Modelle zur Untersuchung des Einflusses von Poreneffekten auf das Trocknungsverhalten kapillarporöser Medien

Habilitationsschrift

von Dr. Thomas Metzger
geb. am 2. Mai 1972 in Berlin-Wilmersdorf

zur Verleihung des akademischen Grades

Doktor-Ingenieur habilitatus
(Dr.-Ing. habil.)

genehmigt von der Fakultät für Verfahrens- und Systemtechnik
der Otto-von-Guericke-Universität am 6. November 2012.

Gutachter:

Prof. Dr.-Ing. habil. Evangelos Tsotsas	Otto-von-Guericke-Universität Magdeburg
Prof. Dr.-Ing. Matthias Kind	Karlsruher Institut für Technologie
Prof. Dr.-Ing. habil. Stefan Heinrich	Technische Universität Hamburg-Harburg

Meiner lieben Frau Nicole
und unseren Kindern Amélie, Benjamin und Ann-Sophie

Danksagung

In diese Habilitation mündete ein wesentlicher Teil meiner beruflichen Aktivität am Lehrstuhl für Thermische Verfahrenstechnik der Otto-von-Guericke-Universität. Zugleich setzt die Schrift einen Schlusspunkt unter meine Magdeburger Jahre.

Ich möchte hier den Wegbegleitern dieser Zeit danken, die diese Arbeit erst möglich gemacht haben:

Evangelos Tsotsas, der die äußeren Voraussetzungen geschaffen und meinen Blick in wissenschaftlichen Diskussionen geschärft hat;

Thai Hong Vu, Anton Irawan, Vikranth Kumar Surasani und Abdolreza Kharaghani, die in von mir betreuten Promotionen wichtige Beiträge zu den dargestellten Ergebnissen geleistet haben;

Christoph Kirsch, der das Team als Mathematiker bereichert hat;

Nicole Vorhauer, Yujing Wang und Yu Sun, welche in laufenden Promotionsprojekten die Forschung weiterführen;

einigen weiteren Doktoranden und Studenten, die ich in verwandten Themen betreut oder begleitet habe und die meinen Blick weiteten;

den verborgenen Helfern in technischen, administrativen und ökonomischen Belangen, insbesondere Herrn Kürschner, Frau Degen, Frau Hesse und Frau Lotz.

Zuletzt danke ich ausdrücklich meiner Frau Nicole, die mich in vielen entscheidenden Situationen unterstützt und ermutigt hat, bis hin zu diesem Abschluss.

Magdeburg, im Dezember 2011

Zusammenfassung

In dieser Forschungsarbeit wird die Trocknung poröser Materialen mit Modellen theoretisch untersucht, die entscheidende physikalische Phänomene auf der Porenskala beschreiben. Dadurch wird zum einen ein tieferes Prozessverständnis ermöglicht, zum anderen kann der Einfluss von Struktureigenschaften auf das Trocknungsverhalten direkt untersucht werden. Kapillareffekte stehen dabei im Mittelpunkt aller Betrachtungen, da sie mit klassischen Kontinuumsmodellen oft nur unzureichend beschrieben werden können und zudem in hohem Maße von der Porenstruktur abhängen.

Zunächst wird ein diskretes Kapillarbündelmodell vorgestellt, mit dem der Einfluss von Porengrößenverteilung und Prozessbedingungen auf den Trocknungsverlauf in einfacher Weise berechnet werden kann. In einem zweiten Modell wird die Geometrie des Kapillarbündels benutzt, um ein Kontinuumsmodell zu parametrisieren, das den Wärme- und Stofftransport im trocknenden Material vollständig beschreibt.

Den Schwerpunkt der Arbeit bilden jedoch diskrete Porennetzwerkmodelle, welche die Porenstruktur in zwei oder drei Dimensionen nachbilden, und in denen die Porenflüssigkeit nicht notwendig eine räumlich zusammenhängende Phase ist und Feuchtetransport auch ohne makroskopischen Gradienten möglich ist. Mit einem Basismodell wird die Trocknung für unterschiedliche Porenstrukturen simuliert. So wird die entscheidende Rolle räumlicher Korrelationen der Porengröße im Netzwerk beleuchtet, der Einfluss des Vernetzungsgrads der Poren untersucht und die Trocknung von Kompositmaterialien charakterisiert.

Mit Erweiterungen des Porennetzwerkmodells werden die Bedeutung der Flüssigkeitsreibung sowie des Wärmetransports für das Trocknungsverhalten untersucht. Unterschiedliche Arten der Wärmezufuhr – konvektiv bzw. durch Kontakt – werden simuliert, um das jeweils charakteristische Verhalten zu analysieren. Durch eine Kopplung des Porennetzwerks mit einem Partikelnetzwerk, dessen mechanisches Verhalten mit der Diskrete-Elemente-Methode simuliert wird, werden schließlich Rissbildung und Schrumpfung bei der Trocknung von Aggregaten in diskreter Weise beschrieben.

Im Weiteren werden zwei Ansätze vorgestellt, um den Skalenübergang vom repräsentativen Porennetzwerk zur Produktebene zu gestalten. Zum einen wird ein universelles Feuchteprofil mit einem Skalengesetz in einem empirischen Makromodell kombiniert; zum anderen werden die effektiven Transportparameter eines Kontinuumsmodells mit numerischen Experimenten an teilgesättigten Porennetzwerken bestimmt.

Abschließend werden Trocknungsexperimente mit Silizium-Netzwerken und röntgen-tomographische Messungen mit Glaskugelschüttungen diskutiert, die zur Validierung und Weiterentwicklung der Porennetzwerkmodelle dienen sollen, sowie eine Volume-of-Fluid-Methode, mit der die Trocknung hochporöser Strukturen adäquater simuliert bzw. die Annahmen der Porennetzwerkmodelle auf der Mikroebene geprüft werden können.

Inhaltsverzeichnis

Einleitung

Diese Schrift stellt überblicksartig dar, welche Modelle in den vergangenen Jahren entwickelt wurden, um die konvektive Trocknung kapillarporöser Medien unter Berücksichtigung von Poreneffekten zu beschreiben. Ausgangspunkt dieser Forschungsaktivität war das Bedürfnis, den Trocknungsverlauf unterschiedlicher poröser Materialien nicht nur empirisch beschreiben zu können, sondern die Auswirkungen der Porenstruktur auf das Prozessverhalten besser zu verstehen.
Klassische Modelle beschreiben die Trocknung auf der Makro-Ebene und können eingeteilt werden in rein empirische sowie physikalisch begründete. Die einfachsten empirischen Ansätze beschreiben lediglich die zeitliche Abnahme des Gesamtfeuchtegehalts, z.B. mit Hilfe einer Exponentialfunktion; die Modellparameter werden angepasst an gravimetrische Messdaten und erlauben nur in sehr beschränktem Maße Voraussagen für veränderte Prozessbedingungen oder Produktabmessungen.
Eine Modellklasse mit begrenzter physikalischer Grundlage bilden die Diffusionsmodelle. Diese gehen von der vereinfachenden Annahme aus, dass der Feuchtetransport im Inneren des Produkts durch Diffusion beschrieben werden kann. Eine solche Beschreibung erfasst also die räumliche Feuchteverteilung und ist daher prinzipiell auf unterschiedliche Produktgeometrien anwendbar. Häufig wird auch die Abhängigkeit der Trocknungskinetik von der Prozesstemperatur berücksichtigt, indem der Diffusionskoeffizient als Funktion der Temperatur beschrieben wird, z.B. mittels einer Arrhenius-Gleichung. Eine geeignete Randbedingung der Diffusionsgleichung für den gasseitigen Stoffübergang ermöglicht dann eine gewisse Vorhersage des Trocknungsverhaltens für unterschiedliche Prozessbedingungen. Dabei ist jedoch zu betonen, dass der Diffusionskoeffizient für die meisten praktischen Anwendungen als Anpassungsgröße an Messdaten – auch räumlich aufgelöst – interpretiert werden muss. Denn zumeist sind eine Vielzahl von Phänomenen am Wärme- und Stofftransport beteiligt.
Schließlich gibt es Kontinuumsmodelle mit dem Anspruch einer möglichst vollständigen Beschreibung der Transportvorgänge. Ausgehend von den Phänomenen auf der Porenebene werden gemittelte Transportgleichungen für das teilgesättigte poröse Medium abgeleitet, durch Methoden der Volumenmittelung oder Homogenisierung. Im Resultat erhält man ein Modell mit effektiven Parametern zur Beschreibung von Konvektion (sowohl der Kapillarflüssigkeit als auch der Gasphase), Dampfdiffusion und Wärmeleitung, welches den zeitlichen Verlauf der Verteilungen von Feuchte, Temperatur und Druck im trocknenden Produkt darstellen kann. Die Modellparameter sind dabei von der Mikrostruktur des Materials abhängig und zudem Funktionen des Sättigungszustands und der Temperatur. Zur Parametrisierung eines solchen Modells müssen Transporteigenschaften und Gleichgewichtsdaten des Materials in unabhängigen, teils aufwändigen Experimenten bestimmt werden. Dann aber kann das Modell den Trocknungsprozess umfassend beschreiben, und dies unabhängig von Produktgeometrie und Trocknungsbedingungen. Es ist hier ausdrücklich zu betonen, dass die Ableitung aus mikroskaligen Transportgleichungen für die einzelnen Phasen als Ziel hat, die Struktur der Modellgleichungen und den Satz an relevanten Produktparametern zu bestimmen, jedoch (noch) nicht, diese Parameter tatsächlich zu berechnen. In diesem Sinne sind die Parameter zwar als physikalisch fundierte, aber dennoch als empirisch zu ermittelnde Größen anzusehen.
Für ein tieferes Verständnis der Trocknung ist daher ein weiterer Schritt nötig, nämlich die Beschreibung des Prozesses direkt auf der Porenebene. Nur so kann die Wechselwirkung zwischen Porenstruktur und Trocknungsverhalten untersucht werden; nur so kann erklärt werden, warum unterschiedliche Materialien sehr unterschiedlich trocknen. Im Sinne der Produktentwicklung kann dann insbesondere extrapoliert werden, welche Mikrostruktur eine schnelle und gleichförmige Trocknung begünstigen würde. Wie im Kontinuumsmodell kann auch der Einfluss von Prozessparametern beschrieben werden, zudem wird es aber möglich, die Rolle einzelner Transportphänomene auf der Porenebene zu analysieren.
In dieser Arbeit werden unterschiedliche Modelltypen vorgestellt, die alle zum Ziel haben, wesentliche Charakteristika des Porenraums zu erfassen und diese in der Beschreibung der Trocknung zu berücksichtigen. Allen Modellen ist gemeinsam, dass der Porenraum

abstrahiert wird, um den Diskretisierungsaufwand für die Simulationen zu reduzieren. Im weitesten Sinn handelt es sich bei allen Modellen um Netzwerkmodelle, wobei sich aufgrund der verwendeten Dimensionalität unterschiedliche Komplexitätsebenen ergeben.
Zunächst wird ein Kapillarbündelmodell für den Stofftransport während der Trocknung entwickelt. Hierin wird berücksichtigt, dass der Porenradius eine verteilte Größe ist. Charakteristika, welche die räumliche Vernetzung der Poren untereinander beschreiben, können hingegen nicht dargestellt werden. Ein Kapillarbündel erstreckt sich über die gesamte Tiefe des porösen Körpers und repräsentiert den gesamten Porenraum; das Modell ist dadurch strikt eindimensional (siehe Abbildung 1a). Lokal gesehen ist das Porenvolumen auf Kapillaren mit unterschiedlichem Radius verteilt, die widerstandslos miteinander kommunizieren. Dieses Modell kann bereits wichtige Auswirkungen von Porengrößenverteilung des trocknenden Materials und Prozessbedingungen auf das Trocknungsverhalten beschreiben.

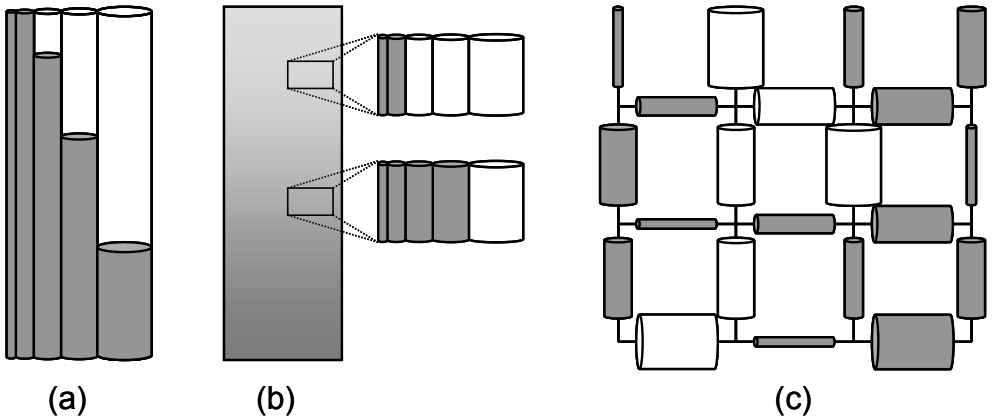

Abbildung 1. Darstellung der unterschiedlichen Modelltypen: (a) Kapillarbündel, (b) Kontinuumsmodell mit Parametern des Kapillarbündels (c) Porennetzwerkmodell. (Die Verdunstung erfolgt jeweils nach oben in überströmende Trocknungsluft; flüssigkeitsbefüllte Poren sind dunkelgrau dargestellt.)

Der zweite Modelltyp verbindet das Kapillarbündel als Abstraktion des Porenraums mit einem etablierten Kontinuumsmodell, das den Wärme- und Stofftransport während der Trocknung physikalisch umfassend beschreibt. Die Kopplung besteht darin, dass alle Parameterfunktionen des Kontinuumsmodells für das Kapillarbündel exakt berechnet werden. In diesem Sinn ist das teilgesättigte Kapillarbündel nur Repräsentant für das feuchte poröse Material innerhalb einer numerischen Volumenzelle des Kontinuumsmodels (siehe Abbildung 1b). Daher ist das Modell auch nicht notwendig eindimensional. Da das Kontinuumsmodell alle relevanten Transportmechanismen erfasst und alle wesentlichen Zustandgrößen liefert, erlaubt dieses hybride Modell eine weitgehende Analyse des Einflusses der Porengrößenverteilung auf den Trocknungsprozess.
Der dritte Modelltyp beschreibt den Porenraum als räumliches Netzwerk einzelner abstrahierter Poren. Die Rechengesetze für die sukzessive Entleerung der Poren können dabei auf zwei- oder dreidimensionale Netzwerke angewendet werden; und diese Netzwerke können von regelmäßiger Struktur, also z.B. quadratisch wie in Abbildung 1c, oder regellos sein. Wesentlicher neuer Aspekt ist, dass Poren unterschiedlicher Größe räumlich verteilt und beliebig miteinander verbunden werden können. Dadurch können wesentliche Charakteristika realer Porenstrukturen abgebildet werden. Und auch die Mechanismen für die Flüssigkeitsverteilung können realistischer beschrieben werden. Während im Kapillarbündel und im Kontinuumsmodel die flüssige Phase stets zusammenhängend bleibt, kann sie sich im Netzwerkmodell in einzelne Cluster aufteilen (siehe Abbildung 1c). Außerdem benötigt die Kapillarströmung nicht – wie in Kontinuumsmodellen – einen makroskopischen Feuchtegradienten, sondern sie wird durch den Druck in den einzelnen Poren bestimmt. In dieser Weise können Netzwerkmodelle bekannte Grenzen der Kontinuumsmodellierung überwinden.

Insbesondere solche Porennetzwerkmodelle werden für grundlegende Untersuchungen des Trocknungsprozesses angewendet und weiterentwickelt. Abbildung 2 gibt einen Überblick über die in dieser Schrift vorgestellte Forschungsarbeit. Als Ausgangspunkt dient eine Modellvariante, welche für die Porenflüssigkeit ideale Kapillarströmung annimmt und diese mit Dampfdiffusion in der Gasphase koppelt. Dieses Modell wird benutzt, um wesentliche Zusammenhänge zwischen Porenstruktur und Trocknungsverhalten aufzuzeigen. Zum einen werden Netzwerke mit monomodaler und bimodaler Porengrößenverteilung mit einander verglichen; dabei wird für bimodale Verteilungen herausgearbeitet, wie sich unterschiedliche räumliche Korrelationen der großen und kleinen Poren auf die Trocknungskinetik auswirken. Zum anderen wird analysiert, welchen Einfluss der Vernetzungsgrad der Poren, ausgedrückt durch die Koordinationszahl, auf das Trocknungsverhalten hat. Neben der Mikrostruktur werden aber auch makroskopische Inhomogenitäten betrachtet: für Kompositmaterialien aus fein- und grobporigen Strukturen wird die Rolle der räumlichen Anordnung dieser beiden Schichten für den Trocknungsprozess untersucht.

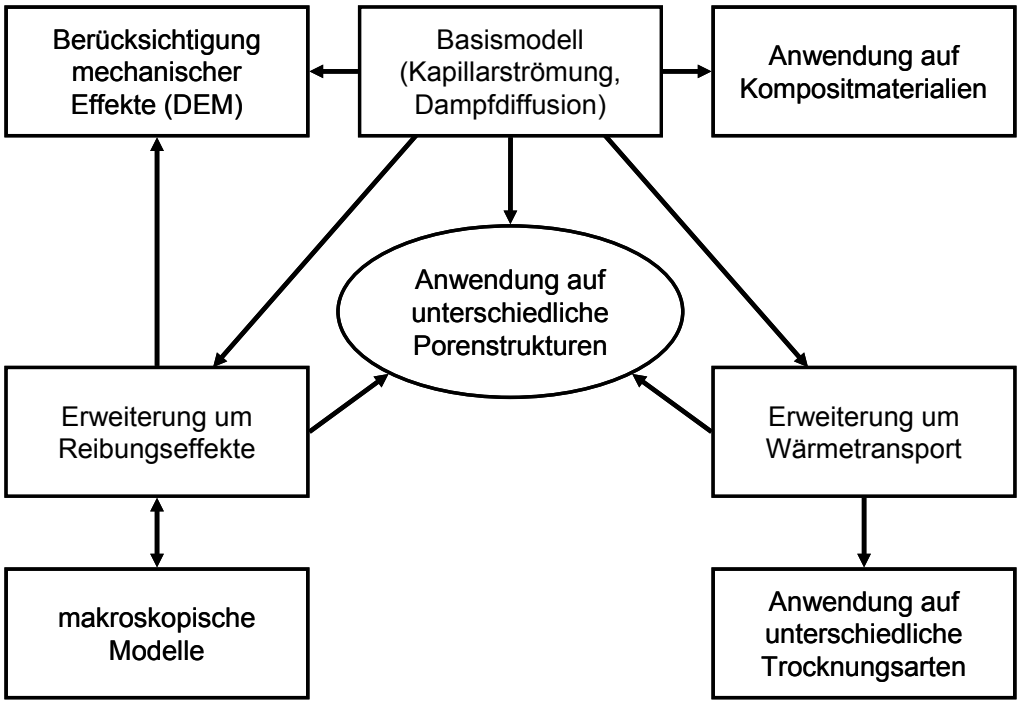

Abbildung 2. Überblick über Forschung mit Porennetzwerken.

Um die Trocknung realistischer beschreiben zu können, wird das Basismodell um bis dahin unberücksichtigte Transportphänomene erweitert. Durch gezieltes Aktivieren einzelner physikalischer Effekte lässt sich deren Rolle bei der Trocknung unterschiedlicher Porenstrukturen in idealer Weise analysieren. Eine erste wesentliche Modellerweiterung betrifft die Reibung beim Flüssigkeitstransport, welche die Reichweite der Kapillarströmung begrenzt. Dieses Modell wird für den einfachen Fall eines Kapillarbündels mit den oben beschriebenen Modelltypen verglichen und so validiert. Durch Simulationen an zwei- bzw. dreidimensionalen Porennetzwerken wird dann gezeigt, wie der Reibungseffekt – je nach Porenstruktur – zu einer Stabilisierung einer sonst unbegrenzten Trocknungsfront führen kann. In einer zweiten Erweiterung des Basismodells wird der Wärmetransport mit einbezogen; neben Temperatureffekten bei Kapillarströmung und Dampfdiffusion wird insbesondere die latente Wärme bei Verdunstung und Kondensation berücksichtigt. Neben der Anwendung auf unterschiedliche Porenstrukturen wird mit dieser Modellvariante auch der Einfluss der Wärmezufuhr bei Konvektions- und Kontakttrocknung untersucht.
Porennetzwerkmodelle eignen sich ideal, um Effekte auf der Porenskala zu untersuchen, können aber wegen des hohen Rechenaufwands nur in ausgewählten Fällen das Verhalten der gesamten porösen Struktur beschreiben, nämlich wenn diese nur eine begrenzte Zahl von Poren enthält. Für die meisten porösen Materialien ist man hingegen auf Modelle mit

gemittelten Größen angewiesen. Um die mit Porennetzwerken gefundenen Erkenntnisse für reale Anwendungen nutzbar zu machen, muss also eine Ankopplung an makroskopische Modelle erfolgen. Der entsprechende Weg wird aufgezeigt für den Fall einer durch Flüssigkeitsreibung stabilisierten Trocknungsfront. Zum einen kann die Tatsache genutzt werden, dass die Ausdehnung der Front mit der dimensionslosen Kapillarzahl skaliert, um ein empirisches Trocknungsmodell zu entwickeln. Zum anderen können für das Kontinuumsmodell, welches die Transportphänomene während der Trocknung durch Gradienten beschreibt, die relevanten Parameter aus geeigneten Netzwerksimulationen bestimmt werden, ganz ähnlich wie mit dem Kapillarbündel.
Neben dem Stoff- und Wärmetransport spielen bei der Trocknung häufig auch mechanische Effekte eine wesentliche Rolle, nämlich die Schrumpfung oder Rissbildung aufgrund der Kapillarkräfte. In der Literatur werden thermo-hydro-mechanische Kontinuumsmodelle zur Beschreibung dieser Effekte vorgeschlagen. Um auch hier den Einfluss der Porenstruktur und der Transportphänomene auf der Porenskala untersuchen zu können, wird das Porennetzwerk an ein Partikelnetzwerk gekoppelt, welches die feste Phase repräsentiert. Dabei ergeben sich aus der Flüssigkeitsverteilung die Kapillarkräfte auf die Partikel, und mittels Diskrete-Elemente-Methode wird deren Wirkung auf die Feststoffbrücken zwischen den Partikeln berechnet. Um den neuen Modellierungsansatz zu etablieren, wird er zunächst für kubische Netzwerke realisiert, und die Trocknung wird als isotherm betrachtet. Mit diesem Basismodell wird untersucht, welchen Einfluss die Gestalt der Trocknungsfront auf die Zahl und Art der Mikrorisse hat.
Die Schrift endet mit einem Ausblick auf aktuelle experimentelle Arbeiten, in denen die unterschiedlichen Porennetzwerkmodelle durch Messungen bewertet und simulierte Effekte real beobachtet werden. Insbesondere die optische Beobachtung zweidimensionaler Mikromodelle während der Trocknung liefert bereits wertvolle Ergebnisse.
Damit ist ein weiter Rahmen gespannt, innerhalb dessen Poreneffekte in Zusammenhang mit der Trocknung kapillarporöser Medien untersucht wurden. Naturgemäß handelt es sich dabei nicht um ein abgeschlossenes Forschungsgebiet. Vielmehr wird neben zahlreichen neuartigen Erkenntnissen auch deutlich, dass einigen der Forschungsansätze noch eine viel versprechende Zukunft bevorsteht.

1 Diskretes Kapillarbündelmodell

In diesem Kapitel soll das einfachste Modell vorgestellt werden, mit dem sich der Einfluss der Porengrößenverteilung auf das Trocknungsverhalten kapillarporöser Medien beschreiben lässt. Bevor jedoch die ihm zugrunde liegende Idee des Kapillarbündels erläutert wird, müssen der Effekt des Kapillardrucks, der daraus resultierende Flüssigkeitstransport sowie der für die Trocknung wesentliche Dampftransport als Grundlage aller in dieser Arbeit vorgestellten Modelle beschrieben werden.

1.1 Stofftransportphänomene

Ist ein poröses Material – oder auch eine einfache zylindrische Kapillare – mit Flüssigkeit gefüllt, so unterscheidet sich der Flüssigkeitsdruck vom Druck der umgebenden Gasphase. Die meisten zu trocknenden Feststoffe sind hydrophil, d.h. die Flüssigkeit benetzt die Porenwände. Dann ist die Flüssig-Gas-Grenzfläche derart gekrümmt (Abbildung 3a), dass der Flüssigkeitsdruck P_w gegenüber dem Gasdruck P_g um den *Kapillardruck* P_c abgesenkt ist. Dieser Druckunterschied hängt ab von der Grenzflächenspannung zwischen Flüssigkeit und Gas σ sowie vom Krümmungsradius r_c, der seinerseits durch Porenradius r und Kontaktwinkel $\theta < 90°$ bestimmt wird (Abbildung 3b):

$$P_w = P_g - P_c = P_g - \frac{2\sigma}{r_c} = P_g - \frac{2\sigma\cos\theta}{r} \tag{1}$$

Diese Beziehung bedeutet insbesondere, dass der Flüssigkeitsdruck in unterschiedlich großen Poren verschieden ist. Ist eine große Pore, oder Kapillare, mit einer kleinen verbunden (Abbildung 3c), so wird Flüssigkeit aufgrund des Druckunterschieds von der großen in die kleine Pore strömen. Erst wenn sich an der gesamten Flüssig-Gas-Grenzfläche eine einheitliche Krümmung einstellen kann, versiegt diese *Kapillarströmung*. Nun strebt ein Meniskus in einer Pore aber stets den vom Kontaktwinkel bestimmten Krümmungsradius an; und nur an singulären Punkten – also an Kanten, wie sie am Ende einer Pore bzw. Kapillare auftreten – kann die Kontaktwinkelbedingung für einen Bereich von Krümmungsradien $r_c > r$ erfüllt werden. Im Beispiel von zwei miteinander verbundenen Kapillaren befüllt sich die kleinere also komplett (Abbildung 3d). In diesem Gleichgewichtszustand ist der Flüssigkeitsdruck dann durch den Kapillardruck der großen Pore bestimmt. Wird nun durch Trocknung die Flüssigkeitsmenge verringert, so bleibt der Meniskus am Ende der kleineren Kapillare stationär und es entleert sich (zunächst) nur die große Kapillare.

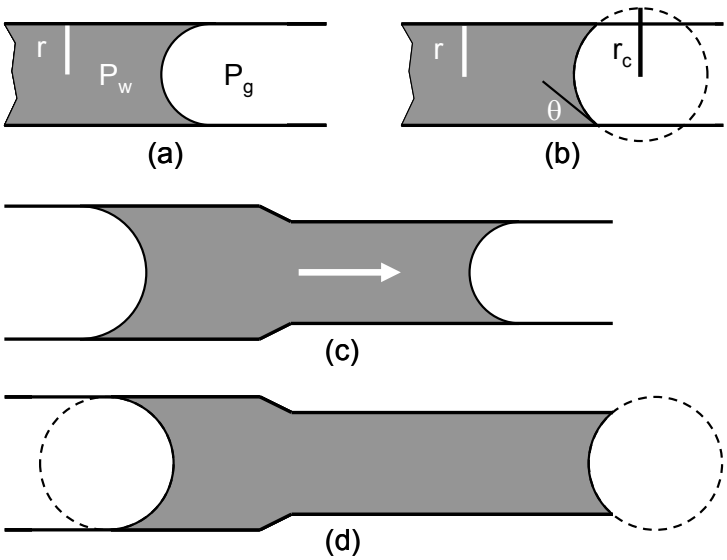

Abbildung 3. Darstellung des Kapillareffekts (siehe Text).

Für vernachlässigbare Reibung lassen sich folgende zwei Regeln zur Kapillarität formulieren, die im Weiteren häufige Anwendung finden werden:

1. Ist ein räumlich zusammenhängendes Flüssigkeitsgebiet auf mehrere Poren verteilt, so bestimmt der Meniskus in der größten Pore den Flüssigkeitsdruck.
2. Wird diesem Gebiet durch Trocknung Flüssigkeit entzogen, so entleert sich jeweils nur die größte Pore, und die Menisken in den anderen Poren bleiben stationär.

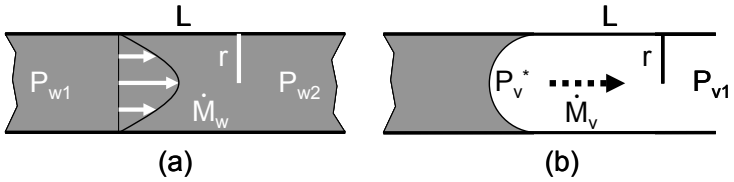

Abbildung 4. Stofftransport in Kapillaren.

Nachdem der Kapillardruck als Triebkraft für den Flüssigkeitstransport in trocknenden Porensystemen ausgewiesen ist, müssen noch kinetische Aspekte diskutiert werden. Aufgrund der üblichen kleinen Porenradien und geringen Geschwindigkeiten ist die Kapillarströmung laminar. Für den Fall einer zylindrischen Pore mit vorgegebenem Druckunterschied bzw. -gradienten berechnen sich Massenstrom bzw. mittlere Strömungsgeschwindigkeit dann gemäß dem Gesetz von Hagen-Poiseuille (Abbildung 4a):

$$\dot{M}_w = \frac{\pi r^4}{8\nu_w}\frac{P_{w1}-P_{w2}}{L} \tag{2a}$$

$$v_w = \frac{\dot{M}_w}{\pi r^2 \rho_w} = \frac{r^2}{8\eta_w}\frac{P_{w1}-P_{w2}}{L} = -\frac{K}{\eta_w}\nabla P_w \tag{2b}$$

wobei L die geometrische Distanz misst, ν_w und η_w kinematische bzw. dynamische Viskosität und ρ_w die Dichte der Flüssigkeit bezeichnen. Gleichung (2b) stellt zugleich das Gesetz von Darcy dar für die Durchströmung poröser Materialien, mit der (intrinsischen) Permeabilität K. Mit abnehmendem Porenradius und abnehmendem Größenunterschied zwischen den Poren (als Ursache des Druckunterschieds) sowie zunehmender Distanz wird die Kapillarströmung also verstärkt durch Reibung behindert.

Ursache für die Konvektionstrocknung ist die Dampfdiffusion in den Luftstrom aufgrund eines Dampfdruckunterschieds. An der Flüssig-Gas-Grenze wird hierzu lokales Gleichgewicht angenommen, also Sattdampfdruck P_v^* (Abbildung 4b). Entsprechend der Diffusionslänge und dem Querschnitt berechnet sich der Diffusionsstrom zu:

$$\dot{M}_v = \delta\frac{\pi r^2}{L}\frac{\tilde{M}_v P_g}{\tilde{R}T}\ln\frac{P_g-P_{v1}}{P_g-P_v^*} \approx \pi r^2\frac{\delta\tilde{M}_v}{\tilde{R}T}\frac{P_v^*-P_{v1}}{L} \tag{3}$$

mit binärem Diffusionskoeffizient δ, Molmasse des Dampfs $\tilde{M}_v$, idealer Gaskonstante $\tilde{R}$ und absoluter Temperatur T (in K). Aufgrund der Luftundurchlässigkeit der Flüssigkeitsoberfläche ist die Diffusion von einem konvektiven Stefanstrom überlagert, und die (beschleunigte) Verdunstung wird durch den logarithmischen Ausdruck beschrieben (S. 179f in [36]), der für moderate Trocknungsbedingungen, d.h. für niedriges Dampfdruckniveau bzw. kleinen Dampfdruckunterschied, auch linear approximiert werden kann.

In den vorgestellten Trocknungsmodellen werden die Poren als groß genug angenommen, so dass der Knudseneffekt, wie er durch Einengung der Gasmoleküle hervorgerufen wird, ohne großen Fehler vernachlässigt werden kann. Entsprechendes gilt für den Kelvineffekt, welcher die Absenkung des Sattdampfdrucks an der gekrümmten Flüssig-Gas-Grenzfläche beschreibt. In den diskreten Modellen – Kapillarbündel und Netzwerk – wird auch die Flüssigkeitsadsorption an den Porenwänden nicht im Modell berücksichtigt, sondern alle Flüssigkeit wird als frei bzw. ungebunden betrachtet.

Im Folgenden wird die Flüssigkeit stets Wasser sein, wie in den meisten realen Trocknungssituationen; die Modelle sind jedoch auf andere Flüssigkeiten übertragbar – gegebenenfalls mit anderen Transportgesetzen, z.B. für nicht-Newtonsche Flüssigkeiten.

1.2 Trocknungsmodell

Die wesentlichen Stofftransportvorgänge bei der konvektiven Trocknung kapillarporöser Medien lassen sich gut an einem Modellsystem aus *zwei Kapillaren* erläutern, wie dies bereits Krischer getan hat (S. 293f in [36]). Abbildung 5 zeigt die beiden parallel angeordneten Kapillaren während der Trocknung. Sie können über ihre gesamte Länge widerstandslos Wasser austauschen und sind zur linken Seite hin offen. (Die horizontale Anordnung ist bewusst gewählt, da Gravitationseffekte nicht diskutiert werden sollen.)

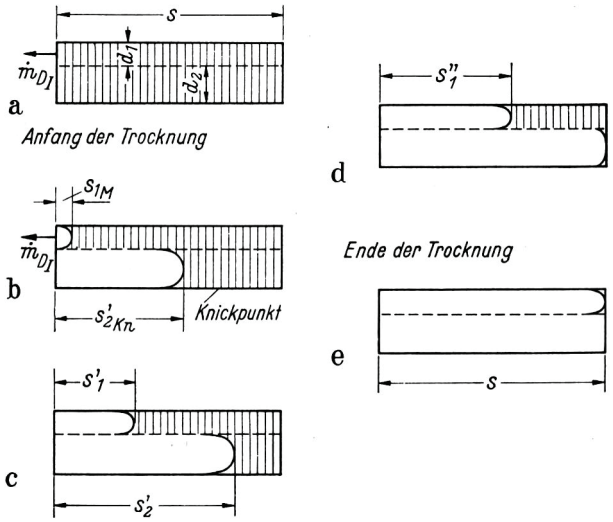

Abbildung 5. Zwei-Kapillaren-Modell der Trocknung von Krischer (S. 293 in [36]).

Zu Beginn des Gedankenexperiments sind die beiden Kapillaren vollständig befüllt (Abbildung 5a), und die Porenflüssigkeit trocknet mit derselben Rate wie eine freie Flüssigkeitsoberfläche. Die Wasserdampfstromdichte hängt also nur ab vom thermodynamischen Zustand der Trocknungsluft, also von Druck, Temperatur und Feuchte (ausgedrückt als Dampfdruck $P_{v\infty}$), sowie von den Strömungsverhältnissen, die den Stoffübergangskoeffizienten β festlegen:

$$\dot{m}_{v,l} = \beta \frac{\tilde{M}_v P_g}{\tilde{R} T} \ln \frac{P_g - P_{v\infty}}{P_g - P_v^*} \tag{4}$$

Wie allgemein bekannt, wird der gasseitige Stoffübergang durch dimensionslose Kennzahlen beschrieben, in welche neben der Luftgeschwindigkeit insbesondere Größe und geometrische Gestalt des trocknenden Objekts eingehen.
Der Sattdampfdruck P_v^* in Gleichung (4) ist eigentlich für die Temperatur der Porenflüssigkeit zu berechnen, die aufgrund der Verdunstungskühlung niedriger ist als die Lufttemperatur. In der Trocknungstechnik ist dies die Gutsbeharrungstemperatur. Vereinfachend nehmen wir hier isotherme Bedingungen an, wie sie für schonende Trocknung (geringes Temperaturniveau bzw. geringe Dampfdruckunterschiede) näherungsweise erfüllt sind.
Mit fortschreitender Trocknung verliert das Modellsystem Flüssigkeit. Den Kapillardruckverhältnissen entsprechend entleert sich dabei zunächst die große Kapillare, und Kapillarströmung hält die kleine Kapillare gefüllt (Abbildung 5b). Im eindimensionalen Modell bleibt der entleerte Abschnitt der großen Kapillare auf Sattdampfniveau, denn er steht mit der kleinen Kapillare im Gleichgewicht. Somit ändert sich an den Verdunstungsbedingungen nichts, und die Trocknungsrate bleibt konstant (hoch).

Die Kapillarströmung ist jedoch nicht reibungsfrei und der benötigte Druckunterschied nimmt nach Gleichung (2a) mit zunehmender Distanz zwischen den Menisken zu. Je nach Trocknungsrate und Größenverhältnissen im Modellsystem reicht der Kapillardruck-unterschied zwischen den Flüssigkeitsmenisken an einem bestimmten Punkt nicht mehr aus, um die kleine Kapillare gefüllt zu halten. Dann weicht die Flüssig-Gas-Grenze von der Oberfläche zurück. (Ist die Reibung vernachlässigbar, so kann sich die große Kapillare vollständig entleeren, bevor dies geschieht.) Als Folge des zusätzlichen Transport-widerstands für die Dampfdiffusion sinkt die Trocknungsrate ab

$$\dot{m}_v = \left(\frac{1}{\beta} + \frac{s_1}{\delta}\right)^{-1} \frac{\tilde{M}_v P_g}{\tilde{R}T} \ln \frac{P_g - P_{v\infty}}{P_g - P_v^*} \tag{5}$$

wobei s_1 die Position des Meniskus in der kleinen Kapillare beschreibt. Diese Gleichung hat auch allgemein Gültigkeit, d.h. für komplexere Porenstrukturen und bei Berücksichtigung der festen Phase: dann ist s_1 durch den Abstand der Verdunstungsfront von der Oberfläche und δ durch einen effektiven Diffusionskoeffizienten für die poröse Struktur zu ersetzen.
Der beschriebene Moment markiert das Ende des 1. Trocknungsabschnitts, in welchem die Trocknung bei konstanter Rate $\dot{m}_{v,I}$ erfolgte. Der 2. Trocknungsabschnitt ist von einer (beständig) abnehmenden Trocknungsrate geprägt. In unserem Modellsystem bewegt sich aber natürlich nicht nur der kleine Meniskus, der für die Trocknungsrate zuständig ist. Schließlich wurde die Kapillarströmung ja nicht ausgeschaltet, sondern hatte nur ihre Grenze erreicht. Der große Meniskus wandert also weiter (Abbildung 5c), und dies sogar schneller als der kleine, denn bei absinkender Trocknungsrate nimmt die maximale Distanz für Kapillarströmung zu, so dass sich der Abstand der Menisken vergrößern kann.
Ist die große Kapillare vollständig entleert (Abbildung 5d), so gibt es keinen Druckunterschied mehr, und damit auch keine Kapillarströmung. Die verbleibende Flüssigkeit verdunstet unbewegt mit allmählich zurückweichender Flüssig-Gas-Grenze entsprechend Gleichung (5). Da Flüssigkeitsadsorption an den Porenwänden nicht modelliert wurde, endet die Trocknung mit einer endlichen – wenn auch meist sehr niedrigen – Rate (Abbildung 5e). Im Modell werden Kelvin-Effekt (Absenkung des Sattdampfdrucks in kleinen Poren) und Knudsen-Effekt (verändertes Diffusionsverhalten von Gasen in kleinen Poren) vernachlässigt, wie dies für alle vorgestellten Simulationen näherungsweise erlaubt ist.

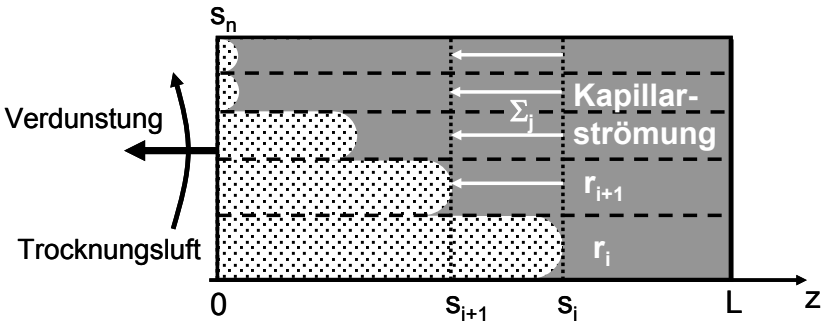

Abbildung 6. Kapillarbündel-Modell der Trocknung.

Das soeben besprochene Modellsystem wird nun erweitert auf ein ganzes *Kapillarbündel* [A], um für eine vorgegebene Porenradienverteilung Trocknungsverläufe berechnen zu können. Wie in Abbildung 6 dargestellt, bewegen sich die Menisken in den einzelnen Kapillaren nacheinander von der Oberfläche weg. Der Meniskus in der größten Kapillare beginnt, und der Meniskus in der nächstkleineren Kapillare muss jeweils dann folgen, wenn der Druckverlust der Flüssigkeitsströmung

$$\Delta P_{w,i} = \frac{8\dot{m}_v \nu_w \sum_{\text{alle}} \pi r_j^2}{\sum_{\text{gefüllte}} \pi r_j^4} \left(s_i - s_{i+1}\right) \tag{6}$$

auf den entsprechenden Kapillardruckunterschied angestiegen ist

$$\Delta P_{c,i} = 2\sigma\left(\frac{1}{r_{i+1}} - \frac{1}{r_i}\right) \tag{7}$$

Die Summen in Gleichung (6) stellen die für die Verdunstung relevante Gesamtquerschnittsfläche des Kapillarbündels bzw. die Strömungseigenschaften des teilweise gefüllten Bündels dar.
Auf diese Weise bildet sich ein Sättigungsprofil aus, das allmählich in die Tiefe wandert. Je nach Parameterwahl werden einige Kapillaren bereits vollständig entleert, noch bevor der letzte Meniskus sich von der Oberfläche lösen musste. Sobald dies jedoch geschieht, beginnt der 2. Trocknungsabschnitt, und die Verdunstungsrate muss der aktuellen Position dieses letzten (kleinsten) Meniskus angepasst werden. Entsprechend Gleichung (6) wird sich das Sättigungsprofil mit abnehmender Trocknungsrate aufweiten.

Das Modell ist insofern elegant, als sich das für den 1. Trocknungsabschnitt universelle Profil einfach aus den diskreten Kapillarradien berechnen lässt und somit jedes beliebige Sättigungsprofil und auch die Dauer des 1. Abschnitts zugänglich sind. Erst im 2. Abschnitt muss eine zusätzliche Diskretisierung (im Wesentlichen der Zeit) erfolgen, dabei sind jedoch keine Stabilitätsbedingungen an die Schrittweite zu beachten. Jede solche Berechnung ergibt direkt ein Sättigungsprofil sowie einen Punkt auf der Trocknungskurve $\dot{m}_v(S)$, wobei S die Gesamtsättigung des Kapillarbündels ist.
Die einzige Eingangsinformation für das Kapillarbündelmodell ist die Porengrößenverteilung. Dabei wird die kontinuierliche Verteilung durch eine Zahl von Kapillarklassen mit Radien r_i dargestellt, denen entsprechend der jeweiligen Klassenbreite Δr_i und dem dazugehörigen Porenvolumen ΔV_i eine Zahl von Kapillaren N_i (nicht notwendig ganzzahlig) angehören; die Summen in Gleichung (6) werden dazu verallgemeinert [A]. Die Verteilung kann dabei experimentell bestimmt oder theoretisch vorgegeben werden. Untersuchungen zum Einfluss der Porengrößenverteilung auf die Trocknung werden in 1.3 vorgestellt.

Zunächst soll jedoch noch auf zwei wesentliche Beschränkungen des Modells eingegangen werden: zum einen die Annahme eines idealen lateralen Stofftransports, insbesondere in der gasseitigen Grenzschicht, zum anderen die starke geometrische Abstraktion des Porenraums, die zugleich die räumliche Kontinuität der Porenflüssigkeit postuliert.

Bisher wurde vorausgesetzt, dass der flüssigkeitsbenetzte Oberflächenanteil beliebig klein werden kann – im Grenzfall besteht er nur noch aus einem Meniskus – ohne dass die Verdunstungsrate geringer werden müsste als jene einer freien Flüssigkeitsoberfläche. Dies kann nur durch idealen lateralen Dampftransport in der Grenzschicht gewährleistet werden, und es soll im Folgenden abgeschätzt werden, ob dies eine sinnvolle Annahme ist. In der Literatur haben sich Suzuki und Maeda [86] und Schlünder [71,72] mit der Oberflächenverdunstung von diskreten Quellen befasst. Beide Untersuchungen haben ergeben, dass die Verdunstungsrate auch bei sehr geringem Bedeckungsgrad noch hoch bleiben kann, wenn die Quellen fein verteilt sind, d.h. wenn es viele von kleiner Größe sind und ihr Abstand gering ist im Vergleich zur Grenzschichtdicke.
Schlünder wählt für die Absenkung der Verdunstungsrate eine für unsere Zwecke geeignete Darstellung mit (mittlerem) Porenradius. Das Kapillarbündel wird zunächst um eine feste Phase erweitert, so dass der Anteil der Poren an der Oberfläche auf einen realistischen Wert absinkt, dann wird die Trocknungsrate des 1. Abschnitts, Gleichung (4), mit Schlünders Modell entsprechend dem Bedeckungsgrad korrigiert. Abbildung 7 zeigt ein Simulationsergebnis für ein Kapillarbündel mit Porosität ψ = 0.5 und normalverteiltem Porenradius (Mittelwert r_0). Die Beschränkung gegenüber dem idealen Fall wird für übliche Stoffübergangsverhältnisse erst bei Porengrößen $r_0 \geq 10$ µm wesentlich und kann deshalb für viele poröse Materialien vernachlässigt werden – zumal jeweils die kleinsten Poren am längsten mit Flüssigkeit befüllt bleiben.

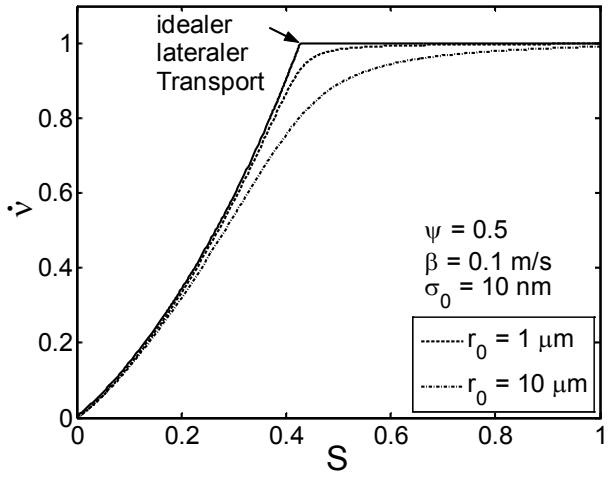

Abbildung 7. Einfluss des Transports in der Grenzschicht auf Trocknungskurve des Kapillarbündels (r_0 ist Mittelwert, σ_0 Standardabweichung der Porenradienverteilung) [B].

In der Literatur ist die Absenkung der Trocknungsrate im 1. Abschnitt für Schüttungen aus großen Partikeln dokumentiert [13,44,81]. Besonders nennenswert ist die Charakterisierung der Wasserverteilung in einer Sandschüttung mittels Neutronenabsorption [81], mit der die Rolle der teilgesättigten Oberfläche für das allmähliche Absinken der Verdunstungsrate eindrucksvoll belegt werden kann.

Obwohl sich das Kapillarbündel geometrisch und topologisch stark von realen Porenstrukturen unterscheidet, ist es traditionell ein abstraktes Modell zur Beschreibung des Fluidtransports in porösen Medien. Eine wesentliche Eigenschaft des Kapillarbündels ist die Kontinuität der Porenflüssigkeit (und der Gasphase). Dies scheint eine schwer zu rechtfertigende Tatsache zu sein, wenn man sich Flüssigkeitsverteilungen in trocknenden dreidimensionalen Strukturen vorstellt, wie sie ab Kapitel 3 mit Porennetzwerkmodellen simuliert werden. Jedoch ist in vielen realen Strukturen die flüssige Phase tatsächlich bis hinunter zu kleinen Sättigungen kontinuierlich; das beste Beispiel hierfür sind Partikelschüttungen und – allgemeiner – auch feste Strukturen aus Primärpartikeln. Moderne Verfahren der Bildgebung und Bildanalyse können dies eindrucksvoll belegen. Insbesondere die Röngtenmikrotomographie konnte in jüngster Zeit die Flüssigkeitstopologie auf der Porenebene analysieren, sowohl in Trocknungsexperimenten mit Sand [44,83] als auch in mechanischen Untersuchungen teilgesättigter Glaskugelschüttungen [70]. Die hydraulische Kontinuität wird dabei durch dicke Flüssigkeitsfilme an Porenverengungen und Kontaktstellen zwischen den Partikeln gewährleistet. Der Übergang von einem kontinuierlichen Flüssigkeitsnetzwerk zu einzelnen Flüssigkeitsbrücken erfolgt je nach Partikelsystem bei Sättigungen von unter 0.1 (Sand in [44]) bis 0.2 (Glaskugelschüttung in [70]).

In diesem Zusammenhang muss die Porengrößenverteilung in verallgemeinertem Sinn verstanden werden. Bereits Krischer (S. 309f in [36]) hat die Analogie zwischen einer Partikelschüttung und zwei, im Winkel zueinander angeordneten Platten etabliert. Wie in Abbildung 8 skizziert, kann ein Porenwinkel – anders als eine idealisierte zylindrische oder kugelförmige Pore – zu einem ganzen Bereich von Porenradien Volumen beitragen. Ganz ähnlich können Tomogramme von Partikelschüttungen zur Bestimmung der Porengrößenverteilung genutzt werden [43]. Insbesondere hängt der Kapillardruck dann vom Sättigungsgrad der Pore bzw. des Porenwinkels ab. (Derselbe Effekt kommt bekanntermaßen bei der Quecksilber-Porosimetrie zum Tragen.) Somit bewirken Sättigungsunterschiede im Plattenwinkel bzw. in den Porenverengungen einer Partikelschüttung eine Kapillarströmung, ganz ähnlich wie beim abstrakten Kapillarbündel. Diese Analogie hat natürlich auch ihre Grenzen, z.B. bei der Berechnung der Permeabilität. Die Rolle von Rauhigkeiten oder Winkeln in den Poren wird auch von Dullien (S. 341 in [23]) betont; er spricht bildhaft von einem zusammenhängenden Netzwerk aus „surface capillaries“.

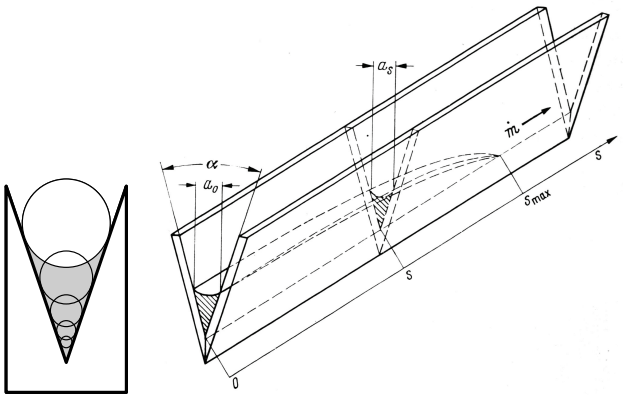

Abbildung 8. Zur Analogie von Plattenwinkel und Kapillarbündel (S. 310 in [36]).

Was die Trocknung einer Partikelschüttung anbelangt, so hat das Kapillarbündelmodell im Bereich der hydraulischen Kontinuität durchaus seine Berechtigung. Mikroskopisch gesehen ist die Entleerung insbesondere der großen Partikelzwischenräume jedoch ein diskreter Prozess, wie er besser mit Netzwerkmodellen beschrieben werden kann. In der Literatur wurde mit geeigneten Vereinfachungen versucht, beiden Aspekten Rechnung zu tragen, indem Porennetzwerkmodelle um Filmeffekte erweitert wurden [63,100].

1.3 Einfluss der Porengrößenverteilung

Mit dem Kapillarbündelmodell kann nun untersucht werden, welchen Einfluss die Porengrößenverteilung auf das Trocknungsverhalten eines porösen Körpers hat, wobei die Simulation Sättigungsprofile und Trocknungskurven liefert. In Abbildung 9 sind einige Ergebnisse für Materialien mit normalverteiltem Porenvolumen (approximiert durch 50 Kapillarklassen) dargestellt, wobei mittlerer Porenradius r_0 und Standardabweichung σ_0 über weite Bereiche variiert wurden. Die Proben haben jeweils eine Dicke von L = 0.1 m und werden einseitig mit trockener Luft bei Umgebungstemperatur getrocknet (mit Stoffübergangskoeffizient β = 0.1 m/s). Die Trocknungsrate wird auf die anfängliche Rate normiert und ist mit $\dot{\nu}$ bezeichnet.

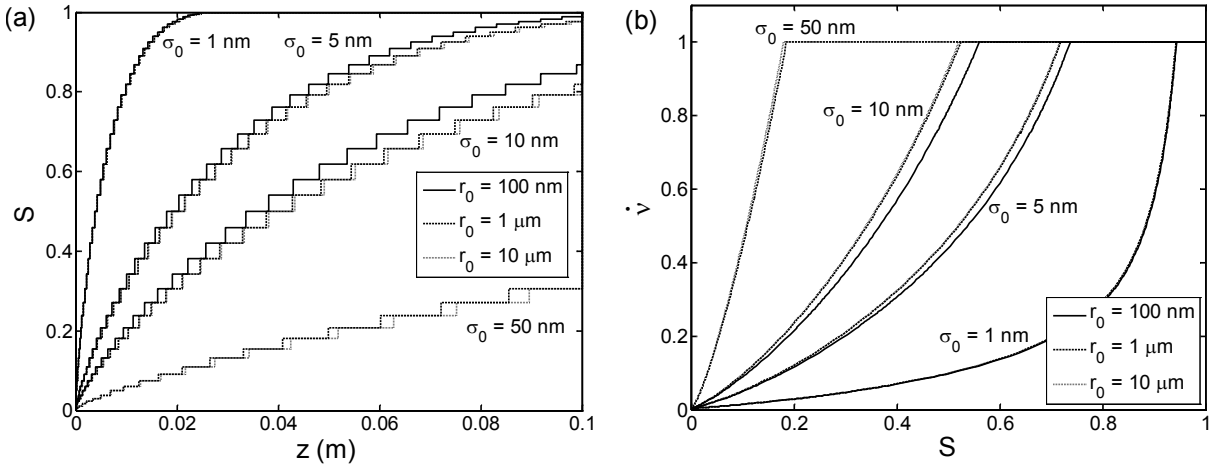

Abbildung 9. (a) Sättigungsprofile am Ende des 1. Trocknungsabschnitts und (b) Trocknungskurven für Kapillarbündel mit normalverteiltem Porenvolumen [A].

Man erkennt, dass die mittlere Porengröße auf das Trocknungsverhalten nur einen geringen Einfluss hat. Dies gilt für Verteilungen mit $\sigma_0 << r_0$ und lässt sich theoretisch begründen [A]. Die Verteilungsbreite hingegen entscheidet maßgeblich, wie viel Wasser im 1. Trocknungsabschnitt entfernt werden kann. Je breiter die Porengröße verteilt ist, desto stärker wird der

treibende Kapillardruckunterschied; dann spielt die Reibung eine untergeordnete Rolle und das Sättigungsprofil bleibt flach – im Grenzfall entleert sich eine Kapillare nach der anderen vollständig. Entsprechend dauert der 1. Abschnitt bis zu niedriger Gesamtsättigung an. Für eng verteilte Porengröße ist die Kapillarströmung stark durch Reibung gehemmt, der Gradient in der Sättigung ist ausgeprägt und die Trocknungsfront weicht früh zurück.
Für enge monomodale Verteilungen lässt sich die Trocknung im 1. Abschnitt gut durch die Kapillarzahl

$$\mathrm{Ca} = \frac{\beta \eta_w L}{1000 \psi \sigma \sigma_0 \cos\theta} \tag{8}$$

charakterisieren [B,F], welche die Reibungseffekte bei vorgegebenen Trocknungsbedingungen zu den Kapillareffekten in Beziehung setzt und alle relevanten Einflüsse beinhaltet. Als Prozessgröße fließt der Stoffübergangskoeffizient β ein (ansonsten wird ein trockener Luftstrom bei Umgebungstemperatur angenommen), und als Stoffeigenschaften die Viskosität η_w und die Grenzflächenspannung σ der Porenflüssigkeit. Außerdem sind Feststoffeigenschaften entscheidend: neben Porosität ψ und Produkttiefe L (gegebenenfalls bis zur Symmetrieebene) beeinflussen die Breite der Porengrößenverteilung σ_0 sowie der Kontaktwinkel θ die Kapillarzahl. (Der Zahlenfaktor approximiert das Dichteverhältnis beim Phasenübergang „flüssig-gasförmig“.)

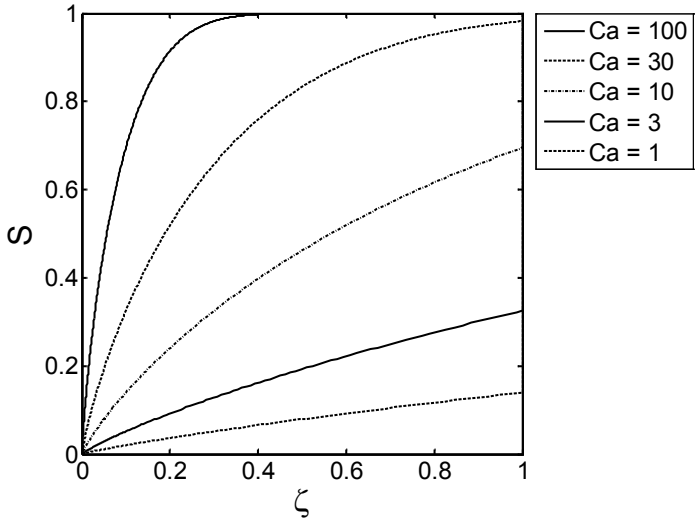

Abbildung 10. Dimensionslose Sättigungsprofile am Ende des 1. Trocknungsabschnitts für Kapillarbündel mit normalverteiltem Porenvolumen (bei Umgebungsbedingungen) [B].

In Abbildung 10 sind für unterschiedliche Kapillarzahlen Ca die Sättigungsprofile über der dimensionslosen Produkttiefe ζ = z/L aufgetragen. Für großes Ca dominiert die Reibung, und der Feuchtegradient ist stark ausgeprägt. Für kleines Ca dominiert der Kapillareffekt, und die Trocknung des Produkts verläuft homogen und mit langem 1. Abschnitt. Dies wird erreicht für (1) moderate Trocknungsraten, (2) kleine Produktabmessungen, (3) hohe Porosität, (4) eine breit verteilte Porengröße sowie (5) gute Benetzbarkeit des Feststoffs.

In neueren Arbeiten auf dem Gebiet der Hydrologie findet das Kapillarenmodell in adaptierter Form Anwendung: Lehmann et al. [44] benutzen zwei Kapillaren in vertikaler Anordnung, um die Porengrößenverteilung in einfacher Weise zu repräsentieren und Reibungs- bzw. Gravitationseffekte mit dem Kapillareffekt in Beziehung zu setzen. Die Autoren leiten die maximale Eindringtiefe der Trocknungsfront im 1. Trocknungsabschnitt in Abhängigkeit von Kapillar- und Bondzahl her. (Gemäß der Definition der Autoren dauert der 1. Abschnitt solange, wie die Oberfläche teilgesättigt ist.) Aufgrund der Porengröße und der vertikalen Abmessungen ist in der Geologie häufig die Gravitation der entscheidende, die Kapillarströmung limitierende Effekt. Lehmann et al. wenden die Theorie auch auf kontinuierliche Porenradienverteilungen an, benutzen jedoch die Kapillardruckkurve, die in

der Sprache der Hydrologie das Wasserrückhaltevermögen als Funktion der Druckhöhe („head“) darstellt. Reibungsverluste werden durch eine makroskopische Permeabilität beschrieben, ganz im Sinne des Kontinuumsmodells, welches im nächsten Kapitel vorgestellt werden wird. Trocknungsexperimente mit Sandschüttungen dienen den Autoren zur Validierung des Modells; darin wird der teilweise mit Flüssigkeit gesättigte Bereich optisch (teils mit Einfärbung) vermessen. Die untersuchten Trocknungsfronten sind in diesen Versuchen nur durch Gravitation stabilisiert. Auch diese Literaturarbeit betont die Bedeutung von Radienkontrast bzw. Breite der Porenradienverteilung, wobei es – für den Fall vernachlässigbarer Reibung – letztlich nur auf den verfügbaren Kapillardruckunterschied ankommt. Die tatsächliche Porengröße bzw. ihre Verteilungsbreite spielt nur für reibungslimitierte Kapillarströmung eine Rolle.

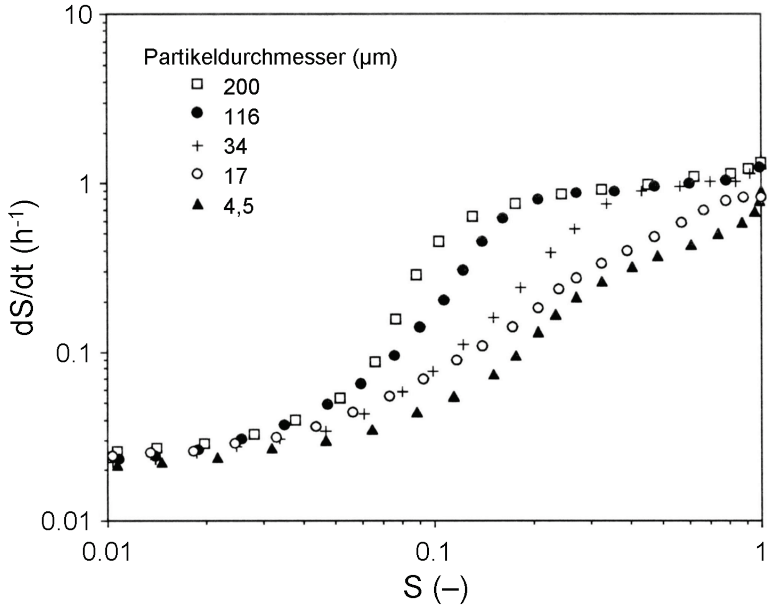

Abbildung 11. Trocknungsversuche mit Glaskugelschüttungen (1,5 cm Höhe) und Ethanol, mit starker Luftströmung bei 23°C (aus [13]).

Coussot [13] berichtet über Trocknungsexperimente mit Glaskugelschüttungen und Ethanol; dabei variiert er die Partikelgröße (4.5 bis 200 µm) und die Geschwindigkeit der Trocknungsluft. Wie in Abbildung 11 zu erkennen, ist der 1. Trocknungsabschnitt durch eine leicht sinkende Verdunstungsrate gekennzeichnet – entsprechend der oben diskutierten Begrenzung des lateralen Dampftransports in der Grenzschicht – und dauert für große Partikel bis zu Sättigungen von nur 0.1 an; für kleinere Partikel verkürzt er sich aufgrund der Reibungseffekte. Dies entspricht den Ergebnissen aus dem Kapillarbündelmodell.
In seinen theoretischen Betrachtungen führt Coussot eine kritische Geschwindigkeit für die Porenflüssigkeit ein, die durch das maximale Kapillardruckpotential und die Flüssig-permeabilität bestimmt ist. Da letztere sättigungsabhängig ist, nimmt die kritische Geschwindigkeit im Laufe der Trocknung ab. Solange sie größer ist als die Trocknungsrate des 1. Abschnitts, verweilt die Verdunstungsfront an der Oberfläche der Schüttung. Dann, zu Beginn des 2. Abschnitts, weicht diese Front stets gerade soweit zurück, dass die reduzierte Verdunstungsrate der kritischen Geschwindigkeit entspricht. Typischerweise genügen geringe Distanzen, d.h. wenige Porendurchmesser, um den Widerstand für die Dampfdiffusion ausreichend zu erhöhen (siehe auch [A]). Erst wenn die Flüssigpermeabilität sehr klein geworden ist, wandert die Verdunstungsfront durch die gesamte Probe. In seiner Analyse bleibt Coussot auf der Kontinuumsebene; daher erreicht er noch nicht die Möglichkeiten des Kapillarbündelmodells, kann aber die grundsätzlichen Phänomene korrekt beschreiben.

In den Simulationen dieser Arbeit wird meist ideale Benetzung angenommen, also $\theta = 0°$. Aus der Definition der Kapillarzahl in Gleichung (8) und Abbildung 10 erkennt man aber den wichtigsten Einfluss des Kontaktwinkels auf das Trocknungsverhalten. Eine Vergrößerung des Kontaktwinkels bewirkt gemäß Gleichung (1) und Abbildung 3 eine Hochskalierung aller Krümmungsradien. Dadurch wird insbesondere die Radienverteilung der Flüssig-Gas-Grenzflächen *breiter*, und – entsprechend den obigen Erfahrungen zum Einfluss der Porenradienverteilung – ist man geneigt, eine Verbesserung der Kapillarströmung zu erwarten. Es geschieht jedoch das Gegenteil: der Kapillareffekt wird geschwächt. Grund ist die Entkopplung der Krümmungsradien von den Porenradien: während erstere sich vergrößern und damit die Kapillardruckunterschiede verringert werden, bleiben die letzteren unverändert, und mit ihnen die Reibungsverluste. In der Folge nimmt die relative Wirkung des Kapillareffekts ab – ähnlich wie für eine *engere* Porenradienverteilung!

Neuere experimentelle Arbeiten aus der Literatur befassen sich mit dem Einfluss des Kontaktwinkels auf das Trocknungsverhalten. Shahidzadeh-Bonn et al. [77] nutzen Gammaabsorption, um Sättigungsprofile in Schüttungen aus hydrophilen ($\theta \approx 0°$) bzw. hydrophobisierten ($\theta \approx 90°$) Glaskugeln zu messen. Im einen Grenzfall sind die Profile aufgrund des dominierenden Kapillareffekts flach und die Schüttung trocknet homogen, im anderen Grenzfall ist der Kapillareffekt ausgeschaltet und eine scharfe Trocknungsfront wandert durch die Schüttung. Shokri et al. [82] betrachten Sandschüttungen mit unterschiedlichen hydrophilen bzw. hydrophobisierten Anteilen. Mittels Neutronenabsorption charakterisieren diese Autoren das Eindringen einer durch Gravitation stabilisierten Trocknungsfront. Mit zunehmendem hydrophobem Anteil, d.h. mit zunehmendem effektivem Kontaktwinkel, verringert sich die vertikale Distanz, über die Kapillarströmung stattfinden kann.

Technische poröse Materialien haben häufig eine bimodale Porengrößenverteilung, denn in vielen Anwendungen sind zugleich große innere Oberflächen, für katalytische Reaktion oder zur Stofftrennung, als auch hohe Permeabilitäten gewünscht. Dies wird durch die Kombination von kleinen und großen Poren erreicht, z.B. in Aggregaten aus porösen Partikeln. Die Trocknung solcher Strukturen kann bei Herstellung, Funktionalisierung oder Regeneration nötig sein. Daher wurde das Kapillarbündelmodell auch auf bimodale Strukturen angewendet [A,B]. Der Vergleich mit einer monomodalen Verteilung anhand von Sättigungsprofilen, wie in Abbildung 12, bringt Aufschluss über die wesentlichen Effekte.

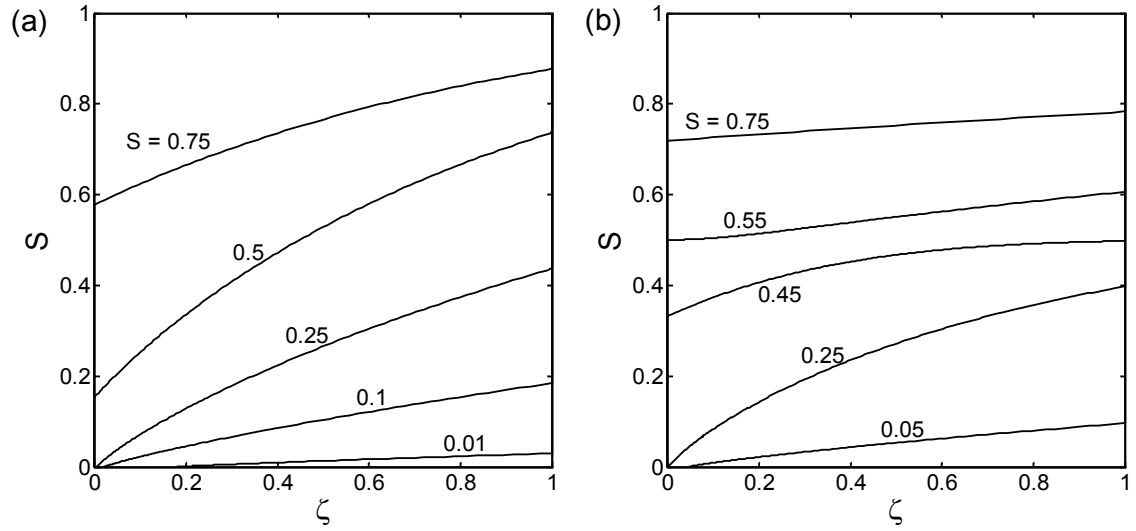

Abbildung 12. Sättigungsprofile für (a) monomodale Porengrößenverteilung (100 ± 10 nm) und (b) bimodale Porengröße (100 ± 10 nm und 1 ± 0.1 µm zu gleichen Volumenanteilen) unter identischen Trocknungsbedingungen, die für (a) mit Ca = 10 charakterisiert sind. Der Kurvenparameter ist die Gesamtsättigung des Kapillarbündels [B].

Im gezeigten Beispiel ist für den monomodalen Fall während des 1. Trocknungsabschnitts (bis $S \approx 0.42$) ein ausgeprägter Sättigungsgradient zu sehen, der sich im 2. Abschnitt allmählich abschwächt. (Die zugehörige Trocknungskurve ist in Abbildung 7 als durchgezogene Linie zu finden.) Wird die Hälfte des Porenvolumens durch große Poren – mit entsprechend breiterer Verteilung – ersetzt, so entleeren sich diese zunächst mit schwachem Gradienten komplett, bis der Gradient bei einer Sättigung von 0.5 gänzlich verschwindet. Erst danach beginnt die Trocknung der kleinen Poren, die ähnlich verläuft wie im monomodalen Fall. In der Folge wird der 1. Trocknungsabschnitt deutlich verlängert. Im Vergleich zum monomodalen Fall trocknen die kleinen Poren jedoch bei einem ungünstigeren Flächenkontrast an der Oberfläche (da sie nur eine Porosität von 0.25 liefern, verdoppelt sich die relevante Kapillarzahl). Somit kann noch etwa die Hälfte ihres Flüssigkeitsvolumens im 1. Abschnitt entfernt werden, und dieser endet bei $S \approx 0.25$. Insgesamt gesehen wirken sich große Poren günstig auf den Trocknungsverlauf aus, sowohl im Hinblick auf die Homogenität der Trocknung als auch auf die Trocknungszeit. Dieser Effekt ist direkt vom Volumenanteil der großen Poren abhängig; und deren Verteilungsbreite ist typischerweise so groß, dass sie keine wesentliche Rolle spielt [A].

Ganz ähnliche Sättigungsprofile wie in Abbildung 12b haben Koptyug et al. [34] mit kernmagnetischer Resonanz in einer trocknenden Aluminiumoxidprobe gemessen. Diese Autoren argumentieren mit der bimodalen Porengrößenverteilung der Probe, um das beobachtete flache Sättigungsprofil mitten im Trocknungsprozess zu erklären: es entspreche der vollständigen Entleerung der großen Poren, während alle kleinen Poren noch gesättigt seien. Es ist jedoch anzumerken, dass die kleinen Poren von Aluminiumoxid noch um eine Größenordnung kleiner sind als die hier betrachteten. Nach Entleerung der großen Poren kann der Transport also nicht ohne weiteres mittels Kapillarströmung beschrieben werden.

Eine erweiterte Version des Kapillarbündelmodells beschreibt die Trocknung von kugelförmigen porösen Materialien [B]. Hierzu wurde die Zahl der Kapillaren in jeder Größenklasse entsprechend der radialen Position in der Probe variiert. In Simulationen wurden gegenüber der Plattengeometrie längere 1. Trocknungsabschnitte beobachtet. Besonders zum Kugelzentrum hin unterschieden sich die berechneten Sättigungsprofile stark: für monomodale Porengröße bildeten sich dort sehr starke Gradienten aus, und für eine bimodale Verteilung blieben dort die großen Poren bis in den 2. Trocknungsabschnitt hinein voll gesättigt. Inwieweit dies real zu erwartende Effekte sind, blieb bisher ungeklärt.

1.4 Nichtisothermes Modell für zwei Kapillaren

Das Kapillarbündelmodell hat den Vorteil, dass es mathematisch einfach ist und dennoch Einsicht in das Wechselspiel der Transportphänomene ermöglicht. Allerdings müssen dafür starke Annahmen gemacht werden: neben der Beschränkung auf eine Dimension, mit allen topologischen Konsequenzen, wird insbesondere der Wärmetransport vernachlässigt. Da die Trocknung ein thermischer Prozess ist, in dessen Verlauf sich die Produkttemperatur teils über weite Bereiche ändert, liegt es nahe, das Modell diesbezüglich zu erweitern. Entscheidend ist dabei die explizite Einbeziehung des Feststoffs, der im isothermen Modell nur als Phasenanteil $1 - \psi$ beim Übergang in die gasseitige Grenzschicht eine Rolle spielt. Wie im Weiteren dargestellt, rechtfertigt der numerische Aufwand einer vollständigen Modellerweiterung nicht den zu erwartenden Erkenntiszuwachs. Daher wird das nichtisotherme Modell nur für zwei Kapillarklassen entwickelt und angewendet [A]. Abbildung 13 zeigt die Modellgeometrie sowie eine nichttriviale Phasenverteilung im Laufe der Trocknung.

Der Stofftransport besteht weiterhin aus Kapillarströmung und Dampfdiffusion; jedoch ist die Temperaturabhängigkeit der Stoffeigenschaften zu berücksichtigen. Sowohl Grenzflächenspannung als auch Viskosität der Flüssigkeit nehmen mit zunehmender Temperatur ab. Für die Kapillarströmung vom kalten Produktinneren zur warmen Oberfläche bedeutet dies eine Absenkung der Triebkraft, mit höherer Temperatur aber auch einen geringeren Widerstand.

Die starke Temperaturabhängigkeit des Sattdampfdrucks an der Phasengrenze hingegen führt dazu, dass im teilgesättigten Bereich ($s_2 < z < s_1$) Dampf von warmen oberflächennahen Regionen ins kältere Produktinnere diffundieren kann, und zwar entgegen der Kapillarströmung. Dieser Diffusionsstrom ist von einem Wärmestrom begleitet, denn das bei s_2 verdunstende Wasser nimmt latente Wärme mit und der bei s_1 kondensierende Dampf gibt diese wieder frei (heat-pipe-Effekt). Ebenso führt die Verdunstung in die Trocknungsluft zu einer Wärmesenke $-\dot{m}_v \Delta h_v$ bei s_2. Umgekehrt erwärmt die Trocknungsluft die Produktoberfläche mit der Wärmestromdichte

$$\dot{q} = \alpha\left(T_\infty - T_{surf}\right) \tag{9}$$

wobei α der (an β gekoppelte) Wärmeübergangskoeffizient ist und T_∞ bzw. T_{surf} die Temperatur von Trocknungsluft bzw. Oberfläche. Innerhalb des Kapillarbündels wird Wärme durch Leitung (näherungsweise nur in Feststoff und Porenwasser) sowie im teilgesättigten Bereich durch einen „effektiven“ Konvektionsstrom (eine Kombination aus Kapillarströmung und Dampfdiffusion) übertragen. Am geschlossenen Ende des Kapillarbündels (z = L) findet weder Wärme- noch Stoffaustausch statt. Zu Trocknungsbeginn wird vollständige Sättigung angenommen, sowie eine einheitliche Temperatur. Die Entwicklung des Temperaturprofils sowie die Meniskenbewegung sind dann Resultat der diskutierten Wärme- und Stoffströme.

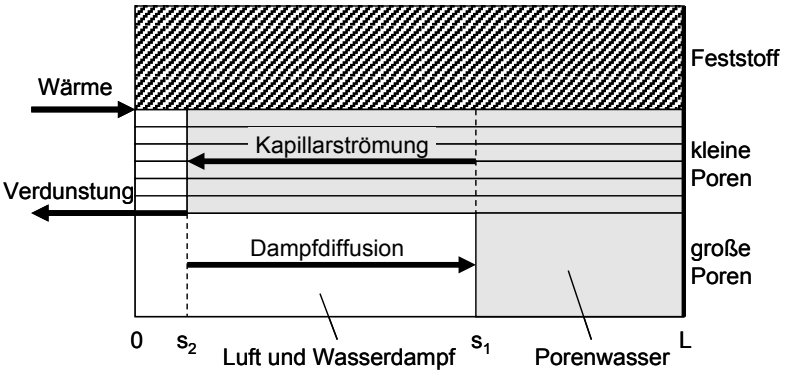

Abbildung 13. Kapillarmodell mit Wärmetransport [A].

Die numerische Lösung des Problems gestaltet sich deutlich aufwändiger als für das isotherme Modell. Die Wärmetransportgleichung wird mit der Finite-Elemente-Methode gelöst; dabei ist zu beachten, dass die Zonengrenzen s_2 und s_1 durch die Elemente wandern. Um den Zeitschritt möglichst groß wählen zu können, wird ein (semi)implizites Verfahren gewählt: aus Temperaturprofil und Meniskenpositionen werden Stoffströme sowie Wärmesenken bzw. -quellen berechnet; damit sind die aktuellen Randbedingungen für die Wärmetransportgleichung gegeben; das zukünftige Temperaturprofil wird nun (semi)implizit berechnet (d.h. ohne zukünftige Meniskenpositionen und Stofftransport auszuwerten); dann werden die Meniskenpositionen aktualisiert. Es ist ganz klar, dass durch die Erweiterung um den – kontinuierlich zu behandelnden – Wärmetransport die numerischen Vorteile des diskreten Modells verloren gehen, denn nun sind bezüglich der Zeitschrittweite Stabilitätskriterien zu beachten.

In Abbildung 14 ist die Temperaturentwicklung während der Trocknung für ein Modellsystem mit Porosität ψ = 0.5 und gleichen Volumenanteilen an großen (r_1 = 1 µm) und kleinen Poren (r_2 = 100 nm) bei L = 0.1 m dargestellt. Als thermische Eigenschaften des Feststoffs wurden die von Glas gewählt. Der Wärmeübergangskoeffizient α = 95 W/m^{2}K entspricht einem Stoffübergangskoeffizienten β = 0.1 m/s. Für die Trocknung wird auf T_∞ geheizte Umgebungsluft (mit Feuchte Y_∞ = 0.01) verwendet.
Zu Beginn der Trocknung erwärmt sich das System von der Oberfläche her auf Gutsbeharrungstemperatur; diese resultiert aus dem dynamischen Gleichgewicht von Wärmezufuhr und Verdunstungskühlung im 1. Trocknungsabschnitt. Wenn alle großen Kapillaren leer sind, wandert der Trocknungsspiegel von der Oberfläche ins Produktinnere; in

der Folge verlangsamt sich die Verdunstung und entsprechend verringert sich der damit verbundene Kühleffekt und das System erwärmt sich weiter. Infolge der unterschiedlichen effektiven Wärmeleitfähigkeiten und der Wärmesenke an der Phasengrenze treten dabei in der trockenen Zone deutliche Temperaturgradienten auf, während die Temperatur im teilgesättigten Inneren homogen ansteigt. Die Wanderung der Phasengrenze zeigt sich im Ablösen einzelner Temperaturkurven von der Masterkurve. Nach abgeschlossener Trocknung, d.h. wenn alle Kapillaren leer sind, erwärmt sich das Produkt allmählich auf die Lufttemperatur.

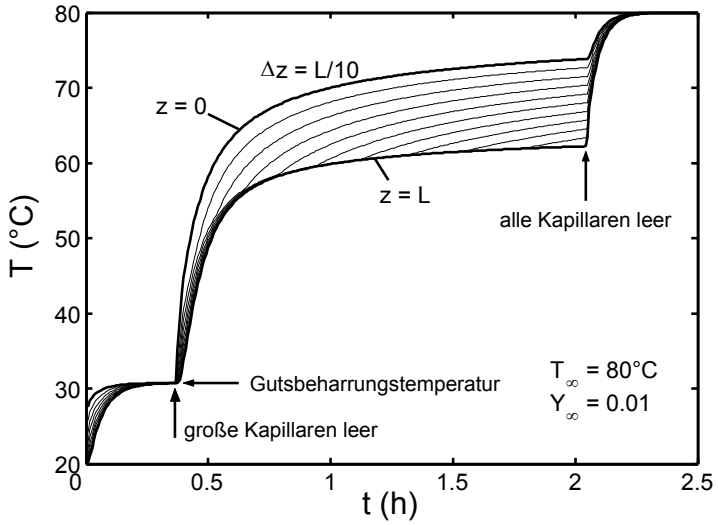

Abbildung 14. Temperaturentwicklung im Trocknungsmodell für zwei Kapillaren [A].

Neben der lokal aufgelösten Temperaturentwicklung kann das Modell Trocknungskurven liefern, wie in Abbildung 15 gezeigt. Für vergleichbare Trocknungsrate im 1. Abschnitt, unterscheidet sich das Verhalten im 2. Abschnitt deutlich vom isothermen Modell. Das dort beobachtete Absinken der Rate auf unrealistisch kleine Werte (aufgrund des zunehmenden Diffusionswiderstands) kann durch die Erwärmung des Systems (und die resultierende Triebkraftverstärkung) teilweise kompensiert werden.

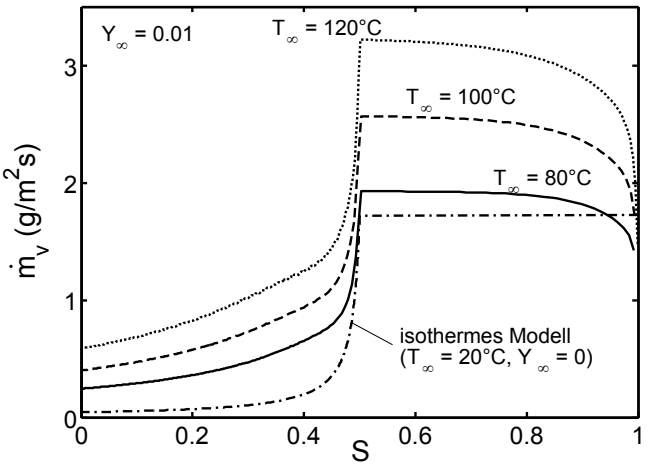

Abbildung 15. Trocknungskurven für nichtisothermes Modell mit zwei Kapillaren [A].

Das Modell eignet sich gut, um den Einfluss der Lufttemperatur auf die Trocknungskinetik zu beleuchten (siehe Abbildung 15). Aufgrund der einfachen Porenradienverteilung endet der 1. Trocknungsabschnitt stets bei S = 0.5, aber der Luftzustand bestimmt das Ausmaß der Erwärmung und somit auch die Trocknungsraten: eine höhere Lufttemperatur erhöht die Gutsbeharrungstemperatur und führt zu einer stärkeren Aufheizung im 2. Abschnitt.

Eine Weiterentwicklung des nichtisothermen Modells auf beliebige Porengrößenverteilungen wurde nicht angestrebt, da jede zusätzliche Kapillarklasse eine weitere wandernde Zonengrenze bedeutet, welche die numerische Lösung erschwert. In seiner jetzigen Form stellt das Modell eine Erweiterung von Krischers Zwei-Kapillaren-Modell dar, mit dem einige grundlegende Phänomene qualitativ untersucht und anschaulich diskutiert werden können. Effekte der Flüssigkeitsreibung, obwohl im Modell berücksichtigt, können wegen der zu restriktiven Darstellung der Porengrößenverteilung durch nur zwei Kapillarklassen jedoch nicht sinnvoll analysiert werden. Im folgenden Kapitel wird daher ein anderer Weg gewählt, um die Trocknung eines Kapillarbündels möglichst vollständig zu beschreiben: ein entsprechend parametrisiertes Kontinuumsmodell.

2 Kontinuumsmodell für Kapillarbündel

Als Alternative zur diskreten Beschreibung der Trocknung mittels Bewegung einzelner Menisken in einem Kapillarbündel wird in diesem Kapitel ein Kontinuumsmodell benutzt, dessen Parameter für den Wärme- und Stofftransport mit einem Kapillarbündel berechnet werden. Unter dem geometrischen Vorbehalt kann damit der Einfluss der Porengrößenverteilung auf das Trocknungsverhalten weitgehend untersucht werden.

2.1 Vorstellung des Literaturmodells

Für die makroskopische Beschreibung der Trocknung wird das Modell von Perré und Turner [54] gewählt, welches auf der Volumenmittelung basiert und alle wesentlichen Transportphänomene berücksichtigt. Insbesondere wird Transport nicht nur aufgrund von Feuchtegradienten (ursächlich für Dampfdiffusion und Kapillarströmung) und Temperaturunterschieden, sondern auch als Folge von Druckunterschieden in der Gasphase formuliert, was besonders für höhere Temperaturen wesentlich sein kann. Entsprechend kann das Modell die zeitliche und räumliche Entwicklung von Sättigung S, Temperatur T und Gasdruck P_g beschreiben. Als Grundlage hierfür dienen Erhaltungsgleichungen für Wasser (Flüssigkeit und Dampf)

$$\frac{\partial}{\partial t}\left(S\psi\rho_w + (1-S)\psi\rho_v\right) = \nabla\cdot\left(\rho_g D_{eff}\nabla y_v\right) - \nabla\cdot\left(\rho_w v_w + \rho_v v_g\right) \tag{10}$$

Luft

$$\frac{\partial}{\partial t}\left((1-S)\psi\rho_a\right) = \nabla\cdot\left(\rho_g D_{eff}\nabla y_a\right) - \nabla\cdot\left(\rho_a v_g\right) \tag{11}$$

und Enthalpie

$$\begin{aligned}&\frac{\partial}{\partial t}\left(S\psi\rho_w h_w + (1-S)\psi(\rho_v h_v + \rho_a h_a) + (1-\psi)\rho_s h_s - (1-S)\psi P_g\right)\\ &\quad = \nabla\cdot\left(\rho_g D_{eff}\left(h_v\nabla y_v + h_a\nabla y_a\right)\right) - \nabla\cdot\left(\rho_w h_w v_w + (\rho_v h_v + \rho_a h_a)v_g\right) + \nabla\cdot\left(\lambda_{eff}\nabla T\right)\end{aligned} \tag{12}$$

mit Dichten ρ_i für Feststoff (s), flüssiges Wasser (w), Wasserdampf (v), Luft (a) und Gas (g), Massenbrüchen $y_i = \rho_i/\rho_g$ in der Gasphase und spezifischen Enthalpien $h_i = c_{pi}(T - T_{ref})$, wobei c_{pi} spezifische Wärmekapazitäten und $T_{ref} = 0°C$ die Referenztemperatur darstellen. Der erste Term auf der rechten Seite der Gleichungen (10)-(12) beschreibt die Diffusion in der Gasphase nach dem Fick'schen Gesetz mit effektivem Diffusionskoeffizienten D_{eff}; der zweite Term stellt den konvektiven Transport in Gasphase und Flüssigkeit durch das Darcy-Gesetz in seiner verallgemeinerten Form dar

$$v_{w,g} = -\frac{K k_{w,g}}{\eta_{w,g}(T)}\cdot\nabla P_{w,g} \tag{13}$$

wobei K intrinsische und k_w bzw. k_g relative Permeabilitäten bezeichnen. In Gleichung (12) für die Enthalpieerhaltung gibt es schließlich einen dritten Term, der die Wärmeleitung mit Hilfe der effektiven Wärmeleitfähigkeit λ_{eff} beschreibt.
Flüssigkeits- und Gasdruck sind durch den Kapillardruck P_c – Gleichung (1) – miteinander gekoppelt; die (Partial)drücke der Gasphase werden nach idealen Gasgesetzen berechnet:

$$P_i = \frac{\rho_i \tilde{R} T}{\tilde{M}_i} \tag{14}$$

wobei $\tilde{R}$ ideale Gaskonstante, T absolute Temperatur (in K) und $\tilde{M}_i$ Molmassen der Gaskomponenten Luft und Dampf bzw. der Mischung $\tilde{M}_g = \tilde{M}_a + (\tilde{M}_v - \tilde{M}_a)\frac{P_v}{P_g}$ darstellen.

Wesentlich ist zudem die Unterscheidung zwischen *freiem* Wasser, das den Gesetzen der Kapillarität folgt, und *gebundenem* Wasser, das mit dem Wasserdampf in der Gasphase im

dynamischen Gleichgewicht steht – charakterisiert durch die Sorptionsisotherme $P_v(S)$, die der letzte wichtige Bestandteil des Modells ist.
Als Randbedingungen dienen die Dampfstromdichte an der Oberfläche

$$\dot{m}_v = \beta \frac{\tilde{M}_v P_{g,\infty}}{\tilde{R}T} \cdot \ln\left(\frac{P_{g,\infty} - P_{v,\infty}}{P_{g,\infty} - P_{v,surf}} \right) \tag{15}$$

wie sie sich durch Verallgemeinerung der Gleichung (4) ergibt, und die Enthalpiestromdichte

$$\dot{q} = \alpha\left(T_\infty - T_{surf}\right) - \Delta h_v \cdot \dot{m}_v \tag{16}$$

Dabei steht der Index ∞ für die Kernströmung der Trocknungsluft; der Dampfdruck an der Oberfläche $P_{v,surf}$ entspricht dem lokalen Sorptionsgleichgewicht. Als dritte Randbedingung ist der Gasdruck an der Oberfläche durch $P_{g,\infty}$ vorgegeben. In Ergänzung dazu gibt es je nach Geometrie der Probe undurchlässige Grenzen (auch um Symmetrieeigenschaften numerisch zu nutzen). Durch Anfangsbedingungen für Sättigung S_0, Temperatur T_0 und Gasdruck $P_{g,0} = P_{g,\infty}$ wird das Problem schließlich eindeutig formuliert.

Das Gleichungssystem mit Anfangs- und Randbedingungen kann nach Diskretisierung in Kontrollvolumina mit einer Newton-Raphson-Methode gelöst werden [51,90]. Aus Gründen der mathematischen Wohldefiniertheit müssen jedoch an jedem Ort Flüssigkeit und Gasphase zugleich existieren. Daher lässt sich die Trocknung eines vollgesättigten Materials (mit S = 1) nicht simulieren. Ebenso wenig darf die Probe nirgendwo komplett trocken sein (mit S = 0), also kann Dampfdiffusion nicht in reiner Form auftreten – wie im Kapillarbündelmodell – sondern muss stets von einem Gradienten in adsorbierter Flüssigkeit begleitet sein. Des Weiteren müssen die Parameterfunktionen des Modells für die numerische Lösung hinreichend glatt sein, so z.B. die Kapillardruckkurve $P_c(S)$ oder die relativen Permeabilitäten $k_w(S)$ und $k_g(S)$.

Eine Parameterstudie für das Kontinuumsmodell findet sich in [93] und [E]; einerseits zum Einfluss der Prozessbedingungen auf den Trocknungsverlauf:

- die Trocknungsrate im 1. Abschnitt wird erhöht durch Erhöhung der Lufttemperatur T_∞, Verringerung der Luftfeuchte ($P_{v,\infty}$) oder Steigerung des Stoffübergangs β (durch Vergrößerung der Strömungsgeschwindigkeit);
- in all diesen Fällen „verkürzt“ sich der 1. Abschnitt, d.h. er endet schon bei höherer Gesamtsättigung, denn die Begrenzung der Kapillarströmung durch Reibungseffekte setzt für höhere Trocknungsraten früher ein;
- im Laufe des 2. Abschnitts kann eine deutliche Steigerung der Trocknungsrate nur durch eine Erhöhung der Lufttemperatur erreicht werden;
- ist die Endfeuchte wesentlich durch das Sorptionsgleichgewicht bestimmt, so kann sie nur verringert werden durch Änderung des Luftzustands (Erhöhung der Temperatur bzw. Verringerung der Luftfeuchte), nicht aber durch Verbesserung des Stoffübergangs;

andererseits zur Rolle der wesentlichen Transportparameter:

- erwartungsgemäß beeinflusst keiner der Parameter zur Beschreibung der inneren Transportvorgänge die Trocknungsrate im 1. Abschnitt;
- eine größere Permeabilität K bedeutet geringere Reibungsverluste und kann daher den 1. Trocknungsabschnitts deutlich verlängern;
- durch Vergrößerung des effektiven Diffusionskoeffizienten werden nur die Trocknungsraten gegen Ende des 2. Abschnitts entscheidend vergrößert;
- eine höhere Wärmeleitfähigkeit (des Feststoffs) bewirkt eine bessere Wärmeabfuhr von der Oberfläche ins Innere der Probe; dadurch dauert die Aufwärmphase bis zum Erreichen der konstanten Trocknungsrate etwas länger, insbesondere erhöhen sich aber die Raten im 2. Trocknungsabschnitt.

2.2 Parametrisierung mit Kapillarbündel

Die vorangehende Analyse des Einflusses der Transportparameter hilft zwar, das Modell besser zu verstehen, ist aber nur bedingt aussagekräftig, da die Parameter nicht unabhängig von der Porenstruktur variiert werden können und durch diese untereinander sowie mit der Kapillardruckkurve (und, genau genommen, auch mit der Sorptionsisotherme) gekoppelt sind. Daher wird das Kontinuumsmodell im Folgenden für eine vorgegebene Porenstruktur parametrisiert. Wieder wird das Kapillarbündel gewählt, da es mit der Porengrößenverteilung eine wesentliche Struktureigenschaft darstellen kann und dennoch einen entscheidenden Vorteil hat: es ist hinsichtlich der Flüssigkeitsverteilung im Porenraum eindeutig (siehe Abbildung 16). Diese Eindeutigkeit ist für die höherdimensionalen Porennetzwerke (siehe Kapitel 3) nicht mehr gegeben: dort hängen die Phasenverteilungen – und damit auch die sättigungsabhängigen Modellparameter – von der Vorgeschichte ab (siehe auch [23]). Das Kapillarbündel hat zudem den Vorteil der Konsistenz mit zwei wesentlichen Eigenschaften des Kontinuumsmodells:

1. Gasphase und Flüssigkeit bleiben während der Trocknung zusammenhängend;
2. Flüssigkeitstransport kann nur aufgrund von Sättigungsgradienten stattfinden.

Bei Porennetzwerken wird die Kontinuität der Flüssigkeit durch Clusterbildung aufgehoben, und Flüssigkeitsströmung ist bedingt durch die Radienverteilung einzelner Poren und kann gradientenfrei erfolgen. Beides sind reale Phänomene, welche die Grenzen der Kontinuumsmodellierung aufzeigen und nur in einer diskreten Beschreibung erfasst werden können.

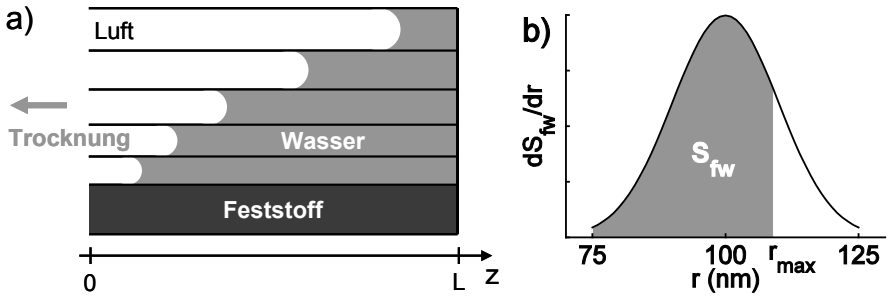

Abbildung 16. Darstellung des Porenraums durch Kapillarbündel mit verteilten Radien: die lokale Sättigung während der Trocknung stellt sich gemäß den Transportvorgängen ein (a), an jedem Ort ist die freie Porenflüssigkeit – beschrieben durch den Sättigungsanteil S_{fw} – in den Poren bis zu einem maximalen Radius r_{max} enthalten (b).

Das Kapillarbündel zur Berechnung der effektiven Parameter ist in Abbildung 16a dargestellt. Die Sättigung an Porenwasser besteht aus freiem und gebundenem Wasser

$$S = S_{fw} + S_{sorb} \tag{17}$$

die im Folgenden unterschiedlich behandelt werden. Die Verteilung des freien Porenwassers auf die Porenradien ist in Abbildung 16b illustriert. Der Transport während der Trocknung erfolgt in z-Richtung entlang den Kapillaren. Tabelle 1 gibt die dieser Geometrie entsprechenden makroskopischen Eigenschaften wieder.

Dampfdiffusion und Wärmeleitung sind unabhängig von der Porengröße, solange der Knudseneffekt vernachlässigbar ist, und werden durch die Querschnittsanteile der beteiligten Phasen charakterisiert. Zu deren Berechnung ist das gesamte Porenwasser (dargestellt durch S) zu berücksichtigen. Dampfdiffusion erfolgt gemäß dem binären Diffusionskoeffizienten δ_{va}, der von Temperatur und Gasdruck abhängt, ist aber beschränkt auf den gasgefüllten Anteil $(1 - S)\psi$; der effektive Diffusionskoeffizient ist entsprechend in Gleichung (18) gegeben. Für die Wärmeleitung wird der Beitrag der Gasphase vernachlässigt, so dass die effektive Wärmeleitfähigkeit in Gleichung (19) einer Parallelschaltung von fester und flüssiger Phase entspricht, mit Temperaturabhängigkeit der Stoffparameter.

Intrinsische und relative Permeabilitäten berechnen sich für das freie Porenwasser durch Integration des Gesetzes von Hagen-Poiseuille (Gleichung (2b)) mit Gewichtung nach der

Porengrößenverteilung. Dabei ergibt gemäß Gleichung (20) die Integration über alle Poren die intrinsische Permeabilität K. Durch Integration über die jeweils mit einer Fluidphase gefüllten Kapillaren und Division durch K erhält man die entsprechenden relativen Permeabilitäten k_w in Gleichung (21) und k_g in Gleichung (22).
Der lokale Kapillardruck ist durch die größte flüssigkeitsgefüllte Kapillare mit Radius r_{max} bestimmt; zudem ist in Gleichung (23) ideale Benetzung (θ = 0°) angenommen, und die Temperaturabhängigkeit der Oberflächenspannung wird berücksichtigt.
Die Adsorption wird unabhängig von der Porengrößenverteilung beschrieben, denn erst bei Porenradien r < 10 nm würde der Kelvin-Effekt zu einer starken Kopplung führen (S. 49 in [36]). Zudem wird die Beziehung zwischen relativer Luftfeuchte φ und Sättigung S vereinfachend als temperaturunabhängig angenommen. Dies ist in der Realität nicht der Fall (S. 54 ff in [36]), jedoch soll gebundenes Wasser nicht Schwerpunkt der folgenden Untersuchung sein. Die Sorptionsisotherme wird durch Gleichung (24) vorgegeben und ist in Abbildung 17 dargestellt.
Damit sind alle Parameter des Kontinuumsmodells vollständig charakterisiert und können in Abhängigkeit von Porengrößenverteilung und Sättigung berechnet werden. Für das Kapillarbündel hängen nur intrinsische und relative Permeabilitäten sowie Kapillardruck von der Porengrößenverteilung ab.

Tabelle 1. Effektive Parameter des Kontinuumsmodells für Geometrie des Kapillarbündels.

effektiver Diffusionskoeffizient	$D_{eff}(S,T,P_g) = (1-S)\psi\delta_{va}(T,P_g)$	(18)
effektive Wärmeleitfähigkeit	$\lambda_{eff}(S,T) = (1-\psi)\lambda_s(T) + S\psi\lambda_w(T)$	(19)
(intrinsische) Permeabilität	$K = \frac{1}{8}\int r^2 \frac{dS_{fw}}{dr} dr$	(20)
relative Permeabilität für Flüssigkeit	$k_w(S_{fw}) = \frac{1}{8K}\int^{r_{max}} r^2 \frac{dS_{fw}}{dr} dr$	(21)
relative Permeabilität für Gas	$k_g(S_{fw}) = 1 - k_w(S_{fw})$	(22)
Kapillardruckkurve	$P_c(S_{fw},T) = \frac{2\sigma(T)}{r_{max}(S_{fw})}$	(23)
Sorptionsisotherme	$\varphi = \frac{P_v}{P_v^*(T)} = \begin{cases} \frac{S}{S_{sorb}}\left(2 - \frac{S}{S_{sorb}}\right), & S < S_{sorb} \\ 1, & S \geq S_{sorb} \end{cases}$	(24)

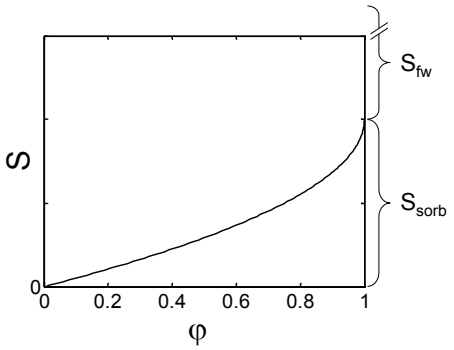

Abbildung 17. Sorptionsisotherme nach Gleichung (24).

Bevor diese Parameterfunktionen für einige ausgewählte Beispiele darstellt werden, soll hier noch auf Arbeiten aus der Literatur eingegangen werden. Das Kapillarbündel wird insbesondere für die Berechnung der relativen Permeabilitäten (und der Kapillardruckkurve)

bei Zwei-Phasen-Strömungen benutzt. Entsprechend der beabsichtigten Anwendung erfolgt die Berechnung dynamisch, d.h. ein nicht benetzendes Fluid wird durch ein benetzendes verdrängt, wobei geeignete Randbedingungen zu wählen sind. Je nach Modell erfolgt die Verdrängungsströmung durch unabhängige parallele Kapillaren [5], oder aber die Kapillaren können über ihre gesamte Länge widerstandslos miteinander kommunizieren [22,66]. Charakteristisch für solche Modelle ist, dass die Kurvenverläufe der relativen Permeabilitäten entscheidend beeinflusst werden vom Viskositätsverhältnis der beiden Fluide sowie von der Strömungsrate. Die dynamischen Ergebnisse unterscheiden sich deutlich von denen des hier betrachteten – und für die Trocknung angemessenen – stationären Falls [5]. Insgesamt ist die Verwendung des verallgemeinerten Darcy-Gesetzes, Gleichung (13), und relativer Permeabilitäten zur Beschreibung der Zwei-Phasen-Strömung wegen zahlreicher (ungeklärter) Abhängigkeiten nicht unstrittig, wird von Dullien [23] aber für dominante Kapillareffekte – wie bei der hier diskutierten Trocknung – als sinnvoll gewertet, denn dann gebe es zwei unabhängige Fluidnetzwerke mit stabilen Phasengrenzflächen.
Bezüglich der Berechnung von Permeabilitäten mit Kapillarbündeln weist Dullien [23] auf die Tatsache hin, dass sich Fehler beim Anteil der großen Poren sehr stark auf das Ergebnis auswirken. Außerdem empfiehlt er, dass nur ein Drittel aller Kapillaren zur Permeabilität in einer Raumrichtung beitragen solle, damit der reale dreidimensionale Fall korrekt wiedergegeben werde. (Hier wird das Kapillarbündel hingegen als idealiertes poröses Material exakt beschrieben.)
Relative Permeabilitäten wurden auch mit Porennetzwerken berechnet, jedoch stellt sich die Frage, nach welchen Regeln die Fluide für eine vorgegebene Sättigung auf den Porenraum verteilt werden sollen [67]. Blunt und King [6] nutzen radiale Verdrängungssimulationen in regellosen dreidimensionalen Netzwerken, um die effektiven Parameter realitätsnah zu bestimmen und den Einfluss von Viskositätsverhältnis und Strömungsrate zu untersuchen.

Um den Einfluss der Porengrößenverteilung auf die effektiven Parameter zu diskutieren, werden die vier in Tabelle 2 aufgelisteten Fälle betrachtet [E]. Die monomodalen Porengrößen sind normalverteilt; die bimodalen Fälle sind aus zwei volumengleichen Normalverteilungen zusammengesetzt, wobei aus numerischen Gründen ein Übergangsbereich zwischen beiden Moden eingefügt wurde. Gebundenes Wasser mit einem Sättigungsanteil $S_{sorb} = 0.15$ ist an der Konvektion nicht beteiligt. Intrinsische Permeabilitäten sind in Tabelle 2 wiedergegeben, die Kurvenverläufe der relativen Permeabilitäten in Abbildung 18.
Für die relativ engen monomodalen Verteilungen bestimmt der Mittelwert r_0 die Permeabilität ($K \approx r_0^2/8$); und die relativen Permeabilitäten sind nahezu linear: $k_w \approx S_{fw}$ und $k_g \approx 1 - S_{fw}$. Je breiter die Verteilung wird (im relativen Maß), desto größer werden die Abweichungen von diesen Näherungen. Für bimodale Verteilungen setzt sich die intrinsische Permeabilität aus zwei Beiträgen zusammen, wobei der Beitrag der großen Poren dominiert. Die Kurven der relativen Permeabilitäten zeigen die unterschiedliche Gewichtung der Beiträge der volumengleichen Moden sehr deutlich: je stärker der Größenkontrast, desto unwesentlicher ist der Beitrag der kleinen Poren und desto stärker variiert die Permeabilität für die einzelnen Phasen während der Trocknung.

Tabelle 2. Mono- und bimodale Porengrößenverteilungen für effektive Parameterfunktionen.

Fall	$r_0 \pm \sigma_0$	K (10^{-15} m^2)
monomodal 1	100 ± 5 nm	1.238
monomodal 2	1 µm ± 100 nm	124.6
bimodal 1	100 ± 10 nm; 200 ± 20 nm	3.119
bimodal 2	100 ± 10 nm; 2 µm ± 200 nm	245.1

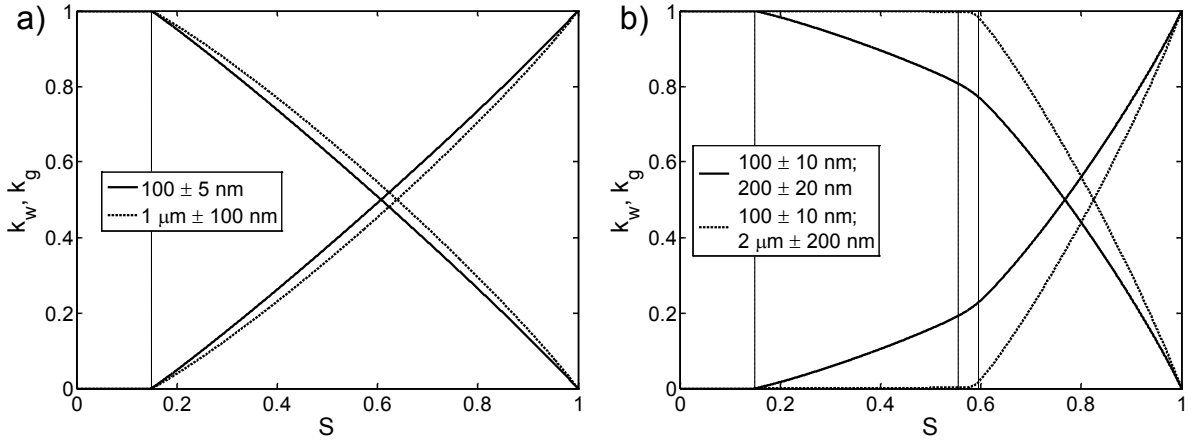

Abbildung 18. Relative Permeabilitäten für (a) monomodale und (b) bimodale Porengrößenverteilungen [E].

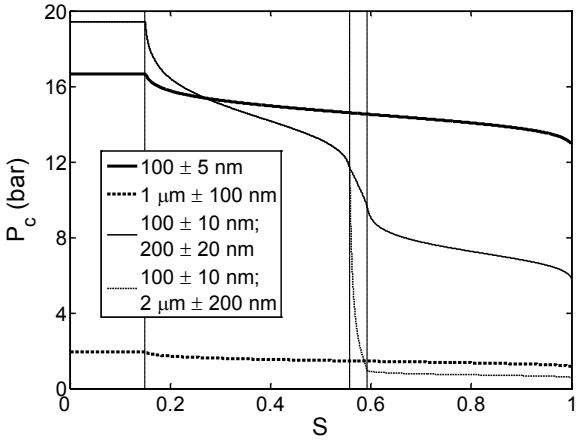

Abbildung 19. Kapillardruckkurven für mono- und bimodale Porengrößenverteilungen [E].

In Abbildung 19 sind die berechneten Kapillardruckkurven für die vier Fälle gezeigt. In den monomodalen Verteilungen bestimmt die mittlere Porengröße das Druckniveau ($P_c \approx 2\sigma/r_0$): dabei erzeugen kleinere Poren einen höheren Kapillardruck. Aus demselben Grund steigt der Kapillardruck während der Trocknung stetig an. Die Druckvariation hängt neben der Verteilungsbreite auch stark vom Mittelwert der Porengröße ab (für enge Verteilungen gilt $\Delta P_c \sim \sigma_0/r_0^2$). Bimodale Porengrößenverteilungen sind durch einen deutlichen Anstieg des Kapillardrucks bei Entleerung der großen Poren charakterisiert; dabei sind die beiden Druckniveaus durch die jeweils mittlere Porengröße festgelegt.

2.3 Vergleich mit diskretem Kapillarbündelmodell

Die für ein Kapillarbündel berechneten Parameterfunktionen werden im Folgenden für Trocknungssimulationen verwendet. In einem ersten Schritt soll dieses hybride Modell mit dem in Kapitel 1 vorgestellten isothermen Kapillarbündelmodell verglichen werden. Die Geometrie des Porenraums ist dabei identisch (monomodale Verteilung mit r_0 = 100 nm und σ_0 = 10 nm), jedoch wird das Problem unterschiedlich diskretisiert: im Kontinuumsmodell ist es die Ortskoordinate, im diskreten Modell, in dem einzelne Flüssigkeitsmenisken verfolgt werden, ist es die Sättigung. Um für den Vergleich auch im Kontinuumsmodell isotherme und isobare Bedingungen zu erhalten, werden sehr große Werte für die Koeffizienten des Wärmetransports angesetzt und eine niedrige Lufttemperatur (20°C) gewählt [E]. Die Trocknungskurven und Sättigungsprofile der beiden Modelle sind in Abbildungen 20 und 21 dargestellt. Die Trocknung mit dem Kontinuumsmodell beginnt aus numerischen Gründen bei der Sättigung S_0 = 0.9; der Anteil gebundenen Wassers wurde auf S_{sorb} = 0.01 gesetzt.

Neben der guten qualitativen Übereinstimmung der Ergebnisse fallen zwei Unterschiede auf: im Kontinuumsmodell ist erstens der 1. Trocknungsabschnitt länger, und zweitens sind die Sättigungsprofile flacher. Dabei unterstützt der zweite Unterschied den ersten, dieser hängt aber zudem mit der unterschiedlichen Diskretisierung zusammen: im diskreten Modell beginnt der 2. Abschnitt mit dem Zurückweichen des letzten Flüssigkeitsmeniskus, und dessen Position kann sich beliebig einstellen; im Kontinuumsmodell muss sich hingegen das Volumenelement an der Oberfläche (im Beispiel von der Größe $\Delta z = 0.2$ mm) erst komplett entleeren, bevor die Trocknungsrate absinkt. Der zweite Unterschied erklärt sich aus den unterschiedlichen Randbedingungen der beiden Ansätze: während im Kontinuumsmodell die Undurchlässigkeit der Probenrückseite einen verschwindenden Sättigungsgradienten bei z = L erfordert, wandern im diskreten Modell die Flüssigkeitsmenisken „aus der Probe heraus“, und effektiv wird eine Druckrandbedingung $P_c(S)$ aufgeprägt [E].

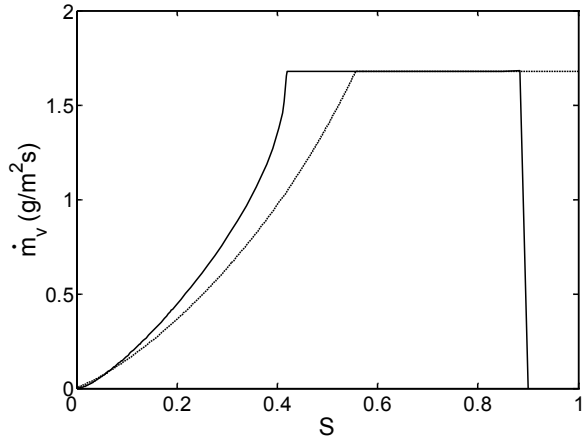

Abbildung 20. Vergleich der Trocknungskurven für ein monomodales Kapillarbündel (durchgezogene Kurve: Kontinuumsmodell, gestrichelte Kurve: diskretes Modell) [E].

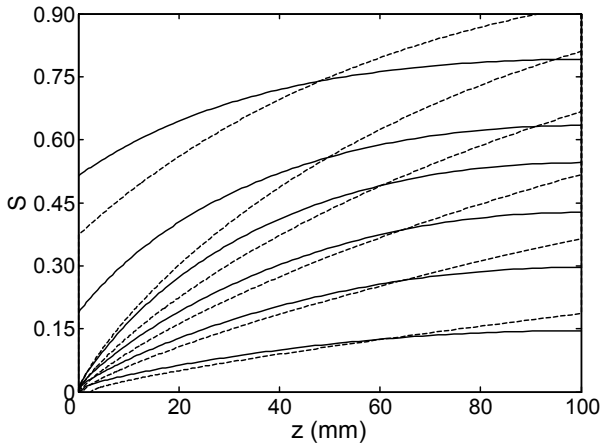

Abbildung 21. Vergleich der Sättigungsprofile für ein monomodales Kapillarbündel (durchgezogene Kurven: Kontinuumsmodell, gestrichelte Kurven: diskretes Modell) [E].

2.4 Trocknungsverhalten für unterschiedliche Porengrößenverteilungen

Das Kontinuumsmodell für das Kapillarbündel wird nun genutzt, um die Einflüsse der Porengrößenverteilung auf das Trocknungsverhalten möglichst umfassend zu untersuchen. Dabei werden die zeitlichen Verläufe von Sättigung, Temperatur und Druck im trocknenden Material sowie die (integrale) Trocknungskurve gezeigt. Die Ergebnisse zu allen in Tabelle 2 aufgelisteten Fällen sind in [E] ausführlicher dargestellt; hier sollen nur die wesentlichen Tendenzen anhand der Beispiele aus [b] diskutiert werden.

Abbildung 22a zeigt je eine monomodale (100 ± 10 nm) und bimodale (100 ± 10 nm und 1 µm ± 100 nm volumengleich) Porengrößenverteilung. Die Porosität ist jeweils $\psi = 0.5$, und die Produkttiefe bis zur undurchlässigen Rückseite (bzw. bis zur Symmetrieebene) beträgt L = 0.1 m. Die Feststoffeigenschaften orientieren sich an Glas, der Anteil gebundenen Wassers ist $S_{sorb} = 0.1$. Von anfänglicher Sättigung $S_0 = 0.9$ bei $T_0 = 20°C$ wird mit trockener Luft bei $T_\infty = 80°C$ und Atmosphärendruck getrocknet. Die Koeffizienten für Wärme- und Stofftransport durch die gasseitige Grenzschicht sind $\alpha = 95$ W/m^2/K und $\beta = 0.1$ m/s.

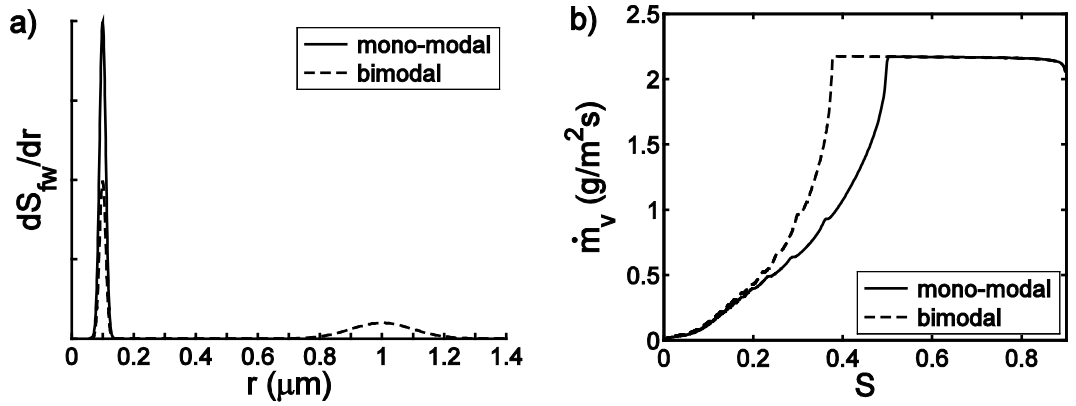

Abbildung 22. Porengrößenverteilungen und zugehörige Trocknungskurven [b].

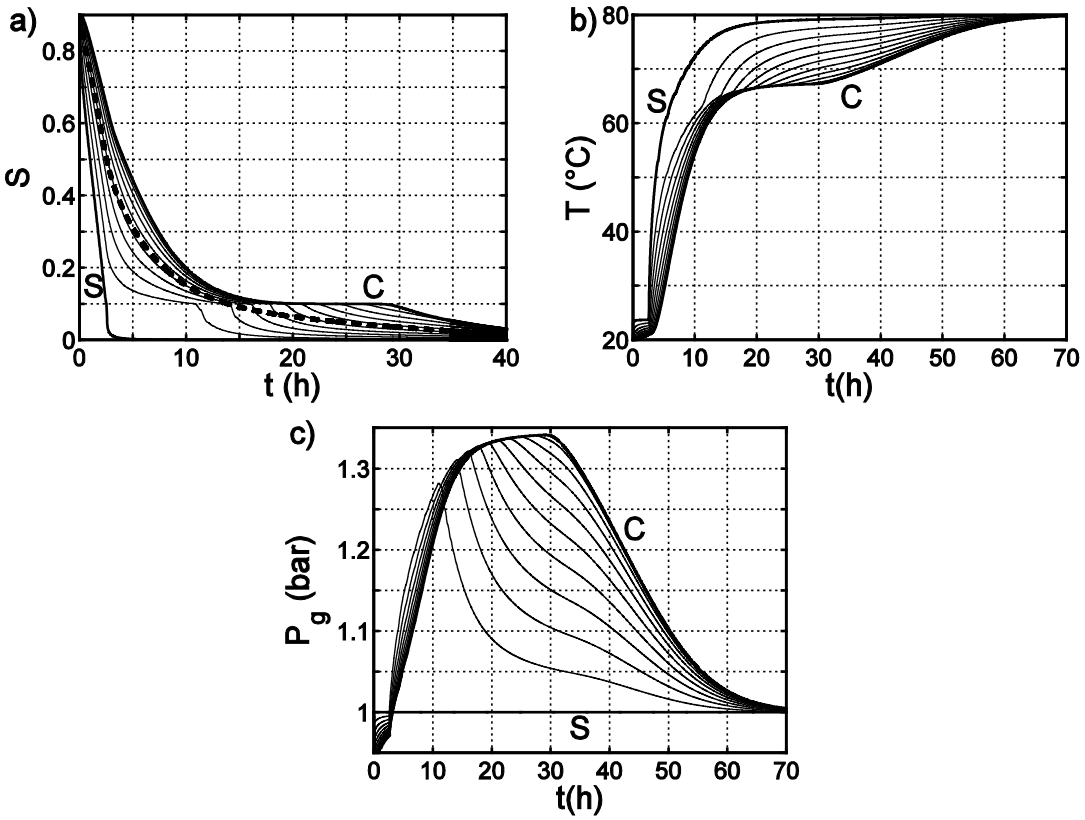

Abbildung 23. Zeitliche Verläufe von (a) Sättigung, (b) Temperatur und (c) Gasdruck für Kapillarbündel mit monomodaler Radienverteilung (siehe Abbildung 22). Durchgezogene Kurven zeigen lokale Werte an äquidistanten Orten zwischen Oberfläche (S) und Kern (C) des porösen Materials; die gestrichelte Kurve in (a) zeigt die mittlere Sättigung [b].

Die Diskussion beginnt mit den Ergebnissen für die monomodale Verteilung, die in Abbildungen 22b, 23 sowie 24a dargestellt sind. Von Beginn der Trocknung an entwickelt sich in der Probe ein ausgeprägter Sättigungsgradient, so dass die Oberfläche früh in den Bereich des gebundenen Wassers austrocknet: bei einer Gesamtsättigung von S = 0.5 (nach

2.6 h) beginnt der 2. Trocknungsabschnitt. Zu diesem Zeitpunkt setzt eine deutliche Erwärmung der Probe von der Oberfläche her ein, wobei die Verdunstungsfront den feuchten Kern (S_{fw} > 0) teilweise abschirmt und dieser sich nur allmählich und ohne deutlichen Temperaturgradienten erwärmt (Abbildung 23b, vgl. auch Abbildung 14). Zugleich entwickelt sich an der Verdunstungsfront (d.h. bei S = S_{sorb}) ein Überdruck, der mit ansteigender Temperatur und zunehmender Distanz zur Oberfläche ansteigt (Abbildung 23c). Wenn schließlich alles freie Wasser in der Probe verdunstet ist (nach etwa 30 h), geht die Trocknung in eine weitere Phase über, die in der Literatur auch als 3. Trocknungsabschnitt bezeichnet wird (S. 304f. in [36]). Durch weiteres Absinken der Verdunstungsrate werden Kühleffekt und Dampfdruck im Inneren der Probe allmählich unbedeutend: die Probe erwärmt sich auf Lufttemperatur und der Überdruck baut sich ab. Der Feststoff strebt das Sorptionsgleichgewicht mit der Luft an. Die Sättigungsprofile aus Abbildung 24a zeigen deutlich den hygroskopischen Bereich (S < 0.1); sehr ähnliche experimentelle Ergebnisse sind in der Literatur dokumentiert (z.B. für Dachziegel und Porenbeton in [36], S. 236).

Zum Einfluss der Porengrößenverteilung auf den Trocknungsverlauf lässt sich feststellen [E]:

- je größer die Verteilungsbreite σ_0, desto schwächer sind die Sättigungsgradienten ausgeprägt, und desto länger ist infolgedessen der 1. Trocknungsabschnitt;
- der Druckanstieg in der Probe nimmt mit zunehmender mittlerer Porengröße r_0 ab;
- der Einfluss auf die Temperaturentwicklung in der Probe erscheint gering.

Diese Ergebnisse untermauern und erweitern die Erkenntnisse aus dem diskreten Kapillarbündelmodell.

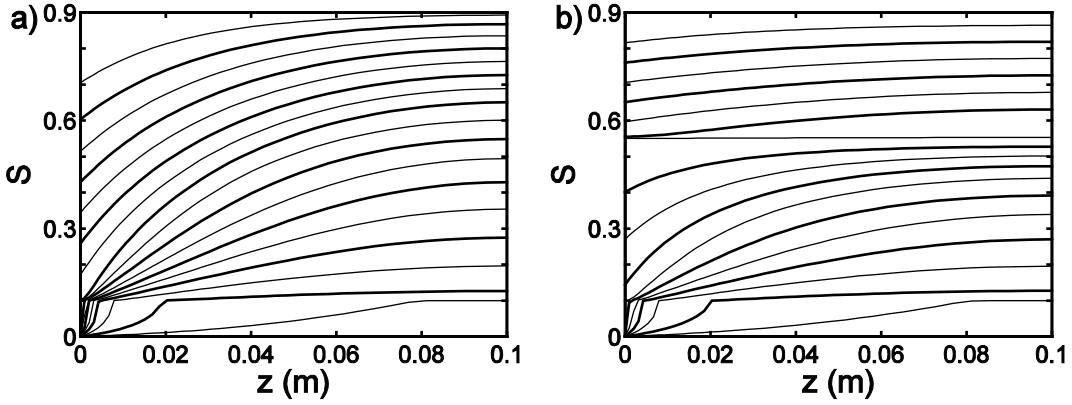

Abbildung 24. Sättigungsprofile für Kapillarbündel mit (a) monomodaler bzw. (b) bimodaler Radienverteilung (siehe Abbildung 22), gezeichnet in Sättigungsschritten von 0.05 (bzw. 0.1 für dick gezeichnete Kurven) [b].

Das Kapillarbündel mit bimodaler Verteilung zeigt ein zweigeteiltes Trocknungsverhalten; dies ist in Abbildungen 22b, 24b und 25 dargestellt. Bei hohen Sättigungen sind die großen Poren teilgesättigt und bestimmen den Trocknungsverlauf: ihre breite Verteilung ermöglicht eine effiziente Kapillarströmung und eine homogene Trocknung der Probe. Erst wenn sich – von der Oberfläche her – die ersten kleinen Poren entleeren, bilden sich signifikante Feuchtegradienten aus, die den Übergang zum 2. Trocknungsabschnitt bestimmen. Über diesen Übergang entscheiden große und kleine Poren gemeinsam, und zwar dauert der 1. Trocknungsabschnitt umso länger

- je größer der Volumenanteil der großen Poren (denn typischerweise entleeren sich zuerst alle großen Poren in der gesamten Probe unabhängig von ihrer Verteilung [E]) und
- je größer die Verteilungsbreite der kleinen Poren.

Im vorliegenden Beispiel ist der 1. Abschnitt für die bimodale Verteilung deutlich länger als im monomodalen Fall.

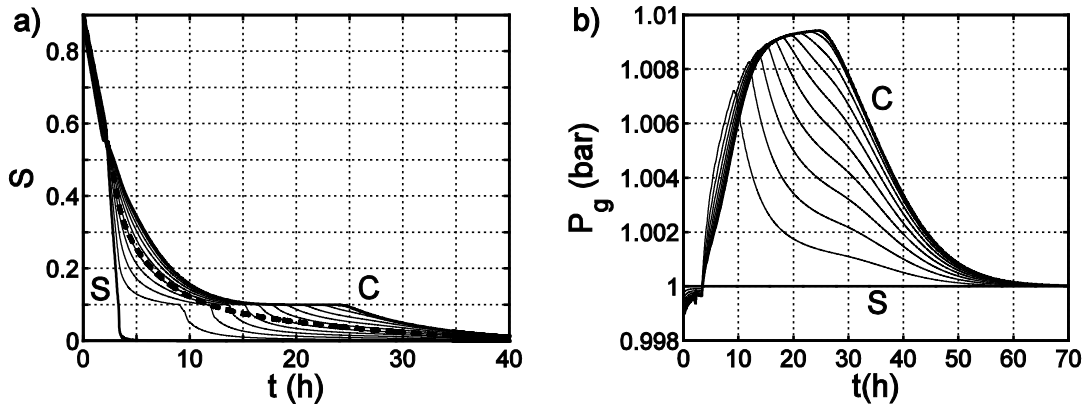

Abbildung 25. Zeitliche Verläufe von (a) Sättigung und (b) Gasdruck für Kapillarbündel mit bimodaler Radienverteilung (siehe Abbildung 22). Durchgezogene Kurven zeigen lokale Werte an äquidistanten Orten zwischen Oberfläche (S) und Kern (C) des porösen Materials; die gestrichelte Kurve in (a) zeigt die mittlere Sättigung [b].

Zum Druckverlauf in der Probe ist festzustellen, dass die schon zu Beginn der Trocknung hohe Gaspermeabilität (vgl. auch Abbildung 18) einen wesentlichen Druckanstieg verhindert. (Die Permeabilität K ist für das bimodale Bündel $6.33 \cdot 10^{-14}$ m^2 gegenüber nur $1.26 \cdot 10^{-15}$ m^2 für das monomodale.) Die Temperaturentwicklung unterscheidet sich nicht wesentlich vom monomodalen Fall – außer in der Dauer des 1. Abschnitts [E].
Das Ende der Trocknung, nämlich die allmähliche Verdunstung des gebundenen Wassers wird nicht mehr von der Porengrößenverteilung bestimmt, denn die entscheidenden Transportparameter für diese Trocknungsphase D_{eff} und λ_{eff} hängen nur von der Porosität ab. (Dies gilt streng genommen nur, wenn das Sorptionsgleichgewicht als unabhängig von der Porengrößenverteilung gesehen werden darf.)

Das Kontinuumsmodell in Kombination mit dem Kapillarbündel zur Parameterberechnung ermöglicht also, den Einfluss einer wesentlichen Strukturcharakteristik, nämlich der Porengrößenverteilung, auf die Trocknung zu untersuchen. Dabei sind neben der Trocknungskurve insbesondere auch lokale Informationen über Feuchte, Temperatur und Gasdruck in der Probe zugänglich.
Kritisch zu erwähnen ist die vereinfachte Geometrie, denn die parallele Anordnung der Poren und des Feststoffs vernachlässigt die Tortuosität realer Porensysteme. Des Weiteren sind die beiden Fluide in der Realität nicht notwendig zusammenhängend. Beides führt zu einer Überschätzung der Transporteigenschaften im Modell. Auf die Parametrisierung des Kontinuumsmodells mit Porennetzwerken wird in 5.2 eingegangen.

Neben dieser Problematik hat das Kontinuumsmodell bekanntermaßen Grenzen in der Anwendbarkeit auf kapillardominierte Prozesse, in denen eine Phase durch eine zweite ersetzt wird [67]. Daher wird in den folgenden Kapiteln die diskrete Modellierung mit Porennetzwerken vorgestellt, die sich für die Beschreibung der grundlegenden Mechanismen als geeignet erwiesen hat [59].

3 Porennetzwerke – Basismodell und Einfluss der Porenstruktur

In den 1980er Jahren wurde in der Beschreibung des Fluidtransports durch poröse Materialien ein Paradigmenwechsel eingeleitet, von Kontinuums- zu diskreten Modellen [67]. Als klassisches – und ökonomisch relevantes – Problem kann die (sekundäre) Erdölgewinnung durch Injektion von Wasser in (poröse) Erdschichten gesehen werden. Dabei handelt es sich um einen Verdrängungsprozess für nichtmischbare Fluide. Aufgrund von Fingerbildung bricht die Wasserphase früh durch, und ein erheblicher Anteil der Ölphase verbleibt in der porösen Struktur – eingeschlossen von der Wasserphase. Diese Phänomene sind von der Größenverteilung der einzelnen Poren bestimmt und können mit Kontinuumsmodellen nicht verstanden werden.

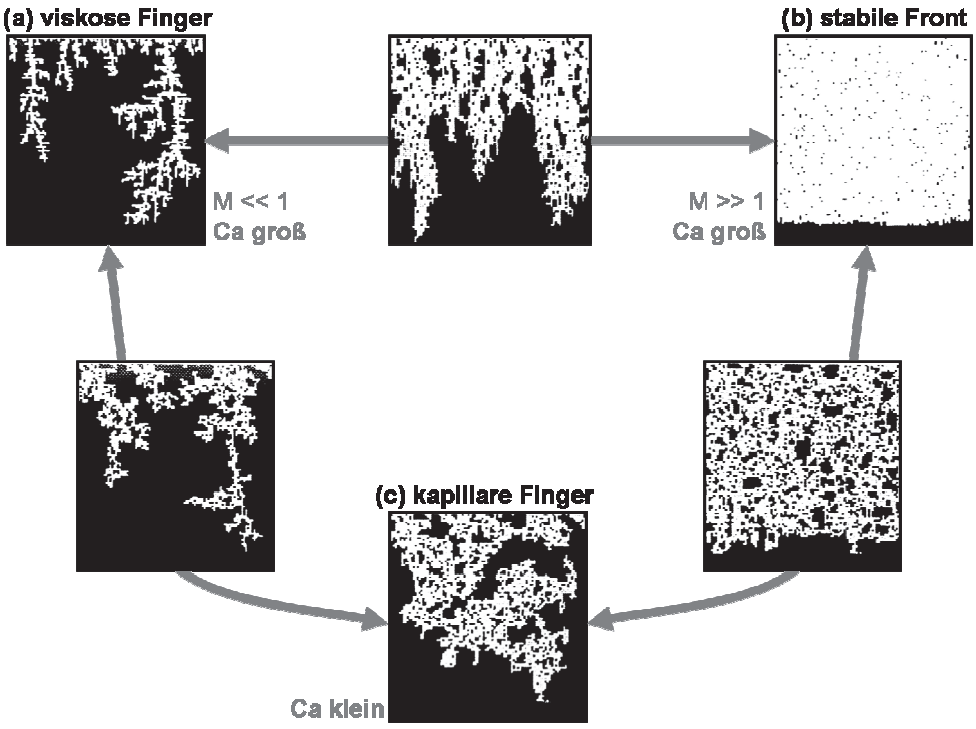

Abbildung 26. Simulierte Frontstrukturen bei der Verdrängung eines benetzenden Fluids (schwarz) durch ein nichtbenetzendes Fluid (weiß), adaptiert aus [46].

Die wohl bedeutendsten Arbeiten zur Untersuchung der Verdrängung eines benetzenden Fluids (1) durch ein nichtbenetzendes (2) wurden von Lenormand et al. durchgeführt [46]. In dynamischen Porennetzwerksimulationen und Experimenten mit zweidimensionalen Mikromodellen wurde bei aufgeprägtem Injektionsvolumenstrom $\dot{V}_2$ der Einfluss von Kapillarität und Reibung untersucht. Sowohl die Kapillarzahl $Ca \sim \dot{V}_2 \eta_2/\sigma$ als auch das Viskositätsverhältnis $M = \eta_2/\eta_1$ wurden über weite Bereiche variiert. Abbildung 26 zeigt typische Phasenverteilungen für die drei Grenzfälle sowie die Übergänge zwischen diesen. Bei schneller Verdrängung entscheidet das Viskositätsverhältnis M über die Frontstruktur: ist das verdrängte Fluid deutlich viskoser als das verdrängende, dann bilden sich viskose Finger aus (a), im gegenteiligen Fall ist die Front stabil (b). Bei langsamer Verdrängung spielt das Viskositätsverhältnis keine Rolle und kapillare Finger gestalten die Front (c). Die Simulationen für 100×100 Netzwerke kann Lenormand eindrucksvoll durch umfassende Experimente mit verschiedenen Fluidkombinationen in 135×150 Netzwerken bestätigen [46].
Für den durch Kapillarität dominierten Fall, d.h. für kleine Kapillarzahl Ca, haben Lenormand und Zarcone die Struktur der Front mit einem 350×350 Netzwerk untersucht, in welchem Öl durch Luft verdrängt wurde [47]. Die Verdrängung wurde dabei durch langsames Absenken des Öldrucks an der Ausströmseite kontrolliert. Theoretisch lässt sich der Prozess dann als Invasionsperkolation in einem Porennetzwerk beschreiben [47]: Luft kann stets nur in Poren

vordringen, in denen der Kapillardruck P_c bereits durch die Druckabsenkung im Öl kompensiert wird; entsprechend wandert die Phasengrenze zu jedem Zeitpunkt nur in solche Poren weiter, die einen kritischen Radius überschreiten; und dieser kritische Radius nimmt mit der Zeit allmählich ab. In der Folge können insbesondere auch ganze Bereiche der Ölphase abgetrennt werden (vgl. Abbildung 26c), sofern sie von großen Poren umschlossen sind, die sich bevorzugt entleeren; die so entstehenden Ölcluster bleiben dann dauerhaft eingeschlossen (trapping).

Ein ganz ähnlicher, ebenfalls kapillardominierter Prozess läuft bei der Hg-Porosimetrie ab. Hierbei wird Quecksilber als nichtbenetzendes Fluid in eine (evakuierte) poröse Probe gedrückt. Mit zunehmendem Druck können immer kleinere Poren befüllt werden, und die Abhängigkeit des Kapillardrucks vom Porenradius wird genutzt, um die Porengrößenverteilung zu messen. Dabei kommt es zu Fehlinterpretationen, wenn z.B. große Poren von kleinen Poren umgeben sind und daher erst verzögert, d.h. bei zu hohen Drücken, befüllt werden können. Wird der Druck zum Ende der Charakterisierung allmählich wieder abgesenkt, zieht sich das Quecksilber wieder aus der Probe zurück – üblicherweise mit einer Hysterese und auch nur unvollständig. Um diese Phänomene besser verstehen zu können, haben Tsakiroglou und Payatakes ein Porennetzwerkmodell entwickelt [88].

Prat schließlich erkannte, dass auch die Trocknung poröser Strukturen mittels Invasionsperkolation beschrieben werden kann [59]. Die Verdunstung der Porenflüssigkeit entspricht dabei weitgehend einer langsamen – und daher kapillardominierten – Verdrängung von Flüssigkeit durch Luft [60]. Allerdings ist das Modell durch die Dampfdiffusion in der Gasphase zu erweitern; diese bestimmt zum einen die Zeitachse für den Prozess und sorgt zum anderen dafür, dass isolierte Flüssigkeitscluster nicht dauerhaft eingeschlossen bleiben, sondern allmählich verdunsten.
Betrachtet man noch einmal die Ergebnisse von Lenormand in Abbildung 26, so erwartet man für die Trocknung Phasenverteilungen, die einem großen Viskositätsverhältnis M entsprechen. Langsame Trocknung ist in der Tat durch kapillare Finger gekennzeichnet (c), wobei die abgetrennten Flüssigkeitscluster nach und nach verschwinden [59]. Eine Stabilisierung der Front (b) kann zum einen für hohe Trocknungsraten beobachtet werden, wenn die Kapillarströmung durch Reibung behindert wird (siehe Kapitel 4). Zum anderen aber auch, wenn Konvektion in der Gasphase eine Rolle spielt, wie bei der Injektion von Trocknungsluft in einen Spalt des porösen Materials [98]; dann wird das Vordringen der Gasphase durch das Druckfeld beeinflusst, zudem werden einzelne Flüssigkeitscluster schneller erodiert.

3.1 Vorstellung des Basismodells

Im Folgenden wird das Basismodell zur Beschreibung der Trocknung von Porennetzwerken vorgestellt, sowohl bezüglich der Rechengesetze als auch hinsichtlich der Form der Simulationsergebnisse. Es basiert auf dem Modell von Prat [59] und ist ausführlich in [G] und [a] erklärt.
Das Basismodell beschreibt den Stofftransport unter isothermen Bedingungen. Der Dampftransport in der Gasphase erfolgt durch molekulare Diffusion. Die Kapillarströmung wird als ideal angenommen, Porenflüssigkeit kann also ohne Reibungsverlust oder Gravitationseffekt von großen in kleine Poren fließen.
Im Regelfall ist das Porennetzwerk je nach Dimensionalität ein quadratisches bzw. kubisches Gitter, dessen Knoten durch zylindrische Poren mit verteiltem Radius r_{ij}, aber konstanter Länge L miteinander verbunden sind (siehe Abbildung 27). Das anfangs voll gesättigte Netzwerk ist zu einer Seite hin offen und wird von dort getrocknet, in der graphischen Darstellung ist dies stets die obere Seite. Um Effekte aufgrund der begrenzten Netzwerkgröße zu reduzieren, werden in lateraler Richtung häufig periodische Randbedingungen angesetzt, d.h. linke und rechte (in drei Dimensionen auch vordere und hintere) Netzwerkseite werden miteinander verbunden.

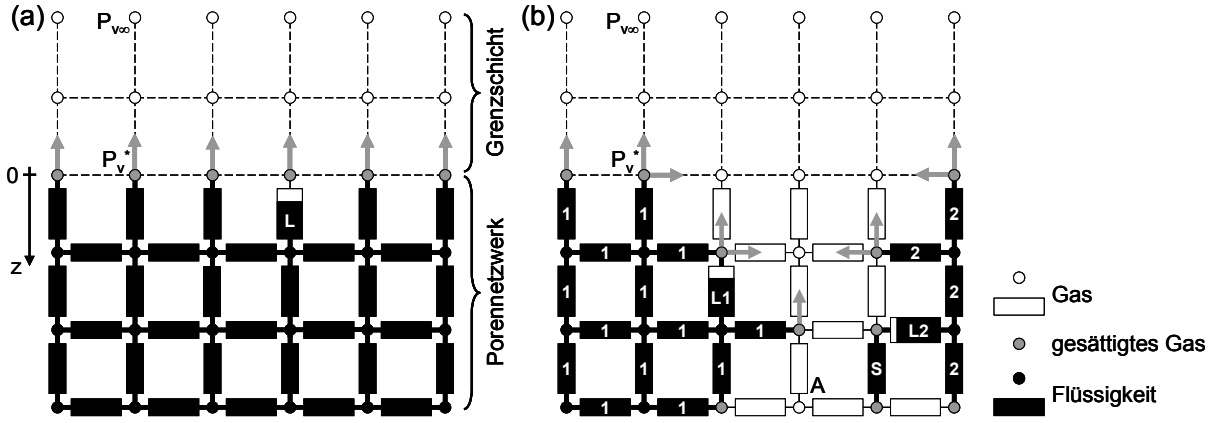

Abbildung 27. Porennetzwerk zur Erläuterung des Trocknungsmodells [a]. Alle Porenradien sind unterschiedlich, es werden jedoch nur die jeweils größten Poren der Phasengrenze (L, L1, L2) graphisch hervorgehoben.

Der gasseitige Dampftransport wird mit einer diskretisierten Grenzschicht beschrieben, um auch laterale Diffusion berücksichtigen und einen 1. Trocknungsabschnitt entsprechend den Überlegungen von Suzuki und Maeda [86] und Schlünder [71,72] abbilden zu können [C]. Laurindo und Prat haben in einer Untersuchung zu den Trocknungsraten zweidimensionaler Netzwerke [39] denselben Ansatz gewählt und die Grenzschichtdicke s experimentell vorgegeben. Allgemein wird man sie aus Korrelationen für den mittleren Stoffübergangskoeffizienten β bzw. die mittlere Sherwoodzahl Sh berechnen

$$s = \frac{\delta}{\beta} = \frac{L_{nw}}{Sh} \tag{25}$$

wobei δ der Diffusionskoeffizient ist und L_{nw} die charakteristische Länge des Netzwerks. (Diese Näherung berücksichtigt weder die Ortsabhängigkeit des Übergangskoeffizienten noch makroskopische Inhomogenitäten in der Oberflächensättigung, welche beide einen Einfluss auf den tatsächlichen Wärme- und Stoffübergang haben [49].)

Die Dampfdiffusion in der Gasphase (Grenzschicht sowie trockene Bereiche innerhalb des Netzwerks) kann in guter Näherung stationär gerechnet werden; dann addieren sich die Dampfmassenströme in jedem Knotenpunkt i zu Null:

$$\sum_j \dot{M}_{v,ij} = \sum_j A_{ij} \frac{\delta}{L} \frac{\tilde{M}_v P_g}{\tilde{R}T} \ln \frac{P_g - P_{v,i}}{P_g - P_{v,j}} = 0 \tag{26}$$

Die Summe läuft über alle Nachbarknoten j, und der Austauschquerschnitt A_{ij} zwischen zwei Knoten beträgt innerhalb des Netzwerks πr_{ij}^2 und in der Grenzschicht L^2. (Aufgrund der einseitigen Diffusion wird mit Stefan-Korrektur gerechnet.) Als Randbedingung wird in der Kernströmung $P_{v\infty}$ und an der Phasengrenze Sattdampfdruck P_v^* gesetzt. Aus dem Dampfdruckfeld berechnen sich dann die Verdunstungsraten für jede Pore an der Phasengrenze.

Zu Beginn der Trocknung befinden sich alle Grenzflächenporen an der Netzwerkoberfläche (siehe Abbildung 27a); sie sind alle durch Flüssigkeit miteinander verbunden und haben alle die gleiche Verdunstungsrate. Aufgrund des Kapillareffekts entleert sich aber nur die größte Pore (L), denn von dieser kann Flüssigkeit in alle anderen nachströmen. Die Zeit für die Entleerung dieser Pore ist durch ihr Volumen und die Gesamttrocknungsrate gegeben.

In dieser Weise entleert sich eine Pore nach der anderen in einem diskreten Prozess. Wegen der zufälligen Größenverteilung wird die Flüssigkeit schon bald in mehrere Cluster getrennt, und die weitere Entleerung schreitet in jedem Cluster unabhängig voran. Wesentlicher Bestandteil des Modells ist also die Clusterkennzeichnung; sie ist in einer Variante des Hoshen-Kopelmann-Algorithmus' umgesetzt [1,D], welche die Vorgeschichte effizient berücksichtigt [G,a]. Abbildung 27b zeigt ein teilgesättigtes Netzwerk mit zwei

Clustern sowie einer einzelnen Flüssigkeitspore (S). Diese ist – wie der gesamte Bereich um den Knoten A – von gesättigter Luft umgeben, also zeitweise von der Trocknung abgeschirmt. Die beiden Cluster trocknen entsprechend ihrer jeweiligen Gesamtverdunstungsrate weiter, es verliert dabei jeweils nur die größte Grenzflächenpore (L1 bzw. L2) Flüssigkeit. Sobald sich eine Pore des Netzwerks vollständig entleert, kann sich die Topologie der Flüssigkeit ändern, so dass die folgenden Schritte iterativ wiederholt werden müssen, bis das Netzwerk trocken ist:

1. Clusterkennzeichnung für aktuelle Flüssigkeitsverteilung;
2. Lösung der Dampfdiffusionsgleichung in der Gasphase;
3. Berechnung des (maximalen) Zeitschritts für jeden Flüssigkeitscluster aus Gesamtverdunstungsrate und Flüssigkeitsmenge in größter Pore an der Phasengrenze;
4. Aktualisierung der Phasenverteilung für kleinsten Clusterzeitschritt.

Als Ergebnis des Algorithmus erhält man eine Abfolge von Phasenverteilungen sowie dazugehörige Trocknungsraten bzw. Zeitschritte, aus denen die integrale Trocknungskurve berechnet werden kann. Abbildung 28 zeigt ein Beispiel für ein zweidimensionales Porennetzwerk mit periodischen Randbedingungen.

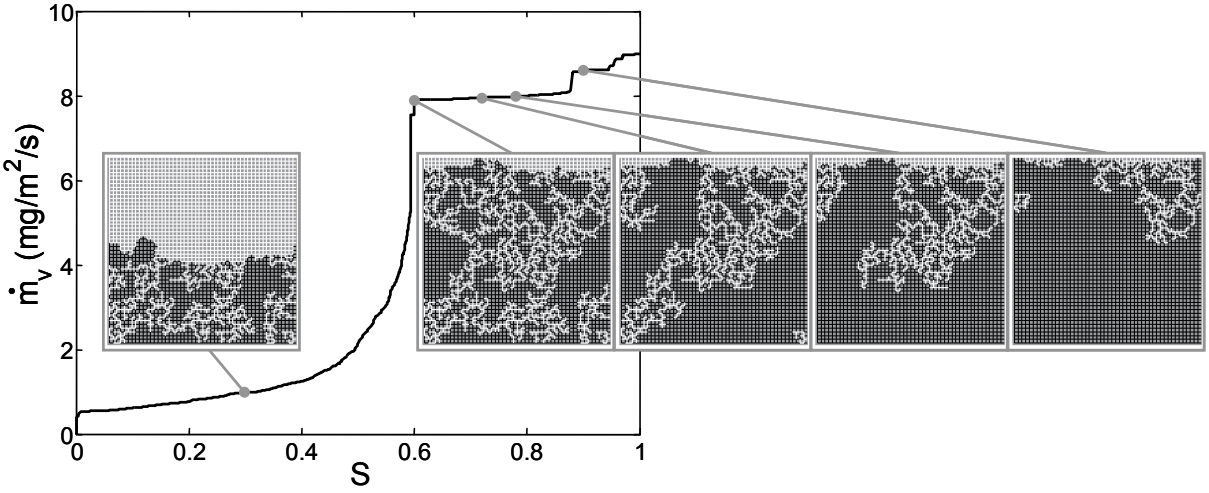

Abbildung 28. Phasenverteilungen und Trocknungskurve [a].

Man erkennt das Vordringen der Gasphase ins Netzwerk sowie die Auftrennung der Flüssigkeit in zahlreiche Cluster. Abhängig von der zufälligen Größenverteilung der Poren bleibt die Netzwerkoberfläche über einen weiten Bereich der Trocknung teilgesättigt, so dass die Trocknungsrate auf hohem Niveau verweilt. Erst wenn die Flüssigkeit in viele kleine Cluster zerfallen und die Oberfläche hydraulisch abgekoppelt ist, trocknet diese aus. Dieser Übergang in den 2. Trocknungsabschnitt ist begleitet von einem deutlichen Einbruch der Trocknungsrate (im Beispiel bei $S \approx 0.6$). Die Kapillarströmung wird als Hauptmechanismus des Stofftransports abgelöst von der Dampfdiffusion. Die Verdunstungsfront weicht ins Netzwerk zurück, während die Flüssigkeitscluster nacheinander von der offenen Seite her austrocknen (tiefer liegende Cluster bleiben temporär von der Trocknung abgeschirmt). Die Trocknungsrate sinkt dabei weiter ab, bis das Netzwerk bei endlicher Rate vollständig getrocknet ist, denn die Simulation berücksichtigt nur freie (und nicht adsorbierte) Flüssigkeit.

Es ist wichtig zu betonen, dass die räumliche Größenverteilung der Poren im Netzwerk zufällig ist und damit auch der Trocknungsverlauf. Das Beispiel in Abbildung 28 wurde zur einfachen zweidimensionalen Darstellung eines Prozessverlaufs gewählt, wie er nur für den dreidimensionalen (also realen) Fall typisch ist: nämlich Vordringen der Gasphase bis zum Durchbruch, dann Auftrennung der Flüssigkeit in viele kleine Cluster und hydraulische Abkopplung der Oberfläche, und schließlich das Zurückweichen der Front [42,102]. Fehlt die dritte Dimension, so führt das Eindringen der Gasphase verstärkt zur Clusterbildung; die Netzwerkoberfläche wird also meist vor dem Gasdurchbruch hydraulisch abgekoppelt.

Häufig bildet sich eine Region kleiner Flüssigkeitscluster aus, die den dahinter liegenden Hauptcluster zeitweise abschirmt; effektiv bewirkt dies eine Stabilisierung der Frontbreite.

Um trotz zufälliger Variationen die charakteristischen Merkmale des Trocknungsverhaltens identifizieren zu können, werden Porennetzwerksimulationen nach dem Monte-Carlo-Prinzip wiederholt. Dabei zeigt sich für zweidimensionale Netzwerke eine große Streuung bei den Trocknungskurven [G]; dreidimensionale Netzwerke weisen hingegen eine deutlich geringere Varianz in der Trocknungskinetik auf. Eine Auswertung der auftretenden Phasenverteilungen ist nur in Form von Sättigungsprofilen sinnvoll. Zur Darstellung des typischen Verhaltens werden die Profile aller Trocknungssimulation für vorgegebene Werte der Netzwerksättigung (nicht der Zeit!) gemittelt. Abbildung 29 zeigt die Ergebnisse für quadratische sowie kubische Netzwerke in normierter Darstellung. Die Rolle der Dimensionalität wird hier sehr deutlich: dem kubischen Netzwerk kann im Volumen und ohne signifikanten Gradienten Flüssigkeit entzogen werden, bevor die kleinen Flüssigkeitscluster mit scharfer Front austrocknen. Das quadratische Netzwerk hingegen trocknet an der Oberfläche früh aus, die Gasphase bricht spät durch, und das komplexe Wechselspiel zwischen dem Vordringen der Gasphase in den Hauptcluster und dem Austrocknen kleiner oberflächennaher Cluster führt in der Mittelung zu einem deutlichen Sättigungsgradienten.

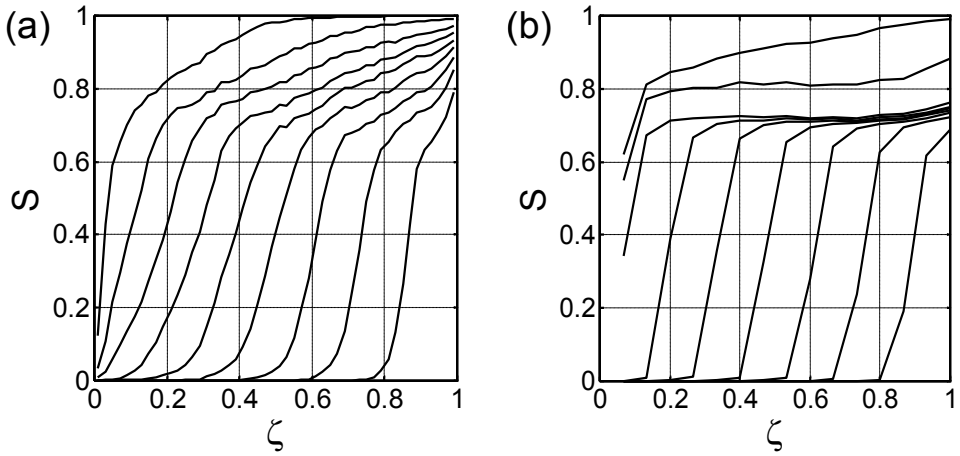

Abbildung 29. Gemittelte Sättigungsprofile aus Monte-Carlo-Simulationen für (a) quadratische bzw. (b) kubische Porennetzwerke [G].

Neben der Entwicklung der Phasenverteilungen soll auch die Gestalt der Trocknungskurve kommentiert werden. Im Beispiel von Abbildung 28 ist die relative Grenzschichtdicke so groß (s = 100 L), dass die Trocknungsrate aufgrund der lateralen Dampfdiffusion fast konstant bleibt, solange die Netzwerkoberfläche teilgesättigt ist: ein 1. Trocknungsabschnitt ist klar identifizierbar, egal ob dieser über die Rate oder die Oberflächensättigung definiert wird. Für kleinere Grenzschichtdicke ist ein deutliches Absinken der Rate mit abnehmender Oberflächensättigung zu beobachten [a,42]; dann ist auch die räumliche Verteilung der flüssigkeitsgefüllten Oberflächenporen entscheidend, insbesondere sind gleichmäßig verteilte Verdunstungszentren günstiger [C]. Im Grenzfall verschwindender Grenzschicht-dicke ($s \rightarrow 0$) und bei Vernachlässigung des Dampftransports durch trockene Poren ist die Trocknungsrate proportional zur Oberflächensättigung.
Auf die Phasenverteilungen hat der Dampftransport in der Grenzschicht kaum einen Einfluss; daher sind diese im Basismodell nahezu unabhängig von der Trocknungsgeschwindigkeit.

Vergleicht man eigene [F,G,I] und fremde [42,102] Trocknungssimulationen an dreidimensionalen Porennetzwerken mit experimentellen Arbeiten aus der Literatur, so stellt man fest, dass entscheidende reale Phänomene dargestellt werden können. Insbesondere die Möglichkeit des gradientenfreien Kapillartransports während des 1. Trocknungs-abschnitts, wie er von Krischer (S. 297 in [36]) und Coussot [13] in abstrahierten Sättigungsprofilen angenommen wird, ist durch die Darstellung des Porenwassers mittels

kernmagnetischer Resonanz eindrucksvoll belegt worden: durch Dicoi et al. [21] in Messungen an Gasbeton, durch van der Heijden et al. für die Trocknung gebrannten Ziegels [91] und durch Faure und Coussot [24] für Kaolin.
Die fraktale Struktur der Trocknungsfront und die Flüssigkeitscluster wurden mit Neutronenabsorption für grobkörnige Sandschüttungen in Hele-Shaw-Zellen von Shokri et al. [81] experimentell dargestellt. Xu et al. [27] haben die Trocknung kolloidaler Suspensionen mit konvokaler Lasermikroskopie dreidimensional dargestellt. Nachdem die Mikropartikel eine Packungsstruktur ausbildeten, konnten diese Autoren den Prozess der Invasionsperkolation direkt beobachten; dabei entleerten sich jedoch häufig ganze Porenregionen, begleitet von einer geringfügigen Umverteilung der Flüssigkeit entlang der restlichen Phasengrenze.

3.2 Porennetzwerkmodelle in der Literatur

Bevor die Anwendung des Basismodells auf unterschiedliche Porenstrukturen diskutiert wird, soll eine Einordnung in andere Literaturarbeiten gegeben werden, die die Beschreibung von Trocknungsphänomenen mit Porennetzwerkmodellen zum Ziel haben.

Daian und Saliba [16] waren 1991 die ersten, die auf diesem Gebiet tätig wurden. Sie haben das Porennetzwerk als repräsentatives Volumenelement angesehen, die Phasenverteilung mit Methoden der Invasionsperkolation gewonnen und dann – als Funktion der Sättigung – einen effektiven Diffusionskoeffizienten für den kombinierten Dampf- und Flüssigkeitstransport berechnet. Dieser Parameter war für den Einsatz in einem einfachen Kontinuumsmodell bestimmt. Im Modell von Daian und Saliba besteht der Porenraum aus kugelförmigen Poren, die durch zylindrische Poren untereinander verbunden sind. In ihrer Analyse stellten sie fest, dass es insbesondere bei der Befeuchtung des Netzwerks darauf ankommt, ob den Knoten eine Pore mit einer definierten Größe zugeordnet wird oder nicht. Entsprechend der Zielsetzung berichten die Autoren nicht über Phasenverteilungen oder Trocknungskurven.
Nowicki et al. [52] simulierten 1992 die Trocknung von 30×30 Netzwerken aus bikonischen Poren; ergänzend zum oben diskutierten Basismodell wird auch die Flüssigkeitsreibung berücksichtigt (siehe auch 4.1). Auch diese Autoren interessierte nicht das Trocknungsverhalten des gesamten Netzwerks, als Repräsentant eines porösen Körpers. Stattdessen wurden Stoffströme und Gradienten in Zustandsvariablen für kleine Unterbereiche des Netzwerks ausgewertet, um Flüssigpermeabilität und effektiven Diffusionskoeffizient für eine Kontinuumsbeschreibung zu berechnen. Außerdem wird der Zusammenhang zwischen Sättigung und Kapillardruck bzw. Dampfdruck während der Trocknung graphisch dargestellt; die gewonnenen Kurven hängen jeoch davon ab, in welcher Tiefe des Netzwerks die Auswertung stattfindet.
Bei beiden Arbeiten handelt es sich um singuläre Beiträge; die jeweiligen Autoren haben ihre Tätigkeit auf dem Forschungsgebiet nicht weitergeführt.

Im Jahr 1993 veröffentlichte Prat sein Trocknungsmodell [59] und hat es seitdem kontinuierlich weiterentwickelt. Die Verbindungen im Netzwerk sind Poren mit rechteckigem Querschnitt, und der offene Bereich um jeden Knotenpunkt wird zu einer eigenen Volumeneinheit zusammengefasst. Das Porennetzwerk wird hier auf der Produktebene betrachtet, und nicht als ein kleiner repräsentativer Ausschnitt. Entsprechend werden Phasenverteilungen dargestellt, Frontstruktur und Flüssigkeitscluster charakterisiert und Trocknungsraten berechnet, zunächst für zwei Dimensionen [60], später auch für ein kubisches Netzwerk [42].
Der Vergleich mit Experimenten an Mikromodellen bestätigt grundsätzlich die simulierten Flüssigkeitsverteilungen [38], die Trocknungszeiten werden in den Simulationen jedoch um ein Mehrfaches überschätzt [39]. Als Grund dafür konnten Flüssigkeitsfilme in den Kanten der Poren nachgewiesen werden [39], welche die hydraulische Kontinuität zwischen den Flüssigkeitsclustern und der Netzwerkoberfläche aufrechterhalten können.

Schon zu Beginn untersucht Prat den Einfluss der Gravitation auf Phasenverteilungen und Trocknungskinetik [38,39,59,60], später auch die Auswirkungen von Flüssigkeitsreibung [61] und Wärmetransport [30,57], die in Kapitel 4 weiter besprochen werden. Außerdem stellt er eine Modellerweiterung für die Verdunstung binärer Flüssigkeitsgemische aus einem Porennetzwerk vor [26].

Um 2000 werden Yiotis et al. in der Porennetzwerkmodellierung der Trocknung aktiv [98]. Ihr Netzwerk besteht aus kugelförmigen Poren; den zylindrischen Verbindungen zwischen diesen wird kein Volumen zugeordnet, sie dienen nur als Kapillarbarrieren bzw. zur Berechnung von Stofftransportwiderständen auf der Porenebene. Das Trocknungsmodell berücksichtigt Reibungseffekte in Gasphase und Flüssigkeit. Wie bei Prat wird das Trocknungsverhalten des gesamten Netzwerks als Abstraktion einer porösen Struktur analysiert. Als wichtiger Beitrag von Yiotis et al. zur Modellentwicklung ist die Beschreibung des Filmtransports in den Kanten von nicht zylindrischen Poren zu sehen [99-101]. Unter vereinfachenden Annahmen und durch geschickte Variablentransformation können sowohl Dampfdiffusion als auch kapillarviskoser Filmtransport – also der gesamte Stofftransport in der gasbefüllten Netzwerkregion – mit einer Laplace-Gleichung dargestellt werden. Im Ergebnis führen Filme dazu, dass den Flüssigkeitsclustern eine Filmregion vorgelagert ist und die Verdunstungsfront dadurch näher an die Netzwerkoberfläche rückt (Abbildung 30). Dies kann insbesondere die von Prat beobachteten hohen experimentellen Trocknungsraten erklären.

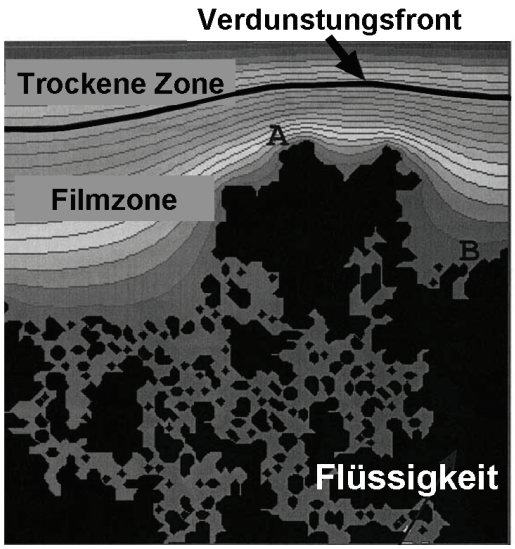

Abbildung 30. Auswirkungen des Filmtransports auf die Trocknung [100].

Ein weiterer wichtiger Beitrag von Yiotis et al. ist die Trocknungssimulation für ein großes Netzwerk (80×80×80) mit dem Basismodell, also ohne viskose Effekte und Filme, jedoch mit gasseitiger Grenzschicht [102]. Hier wird der gradientenfreie Entzug von Porenflüssigkeit bis zu einer Netzwerksättigung von $S \approx 0.4$ dokumentiert, bevor die Trocknungsfront zurückweicht. Dieses Niveau ist sehr niedrig im Vergleich zu eigenen und von Prat publizierten Ergebnissen und resultiert aus der Größe des Netzwerks – und eventuell auch aus der unterschiedlichen Porengeometrie. Entsprechend den eigenen Untersuchungen haben auch Yiotis et al. [102] die Rolle der (Dicke der) gasseitigen Grenzschicht für das Auftreten eines klaren 1. Trocknungsabschnitts diskutiert und dabei auf Schlünder Bezug genommen [72].
Zuletzt soll eine Analyse von Yiotis et al. zum Verhältnis gasseitiger und netzwerkseitiger Transportwiderstände [103] erwähnt werden. In der Grenzschicht werden Diffusion (und auch Konvektion) beschrieben und an die Netzwerkberechnung von Diffusion und Filmtransport gekoppelt. Die Ergebnisse werden auf der Grundlage einer filmbasierten Kapillarzahl und der Grenzschichtdicke (räumlich konstant) diskutiert. Entscheidend für Existenz und Dauer eines 1. Abschnitts mit konstanter Trocknungsrate ist demnach nicht, ob

hinreichend viele Oberflächenporen (voll)gesättigt bleiben, sondern vielmehr, ob sich die Filmregion bis zur Oberfläche erstreckt. Eine dicke Grenzschicht kann eine inhomogene Oberflächensättigung besser ausgleichen; und eine kleine Film-Kapillarzahl ermöglicht eine größere Filmregion. Bei vorgegebener Trocknungsrate kann die Film-Kapillarzahl durch die stoffabhängigen Größen σ und η sowie Porengröße r und Porenquerschnittsgeometrie beeinflusst werden.

In neueren Arbeiten wurde auch Prat in der Erforschung der Filmeffekte aktiv: einerseits in der präzisen theoretischen [8] und experimentellen [11] Untersuchung der Verdunstung aus einer einzelnen Kapillare quadratischen Querschnitts; andererseits bezüglich des Einflusses von Porenquerschnitt und Kontaktwinkel auf die Trocknung von Porennetzwerken [63]. Die im letzteren Fall betrachteten Porenquerschnitte sind regelmäßige Polygone. Je mehr Ecken das Polygon besitzt, d.h. je kleiner die Winkel in diesen Ecken sind (und desto näher man der Kreisform kommt), desto ungünstiger ist dies für den Filmtransport. Außerdem gibt es für jedes Polygon einen kritischen Kontaktwinkel, unterhalb dessen keine Filme existieren können. Aus diesen Gründen kann – in Abhängigkeit vom Porenquerschnitt und für ansonsten identische Netzwerke – der Trocknungsprozess sehr unterschiedlich verlaufen: für bestimmte gasseitige Bedingungen und Kontaktwinkel kann für dreieckige Poren aufgrund des Filmtransports das gesamte Netzwerk mit der anfänglichen Rate trocknen, für hexagonale Poren hingegen gibt es gar keine Filme und daher auch keinen 1. Trocknungsabschnitt [63].
Des Weiteren untersuchte Prat den Einfluss des Kontaktwinkels bis in den hydrophoben Bereich ($\theta > 90°$) [10,12]. Im Porennetzwerk gelten dann andere Regeln für die Porenentleerung, denn nun ist die eindringende Gasphase benetzend; und die Phasenverteilungen sind von einer scharfen Trocknungsfront geprägt [10]. Auch für eine leicht veränderte Porenraumgeometrie (feste Phase als regelmäßig angeordnete Kreise mit Größenverteilung) wird der Übergang zu hydrophoben Bedingungen untersucht – mit sehr ähnlichem Ergebnis: für kleine Kontaktwinkel ($\theta < 90°$) trocknet das Netzwerk mit einer fraktalen Phasengrenze, die durch die zufällige Porengrößenverteilung bestimmt wird, und entsprechend ist auch die Kinetik zufällig; für große Kontaktwinkel ($\theta > 100°$) wird die Front scharf und die Trocknung streng deterministisch.
Obwohl Filmeffekte und der Einfluss des Kontaktwinkels in der Praxis eine wichtige Rolle spielen können, sollen sie in dieser Arbeit nicht weiter untersucht werden. Dies ist theoretisch gerechtfertigt durch eine Beschränkung auf zylindrische Poren sowie durch das Ziel, die Rolle der Kapillarströmung zu charakterisieren, wie sie nur im hydrophilen Fall auftritt. Einflüsse der Porenstruktur sollen insofern untersucht werden, als die Struktur des Netzwerks variiert wird, nicht jedoch die Geometrie der einzelnen Porenelemente.

Neben den wegweisenden Arbeiten der Forschungsgruppen um Prat und Yiotis sind auch die wesentlichen Veröffentlichungen von Segura zu nennen [73-75]. Das dort verwendete Netzwerkmodell unterscheidet sich von den bisher besprochenen. In einem Zeitschritt werden jeweils ganze Porenbereiche entleert, im Sinne einer allmählichen Erhöhung des Invasionsdrucks (bzw. der Krümmung der Flüssigkeitsgrenzfläche). Es wird postuliert (nicht berechnet), dass Filme in den Porenkanten für hydraulische Kontinuität im gesamten Netzwerk sorgen; deren Dicke nimmt jedoch entsprechend der globalen Krümmungsänderung ab – und damit ihre hydraulische Leitfähigkeit. Entsprechend gibt es beim Stofftransport einen Übergang von der Flüssigkeitsabfuhr durch Filme zur Dampfdiffusion durch trockene Poren [75]. Für die Berechnung der Zeitschritte im Trocknungsprozess wird der jeweils dominierende Prozess gewählt. Die Filme erhöhen die Trocknungsraten, so dass Segura die experimentellen Trocknungskurven von Prat [39] gut reproduzieren kann [75]. Auch den Einfluss der Gravitation auf das Trocknungsverhalten untersucht Segura [73], mit ähnlichem Ergebnis wie Prat. Kritisch anzumerken ist, dass der Einfluss von Reibungseffekten auf die Phasenverteilung (hinsichtlich der Flüssigkeitscluster und auch in den Filmen) nicht hinreichend abgebildet wird, denn jederzeit wird kapillares Gleichgewicht angenommen.

In den Untersuchungen werden unterschiedliche polygonale Porenquerschnitte und Porengrößenverteilungen betrachtet, wobei im dargestellten Bereich die Trocknungskinetik von beiden Charakteristika im Wesentlichen unabhängig ist [73]. Für die Phasenverteilungen aus der Trocknungssimulation werden effektive Parameterfunktionen für die Kontinuumsbeschreibung von Dampfdiffusion und viskoser Flüssigkeitsströmung bestimmt; diese Vorgehensweise erscheint fragwürdig, denn beide Phänomene sollten bei den dargestellten Trocknungssimulationen nur eine untergeordnete Rolle spielen [73].
Zuletzt berücksichtigt Segura in einfacher Weise auch die durch den Kapillardruck induzierte Schrumpfung der Poren [74]: (nur) die Radien der Poren an der Phasengrenze verringern sich linear mit zunehmendem Kapillardruck, die Porenlänge bleibt unverändert – und damit auch die Netzwerkgröße. Daher verläuft die Trocknung langsamer und die effektiven Transportparameter haben kleinere Werte. Der positive Einfluss verringerter Distanzen für den Stofftransport wird in dieser Beschreibung nicht berücksichtigt.

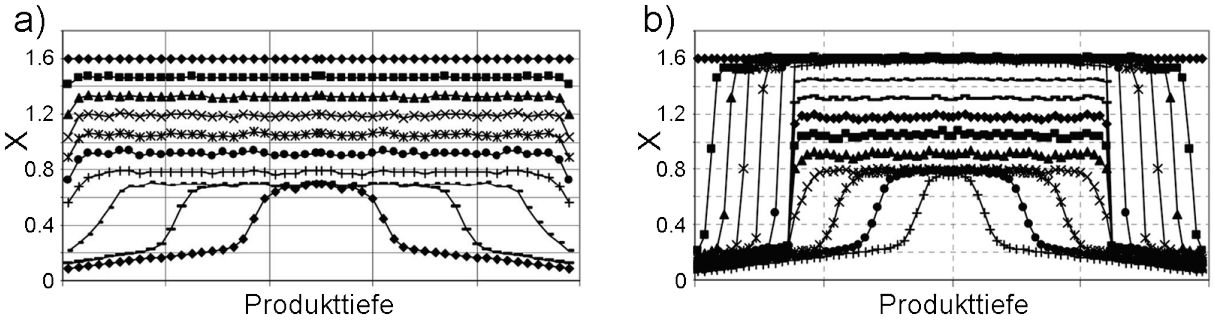

Abbildung 31. Feuchteprofile für beidseitig getrocknete Netzwerke aus hexagonal-rechteckigen Fasern zur Beschreibung der Trocknung von Holz: (a) 60×60×98 Netzwerk mit intakter Oberfläche, (b) 30×30×158 Netzwerk mit beschädigter Oberfläche [68].

Sehr anwendungsnah hat Salin ein Porennetzwerkmodell für die Trocknung von Holz (genauer: Splintholz von Weichholz) entwickelt [68]. Dieses ist dem Basismodell sehr ähnlich, berücksichtigt aber wesentliche Aspekte der Fasergeometrie und bildet die Anisotropie im Stofftransport ab. Um Randeffekte zu minimieren, wird ein lateral periodisches 60×60×98 Netzwerk von beiden Seiten getrocknet. Eindrucksvoll kann so der über einen weiten Bereich gradientenfreie Entzug von Wasser dargestellt werden (siehe Abbildung 31a). Mit einem inhomogenen Porennetzwerk untersucht Salin zudem qualitativ den Einfluss verarbeitungsbedingter Schädigungen der Oberfläche (in Form von Rissen); aufgrund lokal vergrößerter Poren trocknet dann eine oberflächennahe Schicht zunächst vollständig aus, bevor dem Kernbereich – mit verringerter Rate – Wasser entzogen werden kann (siehe Abbildung 31b).
Auch Salin berechnet aus den Phasenverteilungen effektive Transportgrößen für Dampf- und Flüssigkeitstransport, was wie bei Segura inkonsistent erscheint, spielen doch Reibungseffekte im Trocknungsmodell gar keine Rolle. Zuletzt erweitert Salin sein Modell um den Filmtransport, wodurch die gradientenfreie Phase der Trocknung verlängert wird.

Xiao et al. [96] haben die Trocknung von Kartoffeln, als Modellsubstanz für Agrarprodukte, mit einem zweidimensionalen Porennetzwerkmodell beschrieben. Der Trocknungsalgorithmus ist dem Basismodell sehr ähnlich, berücksichtigt aber zudem Wärmeleitung sowie Wärmesenken an der Verdunstungsfront. Originell ist das fraktale, also selbstähnliche, Porennetzwerk; dieses wurde auf der Grundlage von Porengrößenverteilung und fraktaler Dimension der Porenflächen generiert, welche beide aus bildtechnisch verarbeiteten Probenquerschnitten ermittelt wurden. Eine geometrische Ähnlichkeit zwischen experimenteller Probe und Netzwerk ist allerdings nicht zu erkennen. Die Autoren vergleichen die experimentelle Feuchte- und Temperaturverteilung mit Netzwerksimulationen und schlussfolgern (leider wenig nachvollziehbar), dass der reale Prozess durch das fraktale Netzwerk besser abgebildet werde als durch ein einfach quadratisches. Bei diesem

Vergleich ist zudem fraglich, ob das Fehlen der dritten Dimension für die Simulationen nicht eine zu große Einschränkung bedeutet.

Debaste untersucht die Trocknung von Hefegranulaten in der Wirbelschicht [17-20]. Er entwickelt hierzu ein Porennetzwerkmodell, das neben dem Filmtransport auch viskose Effekte in der Kapillarströmung beschreibt. Es entleeren sich also nicht nur die größten Poren sondern auch solche, in denen Flüssigkeit nicht entsprechend der lokalen Verdunstungs- bzw. Filmtransportrate nachströmen kann (siehe auch 4.1). In der konkreten Anwendung spielt diese Reibungshemmung jedoch eine untergeordnete Rolle; der Filmeffekt hingegen ist entscheidend und sorgt für einen langen 1. Trocknungsabschnitt.
Originell an der Arbeit ist das skalenübergreifende Vorgehen: einerseits koppelt Debaste das Netzwerkmodell an ein Wirbelschichtmodell [19] (und simuliert für ein mittleres Prozessverhalten einige Granulate parallel [18]), andererseits versucht er, das Porennetzwerk aus röntgentomographischen Daten der Hefe zu generieren [20]. Letztlich muss sich Debaste in den Simulationen aber mit zweidimensionalen quadratischen Netzwerken (~ 4000 Poren) begnügen, für die zudem nur die Radienverteilung den Tomographiedaten entsprechend gewählt wird [18]. Kritisch anzumerken ist auch die Anpassung eines Modellparameters [18], der den Filmtransport – und damit wesentliche Aspekte des Gesamtprozesses – kontrolliert. In ihrem Anspruch hat die Arbeit wegweisenden Charakter, eine vollständige Umsetzung des Mikro-Makro-Übergangs ist allerdings noch auf weitere Forschung angewiesen.

Abschließend sollen zwei Arbeiten zitiert werden, in denen Porennetzwerke zwar für die Beschreibung von Trocknungsprozessen verwendet werden, die aber qualitativ andere Effekte erfassen. Im Modell von Prachayawarakorn et al. [58] erfolgt Feuchtetransport im Netzwerk nur durch Diffusion; Kapillareffekte werden nicht berücksichtigt. Entsprechend variiert mit der Porengröße nur der lokale Transportwiderstand; und dieser ist in kleinen Poren größer. Zunächst ordnen die Autoren den einzelnen Poren im zweidimensionalen Netzwerk ihre Größe entsprechend einer vorgegebenen Dichteverteilung zufällig zu. Hierfür finden sie, dass bei breiter (und auch bimodaler) Porengrößenverteilung die kleinen Poren die Dampfdiffusion stärker behindern, wodurch die Trocknungszeit länger wird – ganz im Gegensatz zu den in dieser Arbeit vorgestellten Ergebnissen (siehe unten). Die Autoren betrachten schließlich auch eine räumlich korrelierte Variation der Porengröße: erwartungsgemäß trocknet ein Porennetzwerk schneller, wenn die Poren zur Oberfläche hin größer werden.

Chang et al. [9] untersuchen die Trocknung von ruhenden Getreideschüttungen. Hier wird das Volumen zwischen den Getreidekörnern durch ein zweidimensionales Porennetzwerk repräsentiert. Entsprechend spielt Kapillarität wieder keine Rolle; mit dem Netzwerk werden konvektiver Feuchte- und Enthalpietransport in der Gasphase beschrieben. Die Schüttung wird durch abstrahierte, auf einem Gitternetz verteilte Getreidekörner dargestellt, deren interner Stofftransport mit einem Diffusionsmodell beschrieben wird. Die Oberflächenfeuchte bestimmt den Stoffübergang in die Gasphase; die zeitliche Entwicklung der mittleren Partikeltemperaturen ergibt sich aus dem Wärme- und Stoffaustausch.
Chang et al. betrachten relativ breit verteilte Poren- und Partikelgrößen, die zudem unabhängig voneinander gewählt zu sein scheinen. Für Verteilungen mit größerer Standardabweichung finden die Autoren längere Trocknungszeiten bis zum Erreichen der gewünschten mittleren Feuchte sowie eine stärkere lokale Streuung der Einzelkornfeuchte. Die Arbeit ist nicht nur wegen des hohen Abstraktionsgrades kritisch zu bewerten: der Korndurchmesser wird in der Realität selten um den Faktor drei variieren, so dass die betrachteten Effekte künstlich erscheinen; und die eigentliche Problematik der Festbett-Trocknung liegt doch eher in der – deterministischen – räumlichen Variation der Endfeuchte, verbunden mit der systematischen Übertrocknung ganzer Bereiche der Schüttung.

3.3 Anwendung auf unterschiedliche Porenstrukturen

Nach diesem Literaturüberblick wird nun das Basismodell benutzt, um Struktureinflüsse zu untersuchen. Zunächst soll für Netzwerke mit bimodaler Porengrößenverteilung die Rolle der Makroporen beleuchtet werden [G]. (Der Einfachheit halber werden hier die Begriffe „Mikroporen“ und „Makroporen“ verwendet; gemäß UPAC-Definition handelt es sich aber bei beiden Porenklassen um Makroporen.)
Legt man dem Porennetzwerk eine bimodale Radienverteilung zugrunde, so ist entscheidend, wie die Makroporen im Netzwerk verteilt sind. Werden die Radien der beiden Moden den Poren ohne räumliche Korrelation zugeordnet, so unterscheidet sich das Netzwerk hinsichtlich der Trocknung nicht wesentlich von einem monomodalen Netzwerk. Dies soll kurz erläutert werden: solange Reibungseffekte für die Kapillarströmung vernachlässigbar sind, ist die Reihenfolge der Porenentleerung durch die *relative* Porengröße bestimmt; ob die Radienverteilung schmal oder breit ist, oder gar bimodal, spielt nahezu keine Rolle für den Trocknungsverlauf. Nur die Dampfdiffusion wird durch die Verteilungsbreite beeinflusst (siehe [58]), so dass die Verdunstungsraten der einzelnen Cluster leicht verändert werden – und damit auch Details der Phasenverteilungen bzw. der Trocknungskurve.
In Abbildung 32 sind dem monomodalen Netzwerk Repräsentanten der drei grundsätzlich möglichen bimodalen Varianten gegenübergestellt:

1) Im ersten Netzwerk sind die einzelnen Makroporen in langen Kanälen angeordnet, die sich über die gesamte Netzwerktiefe erstrecken; soweit dies in zwei Dimensionen möglich ist, bilden sie eine kontinuierliche „Phase“, ebenso wie die Mikroporen.
2) In der zweiten Variante sind nur die Makroporen kontinuierlich: ein Gitter aus Makrokanälen teilt die Mikroporen in separate Bereiche auf; dieser Fall kann als Abstraktion eines Agglomerats aus mikroporösen Partikeln gesehen werden.
3) Das dritte Porennetzwerk repräsentiert eine feinporige Matrix mit großporigen Einschlüssen; hier sind nur die Mikroporen kontinuierlich.

Alle drei Netzwerke haben dieselben makroskopischen Eigenschaften bezüglich Netzwerkgröße, Porosität und Porenradienverteilung (eine Kombination zweier Normalverteilungen, wobei der Volumenanteil der Makroporen bei 44 % liegt); sie unterscheiden sich nur hinsichtlich der räumlichen Korrelation der Makroporen. Das jeweilige Trocknungsverhalten hängt hiervon aber entscheidend ab und kann – mit Hilfe der Abbildungen 32 und 33 – wie folgt beschrieben werden:

1) Im ersten Netzwerk strömt zunächst die Flüssigkeit der Makrokanäle durch die Mikroporen an die Netzwerkoberfläche, wo sie mit der Rate des 1. Trocknungsabschnitts verdunstet, denn fast die gesamte Oberfläche bleibt gesättigt. Erst wenn alle Makroporen entleert sind (in zwei Dimensionen schon eher), beginnen auch die Mikroporen auszutrocknen. Ist schließlich die hydraulische Kontinuität unterbrochen (in zwei Dimensionen schon bald), so trocknen die entstandenen Cluster nach und nach mit zurückweichender Verdunstungsfront und stark absinkender Rate aus. Die Trocknungskurve dieses Netzwerks ist durch einen markanten 1. Abschnitt gekennzeichnet.
2) Auch für das zweite Netzwerk bleiben die Mikroporen zunächst gesättigt und die Trocknungsrate verharrt auf dem hohen anfänglichen Niveau. Durch die zufällige Entleerung der Makrokanäle werden die mikroporösen Netzwerkregionen aber nach und nach vom Hauptcluster abgekoppelt und trocknen ohne signifikante Kapillarströmung aus (deutlich für S = 0.75). Die Trocknungsrate sinkt früh ab, denn in dieser Weise werden jeweils ganze Oberflächenbereiche inaktiv. Der 1. Trocknungsabschnitt ist also zufälliger Natur und kann für dieses Netzwerk nicht als Charakteristikum gesehen werden. Global gesehen, trocknet das Netzwerk ähnlich wie das monomodale, wobei der zufällige Verlauf durch die Größenverteilung der Makroporen bestimmt wird.
3) Das dritte Porennetzwerk ist dem monomodalen am ähnlichsten. Der zufällige Prozess der Porenentleerung wird nur insofern verändert, als sich ein (kreuzförmiger) Cluster aus Makroporen stets komplett entleeren muss, sobald die Phasengrenze zu ihm

vorgedrungen ist. Die Trocknungskurve unterscheidet sich vom monomodalen Fall auch nur in ihrer zufälligen Ausprägung.

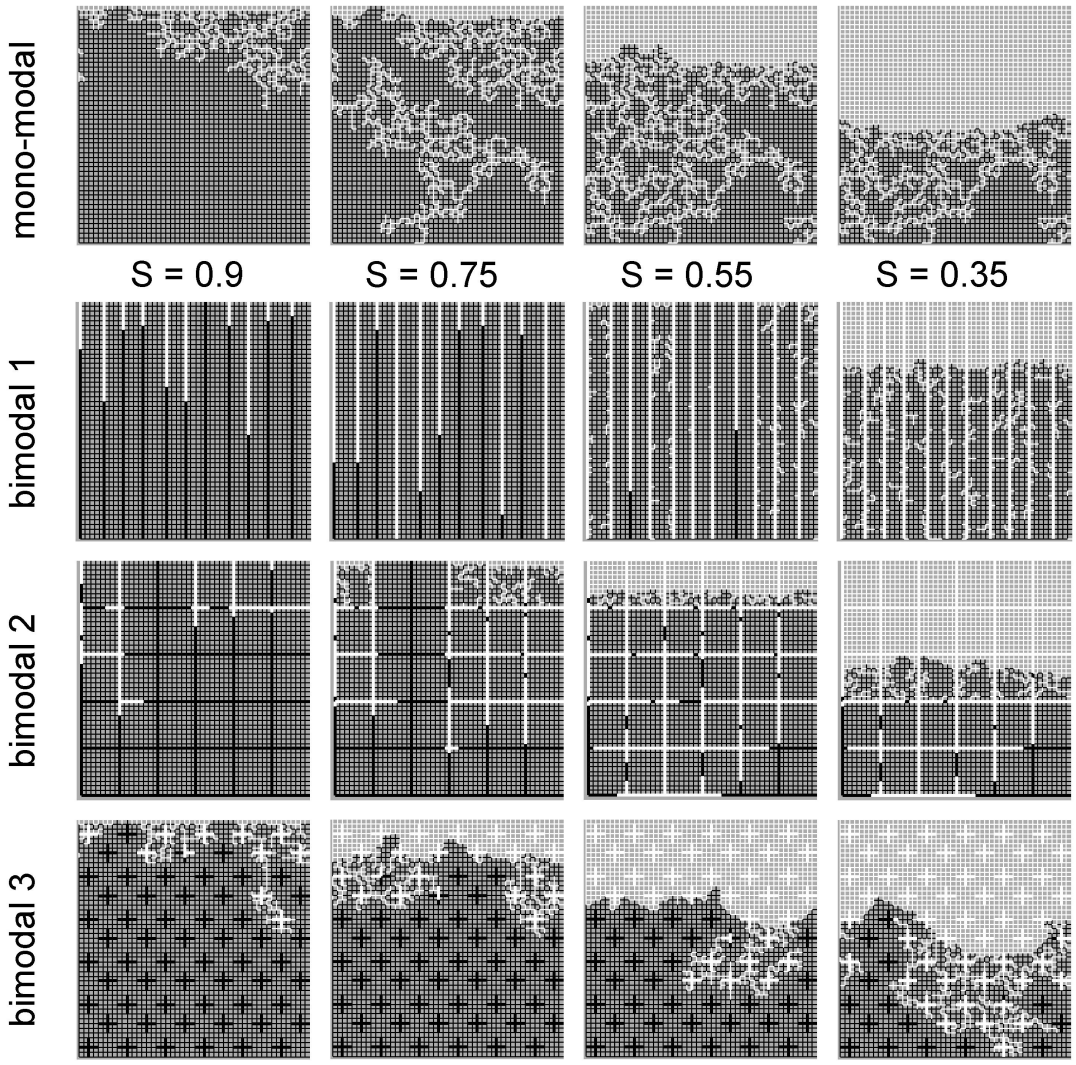

Abbildung 32. Phasenverteilungen in unterschiedlichen Netzwerkstrukturen [G].

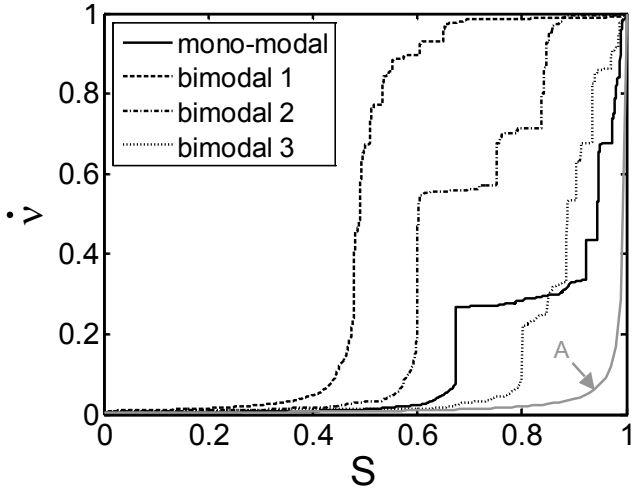

Abbildung 33. Dimensionslose Trocknungskurven für Netzwerke in Abbildung 32 (s = 10 L); Kurve A beschreibt den Fall eines scharfen Trocknungsspiegels, d.h. ohne Kapillareffekt [G].

Für den monomodalen Fall wurde ein günstiger Verlauf dargestellt. Die Phasenverteilungen sind mit den in Abbildung 28 gezeigten vergleichbar; aufgrund der (zehnmal) dünneren Grenzschicht unterscheidet sich aber die Trocknungskurve: die Rate sinkt bei teilgesättigter Oberfläche (bis $S \approx 0.7$) in stärkerem Maße ab. (Für diese gasseitigen Bedingungen lassen sich die netzwerkseitigen Effekte besser diskutieren.)

Die Kapillarwirkung in den unterschiedlichen Netzwerken kann bewertet werden, indem man die Trocknung mit unbeweglicher Porenflüssigkeit, also scharfem Trocknungsspiegel, berechnet. Kurve A in Abbildung 33 zeigt diesen ungünstigsten Verlauf, dessen Raten bereits durch zufällige Kapillarströmung – wie beim monomodalen und dritten bimodalen Netzwerk – deutlich übertroffen werden.
In Monte-Carlo-Simulationen für die vier Netzwerktypen [G] zeigt sich, dass bezüglich der Trocknungsraten gilt:

bimodal 1 > bimodal 2 > bimodal 3 > monomodal

Nur für das erste bimodale Netzwerk führt der Kapillareffekt aber zu einem reproduzierbaren 1. Trocknungsabschnitt; und die Trocknungskurve ist für diesen Fall nahezu deterministisch. Das zweite bimodale Netzwerk weist einen kurzen 1. Trocknungsabschnitt auf, dessen Dauer jedoch von der zufälligen Realisierung abhängt. Das dritte bimodale sowie das monomodale Netzwerk trocknen hingegen ohne 1. Abschnitt.
Gemittelte Sättigungsprofile für die beiden Extremfälle sind in Abbildung 34 wiedergegeben. Eine günstige Anordnung von Makroporen bewirkt also, dass das Netzwerk zunächst im Volumen Flüssigkeit verliert, bei nahezu konstant hoher Oberflächensättigung und mit abnehmendem Feuchtegradienten. Danach wandert eine relativ scharfe Trocknungsfront durch das Netzwerk hindurch. Das Porennetzwerk mit monomodaler Größenverteilung trocknet an der Oberfläche früh aus; das charakteristische Feuchteprofil wandert von Beginn an ohne wesentliche Veränderung durch das Netzwerk.

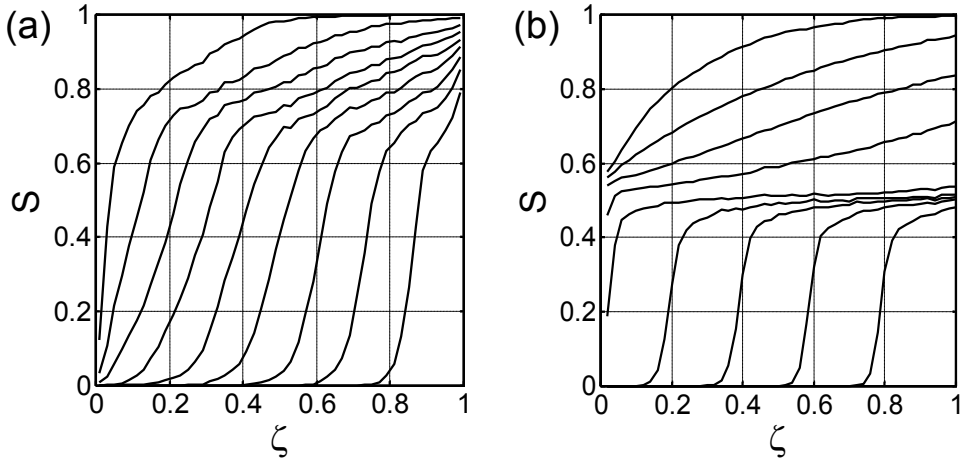

Abbildung 34. Gemittelte Sättigungsprofile aus Monte-Carlo-Simulationen mit zweidimensionalen Netzwerken gemäß Abbildung 32: (a) monomodal, (b) bimodal 1 [G].

Auch für kubische Netzwerke wurde der Einfluss von Makroporen (mit 26 % Volumenanteil) untersucht [B,F,G]. Dabei ist zu bedenken, dass der Kapillareffekt aufgrund der dritten Dimension schon bei monomodaler Porengrößenverteilung eine bedeutende Rolle spielt. Für die gewählte Grenzschichtdicke (s = 10 L), wird jedoch kein 1. Abschnitt mit konstanter Trocknungsrate beobachtet (siehe Abbildung 35).
Die Makroporen wurden hierfür in langen Kanälen angeordnet, entweder senkrecht zur Oberfläche oder als Netzwerk in drei Raumrichtungen (skizziert in Abbildung 35). Beide Typen sind jedoch im Grunde äquivalent (und entsprechen in zwei Dimensionen dem ersten Fall), denn die gesamte in den Makroporen enthaltene Flüssigkeit kann über die Mikroporen an die Netzwerkoberfläche strömen und dort verdunsten, bevor sich die erste Mikropore

entleert. Für diesen Ablauf ist entscheidend, dass jede Makropore von der Oberfläche her ausschließlich über Makroporen erreicht werden kann und dabei zugleich an die mikroporöse Phase angebunden ist, die das gesamte Netzwerk zusammenhängend durchdringen muss. Erwartungsgemäß sind die Trocknungskurven für beide Typen nahezu identisch, wie aus Abbildung 35 ersichtlich. Beide weisen einen 1. Abschnitt auf, in dem alle Makroporen austrocknen; danach sinkt die Rate erst leicht, dann stärker ab – entsprechend der teilweisen bzw. vollständigen Austrocknung der Netzwerkoberfläche.

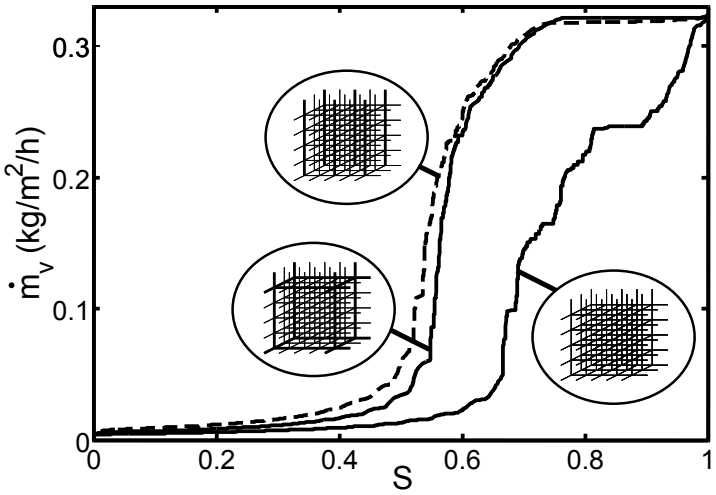

Abbildung 35. Trocknungskurven für 16×16×16 Netzwerke mit mono- bzw. bimodaler Porengrößenverteilung (mit schematischer Darstellung der Anordnung der Makroporen) [B].

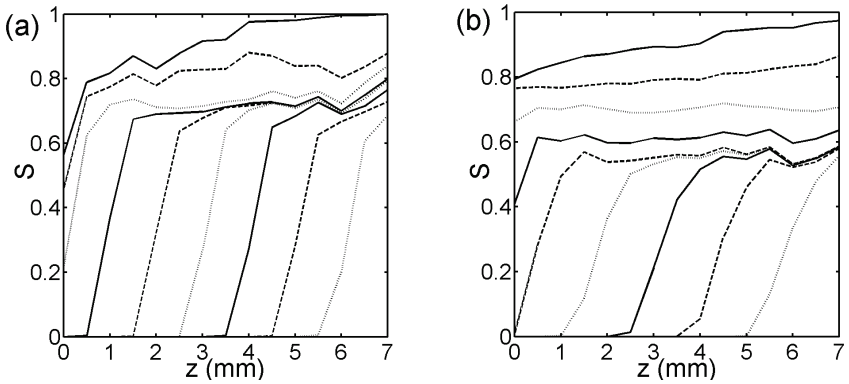

Abbildung 36. Sättigungsprofile zu Netzwerken aus Abbildung 35: (a) für monomodale Porengröße, (b) mit parallelen Makrokanäle senkrecht zur Netzwerkoberfläche [B].

Die Sättigungsprofile in Abbildung 36 zeigen, dass aufgrund der Makroporen mehr Flüssigkeit gradientenfrei aus dem Volumen entfernt werden kann (bis zu $S < 0.6$ statt nur bis $S \approx 0.7$), bevor die Front ins Netzwerk hineinwandert. Auch entsprechende Monte-Carlo-Berechnungen belegen dies [G].

Neben der Porengrößenverteilung ist auch die Netzwerktopologie eine wesentliche Struktureigenschaft. Hierzu wurde für regelmäßige Porennetzwerke der Einfluss der Koordinationszahl Z untersucht [G]. Diese beschreibt, mit wie vielen Nachbarn ein Knoten im Netzwerk direkt verbunden ist. Im Trocknungsalgorithmus entscheidet sie insbesondere, wie viele Flüssigkeitsverbindungen unterbrochen werden, wenn sich eine Pore – und damit auch der benachbarte Knoten – entleert. Es wurden Monte-Carlo-Simulationen sowohl für zwei- als auch für dreidimensionale Porennetzwerke durchgeführt. Die unterschiedlichen Netzwerktypen sollten sich jeweils nur in der Koordinationszahl unterscheiden; daher wurden einerseits Netzwerkabmessungen und Porengrößenverteilung (monomodal) gleich gewählt und andererseits dieselbe Porosität aufgeprägt. Letzteres bedingte eine Anpassung der

Porenlänge, wie man für den dreidimensionalen Fall in Abbildung 37 erkennen kann; im Resultat variierte die Gesamtzahl der Poren um einen Faktor drei (in zwei Dimensionen) bzw. zwei (in drei Dimensionen).
Für den zweidimensionalen Fall wurden hexagonale (Z = 3), quadratische (Z = 4) und trianguläre (Z = 6) Netzwerke betrachtet; die beobachteten Effekte zeigen allerdings keine klaren Tendenzen und lassen sich nur schwer interpretieren [G]. Hier sollen nur die relevanteren dreidimensionalen Ergebnisse dargestellt werden. Die untersuchten Netzwerkstrukturen sind in Abbildung 37 gezeigt.

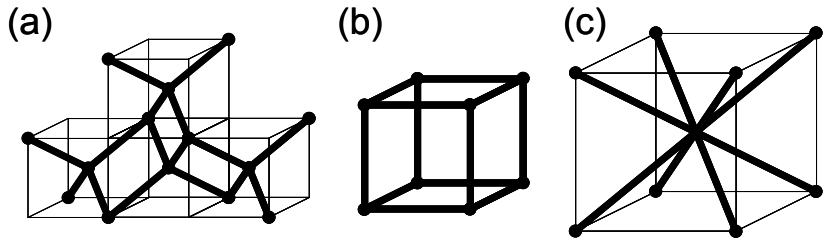

Abbildung 37. Einheitszellen der untersuchten dreidimensionalen Porennetzwerke mit Koordinationszahl (a) Z = 4, (b) Z = 6, (c) Z = 8 [G].

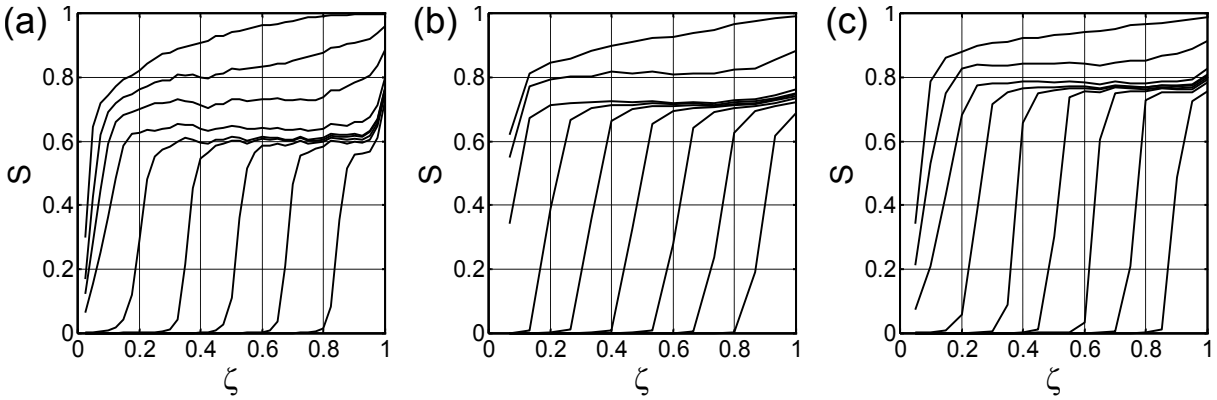

Abbildung 38. Gemittelte Sättigungsprofile für Monte-Carlo-Simulationen mit den in Abbildung 37 dargestellten Netzwerkstrukturen: (a) Z = 4, (b) Z = 6, (c) Z = 8 [G].

Der beobachtete Trend in den Sättigungsprofilen ist eindeutig: eine niedrigere Koordinationszahl erweist sich als günstiger für den Trocknungsverlauf, denn mehr Flüssigkeit kann gradientenfrei aus der Struktur entfernt werden – und je nach Grenzschichtdicke auch mit der hohen anfänglichen Trocknungsrate.
Für die tatsächliche Trocknungsrate bei teilgesättigter Oberfläche scheinen strukturelle Details eine Rolle zu spielen, die jedoch weiterer Untersuchungen bedürfen: anscheinend ist es für eine hohe Trocknungsrate förderlich, wenn die Poren in der ersten Netzwerkschicht nicht senkrecht zur Oberfläche stehen [G].

Nach dieser Betrachtung stellt sich die Frage, welche Netzwerkstrukturen bzw. welche Koordinationszahlen denn in der Realität auftreten. Neuere Untersuchungen widmen sich daher der Netzwerkgenerierung und Trocknungssimulation für regellose Kugelschüttungen, die als einfache Repräsentanten realer Aggregatstrukturen aufgefasst werden [32]. Im einfachsten Fall haben alle Partikel denselben Durchmesser, so dass die Voronoi-Raumtäfelung zur Generierung des Porennetzwerks herangezogen werden kann. Solche Netzwerke haben (abgesehen von Randeffekten) die konstante Koordinationszahl Z = 4. Abbildung 39 zeigt ein kleines Netzwerkbeispiel mit gasseitiger Grenzschicht sowie die Sättigungsprofile für eine große Kugelschüttung. Man erkennt die Schwierigkeiten bei der Definition der räumlichen Grenze zwischen Netzwerk und Grenzsschicht, so dass in der Netzwerksättigung auch Oberflächenwasser berücksichtigt wurde (markierter Bereich).

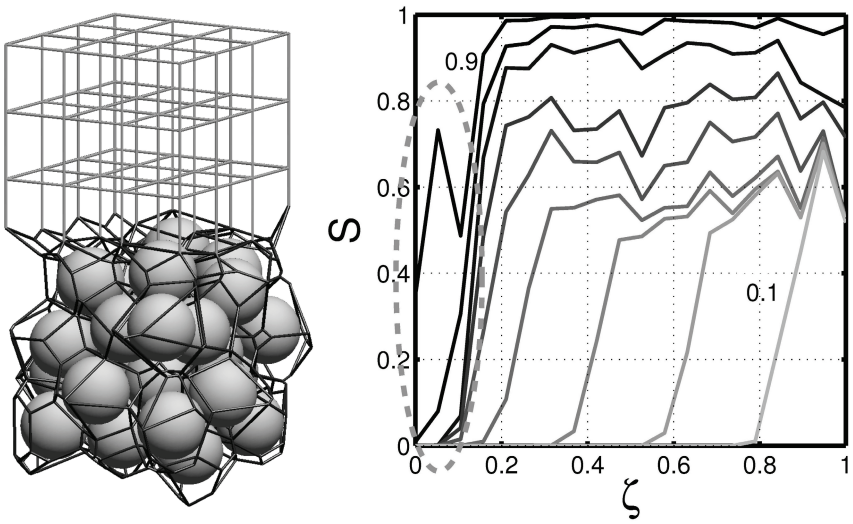

Abbildung 39. Trocknung von Kugelschüttungen: Demonstrationsbeispiel sowie Sättigungsprofile für eine Schüttung aus 1220 Partikeln (16866 Poren) [32].

Ansonsten entsprechen die Sättigungsprofile jedoch qualitativ gut den in Abbildung 38a dargestellten für das regelmäßige Netzwerk mit Z = 4. (Die niedrigeren Sättigungen bei $\zeta = 1$ sind durch die großen Poren zwischen Partikeln und begrenzenden Wänden bedingt [32].)
Wie in Abbildung 39 zu erkennen, sind im Voronoi-Netzwerk manche Poren sehr kurz, so dass ihre Behandlung als Element des Porenvolumens fraglich erscheint. Aktuelle Forschung betrachtet daher Netzwerke, in denen solche kurzen Poren durch Verschmelzen nahe beieinander liegender Knotenpunkte eliminiert werden [bb]; dadurch erhöht sich die Koordinationszahl lokal und wird insgesamt eine verteilte Größe (für den zweidimensionalen Fall siehe [32]).

3.4 Anwendung auf Kompositmaterialien

Porennetzwerke eignen sich in begrenztem Maße auch dazu, den Einfluss makroskopischer Inhomogenitäten auf das Trocknungsverhalten zu untersuchen. So können z. B. Materialien mit Schichtstruktur oder, allgemeiner, Kompositmaterialien simuliert werden. Dabei ist jedoch zu beachten, dass die Netzwerkgröße numerisch begrenzt ist, so dass in Simulationen auf der Produktebene nur wenige makroskopische Regionen betrachtet werden können.

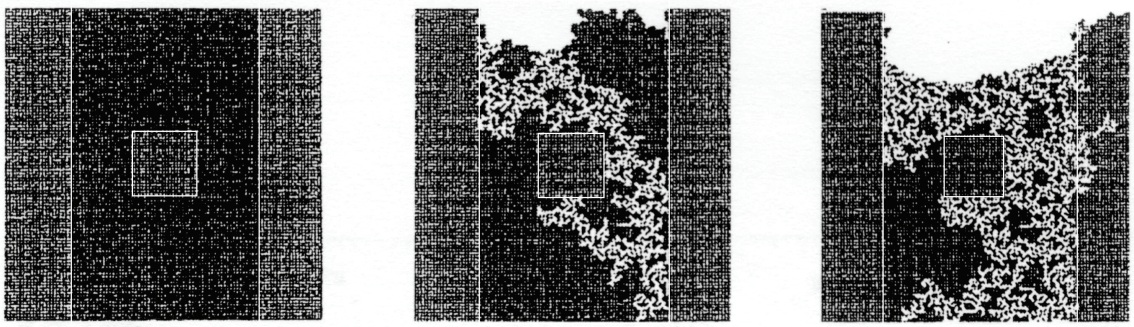

Abbildung 40. Trocknungssimulation für Porennetzwerk mit makroskopischer Inhomogenität (groß- und feinporige Regionen sind durch weiße Linien voneinander getrennt) [40].

Bereits Laurindo und Prat berichten von einer derartigen Simulation, die in Abbildung 40 wiedergegeben ist [40]. Das zweidimensionale Netzwerk besteht an seiner linken und rechten Seite sowie im Zentrum aus feinen Poren, ansonsten sind seine Poren groß. Aufgrund des Kapillareffekts entleeren sich zunächst nur große Poren, während die feinporigen Regionen vollgesättigt bleiben. Erst als die rechte feinporige Region keine

Flüssigkeitsverbindung mehr zu großen Poren hat, beginnt auch sie auszutrocknen; später folgen auch die beiden anderen feinporigen Regionen.

Hier werden nun eigene Simulationen an lateral periodischen 30×30×30 Netzwerken diskutiert, welche die Trocknung von Schichtstrukturen nachbilden sollen [aa]. Die mittleren Porenradien der fein- bzw. großporigen Regionen sind 10 µm bzw. 15 µm, die Porenlänge im gesamten kubischen Gitter beträgt 100 µm; daher haben die Regionen eine unterschiedliche Porosität (ψ = 0.09 bzw. ψ = 0.21).
Im ersten betrachteten Fall sind fein- und großporige Region *nebeneinander* angeordnet. In Abbildung 41 sind dreidimensionale Phasenverteilungen dargestellt: zu Beginn der Trocknung entleeren sich nur Poren der großporigen Region, bis dort die Flüssigkeit in kleine separate Cluster aufgeteilt ist; dann beginnt die Entleerung der kleinen Poren. Die Oberfläche der großporigen Region trocknet zuerst vollständig aus, und die Trocknungsfronten in den beiden Regionen propagieren zeitlich versetzt durch das Netzwerk. Dadurch unterscheiden sich auch die lokalen Dampfstromdichten an der Oberfläche.

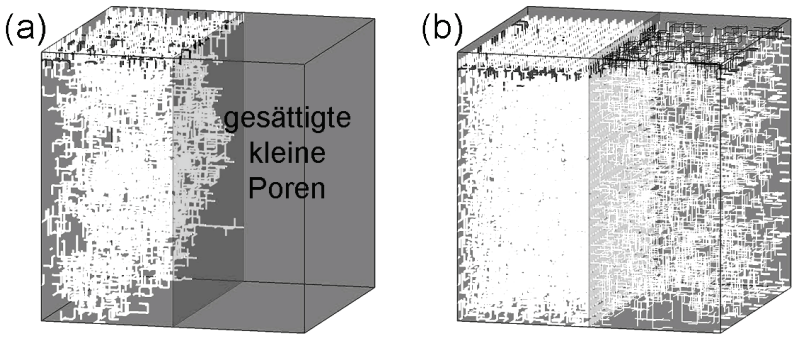

Abbildung 41. Phasenverteilungen in einem Netzwerk mit vertikaler Schichtstruktur für (a) S = 0.9 und (b) S = 0.7 (weiß: leere Poren, dunkelgrau: teilgesättige Poren) [O].

An dieser Stelle sei auf eine sehr ähnliche Arbeit aus der Hydrologie von Lehmann und Or hingewiesen [45], in welcher der Einfluss von Inhomogenitäten auf den Wasserverlust des Bodens untersucht wird. Trocknungsexperimente mit gefärbtem Wasser an Hele-Shaw-Zellen, die in benachbarten Regionen mit feinem bzw. grobem Sand befüllt sind, zeigen, wie der grobe Sand zuerst trocknet. Die Kapillarströmung wird zudem elegant mit Neutronenabsorptionsmessungen und schwerem Wasser (D_2O) nachgewiesen. In den Messungen ist der Kapillareffekt allerdings im weiteren Verlauf durch Gravitation begrenzt.
Ferner können Lehmann und Or mit einem Kapillarmodell (ähnlich dem in [44]) darstellen, wie Texturkontraste – als feinporige Zonen in einem großporigen Boden – neben einem längeren 1. Trocknungsabschnitt auch die Austrocknung des Bodens bis in eine größere Tiefe bewirken. Dabei werden charakteristische Längen für Reibung und Gravitation benutzt, um die Wassereinzugsgebiete der feinporigen Zonen abzuschätzen; die typische Längenskala der Inhomogenitäten beträgt in dieser Anwendung einige Meter.
In einer verwandten Untersuchung benutzen Shahraeeni und Or eine Infrarotkamera, um Variationen der lokalen Trocknungsrate an der Oberfläche von heterogenen Materialien zu messen [78].
Für den Fall der kombinierten Salzmigration und Verdunstung an der Oberfläche einer gesättigten Struktur hat Veran [92] den Kontrast in der Permeabilität mit einem Kontinuumsmodell beschrieben und als Ursache für das experimentell beobachtete bevorzugte Auskristallisieren von Salz an der Oberfläche der feinporigen Region identifiziert.
Xu et al. [97] haben die diskutierten Effekte auf einer kleineren Längenskala experimentell nachgewiesen. Bei der Trocknung kolloidaler Suspensionen mit Regionen unterschiedlicher Partikelgröße haben sie die Phasenverteilungen mittels konvokaler Lasermikroskopie dreidimensional aufgelöst beobachtet. Sie weisen nach, dass die Entleerung der beiden Schichten nacheinander und jeweils mit fraktalen Strukturen erfolgt.

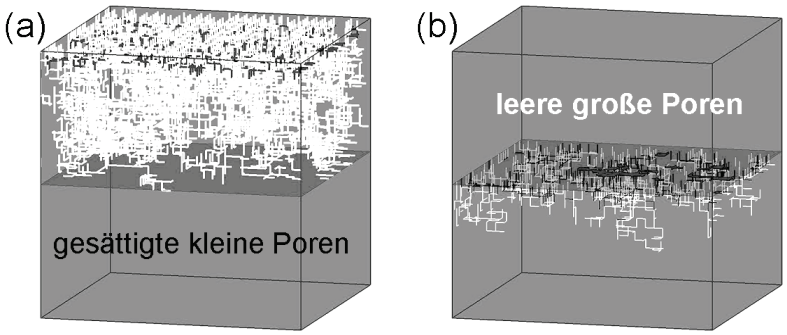

Abbildung 42. Phasenverteilungen in einem Netzwerk mit horizontaler Schichtstruktur für (a) S = 0.9 und (b) S = 0.3 (weiß: leere Poren, dunkelgrau: teilgesättigte Poren) [O].

In den beiden weiteren Fällen liegen die zwei unterschiedlichen Schichten *übereinander*. Ist die oberflächennahe Region großporig, so stellt die Schichtgrenze eine Kapillarbarriere dar, wie man aus den Phasenverteilungen in Abbildung 42 ersehen kann: die großporige Region trocknet in diesem Fall vollständig aus, bevor sich die erste Pore der kleinen Region entleert. Dabei verläuft die Trocknung der beiden Zonen jeweils nach dem bekannten Schema: gradientenfreier Wasserentzug bis die Flüssigkeit nur noch aus kleinen separaten Clustern besteht, die dann von der Verdunstungsseite her nach und nach austrocknen.
Hier sei noch einmal auf Salin [68] verwiesen, der ein ähnliches Verhalten simuliert hat; in Salins Modell nimmt die Porengröße allerdings von der Oberfläche her *allmählich* auf das Niveau der feinporigen Region ab, weshalb die Trocknungsfront bei ihm schärfer ist.

Zuletzt wird der Fall einer feinporigen Oberflächenschicht betrachtet; die entsprechenden Phasenverteilungen sind in Abbildung 43 gegeben. Hier beobachtet man, dass die Trocknung der feinporigen Schicht stoppt, sobald die Gasphase zur darunter liegenden großporigen Schicht durchgebrochen ist. Diese wird dann zunächst soweit entfeuchtet, bis die Flüssigkeit nur noch als kleine Cluster vorliegt. Danach schreitet die Trocknung in der oberen, feinporigen Schicht voran, bis auch dort die makroskopische Kontinuität der Flüssigkeit aufgehoben ist. Dann beginnt schließlich der 2. Trocknungsabschnitt, und die Trocknungsfront der verdunstenden Cluster wandert durch das gesamte Netzwerk.

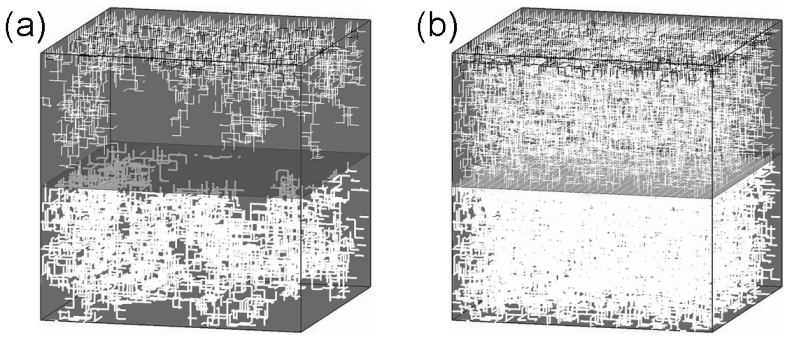

Abbildung 43. Phasenverteilungen in einem Netzwerk mit horizontaler Schichtstruktur für (a) S = 0.9 und (b) S = 0.7 (weiß: leere Poren, dunkelgrau: teilgesättigte Poren) [O].

Die Betrachtung der Phasenverteilungen (in Abbildungen 42 und 43) legt nahe, dass von den letzten beiden Fällen derjenige hinsichtlich der Trocknungsdauer günstiger ist, für den die feinporige Region an der Oberfläche liegt - denn der Kapillareffekt wird hier effizient für den Stofftransport genutzt. Aufgrund des Porositätskontrasts muss in diesem Fall jedoch gegen Ende des Trocknungsprozesses noch relativ viel Flüssigkeit aus der oberflächenfernen Schicht verdunsten – und dies durch eine Schicht mit niedriger Porosität, also kleinem effektivem Dampfdiffusionskoeffizienten. Daher ist die Trocknungsdauer tatsächlich *länger*.
Für eine Schichtstruktur ohne Porositätskontrast, wie bei Schüttungen aus Glaskugeln oder Sand, ist hingegen zu erwarten, dass die bessere Nutzung des Kapillareffekts die

Trocknungskurve günstig beeinflusst. In der Tat haben Pillai et al. in zweidimensionalen Netzwerksimulationen den Porositätskontrast künstlich aufgehoben (indem sie Porenvolumina und Transportkoeffizienten angeglichen haben, ohne das Netzwerk selbst zu ändern) und konnten diese Erwartung bestätigen [56].

Die Trocknung einer Schicht kleiner Glaskugeln auf einer grobkörnigen Schüttung wurde von Shahidzadeh-Bonn et al. [77] durch Absorption von Gammastrahlung experimentell charakterisiert. Die gemessenen Sättigungsprofile belegen den bevorzugten Wasserentzug aus der tiefer liegenden Schicht, bevor die obere Schicht weitertrocknet.

Eine realitätsnahe Abbildung von Schichten unterschiedlicher Porengröße durch ein Netzwerk ist nicht trivial, denn die Porenlänge (bzw. im regulären Fall die Gitterkonstante) ändert sich an der Schichtgrenze. Abbildung 44 soll anhand von Sättigungsprofilen zeigen, dass es beim Übergang von fein- zu grobporiger Region ohnehin zu Randeffekten – nämlich zu einem Überschwingen der Sättigung auf beiden Seiten – kommt. Dies lässt vermuten, dass die Umsetzung der Ankopplung der beiden Zonen einen kritischen Schritt darstellt, der sich für Regionen mit unterschiedlicher Gitterkonstante noch schwieriger gestaltet.

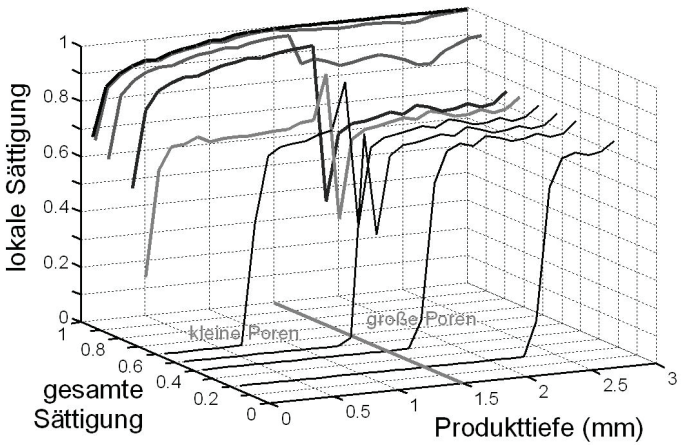

Abbildung 44. Sättigungsprofile für das Netzwerk aus Abbildung 43.

Pillai et al. [56] haben neben den zweidimensionalen Simulationen, welche die hier besprochenen Effekte bestätigen, auch Trocknungsexperimente an Mikromodellen (12×12 Netzwerke) durchgeführt, in denen zwei Schichten übereinander liegen. Filmtransport spielt hierbei jedoch eine entscheidende Rolle und führt zu einem schärferen Kontrast: sobald Gas in die großporige Region eindringt, entleert sich diese *vollständig*, bevor die kleinporige Region (weiter)trocknen kann. Außerdem wird beim Durchbruch der Gasphase durch eine feinporige Oberflächenregion in eine tiefer liegende großporige Region eine spontane Umverteilung von Porenflüssigkeit beobachtet, wobei bereits entleerte kleine Poren wieder befüllt werden. Dieses Phänomen kann mit den bisherigen Porennetzwerkmodellen noch nicht beschrieben werden.

Eine wichtige Arbeit zur Trocknung geschichteter Strukturen haben jüngst Shokri, Lehmann und Or [84] veröffentlicht. Sie betrachten insbesondere den Fall einer feinen Sandschicht auf einer groben Sandschüttung. Mittels Neutronenabsorption an Hele-Shaw-Zellen (gefüllt mit geschichteten H_2O und D_2O) werden sowohl der frühe Durchbruch der Gasphase durch die obere feine Schicht und ihr Vordringen in die untere grobkörnige Schicht als auch die Kapillarströmung eindrucksvoll nachgewiesen. Außerdem messen die Autoren einen sprunghaften Anstieg des Flüssigkeitsdrucks im Moment des Durchbruchs.
In weiteren Untersuchungen betrachten die Autoren unterschiedliche Abfolgen von zwei bis drei fein- und grobkörnigen Sandschichten und entwickeln ein Kapillarbündelmodell zum Verständnis der Phänomene. Die Abfolge, die Dicken (bzw. Positionen) und die Porengrößenverteilungen der Schichten bestimmen, bis zu welcher Tiefe die Trocknungsfront im Schwerefeld vordringen kann, bevor die Oberfläche austrocknet und die Trocknungsrate

deutlich absinkt. Die Ergebnisse bedeuten einen entscheidenden Fortschritt für Verständnis und gezielte Beeinflussung des Wasserverlusts von Böden. Dieselben Autoren untersuchten in einer früheren Arbeit [80] bereits die Wirkung einer dünnen hydrophoben Schicht – an der Oberfläche oder eingebettet – um den Wasserverlust zu bremsen.

Zuletzt soll eine Untersuchung von Yiotis et al. zum Einfluss makroskopischer Inhomogenität der Porengröße erwähnt werden [106]. In $70\times70\times70$ Netzwerken wird der mittlere Porenradius linear mit dem Abstand zur Netzwerkoberfläche variiert. Nimmt die Porengröße ins Netzwerk hinein ab, so trocknet das Netzwerk von der Oberfläche her aus, mit einer begrenzten teilgesättigten Zone, denn der Kapillareffekt ist abgeschwächt. Werden hingegen die Poren ins Netzwerk hinein größer, so entleert es sich zunächst von der oberflächenfernen Seite. Dieser Fall kann als Verallgemeinerung der bisher betrachteten Situationen mit scharf abgegrenzten homogenen Schichten betrachtet werden.

Damit sind die Betrachtungen zu Struktureinflüssen auf das Trocknungsverhalten abgeschlossen, und im folgenden Kapitel wird die Bedeutung wesentlicher Transport-phänomene für den Trocknungsprozess beleuchtet sowie die Modellerweiterung um mechanische Effekte vorgenommen.

4 Porennetzwerke – Modellerweiterungen und Rolle einzelner Transportphänomene

Das Basismodell wird nun um Flüssigkeitsreibung, Wärmetransport bzw. mechanische Effekte erweitert, damit deren Rolle für das Trocknungsverhalten untersucht werden kann.

4.1 Flüssigkeitsreibung

In der Literatur gibt es mehrere Porennetzwerkmodelle, in denen die Viskosität der Flüssigkeit mehr oder weniger vollständig berücksichtigt wird [17,52,75,98]. In deren Anwendung spielen die entsprechenden Reibungseffekte aber entweder eine untergeordnete Rolle oder ihre Wirkung auf das Trocknungsverhalten wurde nicht untersucht. Prat allein scheint den stabilisierenden Einfluss auf die Trocknungsfront – als teilgesättigten Bereich zwischen trockener und vollgesättigter Zone – mit Methoden der Porennetzwerke beleuchtet zu haben, allerdings nur für den stationären Fall [61]; dabei betont er Parallelen zur Wirkung der Gravitation [62].
Entscheidende Motivation für die Erweiterung des Basismodells um die Flüssigkeitsreibung sind die Erfahrungen mit dem Kapillarbündelmodell (siehe Kapitel 1). Nur mit Viskositätseffekten kann die Trocknung von feinporigen makroskopischen Objekten korrekt beschrieben und der Einfluss der äußeren Trocknungsbedingungen (als Rate des 1. Trocknungsabschnitts) angemessen berücksichtigt werden.

Das viskose Modell ist in [H] und [31] ausführlich beschrieben und soll hier nur in groben Zügen skizziert werden. Als wesentliche Neuerung wird nun nicht mehr angenommen, dass die Kapillarströmung mit beliebiger Rate und über beliebige Distanzen Porenflüssigkeit transportieren kann. Stattdessen wird für jeden Flüssigkeitsmeniskus geprüft, ob der Kapillardruckunterschied ausreicht, um Flüssigkeit mit der lokalen Verdunstungsrate nachzuliefern; falls nicht, bewegt sich der Meniskus entsprechend der Differenz der Massenströme für Flüssigkeit und Dampf. Druckfeld und Konvektionsströme in der Flüssigkeit berechnen sich dabei aus Massenbilanzen um die Knotenpunkte:

$$\sum_j \dot{M}_{w,ij} = \sum_j \frac{\pi r_{ij}^2}{8 \nu_w L_{ij}} \left(P_{w,i} - P_{w,j} \right) = 0 \qquad (27)$$

Die Randbedingungen für dieses Gleichungssystem sind an der Phasengrenze gegeben und hängen davon ab, ob der jeweilige Meniskus stationär ist oder nicht. An stationären Menisken wird die lokale Verdunstungsrate als Randbedingung 2. Art vorgegeben; an bewegten Menisken der um den Kapillardruck abgesenkte Gasdruck in einer Randbedingung 1. Art, entsprechend Gleichung (1). Um das System zu lösen, muss also ein iteratives Verfahren gewählt werden, denn die Randbedingungen hängen von der Lösung selbst ab. Zwei mögliche Strategien hierzu sind in [H] dargestellt.
Das Modell rechnet – wie schon das Basismodell – mit quasistationären Bedingungen; die Menisken bewegen sich also jeweils mit konstanter Geschwindigkeit, bis einer von ihnen das Ende einer Pore erreicht hat. Beim Übergang zum nächsten quasistationären Zustand werden insbesondere keine Trägheitseffekte berücksichtigt. Aufgrund der diskreten Änderungen im Druckfeld kann es zur Wiederbefüllung teilweise entleerter Poren kommen – im Sinne eines kleinen „Haines-Jump“; vollständig entleerte Poren bleiben jedoch leer [H].
Um die Äquivalenz mit den anderen Modelltypen zu untersuchen, wurde das erweiterte Porennetzwerkmodell zunächst auf ein Abbild des Kapillarbündels angewendet. (Eine schematische Darstellung ist in Abbildung 45 gegeben; für die Simulationen wurden 50×50 Netzwerke verwendet.) Dabei können die horizontalen Poren den widerstandslosen Stoffaustausch zwischen den Kapillaren trotz numerischer Tricks [H] nur unzureichend gewährleisten. Außerdem ist die vertikale Position im Porennetzwerkmodell diskretisiert: zwar können sich die Flüssigkeitsmenisken beliebig bewegen, aber die Randbedingung des Sattdampfdrucks in der Luft springt jeweils von einem Knoten zum nächsten [H].

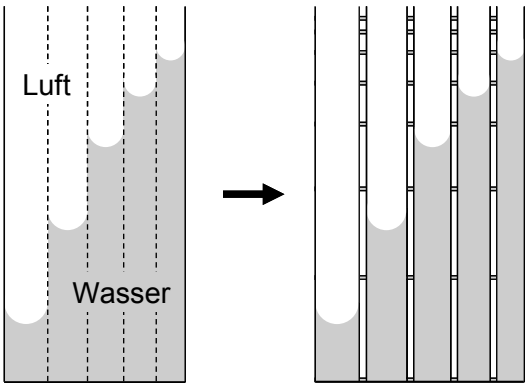

Abbildung 45. Abbildung des Kapillarbündels durch ein Porennetzwerk [H].

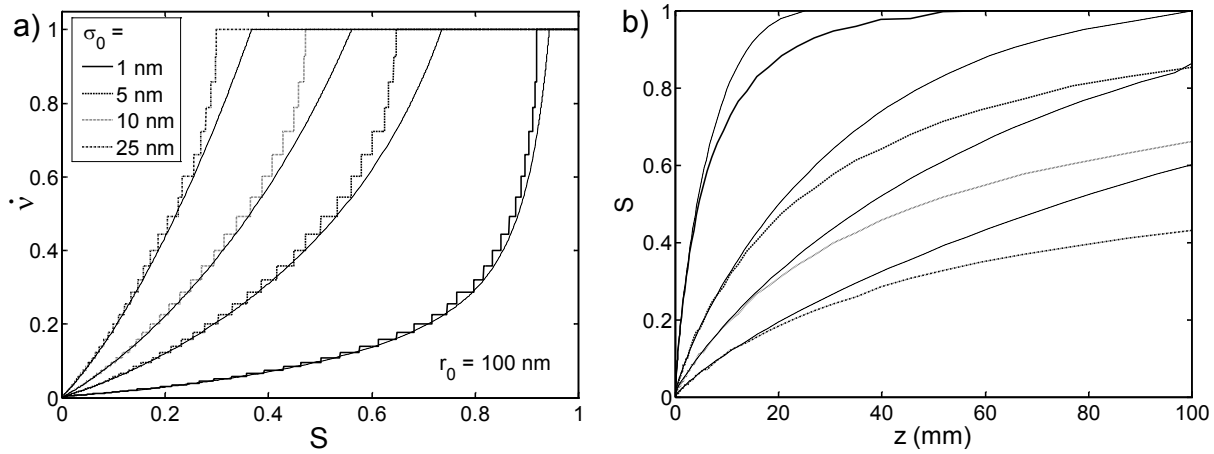

Abbildung 46. Trocknungskurven (a) und Sättigungsprofile am Ende des 1. Abschnitts (b) für Kapillarbündel mit normalverteiltem Radius (Mittelwert r_0 und Standardabweichung σ_0). Dünn gestrichelte Kurven zeigen Ergebnisse des Kapillarbündelmodells aus Kapitel 1 [H].

In Abbildung 46 sind für vier unterschiedliche Porenradienverteilungen sowohl die Trocknungskurven als auch die Sättigungsprofile am Ende des 1. Trocknungsabschnitts für beide Modelle gegenübergestellt. Neben einer grundsätzlichen Übereinstimmung der Ergebnisse beobachtet man für die Netzwerksimulationen flachere Sättigungsprofile, besonders zum unteren Ende des Netzwerks hin, wo die Randbedingung verschwindenden Stoffstroms nun korrekt umgesetzt ist – im Gegensatz zum Kapillarbündelmodell (vgl. 2.3). Teilweise als Folge dieses Effekts, sagt das Netzwerkmodell einen längeren 1. Trocknungsabschnitt voraus. Insgesamt liegen die Ergebnisse des Netzwerkmodells nahe an denen des Kontinuumsmodells (siehe Abbildung 21).
Nachdem das Modell in dieser Weise erfolgreich getestet wurde, wurde es auf Porennetzwerke mit räumlich zufällig verteiltem Radius angewendet [H,I] und Parallelen zwischen Reibungs- und Gravitationseffekten wurden beleuchtet [a].

Im Folgenden werden die wesentlichen Änderungen im Trocknungsprozess durch Flüssigkeitsreibung anhand einer dreidimensionalen Simulation [I] diskutiert. Das 25×25×50 Netzwerk hierfür besteht aus Poren der Länge 500 nm und mit eng verteiltem Radius (r_0 = 50 nm, σ_0 = 1 nm); es trocknet mit einem sehr hohen Stoffübergangskoeffizienten (β = 0.51 m/s). Die Parameter wurden bewusst extrem gewählt, um charakteristische Reibungseffekte beobachten zu können, wie sie in der Realität nur in wesentlich größeren – und damit der direkten Simulation unzugänglichen – Porensystemen auftreten. In Abbildung 47 wird das Netzwerk unter Vernachlässigung von Reibungseffekten, d.h. entsprechend den Regeln des Basismodells, getrocknet; Abbildung 48 zeigt die Trocknungssimulation für das erweiterte Netzwerkmodell. Zur besseren Sichtbarkeit sind in den einzelnen Lagen des Netzwerks jeweils nur entweder leere (weiße) oder gesättigte (schwarze) Poren dargestellt.

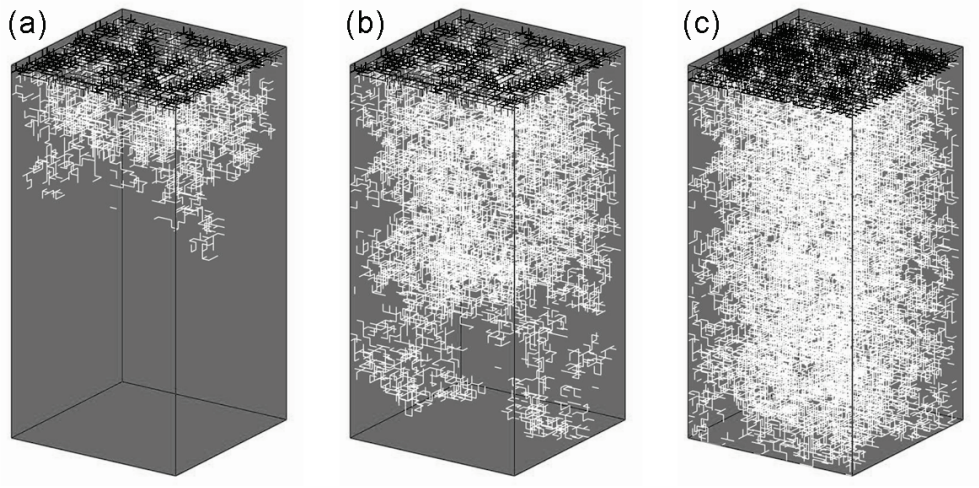

Abbildung 47. Phasenverteilungen für Netzwerksättigungen
(a) 0.95, (b) 0.86 und (c) 0.75 für vernachlässigte Flüssigkeitsreibung [l].

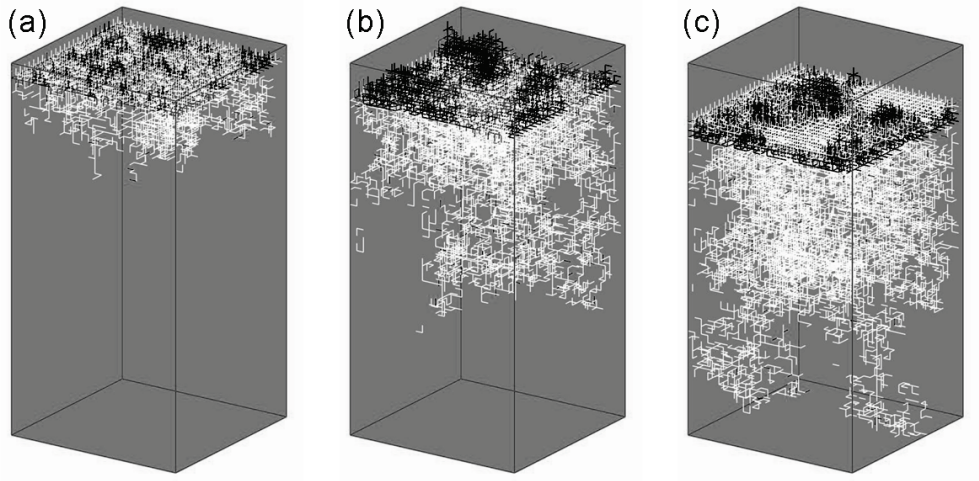

Abbildung 48. Phasenverteilungen für Netzwerksättigungen
(a) 0.95, (b) 0.86 und (c) 0.75 mit berücksichtigter Flüssigkeitsreibung [l].

Spielt Reibung keine Rolle, so kann durch den Kapillareffekt Flüssigkeit aus dem gesamten Netzwerk an die Oberfläche strömen: solange die Flüssigkeit einen zusammenhängenden Cluster bildet, entleert sich an der Phasengrenze jeweils nur die größte Pore, egal wo sie sich befindet. Daher ist schon bei einer Netzwerksättigung von 0.86 der Durchbruch der Gasphase zu beobachten. Die Oberflächensättigung ändert sich über den dargestellten Sättigungsbereich nur unmerklich; und die Oberfläche trocknet erst bei einer Netzwerksättigung von 0.67 vollständig aus.
Ganz anders verläuft die Trocknung, wenn Flüssigkeitsreibung berücksichtigt wird. Dann ist die Reichweite der Kapillarkräfte durch Reibungsverluste beschränkt. Bei der anfänglichen hohen Trocknungsrate sind diese sehr stark, so dass die Oberfläche schon bei einer Netzwerksättigung von 0.95 austrocknet. Mit zurückweichender Front sinkt die Verdunstungsrate ab, und der Kapillareffekt gewinnt an Bedeutung: die Frontbreite des teilgesättigten Bereichs nimmt zu, und bei einer Netzwerksättigung von 0.75 bricht die Gasphase durch. Am Ende des Prozesses, wenn die Trocknungsrate stark abgesunken ist, spielen viskose Effekte keine entscheidende Rolle [l].
Eine bedeutende Publikation in diesem Kontext stammt von Shaw [79], der eine dünne dreidimensionale Kugelschüttung bei der Trocknung optisch beobachtet und die Frontbreite untersucht hat. In seinen Experimenten beobachtete er dasselbe Verhalten, nämlich dass sich die Front aufweitet, wenn sie in die Schicht hineinwandert.

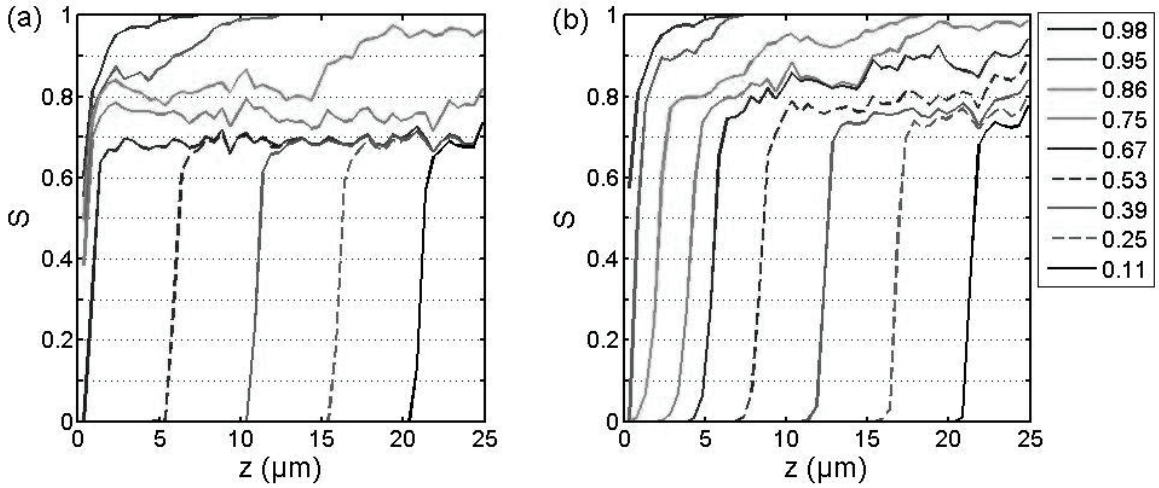

Abbildung 49. Sättigungsprofile zu den Simulationen aus Abbildungen 47 und 48: (a) ohne Reibung, (b) mit Reibung (die Legende gibt die Netzwerksättigung an) [I].

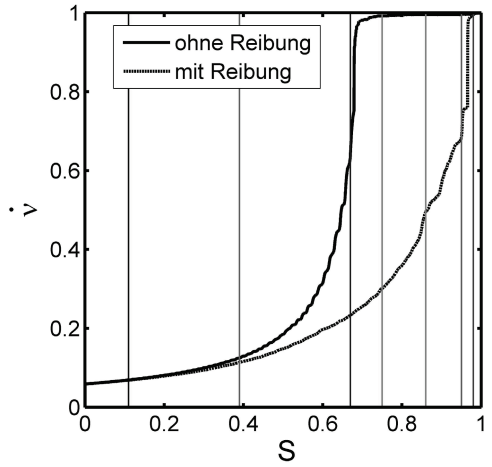

Abbildung 50. Trocknungskurven für die Simulationen aus Abbildungen 47 und 48 (Sättigungen der Profile aus Abbildung 49 sind gekennzeichnet) [I].

Unter makroskopischem Blickwinkel werden die Flüssigkeitsverteilungen während der Trocknung in Abbildung 49 betrachtet. Die dargestellten Sättigungsprofile weisen unter dem Einfluss der Reibung deutliche Gradienten auf, ganz im Gegensatz zum gradientenfreien Flüssigkeitstransport des Basismodells (besonders für $S \approx 0.75$, siehe auch Abbildung 47c). Kapillarströmung wird nun nicht erst aufgrund fehlender hydraulischer Kontinuität gestoppt, sondern bereits deutlich früher aufgrund viskoser Effekte gehemmt. Damit rückt das Porennetzwerkmodell näher an das klassische Kontinuumsmodell mit seinem gradientengetriebenen Transport (siehe Kapitel 2); mögliche Übergange zur Makroskala werden in Kapitel 5 diskutiert.
Schließlich sind in Abbildung 50 die Trocknungskurven für die beiden Modelle dargestellt. Während im reibungsfreien Fall ein deutlicher 1. Trocknungsabschnitt beobachtet wird, sinkt die Trocknungsrate bei berücksichtigter Reibung praktisch sofort ab. Nur die Grenzfälle sind für beide Modelle identisch: die anfängliche Trocknungsrate ist durch die gasseitige Grenzschicht vorgegeben, und die letzten Poren trocknen jeweils mit dem kombinierten Stofftransportwiderstand für Netzwerk und Grenzschicht aus.

Für zweidimensionale Porennetzwerke wurde der Einfluss viskoser Effekte auf die Kapillarströmung auch für bimodale Strukturen untersucht [H, 31]. Unter realistischen Bedingungen ist der Kontrast im Porenradius für die beiden Moden jedoch so groß, dass die bevorzugte Entleerung der Makroporen nicht durch Reibung beeinträchtigt wird. Und

gewöhnlich haben nur die Mikroporen eine so kleine Verteilungsbreite σ_0, dass Reibungseffekte erst bei ihrer Entleerung eine bedeutende Rolle spielen. Neben einer eng verteilten Porengröße bleiben relativ große Abmessungen sowie hohe Trocknungsraten wichtige Kriterien für das Auftreten der viskosen Effekte.

4.2 Wärmetransport

In der zweiten Modellerweiterung wird das Basismodell, mit reibungsfreiem Stofftransport, um die Beschreibung des Wärmetransports ergänzt. In der Literatur sind nur zwei Arbeiten zur nicht-isothermen Trocknung von Porennetzwerken bekannt, die vorab kurz diskutiert werden sollen.

Plourde und Prat [57] interessieren sich für den Einfluss von Temperaturgradienten auf die Phasenverteilungen. Sie untersuchen, wie für Netzwerke mit eng verteiltem Porenradius die Reihenfolge der Porenentleerung wegen der Temperaturabhängigkeit der Oberflächenspannung (für Wasser etwa 0.2 % Absenkung pro 1 K Temperaturerhöhung) vom Temperaturfeld mitbestimmt wird. Für den lokalen Flüssigkeitsdruck gilt nämlich im nicht-isothermen Fall:

$$P_{w,ij} = P_g - \frac{2\sigma(T_{ij})}{r_{ij}} \tag{28}$$

so dass nicht nur größere, sondern auch wärmere Poren bevorzugt entleert werden. In ihren zweidimensionalen Simulationen geben Plourde und Prat die Temperatur an Ober- und Unterseite des Netzwerks vor und berechnen für quasistationäre Bedingungen die Phasenverteilungen und Temperaturfelder innerhalb des Netwerks. Dabei wird die Wärmeleitung abhängig von der lokalen Porensättigung beschrieben und die latente Wärme beim lokalen Phasenübergang berücksichtigt. Für eine höhere Temperatur an der offenen Netzwerkseite (dT/dz < 0) wird die Trocknungsfront stabilisiert; andernfalls (dT/dz > 0) ist eine Destabilisierung zu beobachten.

Huinink et al. [30] betrachten den Einfluss eines linearen Temperaturfeldes auf die Trocknung und setzen ihren Schwerpunkt auf die Variation des Sattdampfdrucks mit der Temperatur $P_v^*(T_i)$, wobei sie eine lineare Abhängigkeit postulieren. Effektiv wird also an der gesamten Phasengrenze ein lineares Sattdampfdruckprofil aufgeprägt. (Für die Oberflächenspannung wird die Temperaturabhängigkeit vernachlässigt.) Das sich daraus ergebende Dampfdruckfeld bestimmt die lokalen Übergangsraten an der Phasengrenze. Unter Annahme reibungsfreier Kapillarströmung in jedem Flüssigkeitscluster wird dann jeweils die größte Grenzflächenpore gemäß der Übergangsrate des gesamten Clusters entleert bzw. die kleinste befüllt. Je nach Temperaturgradient beobachten auch Huinink et al. eine (leichte) Stabilisierung bzw. eine (ausgeprägte) Destabilisierung der Trocknungsfront – ähnlich wie bei Plourde und Prat, jedoch aufgrund anderer Mechanismen. Die Destabilisierung für dT/dz > 0 erklärt sich wie folgt: oberflächennahe Flüssigkeitscluster verdunsten nur solange, bis der Dampfdruckgradient in der trockenen Region auf den aufgeprägten Gradienten in der teilgesättigten Region abgesunken ist; Cluster an der Unterseite des Netzwerks verdunsten durch die teilgesättigte Region hindurch; und Flüssigkeitscluster, die gänzlich von gesättigtem Gas umschlossen sind, sind stationär.

Ziel des hier vorgestellten Modells ist es nicht, eine Temperatur aufzuprägen, sondern ihre zeitliche und räumliche Entwicklung als Folge des gekoppelten Wärme- und Stofftransports bei der Trocknung zu berechnen. Neben dem Basismodell für den Stofftransport, in dem einige stoffliche Parameter temperaturabhängig werden, muss also insbesondere der Wärmetransport zeitabhängig beschrieben werden. Hierzu wird um jeden Knoten des Porennetzwerks ein Kontrollvolumen gelegt, das jeweils die halbe Länge der Nachbarporen sowie den entsprechenden Feststoff enthält; für die zeitliche Entwicklung der Temperatur eines Kontrollvolumens gilt

$$\left(\rho c_p V\right)_i \frac{dT_i}{dt} = \sum_j \dot{Q}_{ij} - \Delta h_v\left(T_i\right)\sum_j \dot{M}_{ev,ij} \tag{29}$$

Dabei ist $(\rho c_p V)_i$ seine Wärmekapazität unter Berücksichtigung von Feststoff und Flüssigkeit. Die Wärmeströme zwischen dem Knoten und seinen Nachbarn berechnen sich zu

$$Q_{ij} = \frac{\left(\lambda A\right)_{ij}}{L}\left(T_i - T_j\right) \tag{30}$$

wobei $(\lambda A)_{ij}$ das Produkt aus effektiver Wärmeleitfähigkeit und Gesamtaustauschfläche zwischen den jeweiligen Kontrollvolumina darstellt. Zuletzt werden die Wärmesenken berücksichtigt, entsprechend der sich aus dem diffusiven Dampftransport in der Gasphase ergebenden Verdunstungsraten $\dot{M}_{ev,ij}$. Bei lokaler Kondensation ändert sich das Vorzeichen, so dass eine Wärmequelle vorliegt. Konvektive Beiträge zum Wärmetransport bleiben unberücksichtigt; zudem wird lokales thermisches Gleichgewicht angenommen. (Beide Annahmen könnten durch zukünftige Modellerweiterungen wegfallen.) Als Randbedingungen für die Gleichungen (29) wird der Wärmeübergang durch die gasseitige Grenzschicht mit Gleichung (9) beschrieben, und die übrigen Netzwerkseiten werden als thermisch isoliert behandelt.
Da der Wärmetransport ein kontinuierlicher Prozess ist – im Gegensatz zum Stofftransport, der entsprechend den Regeln der Invasionsperkolation diskret abläuft – müssen bei der numerischen Lösung der Gleichungen (29) Stabilitätskriterien für die Zeitschrittweite beachtet werden. Dadurch steigt der Aufwand im Vergleich zum isothermen Fall in zweifacher Weise: es muss nicht nur ein weiteres Gleichungssystem gelöst werden, sondern auch die Zeitdiskretisierung wird feiner.
Zur Kondensation ist noch folgende wichtige Einschränkung zu nennen: da auch das erweiterte Modell nur Regeln für die Poren*entleerung* benutzt, wird lokale Kondensation nur berücksichtigt, sofern sie innerhalb eines Flüssigkeitsclusters durch lokale Verdunstung kompensiert werden kann bzw. solange keine leere Pore befüllt werden muss. Darüber hinausgehende Kondensation wird vernachlässigt.
Weitere Details zum Modell und zum numerischen Lösungsverfahren sind in [J] und [85] nachzulesen.

Mit dem vorgestellten Modell wurde die nicht-isotherme Trocknung von quadratischen [J] und kubischen [M] Porennetzwerken jeweils mit monomodaler und bimodaler Porengrößenverteilung simuliert. Und auch der stabilisierende Effekt der Gravitation wurde für ein quadratisches monomodales Netzwerk für nicht-isotherme Trocknung untersucht [L].
Zunächst soll der Einfluss des Wärmetransports für den zweidimensionalen Fall diskutiert werden; da nur bimodale Netzwerke einen 1. Trocknungsabschnitt aufweisen, beschränken sich die Ausführungen darauf, und für monomodale Netzwerke sei auf [J] verwiesen. Das betrachtete 51×51 Netzwerk hat Poren mit Radien $r_0 \pm \sigma_0$ = 40 ± 2 µm bzw. 100 ± 5 µm und einheitlicher Länge 500 µm (43 % des Porenvolumens liegt in Makroporen); es wird langsam getrocknet (β = 0.007 m/s). Die feste Phase hat die stofflichen Eigenschaften von Glas und ist in der dritten Dimension 500 µm dick; daraus ergibt sich die Porosität zu ψ = 0.17.
In Abbildung 51 sind Phasenverteilungen und Temperaturfelder zu ausgewählten Trocknungszeiten gezeigt. Zu Beginn der Trocknung erwärmt sich das Netzwerk von der Oberfläche her auf die Gutsbeharrungstemperatur. Wenn dann erste Bereiche der Netzwerkoberfläche austrocknen, kommt es lokal zur weiteren Aufheizung, da mit der Verdunstungsrate auch die Kühlwirkung abnimmt (siehe auch [78]). Wenn schließlich die ganze Oberfläche trocken ist, so setzt eine starke Aufheizung ein, die von signifikanten Temperaturgradienten begleitet wird. Ist die Verdunstungsfront ins Netzwerk hineingewandert, so nehmen Temperaturunterschiede im Netzwerk ab; insbesondere ist der gesamte teilgesättigte Bereich im Wesentlichen vom Wärmeeintrag abgeschirmt und daher isotherm. Der entsprechende zeitliche Verlauf von Temperatur und Netzwerksättigung ist in

Abbildung 52 dargestellt. Die Trocknungskurve wird in Abbildung 53 mit dem isothermen Fall (Anwendung des Basismodells auf dasselbe Netzwerk) verglichen.

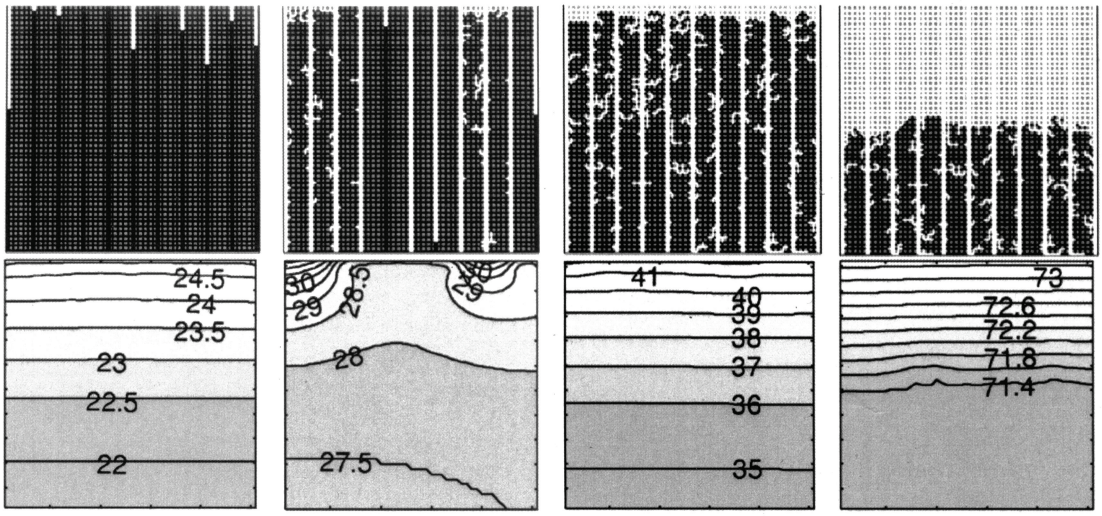

Abbildung 51. Phasenverteilungen und Temperaturfelder für die Trocknung eines bimodalen Netzwerks mit 80°C warmer, trockener Luft (S = 0.95, 0.6, 0.48 und 0.1) [J].

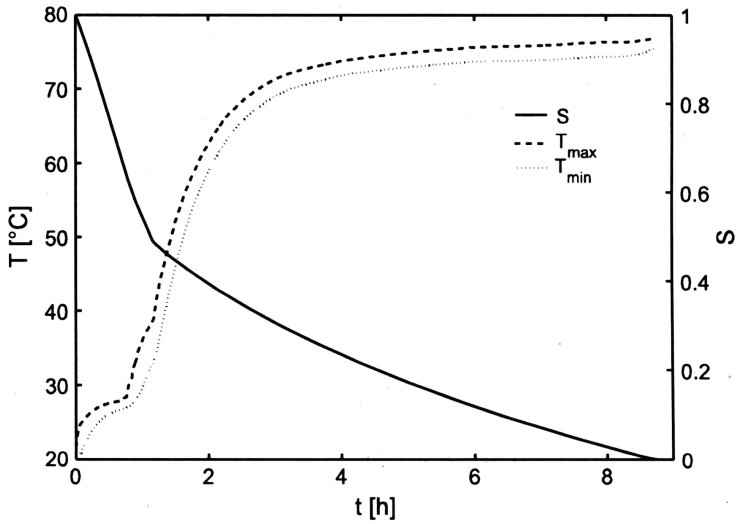

Abbildung 52. Zeitlicher Verlauf von Netzwerksättigung und des im Netzwerk auftretenden Temperaturbereichs für Simulation aus Abbildung 51 [J].

Insgesamt ist festzustellen, dass die Reihenfolge der Porenentleerung durch die Berücksichtigung der Aufheizung nicht wesentlich beeinflusst wird (siehe Abbildung 32) [85], denn die Temperaturunterschiede im teilgesättigten Bereich sind aufgrund der Abschirmung klein und verändern den Kapillardruck entsprechend Gleichung (28) nur wenig. Auch für monomodale Netzwerke beobachtet man nur geringfügige Änderungen bei den Phasenverteilungen [J,b].
Die Trocknungsraten jedoch werden im Vergleich zum isothermen Fall deutlich angehoben: insbesondere sinkt die Rate im 2. Trocknungsabschnitt nicht mehr so stark ab, denn der wachsende Diffusionswiderstand kann durch den zunehmenden Dampfdruckunterschied teilweise kompensiert werden. Die Trocknungskurven in Abbildung 53 sind nicht glatt, da das Porensystem relativ klein ist und diskrete Ereignisse im Gesamtverhalten sichtbar werden. So ist das spontane Absinken der Trocknungsrate durch ein lokales Zurückweichen der Phasengrenze bedingt; für den nicht-isothermen Fall erfolgt daraufhin eine lokale Aufheizung, sodass die Rate allmählich wieder ansteigt.

Kondensationseffekte spielen eine untergeordnete Rolle und können großteils berücksichtigt werden [85]: während des gesamten Trocknungsprozesses kondensieren nur 1.7 % der anfänglichen Flüssigkeitsmenge, und etwa ein Viertel der Kondensation wird vernachlässigt; Ähnliches gilt für ein monomodales Porennetzwerk.

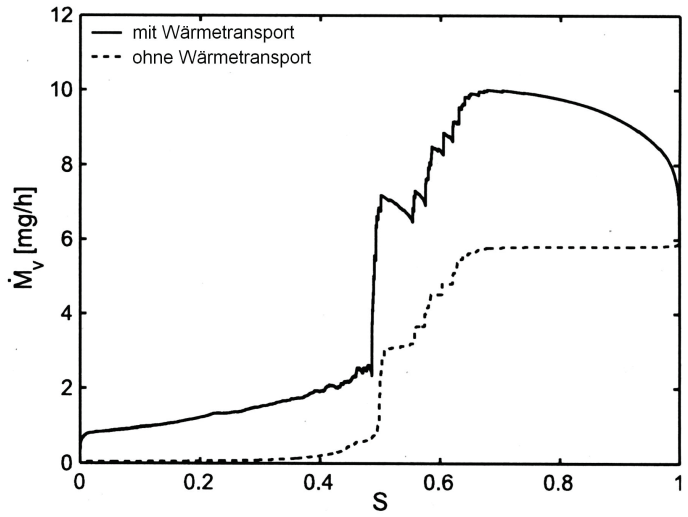

Abbildung 53. Trocknungsrate als Funktion der Sättigung für die nicht-isotherme Simulation aus Abbildung 51 und Vergleich mit einer Simulation ohne Aufheizung (mit Basismodell) [J].

Der dreidimensionale Fall wurde in [M] untersucht, wobei aus rechentechnischen Gründen nur relativ kleine Netzwerke der Größe 13×13×13 simuliert werden konnten. Die Mikro- bzw. Makroporen haben jeweils normalverteilte Radien mit $r_0 \pm \sigma_0$ = 40 ± 2 µm bzw. 100 ± 5 µm und eine einheitliche Länge von 350 µm. Das monomodale Porennetzwerk besteht nur aus Mikroporen und hat die Porosität ψ = 0.15. Im bimodalen Fall sind Makrokanäle in allen drei Raumrichtungen als übergeordnetes Netzwerk eingebaut; die Gesamtporosität erhöht sich auf ψ = 0.22, und die Makroporen machen 36 % des Porenvolumens aus [85]. Beide Netzwerke werden langsam mit trockener, 80°C warmer Luft getrocknet. Die feste Phase hat die stofflichen Eigenschaften von Glas. Die Phasenverteilungen und Temperaturfelder sind in [M] dokumentiert; wie schon in zwei Dimensionen korreliert die Oberflächenfeuchte mit der Temperatur: trockene Bereich heizen sich stärker auf. Auch ansonsten verläuft die Trocknung sehr ähnlich wie für das quadratische bimodale Netzwerk.

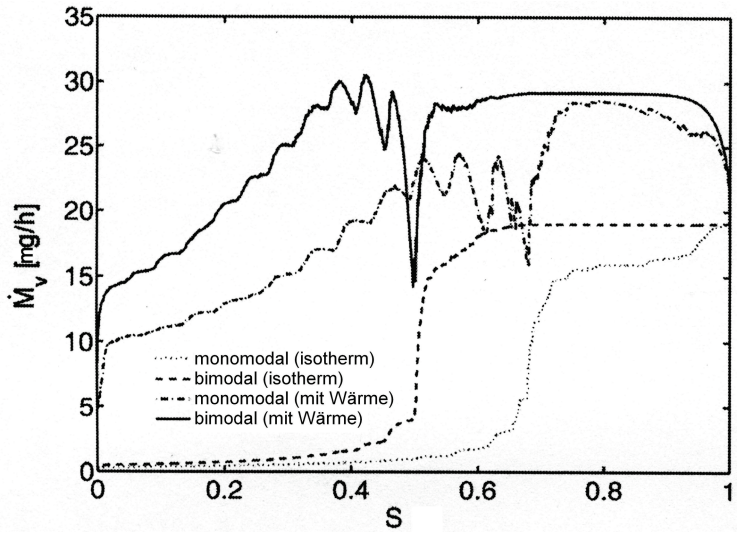

Abbildung 54. Trocknungsraten für kubische 13×13×13 Porennetzwerke von mono- bzw. bimodaler Porengrößenverteilung; der Einfluss des Wärmetransports wird durch Vergleich mit dem Basismodell gezeigt [M].

Die Phasenverteilungen unterscheiden sich nicht wesentlich von isothermen Simulationen, so dass der Haupteinfluss des Wärmetransports wieder die Trocknungsraten betrifft; diese sind in Abbildung 54 wiedergegeben. Für beide Netzwerktypen ist ein 1. Trocknungsabschnitt erkennbar (im monomodalen Fall auf leicht abgesenktem Niveau); für das bimodale Netzwerk ist er jedoch deutlich länger. Die Aufheizung der Netzwerke führt dazu, dass die Trocknungsrate im 2. Abschnitt nur mäßig absinkt. Dabei sind die Diffusionsraten für das bimodale Netzwerk aufgrund der größeren Porenquerschnitte höher. Die Trocknungskurven haben wieder eine „Feinstruktur“, die vom Austrocknen und der anschließenden Erwärmung einzelner Poren(bereiche) herrührt. (Die generell recht hohen Raten am Ende des Prozesses sind teilweise der geringen Netzwerktiefe geschuldet.)

Zusammenfassend kann man sagen, dass das nicht-isotherme Trocknungsmodell auf dreidimensionale Netzwerke angewendet das reale Trocknungsverhalten von großporigen, nicht-hygroskopischer Materialien qualitativ am besten beschreibt: unabhängig von der Porengrößenverteilung gibt es einen 1. Trocknungsabschnitt, die Absenkung der Trocknungsrate im 2. Abschnitt bleibt moderat; und ein „3. Abschnitt“ mit sehr kleinen Trocknungsraten wird nicht beobachtet (vgl. S. 304f in [36]).

Die Betrachtungen zum Wärmetransport abschließend, soll nun noch der Einfluss der Art des Wärmeeintrags diskutiert werden, wie er in [K] untersucht wurde. Die Trocknung eines bimodalen quadratischen Netzwerks mit warmer Luft wird hierzu verglichen mit der Trocknung im unbeheizten Luftstrom, aber mit Kontaktheizung. Während im ersten Fall ein leicht negativer Gradient dT/dz mit vernachlässigbarer Auswirkung auf die Phasenverteilung zu beobachten ist (siehe oben), wird der zweite Fall von einem stark positiven Gradienten dT/dz geprägt, mit großen Temperaturunterschieden ($\Delta T \sim 40$ K), so dass die Reihenfolge der Porenentleerung entscheidend beeinflusst wird. Weitere Details zu den Simulationen finden sich in [K]. Abbildung 55 gibt die Phasenverteilungen während der Trocknung für beide Fälle wieder.

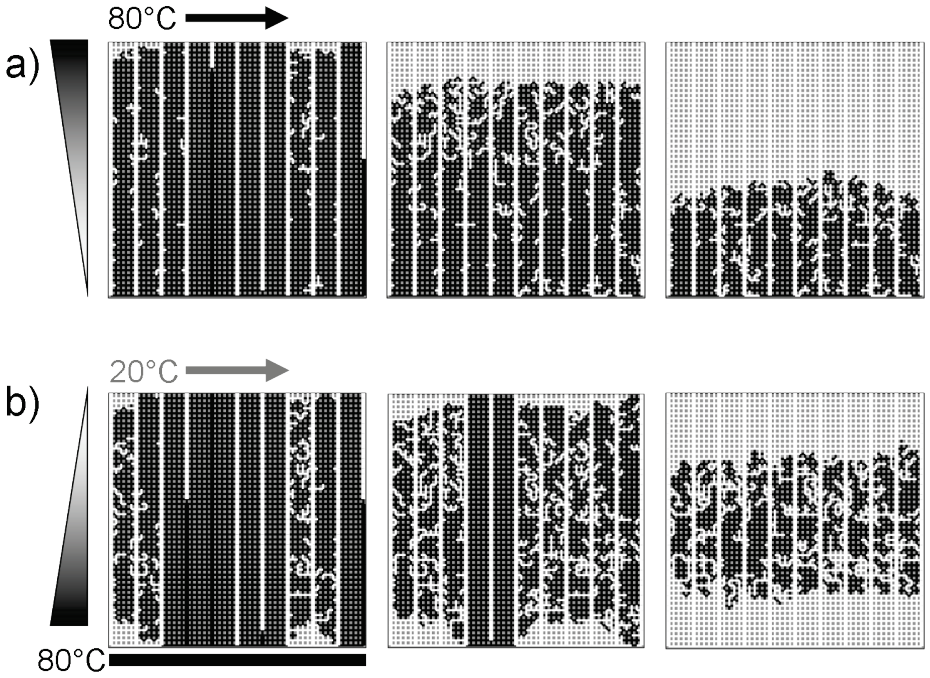

Abbildung 55. Einfluss der Wärmezufuhr auf die Phasenverteilungen bei der Trocknung eines bimodalen Netzwerks (S = 0.6, 0.48 und 0.2): (a) konvektiv, (b) durch Kontakt. [K].

Sobald die Makrokanäle entleert sind, und damit die Gasphase den Netzwerkboden erreicht hat, unterscheiden sich die Phasenverteilungen grundsätzlich. Im Folgenden soll hauptsächlich der neue Fall der Kontaktheizung diskutiert werden. Solange sich

Flüssigkeitscluster noch über das ganze Netzwerk erstrecken ($S \approx 0.6$), trocknen die Poren am warmen Netzwerkboden bevorzugt aus, denn die Variation in der Oberflächenspannung $\Delta\sigma \sim 8$ % übertrifft die Variation im Porenradius $\sigma_0/r_0 = 5$ %, ähnlich wie bei [57]. In zwei Dimensionen ist dieser Abschnitt kurz; für dreidimensionale Porennetzwerke sollte er aber eine bedeutende Rolle spielen.
Wenn viele getrennte Flüssigkeitscluster über das Netzwerk verteilt sind, dann kontrolliert der Gradient im Sattdampfdruck den weiteren Verlauf, ähnlich wie in [30]. Es bilden sich zwei Fronten aus, denn nicht nur oberflächennahe Flüssigkeitscluster trocknen aus, sondern auch Cluster an der warmen Netzwerkseite. Deren Dampf diffundiert durch die teilgesättigte Netzwerkregion hindurch; in dieser Region finden sowohl Verdunstung als auch Kondensation statt. Insgesamt sollten 24 % der anfänglichen Flüssigkeitsmenge während der Trocknung wieder kondensieren, etwa ein Fünftel – also 5 % der Gesamtflüssigkeit – muss jedoch vernachlässigt werden, da eine Porenbefüllung im Modell nicht beschreibbar ist [85]. Im Gegensatz zur Konvektionstrocknung mit warmer Luft stößt das Modell hier an seine Grenzen und kann den Prozess nur noch qualitativ abbilden (siehe auch 6.1). Die Trocknungskurven [K] sind daher mit Vorbehalt zu betrachten. Für die Kontaktheizung sind die Raten jedoch, aufgrund des höheren Temperaturniveaus im Netzwerk, während der gesamten Trocknung deutlich höher als für die konvektive Wärmezufuhr.

Insgesamt gesehen, kann die diskutierte Modellerweiterung wesentliche nicht-isotherme Effekte bei der Trocknung darstellen, auch wenn eine vollständige Beschreibung der Kondensation noch nicht umgesetzt wurde. Dies erfordert die Implementierung neuer diskreter Rechengesetze für die Porenbefüllung, wie z.B. in [10].

4.3 Mechanische Effekte

Kapillareffekte kontrollieren nicht nur den Flüssigkeitstransport während der Trocknung, sondern führen aufgrund des Kapillardrucks auch – besonders bei feinporigen Materialien – zu einer starken mechanischen Belastung mit der Folge von Schrumpfung oder Rissbildung. Üblicherweise werden die mechanischen Effekte mit Kontinuumsmodellen beschrieben (siehe z.B. [14,35] und Literaturstellen in [f]). Solche Modelle berücksichtigen die lokale Schrumpfung bzw. Ausdehnung des Materials entsprechend der lokalen Feuchte und Temperatur, die ihrerseits mit Kontinuumsansätzen für den Wärme- und Stofftransport berechnet werden. Auf der Basis der mechanischen Materialeigenschaften (elastisch, plastisch, etc.) wird dann das Spannungsfeld in der trocknenden Probe gewonnen. Bei Kenntnis der Modellparameter lässt sich so vorhersagen, wie die Probe schrumpfen wird, an welchem Ort sie den größten Belastungen ausgesetzt und ob dort Risse zu erwarten sind.

Motivation für das im Folgenden dargestellte Modell war die Vorstellung, dass die mechanische Belastung der Probe von der Flüssigkeitsverteilung abhängen sollte, die ihrerseits von Porenstruktur und Trocknungsbedingungen bestimmt wird. Das Modell soll also die Kapillarkräfte auf der Porenskala berücksichtigen und ihre Wirkung auf die Feststoffmatrix abbilden. Die feste Phase ist dann auch diskret zu betrachten, in Einheiten von ähnlicher Größe wie die Poren selbst. Für viele reale Strukturen ist diese Diskretisierung in natürlicher Weise vorgegeben, denn sie sind aus kleinen Primärpartikeln aufgebaut. Und so wird das Modell insbesondere für Partikelaggregate entwickelt. Abbildung 56 erläutert das Konzept: das Porenvolumen wird durch ein Porennetzwerk dargestellt, der Feststoff durch ein Partikelnetzwerk. Für die Modellentwicklung wird ein abstrahiertes Aggregat mit kubischer Struktur gewählt, eine Verallgemeinerung auf regellose Partikelanordnungen ist aber möglich [32]. Der Flüssigkeitstransport während der Trocknung wird dann mit einem Porennetzwerkmodell berechnet, wobei die Porenradien für ein streng kubisches Netzwerk alle identisch sind und deswegen künstlich randomisiert werden müssen.

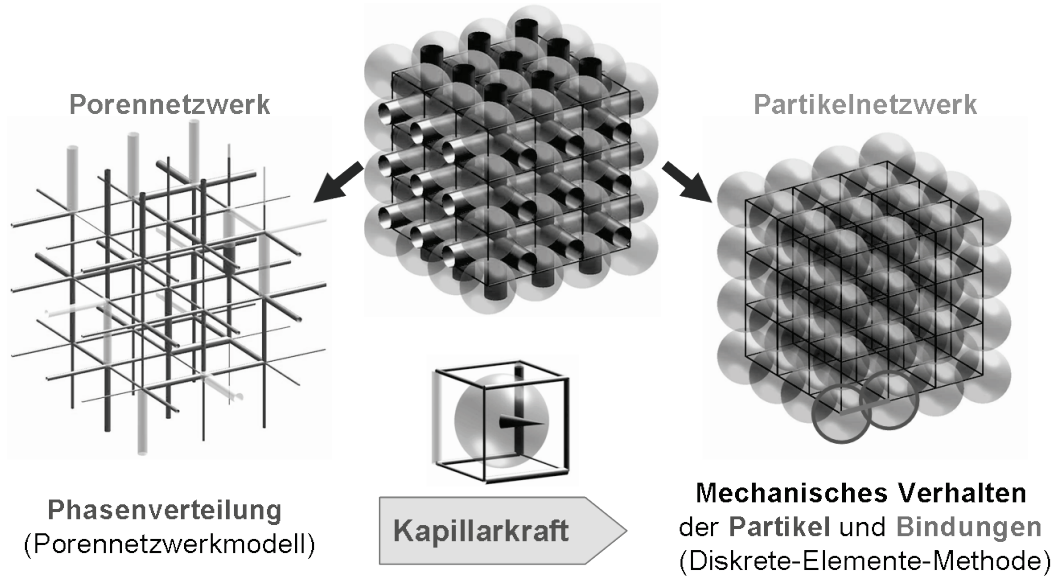

Abbildung 56. Konzept zur diskreten Beschreibung mechanischer Effekte [O].

Das mechanische Verhalten des Aggregats wird beschrieben mit den einzelnen Partikeln, welche durch diskrete Bindungen zu einem Netzwerk zusammengefügt sind. Hierzu wird die Diskrete-Elemente-Methode (DEM) benutzt [15,55], die die Bewegung der Partikel gemäß den auf sie wirkenden Kräften in einem Zeitschrittverfahren berechnet; dabei werden äußere Kräfte und von den direkten Nachbarn übertragene Kräfte berücksichtigt. Je nach Anwendung spielen unterschiedliche äußere und interpartikuläre Kräfte eine Rolle. Klassisch wird DEM zur Simulation des Schüttverhaltens frei beweglicher Partikel verwendet; dann spielen Gravitation, Partikel-Wand-Wechselwirkungen und Partikel-Partikel-Kontaktkräfte eine Rolle. Aber auch Partikelaggregate wurden bereits mittels DEM beschrieben [2,3]: dann sind die Relativbewegungen der Partikel typischerweise sehr klein, und die Kräfte werden hauptsächlich durch Feststoffbindungen übertragen, die ab einer kritischen mechanischen Belastung aufbrechen. Entscheidend – und sehr aufwändig – ist die Kalibrierung des Modells, d.h. die Bestimmung der mechanischen Mikroparameter. Die vorgestellten Simulationen mit Partikelaggregaten hoher Steifigkeit orientieren sich daher an Werten aus der Literatur [2]. Weitere allgemeine Ausführungen zur Diskrete-Elemente-Methode finden sich in [P] und [32].

Die beiden Netzwerke, respektive für Stofftransport und Mechanik, sind gekoppelt durch die Kapillarkräfte, wie sie sich aus der Flüssigkeitsverteilung ergeben. Vereinfachend wird die Kraft auf ein Partikel als Summe der Kapillarkraftbeiträge der 12 Nachbarporen berechnet, welche durch deren momentane Sättigung und relative Position im Raum bestimmt sind:

$$\mathbf{F}_c(\mathbf{x}_n, t) \propto \sum_{k=1}^{12} S_k(t) \frac{\mathbf{x}_k - \mathbf{x}_n}{|\mathbf{x}_k - \mathbf{x}_n|} \tag{31}$$

Hierbei sind $\mathbf{x}_n$ und $\mathbf{x}_k$ die Schwerpunktskoordinaten von Partikel bzw. Pore. Die alleinige Abhängigkeit von der Porensättigung S_k setzt implizit ein konstantes Kapillardruckniveau voraus. In Abbildung 56 ist beispielhaft gezeigt, wie sich die Kapillarkraft (Kegelpfeil) aus der Porensättigung ergibt (die Flüssigkeit ist dunkel dargestellt). Dieser einfache Ansatz berücksichtigt keine binären Flüssigkeitsbrücken zwischen den Partikeln, deren Kapillarkräfte eher für Partikelschüttungen relevant wären; im Partikelaggregat hingegen ist der Raum zwischen zwei Partikeln typischerweise durch eine Feststoffbrücke besetzt.

Im Trocknungsmodell werden die Kapillarkräfte in einer Ein-Weg-Kopplung als äußere Kräfte auf die Partikel des Aggregats gegeben. Dazu werden zuerst die Flüssigkeitsverteilungen für den gesamten Prozess berechnet. Daraus wird mit Gleichung (31) ein Kapillarkräfteprotokoll erstellt. In der DEM-Simulation schließlich wird die mechanische Antwort des Partikel-

aggregats schrittweise berechnet. Für jeden Satz von Kapillarkräften wird mechanisches Gleichgewicht etabliert, bevor die Kapillarkräfte für den nächsten Trocknungsschritt angewendet werden [32].

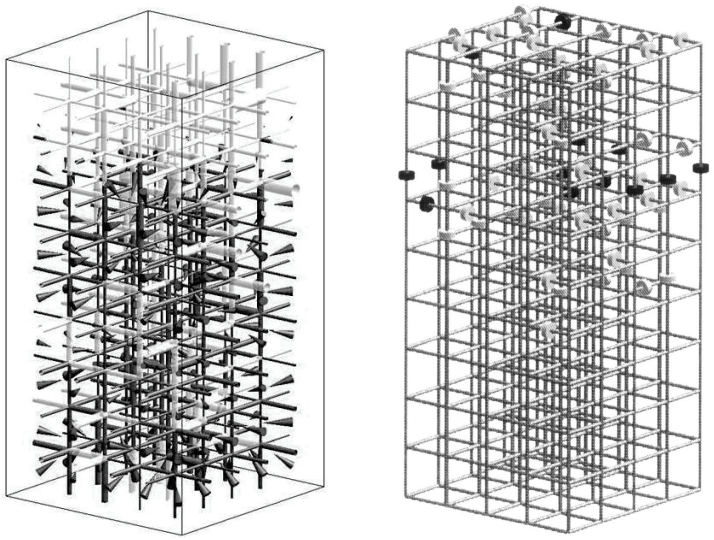

Abbildung 57. Flüssigkeitsverteilung und Kapillarkräfte (links) sowie Brüche (rechts) unter Scher- (hell) bzw. Zugspannung (dunkel) für ein 5×5×10 Partikelnetzwerk [32].

Ein typisches Simulationsergebnis für ein kleines Netzwerk ist in Abbildung 57 dargestellt. Für die Trocknung wurde hier das Basismodell benutzt, d.h. Flüssigkeitsreibung wurde vernachlässigt. Entsprechend wird erst dem gesamten Porennetzwerk Flüssigkeit entzogen, bevor die Trocknungsfront zurückweicht. Ist ein Partikel nur von trockenen oder vollgesättigten Poren umgeben, so wirken darauf keine direkten Kapillarkräfte, sondern nur bei Partikeln an der Phasengrenze. Solange eine große Region vollgesättigt ist, steht sie insgesamt unter Druckspannung, denn von allen Seiten wirkt der Kapillardruck. In teilgesättigten Bereichen ist die Phasengrenze sehr zerklüftet, und die Kapillarkräfte weisen lokal in sehr unterschiedliche Richtungen. Dadurch können einzelne Bindungen unter Zug- bzw. Scherspannung geraten und – je nach Belastungsniveau – auch aufbrechen.
Diese Brüche können als Mikrorisse gewertet werden, die das Material schädigen, jedoch nicht zu makroskopischen Rissen oder zur Zerstörung der Probe führen. Solche Mikrorisse können experimentell mit einem akustischen Sensor beobachtet werden [35].

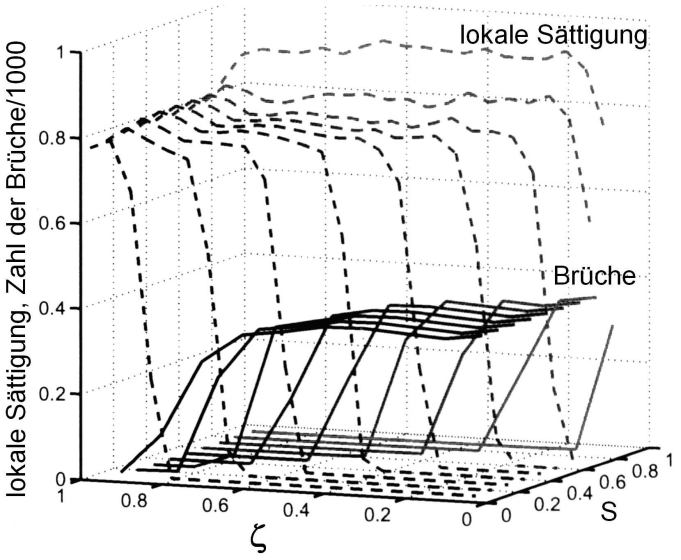

Abbildung 58. Sättigungsprofile und Lokalisierung der Brüche bei der Trocknung von 10×10×20 Partikelnetzwerken (Mittelung über 10 Monte-Carlo-Simulationen) [32].

Monte-Carlo-Simulationen mit größeren Netzwerken sollen das charakteristische Verhalten zeigen. Abbildung 58 veranschaulicht, dass Partikelbindungen nur an der zurückweichenden Trocknungsfront aufbrechen, also dann, wenn die Kapillarkräfte nach und nach ausgeschaltet werden. Beim anfänglichen Vordringen der Gasphase im 1. Trocknungsabschnitt sowie im trockenen Bereich treten keine Brüche auf.

Mit dem Modell kann qualitativ auch der Einfluss der mechanischen Eigenschaften des Partikelaggregats untersucht werden. Wie Abbildung 59 zeigt, nimmt die Zahl der Brüche ab, wenn die Stärke der Bindungen erhöht wird. Für sehr schwache Bindungen kommt es praktisch zu einer „Atomisierung“ des Aggregats.

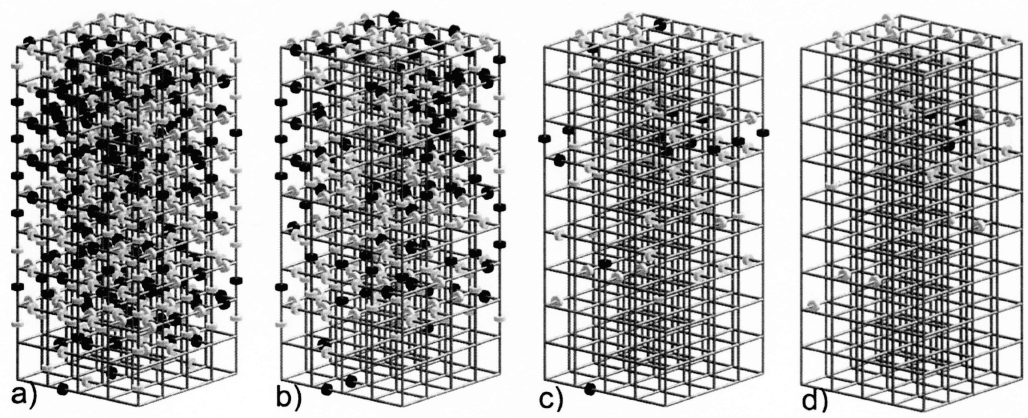

Abbildung 59. Brüche für Bindungsstärke (a) 4, (b) 8, (c) 16 und (d) 20 kN/m^2 [P].

Neben der Materialseite ist insbesondere auch der Einfluss der Trocknungsbedingungen von Interesse. So ist bekannt, dass eine Materialschädigung im Allgemeinen durch schonende Trocknung, d.h. niedrige Trocknungsraten, vermieden werden kann. Entsprechend den oben gewonnenen Erkenntnissen über die Stabilisierung der Trocknungsfront durch Reibungseffekte, wurde neben dem bereits diskutierten Grenzfall vernachlässigbarer Reibung auch der andere Grenzfall einer scharfen Trocknungsfront, d.h. ohne jegliche Kapillarströmung, betrachtet. In Monte-Carlo-Simulationen [P,32] zeigte sich, dass die Gesamtzahl der Mikrobrüche unabhängig von den Trocknungsbedingungen ist. Nur die relativen Anteile von Zug- und Scherbrüchen verschieben sich leicht, und das räumliche Muster der Brüche wird für unterdrückte Kapillarströmung regelmäßig.
Diese Invarianz lässt sich nur so erklären, dass eine Feststoffbrücke anscheinend – unabhängig vom makroskopischen Prozess – ähnlichen lokale Belastungen ausgesetzt wird, und zwar zu dem Zeitpunkt, zu dem die umliegenden Poren entleert werden. Je nach Trocknungsbedingungen und Frontstruktur geschieht dies allerdings zu einem früheren oder späteren Zeitpunkt.

Da dieses simulierte Verhalten nicht den allgemeinen Erfahrungen entspricht, ist die rein mikroskalige Beschreibung der Kapillarkräfte offenbar nicht ausreichend, um wesentliche Tendenzen korrekt abzubilden. Wie in [f] ausführlich diskutiert, spielt der makroskopische Druckgradient eine entscheidende Rolle bei der Rissbildung: je höher die anfängliche Trocknungsrate, desto größer ist auch das Gefälle im Flüssigkeitsdruck, das sich aufgrund der Kapillarströmung entwickelt. Dadurch kommt es zu makroskopischen Zugspannungen an der Oberfläche. Vermutlich ist es die Kombination dieser mechanischen Vorbelastung mit dem lokalen Abschalten von Kapillarkräften beim Austrocknen einzelner Poren, welche die Brüche auf der Partikelebene zu makroskopischen Rissen propagieren lassen (siehe auch [7]). Zukünftige Modelle sollten daher dem Druckgradienten – zumindest als von außen aufgeprägter effektiver Größe – Rechnung tragen.

Das Modell wurde schließlich auch auf reversibel schrumpfende Materialien angewendet [P]. Dann kann es folgendes Trocknungsszenario beschreiben (siehe hierzu Abbildung 60): das anfänglich vollgesättigte Partikelnetzwerk (a) schrumpft solange gleichförmig, bis die abstoßenden Partikelkräfte das Niveau des Kapillardrucks erreicht haben (b); dann entleeren sich die Poren entsprechend dem Stofftransportmodell, und die Probe entspannt sich von der Oberfläche her (c), bis sie die anfänglichen Dimensionen wieder erreicht hat (d). In der DEM-Simulation wird die gleichförmige Schrumpfung in einem einzigen Berechnungsschritt durch Anlegen der vollen Kapillarkräfte zusammengefasst und nur die Austrocknung der Poren mit der lokalen Abschaltung von Kapillarkräften wird zeitlich aufgelöst.

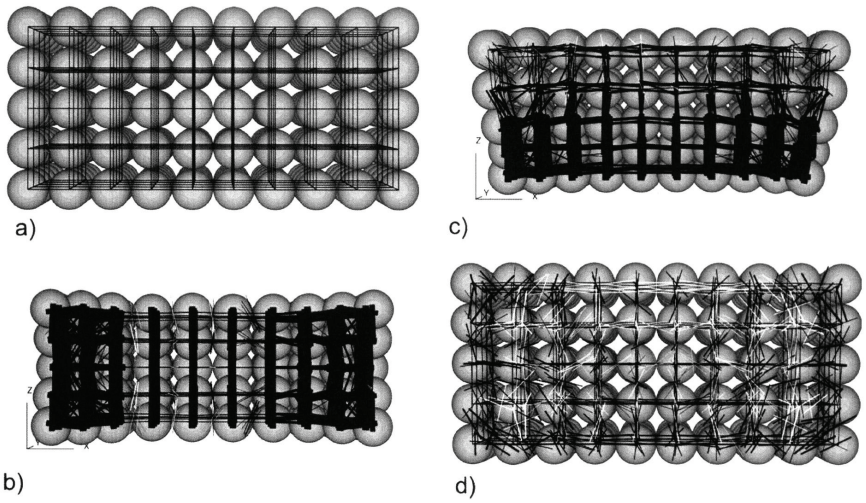

Abbildung 60. Trocknung eines reversibel schrumpfenden 10×5×5 Partikelnetzwerks; Linien stellen Kontaktkräfte dar (Dicke: Stärke, schwarz: Kompression, weiß: Zug) [P].

Da die kubische Struktur einen sehr hohen Abstraktionsgrad bedeutet, wurde das Porennetzwerkmodell für den Stofftransport bereits auf regellose Netzwerke von Partikeln gleicher Größe erweitert; hierzu kam die Voronoi-Täfelung zum Einsatz [32]. Die Kapillarkraftberechnung und die Anwendung auf das Partikelaggregat wurden auch schon für zwei Dimensionen umgesetzt [c].

Abschließend soll eine neue Arbeit aus der Literatur erwähnt werden, die konzeptionell einen ähnlichen Ansatz verfolgt. Musielak und Sliwa [50] beschreiben die Mechanik durch ein zweidimensionales Partikelnetzwerk mit elastischen Bindungen. Der Feuchtetransport wird mit einem einfachen Kontinuumsmodell berechnet. Sowohl die Federkonstanten als auch die Belastbarkeit der Bindungen werden (gemäß empirischer Gleichungen) mit abnehmender Feuchte größer. Dadurch kommt es zu Mikrorissen, welche die Belastung der umliegenden Bindungen erhöhen; in der Folge propagieren die Risse und es kommt zu makroskopischer Schädigung. Bei Musielak und Sliwa sorgt also der makroskopische Feuchtegradient – über den Umweg feuchteabhängiger effektiver Parameter – für ein realistisches mechanisches Verhalten des Partikelnetzwerks.
Entsprechend sollte mit der oben empfohlenen Erweiterung des hier vorgestellten Modells um makroskopische Druckgradienten eine realistische Prozessbeschreibung möglich sein.

5 Porennetzwerke – Verbindung zu makroskopischen Modellen

In diesem Kapitel werden zwei Ansätze vorgestellt, die zeigen sollen, wie der Übergang vom Porennetzwerk zur Makroskala gestaltet werden kann. Dies ist nötig, da aus rechentechnischen Gründen meist nur ein sehr kleiner Ausschnitt der trocknenden Probe auf der Porenskala simuliert werden kann. Ausgangspunkt für beide vorgestellten Methoden ist das Modell aus 4.1, d.h. das um die Flüssigkeitsreibung erweiterte (isotherme) Basismodell. In Abbildung 61 sind typische Phasenverteilungen für den zweidimensionalen Fall dargestellt: die Trocknungsfront ist durch Reibung stabilisiert und weitet sich mit absinkender Trocknungsrate auf; die Sättigungsprofile weisen einen Gradienten auf. Diese Charakteristika werden in den beiden Ansätzen genutzt.

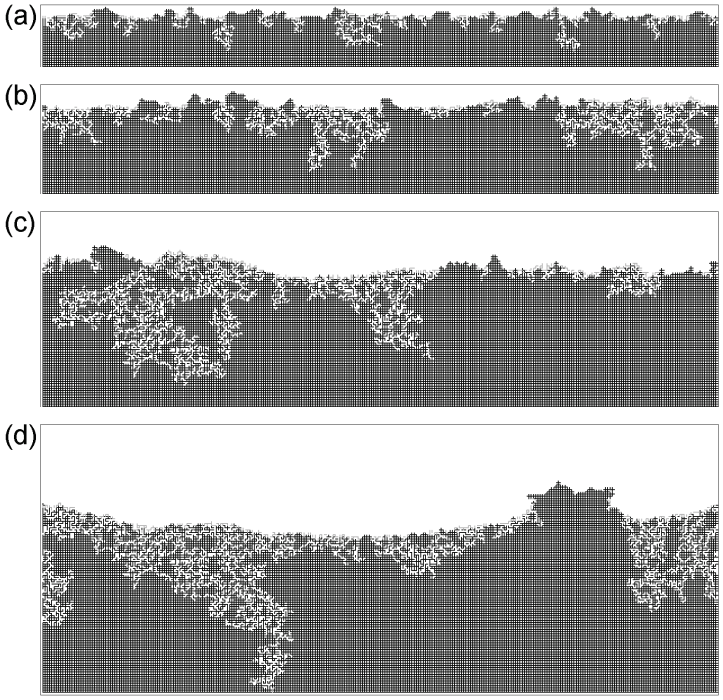

Abbildung 61. Flüssigkeitsverteilungen mit viskoser Stabilisierung der Trocknungsfront für ein 300×120 Netzwerk; die Gesamtsättigung beträgt (a) 0.95, (b) 0.9, (c) 0.75, (d) 0.583 [b].

5.1 Empirisches Modell mit Skalengesetz

Die Grundlage für den ersten Modellansatz bilden Arbeiten von Tsimpanogiannis et al. [89] sowie Prat und Bouleux [61], in denen Skalengesetze für stabilisierte Trocknungsfronten hergeleitet werden, insbesondere für die Frontbreite. Die Frontbreite (in z-Richtung) kann durch zwei Größen beschrieben werden: L_f charakterisiert die absolute Ausdehnung der teilgesättigten Zone, σ_f ist die Standardabweichung der Sättigungsverteilung einzelner Poren [61]. Beide Längen skalieren für den betrachteten viskos stabilisierten Fall mit der Kapillarzahl, die für das hier vorgestellte Model [N] definiert wird als

$$\mathrm{Ca} = \frac{4\nu_w L^3 \dot{m}_v}{\sigma \pi r_0^2 \sigma_0} \tag{32}$$

mit Porenlänge L und (über die Netzwerkoberfläche gemittelter) Dampfstromdichte $\dot{m}_v$.
In zwei Dimensionen lautet das Skalengesetz für die Frontbreite

$$\frac{L_f}{L} = B \cdot \mathrm{Ca}^{-\chi} \tag{33}$$

wobei χ = 0.52 [61] (der Vorfaktor B wird nicht diskutiert); σ_f/L skaliert mit χ = 0.57 [89,61].

Abbildung 62 zeigt für eine Porennetzwerksimulation, wie die Frontbreite mit abnehmender Kapillarzahl zunimmt. Der Bereich, in dem die Front sich im Netzwerkinneren befindet, d.h. von der Austrocknung der Oberfläche bis zum Durchbruch der Gasphase (bei S = 0.5514), kann in doppelt-logarithmischer Darstellung durch eine Gerade angepasst werden.

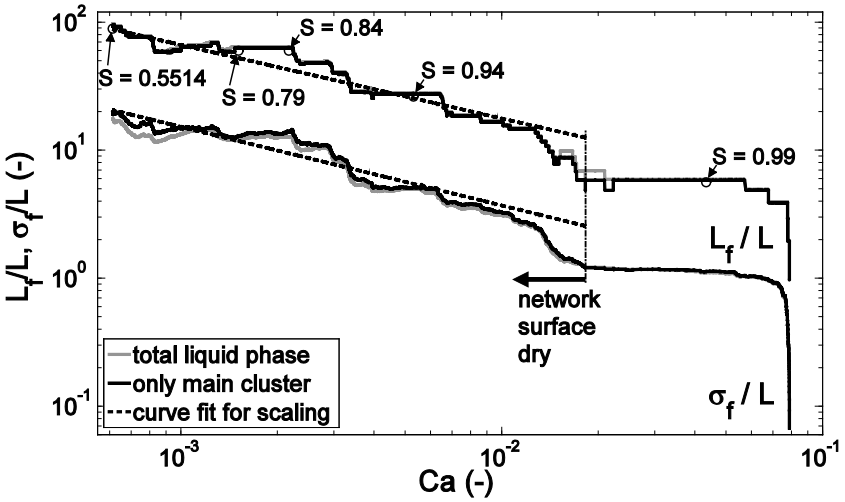

Abbildung 62. Variation der Frontbreite mit der Kapillarzahl für die Trocknung eines 300×120 Netzwerks mit Kurvenfit zur Bestimmung von (B und) χ in Gleichung (33) [N].

Wiederholt man solche Trocknungssimulationen, so findet man $\chi \approx 0.54$ für L_f und $\chi \approx 0.57$ für σ_f [N], was in Einklang mit den Literaturwerten steht; jedoch reichen simulierte Netzwerkgröße sowie Anzahl der Simulationen noch nicht für eine präzise Bestimmung der Skalierungsparameter aus.
Auch in der Literatur wurde χ mittels Netzwerksimulationen bestimmt, allerdings für eine durch Gravitation stabilisierte Trocknungsfront; dann wird Ca durch die Bondzahl ersetzt. Die ermittelten Werte liegen bei 0.57 [61] bzw. 0.58 [104] für das Skalengesetz von σ_f.

Nachdem die Breite der Trocknungsfront beschrieben ist, benötigt man für das Modell noch Informationen über die Flüssigkeitsverteilung innerhalb der Front, in einfachster Form als eindimensionales Profil. Zeichnet man die während der Trocknung auftretenden Sättigungsprofile über die dimensionslose Koordinate ζ innerhalb der Front (Abbildung 63), dann stellt man fest, dass sie alle gut durch eine einzige Kurve beschrieben werden können [N].

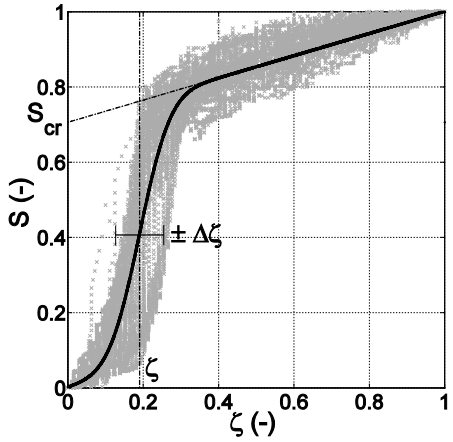

Abbildung 63. Dimensionslose Darstellung der Sättigungsprofile zu unterschiedlichen Zeitpunkten der Trocknung [N].

Im Trocknungsmodell sollen diese Informationen nun kombiniert werden: Gleichungen (32) und (33) beschreiben, wie sich L_f in Abhängigkeit von $\dot{m}_v$ verändert; und das dimensionslose Profil approximiert die Flüssigkeitsverteilung innerhalb der Front; es fehlt also nur eine Beziehung, welche das Vorrücken der Front erfasst. Hierzu wird die Frontposition z_f definiert als die oberflächennahe Grenze der Front. Nimmt man für die eindimensionale Beschreibung vereinfachend an, dass der gesamte teilgesättigte Bereich zwischen z_f und $z_f + L_f$ auf Sattdampfdruck liegt, dann wird die momentane Trocknungsrate beschrieben durch

$$\dot{m}_v = \left(\frac{1}{\beta} + \frac{z_f}{D_{eff}(S=0)} \right)^{-1} \frac{\tilde{M}_v P_g}{\tilde{R}T} \ln \frac{P_g - P_{v\infty}}{P_g - P_v^*} \tag{34}$$

(vgl. Gleichung (5)) mit dem effektiven Diffusionskoeffizienten des trockenen Netzwerks $D_{eff}(S = 0) \approx \delta\pi r_0^2/L^2$. Der Trocknungsverlauf kann nun mit z_f als Parameter berechnet werden und ist in Abbildung 64 als wandernde Front und in Abbildung 65 als Trocknungskurve dargestellt, und einer Porennetzwerksimulation gegenübergestellt. Zudem wurde die Trocknungskurve für eine scharfe Trocknungsfront ($L_f = 0$) mit Gleichung (34) berechnet.

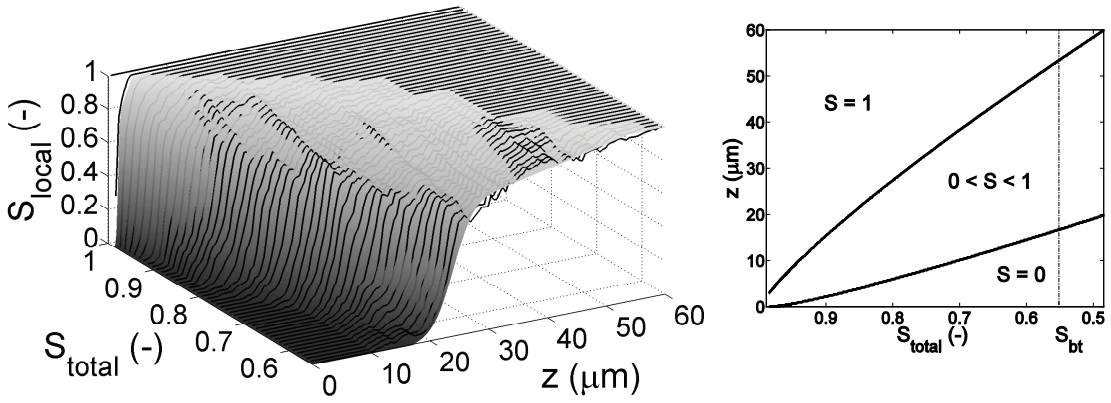

Abbildung 64. Sättigungsprofile für eine Netzwerksimulation und das Makromodell (links) sowie Bewegung des teilgesättigten Bereichs von z_f bis $z_f + L_f$ (rechts) [N].

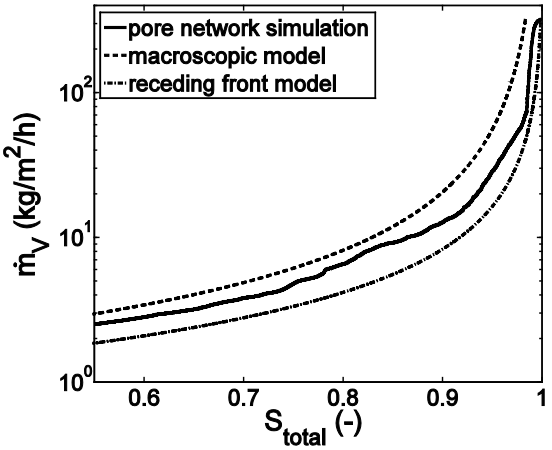

Abbildung 65. Trocknungskurven für eine Netzwerksimulation, das Makromodell sowie für eine scharf zurückweichende Front ohne Kapillareffekte [N].

Insgesamt gesehen werden die Feuchteprofile durch das empirische Makromodell gut beschrieben. Die Trocknungsrate wird jedoch unterschätzt aufgrund der Annahmen, dass die Front glatt und die Flüssigkeit innerhalb der Front gut verteilt sei. Anhand von Abbildung 61 sieht man jedoch, dass nur einzelne Netzwerkbereiche bis hin zu z_f gesättigt sind. Außerdem kann das Modell den Beginn der Trocknung nicht korrekt wiedergegeben, denn die Front muss sich erst entwickeln. Und auch der Durchbruch der Gasphase wird nur unzureichend vorhergesagt.

Das vorgestellte Modell ist nicht einfach auf den dreidimensionalen Fall übertragbar, da die Front dann in zwei Regionen eingeteilt werden muss, deren Breiten zwar beide entsprechend Gleichung (33), aber mit unterschiedlichen Exponenten skalieren. Der Exponent χ = 0.57 gilt dann nur noch für die fraktale Region im Bereich hoher Flüssigkeitssättigungen, für die Breite der kompakten Region wird hingegen χ = 1 erwartet [69]. Mit fortschreitender Trocknung wächst die kompakte Region daher verhältnismäßig stärker und die fraktale Region verliert zunehmend an Bedeutung.
In [N] wurde das Modell für dreidimensionale Porennetzwerke benutzt; die Ergebnisse sind allerdings – rückblickend – kritisch zu bewerten. Die dimensionslosen Sättigungprofile (Abbildung 9 in [N]) lassen sich nicht elegant durch eine einzige Kurve approximieren; vielmehr scheinen sie die unterschiedliche Skalierung der beiden Regionen widerzuspiegeln. Ferner ist damit zu rechnen, dass die begrenzte Netzwerkgröße (15×15×121) selbst einen Skaleneffekt bewirkt. Weitere Untersuchungen, insbesondere für drei Dimensionen, sind daher nötig, erscheinen aber lohnend.

Für den Fall des reibungsfreien Flüssigkeitstransports (Basismodell) könnte der Trocknungsprozess durch ein einfacheres Makromodell approximiert werden, das bis zu einer kritischen Sättigung gleichförmigen Flüssigkeitsentzug in der gesamten Probe annimmt, und danach das Zurückweichen der Verdunstungsfront mit Dampfdiffusion durch die trockene Zone beschreibt (siehe S. 297 in [36] sowie [13]). Als wesentlicher Modellparameter ist dann die kritische Sättigung zu bestimmen, unterhalb derer die Flüssigkeit nicht mehr makroskopisch zusammenhängt; diese ist durch die Perkolationstheorie bestimmt und hängt von der Netzwerkgröße ab.

5.2 Parametrisierung des Kontinuumsmodells

Der zweite Modellansatz verfolgt das gleiche Ziel wie in Kapitel 2, nämlich die Bestimmung der effektiven Parameter des Kontinuumsmodells durch Simulationen auf der Porenebene. Abbildung 66 skizziert die auf viskose Kapillarströmung und Dampfdiffusion reduzierte Variante des Kontinuumsmodells, die den Netzwerksimulationen in Abbildung 61 entspricht. Die Gleichung für den Feuchtetransport ist gegeben durch

$$\frac{\partial}{\partial t}\left(S\psi\rho_w + (1-S)\psi\frac{\tilde{M}_v P_v}{\tilde{R}T}\right) = \frac{\partial}{\partial z}\left(D_{eff}\frac{\tilde{M}_v P}{\tilde{R}T}\frac{\partial \ln(P-P_v)}{\partial z} - \frac{Kk_w}{\nu_w}\frac{\partial P_c}{\partial z}\right) \tag{35}$$

mit den drei Parameterfunktionen effektiver Diffusionskoeffizient $D_{eff}(S)$, Flüssigpermeabilität Kk_w (S) und Kapillardruck $P_c(S)$, welche für eine gegebene Porenstruktur zu ermitteln sind. Aus numerischen Gründen muss zudem jedem Dampfdruck eindeutig eine Sättigung zugeordnet werden, also (zumindest geringfügig) hygroskopisches Verhalten in einer Sorptionsisotherme $P_v(S)$ definiert werden.

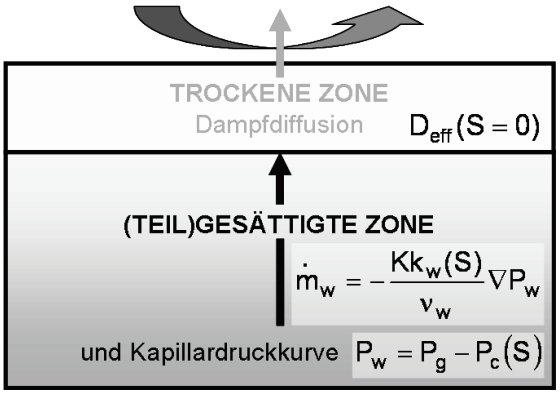

Abbildung 66. Kontinuumsmodell für Trocknung (isotherm, ohne Gradient im Gasdruck).

In einem Demonstrationsprojekt [e] wurde für ein Porennetzwerk wie in Abbildung 61 die Trocknung simuliert. Während des Trocknungsprozesses wurden teilgesättigte Scheiben aus dem Netzwerk "entnommen", und daran wurden numerische Experimente zur Bestimmung der effektiven Parameter durchgeführt.
Für die Flüssigpermeabilität wurde an die Scheibe (mit Dicke Δz und Querschnittsfläche A) ein Druckunterschied ΔP_w angelegt und der Massenstrom $\dot{M}_w$ durch alle Flüssigkeitscluster berechnet, wie in [68,73]:

$$Kk_w(S) = \nu_w \frac{\dot{M}_w(S)}{A} \frac{\Delta z}{\Delta P_w} \tag{36}$$

Da separate Flüssigkeitscluster (wie in Abbildung 61d) hierbei auch berücksichtigt wurden, ergibt sich das Problem, dass sie für dünne Scheiben zu Kk_w beitragen können, nicht aber zum Flüssigkeitstransport auf der Netzwerkebene.
Der Kapillardruck P_c wurde für kapillares Gleichgewicht in der Scheibe bestimmt, d.h. er ist durch die größte Grenzflächenpore des jeweiligen Flüssigkeitsclusters vorgegeben; entsprechend trägt jeder Cluster in der Scheibe einen Kapillardruckwert bei, obwohl die separaten Cluster für den makroskopischen Flüssigkeitstransport keine Rolle spielen.
Die numerischen Experimente zur Parameterbestimmung wurden zwar bewusst unabhängig und ohne Kenntnis vom Makro-Prozess durchgeführt; aufgrund der genannten Inkonsistenz ist zukünftig aber eine Beschränkung auf den Hauptcluster zu empfehlen.

Der effektive Diffusionskoeffizient wurde ganz analog durch Anlegen eines Dampfdruckunterschieds ΔP_v und Berechnung des zugehörigen Massenstroms $\dot{M}_v$ bestimmt:

$$D_{eff}(S) = \frac{\tilde{R}T}{\tilde{M}_v} \frac{\dot{M}_v(S)}{A} \frac{\Delta z}{\Delta P_v} \tag{37}$$

Hierbei wurde die Flüssig-Gas-Grenzfläche als undurchlässig angenommen (wie auch in der Literatur [68,73]); diese Randbedingung ist jedoch kritisch zu bewerten, denn in einem Dampfdruckgradienten ist Verdunstung bzw. Kondensation möglich.

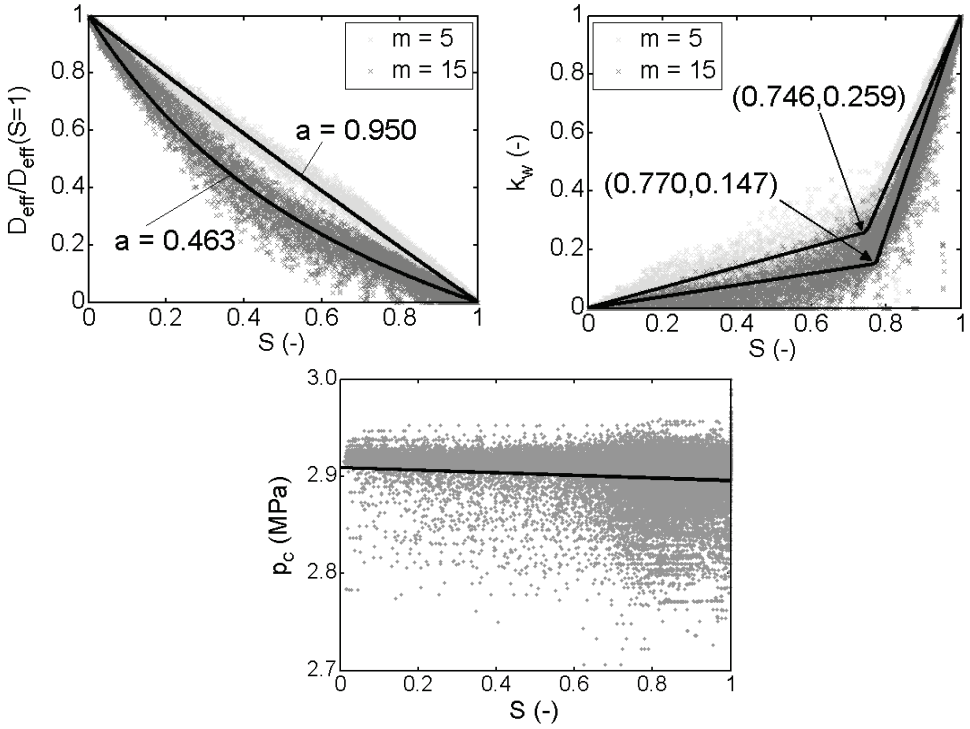

Abbildung 67. Parameterfunktionen aus Netzwerksimulationen: $D_{eff}/D_{eff}(S = 1)$ wurde mit einer Kurve $\frac{a(1-S)}{1+(a-1)(1-S)}$ angepasst, k_w und P_c mit (abschnittsweise) linearen Kurven [e].

Die Ergebnisse der Parameterbestimmung sind in Abbildung 67 dargestellt. Die Funktionen für D_{eff} und k_w hängen stark von der verwendeten Scheibendicke ab (m ist die Zahl der Knotenebenen). Dies ist ein bekanntes Phänomen [65,68]; im zweidimensionalen Fall kommt allerdings hinzu, dass kein repräsentatives Volumenelement existiert, da die gesamte Flüssigkeitsfront fraktal ist.
Für den Kapillardruck kann aus der Punktewolke keine geeignete Funktion abgeleitet werden, daher wurde vereinfachend eine lineare Abhängigkeit angenommen; die Streuung sollte deutlich kleiner werden, wenn nur der Hauptcluster berücksichtigt wird. In der Literatur wurde für dreidimensionale Verdrängungssimulationen bei hohen Sättigungen eine starke Abhängigkeit der Kurve von der Netzwerkgröße festgestellt, denn im fraktalen Bereich der Front gibt es kein repräsentatives Netzwerk [69].

Nun werden die Parameterfunktionen ins Kontinuumsmodell – Gleichung (35) – eingesetzt, um die Trocknung zu simulieren. Im zweidimensionalen Fall kann dies leider nur der Demonstration dienen, denn im Kontinuumsmodell skaliert die Frontbreite mit $\chi = 1$ [69], was grundsätzlich nicht mit der Netzwerksimulation ($\chi = 0.57$) vereinbar ist. In drei Dimensionen hingegen skaliert der Hauptteil der diskreten Trocknungsfront ebenfalls $\chi = 1$, so dass eine Äquivalenz mit dem Kontinuumsansatz möglich, und damit eine Parametrisierung sinnvoll erscheint.
Die Sättigungsprofile für das Kontinuumsmodell sind in Abbildung 68 denen aus mehreren Netzwerksimulationen gegenübergestellt. Besonders für kleine und für hohe lokale Sättigungen gibt es qualitative Abweichungen.

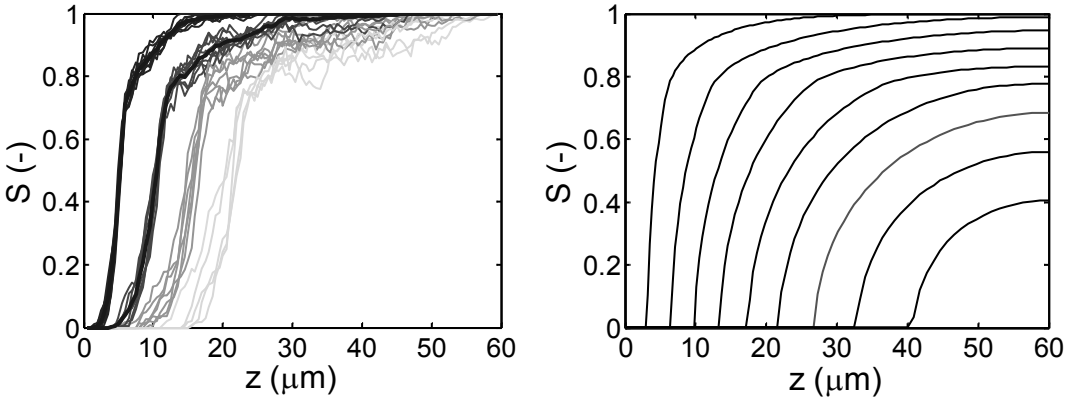

Abbildung 68. Sättigungsprofile für Netzwerksimulationen (links) und für das mittels Porennetzwerk parametrisierte Kontinuumsmodell (rechts) [e].

Neben dem erwähnten Problem der Dimensionalität bleiben weitere kritische Aspekte, die eine gute Übereinstimmung der Modelle behindern können. Insbesondere nimmt das Kontinuumsmodell stark vereinfachend an, dass der gesamte teilgesättigte Bereich von z_f bis $z_f + L_f$ auf Sattdampfdruck liegt. Somit wird die Sättigungsabhängigkeit von D_{eff} überhaupt nicht genutzt; außerdem kann die Voraussetzung am oberflächennahen Ende der Trocknungsfront durch einige wenige isolierte Cluster gar nicht gewährleistet werden (siehe Dampfdruckprofile in [41]). Dieses Problem könnte eine Erweiterung des Kontinuumsmodells nötig machen, die den isolierten Clustern Rechnung trägt.
Als weitere offene Frage ist unklar, wie die effektiven Parameter am besten bestimmt werden sollen: so wie hier, d.h. unter Nutzung von Informationen aus dem Trocknungsprozess, oder für gänzlich unabhängig gewonnene Phasenverteilungen (für Kapillardruck siehe z.B. [69]).

Aus den Ausführungen wird deutlich, dass noch einige Forschungsarbeit zu leisten sein wird, bis Porennetzwerke zur Parametrisierung eines Kontinuumsmodells für den Wärme- und Stofftransport genutzt werden können. Für die praktische Anwendung von Netzwerkmodellen wäre diese Möglichkeit aber ein sehr bedeutender Fortschritt und ist daher unbedingt weiter anzustreben.

6 Parallele und zukünftige Arbeiten

Dieses letzte Kapitel gibt zunächst einen kurzen Überblick über laufende experimentelle Projekte, die den Trocknungsprozess auf der Porenebene untersuchen – zur Bewertung und Weiterentwicklung der Modelle. Außerdem wird ein theoretischer Ansatz zur Beschreibung der Flüssig-Gas-Grenze in der exakten Porengeometrie skizziert, der komplementär zur Porennetzwerkmodellierung verwendet werden kann – oder zur Prüfung der dort getroffenen Annahmen. Zuletzt wird auf über die reine Trocknung hinausgehende Anwendungen von Netzwerkmodellen eingegangen.

6.1 Experimentelle Phasenverteilungen

Für die experimentelle Untersuchung der Trocknung auf der Porenebene eignen sich einerseits zweidimensionale Mikromodelle, in welchen die gewünschte Porenstruktur mit Methoden der Siliziumtechnologie präzise hergestellt werden kann. Andererseits sind Schüttungen aus monodispersen Glaskugeln – auch als quasi zweidimensionale Monolage zwischen zwei Platten – beliebte Modellsysteme. Bei letzteren muss die zufällige Struktur erst charakterisiert werden, um Experimente und Simulationen vergleichen zu können.
Zweidimensionale Systeme können mit einer einfachen optischen Kamera hinreichend dargestellt werden; für einen guten Kontrast zwischen Flüssigkeit und Gas kommt es jedoch entscheidend auf die richtige Beleuchtung an. Dreidimensionale Schüttungen können nur mit einer tomographischen Messmethode charakterisiert werden; aufgrund der hohen Ortsauflösung bietet sich hier die Röntgen-Mikrotomographie an.
Im Folgenden sollen nun ausgewählte Beispiele aktueller eigener Trocknungsexperimente mit den genannten Modellsystemen gezeigt werden.

In Abbildung 69 ist die Trocknung eines Siliziumnetzwerks mit aufgeprägtem destabilisierenden Temperaturgradienten gezeigt. Hierzu wurde das Netzwerk horizontal auf eine temperierte Metallplatte gelegt und an seiner offenen Seite mit Trocknungsluft beströmt. Die Trocknungsbedingungen sind also ähnlich wie für die in Abbildung 55 dargestellte Simulation; allerdings wird für das zweidimensionale Siliziumnetzwerk das gesamte Temperaturfeld durch die äußeren Bedingungen vorgegeben und entwickelt sich nicht frei.

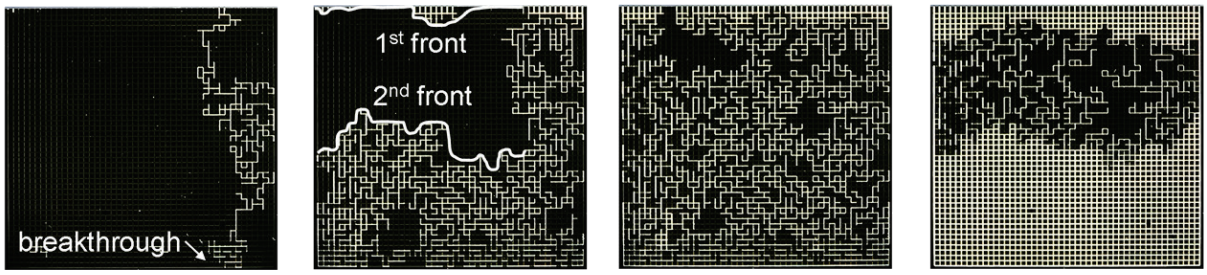

Abbildung 69. Kamerabilder eines trocknenden 50×50 Netzwerks aus Silizium; die Temperatur an der offenen Seite (oben) beträgt 27°C, am Netzwerkboden 49°C [ee].

Entsprechend den Erwartungen aus den Simulationen, beobachtet man einen frühen Durchbruch der Gasphase und eine bevorzugte Entleerung des warmen Bereichs durch Kapillareffekte. Wenn die Flüssigkeit dann nur noch aus einzelnen kleinen Clustern besteht, trocknen diese nicht nur von der offenen Netzwerkseite, sondern auch vom warmen Netzwerkboden her. Dabei kondensiert ein beträchtlicher Teil des diffundierenden Dampfs, was zu einer Kompaktierung der Flüssigkeitscluster im Inneren des Netzwerks führt. (Vermutlich ist dieser Effekt deshalb besonders stark, weil das aufgeprägte Temperaturprofil linear ist.) Die nicht-isotherme Modellierung des Prozesses kann den Verlauf bereits teilweise wiedergeben [ee], muss aber noch um den Effekt der Porenbefüllung durch Kondensation erweitert werden.

(Oyarzun und Segura haben jüngst ähnlich hergestellte Mikromodelle getrocknet, welche die charakteristische Poren- bzw. Zellenstruktur von Holz nachbilden sollten [53].)

Ein Trocknungsexperiment für eine zufällige Monolage von Glaskugeln ($\varnothing \approx 1.3$ mm) zwischen zwei Glasplatten ist in Abbildung 70 dargestellt. Die Schicht wurde mit Durchlicht beobachtet, und der Kontrast zwischen trockenen und flüssigkeitsbenetzten Glaskugeln wurde bildanalytisch genutzt, um den gesättigten Bereich (schwarz) darzustellen [4]. Die Gesamtsättigung wird als Anteil der schwarzen Fläche berechnet.

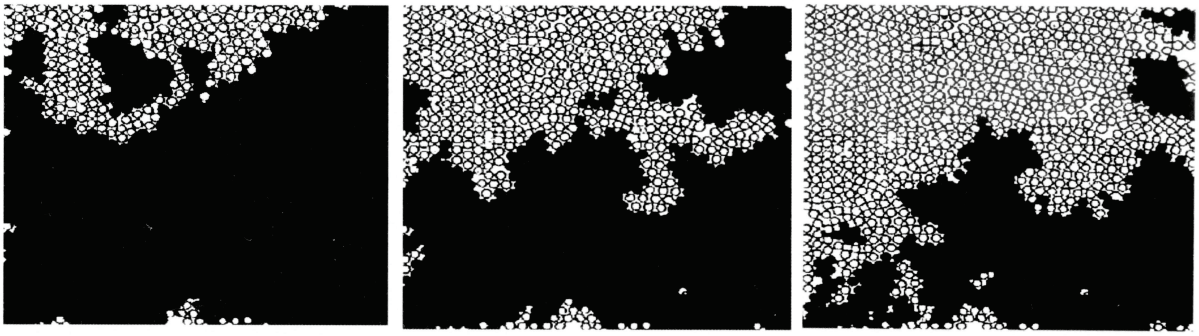

Abbildung 70. Bildanalytisch bearbeitete Kamerabilder einer trocknenden regellosen Schicht aus Glaskugeln (schwarz: Flüssigkeit) [4].

Die Phasenverteilungen sind qualitativ von gleicher Struktur wie bei Simulationen mit quadratischen Porennetzwerken. Da die Ränder der Schüttung nicht perfekt verschlossen wurden, konnte auch von dort Gas eindringen. Flüssigkeitsfilme scheinen im Prozess eine wichtige Rolle zu spielen, denn die Trocknungsrate ist bis zu sehr niedrigen Sättigungen ($S \approx 0.06$) konstant; allerdings sind sie optisch nur sehr schwer zu erkennen und nicht quantitativ zu erfassen [4]. Außer der homogenen Schüttung wurden auch aus zwei unterschiedlichen Zonen bestehende Schüttungen getrocknet (vgl. Simulationen in 3.4) [4].

(Ähnliche Messungen – jedoch mit mehreren Kugellagen Schichtdicke – wurden jüngst auch von Yiotis et al. durchgeführt und zur Bestimmung von χ im Skalengesetz für die Frontbreite benutzt [105]. Im Gegensatz zu Shaw [79], der mit größerer Schichtdicke arbeitete, können Yiotis et al. den theoretischen Wert für den zweidimensionalen Fall gut reproduzieren.)

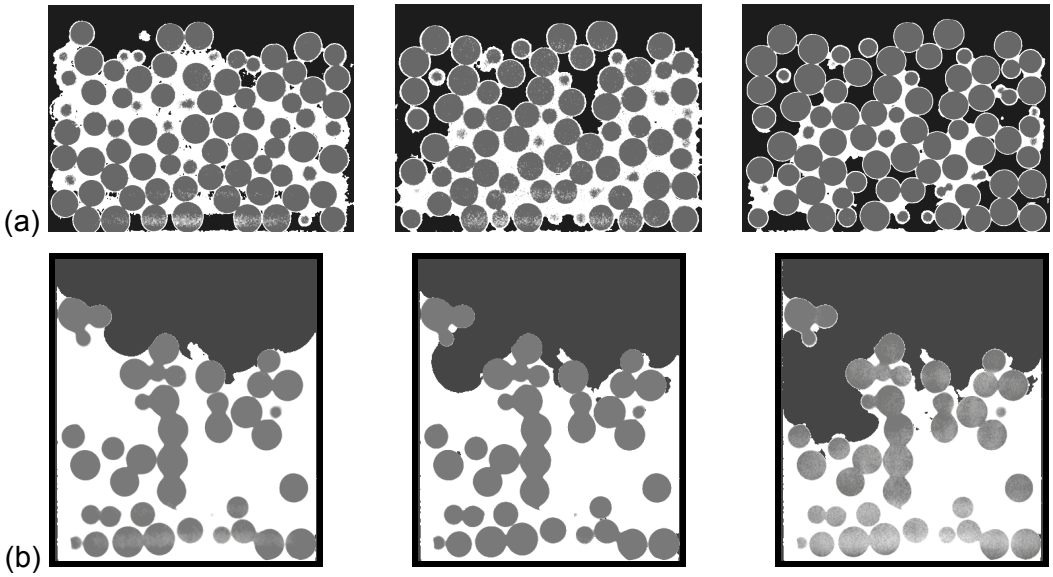

Abbildung 71. Querschnitte aus bildtechnisch verarbeiteten Röntgentomogrammen einer trocknenden Schüttung aus (a) Glaskugeln [bb], (b) gesinterten Anordnungen von Glaskugeln [cc] (schwarz: Luft, dunkelgrau: Glas, hellgrau: Flüssigkeit).

Röntgentomographische Messungen an Schüttungen aus Glaskugeln sind in Abbildung 71a gezeigt. Die Probe wurde im Tomographen getrocknet und für die Dauer einer Aufnahme abgedeckt, um Artefakte durch Bewegung der Menisken zu vermeiden. Aufgrund von Wandeffekten entleeren sich die Poren von allen Seiten. Mittels Bildanalyse können die drei Phasen unterschieden und Koordinaten und Radien der Glaskugeln bestimmt werden. Aktuell werden die Messungen verwendet, um ein Porennetzwerkmodell [32] für regellose dreidimensionale Kugelschüttungen zu testen und weiterzuentwickeln.
Zudem wurden Trocknungsexperimente mit hochporösen Partikelanordnungen durchgeführt [cc]. Die Ergebnisse in Abbildung 71b zeigen, wie große Zwischenräume aufgrund des Kapillareffekts zuerst austrocknen. In beiden Experimenten wurde jeweils nur eine kleine Schüttung aus relativ großen Kugeln ($\varnothing \sim 1$ mm) verwendet, damit die Flüssigkeit in den Poren gut aufgelöst werden kann.

6.2 Mikroskalige Modellierung

Da die Beschreibung mit Porennetzwerken nicht für alle Porenstrukturen geeignet scheint, wird auch ein alternativer Modellierungsansatz verfolgt, mit dem die Flüssigkeitsverteilung in beliebigen Geometrien berechnet werden kann. Ein Anwendungsbeispiel ist die Trocknung hochporöser Gele, die aus Netzwerken von Nanopartikeln bestehen.
Abbildung 72 zeigt, wie hierzu die gesamte Struktur mit einem raumfesten Gitter diskretisiert wird. Mit einem Volume-of-Fluid-Ansatz wird die Phasenverteilung durch die Volumenanteile f_i der drei Phasen (fest s, flüssig w, gasförmig g) in den einzelnen Raumzellen beschrieben. Um aufwändige fluiddynamische Berechnungen zu vermeiden, wird die Trocknung als Abfolge kapillarer Gleichgewichtszustände behandelt. Nachdem durch Dampfdiffusion etwas Flüssigkeit entfernt wurde, relaxiert jeder Flüssigkeitscluster, so dass die Bedingung für den Kontaktwinkel θ erfüllt ist und die Flüssig-Gas-Grenzfläche eine konstante Krümmung κ hat. Hierzu werden die Normalenvektoren $\mathbf{n}_i$ der Grenzflächen und die Krümmung aus den Volumenanteilen f_i berechnet. Diese numerische Methode ist an die Arbeiten von Štěpánek (siehe z.B. [73]) angelehnt.

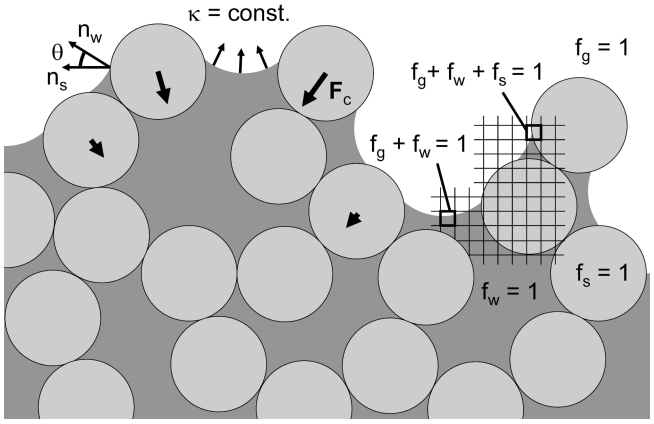

Abbildung 72. Illustration der Volume-of-Fluid-Methode zur Berechnung des kapillaren Gleichgewichts in einem Partikelaggregat [f].

In Abbildung 73 ist die Trocknung eines hochporösen Partikelnetzwerks für zwei unterschiedliche Kontaktwinkel gezeigt. Man erkennt deutlich, wie die Kapillarströmung bei hydrophilen Partikeln begünstigt und bei hydrophoben Partikeln unterdrückt wird.

Das Modell soll nicht nur für die Simulation von Phasenverteilungen und Trocknungskurven verwendet werden, sondern auch für die Berechnung der Kapillarkräfte $\mathbf{F}_c$ auf die Primärpartikel (siehe Abbildung 72). In einer Kopplung mit der Diskrete-Elemente-Methode sollen dann mechanische Effekte bei der Trocknung dargestellt werden. Um erfassen zu können, wie Phasenverteilungen und mechanische Schädigung von den Trocknungs-

bedingungen abhängen, soll der Probe ein makroskopischer Gradient im Flüssigkeitsdruck bzw. in der Krümmung aufgeprägt werden.
Die mikroskalige Beschreibung kann aber auch dazu genutzt werden, die vereinfachenden Regeln für die Porenentleerung in abstrahierten Netzwerkmodellen zu überprüfen.

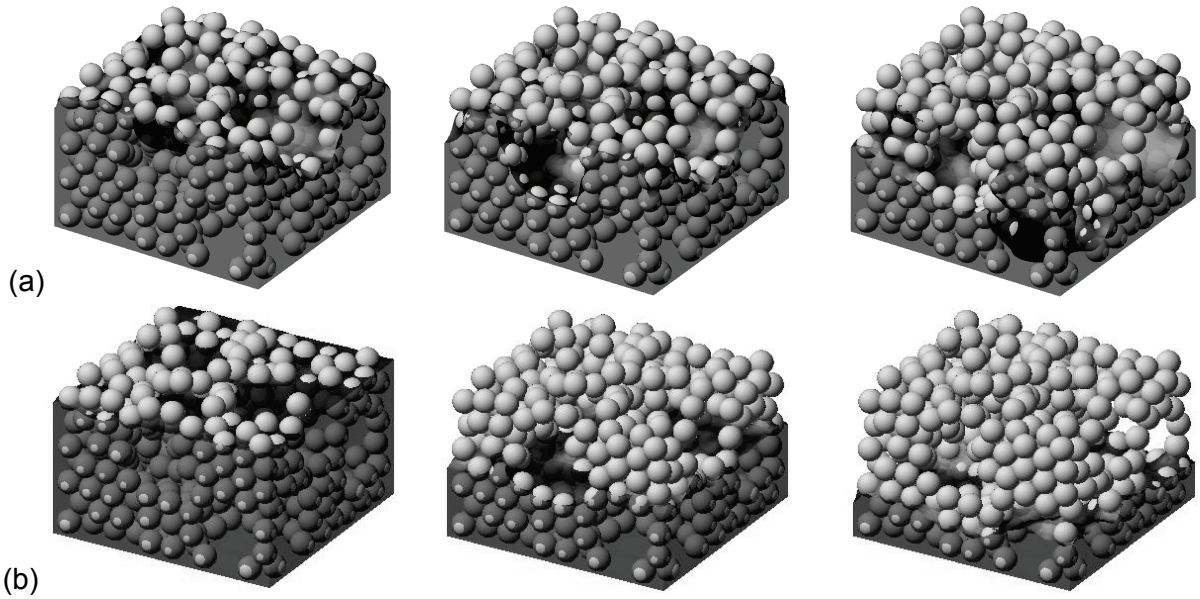

Abbildung 73. Mit Volume-of-Fluid-Methode simulierte Flüssigkeitsverteilungen für trocknendes Partikelaggregat; Einfluss des Kontaktwinkels (a) θ = 18° [d], (b) θ = 60°.

An dieser Stelle sei auf eine Arbeit von Lehmann et al. [43] hingewiesen, welche die Phasenverteilungen für kapillaritätsdominierte Verdrängung ebenfalls mit einer Raumdiskretierung deutlich unterhalb der Porengröße beschreiben, die Phasengrenze aber nicht als frei bewegliche Fläche behandeln, welche sich entsprechend der Grenzflächenkräfte einstellt. Vielmehr wird die Methode der Invasionsperkolation verallgemeinert, so dass die unterschiedliche Geometrie der Poren besser berücksichtigt werden kann als bei den in dieser Arbeit verwendeten Porennetzwerken. Lehmann et al. stellen ein morphologisches Porennetzwerkmodell vor, in welchem jedem Raumelement entsprechend seiner geometrischen Lage im Porenraum ein Invasionsradius zugeordnet wird. In einem Invasionsschritt werden dann jeweils ganze Porenbereiche entleert.

6.3 Weitere Anwendungen von Porennetzwerkmodellen

In vielen praktisch relevanten Trocknungsprozessen sind die Poren nicht mit reiner Flüssigkeit gefüllt, sondern mit einem Flüssigkeitsgemisch, einer Lösung oder einer Suspension.
In der Literatur haben Prat et al. [8,76,92] die Verdunstung von Salzlösungen aus porösen Materialien behandelt. Durch Kapillarströmung reichert sich das Salz an den Orten der Verdunstung an. Dies ist z. B. für Gebäude in Gegenden hohen Grundwassersalzgehalts (in Meeresnähe) relevant: während Kristallisation an der Oberfläche (nur) zu Salzflecken führt, kann die Bausubstanz zerstört werden, wenn das Salz im Inneren auskristallisiert [92]. In der Modellierung muss neben dem Wassertransport insbesondere der konvektive und diffusive Salztransport in der Porenflüssigkeit berücksichtigt werden. Zum grundlegenden Verständnis der Effekte wurde zunächst eine einzelne Kapillare betrachtet [8], dann folgten Experimente mit Kugelschüttungen [76,92] und erste Porennetzwerksimulationen [92].

Lewis et al. [48] haben die Trocknung von Keramik mit organischem Binder simuliert; dazu haben sie ein Porennetzwerkmodell (im weitesten Sinn) verwendet und die Diffusion der

volatilen Komponenten in der Porenflüssigkeit als Brownsche Bewegung virtueller Teilchen mit einer Monte-Carlo-Methode beschrieben. Als Simulationsergebnis präsentieren die Autoren die Verteilung der nichtvolatilen Polymere in den Zwischenräumen der Keramikpartikel.
Ähnlich könnte auch der Trocknungsschritt bei der Herstellung keramischer Filterkörper simuliert werden. Im üblichen Produktionsablauf wird dazu ein Formkörper aus Papier zunächst mit einer submikronen Keramiksuspension getränkt, dann getrocknet und schließlich gebrannt. Für die Qualität des Keramikkörpers ist eine möglichst homogene Dichteverteilung sehr wichtig. Ein Porennetzwerkmodell könnte die Wanderung der Keramikpartikel aufgrund von Kapillarströmung und Diffusion untersuchen.
Ein weiteres praktisches Beispiel mit ähnlichen Effekten ist die Funktionalisierung poröser Strukturen zu Katalysatoren in einem nassen Produktionsschritt.

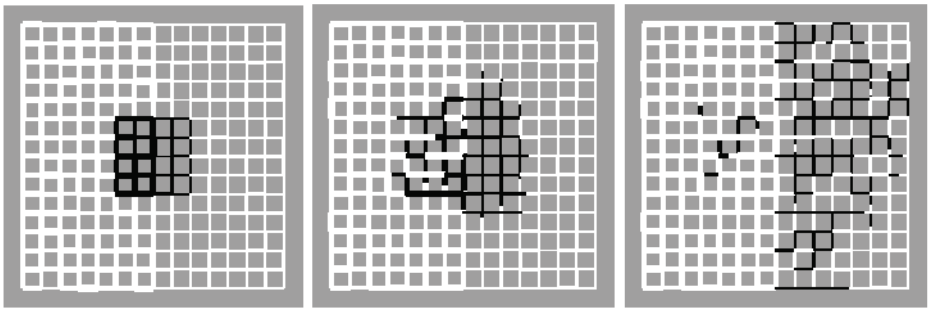

Abbildung 74. Kapillarwasserbewegung in einem Netzwerk mit Regionen unterschiedlicher Porengröße [dd].

Neben der Trocknung sind auch Befeuchtung und kapillare Feuchtemigration wichtige Prozesse, die mit Porennetzwerkmodellen beschrieben werden können. Eine eigene Simulation für die Kapillarwasserbewegung in einem Porennetzwerk mit Kontrast in der Porengröße ist in Abbildung 74 gezeigt. Das Netzwerkmodell berücksichtigt die Porenentleerung und -befüllung sowie die Auftrennung der Flüssigkeit in Cluster unter der Wirkung viskoser Kapillarströmung. Für die getroffenen Modellannahmen strömt der Hauptteil der Flüssigkeit in den feinporigen Bereich, ein Teil verbleibt aber auch isoliert in großen Poren. Diese Modellentwicklung steht noch am Anfang und muss von entsprechenden Befeuchtungsexperimenten begleitet werden.

Ein Beispiel für eine technische Anwendung ist die Beschichtung von Papier, die mit einem Porennetzwerkmodell [28] untersucht wurde.
In anderen Prozessen sind Befeuchtung und Trocknung gekoppelt, z.B. bei der Sprühagglomeration poröser Partikel in der Wirbelschicht: hierbei muss die Zeit, die ein Tropfen Binderflüssigkeit benötigt, um durch Trocknung bzw. Einsaugung von der Partikeloberfläche zu verschwinden, im richtigen Verhältnis zum typischen Kollisionsintervall stehen [87]. Porennetzwerkmodelle könnten hier zum besseren Verständnis der Tropfenkinetik beitragen.

Weitere Anwendungen kapillardominierter Prozesse finden sich in der Raumfahrt. Wärmetauscher nach dem heat-pipe-Prinzip nutzen Verdunstungskühlung und kapillare Flüssigkeitsrückführung und wurden bereits mit Porennetzwerken modelliert [25, 64]. Aber auch das Treibstoffmanagement in der Schwerelosigkeit basiert auf Kapillareffekten, z.B. werden Metallgewebe benutzt, um den Treibstoff aus dem Tank abzusaugen. Dabei spielt das Befeuchtungsverhalten der Gewebe eine wichtige Rolle. Über Experimente und ein Kontinuumsmodell, das auch den Einfluss der Verdunstung berücksichtigt, berichten Fries et al. [27]. Auch hier könnten Porennetzwerkmodelle wertvolle Beiträge liefern.

Zuletzt soll die jüngste Bedeutung von Porennetzwerken bei der Modellierung des Stofftransports in Brennstoffzellen (vom Typ PEM) betont werden. Diese sind aus mehreren dünnen porösen Schichten aufgebaut, die je nach Funktion hydrophil oder hydrophob

gewählt werden. Für die Leistungsfähigkeit einer PEM-Brennstoffzelle ist der Wasserhaushalt besonders in der Gasdiffusionsschicht entscheidend: von der Membran her dringt Wasser ein, aber der Gastransport darf nicht beeinträchtigt werden [64]. Die Transportvorgänge sind kapillar dominiert und können wegen der geringen Schichtdicken mit den üblichen Kontinuumsansätzen nicht zufrieden stellend beschrieben werden [64,65].
Besonders das Eindringen des Wassers in die (teilweise) hydrophobe Gasdiffusionsschicht wurde mit Porennetzwerken modelliert, wobei der Einfluss des Anteils hydrophober Poren und die Auswirkung einer alterungsbedingten Verschiebung untersucht wurden [37]; für die teilgesättigte Schicht wurden effektive Transportparameter für Flüssigkeit und Gas zum Gebrauch in Kontinuumsmodellen bestimmt [29,37,65] – auch abhängig von der Schichtdicke [65]. Aber auch die Trocknung der Schicht wurde beleuchtet, wobei insbesondere die Rolle des Kontaktwinkels interessierte [12]. Schließlich wurde die Bedeutung einer feinporigen Schicht zur Verbesserung des Wasserhaushalts mit Porennetzwerken untersucht [94,95].

Diese Auswahl zeigt bereits die Breite möglicher Anwendungen von Porennetzwerken zur Beschreibung von Kapillareffekten bei Befeuchtung und Trocknung. Sie basiert auf bisherigen Arbeiten und ist bei weitem nicht vollständig; in Zukunft werden mit Sicherheit noch eine Vielzahl weiterer Prozesse und Phänomene mit Netzwerkmodellen untersucht werden.

Schlussbemerkungen

In dieser Arbeit wurden Modelle vorgestellt, die das Ziel haben, den komplexen Prozess der Trocknung poröser Feststoffe ausgehend von den Phänomenen auf der Porenebene besser zu verstehen. Die kapillare Flüssigkeitsbewegung nimmt dabei eine zentrale Stellung ein, denn sie bestimmt wesentlich den Trocknungsverlauf und hängt ihrerseits stark von der Porenstruktur und von den Prozessbedingungen ab.

Da Kapillareffekte in den einzelnen Poren des Feststoffs wirken, basieren die Modelle auf entsprechenden Darstellungen des Porenraums. In abstrahierter Weise berücksichtigen sie, dass das Porenvolumen auf viele Poren unterschiedlicher Größe verteilt ist. Bereits mit einem Kapillarbündel – im diskreten Modell oder als Einheitszelle des Kontinuumsmodells – lassen sich viele wesentliche Effekte darstellen und die Auswirkungen einzelner Produkteigenschaften oder Prozessparameter auf den Trocknungsverlauf untersuchen.

Die Flüssigkeitsbewegung hängt aber auch entscheidend von der räumlichen Vernetzung der Poren und von räumlichen Korrelationen in diesem Porennetz ab. Daher liegt der Schwerpunkt der Arbeit auf Porennetzwerkmodellen. Diese stellen den Porenraum durch räumlich vernetzte geometrisch ähnliche Poren dar; der Trocknungsprozess wird als kapillaritätskontrolliertes Eindringen der Gasphase mit Regeln der Invasionsperkolation beschrieben. Bereits mit einem Basismodell konnten wesentliche Einflüsse der Porenstruktur auf das Trocknungsverhalten herausgearbeitet werden.
Mit Erweiterungen des Basismodells wurde die Rolle wichtiger weiterer Transportphänomene – Flüssigkeitsreibung und Wärmetransport – für die Trocknung unterschiedlicher Strukturen untersucht und damit das Prozessverständnis verbessert. Erste Erkenntnisse zu mechanischen Effekten während der Trocknung wurden mit einer diskreten Beschreibung der auf die Feststoffmatrix wirkenden Kapillarkräfte gewonnen.

Aufgrund ihres diskreten Charakters können Porennetzwerkmodelle Phänomene abbilden, die mit klassischen Kontinuumsmodellen nicht beschrieben werden können: gradientenfreie Kapillarwasserbewegung oder Durchbruch der Gasphase können nur mit solchen diskreten Methoden untersucht werden.
Unter bestimmten Voraussetzungen besitzen Kontinuumsmodelle aber auch ihre Gültigkeit; dann können mit repräsentativen Porennetzwerke die effektiven Modellparameter bestimmt werden. Dies ist aus numerischen Gründen erstrebenswert, denn zwischen Porennetzwerk-simulation und Produktebene liegen oft mehrere Größenordnungen. Erste Schritte für den Skalenübergang – empirisch bzw. im Sinne einer Volumenmittelung – wurden präsentiert; der Weg zur vollen Äquivalenz von Mikro- und Makromodell scheint allerdings noch weit.

In neuartigen, nicht-isothermen Experimenten mit Siliziumnetzwerken, aber auch bei der Trocknung von klassischen Kugelschüttungen werden die Porenphänomene derzeit mit optischen oder tomographischen Methoden direkt beobachtet und analysiert. Die diskreten Regeln der Porennetzwerkmodelle können so geprüft, aber auch weiterentwickelt werden.

Mit den diskutierten Modellen können zum jetzigen Zeitpunkt nur qualitative Aussagen zum Trocknungsverhalten getroffen werden, die aber durchaus zum Zwecke der Optimierung von Porenstruktur oder Prozessbedingungen genutzt werden können.
Mit neuen experimentellen Methoden zur Herstellung und Analyse von Porenstrukturen sowie und zur räumlichen Darstellung der Vorgänge in einzelnen Poren wachsen auch die Chancen, dass Porennetzwerke für quantitative Vorhersagen verwendet werden können.

Je nach Auswahl der simulierten Transportphänomene können mit Porennetzwerkmodellen neben Varianten der Trocknung auch sehr unterschiedliche andere Prozesse beschrieben werden. Diese Flexibilität lässt das Forschungsgebiet auf lange Sicht attraktiv und ergiebig erscheinen.

Symbolverzeichnis

A	Querschnittsfläche, Austauschfläche	M^2
B	Vorfaktor im Skalengesetz	–
c_p	spezifische Wärmekapazität	$J\ kg^{-1}\ K^{-1}$
Ca	Kapillarzahl	–
D_{eff}	effektiver Diffusionskoeffizient	$m^2\ s^{-1}$
$\mathbf{F}$	Kraftvektor	N
f	Volumenanteil einer Phase in einer Raumzelle	–
h	spezifische Enthalpie	$J\ kg^{-1}$
Δh_v	spezifische Verdunstungsenthalpie	$J\ kg^{-1}$
K	intrinsische Permeabilität	m^2
k	relative Permeabilität	–
L	Länge der Kapillaren bzw. Poren	m
L_f	(absolute) Breite der Trocknungsfront	m
M	Viskositätsverhältnis für nichtmischbare Fluide	–
$\tilde{M}$	Molmasse	$kg\ mol^{-1}$
$\dot{M}$	Massenstrom	$kg\ s^{-1}$
m	Dicke einer Netzwerkschicht (in Einheiten von L)	–
$\dot{m}$	Massenstromdichte	$kg\ m^{-2}\ s^{-1}$
N	Zahl der Kapillaren in einer Klasse	–
$\mathbf{n}$	Normalenvektor	–
P	Druck	Pa
$\dot{Q}$	Wärmestrom	W
$\dot{q}$	Wärmestromdichte	$W\ m^{-2}$
$\tilde{R}$	ideale Gaskonstante	$J\ mol^{-1}\ K^{-1}$
r	Radius	m
r_c	Krümmungsradius der Flüssig-Gas-Grenze	m
r_0	mittlerer Porenradius	m
r_{max}	Radius der größten gefüllten Kapillare	m
S	Sättigung	–
s	Grenzschichtdicke	m
s_i	Position der Menisken im Kapillarbündel	m
Sh	Sherwoodzahl	–
T	Temperatur	°C oder K
t	Zeit	s
V	Voumen	m^3
$\dot{V}$	Volumenstrom	$m^3\ s^{-1}$
v	(mittlere) Strömungsgeschwindigkeit	$m\ s^{-1}$
X	Feststofffeuchte	$kg_{Wasser}\ kg_{trockener\ Feststoff}^{-1}$
$\mathbf{x}$	Raumkoordinate	m
Y	absolute Luftfeuchte	$kg_{Wasser}\ kg_{trockene\ Luft}^{-1}$

y	Massenbruch	–
Z	Koordinationszahl / Zahl der Nachbarn	–
z	ins poröse Material hinein gerichtete Koordinate	m
z_f	Position der Trocknungsfront	m

Griechisch

α	Wärmeübergangskoeffizient	$W\ m^{-2}\ K^{-1}$
β	Stoffübergangskoeffizient	$m\ s^{-1}$
δ	Diffusionskoeffizient	$m^2\ s^{-1}$
ζ	dimensionslose Produkttiefe	–
η	dynamische Viskosität	Pa s
θ	Kontaktwinkel	°
κ	Krümmung	m^{-1}
λ	Wärmeleitfähigkeit	$W\ m^{-1}\ K^{-1}$
λ_{eff}	effektive Wärmeleitfähigkeit	$W\ m^{-1}\ K^{-1}$
ν	kinematische Viskosität	$m^2\ s^{-1}$
$\dot{\nu}$	dimensionslose Trocknungsrate	–
ρ	Dichte	$kg\ m^{-3}$
σ	Oberflächenspannung	$N\ m^{-1}$
σ_f	Standardabweichung für Trocknungsfront	m
σ_0	Standardabweichung des Porenradius	m
φ	relative Luftfeuchte	–
χ	Exponent in Skalengesetzen	–
ψ	Porosität	–

Indizes

a	trockene Luft
c	Kapillar-
ev	Verdunstung
fw	ungebundenes Wasser
g	Gas, (feuchte) Luft
ij	Pore zwischen Knoten i und j
nw	Netzwerk
ref	Referenz-
s	Feststoff
surf	Oberfläche
sorb	gebundenes bzw. adsorbiertes Wasser
v	Dampf
w	Wasser bzw. flüssige Phase
0	Anfangswert
I	1. Trocknungsabschnitt
∞	Kernströmung
*	Sättigung, Gleichgewicht

Literatur im Anhang

[A] T. Metzger, E. Tsotsas,
Influence of pore size distribution on drying kinetics: a simple capillary model,
Drying Technology 23, 1797-1809, 2005.
[B] T. Metzger, A. Irawan, E. Tsotsas,
Discrete modelling of drying kinetics of porous media,
in: T.M. Eikevik, O. Alves-Filho, I. Strommen (Eds.), Proceedings 3rd Nordic Drying Conference (NDC05), Karlstad, Schweden, 2005.
[C] A. Irawan, T. Metzger, E. Tsotsas,
Pore network modelling of drying: combination with a boundary layer model to capture the first drying period,
Proc. 7th World Congress of Chemical Engineering, Glasgow, Scotland, 2005, P42-033.
[D] T. Metzger, A. Irawan, E. Tsotsas,
Remarks on the paper “Extension of Hoshen-Kopelman algorithm to non-lattice environments” by A. Al-Futaisi and T.W. Patzek, Physica A 321 (2003) 665-678,
Physica A 363, 558-560, 2006.
[E] T.H. Vu, T. Metzger, E. Tsotsas,
Influence of pore size distribution via effective parameters in a continuous drying model,
Proc. 15th International Drying Symposium, 2006, Budapest, Vol. A, 554-560
[F] T. Metzger, M. Kwapinska, M.Peglow, G. Saage, E. Tsotsas,
Modern modelling methods in drying,
Transport in Porous Media 66, 103-120, 2007.
[G] T. Metzger, A. Irawan, E. Tsotsas,
Influence of pore structure on drying kinetics: a pore network study,
AIChE Journal 53, 3029-3041, 2007.
[H] T. Metzger, A. Irawan, E. Tsotsas,
Isothermal drying of pore networks: influence of friction for different pore structures,
Drying Technology 25, 49-57, 2007.
[I] T. Metzger and E. Tsotsas,
Viscous stabilization of drying front: three-dimensional pore network simulations,
Chemical Engineering Research and Design, 86, 739-744, 2008.
[J] V.K. Surasani, T. Metzger, E. Tsotsas,
Consideration of heat transfer in pore network modelling of convective drying,
International Journal of Heat and Mass Transfer, 51, 2506-2518, 2008.
[K] V.K. Surasani, T. Metzger, E. Tsotsas,
Influence of heating mode on drying behavior of capillary porous media: pore scale modelling,
Chemical Engineering Science 63, 5218-5228, 2008.
[L] V.K. Surasani, T. Metzger, E. Tsotsas,
A non-isothermal pore network drying model with gravity effect,
Transport in Porous Media 80, 431-439, 2009.
[M] V.K. Surasani, T. Metzger, E. Tsotsas,
Drying simulations of various 3D pore structures by a non-isothermal pore network model,
Drying Technology 28, 615-623, 2010.
[N] N. Vorhauer, T. Metzger, E. Tsotsas,
Empirical macroscopic model for drying of porous media based on pore networks and scaling theory,
Drying Technology 28, 991-1000, 2010.
[O] T. Metzger, E. Tsotsas,
Network models for capillary porous media: application to drying technology,
Chemie Ingenieur Technik 82, 869-879, 2010.
[P] A. Kharaghani, T. Metzger, E. Tsotsas,
A proposal for discrete modeling of mechanical effects during drying, combining pore networks with DEM,
AIChE Journal 57, 872-885, 2011.

Weitere eigene Arbeiten

[a] T. Metzger, E. Tsotsas, M. Prat,
Pore-network models: A powerful tool to study drying at the pore level and understand the influence of structure on drying kinetics,
Chapter 2 in: E. Tsotsas, A.S. Mujumdar (Eds.), Modern drying technology, Vol. 1: Computational tools at different scales, 57-102, Wiley-VCH, Weinheim, 2007.

[b] T. Metzger, T.H. Vu, A. Irawan, V.K. Surasani, E. Tsotsas,
Pore-scale modelling of transport phenomena in drying,
in: A. Bertram, J. Tomas (Eds.), Micro-macro-interactions in structured media and particle systems, 187-204, Springer, Berlin, 2008.

[c] Kharaghani, T. Metzger, E. Tsotsas,
An irregular pore network model for convective drying of aggregates: capillary and micro-mechanical effects,
Proceedings 17th International Drying Symposium, 2010, Magdeburg, Vol. A, 132-140.

[d] Kirsch, T. Metzger, E. Tsotsas,
Micro-scale model for drying of highly porous particle aggregates,
Proceedings 17th International Drying Symposium, 2010, Magdeburg, Vol. A, 407-414.

[e] N. Vorhauer, T. Metzger, E. Tsotsas,
Extraction of effective parameters for continuous drying model from discrete pore network model,
Proceedings 17th International Drying Symposium, 2010, Magdeburg, Vol. A, 415-422.

[f] T. Metzger, A. Léonard, W. Jomaa, H. Tamon,
Understanding and preventing structural changes during drying of gels,
Chapter 5 in: E. Tsotsas, A.S. Mujumdar (Eds.), Modern drying technology, Vol. 3: Product quality and formulation, Wiley-VCH, Weinheim, 2011.

[aa] T. Metzger, E. Tsotsas,
Simulation der Trocknung von Kompositmaterialien,
Poster auf ProcessNet-FA-Sitzung Trocknungstechnik, Halle, 5.-7. März 2008.

[bb] Y. Wang, A. Kharaghani, T. Metzger, E. Tsotsas,
Pore network drying model for particle aggregates: assessment by X-ray microtomography,
Vortrag auf 7th Asia-Pacific Drying Conference (ADC 2011), Tianjin, China, 18.-20. September 2011.

[cc] A. Kharaghani, Y. Wang, C. Kirsch, T. Metzger, E. Tsotsas,
Drying of highly porous particle aggregates: X-ray microtomography and pore-scale simulation,
Poster auf 7th Asia-Pacific Drying Conference (ADC 2011), Tianjin, China, 18.-20. September 2011.

[dd] Yu Sun, T. Metzger, E. Tsotsas, J. Müller,
Network model for liquid migration in porous media – capillarity, friction and gravity,
Poster auf 8th European Congress of Chemical Engineering, Berlin, 25.-29. September 2011.

[ee] N. Vorhauer, T. Metzger, E. Tsotsas,
On the influence of temperature gradients on drying of pore networks,
Vortrag auf European Drying Conference, Palma de Mallorca, 26.-28. Oktober 2011.

Fremde Literatur

[1] A. Al-Futaisi, T.W. Patzek, Extension of Hoshen-Kopelman algorithm to non-lattice environments, Physica A 321, 665-678, 2003.

[2] S. Antonyuk, Deformations- und Bruchverhalten von kugelförmigen Granulaten bei Druck- und Stoßbeanspruchung, Dissertation, Otto-von-Guericke-Universität Magdeburg, 2006.

[3] S. Antonyuk, M. Khanal, J. Tomas, S. Heinrich, L. Mörl, Impact breakage of spherical granules: experimental study and DEM simulation, Chem. Eng. Process. 45, 838-856, 2006.

[4] D. Anyamene, Direct imaging of pore-scale phenomena during drying of 2-D particle aggregate, Masterarbeit, Otto-von-Guericke-Universität Magdeburg, 2011.

[5] J.T. Bartley, D.W. Ruth, Relative permeability analysis of tube bundle models, including capillary pressure, Transport in Porous Media 45, 447-480, 2001.

[6] M. Blunt, P. King, Relative permeabilities from two- and three-dimensional pore-scale network modelling, Transport in Porous Media 6, 407-433, 1991.

[7] C.J. Brinker, G.W. Scherer, Sol-gel science, Academic Press, New York, 1990.

[8] B. Camassel, N. Sghaier, M. Prat, S. Ben Nasrallah, Ions transport during evaporation in capillary tubes of polygonal cross section, Chem. Eng. Sci. 60, 815-826, 2005.

[9] J. Chang, Y.J. Yuan, D.Y. Yang, X.D. Liu, Pore network model and simulation of transport process for grain drying, Chem. Eng. Technol. 34, 1049-1056, 2011.

[10] O. Chapuis, M. Prat, Influence of wettability conditions on slow evaporation in two-dimensional porous media, Phys. Rev. E 75, 046311, 2007.

[11] F. Chauvet, P. Duru, S. Geoffroy, M. Prat, Three periods of drying of a single square capillary tube, Phys. Rev. Lett. 103, 124502, 2009.

[12] H. Chraïbi, M. Prat, O. Chapuis, Influence of contact angle on slow evaporation in two-dimensional porous media, Phys. Rev. E 79, 026313, 2009.

[13] P. Coussot, Scaling approach of the convective drying of a porous medium, Eur. Phys. J. B 15, 557-566, 2000.

[14] F. Couture, P. Bernada, M.A. Roques, Continuous thermomechanical models using volume-averaging theory, Chapter 3 in: E. Tsotsas, A.S. Mujumdar (Eds.), Modern drying technology, Vol. 1: Computational tools at different scales, Wiley-VCH, Weinheim, 2007.

[15] P.A. Cundall, O.D.L. Strack, A disrete numerical model for granular assemblies, Géotechnique 29, 47-65, 1979.

[16] J.F. Daian, J. Saliba, Determination d'un réseau aleatoire de pores pour modéliser la sorption et la migration d'humidité dans un mortier de ciment, Int. J. Heat Mass Transfer 8, 2081-2096, 1991.

[17] F. Debaste, V. Halloin, Application of discrete modelling approach to yeast drying, Proceedings of European Congress of Chemical Engineering, Copenhagen, 16-20 September 2007.

[18] F. Debaste, Modélisation de l'évaporation en milieu poreux: développement de modèles fondamentaux et appliqués, Dissertation, Université Libre de Bruxelles, Belgien, 2008.

[19] F. Debaste, V. Halloin, Application of discrete modeling approach to fluidized bed yeast drying, Journal of Food Process Engineering 33 (Suppl. 1), 2-22, 2010.

[20] F. Debaste, A. Léonard, V. Halloin, B. Haut, Microtomographic investigation of a yeast grain porous structure, Journal of Food Engineering 97, 526-532, 2010.

[21] O. Dicoi, P. Walzel, B. Blümich, W. Rähse, Untersuchung des Trocknungsverhaltens von Feststoffen mit kernmagnetischer Resonanz, Chemie Ingenieur Technik 76, 94-99, 2004.

[22] M. Dong, F.A.L. Dullien, L. Dai, D. Li, Immiscible displacement in the interacting capillary bundle model, Part I. Develepment of interacting capillary bundle model, Transport in Porous Media 59, 1-18, 2005.

[23] F.A.L. Dullien, Porous Media, Fluid Transport and Pore Structure, 2nd Ed., Academic Press, 1992.

[24] P. Faure, P. Coussot, Drying of a model soil, Phys. Rev. E 82, 036303, 2010.

[25] C. Figus, Y. Le Bray, S. Bories, M. Prat, Heat and mass transfer with phase change in a porous structure partially heated: continuum model and pore network simulations, Int. J. Heat Mass Transfer 42, 2557-2569, 1999.

[26] D.S. Freitas, M. Prat, Pore network simulation of evaporation of a binary liquid from a capillary porous medium, Transport in Porous Media 40, 1-25, 2000.

[27] N. Fries, K. Odic, M. Conrath, M. Dreyer, The effect of evaporation on the wicking of liquids into a metallic weave, J. Colloid Interface Science 321, 118-129, 2008.

[28] J. Ghassemzadeh, M. Hashemi, L. Sartor, M. Sahimi, Pore network simulation of imbibition into paper during coating: I. Model development, AIChE J. 47, 519-535, 2001.

[29] J.T. Gostick, M.A. Ioannidis, M.W. Fowler, M.D. Pritzker, Pore network modeling of fibrous gas diffusion layers for polymer electrolyte membrane fuel cells, J. Power Sources 173, 277-290, 2007.

[30] H.P. Huinink, L. Pel, M.A.J. Michels, M. Prat, Drying processes in the presence of temperature gradients. Pore-scale modelling, Eur. Physical J. E 9, 487-498, 2002.

[31] A. Irawan, Isothermal drying of pore networks: influence of pore structure on drying kinetics, Dissertation, Otto-von-Guericke-Universität Magdeburg, 2006.

[32] A. Kharaghani, Irregular pore networks and mechanical effects during drying of porous media, Dissertation, Otto-von-Guericke-Universität Magdeburg, 2010.

[33] M. Kohout, Z. Grof, F. Štěpánek, Pore-scale modelling and tomographic visualisation of drying in granular media, J. Colloid Interface Science 299, 342-351, 2006.

[34] I.V. Koptyug, S.I. Kabanikhin, K.T. Iskakov, V.B. Fenelonov, L.Yu. Khitrina, R.Z. Sagdeev, V.N. Parmon, A quantitative NMR imaging study of mass transport in porous solids during drying, Chem. Eng. Sci. 55, 1559-1571, 2000.

[35] S.J. Kowalski, Control of mechanical processes in drying. Theory and experiment, Chem. Eng. Sci. 65, 890-899, 2010.

[36] O. Krischer, Trochnungstechnik Erster Band, Die wissenschaftlichen Grundlagen der Trocknungstechnik, Springer Verlag, Berlin, 1956. *Alle Seitenzahlen beziehen sich auf die korrigierte 3. Auflage von 1992*.

[37] S. Pulloor Kuttanikkad, M. Prat, J. Pauchet, Pore-network simulations of two-phase flow in a thin porous layer of mixed wettability: application to water transport in gas diffusion layers of proton exchange membrane fuel cells, J. Power Sources 196, 1145-1155, 2011.

[38] J.B. Laurindo, M.Prat, Numerical and experimental network study of evaporation in capillary porous media. Phase distributions, Chem. Eng. Sci. 51, 5171-5185, 1996.

[39] J.B. Laurindo, M. Prat, Numerical and experimental network study of evaporation in capillary porous media. Drying rates, Chem. Eng. Sci. 53, 2257-2269, 1998.

[40] J.B. Laurindo, M. Prat, Modeling of drying in capillary-porous media: a discrete approach, Drying Technology 16, 1769-1787, 1998.

[41] Y. Le Bray, Contributions à l'étude du changement de phase liquide-vapeur en milieu poreux. Simulations numériques sur réseaux de pores, Dissertation, INP Toulouse, 1997.

[42] Y. Le Bray, M. Prat, Three-dimensional pore network simulation of drying in capillary porous media, Int. J. Heat Mass Transfer 42, 4207-4224, 1999.

[43] P. Lehmann, P. Wyss, A. Flisch, E. Lehmann, P. Vontobel, M. Krafczyk, A. Kaestner, F. Beckmann, A. Gygi, H. Flühler, Tomographical imaging and mathematical description of porous media used for the prediction of fluid distribution, Vadose Zone J. 5, 80-97, 2006.

[44] P. Lehmann, S. Assouline, D. Or, Characteristic lengths affecting evaporative drying of porous media, Phys. Rev. E 77, 056309, 2008.

[45] P. Lehmann, D. Or, Evaporation and capillary coupling across textural contrasts in porous media, Phys. Rev. E 80, 046318, 2009.

[46] R. Lenormand, E. Touboul, C. Zarcone, Numerical models and experiments on immiscible displacements in porous media, J. Fluid Mech. 189, 165-187, 1988.

[47] R. Lenormand, C. Zarcone, Capillary fingering: percolation and fractal dimension, Transport in Porous Media 4, 599-612, 1989.

[48] J.A. Lewis, M.A. Galler, D.P. Bentz, Computer simulations of binder removal from 2-D and 3-D model particulate bodies, J. Am. Ceram. Soc. 79, 1377-1388, 1996.

[49] W. Masmoudi, M. Prat, Heat and mass transfer between a porous medium and a parallel external flow, Application to Drying of Capillary Porous Materials, Int. J. Heat Mass Transfer 34, 1975-1989, 1991.

[50] G. Musielak, T. Sliwa, Simulation of crack generation during drying, Proceedings 17th International Drying Symposium, 2010, Magdeburg, Vol. A, 125-131.

[51] S.B. Nasrallah, P. Perré, Detailed study of a model of heat and mass transfer during convective drying of porous media, Int. J. Heat Mass Transfer 31, 957-967, 1988.

[52] S.C. Nowicki, H.T. Davis, L.E. Scriven, Microscopic determination of transport parameters in drying porous media, Drying Technology 10, 925-946, 1992.

[53] C.A. Oyarzun, L.A. Segura, Design and construction of glass micromodels for the study of moisture transport in softwoods, Drying Technology 27, 14-29, 2009.

[54] P. Perré, I.W. Turner, A 3-D version of TransPore: a comprehensive heat and mass transfer computational model for simulating the drying of porous media, Int. J. Heat Mass Transfer 42, 4501-4521, 1999.

[55] Particle flow code in three dimensions, version 3.10, Itasca Consulting Group Inc., Minneapolis, 2005.

[56] K.M. Pillai, M. Prat, A study on slow evaporation of liquids in a dual-porosity porous medium using square network model, Int. J. Heat Mass Transfer 52, 1643-1656, 2009.

[57] F. Plourde, M. Prat, Pore network simulations of drying of capillary media. Influence of thermal gradients, Int. J. Heat Mass Transfer 46, 1293-1307, 2003.

[58] S. Prachayawarakorn, P. Prakotmak, S. Soponronnarit, Effects of pore size distribution and pore-architecture assembly on drying characteristics of pore networks, Int. J. Heat Mass Transfer 51, 344-352, 2008.

[59] M. Prat, Percolation model of drying under isothermal conditions in porous media, Int. J. Multiphase Flow 19, 691-704, 1993.

[60] M. Prat, Isothermal drying of non-hygroscopic capillary-porous materials as an invasion percolation process, Int. J. Multiphase Flow 21, 875-892, 1995.

[61] M. Prat, F. Bouleux, Drying of capillary porous media with a stabilized front in two dimensions, Phys. Rev. E 60, 5647-5656, 1999.

[62] M. Prat, Recent advances in pore-scale models for drying of porous media, Chem. Eng. J. 86, 153-164, 2002.

[63] M. Prat, On the influence of pore shape, contact angle and film flows on drying of capillary porous media, Int. J. Heat Mass Transfer 50, 1455-1468, 2007.

[64] M. Prat, Pore-scale network models and their applications to capillary evaporators and gas diffusion layers of PEM fuel cells, Proc. 6th Int. Sympos. Multiphase Flow, Heat Mass Transfer and Energy Conversion, Xi'an, China, 11-15 July 2009.

[65] M. Rebai, M. Prat, Scale effect and two-phase flow in a thin hydrophobic porous layer. Application to water transport in gas diffusion layers of proton exchange membrane fuel cells, J. Power Sources 192, 534-543, 2009.

[66] D. Ruth, J. Bartley, Capillary tube models with interaction between the tubes [A note on „Immiscible displacement in the interacting capillary bundle model“, by Dong, M., Dullien, F.A.L., Dai, L. and Li, D., 2005, Transport Porous Media], Transport in Porous Media 86, 479-482, 2011.

[67] M. Sahimi, Flow and transport in porous media and fractured rock. From classical methods to modern approaches, VCH Weinheim, 1995.

[68] J.G. Salin, Drying of liquid water in wood as influenced by the capillary fiber network, Drying Technology 26, 560-567, 2008.

[69] V. Sarrot, M. Prat, Hyperslow drainage in a porous medium, Influence of retention curve, Adv. Water Resour. 33, 987-996, 2010.

[70] M. Scheel, R. Seemann, M. Brinkmann, M. Di Michiel, A. Sheppard, S. Herminghaus, Liquid distribution and cohesion in wet granular assemblies beyeond the capillary bridge regime, J. Phys.: Condens. Matter 20, 494236, 2008.

[71] E.U. Schlünder, Über den Mechanismus des ersten Trocknungsabschnittes und seine mögliche Bedeutung für diffusionskontrollierte katalytische Gasphasenreaktionen, Chemie Ingenieur Technik 60, 117-120, 1988.

[72] E.U. Schlünder, On the mechanism of the constant drying rate period and its relevance to diffusion controlled catalytic gas phase reactions, Chem. Eng. Sci. 43, 2685-2688, 1988.

[73] L.A. Segura, P.G. Toledo, Pore-level modeling of isothermal drying of pore networks. Effects of gravity and pore shape and size distributions on saturation and transport parameters, Chem. Eng. J. 111, 237-252, 2005.

[74] L.A. Segura, P.G. Toledo, Pore-level modeling of isothermal drying of pore networks accounting for evaporation, viscous flow, and shrinking, Drying Technology 23, 2007-2019, 2005.

[75] L.A. Segura, Modeling at pore-scale isothermal drying of porous materials: liquid and vapour diffusivity, Drying Technology 25, 1677-1686, 2007.

[76] N. Sghaier, M. Prat, Effect of efflorescence formation on drying kinetics of porous media, Transp. Porous Med. 80, 441-454, 2009.

[77] N. Shahidzadeh-Bonn, A. Azouni, P. Coussot, Effect of wetting properties on the kinetics of drying of porous media, J. Phys.: Condens. Matter 19, 112101, 2007.

[78] E. Shahraeeni, D. Or, Thermo-evaporative fluxes from heterogeneous porous surfaces resolved by infrared thermography, Water Resour. Res. 46, W09511, 2010.

[79] T.M. Shaw, Drying as an immiscible displacement process with fluid counterflow, Phys. Rev. Lett. 59, 1671-1674, 1987.

[80] N. Shokri, P. Lehmann, D. Or, Effects of hydrophobic layers on evaporation from porous media, Geophys. Res. Lett. 35, L19407, 2008.

[81] N. Shokri, P. Lehmann, P. Vontobel, D. Or, Drying front and water content dynamics during evaporation from sand delineated by neutron radiography, Water Resour. Res. 44, W06418, 2008.

[82] N. Shokri, P. Lehmann, D. Or, Characteristics of evaporation from partially wettable porous media, Water Resour. Res. 45, W02415, 2009.

[83] N. Shokri, P. Lehmann, D. Or, Liquid-phase continuity and solute concentration dynamics during evaporation from porous media: pore-scale processes near vaporization surface, Phys. Rev. E 81, 046308, 2010.

[84] N. Shokri, P. Lehmann, D. Or, Evaporation from layered porous media, J. Geophys. Res. 115, B06204, 2010.

[85] V.K. Surasani, A non-isothermal pore network drying model, Dissertation, Otto-von-Guericke-Universität Magdeburg, 2008.

[86] M. Suzuki, S. Maeda, On the mechanism of drying of granular beds, J. Chem. Eng. Japan 1, 26-31, 1968.

[87] K. Terrazas-Velarde, M. Peglow, E. Tsotsas, Investigation of fluidized bed spray agglomeration based on stochastic methods, AIChE J. 57, 3012-3026, 2011.

[88] C.D. Tsakiroglou, A.C. Payatakes, A new simulator of mecury porosimetry for the characterization of porous materials, J. Colloid Interface Sci. 137, 315-339, 1990.

[89] I.N. Tsimpanogiannis, Y.C. Yortsos, S. Poulou, N. Kanellopoulos, A.K. Stubos, Scaling theory of drying in porous media, Phys. Rev. E 59, 4353-4365, 1999.

[90] I.W. Turner, P. Perré, A synopsis of strategies and efficient solution techniques used for modelling and numerically simulating the drying process. In: I. Turner, A.S. Mujumdar (Eds.), Mathematical modeling and numerical techniques in drying technology, Marcel Dekker, New York, 1996.

[91] G.H.A. van der Heijden, H.P. Huinink, L. Pel, K. Kopinga, Non-isothermal drying of fired-clay brick, an NMR study, Chem. Eng. Sci. 64, 3101-3018, 2009.

[92] S. Veran-Tissoires, Sur le phénomène de cristallisation discrète à la surface ou à l'intérieur d'un milieu poreux, Dissertation, INP Toulouse, 2011.

[93] T.H. Vu, Influence of pore size distribution via effective parameters in a continuous drying model, Dissertation, Otto-von-Guericke-Universität Magdeburg, 2006.

[94] R. Wu, X. Zhu, Q. Liao, H. Wang, Y. Ding, J. Li, D. Ye, A pore network study on water distribution in bi-layer gas diffusion media: effects of inlet boundary condition and micro-porous layer properties, Int. J. Hydrogen Energy 35, 9134-9143, 2010.

[95] R. Wu, X. Zhu, Q. Liao, H. Wang, Y. Ding, J. Li, D. Ye, A pore network study on the role of micro-porous layer in control of liquid water distribution in gas diffusion layers, Int. J. Hydrogen Energy 35, 7588-7593, 2010.

[96] Z. Xiao, D. Yang, Y. Yuan, B. Yang, X. Liu, Fractal pore network simulation on the drying of porous media, Drying Technology 26, 651-665, 2008.

[97] L. Xu, S. Davies, A.B. Schofield, D.A. Weitz, Dynamics of drying in 3D porous media, Phys. Rev. Lett. 101, 094502, 2008.

[98] A.G. Yiotis, A.K. Stubos, A.G. Boudouvis, Y.C. Yortsos, A 2-D pore-network model of the drying of single-component liquids in porous media, Adv. Water Resour. 24, 439-460, 2001.

[99] A.G. Yiotis, A.G. Boudouvis, A.K. Stubos, I.N. Tsimpanogiannis, Y.C. Yortsos, Effect of liquid films on the isothermal drying of porous media, Phys. Rev. E 68, 037303, 2003.

[100] A.G. Yiotis, A.G. Boudouvis, A.K. Stubos, I.N. Tsimpanogiannis, Y.C. Yortsos, The effect of liquid films on the drying of porous media, AIChE J. 50, 2721-2737, 2004.

[101] A.G. Yiotis, A.K. Stubos, A.G. Boudouvis, I.N. Tsimpanogiannis, Y.C. Yortsos, Pore-network modeling of isothermal drying in porous media, Transport in Porous Media 58, 63-86, 2005.

[102] A.G. Yiotis, I.N. Tsimpanogiannis, A.K. Stubos, Y.C. Yortsos, Pore-network study of the characteristic periods in the drying of porous materials, J. Colloid Interface Science 297, 738-748, 2006.

[103] A.G. Yiotis, I.N. Tsimpanogiannis, A.K. Stubos, Y.C. Yortsos, Coupling between external and internal mass transfer during drying of a porous medium, Water Resour. Res. 43, W06403, 2007.

[104] A.G. Yiotis, I.N. Tsimpanogiannis, A.K. Stubos, Fractal characteristics and scaling of the drying front in porous media: a pore network study, Drying Technology 28, 981-990, 2010.

[105] A.G. Yiotis, I.N. Tsimpanogiannis, A.K. Stubos, Experimental study of drying/evaporation in an effective 2-D porous medium, NSTI-Nanotech 2010, Vol. 2, 432-435, 2010.

[106] A.G. Yiotis, I.N. Tsimpanogiannis, A.K. Stubos, Three-dimensional modeling of the evaporation of volatile hydrocarbons from anisotropic porous media, Journal of Porous Media 13, 209-219, 2010.

Anhang

Drying Technology, 23: 1797–1809, 2005

ISSN: 0737-3937 print/1532-2300 online
DOI: 10.1080/07373930500209830

Taylor & Francis
Taylor & Francis Group

Influence of Pore Size Distribution on Drying Kinetics: A Simple Capillary Model

Thomas Metzger and Evangelos Tsotsas
Thermal Process Engineering, Otto-von-Guericke University, Magdeburg, Germany

Abstract: In this article, convection drying of a porous medium is described by a capillary model. The simplest form of this model was introduced by Krischer for two parallel capillaries to describe fundamental phenomena of drying kinetics such as the existence of a constant rate period and a falling rate period. The model accounts for capillary pressure, mass transfer is described by liquid water convection and vapor diffusion in the capillaries and at the surface, and isothermal conditions are assumed. This theoretical model is extended to a larger (arbitrary) number of capillaries with a size distribution in order to better represent the situation in a real porous medium. Drying curves as well as moisture profiles in the solid are presented for different pore size distributions. In a second step, the isothermal condition is abandoned and heat transfer into the porous medium is included into the theoretical description for the case of two capillaries. Drying curves and the time-dependent temperature profile in the solid are shown.

Keywords: Capillary porous media; Drying curves; Moisture profiles; Temperature profiles

INTRODUCTION

One of the most demanding tasks in drying technology is to find a way to correlate the drying behavior of a product to its pore structure or to predict the drying curve for a given pore geometry. Until now, drying curves must be determined experimentally or estimated qualitatively on the basis of experience. The present study aims to give a theoretical contribution to better understand the influence of the pore size distribution on the drying kinetics.

Correspondence: Thomas Metzger, Thermal Process Engineering, Otto-von-Guericke University, P.O. 4120, D-39106 Magdeburg, Germany; E-mail: thomas.metzger@vst.uni-magdeburg.de

We start from a two capillary representation of a porous medium, which was to our knowledge introduced by Krischer.[1] The two parallel capillaries (set perpendicular to the product surface) are connected all along their length without any resistance. Fluid transport is a result of the combined action of capillary and viscous forces; vapor transport is due to diffusion in the gas phase. Isothermal conditions are assumed so that the solid phase may be neglected. The model is useful to illustrate fundamental phenomena of drying kinetics, such as the existence of a constant rate period and a falling rate period, as well as the influence of mass transfer conditions outside the product on the drying curve.

We extended this isothermal model to a large number of capillaries with a size distribution and used it to investigate—in a simple and, of course, limited way—the influence of pore size distribution on the drying kinetics. The extended model as well as the simulation results will be presented in the following section. In the third section, we present a two capillary model that has been extended to include heat transfer and allows calculation of temperature profiles during drying. This work gives a valuable contribution to the prevailing discussion on the relevant transport mechanisms during the falling rate period.[2]

ISOTHERMAL DRYING

Figure 1 shows five parallel capillaries (not to scale) that are at first completely filled with water (a). The left end of the capillaries is open for evaporation; the right end is closed. The positions $x = 0$ and L correspond to the surface and the center (or sealed back) of the porous medium, respectively. The length of the capillaries is $L = 0.1\,m$; their radii are $r_i = 110$, 105, 100, 95, and 90 nm.

At the beginning of the drying process, the meniscus of the biggest capillary retreats from the surface (position s_1) while the others remain stationary due to capillary forces (b). Liquid water is pumped out of the biggest capillary through the other four capillaries to the surface. If the pressure drop in the full capillaries Δp_f (due to friction) equals the difference in capillary pressure Δp_c, another meniscus retreats from the surface (c) until only one meniscus is left at the surface (d). This marks the end of the first drying period. Up to this point, part of the surface is still wet, and the drying rate may be set equal to that for a completely wet surface. This is a good approximation as long as the radius of the wet patches is small compared to the thickness of the boundary layer and as long as the fraction of wet surface is not too small.[4] (Note that for a different capillary geometry, some capillaries may empty before the end of the first drying period.)

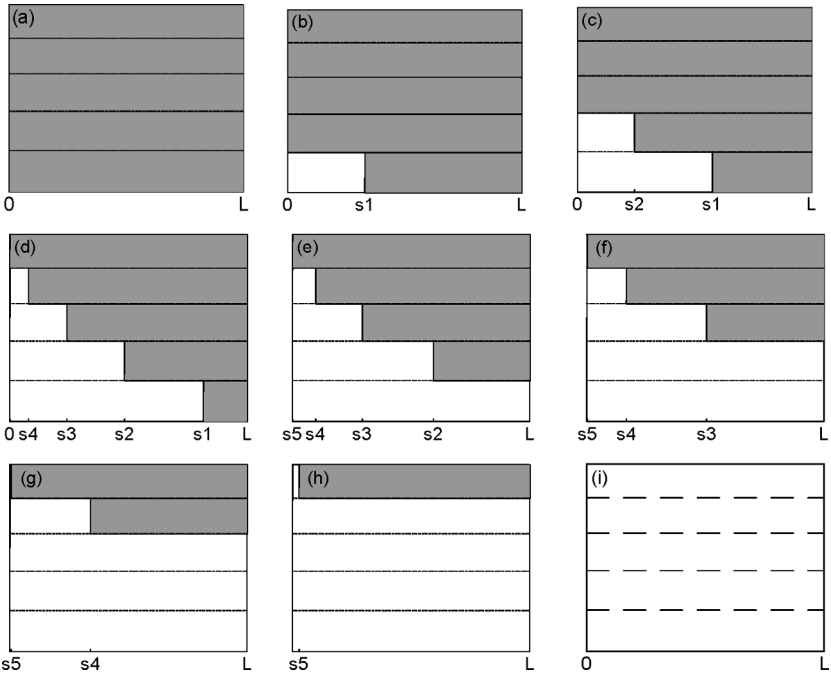

Figure 1. Filling of capillaries at distinct times during isothermal drying (the evaporation surface is on the left, shown are all meniscus positions for which $0 < s_i < L$).

Then the meniscus of the smallest capillary (s_5) moves back from the surface (the distance is too small to be seen in Figure 1). This introduces an additional mass transfer resistance for evaporation so that the drying rate is reduced. As a consequence, the frictional forces in the capillaries decrease, whereas the capillary forces stay constant. Hence the distance between the menisci may increase and one capillary after the other will empty (e-g) while the last meniscus is still relatively close to the surface (h). Then the drying rate will decrease even stronger as the evaporating meniscus retreats without supply from other capillaries. We assume that all empty capillaries are saturated with vapor up to the last meniscus (no resistance between capillaries) and that consequently the whole cross section serves as an evaporation area. Drying is completed at a small but non-zero drying rate (i). Residual moisture in the form of sorbed water is not accounted for.

Figure 2 shows the drying curve for the complete process. We use saturation S to describe the moisture content because volume fraction and density of the solid phase are not relevant in this model.

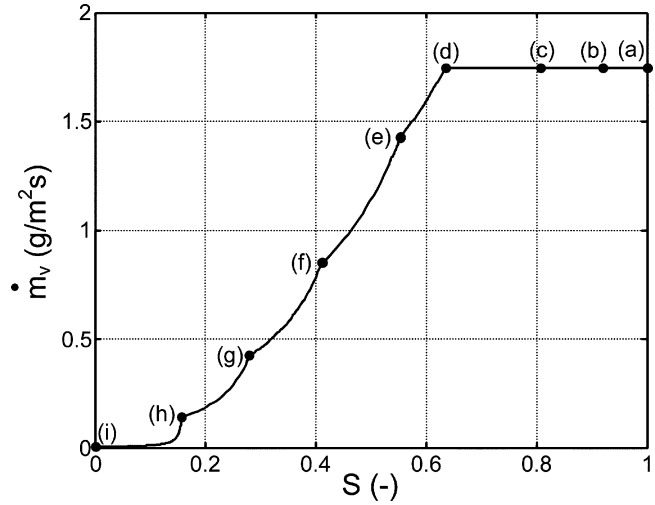

Figure 2. Drying curve for capillaries as in Figure 1 (the distinct times are shown on the curve).

Model Equations

Evaporation of water is described as a diffusive vapor flux (with Stefan correction) given by

$$\dot{m}_v = -\left(\frac{1}{\beta} + \frac{s_n}{\delta_{va}}\right)^{-1} \frac{p\tilde{M}_v}{\tilde{R}T} \cdot \ln\left(\frac{p - p_{v,\infty}}{p - p_v^*}\right) \tag{1}$$

where β is the mass transfer coefficient at the surface, s_n is the position of the meniscus in the smallest capillary, δ_{va} is the diffusion coefficient of vapor in air, p is the total pressure, $\tilde{M}_v$ is the molar mass of vapor, $\tilde{R}$ is the universal gas constant, T is the temperature (in K), $p_{v,\infty}$ is the vapor pressure in the bulk drying air, and p_v^* is the saturation vapor pressure. The Knudsen effect in vapor diffusion is neglected, which is reasonable as long as the radius of the capillaries is bigger then the mean free path of the vapor molecules ($\approx$40 nm). The reduction of vapor pressure above the curved liquid surfaces (Kelvin effect) is not taken into account, which is a good approximation for $r > 10$ nm. We take $\beta = 0.1$ m/s as well as atmospheric pressure throughout this article, and $T = 20°C$, $p_{v,\infty} = 0$, and $L = 0.1$ m for the isothermal case. The water that evaporates must also flow as liquid through the capillaries. The number of liquid-filled capillaries varies according to the position in the product. The positions of the menisci s_i give a natural subdivision of space. Between two consecutive meniscus positions, the pressures that must balance are the difference in capillary pressure (due to different

radii)

$$\Delta p_{c,i} = 2\sigma \cdot \left(\frac{1}{r_{i+1}} - \frac{1}{r_i}\right) \qquad \text{for } i = 1, \ldots, n-1 \tag{2}$$

and the pressure drop due to friction (Poiseuille flow)

$$\Delta p_{f,i} = 8\eta \frac{\dot{m}_v}{\rho_w} \left(\sum_{j=1}^{n} N_j \pi r_j^2\right) \cdot \left(\sum_{j=i+1}^{n} N_j \pi r_j^4\right)^{-1} (s_i - s_{i+1}) \qquad \text{for } i = 1, \ldots, n-1 \tag{3}$$

where σ is the surface tension, η is the dynamic viscosity, ρ_w is the density of water, and N_j denotes the number of capillaries for each class. (The first sum is over all capillaries and gives the total surface for evaporation; the second sum is only over liquid-filled capillaries to account for friction.) Note that we have assumed a zero contact angle, i.e., complete wetting of walls, in Eq. (2).

The pressure balance between Eqs. (2) and (3) defines the distances of the menisci $s_i - s_{i+1}$ as a function of the drying rate, while Eq. (1) gives the absolute position of the last meniscus s_n. Hence the model is complete, and integration over time can yield moisture profiles and the drying curve.

Mono-Modal Pore Size Distributions

At first we look at porous media that may be described by a normally distributed pore volume

$$\frac{dV}{dr} = \frac{V_{total}}{\sqrt{2\pi}\sigma_0} e^{-\frac{1}{2}\left(\frac{r-r_0}{\sigma_0}\right)^2} \tag{4}$$

where r_0 is the mean pore radius and σ_0 is the standard deviation. This pore size distribution is then approximated by 50 capillary classes that are equidistantly distributed in the range $r_0 \pm 2.5 \cdot \sigma_0$. The number of capillaries per class N_k is chosen according to the volume distribution. (Then the surface of the smallest capillary class is still 0.2% of the total surface.)

Figure 3 shows results for different pore volume distributions: (a) gives local moisture profiles in the pores at the end of the first drying period (the area below the curves corresponds to the total moisture) and (b) shows the corresponding normalized drying curves.

The most important result is that the drying behavior depends strongly on the standard deviation of the distribution, whereas the size of the pores has negligible influence, a fact that was reported from

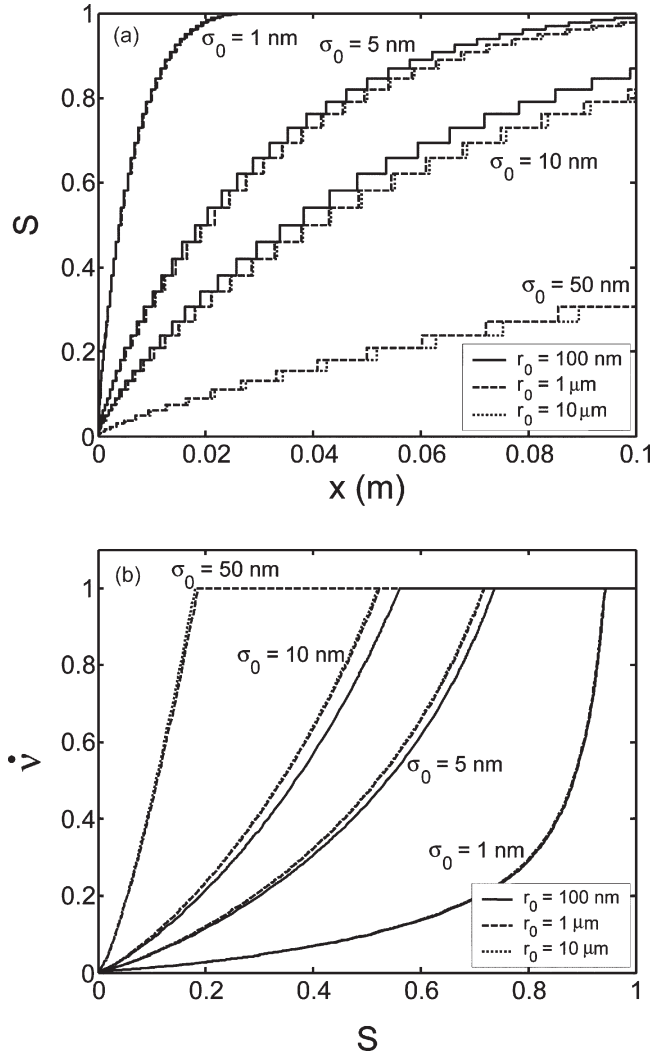

Figure 3. Moisture profiles at the end of the first drying period (a) and normalized drying curves (b) for normal pore volume distributions of different mean radius r_0 and standard deviation σ_0.

experimental results.[3] This can be understood by the following reasoning: if $\sigma_0 << r_0$, then $r_i \approx r_0$ and $1/r_{i+1} - 1/r_i \approx (r_i - r_{i+1})/r_0^2$ so that we may approximate the pressure balance of Eqs. (2) and (3) by

$$\frac{s_{i+1} - s_i}{r_{i+1} - r_i} \approx \frac{\sigma\rho}{4\eta\dot{m}_v} \left(\sum_{j=1}^{n} N_j \right)^{-1} \cdot \sum_{j=i+1}^{n} N_j \tag{5}$$

This means that the model is independent of the absolute size of the capillaries and that only differences in radii and numbers of capillaries per class play a role.

As a second result, we might state that for distributions with $\sigma_0 > 50\,\text{nm}$ most of the water can be evaporated at the high rate of the first drying period.

Bi-Modal Pore Size Distributions

In order to investigate the drying behavior of porous media that have micro and macropores, we combined two pore volume distributions as given in Eq. (4). The small capillaries had a radius of 100 nm with a standard deviation of either 1 nm or 10 nm; the big pores had a radius of 1 μm or 10 μm with a standard deviation that corresponds to either 1% or 10 % of the radius. Furthermore, the volume fractions assigned to the micro and macropores was varied: either they were set equal or one was set four times bigger than the other.

The obtained results are shown in Figure 4. We found that the pore size distribution of the macropores did not influence the drying behavior. The length of the first drying period depends on the volume fraction of the macropores: more big pores are favorable for drying. But it can also be influenced by the pore size distribution of the micropores: a broad distribution is favorable in the sense that the first drying period is longer and that the drying rate in the second period is higher, as in the case of monomodal distributions.

DRYING WITH HEAT TRANSFER

In order to get a more realistic model, heat transfer has been included for the case of two classes of capillaries. Figure 5 shows the heat and mass transfer phenomena during drying for the most general situation. Heat is transferred from the drying air to the surface of the product, and water is evaporated from the menisci to the drying air. Liquid water is flowing through the thin capillaries toward the surface due to capillary forces, and vapor diffusion may occur between the two meniscus positions because of differences in saturation vapor pressure at the menisci (due to different temperatures). Heat is transferred by conduction in the solid and the liquid as well as by convection of liquid and vapor. Contributions of the gas phase are neglected. The heat flux to the surface and due to evaporation or condensation of water is accounted for by the source terms

$$\dot{q} = \alpha \cdot (T_\infty - T_{surf}) \tag{6}$$

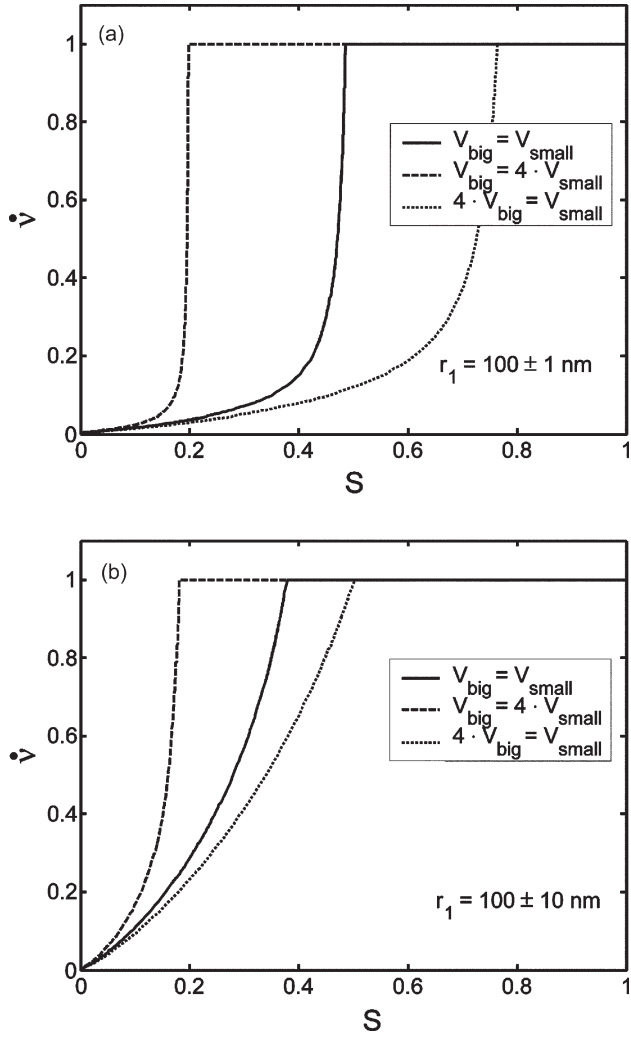

Figure 4. Drying curves for different bimodal pore volume distributions; the curves are identical for $r_2 = 1 \pm 0.01\,\mu m$, $r_2 = 1 \pm 0.1\,\mu m$, $r_2 = 10 \pm 0.1\,\mu m$, and $r_2 = 10 \pm 1\,\mu m$.

and

$$\dot{q}_v = \Delta h_v \cdot \dot{m}_v \tag{7}$$

where α is the heat transfer coefficient; T_∞ and T_{surf} are the temperatures of the fluid bulk and the surface, respectively; Δh_v is the evaporation enthalpy; and $\dot{m}_v$ is the mass flux of vapor. There is no flux at the right end of the system, and we neglect any resistances in the lateral direction. Kelvin and Knudsen effects are not included in the model.

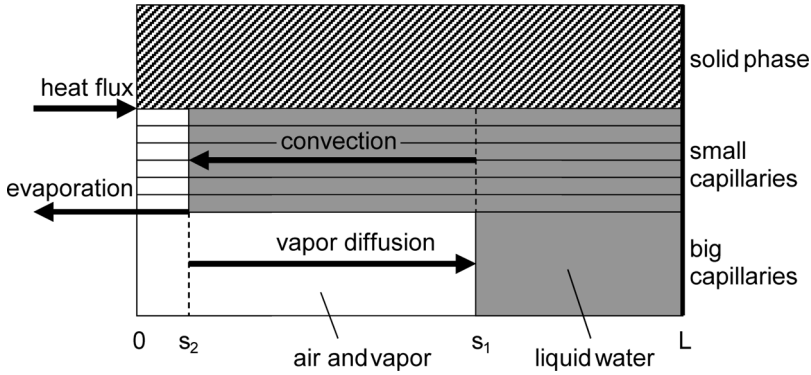

Figure 5. Geometry and transport phenomena in capillary model.

The model consists of a partial differential equation for heat transfer with different coefficients for the different zones, the boundaries of which are moving, and algebraic equations for mass transfer from which the motion of the boundaries may be calculated. The system is solved by successively updating the temperature profile and the meniscus positions as well as all mass fluxes. (Evaporation enthalpy, thermal conductivity, surface tension, and viscosity of water, as well as the diffusion coefficient, are functions of temperature, whereas density and heat capacity of water are taken as constant.)

Results for Two Classes of Capillaries

In our simulations we took capillaries of radius 100 nm and 1 μm and length $L = 0.01\,m$; both capillary classes had the same volume fraction. The porosity of the capillary system was $\psi = 0.5$; the solid had the specific heat capacity $(\rho c_p)_s = 2 \cdot 10^6\,J/m^3K$ and the thermal conductivity $\lambda = 1\,W/mK$. The moisture content of the drying air was set to $Y_\infty = 0.01$; its temperature was 80°C, 100°C, or 120°C, respectively. The initial temperature of the system was 20°C. The analogy between heat and mass transfer gives $\alpha = 95\,W/m^2K$ (for 50°C).

The results are shown as drying curves in Figure 6. For comparison, the drying curve for isothermal drying (at 20°C, completely dry air) is also given. The time-dependent temperature profile in the porous system is presented in Figure 7 for drying at 80°C. During the first drying period the drying rate is not constant due to warming up (to the wet-bulb temperature). For the given geometry and drying conditions, the big capillaries empty completely before the evaporation front (in the small capillaries) moves back from the surface and the second drying period begins. Then, the evaporation rate decreases, and the associated cooling

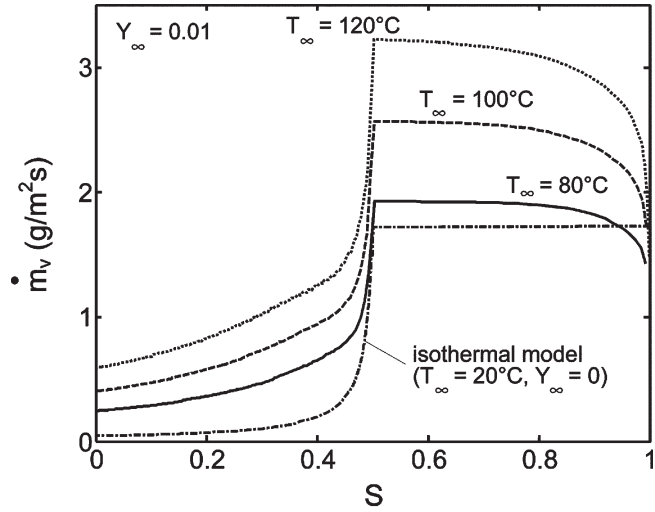

Figure 6. Drying curves for capillary model with heat transfer.

effect is reduced so that the product heats up, leading to an increased drying rate as compared to the isothermal case (Figure 6). A considerable temperature gradient develops between product surface and evaporation front (Figure 7), most of the transferred heat being used for evaporation.

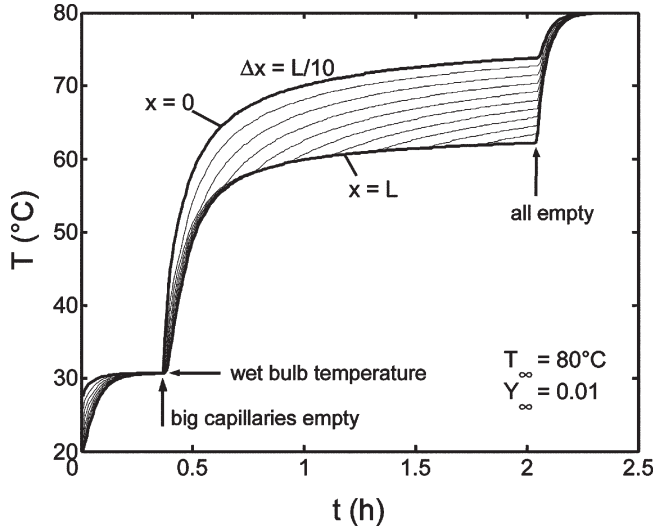

Figure 7. Temperature profiles during drying. (The uppermost curve shows the temperature at the product surface, the lowest curve the temperature at the sample center.)

Therefore, the temperature beyond the evaporation front is almost uniform, slowly increasing with time. When the evaporation front passes by a given position, there is a sudden increase in temperature. After all capillaries are dried out, the product heats up to the dry-bulb temperature.

One can state the well-known fact that drying is faster at higher temperatures (Figure 6). Concerning the constant drying period, this can also be explained by an isothermal model, but the additional enhancement due to heating up in the second drying period can only be captured by a model that includes heat transfer.

CONCLUSIONS

We have presented an isothermal capillary model that gives some insight in how the pore size distribution influences the drying behavior. In general, porous media with broad pore size distributions or with a binary pore size distribution, i.e., having micro and macropores, will dry more easily (with an extended first drying period) than porous media with a narrow pore size distribution. Secondly, a drying model for two capillary classes including heat transfer has been presented that can additionally explain the several stages of heating up of the porous medium during drying. In future work, this model will be extended to pore size distributions.

The main problem of the presented models seems to be the assumption of a completely wet surface during the first drying period, which, toward the end of this period, must be ensured by a few small capillaries. For the isothermal model, a factor might be introduced that relates the drying rate to the fraction of really wet surface.[4] For the model including heat transfer, this problem is more severe because dry surface regions will heat up, leading to hot spots that might require three-dimensional modeling. The limitations of the model in this sense are not yet clear. In order to model pores of smaller size, Knudsen and Kelvin effects should be included in the model.

As a natural extension of the presented capillary model, pore network models[5,6] can be used to investigate the influence of pore structure on drying behavior because they can better represent the complex three-dimensional pore geometry of real porous media.

NOMENCLATURE

c_p	Heat capacity (J/kgK)
Δh_v	Evaporation enthalpy (J/kg)
L	Length of capillaries (m)
$\tilde{M}$	Molar mass (kg/kmol)
$\dot{m}$	Mass flux (kg/m^{2}s)

N	Number of capillaries in one class
p	Pressure (Pa)
p_v^*	Saturation vapor pressure (Pa)
$\dot{q}$	Heat flux (W/m^2)
$\tilde{R}$	Universal gas constant (J/kmolK)
r	Radius of capillary (m)
S	Saturation
s	Position of meniscus (m)
T	Temperature (K, °C)
V	Volume (m^3)
x	Position (m)
Y	Moisture content (of air) ($kg_{vapor}/kg_{dry\ air}$)

Greek Symbols

α	Heat transfer coefficient (W/m^2K)
β	Mass transfer coefficient (m/s)
δ	Diffusion coefficient (m^2/s)
η	Dynamic viscosity (Pa·s)
λ	Thermal conductivity (W/mK)
$\dot{\nu}$	Normalized drying rate
ρ	Density (kg/m^3)
σ	Surface tension of water (N/m)
σ_0	Standard deviation of pore distribution (m)
ψ	Porosity

Subscripts

a	Air
c	Capillary
i	Class index
f	Friction
s	Solid
v	Vapor
w	Liquid water
∞	Bulk

ACKNOWLEDGEMENTS

The authors would like to thank the Graduiertenkolleg 828 *Micro-Macro-Interactions in Structured Media and Particle Systems* (funded by the German Research Foundation) for its financial support.

REFERENCES

1. Krischer, O. *Die wissenschaftlichen Grundlagen der Trocknungstechnik*, 1st Ed; Springer-Verlag: Berlin, 1956.

2. Schlünder, E.-U. Drying of porous material during the constant and the falling rate period: A critical review of existing hypotheses. Drying Technology **2004**, *22* (6), 1517–1532.
3. Groenewold, C.; Groenewold, H.; Tsotsas, E. Interrelations between porous structure and convective drying kinetics in theory and experiment. In Proceedings of 12th International Drying Symposium, Nordwijkerhout, The Netherlands, 2000; Paper No. 59.
4. Schlünder, E.-U. On the mechanism of the constant drying rate period and its relevance to diffusion controlled catalytic gas phase reactions. Chemical Engineering Science **1988**, *43* (4), 2685–2688.
5. Laurindo, J.B.; Prat, M. Modeling of drying in capillary-porous media: A discrete approach. Drying Technology **1998**, *16* (9&10), 1769–1788.
6. Segura, L.A.; Toledo, P.G. Pore-level modeling of isothermal drying in pore networks accounting for evaporation, viscous flow and shrinking. In Proceedings of 14th International Drying Symposium, Sao Paulo, Brazil, 2004.

DISCRETE MODELING OF DRYING KINETICS OF POROUS MEDIA

Thomas Metzger, Anton Irawan, Evangelos Tsotsas

Chair of Thermal Process Engineering, Otto-von-Guericke University,
P.O. 4120, D-39106 Magdeburg, Germany,
E-mail: thomas.metzger@vst.uni-magdeburg.de

Keywords: capillary model, pore network model, pore size distribution, pore structure

ABSTRACT

Discrete models of different dimensionality and complexity are presented for isothermal drying of capillary porous media. The simplest is a one-dimensional capillary model, in which liquid water flow is governed by the counter-acting mechanisms of capillary pumping and friction; vapour transport in the capillaries is diffusive. A variant of this plane model allows to describe the drying of spherical objects.
More realistically, a porous object can be represented by two- or three-dimensional networks of capillaries. We present a network model, in which capillary forces are assumed to dominate over friction forces – restricting the model to larger pore radii and moderate drying conditions; vapour transport in the network is purely diffusive. Lateral transport of vapour in the boundary layer is modelled explicitly so that the constant drying period can be reproduced.
The proposed models are used to investigate the influence of drying air velocity and plate thickness or particle diameter. Different pore size distributions, mono-modal and bi-modal, are modeled to study the influence on drying kinetics. The results are presented as drying curves and plots of moisture distribution.

INTRODUCTION

In drying technology, we are still far from predicting the drying behavior for a given pore structure, although this is one of the most interesting goals. A promising way to make progress in this direction seems to be discrete modeling of the drying process, where drying curves are computed from pore-level phenomena in representative porous media. Depending on the number of effects included in such models, they might become applicable to a more or less wide range of materials and drying conditions. The most popular tool are pore network models, in which capillary forces are usually assumed to dominate over

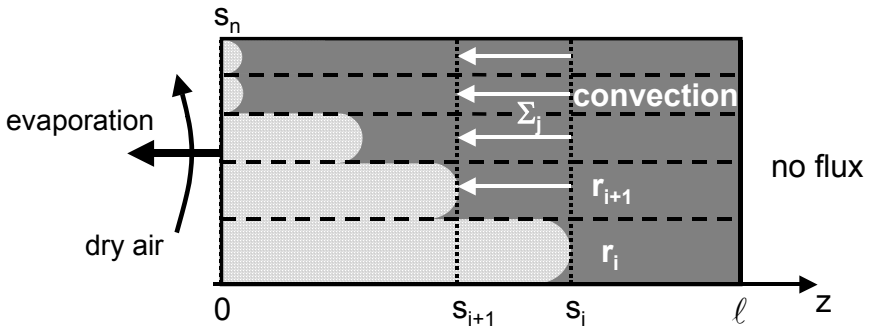

Figure 1 – Geometry of one-dimensional capillary model.

friction forces and which are hence restricted to large pore radii in the hundred micrometer range (Laurindo and Prat, 1998; Segura, 2005); but models accounting for viscous effects have also been developed (e.g. Yiotis, 2005). Most of the literature models are restricted to isothermal conditions. The general idea of a network model is to represent the pore space by discrete pores connected by throats. The exact geometry may vary, but commonly pores are taken as nodes without volume. Recently we proposed a one-dimensional discrete model (Metzger, 2005) which includes friction forces and can give some insight in the influence of the pore size distribution on the drying behavior. This model is analysed and further developed in the present paper; two- and three-dimensional network models, based on the work of Prat and neglecting viscous forces, are used for complementary investigations.

ONE-DIMENSIONAL CAPILLARY MODEL

In a first approach we represent the pore space by a large number of cylindrical capillaries which are set perpendicular to the product surface and connected all along their length ℓ without any resistance. Figure 1 illustrates this for a flat product geometry. The capillaries are divided into n classes of decreasing radii r_i according to a volume distribution. Initially, all capillaries are completely filled by water; during drying, capillary pumping ensures that large capillaries will empty first. The difference in capillary pressure between two classes – for surface tension σ and zero contact angle –

$$\Delta p_{c,i} = 2\sigma \cdot \left(\frac{1}{r_{i+1}} - \frac{1}{r_i} \right) \quad \text{for } i = 1, \ldots, n-1 \tag{1}$$

gives an upper limit for the laminar pressure drop between the corresponding meniscus positions s_i

$$\Delta p_{f,i} = \frac{8\eta \dot{M}_v}{\rho} \cdot \left(\sum_{j=i+1}^{n} N_j \pi r_j^4 \right)^{-1} (s_i - s_{i+1}) \quad \text{for } i = 1, \ldots, n-1 \tag{2}$$

where η denotes dynamic viscosity, ρ density of water and N_j the number of capillaries for one class. Whenever this limit is reached, another meniscus retreats from the surface. The mass flow rate of evaporation is given by

$$\dot{M}_v = -\left(\frac{1}{\beta} + \frac{s_n}{\delta} \right)^{-1} \frac{A_{tot}}{\psi} \frac{p \tilde{M}_v}{\tilde{R} T} \cdot \ln\left(\frac{p - p_{v,\infty}}{p - p_v^*} \right) \tag{3}$$

where β is mass transfer coefficient, δ diffusivity of vapor in air, A_{tot} total cross-sectional area of capillaries, ψ porosity, p total pressure, $\tilde{M}_v$ molar mass of vapor, $\tilde{R}$ universal gas constant, T absolute temperature, $p_{v,\infty}$ vapor pressure of drying air and p_v^* saturation vapor pressure. Consequently neglecting any lateral resistances, we assume that all capillaries are saturated with vapor up to the last meniscus and that the total product surface is active. Therefore, as long as part of the product surface is still wet,

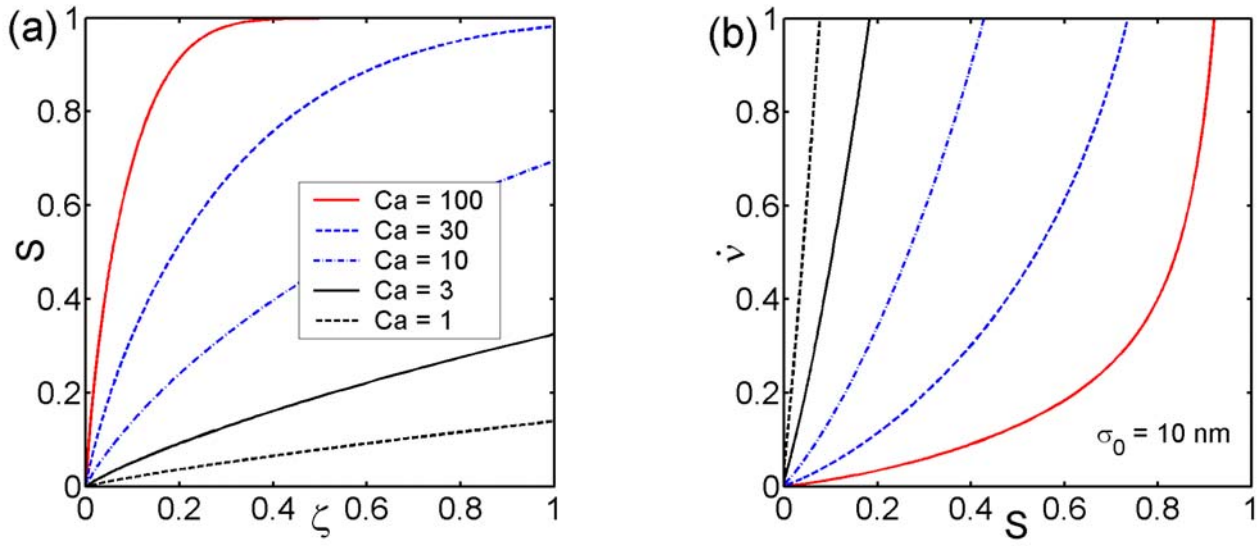

Figure 2 – (a) Moisture profiles at end of first drying period and (b) corresponding drying curves for a plate.

drying is at a constant rate. This strong assumption which will be critically discussed later on. Furthermore, we neglect Knudsen and Kelvin effects which is a reasonable approximation for $r_i > 40$ nm (mean free path of vapor molecules); residual moisture in form of sorbed water is not accounted for.

Mono-modal pore size distributions

If we apply this model to a normally distributed pore volume, with mean pore radius r_0 and standard deviation σ_0, we find that the drying behavior strongly depends on σ_0 whereas r_0 plays only a minor role (Metzger, 2005). Indeed, if $\sigma_0 << r_0$, then the first drying period can be completely described in terms of the following Capillary number

$$\mathrm{Ca} = \frac{\beta\eta\ell}{1000\cdot\psi\sigma\sigma_0} \tag{4}$$

It is the ratio of the evaporation velocity β, transformed into an interstitial velocity β/ψ, to a typical water velocity v through a capillary of radius r_0

$$v = \frac{r_0^2}{8\eta}\frac{\Delta p_c}{\ell} \quad \text{with} \quad \Delta p_c = 2\sigma\cdot\left(\frac{1}{r_0-2\sigma_0}-\frac{1}{r_0+2\sigma_0}\right)\approx\frac{8\sigma\sigma_0}{r_0^2} \tag{5}$$

(The factor was introduced to account for the difference in liquid and gas densities.) In the second drying period, the vapor velocity becomes dependent on the size distribution of the capillaries; therefore, we must give its standard deviation σ_0 in order to uniquely define the process.

Figure 2a shows the saturation profiles at the end of the first drying period as a function of dimensionless depth $\zeta = z/\ell$; the corresponding dimensionless drying rates $\dot{v}$ are given in Figure 2b for $\sigma_0 = 10$ nm. As in the remainder of this paper, the temperature is set to 20°C and the drying air contains no moisture at all. The results were computed for $\sigma_0 << r_0$; effects of the necessary truncation and discretization of the distribution are negligible. One can see that for a low capillary number, e.g. for moderate drying conditions, thin products or broad pore size distribution, more water can be removed during the first drying period and the gradient in moisture content becomes lower.

Figure 5a gives an example of the evolution of the moisture profile during drying.

Spherical geometry

The capillary model can be adapted to describe the drying of spherical bodies. The plate thickness L is then replaced by the radius of the sphere R, and the number of capillaries depends on the radial position

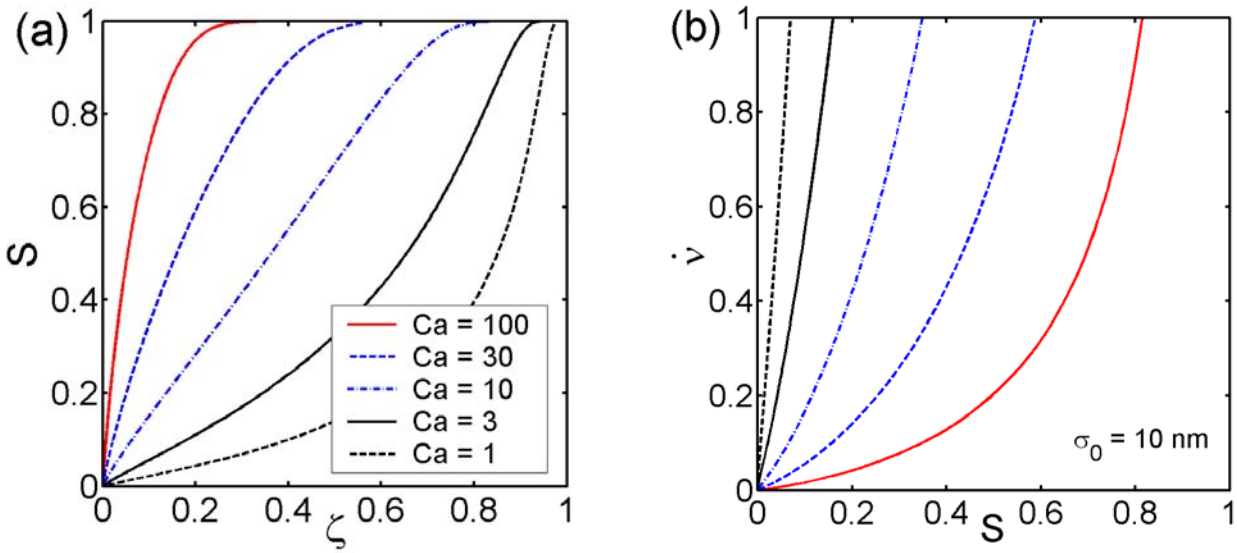

Figure 3 – (a) Moisture profiles at end of first drying period and (b) corresponding drying curves for a sphere.

$$N_j(s) = \frac{(R-s)^2}{R^2} N_{0,j} \quad \text{for } j = 1,\ldots,n \tag{6}$$

As a result, $\Delta p_{f,i}$ must be computed from an integral, and the distances between the menisci become dependent on their absolute positions. Figure 3 shows moisture profiles at the end of the first drying period as well as drying curves; in Figure 5a the evolution of the moisture profile during is given. All can be directly compared to the results for the plate geometry. Most remarkable are more favorable drying curves with an extended first drying period, and the distortion of the moisture profile towards the centre of the sphere. The menisci reach the center of the sphere only asymptotically; this is due to the local decrease in permeability.

Lateral resistance for vapor diffusion

So far we made the assumption that the high drying rate of the first period can be maintained as long as there are still wet spots (menisci) at the surface, no matter how small their number. We now ignore all lateral vapor transport in the pore space and introduce lateral mass transfer resistances in the laminar boundary layer by taking up an idea by Schlünder (1988). In his model, the drying rate is a function of wet surface fraction φ, boundary layer thickness ε = β/δ and average radius of the wet spots r

$$\dot{v} = \frac{1}{1+\Phi} \quad \text{with} \quad \Phi = \frac{2}{\pi}\frac{r}{\varepsilon}\sqrt{\frac{\pi}{4\varphi}}\left(\sqrt{\frac{\pi}{4\varphi}} - 1\right) \tag{7}$$

Typical drying curves are given in Figure 4 for a plate with porosity 50 %. For simplicity we modeled only the period in which at least one meniscus is still at the surface; note that nevertheless we can almost produce the complete drying curve. This can be understood from the fact that the moisture profile primarily depends on the drying rate – with no importance by what kind of addictional resistance this rate is reduced. Note that only for large pore radii the drying curve is significantly changed. Therefore we retain the simple (and consistent) model of negliglible lateral resistance for liquid *and* gas.

Bi-modal pore size distributions

In order to investigate the drying behavior of porous media with bi-modal pore size distributions, we combined two normal pore volume distributions, with $r_1 \pm \sigma_1$ for macro and $r_2 \pm \sigma_2$ for micro pores. In previous work (Metzger, 2005) we found for the plate geometry that usually the macro capillaries dry out completely before the first micro capillaries start to empty (due to the high difference in capillary pressure between the two modes). The onset and the kinetics of the second drying period are then

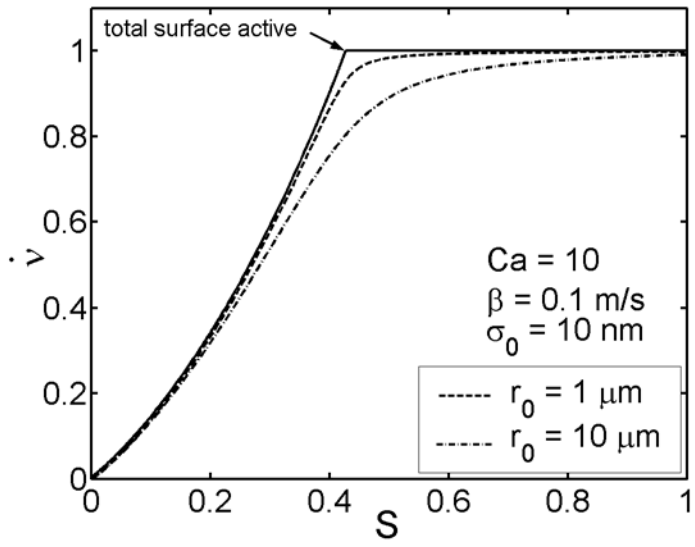

Figure 4 – Effect of lateral resistance for vapor diffusion.

determined by the micro capillaries. Therefore the size distribution of the macro pores is of minor importance and their volume fraction just gives an additional contribution to the first drying period. The only significant capillary number Ca_2 is computed from the size distribution of the micro capillaries.

For these reasons, we give only one example of a bi-modal distribution with equal volumes $V_1 = V_2$ for macro and micro capillaries. The evolution of moisture profiles is shown in Figure 5b for both plate and sphere, the corresponding drying curve for a plate is obtained from the solid curve in Figure 4 (by shrinking it to $0 \le S \le 0.5$). In the case of a plate, one can see that the macro capillaries dry out with a low gradient in moisture content, before this gradient increases to empty the micro capillaries. For a sphere, the large capillaries retain some water for $S < 0.5$ in a shrinking wet core.

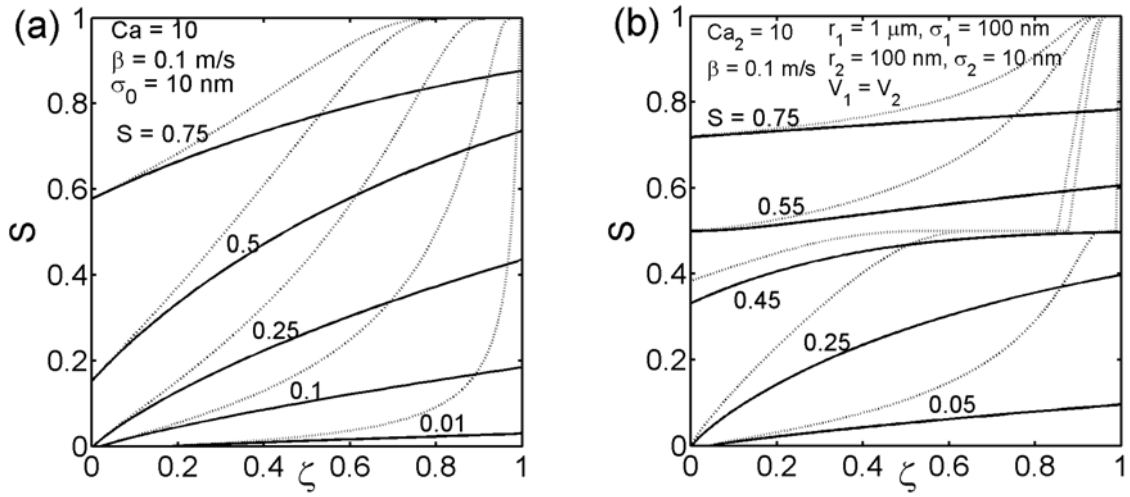

Figure 5 – Evolution of moisture profiles for (a) mono-modal and (b) bi-modal pore size distribution, parameter is the overall saturation; solid lines are for plate, dotted lines for spherical geometry.

The major drawbacks of the one-dimensional capillary model are the absence of lateral resistances and the fact that the liquid phase is always continuous which is not true in reality. We will now present and apply a network model which does not have these deficiencies, but does not account for viscous forces.

TWO- AND THREE-DIMENSIONAL PORE NETWORKS

In this second approach, we represent porous media by regular square or cubical networks of cylindrical capillaries with a radius distribution. Figure 6 shows three examples of two-dimensional networks in the course of drying. Up to now, all viscous forces are neglected in our model which is only reasonable for relatively large capillaries. (The validity of this assumption is checked in our algorithm.)

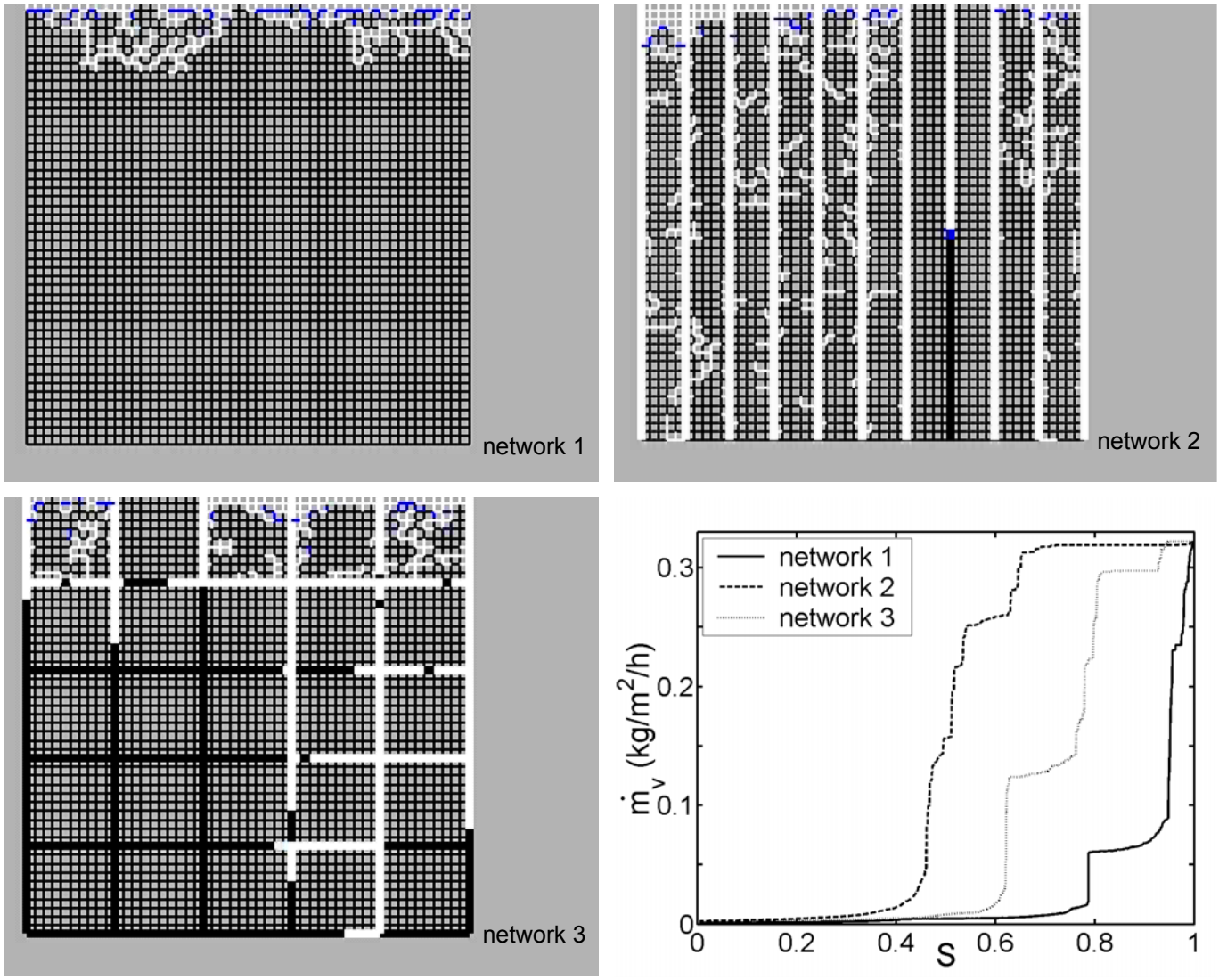

Figure 6 – Drying curves for different two-dimensional networks; the filling of capillaries is shown for $\dot{\nu} = 0.5$ (black stands for completely filled, blue for partially filled and white for empty).

The pore network is open for evaporation at the top. Initially, all capillaries are filled by water; in the course of drying, the liquid phase typically splits up into several clusters, and the capillaries need to be labeled according to their cluster affiliation (by the Hoshen-Kopelman algorithm). Within one liquid cluster, water is pumped into throats of small radius, and large throats empty first – due to the dominance of capillary forces over friction forces.

For any time step, the state of all capillaries (empty, partially or completely filled by water) must be known. A connection site is defined as gas node if at least one empty capillary is connected to it, and as liquid node otherwise. The main task is to compute the vapour pressure field $p_{v,i}$ for the gas nodes of the network; assuming quasi-steady diffusive vapour transport this leads to solving mass balances

$$\sum_j \dot{M}_{v,ij} = \sum_j A_{ij} \frac{\delta}{\ell} \frac{p\tilde{M}_v}{\tilde{R}T} \cdot \ln\left(\frac{p - p_{v,i}}{p - p_{v,j}}\right) = 0 \qquad (8)$$

for all gas nodes i (the sum is over all neighboring gas nodes j that are connected to node i by an empty capillary). Here $A_{ij} = \pi r_{ij}^2$ denotes the cross section and ℓ the length of the respective capillaries. Inside the network, the boundary condition is that any gas node which is connected to a (partially) filled capillary is at saturation vapour pressure.

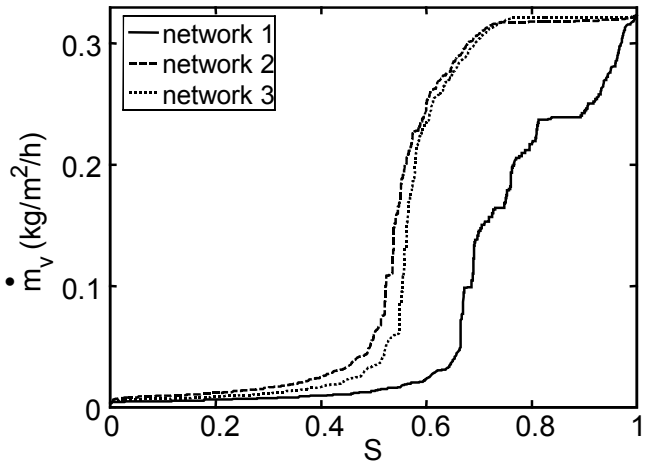

Figure 7 – Drying curves for 3D networks.

The (diffusive) boundary layer of drying air is discretized by naturally extending the nodes of the network up to the average boundary layer thickness as computed by laminar theory. Then Eq. (8) also holds for these nodes if the cross sections A_{ij} are chosen appropriately. The (zero) vapour pressure of the drying air gives the remaining boundary condition. From solving Eq. (8), we immediately get the vapour flow rates and can easily compute the total evaporation rate for every cluster – and hence the time for emptying its largest throat. The minimum time of all clusters is chosen as the time step and the liquid saturation of capillaries is updated accordingly.

Influence of pore structure

In two dimensions, drying simulations were done for three different 51×51 networks as depicted in Figure 6. The length of the capillaries was chosen to be ℓ = 500 µm (giving a network size L = 2.5 cm), their radii according to a normal distribution with mean 40 µm and standard deviation 2 µm. The second and third network additionally contain larger capillaries of radius 100 ± 5 µm (43 % of total pore volume) forming long channels either only towards the network surface or in both directions. These latter geometries were chosen to assess the effect of capillary pumping. The velocity of the drying air was set to a low value of u_4 = 0.05 m/s which yields the mass transfer coefficient β_4 = 5.1 mm/s (using dimension L in Reynolds and Sherwood numbers). This corresponds to a relatively large (average) boundary layer thickness of 5 mm or 10 nodes, so that lateral vapour transfer in the boundary layer may ensure that regions above already dry capillaries are also used for exchange, and a first drying period can be observed. Figure 6 shows the resulting drying curves; saturation is shown at the moment when the drying rate drops below 50 % of its initial value.

For a completely random radius distribution (network 1), capillary pumping only plays a minor role; the surface dries out rapidly, leaving most of the water to evaporate at very low rates. In contrast, the second network dries at an almost constant rate down to a saturation of 60 %, because the large vertical channels dry out first while water is pumped to the surface in the micro channels keeping the wet surface fraction high. In the drying of the third network, the strong action of capillary pumping cannot prevail

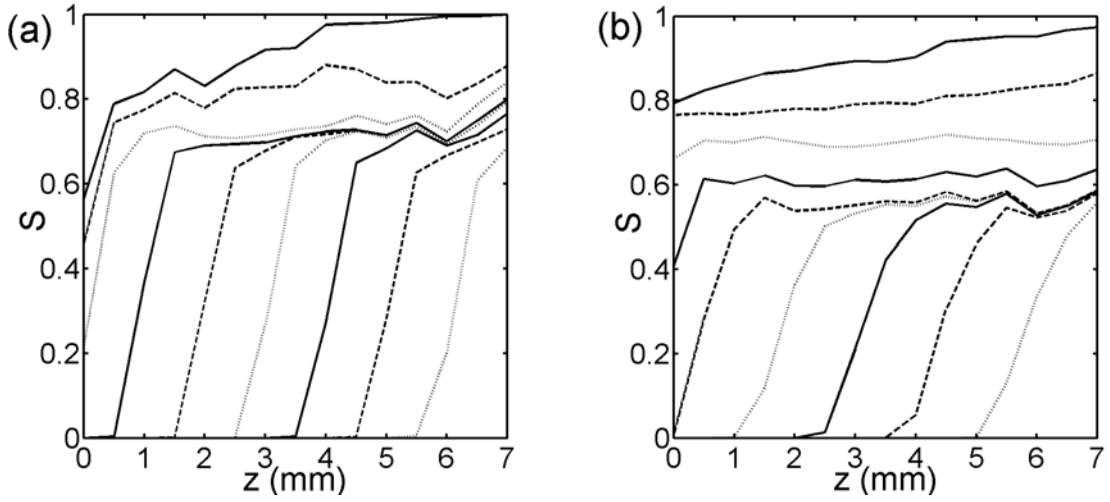

Figure 8 – Evolution of moisture profiles for 3D network 1 (a) and 3D network 2 (b); lines correspond to multiples of 10% in overall saturation.

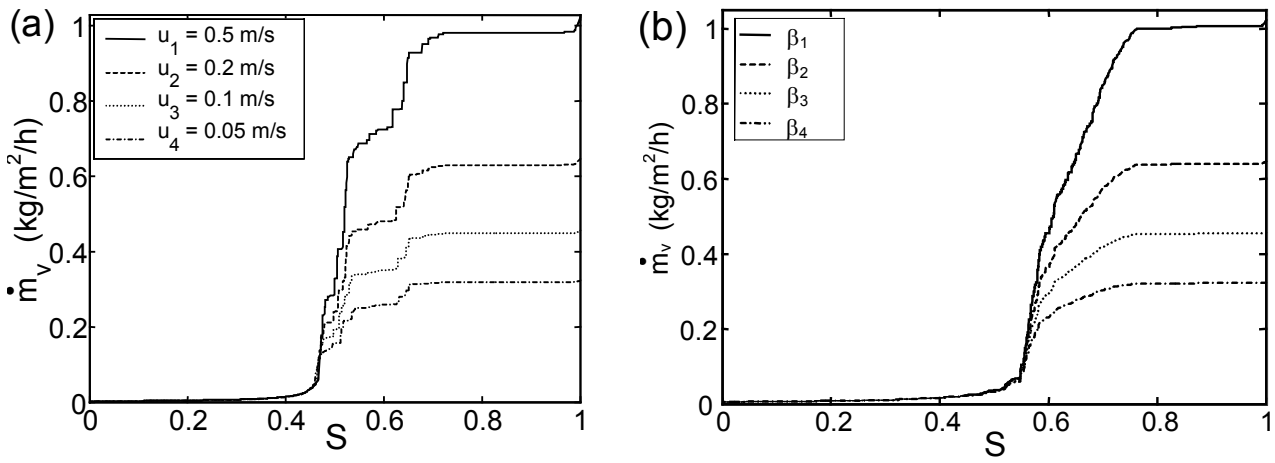

Figure 9 – Influence of mass transfer coefficient on drying curves of (a) 2D network 2 and (b) 3D network 3.

for long because the emptying of horizontal macro channels cuts off capillary flow to the surface; as a consequence whole surface regions dry out – making lateral diffusion in the boundary layer less efficient. A significant first drying period can only be found for network 2.

Analysis of drying curves for several networks of each class has shown that the quasi-constant periods (as for network 1 around S ≈ 0.8) are not a characteristic of the network class but random effects.

In three dimensions, 16×16×16 networks, i.e. with network length L = 7.5 mm, of the same three types have been generated; the large capillaries in networks 2 and 3 making up 26 % of the total pore volume and being oriented towards the network surface or in all three space directions, respectively. The networks were dried using the same mass transfer coefficient β_4 as in the two-dimensional case.

The drying curves are shown in Figure 7. As a first result, we may state that the different drying behaviour of networks 2 and 3 was a two-dimensional effect. Secondly, we see that the third dimension enhances the drying rates in general. Despite the significantly lower fraction of large capillaries in the 3D networks, the first drying period is almost as long as for the 2D networks. Both effects are due to the fact that, in three dimensions, flow paths can be maintained more easily. Figure 8 shows the evolution of moisture profiles; generally, we see that during the first drying period the saturation decreases in the whole network – more or less uniformly, depending on the effectiveness of capillary pumping – and that during the second drying period, an evaporation front penetrates into the network.

Influence of drying air velocity

Naturally, the thickness of the boundary layer is of major importance for the extent of the first drying period. In the limit of a very thin boundary layer, lateral vapour transfer becomes negligible and the drying rate drops from the start (as the first surface capillary dries out). In Figure 9a, we show drying curves for the two-dimensional network 2 for four different drying air velocities; results for the three-dimensional network 3 are shown for the same four mass transfer coefficients in Figure 9b.

We can see that, for more gently drying conditions, the drying curve is smoother and their dimensionless form maintains closer to one down to lower saturations.

Influence of network depth

Finally, drying simulations at the low mass transfer coefficient were carried out for two- and three-dimensional networks of different depth (51×11…71 and 16×16×11…21, respectively). The results are shown in Figure 10 as drying rates over evaporated mass of water. We can see that the amount of water evaporated in the first period increases quasi linearly with network depth – due to the fact that the large capillaries first empty completely before the drying rate decreases. If the drying curves were plotted as a function of saturation, they would more or less coincide, i.e. be independent of depth.

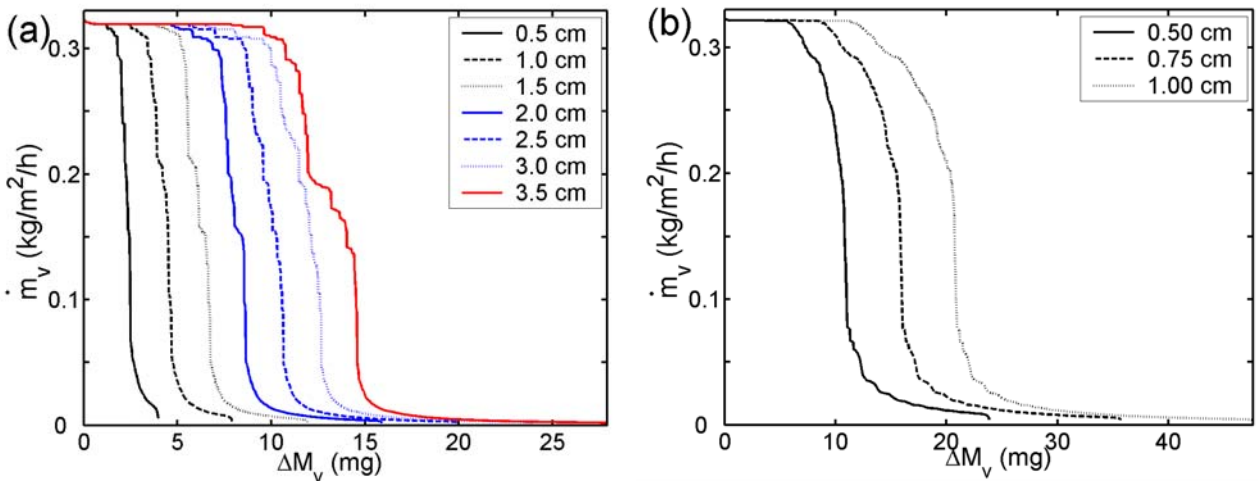

Figure 10 – Influence of network depth on drying curves for (a) 2D network 2 and (b) 3D network 3; the abscissa gives the mass of evaporated water.

CONCLUSION

Two different approaches have been presented in order to study drying behavior for different pore size distributions. Both models have strong assumptions, namely continuous liquid phase for the one-dimensional capillary model and no viscosity for the two-and three-dimensional network model; hence different effects counteract capillary pumping and lead to a decrease in drying rate: either friction forces or discontinuity of the liquid phase. Therefore the conclusions for both models may well be different.

The capillary model predicts that a broad mono-modal pore-size distribution is favorable for drying. Segura (2005) has investigated such an influence for networks but did not report a significant effect. As a common result for both models, we find confirmed the fact that bi-modal distributions are favorable.

In the capillary model, the mass transfer coefficient has a strong influence on the dimensionless drying curve (via the capillary number) whereas the network model only states a minor effect. The product depth has no influence for bi-modal networks but plays an important role in the capillary model.

For a more comprehensive view on the effects of pore structure on drying behavior, we will need to upgrade the network model to include viscous effects. Then drying of porous structures with smaller pore sizes can be described more realistically. Additionally, we will investigate networks with randomized connection sites and capillary connections with a correlated radius distribution, to get closer to real porous structures.

NOTATION

A	cross section	m^2
Ca	capillary number, see Eq. (4)	–
L	length of network	m
ℓ	length of capillaries	m
$\tilde{M}$	molar mass	kg/kmol
$\dot{M}$	mass flow rate	kg/s
$\dot{m}$	mass flux	kg/m²s
N	number of capillaries in one class	–
p	pressure	Pa
p_v^*	saturation vapor pressure	Pa
r	radius of capillary	m

R	radius of spherical porous particle		m
$\tilde{R}$	universal gas constant		J/kmolK
S	saturation		–
s	position of meniscus		m
T	absolute temperature		K
u	drying air velocity		m/s
V	volume		m^3
z	position		m

Greek Symbols

β	mass transfer coefficient		m/s
δ	diffusivity of vapr in air		m^2/s
ζ	dimensionless length of capillaries		–
η	dynamic viscosity		Pa s
$\dot{\nu}$	dimensionless drying rate		–
ρ	density		kg/m^3
σ	surface tension of water		N/m
σ_0	standard deviation of pore volume distribution		m
φ	wet surface fraction		–
ψ	porosity		–

Subscripts

c	capillary	s	surface
i	index of capillary class	v	vapor
f	friction	∞	bulk

ACKNOWLEDGEMENTS

The authors would like to thank the Graduiertenkolleg 828 «Micro-Macro-Interactions in Structured Media and Particle Systems» (by the German Research Foundation) which financed part of this work.

LITERATURE

Metzger, T., Tsotsas, E. (2005). Influence of pore size distribution on drying kinetics: a simple capillary model. Drying Technology, accepted for publication.

Schlünder, E.-U. (1988). On the mechanism of the constant drying rate period and its relevance to diffusion controlled catalytic gas phase reactions. Chem. Eng. Sci., Vol 43 (4).

Segura, L.A., Toledo, P.G. (2005). Pore-level modeling of isothermal drying of pore networks. Effects of gravity and pore shape and size distributions. Chemical Engineering Journal, article in press.

Laurindo, J.B., Prat, M. (1998). Numerical and experimental network study of evaporation in capillary porous media. Drying Rates. Chem. Eng. Sci., Vol 53 (12).

Yiotis, A.G., Stubos, A.K., Boudouvis, A.G., Tsimpanogiannis, I.N., Yortsos, Y.C. (2005). Pore-network modeling of isothermal drying in porous media. Transport in Porous Media, Vol 58.

PORE NETWORK MODELLING OF DRYING: COMBINATION WITH A BOUNDARY LAYER MODEL TO CAPTURE THE FIRST DRYING PERIOD

Anton Irawan, Thomas Metzger, Evangelos Tsotsas

Chair of Thermal Process Engineering, Otto-von-Guericke-University,
P.O. 4120, D-39016 Magdeburg, Germany,
E-mail: thomas.metzger@vst.uni-magdeburg.de

Keywords: drying kinetics, pore size distribution, capillary porous media

ABSTRACT

Although drying of porous materials has always been a crucial step in solids processing, modelling of the involved transport phenomena is still a challenging task. Within the last few years, network models, in which the pore space is represented by a network of interconnected pores, have become very popular in order to describe physical phenomena in porous media, including drying. However, most existing network drying models fail to reproduce the first drying period, in which the material dries at a constant rate. Instead, the drying rate falls from the very beginning of drying. In this paper, we show that this deficiency may be overcome by properly accounting for vapour transfer in the boundary layer. Laurindo and Prat (1998) introduced a diffusive boundary layer into their network model without commenting on its thickness. We carried on this idea by choosing the thickness according to the flow conditions using Prandtl's relationship for mass transfer through a laminar boundary layer. From such an extended network model, drying curves were calculated under isothermal conditions for two-dimensional networks with different pore size distributions. Depending on flow conditions and pore structure a more or less extensive constant rate period can be observed in the drying curves. We compared our results to the work of Schlünder (1988) on the existence of the first drying period. He proposed a model which gives criteria for evaporation of moisture from a partially dry surface at the same rate as from a completely wet surface, and defines the reduction of evaporation rate, if these criteria are not fulfilled.

INTRODUCTION

Several research groups have applied pore network models to isothermal drying of capillary porous media. All of these models use regular square networks, but differ in their exact geometry and in the assumptions made on the importance of viscous effects. Prat (1993) proposed a percolation model for a

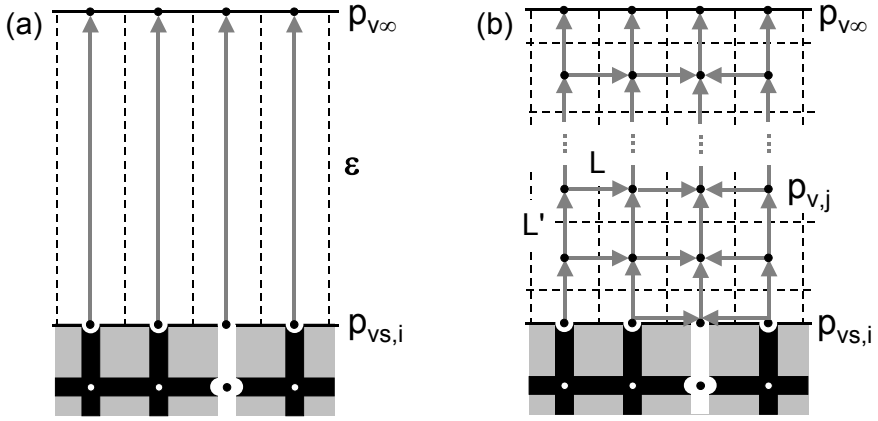

Figure 1 – Vapour transfer in the boundary layer for (a) conventional and (b) extended network model.

network of cylindrical pore throats which are the connections between nodes without volume. In his model, all viscous effects are neglected and capillary forces ensure that pore throats that are accessible for evaporation empty in order of decreasing radius. Quasi-steady vapour diffusion in gas-filled throats is assumed between the drying of two throats. Recently, Segura (2004) used a similar model with throats of rectangular cross section, accounting for corner flow as well as Haines jumps in the emptying of throats.

Nowicki (1992) developed a drying model with bi-conical pore throats, hence better representing the converging-diverging character of pore geometry. Vapour transport in the gas-filled pores is diffusive. The model additionally accounts for friction forces in the liquid phase that counteract capillary pumping; consequently, the positions of menisci in the throats is tracked continuously.

Another network model was presented by Yiotis (2001) for the case of non-negligible pressure differences in the gas phase, as for the drying of a rock by a fracture. Therefore, the model accounts for viscous effects in both liquid and gas phase. The pore bodies have volume and may be partially filled, whereas the pore throats have no volume and empty instantly.

All above mentioned network drying models reduce the gas-side boundary layer to a mass transfer coefficient β, which describes the vapour transfer between any surface pore (at vapour pressure $p_{vs,i}$) and the bulk drying gas (at vapour pressure $p_{v,\infty}$) without allowing for lateral vapour transfer (see Figure 1a). The local mass flux of evaporation is given by

$$\dot{m}_{v,i} = \beta \frac{p\widetilde{M}_v}{\widetilde{R}T} \cdot \ln\left(\frac{p - p_{v,\infty}}{p - p_{vs,i}}\right) \approx \beta \frac{p\widetilde{M}_v}{\widetilde{R}T} \cdot \left(p_{vs,i} - p_{v,\infty}\right) \tag{1}$$

with total pressure p, molar mass of vapour $\widetilde{M}_v$, universal gas constant $\widetilde{R}$ and absolute temperature T. Hence, the drying rate for the whole network decreases every time that another surface pore is emptied; and, consequently, the first drying period, during which the drying rate is constant, cannot be reproduced. This constant rate period is however a reality, and it can last down to relatively low liquid saturation of the porous medium.

Schlünder (1988) proposed a model to compare the drying rate for a partially wetted surface to that for a completely wet surface. If one may assume that the liquid patches are small and evenly distributed over the product surface, then the drying rate may remain at the high reference level down to a wet surface fraction of several percent. The reason for this is diffusive lateral vapour transfer, which – for sufficient boundary layer thickness – can ensure that the region above dry pores is also used for exchange.

To our knowledge, Laurindo and Prat (1998) were the only researchers to include lateral vapour transfer in the boundary layer into their network model. The idea is to extend the discrete model of the network into the gas phase (see Figure 1b); the nodes in the gas phase are separated by the same (constant) length L as the pore nodes in the network but are connected by a square cross section L^2 (or

by a rectangular cross section $L^2/2$ next to the product surface) instead of small cylindrical throats. (Note that this approach is equivalent to the finite volume method with corresponding exchange interfaces.)

In our work, we round off this idea by choosing the thickness of the boundary layer, which depends on gas flow velocity and dimensions of the porous body, according to laminar boundary layer theory.

NETWORK MODEL

Both network geometry and drying algorithm are based on the work of Prat, but shall be briefly presented. The pore structure consists of a two-dimensional regular square network of nodes (without associated pore volume), which are connected by cylindrical throats of variable radius. The network is open for evaporation at the top. Initially, all throats are filled by water. In the course of drying, the liquid phase typically splits up into separate clusters, whereas the gas phase remains continuous. The main assumption of the model is that capillary forces dominate over friction forces so that, within one liquid cluster, water is pumped into pore throats of small radius and large throats empty first.

For any time step, the state of all throats – empty, partially or completely filled by water – must be known. This defines the state of the nodes: any node which is connected to at least one empty throat is a gas node, all others are liquid nodes. The liquid filled throats are labelled according to their cluster affiliation using the Hoshen-Kopelman algorithm.

Then, the vapour pressure field is computed for the gas-filled part of the network. For this, we assume quasi-steady diffusive vapour transport between nodes leading to the mass balances

$$\sum_j \dot{M}_{v,ij} = \sum_j A_{ij} \frac{\delta}{L} \frac{p\tilde{M}_v}{\tilde{R}T} \cdot \ln\left(\frac{p - p_{v,i}}{p - p_{v,j}}\right) = 0 \qquad \text{for all gas nodes i} \tag{2}$$

where δ is the diffusion coefficient of vapour in air, $A_{ij} = \pi r_{ij}^2$ is the cross section and L the length of the connecting throat. The sum is over all neighbouring gas nodes that are connected by an empty throat. Note that the problem becomes linear by switching from $p_{v,i}$ to the variable $\ln\left(1 - p_{v,i}/p\right)$. The inner-network boundary conditions are given by the assumption that any gas node which is connected to a (partially) filled throat is at saturation vapour pressure; the boundary conditions at the top of the network are discussed in the next section. From the solution of Eq. (2) we know the vapour flow rate through every gas throat and can easily compute the evaporation rate from any meniscus. If several (partially) filled throats are connected to a gas node, the evaporative flow is distributed to the menisci according to their cross sections.

Now, for every liquid cluster, the total evaporation rate is computed, and the largest meniscus defines the candidate throat for drying. In order to check that water can flow from the candidate to the other menisci at the required rate, maximal liquid flow rates (Poiseuille law) are computed from mass balances

$$\sum_j \dot{M}_{w,ij} = \sum_j \frac{\pi r_{ij}^4}{8 \nu_w L_{ij}} \left(p_{w,i} - p_{w,j}\right) = 0 \qquad \text{for all liquid nodes i} \tag{3}$$

– the sum being over all neighbouring (partially) filled throats – where p_w is liquid pressure, ν_w kinematic viscosity of water, r_{ij} throat radius and $0 < L_{ij} \le 1$ liquid filled length. Gravitational effects are neglected. As boundary conditions we have liquid pressures at the menisci, which are equal to the total gas pressure reduced by the capillary pressure $p_{w,i} = p - 2\sigma/r_i$, where σ is the surface tension of water (for zero contact angle). Only if friction forces are indeed negligible, the drying algorithm may continue.

At last, the time for emptying the candidate throat is computed for every liquid cluster and the minimum time chosen as the time step. The liquid saturation of throats is updated accordingly.

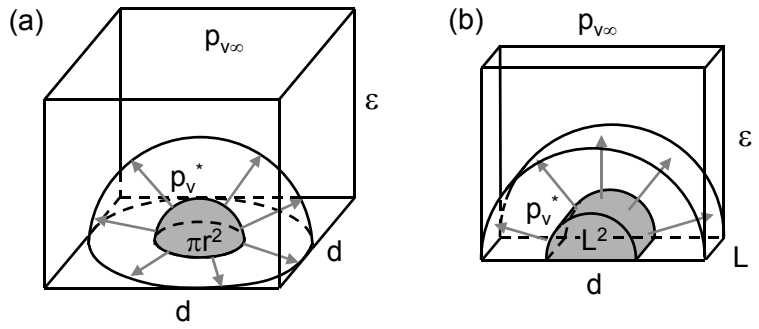

Figure 2 – Geometry for evaporation from wet patches in Schlünder's model (a) and the two-dimensional equivalent (b).

BOUNDARY LAYER MODELLING

In this section, we present three approaches to model vapour transfer in the boundary layer: at first, the use of an average mass transfer coefficient as in conventional network models; then, our proposal of a discretized diffusive boundary layer – with flow dependent thickness – to account for lateral vapour transfer; at last, an average model for diffusive boundary layer mass transfer as proposed by Schlünder.

Average mass transfer coefficient

If a plate is set in fluid flow, a boundary layer of increasing thickness develops. In this paper, all boundary layers are laminar and assumed to be fully developed. In this case, an average mass transfer coefficient β can be computed from the relationship

$$\mathrm{Sh} = 0.664\,\mathrm{Re}^{1/2}\,\mathrm{Sc}^{1/3} \tag{4}$$

with Reynolds number $\mathrm{Re} = uL_{tot}/\nu$, Schmidt number $\mathrm{Sc} = \nu/\delta$ and Sherwood number $\mathrm{Sh} = \beta L_{tot}/\delta$, where u is bulk fluid velocity, L_{tot} total length of the plate and ν kinematic fluid viscosity.

This mass transfer coefficient can be used to complete the boundary conditions in the network model: the vapour pressure at the surface nodes is then linked to the vapour pressure of the bulk fluid by Eq. (1) which is multiplied by L^2 (maximum cross section for vapour transfer) to get a mass flow rate.

Discretized diffusive boundary layer

We can use the above mass transfer coefficient to define an average thickness of the boundary layer by $\varepsilon = \delta/\beta$. This defines the region into which the network needs to be extended by gas nodes. The vertical distance L′ is adjusted so that the last row of nodes is on the edge of the boundary layer (see Figure 1b). These nodes are at bulk vapour pressure and give the missing boundary condition for the network model. Mass transfer between boundary layer nodes is described by Eq. (2) with an adjusted cross section A_{ij}.

Average model for diffusive boundary layer mass transfer

In his model, Schlünder assumes spherical droplets of diameter r which are evenly distributed on a dry surface, the distance between the droplets being d; inherently, both quantities are averages. Vapour diffusion from the droplet surface (at p_v^*) through the boundary layer to the bulk air (at $p_{v\infty}$) is approximated by diffusion in series as depicted in Figure 2a: first, from a hemisphere of radius r to one of radius d/2, then from the product surface through the boundary layer via a square chimney of cross section d^2. By this, Schlünder obtains the dimensionless drying rate

$$\dot{\nu} = \frac{\dot{m}_v}{\dot{m}_{v,I}} = \frac{1}{1+\Phi} \qquad \text{with} \qquad \Phi = \frac{2}{\pi}\frac{r}{\varepsilon}\sqrt{\frac{\pi}{4\varphi}}\left(\sqrt{\frac{\pi}{4\varphi}} - 1\right) \tag{5}$$

where $\dot{m}_{v,I}$ is the drying rate for a completely wet surface and $\varphi = \pi r^2/d^2$ the wet surface fraction.

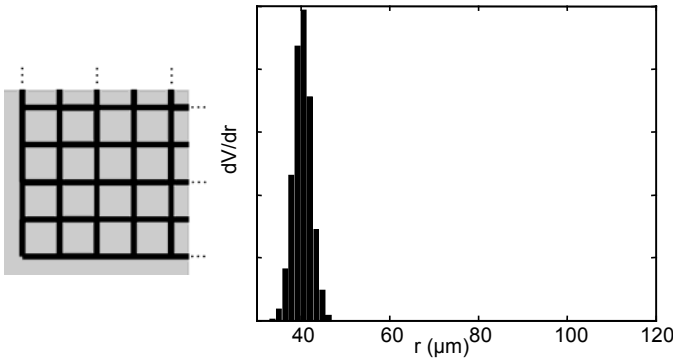

Network 1 – monomodal pore size distribution
(total pore volume 12.7 mm^3, only micro pores)

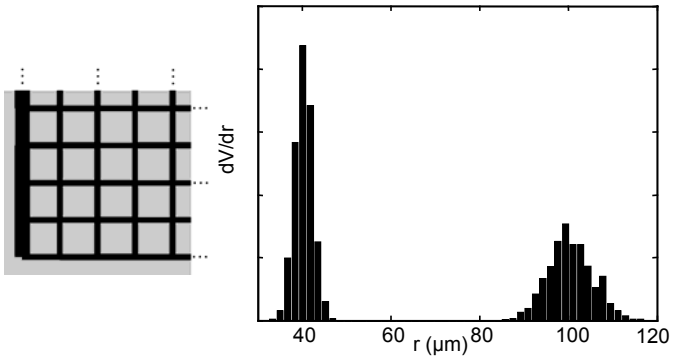

Network 2 – bimodal distribution with vertical macro pores
(total pore volume 20.0 mm^3, 43.3 % macro pores)

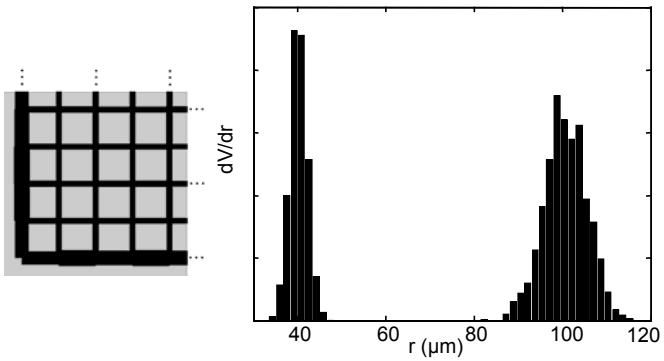

Network 3 – bimodal distribution with vertical and horizontal macro pores
(total pore volume 26.7 mm^3, 62.2 % macro pores)

Figure 3 – Lower left hand corner of three different 51×51 networks – the presented cell is repeated in both spatial directions with random variation of micro and macro pore diameters according to the respective distributions. (See Figure 4 for complete networks in the course of drying.)

Note that the reduction factor Φ depends on the thickness of the boundary layer ε.

We will use an adaptation of this model to our case of a one-dimensional product surface with depth L in order to assess our results later in this paper. For every (partially) filled surface throat we assume a square wet patch of area L^2, so that we need to consider diffusion from a half-cylinder of radius L/2 to one of radius d/2 and then via a rectangular chimney of cross section L×d and length ε to the bulk fluid (see Figure 2b). This yields a reduction factor

$$\Phi = \frac{1}{\pi}\frac{L}{\varepsilon}\frac{1}{\varphi}\ln\left(\frac{1}{\varphi}\right) \tag{7}$$

where $\varphi = L/d$ is the wet surface fraction. (In absence of lateral transfer, we would simply get $\dot{v} = \varphi$.)

NUMERICAL DRYING EXPERIMENTS

Three different 51×51 networks are simulated in this paper, all having a throat length of 500 µm, leading to a total size of 2.5×2.5 cm^2. The first network has a normal random distribution of throat radii with mean 40 µm and standard deviation 2 µm; part of the network is shown in Figure 3 along with the pore volume distribution. Figure 4 shows the full network in the course of drying.

A second network contains micro pores with radii of 40 ± 2 µm and macro pores with radii of 100 ± 5 µm, the macro pores forming long channels towards the network surface. This geometry was chosen to study the effect of capillary pumping.

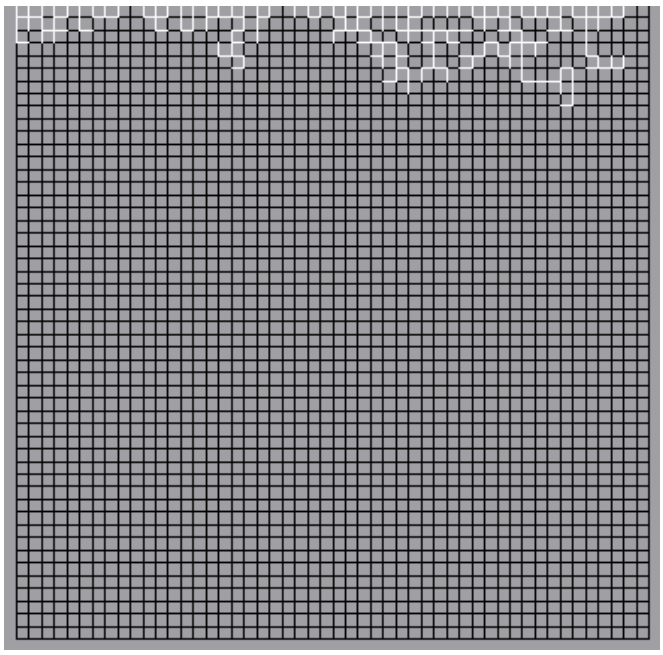

Network 1

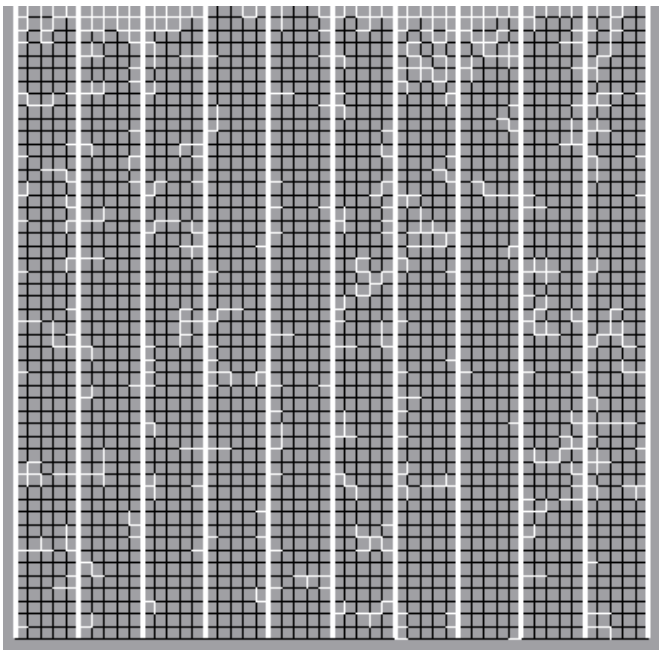

Network 2

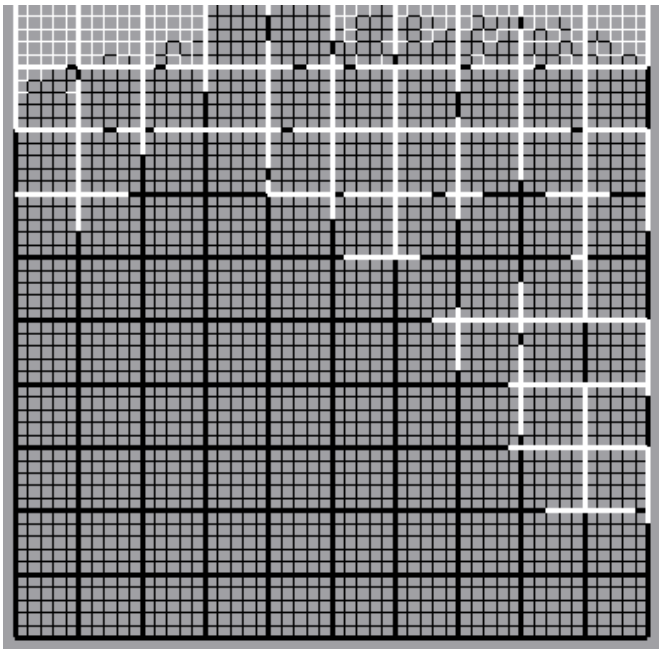

Network 3

Figure 4 – Moisture distribution for the three networks when the drying rate falls below 50% of its initial value (for drying at low air velocity u = 0.05 m/s, with lateral vapour transfer in boundary layer).

u (m/s)	Re	Sh	β (mm/s)	ε (mm)
0.5	830.6	16.12	16.24	1.58
0.2	332.2	10.19	10.27	2.50
0.1	166.1	7.21	7.26	3.54
0.05	83.1	5.10	5.13	5.00

Table 1 – Air flow velocities with respective mass transfer coefficient and boundary layer thickness.

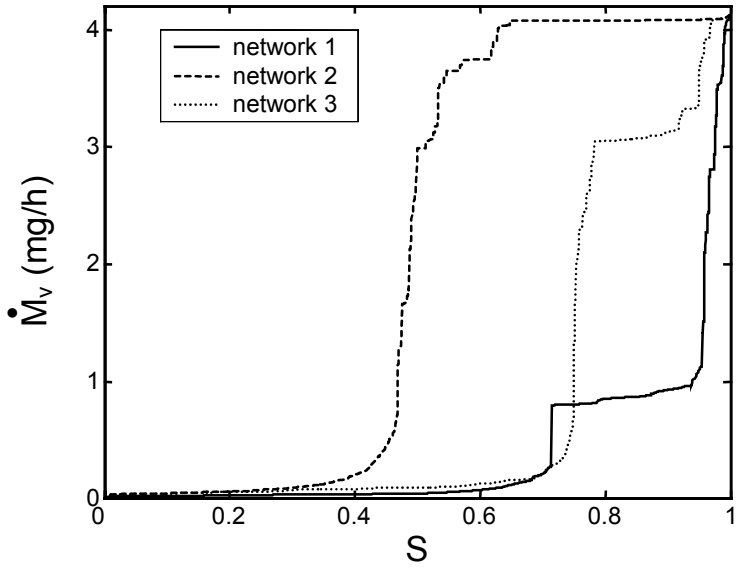

Figure 5 – Drying curves for three different networks (for u = 0.05 m/s, with lateral vapour transfer in boundary layer).

The last network also has micro and macro pores, but this time the macro pores are oriented in both directions – hence cutting off capillary flow towards the surface. This network may be seen as a simple representation of an agglomerate of microporous particles.

Note that, in general, the throat radii are chosen relatively large so that the assumption of negligible viscous effects can be fulfilled.

All three networks are dried at atmospheric conditions with a convective flow of absolutely dry air. In order to study the effect of boundary layer thickness we chose four different velocities (see Table 1).

The drying curves shown in Figure 5 were obtained for the extended network model (including lateral mass transfer in the boundary layer) for the lowest air velocity; in this case, the boundary layer is thickest and contains 10 nodes in vertical direction. The moisture distribution in the three networks is shown in Figure 4, at the moment when the drying rate falls below 50% of the initial drying rate.

One can see that for a completely random pore size distribution, such as in the first network, capillary pumping only plays a minor role; the surface dries out rapidly, leaving most of the water to evaporate at very low rates. (During a quasi-constant drying period around saturation $S \approx 0.8$, the filling of pores happens to be more favourable for capillary pumping; at this stage, the surface is almost dry, whereas many near-surface pores remain filled due to capillary flow from deeper layers.)

In contrast, the second network dries at almost the initial drying rate down to $S \approx 0.6$, the reason for which can be seen in Figure 4; the large vertical channels dry out first, while water is pumped to the surface in the micro pores keeping the wet surface fraction at a high level.

In the drying of the third network, the strong action of capillary pumping cannot prevail for long because the emptying of horizontal macro pores cuts off the capillary flow to the surface. Whole surface regions (corresponding to microporous particles in an agglomerate) dry out whereas others may stay wet. Altogether, the drying behaviour is not so different from that of the first network.

Figure 6 shows (the first part of the) drying curves for all three networks at all four air velocities, both with and without lateral mass transfer in the boundary layer, in order to show its influence. In all cases, one can see that proper modelling of vapour transport in the boundary layer leads to a higher drying rate and smoothens the drying curve, both effects being more pronounced at lower air velocities for which the boundary layer is thicker. For all three networks, a more or less extended first drying period can be observed, but it is clear that the pore structure plays the dominant role concerning its duration. None of these first drying periods can be reproduced without accounting for lateral vapour diffusion.

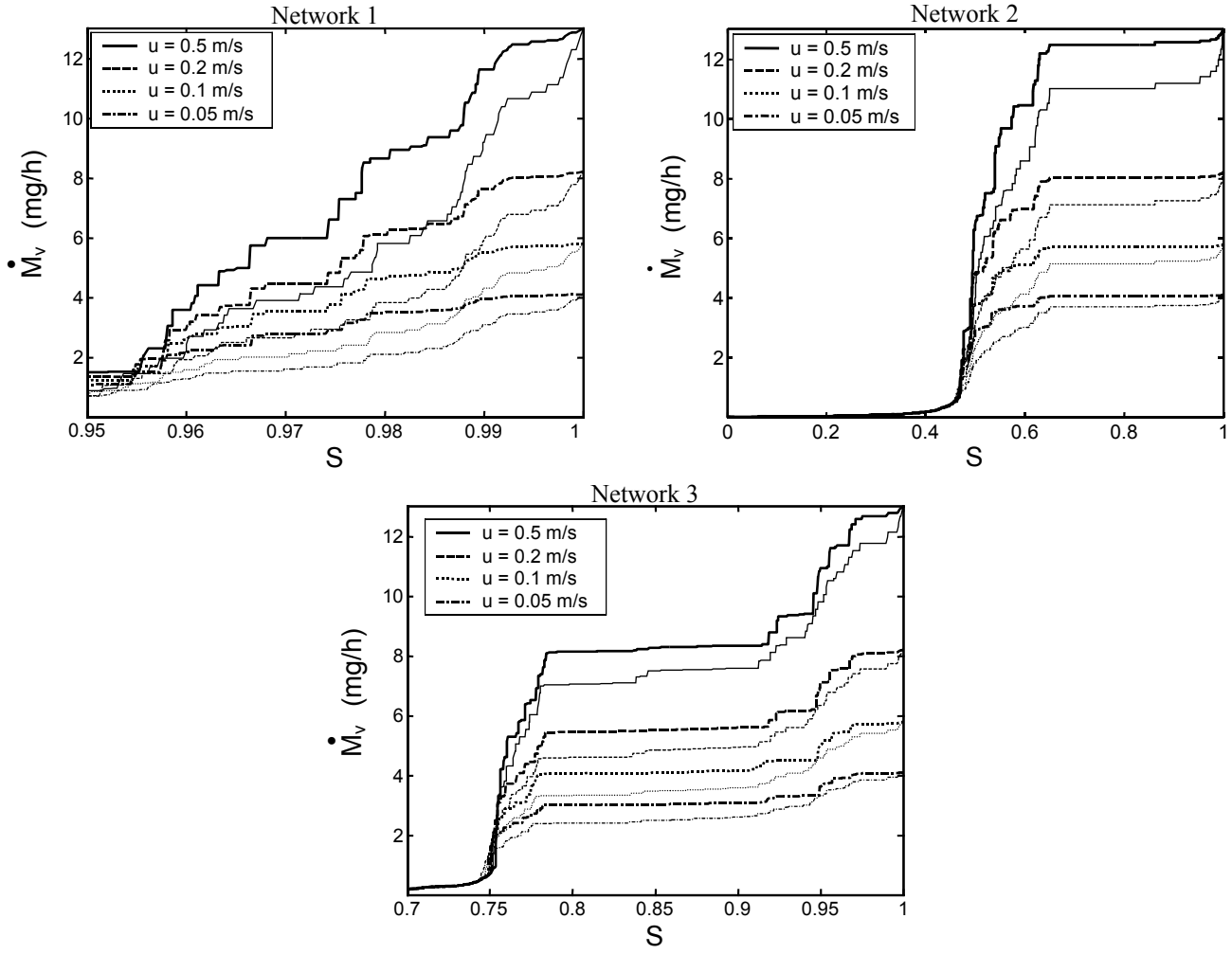

Figure 6 – Influence of lateral vapour transfer in the boundary layer for the three different networks at different air flow rates. Bold drying curves are computed with a diffusive boundary layer; thin curves with a mass transfer coefficient.

Finally, we compare the network simulation with the averaged model for diffusive boundary layer mass transfer. This allows an assessment of the quality of drying because the averaged model describes the most favourable case. The comparison is shown in Figure 7 for all networks and air velocities, where the dimensionless drying rate is plotted versus the wet surface fraction. We see confirmed that a lower air velocity, i.e. a larger boundary layer, is favourable for maintaining the drying rate at its high initial value.

For the first network, the high values predicted by the average model are almost obtained, the reason being the almost even distribution of wet patches due to the randomness of throat radii. In the second network, the drying out of surface throats is not completely random due to the spatial correlation of throat radii. This deviation from an ideal distribution of wet patches leads to a reduced drying rate with respect to the averaged model. The same effect is much more pronounced for the third network, for which the drying of the surface occurs in groups of throats (see Figure 4) according to high correlation of pore size. For this unfavourable case, we also show the lowest limit for the dimensionless drying rate – proportionality to the wet surface fraction – in Figure 7.

(For low values of φ, the network drying rate may be higher than that predicted for the averaged model because dry surface regions are not necessarily at zero vapour pressure.)

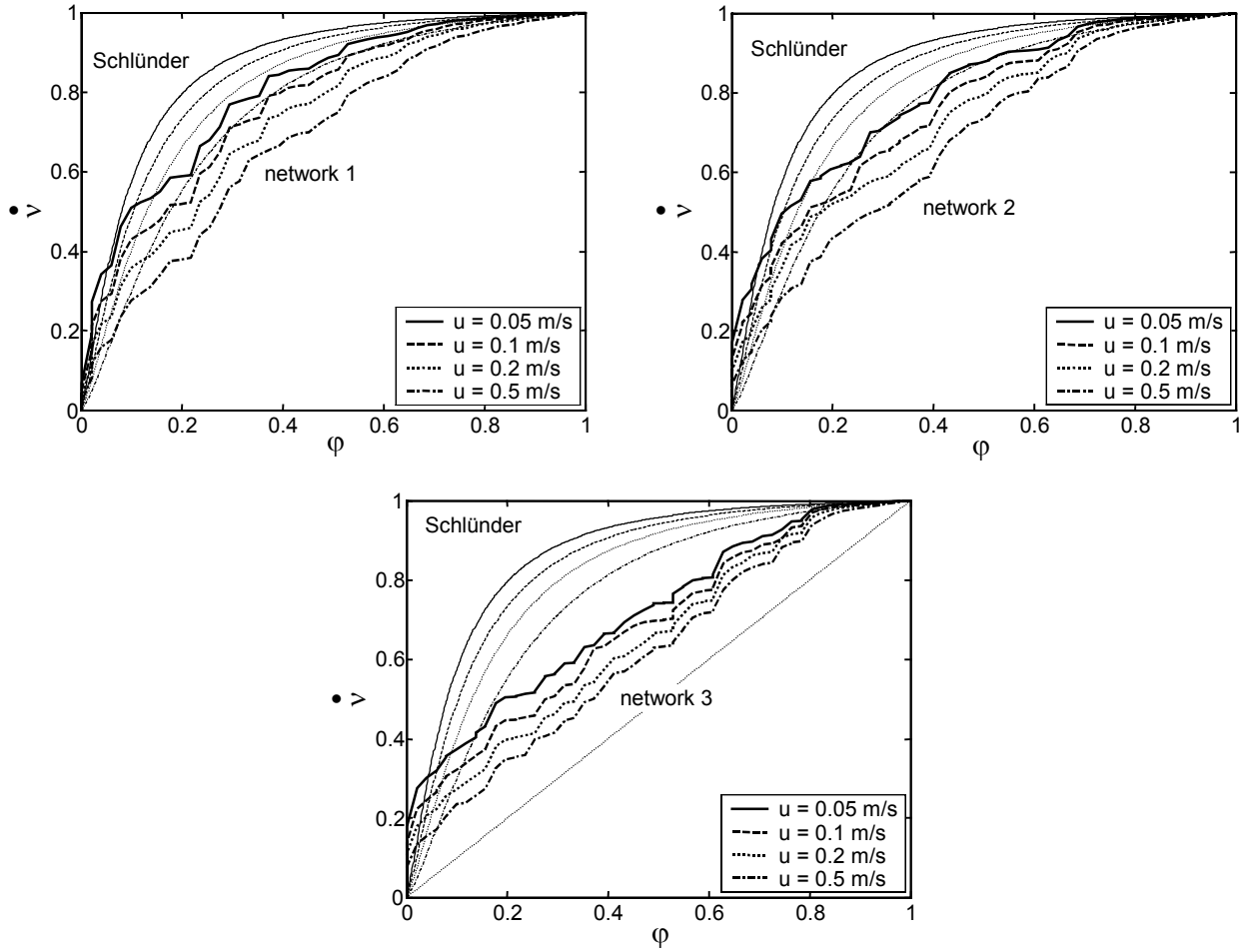

Figure 7 – Dimensionless drying rate as a function of wet surface fraction, for network simulations and Schlünder's model.

CONCLUSION

The above results confirm the importance of properly including the boundary layer into pore network drying models, if one aims to reproduce realistic drying behaviour such as the constant drying period at the beginning of drying. Unfortunately, it is not possible to link a discrete network model to an averaged boundary layer description, because this would mask the influence of pore structure on drying behaviour. Therefore, a discrete model of a diffusive boundary layer has been proposed and proven adequate.

Furthermore, the influence of the pore structure has been found to be of extreme importance for the duration of the constant drying period. Only if capillary flow paths can be maintained over a significant time, a relevant constant drying period is possible. Furthermore, a spatially random drying out of the surface is favourable for high drying rates.

In future work, the above simulations will be repeated for three-dimensional networks in order to exclude artefacts due to the restriction to two dimensions. More important, viscous effects in the liquid phase must be included in the model if one wants to describe drying of porous structures with smaller pore sizes – frequent in nature and technology. This will be especially attractive, since the model of Schlünder suggests that the role of the boundary layer becomes more important if throat size is smaller.

NOTATION

d	average distance of wet patches on surface	m

L	length of pore throat	m
$\tilde{M}$	molar mass	kg/kmol
$\dot{M}$	mass flow rate	kg/s
$\dot{m}$	mass flux	kg/m²s
p	(total) pressure	Pa
p_v^*	saturation vapour pressure	Pa
r	radius of pore throat	m
$\tilde{R}$	universal gas constant	J/kmolK
S	saturation	–
T	temperature	K

Greek Symbols

β	mass transfer coefficient	m/s
δ	diffusion coefficient (vapour in air)	m²/s
ε	boundary layer thickness	m
$\dot{\nu}$	dimensionless drying rate	–
ν	kinematic viscosity	m²/s
σ	surface tension of water	N/m
Φ	reduction factor in drying rate	–
φ	wet surface fraction	–

Subscripts

c	capillary	w	liquid water
v	vapour	∞	bulk

ACKNOWLEDGEMENTS

We gratefully state that this research has been financed by the Graduiertenkolleg 828 «Micro-Macro-Interactions in Structured Media and Particle Systems» (funded by the German Research Foundation).

LITERATURE

Laurindo, J.B., Prat, M., (1998), Numerical and experimental network study of evaporation in capillary porous media. Drying rates, Chem. Eng. Sci., Vol. 53, no. 12, pp. 2257-2269

Nowicki, S.C., Davis, H.T., Scriven, L.E., (1992), Microscopic determination of transport parameters in drying porous media, Drying Technology, Vol. 10, no. 4, pp. 925-946

Prat, M., (1993), Percolation model of drying under isothermal conditions in porous media, Int. J. Multiphase Flow, Vol. 19, no. 4, pp. 691-704

Schlünder, E.-U., (1988), On the mechanism of the constant drying rate period and its relevance to diffusion controlled catalytic gas phase reactions, Chem. Eng. Sci., Vol. 43, no. 4, pp. 2685-2688

Segura, L.A., Toledo, P.G. (2004), Pore-level modeling of isothermal drying in pore networks accounting for evaporation, viscous flow and shrinking, Proc. 14th Int. Drying Conference, Sao Paulo, Brazil

Yiotis, A.G., Stubos, A.K., Boudouvis, A.G., Yortsos, Y.C. (2001), A 2-D pore-network model of the drying of single-component liquids in porous media, Adv. Water Resources, Vol. 24, pp. 439-460

Available online at www.sciencedirect.com
SCIENCE DIRECT®
Physica A 363 (2006) 558–560
PHYSICA A
www.elsevier.com/locate/physa

Remarks on the paper "Extension of Hoshen–Kopelman algorithm to non-lattice environments" by A. Al-Futaisi and T.W. Patzek, Physica A 321 (2003) 665–678

T. Metzger*, A. Irawan, E. Tsotsas

Thermal Process Engineering, Otto-von-Guericke-University, P.O. 4120, 39016 Magdeburg, Germany

Received 26 May 2005; received in revised form 26 May 2005
Available online 7 September 2005

Abstract

In this paper, two examples are given where the cluster labeling algorithm of Al-Futaisi and Patzek for arbitrary networks produces incorrect results. The reason for this is pointed out, and an improvement to the algorithm is proposed so that such errors can be avoided in future.

Keywords: Cluster labeling; Pore networks; Capillary flow

In the above-mentioned article, Al-Futaisi and Patzek propose an algorithm to label occupied links and nodes of an arbitrary network according to their cluster affiliation. We applied this algorithm to our own research, where we investigate the drying behaviour of porous media by network models [1]. During drying, capillary pumping of the liquid phase is an important mechanism. Naturally, capillary flow can only occur between pores which are part of the same liquid cluster, so that cluster labeling is an essential step of our drying model. We chose the non-lattice data structure of Al-Futaisi and Patzek because it allows to investigate both regular and random pore networks. However, we found that their labeling algorithm does not always produce correct results and therefore needs some improvement.

First, we will give a simple one-dimensional example where unfavourable node numbering makes the algorithm fail. Then, a two-dimensional example from pore network modelling is presented where the specific node occupancy leads to wrong results. At last, we present a simple modification of the labeling algorithm to avoid such errors.

Fig. 1 shows a linear one-dimensional network, all nodes and links of which are occupied; therefore all nodes belong to the same cluster. In the algorithm of Al-Futaisi and Patzek, node numbers give the order of labeling; in this example, node numbering is not sequential so that relabeling will be needed.

*Corresponding author. Tel.: +49 391 6711362; fax: +49 391 6711160.
E-mail address: thomas.metzger@vst.uni-magdeburg.de (T. Metzger).

0378-4371/$ - see front matter © 2005 Elsevier B.V. All rights reserved.
doi:10.1016/j.physa.2005.08.026

After the labeling of the first four nodes, every labeled node has a different label, stored in `NodeL`; the vector `NodeLP` contains all four label numbers

$$\texttt{NodeL} = \{1,2,3,4,0,0,0\}, \quad \texttt{NodeLP} = [1,2,3,4]\,. \tag{1}$$

During the labeling of each of the remaining nodes, two labeled neighbours do already exist—case 4(c)(ii) in the work of Al-Futaisi and Patzek—and labels are subsequently corrected in the following way:

$$\texttt{NodeL} = \{1,2,3,4,3,0,0\}, \quad \texttt{NodeLP} = [1,2,3,3]\,. \tag{2}$$

$$\texttt{NodeL} = \{1,2,3,4,3,2,0\}, \quad \texttt{NodeLP} = [1,2,2,3]\,. \tag{3}$$

$$\texttt{NodeL} = \{1,2,3,4,3,2,1\}, \quad \texttt{NodeLP} = [1,2,1,3]\,. \tag{4}$$

In step 5(a) of the algorithm, the labels in `NodeLP` are corrected recursively: label 4 is equivalent to label 3 which is in turn equivalent to label 1; however, label 2 is not corrected so that nodes 2 and 6 are treated as a separate cluster

$$\texttt{NodeLP} = [1,2,1,1]\,. \tag{5}$$

This error already occurs during the labeling of node 7: its two neighbours have labels 1 and 4; according to the algorithm, former label corrections are—*partially*—accounted for by taking the function `NodeLP(NodeLP)` of these labels and computing its minimum. `NodeLP` of the neighbouring labels are then set to this value. By this, the reference from label 3 to label 2 is lost.

A second example is now given from pore network modeling. The network consists of pore nodes without any volume which are connected by cylindrical throats. All information which is relevant for drying kinetics (total network saturation, capillary pumping, vapour diffusion) can be given in terms of liquid saturation and cluster affiliation of liquid filled throats. The state of pore nodes is determined by the connected throats: if one

Fig. 1. Completely occupied one-dimensional network of seven nodes.

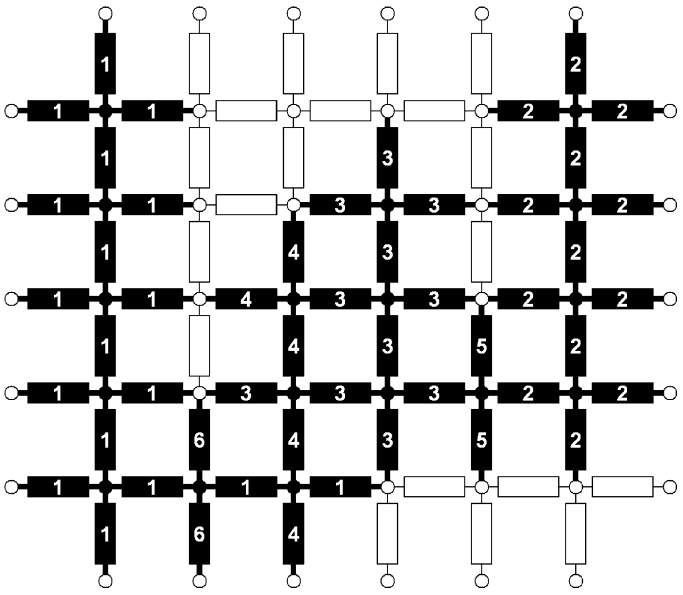

Fig. 2. Partially filled two-dimensional pore network with throat labels before correction.

or more of them are empty, the node is also empty and liquid cannot pass through it. In the nomenclature of Al-Futaisi and Patzek, pore throats take up the role of *nodes*, and pore nodes the role of *links*.

Fig. 2 shows part of such a network, white throats being empty and black throats filled with liquid. The throats are numbered from top left to down right row by row: first all vertical throats, then all horizontal ones. The cluster labeling of the liquid filled throats is shown before correction in step 5(a). Then, the labels of the throats are corrected according to the vector of labels

$$\texttt{ThroatLP} = [1, 2, 1, 1, 1, 1]\,. \tag{6}$$

As in the first example, we have a single cluster which is not recognized as such: all throats with label 2 are interpreted as belonging to a separate cluster.

In order to repair this deficiency of the otherwise very useful algorithm by Al-Futaisi and Patzek, we propose the following modification of case 4(c)(ii) in their Matlab code:

```
N = nonzeros(NodeNextL)';
for k = 1:length(N)
   M = NodeLP(N(k));
   while M<N(k)
      N(k) = M;
      M = NodeLP(N(k));
   end
end
NodeLPmin = min(N);
NodeL(i) = NodeLPmin;
NodeLP(N) = NodeLPmin;
```

In this way, an already existing recursive sequence for correction of labels `NodeLP(NodeLP(...))` is not interrupted, and further corrections are only made for the last element of any such sequence—and therefore for *all* its elements.

Several other versions of a corrected algorithm have been tested and the proposed one found to be both easily structured and fast in computation time.

References

[1] A. Irawan, T. Metzger, E. Tsotsas, Pore network modelling of drying: combination with a boundary layer model to capture the first drying period, Seventh World Congress of Chemical Engineering, Glasgow, Scotland, July 2005.

15th International Drying Symposium (IDS 2006)
Budapest, Hungary, 20-23 August 2006

INFLUENCE OF PORE SIZE DISTRIBUTION VIA EFFECTIVE PARAMETERS IN A CONTINUOUS DRYING MODEL

T.H. Vu, T. Metzger and E. Tsotsas

Thermal Process Engineering, Otto-von-Guericke-University Magdeburg
Universitatesplatz 2, 39106 Magdeburg, Germany
Tel.:+49-391-6711362, E-mail: thomas.metzger@vst.uni-magdeburg.de

Abstract: In the present work, the influence of pore size distribution on drying kinetics is investigated by use of a bundle of capillaries as a simple representative for porous media. First, effective transport coefficients and capillary pressure are computed as functions of liquid saturation. Then, these effective properties are used in a rigorous continuous drying model (Perré and Turner, 1999) which is capable of describing the spatial and temporal evolution of moisture content, temperature and gaseous pressure. In this way, the drying behavior of mono- and bi-modal pore size distributions is investigated and discussed.

Keywords: bundle of capillaries, drying kinetics, relative permeability, capillary pressure

INTRODUCTION

Within the last decades, continuous modeling of drying of porous media has attained a high level: not only have macroscopic transport equations been derived from the microscopic ones in a mathematically rigorous way, but also has their numerical solution become very efficient (Perré and Turner, 1999). Recent modeling even aims at realistically describing the strongly non-isotropic and heterogeneous behavior of wood though the numerical challenges are very demanding (e.g. Truscott and Turner, 2005).

However, one of the major problems clearly remains the estimation of the numerous model parameters for a given material; these may be divided into effective transport parameters, namely effective diffusivity, absolute and relative permeabilities and effective thermal conductivity, as well as equilibrium data, capillary pressure and sorption isotherms, all of which are (not necessarily unique) functions of saturation.

In the present work, these parameters are computed for the simple geometry of a bundle of capillaries with a radius distribution which shall – in a simple way – represent the porous medium. The aim of this approach is to understand, on a fundamental basis, how variation of pore size distribution changes drying behavior. Certainly, the idea to use a bundle of capillaries to describe the pore space is not new: as a prominent example, Krischer (1956) may be mentioned who described liquid water transport in porous media using this geometry. But to our knowledge it was never used for a systematic investigation of the whole drying process.

It shall be stated that at the time of Krischer, continuous drying models still had a less rigorous theoretical basis and contained rather empirical parameters. Also, the "language" in drying modeling has changed: for instance, liquid water transport was then computed from gradients in moisture content using a moisture migration coefficient, the roles of which are today taken up by liquid pressure and permeability, respectively.

Recently, we used a bundle of capillaries for developing a discrete model of isothermal drying and, with this, investigated the drying behavior for a range of mono- and bimodal pore size distributions (Metzger and Tsotsas, 2005). The present work shall be understood as the continuous equivalent – and also extension – of our former research because, by virtue of the employed continuous model, it additionally accounts for gradients in temperature and gas pressure.

Naturally, pore size distribution is not enough to characterize a porous medium; it is only the most accessible structural information. Pore structure can be more realistically described by networks of pores which can be used for developing a discrete drying model or to compute effective transport parameters for continuous modeling (e.g. Nowicki et al., 1992). Therefore, a parallel research activity uses a network drying model in order to investigate the influence of pore structure on drying behavior (Irawan et al., 2005). This model is currently extended to account for liquid viscosity (Irawan et al., 2006) and heat transfer (Surasani et al., 2006) so that it will soon comprise the same transport phenomena as the reference continuous drying model.

This shall offer the possibility to directly compare the modern way of discrete and the traditional way of continuous modeling; and to investigate to what extent they are equivalent and where the limits of continuous modeling are (Metzger et al., 2006). The bundle of capillaries, as simple reference geometry, allows doing the first step into this direction, since it was used for discrete modeling and is now used in the continuous model.

The structure of the paper is as follows: first, the bundle of capillaries is introduced and characterized with respect to its equilibrium and transport properties; these are computed for different mono-modal and bi-modal pore size distributions. Then, the continuous drying model is presented and a parametric study is performed revealing the sensitivity of drying behavior to the different transport parameters and to a variation of drying conditions. In the main part, the effective parameters of the different pore size distributions are used to compute time-dependent profiles of moisture content, temperature and gas pressure for the drying process. For the isothermal case, results are compared to those of the discrete model.

BUNDLE OF CAPILLARIES AS POROUS STRUCTURE

In order to investigate the influence of pore size distribution on drying kinetics, we take the simplest possible geometry – a bundle of capillaries – and assume that it represents the void space of a porous medium. The capillary tubes are set perpendicular to the surface of the porous body and the solid phase is arranged in parallel; there is no lateral resistance to heat or mass transfer between solid and capillaries, making the model strictly one-dimensional. Figure 1 illustrates this pore geometry and how it will behave during drying. We restrict ourselves to large enough pore sizes so that for every capillary the gas-liquid phase boundary can be described by a meniscus having a capillary pressure. During drying, larger capillaries will empty first, because they have the lower capillary pressure; however, this capillary pumping is subject to friction leading to a non-trivial moisture profile.

Pores size distribution and saturation

For our investigation, we use either mono-modal capillary radius distributions with a normal volume distribution

$$\frac{dV}{dr} = \frac{1}{\sqrt{2\pi}\sigma_0} e^{-\frac{1}{2}\left(\frac{r-r_0}{\sigma_0}\right)^2} \qquad (1)$$

where r_0 is mean pore radius and σ_0 standard deviation, or bimodal distributions which consist of two such normal modes. We consider this choice to be enough for systematic investigation but, of course, other distributions are possible. The integral of the pore size distribution in Eq. (1) must be equal to the void volume of the sample, but is here set to unity for simplicity. (For the computations, all normal distributions will be truncated at 2.5 σ_0.)

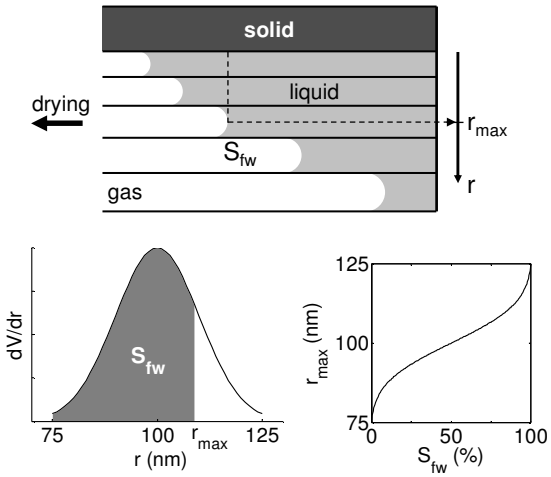

Fig. 1. Partially saturated bundle of capillaries: relationship between free water saturation S_{fw} and maximum radius filled r_{max}.

If the porous medium is partially saturated with water, the assumption of ideal lateral transfer between the capillaries implies that, for given local free water saturation S_{fw} small capillaries are filled up to a maximum radius r_{max} (see Figure 1) so that

$$S_{fw} = \int^{r_{max}} \frac{dV}{dr} dr \qquad (2)$$

We will soon see that this localization of free water is the key for computing effective properties as function of saturation.

Adsorbed water, which may play an important role in drying of hygroscopic materials and is necessary for the continuous drying model (see below), needs to be modeled separately since it depends mainly on material properties. (The influence of pore size distribution is neglected because condensation due to the Kelvin effect only occurs at very high relative humidity.) We use here the same type of temperature independent sorption isotherm as Perré and Turner (1999) did for concrete (see Figure 2)

$$\varphi = \frac{S}{S_{sorb}} \cdot \left(2 - \frac{S}{S_{sorb}}\right) \quad \text{for } S \le S_{sorb} \qquad (3)$$

where φ is relative humidity, S_{sorb} maximum amount of adsorbed water and $S = S_{sorb} + S_{fw}$; in the presence of free water, $\varphi = 1$. We set $S_{sorb} = 15\%$ so that we can investigate hygroscopic material. The total volume fraction of liquid for $S = 100\%$ must correspond to the porosity ψ of the sample.

Instead of saturation S, often moisture content X is used in drying; both quantities are proportional by

$$S\psi\rho_w = X\rho_s \quad (4)$$

where ρ_w and ρ_s are densities of liquid and solid.

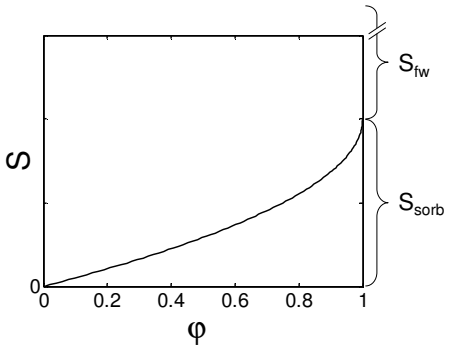

Fig. 2. Sorption isotherm.

Table 1. Studied distributions with permeability.

	$r_0 \pm \sigma_0$ (nm)	K (10^{-15} m^2)	
Reference	100 ±10	1.246	mono-modal
Case 1	100 ± 5	1.238	
Case 2	1000 ± 100	124.6	
Case 3	100 ± 10 200 ± 20	3.119	bimodal
Case 4	100 ± 10 2000 ± 200	245.1	

In the following, effective parameters are computed for the four different cases of pore size distributions in Table 1 (the reference case will be needed later). For bimodal distributions, pore volume is equally distributed to the two modes.

Capillary pressure

Besides vapor pressure, also capillary pressure is linked to saturation by a state equation: it is given by the meniscus in the largest filled capillary

$$P_c(S_{fw}, T) = \frac{2 \cdot \sigma(T)}{r_{max}(S_{fw})} \quad (5)$$

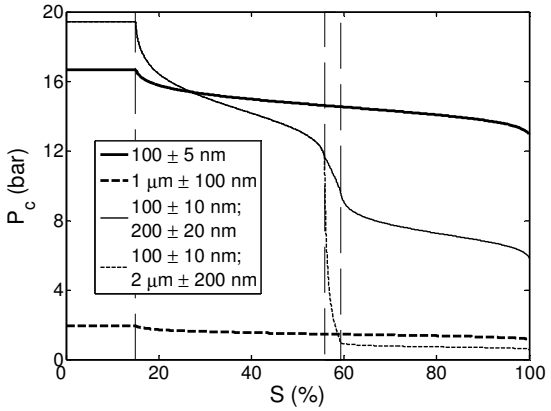

Fig. 3. Capillary pressure curves for the four cases. (Adsorbed water region for S < 15%, and transition region for bimodal distributions for S ≈ 57.5%.)

where the surface tension of water σ depends on temperature T. (Zero contact angle is assumed.) Figure 3 shows the capillary pressure curves for the four pore size distributions. Naturally, with decreasing saturation, capillary pressure increases. The overall level is determined by the mean pore size r_0 (of a mode) and its range of variation by the standard deviation σ_0. For bimodal distributions, a sudden change of capillary pressure is observed when the larger mode is emptied, which – for numerical reasons – is extended into a transition region (see below). In the sorption region, capillary pressure is set constant at the value corresponding to only the smallest pores being filled.

Permeabilities

In the continuous model, convective transport of liquid and gas in the partially saturated porous medium are described by the generalized Darcy law

$$v_{w,g} = -\frac{K k_{w,g}}{\eta_{w,g}(T)} \cdot \nabla P_{w,g} \quad (6)$$

where, for each phase (w: liquid water, g: gas), v is mean velocity (volumetric flow rate per total cross section of porous medium), η dynamic viscosity (temperature dependent) and P pressure. Velocities are assumed to be small enough to neglect inertial effects. The effective transport parameters – with computation rules for the bundle of capillaries – are absolute permeability

$$K = \frac{1}{8}\int r^2 \frac{dV}{dr} dr \quad (7)$$

and relative permeabilities for the two phases

$$k_w(S_{fw}) = \frac{1}{8K}\int_{r_{max}} r^2 \frac{dV}{dr} dr \quad (8)$$

$$k_g(S_{fw}) = 1 - k_w(S_{fw}) \quad (9)$$

These do not depend on temperature or pressure. Adsorbed water plays no role in convection. The absolute permeabilities for the different pore size distributions are given in Table 1, relative ones in Figure 4. It can be seen that K is mainly determined by the mean radius (of the large pores) and that broadness of the distribution and small pores (for the bimodal cases) contribute only little. Relative permeabilities are almost proportional to respective phase saturation for the monomodal distributions, but curvature of the functions $k_{w,g}(S)$ increases with broader (or bimodal) pore size distribution – in an unfavorable way for liquid transport and favorably for gas transport. Again, the contribution of small pores (bimodal cases) is small.

Effective vapor diffusivity and thermal conductivity

The other two transport parameters, i.e. effective vapor diffusivity and thermal conductivity, are assumed to be independent of pore size distribution.

Saturation alone describes by how much the presence of liquid water reduces the void cross section for vapor diffusion

$$D_{eff}(S,T,P) = (1-S)\cdot\psi\cdot\delta_{va}(T,P) \qquad (10)$$

The binary diffusion coefficient δ_{va} is modeled as temperature and pressure dependent. (Knudsen effect can be neglected for investigate pore sizes.)

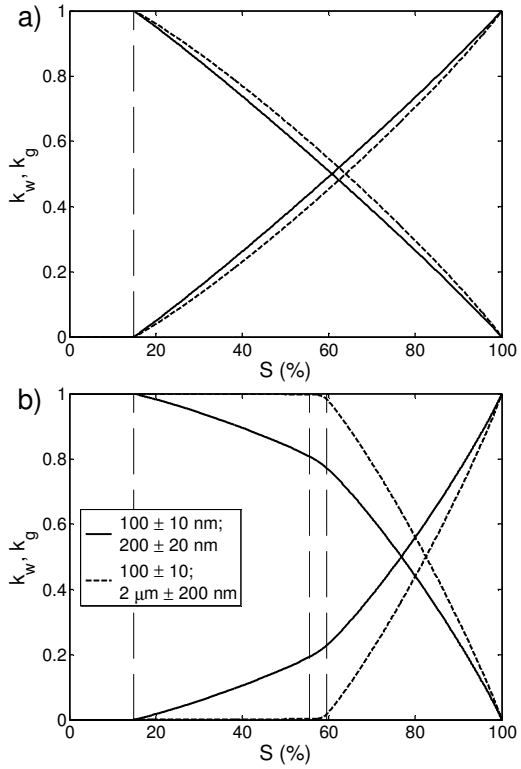

Fig. 4. Relative permeabilities for the four cases.

On the contrary, heat conduction occurs in all phases weighted according to their respective volume fractions; if the contribution of gas is neglected

$$\lambda_{eff}(S,T) = (1-\psi)\cdot\lambda_s(T) + S\cdot\psi\cdot\lambda_w(T) \qquad (11)$$

where the thermal conductivities of solid and liquid water λ_s and λ_w introduce temperature dependence.

CONTINUOUS DRYING MODEL

After having characterized the porous structure with respect to its drying relevant properties, we now briefly describe the drying model which was derived from microscopic transport equations by volume averaging (Perré and Turner, 1999).

Model equations

The conservation equations for water (liquid and vapor), air and enthalpy are given as

$$\begin{aligned}&\frac{\partial}{\partial t}\left(S\psi\rho_w + (1-S)\psi\rho_v\right)\\ &\quad = \nabla\cdot\left(\rho_g D_{eff}\nabla y_v\right) - \nabla\cdot\left(\rho_w v_w + \rho_v v_g\right)\end{aligned} \qquad (12)$$

$$\frac{\partial}{\partial t}\left((1-S)\psi\rho_a\right) = \nabla\cdot\left(\rho_g D_{eff}\nabla y_a\right) - \nabla\cdot\left(\rho_a v_g\right) \qquad (13)$$

$$\begin{aligned}&\frac{\partial}{\partial t}\left(S\psi\rho_w h_w + (1-S)\psi(\rho_v h_v + \rho_a h_a)\right.\\ &\qquad \left. + (1-\psi)\rho_s h_s - (1-S)\psi P_g\right)\\ &= \nabla\cdot\left(\rho_g D_{eff}\left(h_v\nabla y_v + h_a\nabla y_a\right)\right)\\ &\qquad - \nabla\cdot\left(\rho_w h_w v_w + (\rho_v h_v + \rho_a h_a)v_g\right)\\ &\qquad + \nabla\cdot\left(\lambda_{eff}\nabla T\right)\end{aligned} \qquad (14)$$

ρ_v and ρ_a denote densities of vapor and air, y_v and y_a are respective mass fractions and $h_i = c_{pi}(T - T_{ref})$ specific enthalpies of each phase, with $T_{ref} = 0°C$. The phase velocities are given by the generalized Darcy law in Eq. (6).

Additionally, equilibrium between liquid and gas pressure is given by capillary pressure $P_w = P_g - P_c$; the sorption isotherm describes liquid vapor equilibrium; and ideal gas laws are assumed for partial and total gas pressures

$$P_i = \frac{\rho_i\tilde{R}T}{\tilde{M}_i} \qquad (16)$$

where i stands for air, vapor or gas; $\tilde{R}$ is ideal gas constant; and $\tilde{M}_i$ are molar masses of air, vapor or gas average

$$\tilde{M}_g = \tilde{M}_a + (\tilde{M}_v - \tilde{M}_a)\frac{P_v}{P_g} \qquad (17)$$

To solve this set of equations, three boundary conditions for the porous body are required. At the open surface, vapor and heat flux are described for convective drying by boundary layer theory (with Stefan correction)

$$\dot{m}_v = \beta\frac{P_g\tilde{M}_v}{\tilde{R}T}\cdot\ln\left(\frac{P_g - P_{v,\infty}}{P_g - P_v}\right) \qquad (18)$$

$$\dot{q} = \alpha(T - T_\infty) + \Delta h_v\cdot\dot{m}_v \qquad (19)$$

where $P_{v,\infty}$ and T_∞ are vapor pressure and temperature of bulk drying air, respectively; additionally, gas pressure is imposed $P_g = P_\infty$. The other side is impervious to heat and mass transfer. Finally, initial values of saturation S_0 and product temperature T_0 must be given, while $P_{g,0} = P_\infty$.

Numerical solution

The above set of model equations is solved using the control-volume finite-element method and a Newton Raphson scheme with variable time step (Nasrallah and Perré, 1988; Turner and Perré, 1996) and non-uniform grid (41 elements) of geometric progression to better describe steep gradients near the product surface.

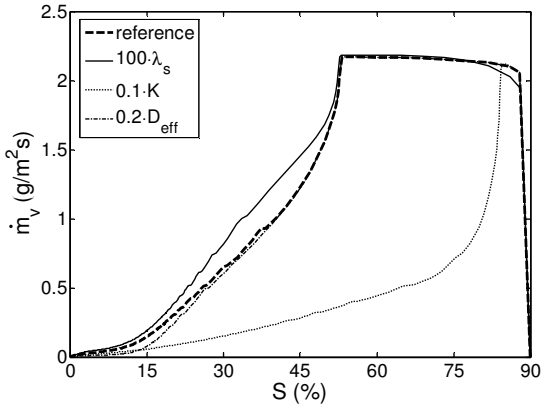

Fig. 5. Parametric study for drying model.

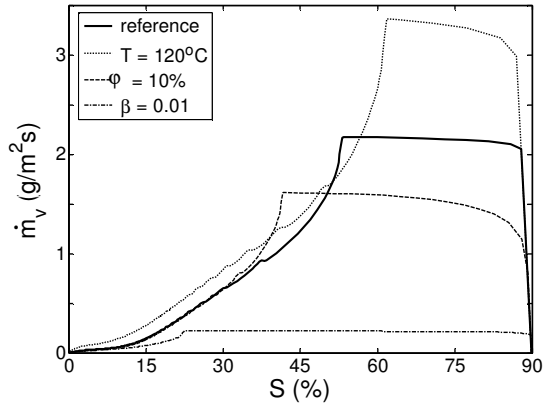

Fig. 6. Variation of drying conditions.

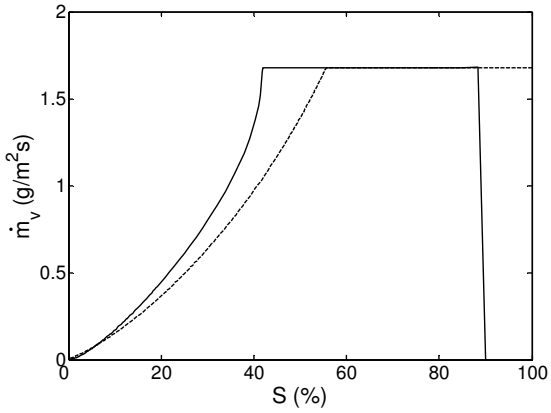

Fig. 7. Drying curves for continuous (solid line) and discrete capillary model (dashed line).

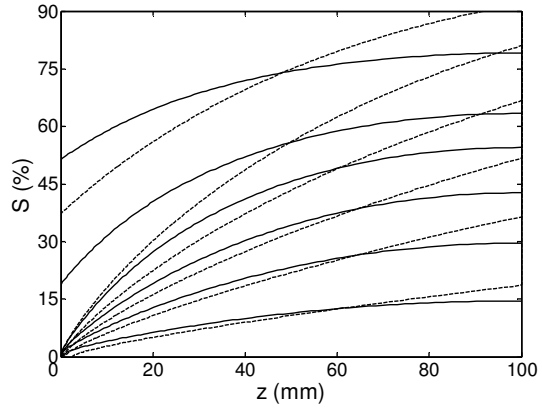

Fig. 8. Moisture profiles for continuous (solid lines) and discrete capillary model (dashed lines).

It shall be mentioned that the algorithm only converges for initial saturations less than unity. Furthermore, pore size distribution had to be slightly modified (esp. pores making up 4% of free saturation were introduced in the transition region for bimodal distributions) to get a smooth capillary pressure curve and transport parameter functions, because sudden changes of slope or even jumps can not be handled by the numerical solution technique.

Last, it has to be emphasized that the model needs a unique relation $S(P_v)$ so that a small amount of adsorbed water with a defined sorption equilibrium is required – although, vapor pressure gradients also exist in completely empty sections of the pore space ($S \equiv 0$) if vapor is transferred by diffusion.

Parametric study

For all investigated cases, the bundle of capillaries is 0.1 m long. The porosity is $\psi = 0.5$; the solid has thermal conductivity $\lambda_s = 1$ W/m/K and volumetric heat capacity $(\rho c)_s = 2 \cdot 10^6$ J/m^3/K. Initial saturation and product temperature are $S_0 = 90\%$ and $T_0 = 20°C$. Gas pressure is always $P_\infty = 1$ bar, and, if not indicated otherwise, drying air has zero moisture and temperature $T_\infty = 80°C$. Transfer coefficients for the boundary layer are $\alpha = 95$ W/m^2/K for heat and $\beta = 0.1$ m/s for mass.

To see how the three transport parameters influence drying behavior, we first take the reference bundle of capillaries with normal distribution 100 ± 10 nm and then vary its parameters one by one. The results are shown in Figure 5. An increase of (solid) thermal conductivity slightly slows down initial warming up of product surface and increases drying rates in the second period since heat is better transferred to the place of evaporation. A reduction of absolute permeability (by decrease of pore size) dramatically shortens the first drying period whereas a decrease of effective diffusivity (by introducing tortuosity) only reduces the already low rates at the end of the second period when adsorbed water removal dominates.

Variation of drying conditions

Next the influence of drying conditions is studied (Figure 6): the well known fact is confirmed that hotter and drier air with higher velocity (i.e. higher transfer coefficients) produces higher drying rates in the first period, but its duration is shorter. (The low residual moisture for $\varphi = 10\%$ cannot be seen.)

COMPARISON WITH CAPILLARY MODEL

For comparison with the isothermal capillary model (Metzger and Tsotsas, 2005), we use a finer mesh of 101 elements and enhance heat transfer by setting $\alpha = 6000$ W/m^2/K and $\lambda_s = 6000$ W/m/K. For $T_\infty = 20°C$, the *imaginary* wet bulb temperature

was 19.3°C (to be used in isothermal model); and gas pressure varied only by 20 mbar as compared to being constant in the capillary model. The amount of adsorbed water was set to 1% to approach the case of no sorption in the discrete model.

Figures 7 and 8 show that the continuous model version yields a slightly longer first drying period and flatter moisture profiles than the discrete one. (The discrete model can cope with full saturation.) We think that this can be explained by two differences in modeling. The first concerns discretization: in the capillary model, the pore size distribution is represented by discrete capillary classes with menisci continuously moving in space whereas, in the continuous model, only space is discretized. At the end of the first period, the last meniscus moves back from the surface and a small additional distance to vapor diffusion immediately causes a dramatic drop in drying rate. In the capillary model, the meniscus can move to any distance whereas, in the continuous model, the whole surface element (0.2 mm in size) must dry below S_{sorb} before the rate drops. Second, the no-flux condition of the continuous model for the impervious boundary (which leads to locally vanishing moisture gradients) does not exist in the capillary model. Instead, menisci disappear one by one at the right hand side, rather imposing a (capillary) pressure boundary condition.

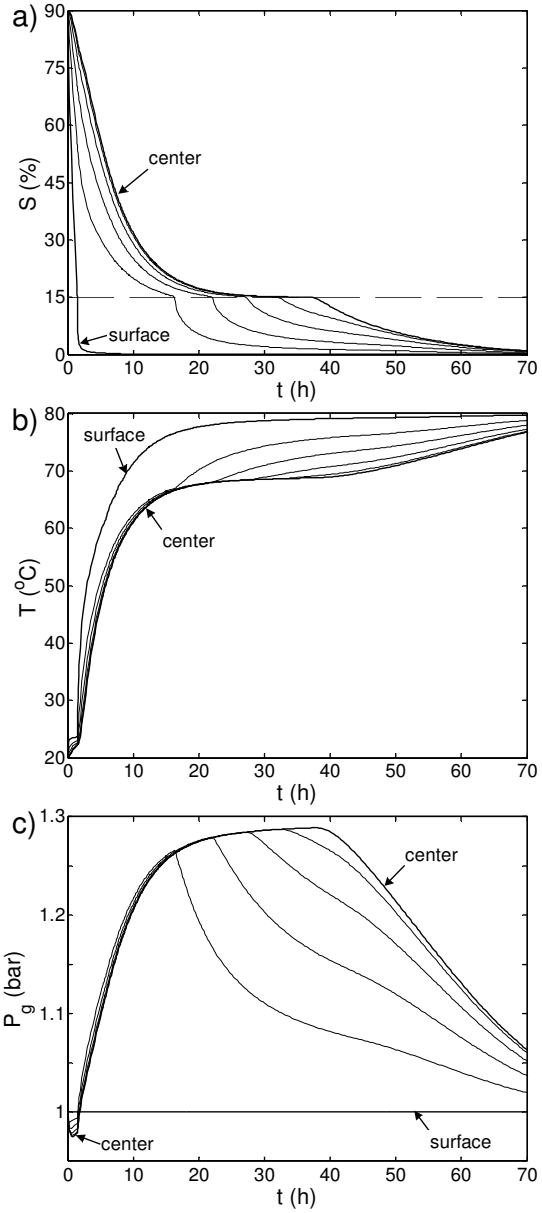

Fig. 9. Drying 100 ± 5 nm distribution (case 1).

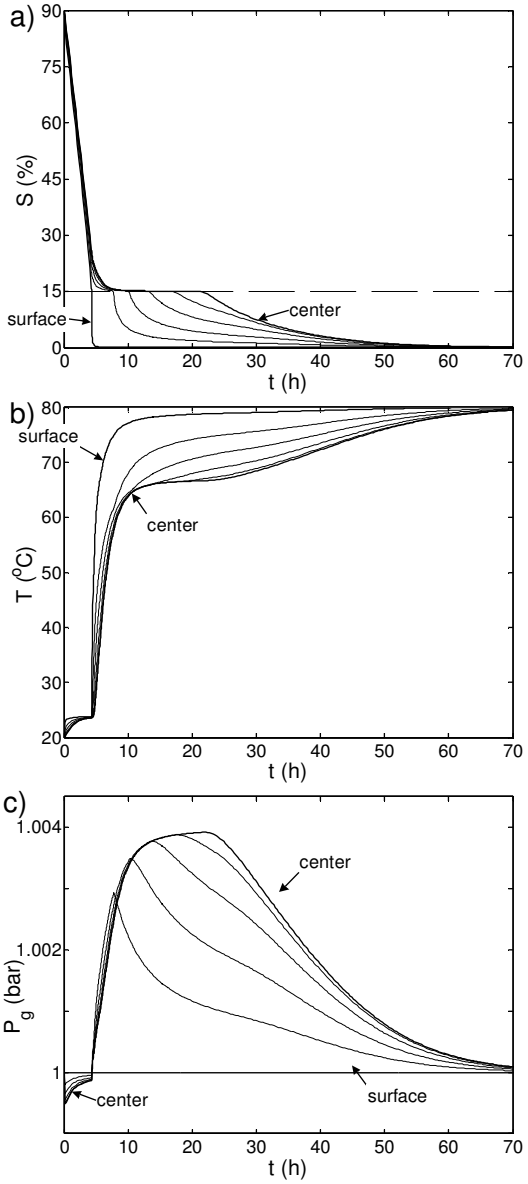

Fig. 10. Drying 1 µm ±100 nm distribution (case 2).

VARIATION OF PORE SIZE DISTRIBUTION

Now the results of drying simulations for the four cases of pore size distribution are presented.

Mono-modal distributions

Figures 9 and 10 show the evolution of moisture content, temperature and gas pressure at (almost) equidistant positions in the porous medium. Figure

11 gives the drying curve, and Figure 12 shows moisture profiles (fat line for end of first period).

For the small pores with a narrow distribution, the first drying period is short, moisture gradients are steep throughout the drying, and significant gas pressure gradients occur in the second period. The large pore case with a broad distribution has a long first drying period, and moisture and pressure gradients are much smaller. On the contrary, variation of the pore size distribution has little effect on the temperature evolution: only the wet bulb temperature prevails longer if the surface stays wet for longer (broader distribution).

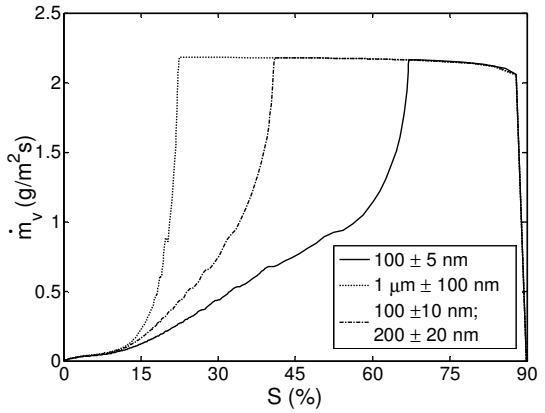

Fig. 11. Drying curves for different pore size distributions (cases 3 and 4 yield identical curves).

Bimodal distributions

Figures 11 and 13 show overall drying curve and evolution of local saturation for the distribution with two close modes (case 3). The large pores dry out completely at the high drying rate of the first period with only small low moisture gradients (broad mode); in the transition region, the moisture profile is flat; during the drying of the small pores, steeper gradients develop (narrow mode) and the second drying period starts. For case 4, with a more important difference in size between the two modes and a broader large mode, moisture profiles are even flatter during the drying of the large pores, but the overall drying curve is unchanged.

One may say that the large pores in a bimodal distribution can significantly prolong the first drying period, but that the second drying period is entirely determined by the small pores.

CONCLUSIONS

A continuous drying model has been used together with a bundle of capillaries to investigate the influence of pore size distribution on drying behavior. It was found that broader or bimodal pore size distributions dry more favorably in terms of higher drying rates and lower moisture gradients. Significant gas pressure differences build up if all pores are of small size. The present work could

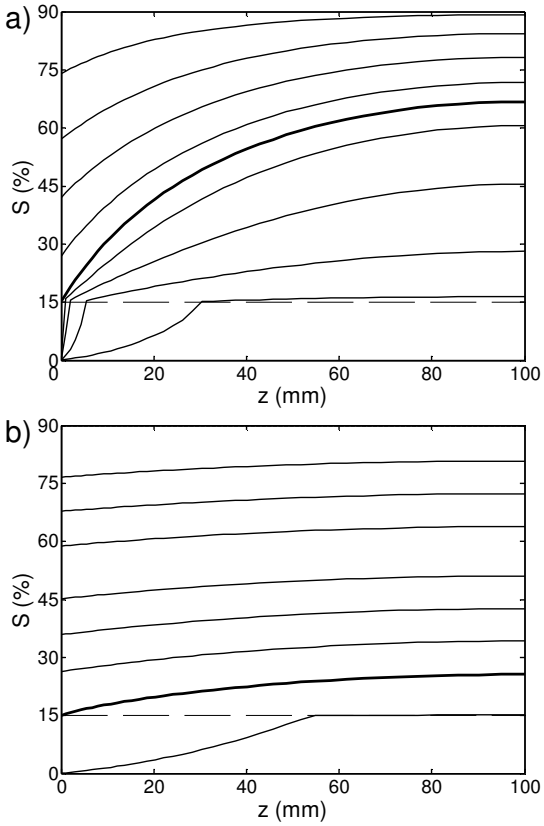

Fig. 12. Drying moisture profiles for mono-modal distributions a) 100 ± 5 nm and b) 1µm ± 100 nm.

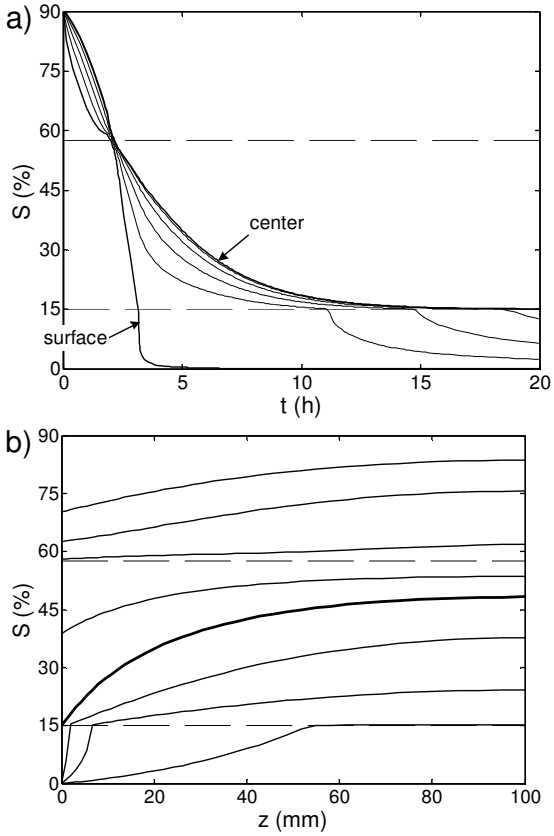

Fig. 13. Drying of bimodal pore size distribution 100 ± 10 nm, 200 ± 20 nm (case 3).

confirm and extend previous investigations with an isothermal capillary model.

Future work shall use pore networks to obtain the effective parameters of the continuous model. For a given network saturation, gradients of liquid and gas pressure, vapor pressure and temperature may be applied and corresponding effective parameters computed. These are to be used in the continuous model which will allow checking to what extent the discrete and continuous approach are equivalent. In this context, an interesting question is how the liquid is to be distributed in the network for a given overall saturation since phase distributions are dependent on drying history.

NOMENCLATURE

c	specific heat capacity	$kJ\ kg^{-1}K^{-1}$
D	diffusion coefficient	m^2s^{-1}
h	specific enthalpy	$kJ\ kg^{-1}$
Δh_v	evaporation enthalpy	$kJ\ kg^{-1}$
K	absolute permeability	m^2
k	relative permeability	–
$\tilde{M}$	molar mass	$kg\ kmol^{-1}$
$\dot{m}$	mass flux	$kg\ s^{-1}m^{-2}$
P	pressure	Pa
$\dot{q}$	heat flux	$W\ m^{-2}$
$\tilde{R}$	ideal gas constant	$J\ kmol^{-1}K^{-1}$
r	capillary radius	m
r_0	mean capillary radius	m
S	saturation	–
T	temperature	K
V	volume	m^3
X	moisture content	kg_w/kg_s
y	mass fraction	–

Greek letters

α	heat transfer coefficient	$Wm^{-2}K^{-1}$
β	mass transfer coefficient	ms^{-1}
δ	vapor diffusion coefficient	m^2s^{-1}
η	dynamic viscosity	m^2s^{-1}
λ	thermal conductivity	$Wm^{-1}K^{-1}$
ρ	density	$kg\ m^{-3}$
σ	surface tension	$N\ m^{-1}$
σ_0	standard deviation of radius	m
φ	relative humidity	–
ψ	porosity	–

Subscripts

a	air	g	gas
c	capillary	s	solid
eff	effective	v	vapor
fw	free water	w	liquid water

ACKNOWLEDGEMENTS

This work was financed by the German Research Foundation (DFG) in the frame of Graduate School 828 “Micro-Macro-Interactions in Structured Media and Particle Systems”.

REFERENCES

Irawan, A., T. Metzger and E. Tsotsas (2005), Pore network modelling of drying: combination with a boundary layer model to capture the first drying period, 7th World Congress of Chemical Engineering, Glasgow, Scotland

Irawan, A., T. Metzger and E. Tsotsas (2006), Isothermal drying of pore networks: influence of friction for different pore structures, 15th International Drying Symposium, Budapest, Hungary, August 20-23, 2006.

Krischer, O. (1956), Die wissenschaftlichen Grundlagen der Trocknungstechnik, 1er Band, 1st Edition, Springer-Verlag, Berlin, Germany.

Metzger, T. and E. Tsotsas (2005), Influence of pore size distribution on drying kinetics: a simple capillary model, Drying Technology, Vol. 23, pp. 1797-1809.

Metzger, T., M. Kwapinska, M. Peglow, G. Saage and E. Tsotsas (2006), Modern modeling methods in drying, submitted to Transport in Porous Media.

Nasrallah, S. B. and P. Perré (1998), Detailed study of a model of heat and mass transfer during convective drying of porous media, Int. J. Heat. Mass Transfer, Vol. 31, pp. 957-967.

Nowicki, S.C., H.T. Davis and L.E. Scriven (1992), Microscopic determination of transport parameters in drying porous media, Drying Technology, Vol. 10, pp. 925-946.

Perré, P. and I.W. Turner (1999), A 3-D version of TransPore: a comprehensive heat and mass transfer computational model for simulating the drying of porous media, Int. J. Heat Mass Transfer , Vol. 42, pp. 4501-4521.

Surasani, V.K., T. Metzger and E. Tsotsas (2006), Towards a complete pore network drying model: first steps to include heat transfer, 15th International Drying Symposium, Budapest, Hungary, August 20-23, 2006.

Truscott, S. L. and I. W. Turner (2005), A heterogeneous three-dimensional computational model for wood drying, Applied Mathematical Modelling, Vol. 29 , pp. 381-410.

Turner, I. W. and P. Perré (1996), A synopsis of the strategies and efficient resolution techniques used for modelling and numerically simulating the drying process. In: Turner, I. and Mujumdar, A. S. (Eds.), Mathematical modeling and numerical techniques in drying technology, Marcel Dekker, New York.

Transp Porous Med (2007) 66:103–120
DOI 10.1007/s11242-006-9025-z

ORIGINAL PAPER

Modern modelling methods in drying

Thomas Metzger · Marzena Kwapinska · Mirko Peglow · Gabriela Saage · Evangelos Tsotsas

Received: 15 November 2005 / Accepted: 26 March 2006 /
Published online: 30 August 2006

Abstract Several modern modelling techniques are presented as tools for drying science and technology, namely pore networks, discrete element method and population balances. After first presenting results from their own research, the authors indicate what future contributions to a better understanding of the drying process at different levels—single porous particles, agitated and fluidised beds—may be expected.

Keywords Drying kinetics · Agitated bed · Mixing · Fluidised bed · Agglomeration · Pore networks · Discrete element method · Population balances

Nomenclature

A	Pore throat cross section [m^2]
c_p	Heat capacity [$kJ\,kg^{-1}\,K^{-1}$]
f	Number density [$m^{-3}\,kg^{-1}$]
G	Rate of drying/wetting [$kg\,s^{-1}$]
L	Capillary or pore throat length [m]
l	Amount of liquid [kg]
$\dot{M}$	Mass flow rate [$kg\,s^{-1}$]
$\tilde{M}$	Molar mass [$kg\,kmol^{-1}$]
m_l	Liquid mass density [kg^{-3}]
N_{mix}	Mixing number [–]
n	Rotational frequency [s^{-1}]
n	Number density [s^{-1}] or [m^{-3}]
$\dot{n}$	Number flow rate [s^{-2}]

T. Metzger (✉) · M. Kwapinska · M. Peglow · G. Saage · E. Tsotsas
Chair of Thermal Process Engineering,
Otto-von-Guericke-University,
P.O. 4120, D-39016 Magdeburg, Germany
e-mail: thomas.metzger@vst.uni-magdeburg.de

$\tilde{R}$ Ideal gas constant [kJ kmol^{-1} K^{-1}]
p Pressure [Pa]
r Radius [m]
r_0 Mean radius [m]
s Meniscus position [m]
T Absolute temperature [K]
t Time [s]
t_{mix} Revolution time [s]
t_{R} Mixing time [s]
v Particle volume [m^3]
z Space coordinate [m]

Greek symbols
α Heat transfer coefficient [W m^{-2} K^{-1}]
β Mass transfer coefficient [m s^{-1}]
β Agglomeration kernel [s^{-1}]
δ Binary diffusion coefficient [m^2 s^{-1}]
ζ Dimensionless position [–]
η Dynamic viscosity [Pa s]
λ Thermal conductivity [Wm^{-1} K^{-1}]
$\dot{\nu}$ Dimensionless drying rate [–]
ρ Density [kg m^{-3}]
σ Surface tension [N m^{-1}]
σ_0 Radius standard deviation [m]
τ Age of particle [s]
ψ Porosity [–]

Subscripts
bed (Penetration into) Bed
I First drying period
v Vapour
ws Wall-to-bed

1 Introduction

In recent years, new approaches have been taken to the modelling of drying; unlike traditional models that describe the drying process in terms of average quantities and at a continuous level, they are able to give values of local or distributed character. These advances have become possible due to the development of fast computers, which can handle large amounts of data, and new numerical techniques.

In the present paper the following approaches will be discussed: first, network modelling, which is able to describe drying of porous media at the pore level and will permit a systematic investigation of the influence of structure on drying kinetics. For realistic results, simulations with large pore networks are required, which became possible only with increasing computer performance. In the past, intra-particle transport processes were modelled in continuous approaches, such as purely diffusional

models, using lumped parameters. In contrast, the new discrete approach aims at a microscopic description of all relevant physical phenomena.

Second, discrete element modelling will be presented, which describes individual particle motion in agitated beds based on mechanical principles. Recent model upgrades include thermal contacts between the particles, so that modelling of heat transfer in contact dryers is possible. The individual description allows us to assess traditional models which use a continuum approach. A full description of the drying process in contact dryers is expected in the near future. As in the case of networks, this kind of modelling only became possible with powerful computers.

Finally, population balances are discussed. These are used in fluidised bed operations to model the evolution of properties that may differ from particle to particle, such as moisture content or temperature. Instead of computing only averages for all particles, as in traditional models, distributions of these quantities are obtained. This permits a better assessment of product quality, even more so as the history of particles and its influence on other important properties, e.g. bioactivity, are accessible.

2 Network models: influence of pore structure on drying kinetics

It is well known that drying kinetics of a porous body depend on two different groups of parameters: one refers to the drying conditions, the other to the material itself. In convection drying, the first drying period is described by temperature, humidity and velocity of the drying air as well as the outer geometry of the body (needed to compute transfer coefficients); the second drying period depends, from its beginning, on the internal structure of the solid. Naturally, the factors determining the constant drying rate are easily accessible whereas the modelling of the second drying period must be based on a range of parameters that need to be measured in well-designed experiments. These parameters can either be effective transport parameters for a partially saturated porous medium that are to be used in a volume-averaged drying model (Perré and Turner 1999); or they may be structural parameters describing pore size distribution, connectivity of pores, etc.

In order to investigate the influence of structural parameters on drying kinetics there are, in principle, two possibilities: one can aim to describe their influence on the effective transport parameters; or one can use the structural information to simulate the drying process directly at the pore level. For both approaches, a suitable tool is pore networks consisting of regularly or randomly located pores that are interconnected by throats. To be representative of a real porous medium, such networks should be chosen large enough and have the same structural properties. At present, these requirements can only be partially fulfilled, because experimental tools to analyse porous media in terms of their structure down to the nanoscale are not available. Therefore, network simulations are qualitative in nature or must be restricted to macroporous structures.

In the past decade, pore network models, which were traditionally used to model drainage, have become very popular in the field of drying (e.g. Nowicki et al. 1992; Laurindo and Prat 1998; Plourde and Prat 2003; Yiotis et al. 2001, 2005; Segura and Toledo 2005). To our knowledge, all networks used for drying simulations were regular ones: square for two-dimensional and cubic for three-dimensional modelling. However, literature models vary in the geometry of pores and throats: throats have cylindrical, rectangular or polygonal cross sections or they are bi-conical to better

represent the converging–diverging character of a real pore space; pores are chosen as nodes without volume or as pore bodies. Viscous effects are either completely neglected or accounted for in the liquid phase (Nowicki et al.) or in both liquid and gas phase (Yiotis et al.). Most approaches assume isothermal conditions; heat transfer has only been modelled by Prat and coworkers who also used experiments with micromodels to validate their model. Film and corner flow in gas-filled throats has remained an important issue over the years. Gravitational effects on drying rates have been investigated as well.

In the early research, Nowicki et al. derived, among other properties, effective vapour diffusivity and relative liquid permeability as a function of saturation—using local vapour or liquid fluxes and corresponding gradients in vapour or capillary pressure, as they occur during the drying of the network. However, the influence of network structure on drying behaviour or on effective transport parameters was not investigated. For a long period, other researchers only simulated the drying process for networks—without computing effective transport parameters, and also without variation of the pore structure. Only recently, Segura and Toledo (2005) computed drying curves as well as diffusivity and permeablities for pore saturations of obtained from drying simulations. In their work, pore size distribution as well as throat shape were varied to study structural influences, but the small range of variations in pore size and the absence of viscosity in the model make it difficult to draw conclusions.

On the way to a better understanding of the influence of pore size distribution on drying behaviour, we lately introduced a one-dimensional capillary model (Metzger and Tsotsas 2005; Metzger et al. 2005). The pore space is represented by a bundle of cylindrical capillaries, set perpendicular to the product surface and connected without any lateral resistances (see Fig. 1). Isothermal drying was modelled for a viscous liquid, both for plate and spherical porous objects. The major condition for liquid flow is that between any two menisci the difference in capillary pressure $\Delta p_{\mathrm{c},i}$ must overcome the pressure drop due to friction $\Delta p_{\mathrm{f},i}$. For plate geometry, we have

$$2\sigma\left(\frac{1}{r_{i+1}}-\frac{1}{r_i}\right)=\Delta p_{\mathrm{c},i}\geq\Delta p_{\mathrm{f},i}=\frac{8\eta\dot{M}_v\left(s_i-s_{i+1}\right)}{\rho\sum_j\pi r_j^4} \tag{1}$$

where σ is surface tension, ρ density and η dynamic viscosity for liquid water, $\dot{M}_{\mathrm{v}}$ total evaporation rate, and r_i are radii of capillaries and s_i positions of respective menisci. Assuming ideal lateral transfer, $\dot{M}_{\mathrm{v}}$ depends only on the mass transfer coefficient β for the boundary layer until the last meniscus withdraws from the surface; then an additional resistance for vapour diffusion appears over the distance s_n.

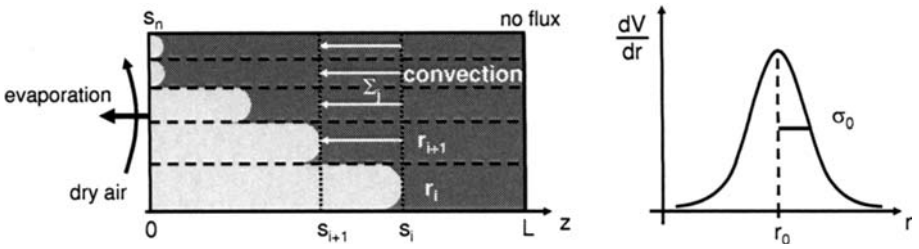

Fig. 1 Bundle of capillaries with normal pore volume distribution

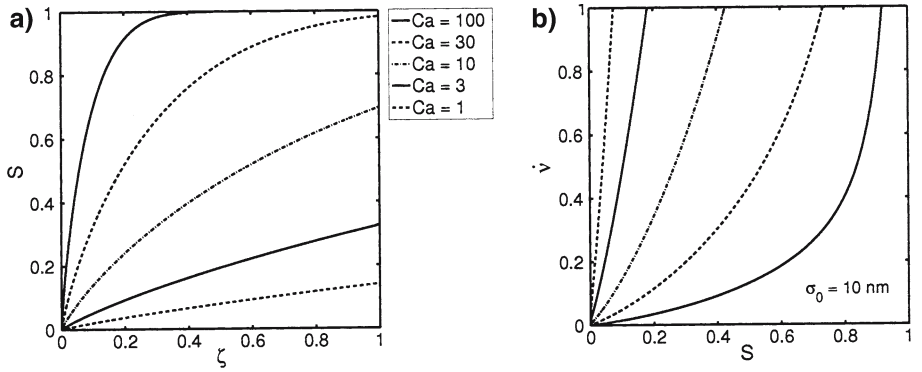

Fig. 2 Moisture profiles at the end of the first drying period and dimensionless drying curves for different Capillary number

For mono-modal pore volume distributions (normal with mean r_0 and standard deviation σ_0) we found that the absolute size of pores plays only a minor role, especially if $\sigma_0 \ll r_0$, but that the duration of the first drying period is significantly increased as the distribution becomes broader. In Fig. 2, saturation profiles for the dimensionless coordinate $\zeta = z/L$ as well as dimensionless drying rates $\dot{v} = \dot{M}_\mathrm{v}/\dot{M}_{\mathrm{v},I}$ are plotted for different values of the Capillary number

$$\mathrm{Ca} = \frac{\beta \eta L}{1000 \cdot \psi \sigma \sigma_0} \tag{2}$$

where ψ is porosity (equal to unity if solid phase is not included) and L capillary length. (The factor is to account for the density difference between liquid water and vapour.) For $\beta = 0.1\,\mathrm{m/s}$, $L = 0.1\,\mathrm{m}$, $\psi = 0.5$ and $\sigma_0 = 10\,\mathrm{nm}$, we have $Ca \approx 30$. Whereas the first drying period only depends on Ca, the second period needs one more parameter, i.e. distribution width σ_0.

For bi-modal distributions drying is generally faster because the large pores dry out first, more or less completely; consequently, their volume fraction significantly influences the drying curve. It is clear that the validity of the model is limited due to its restriction to one dimension and the resulting continuity of the liquid phase. Currently, the geometry of this model is used to derive all relevant macroscopic properties of the corresponding porous medium; these are then employed in volume-averaged drying simulations to show the equivalence of continuous and discrete approach. In this frame, we already extended the capillary model to simulate drying with heat transfer for two (classes of) capillaries of different radius in plate geometry (Metzger and Tsotsas 2005).

In parallel, the isothermal pore network model of Prat was used to study how drying kinetics depend on pore structure (Irawan et al. 2005; Metzger et al. 2005). The network consists of pore nodes connected by cylindrical throats of random radii, which are chosen according to a pore size distribution. Initially, all throats are filled by liquid, which can then evaporate through one surface of the two- or three-dimensional network. During drying, the liquid phase typically becomes discontinuous, splitting up into many clusters. The major model assumption (valid only for relatively large pores) is that capillary forces dominate over friction, so that within one such cluster the throats empty one by one with decreasing radius because liquid is always pumped

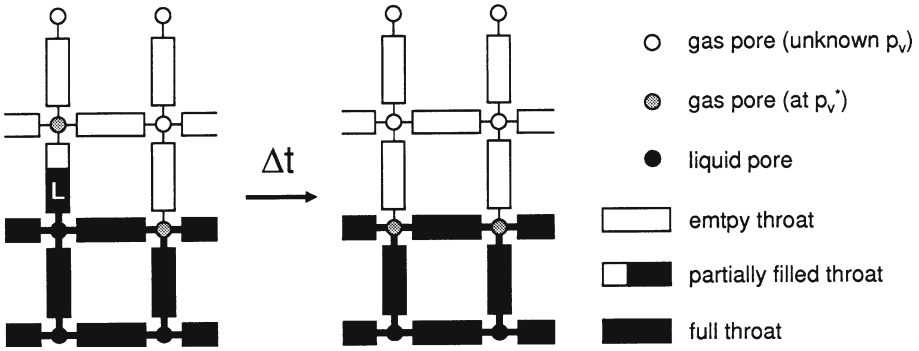

Fig. 3 Emptying of the largest throat (L) in a liquid cluster

to small throats. Figure 3 shows schematically the state of pores and throats, before and after the emptying of a throat. The drying rate is determined by vapour diffusion as computed from mass balances for all gas filled pores (i and j)

$$\sum_j \dot{M}_{\mathrm{v},ij} = \sum_j A_{ij} \frac{\delta}{L} \frac{p\tilde{M}_\mathrm{v}}{\tilde{R}T} \cdot \ln\left(\frac{p - p_{\mathrm{v},i}}{p - p_{\mathrm{v},j}}\right) = 0 \tag{3}$$

where A_{ij} is cross section and L length of connecting empty throats, δ vapour diffusion coefficient, p total pressure, p_v vapour pressure, $\tilde{M}_\mathrm{v}$ molar mass of vapour, $\tilde{R}$ ideal gas constant and T absolute temperature. We combined the idea of a discretised boundary layer proposed by Laurindo and Prat (1998) with laminar boundary layer theory, so that the network of nodes is naturally extended up to the average boundary layer thickness (see Fig. 4). The boundary conditions for Eq. (3) are then given by the vapour pressure of bulk drying air and saturation vapour pressure p_v^* at any liquid surface inside the network. The amount of water in the largest throat divided by the total evaporation rate for the cluster (sum over all menisci) gives the time step Δt. Emptying of a throat may create new clusters.

Figure 4 shows a typical phase distribution with several liquid clusters along with the vapour pressure field. In the network, vapour pressure is uniform except near the surface so that some of the clusters are not (yet) evaporating; in the boundary layer one can see the lateral vapour transfer.

With this model, we computed drying curves for two- and three-dimensional networks with different structures and pore size distributions; two examples are shown in Figs. 5 and 6; the corresponding moisture profiles are plotted in Fig. 7. Additionally, the influence of boundary layer thickness (or drying air velocity) and product depth were analysed for different structures. It could be shown that the first drying period can only be reproduced if a discretised boundary layer is included in the model.

As a consequence of neglecting any viscous forces, the only counter mechanism to capillary pumping is the discontinuity of the liquid phase: the network dries out rapidly only if capillary flow paths can be maintained over a significant time. For a network 1 with normally distributed throat radii, this is not the case; in the present model, a change of mean pore size and broadness of the distribution will not change the drying behaviour, since the splitting up into clusters is determined by the order of throat emptying which proceeds according to relative decrease in size. For bimodal

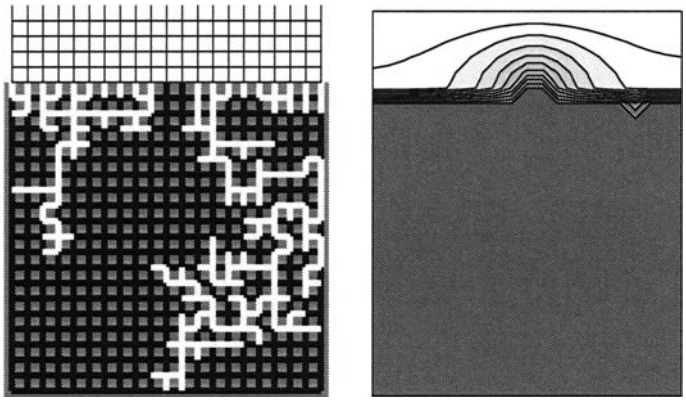

Fig. 4 Pore saturation and vapour pressure field for a small two-dimensional network

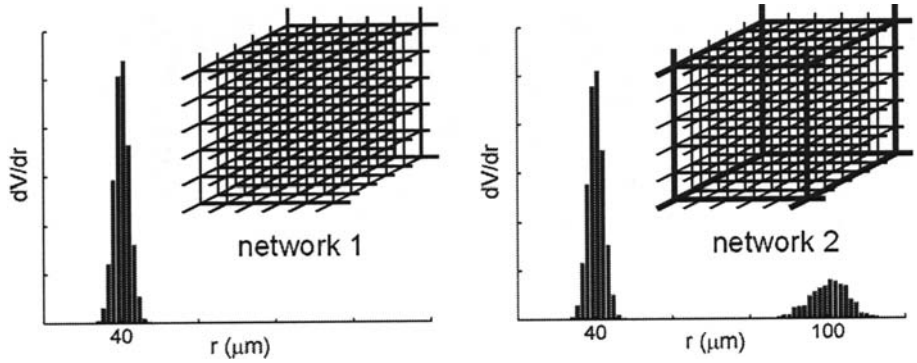

Fig. 5 Pore size distribution and pore structure for two different $16 \times 16 \times 16$ networks with $L = 500\,\mu$m (only part of the network is sketched)

Fig. 6 Drying curves for the two networks in Fig. 5 (evaporation flux as a function of network saturation)

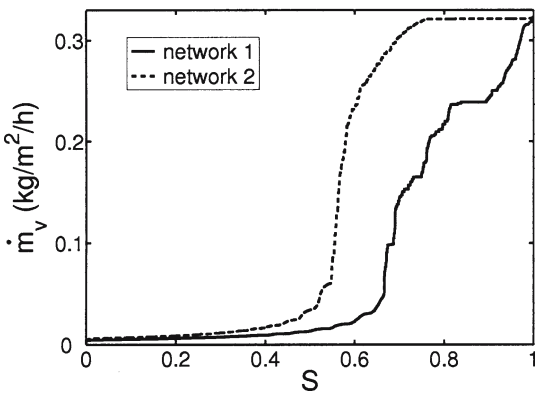

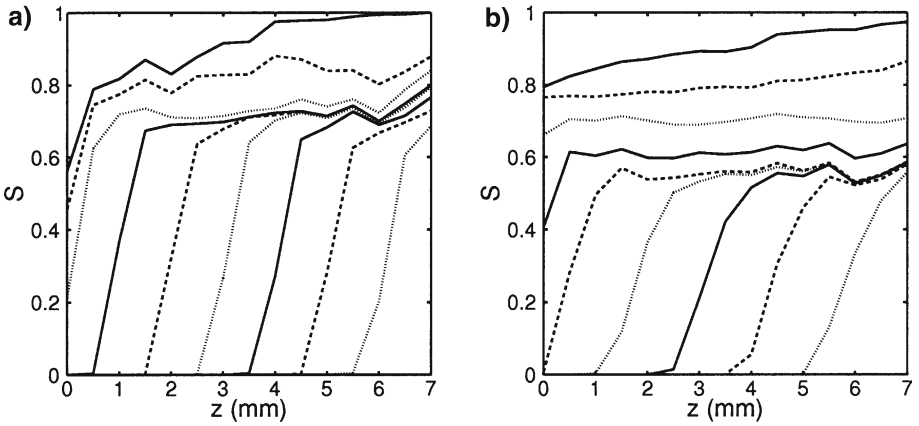

Fig. 7 Moisture profiles for (**a**) network 1 and (**b**) network 2 as in Fig. 5, drawn for multiples of 10% in network saturation

pore size distributions with highly correlated pore structures, as in network 2, where large throats are forming long channels, drying rates can be significantly higher, and a first drying period is observed. As can be seen in Fig. 7, moisture gradients for network 1 are steeper than for network 2.

We found that drying simulations in two and three dimensions may lead to contradictory conclusions: in the two-dimensional version of network 2, for example, capillary flow paths are easily cut off by emptying large throats. Therefore, three-dimensional modelling is imperative when structural influences are to be investigated.

It is clear that these first findings from network simulations are quite different from the results of the one-dimensional capillary model in which the liquid is viscous and forms a continuous phase. These contradictions will be overcome and a more comprehensive view become possible only by our current activity of including viscosity into the network model.

The next crucial step is to extend the model to heat transfer, since real drying can rarely be described by an isothermal model; previous work by Plourde and Prat (2003) and Huinink et al. (2002) will serve as basis. Due to non-uniform temperature and therefore non-uniform saturation vapour pressure, such a model must be able to describe vapour condensation and not only evaporation. Only then will the network model account for all transport effects, and it will make sense to compare its results with those of a continuous model.

Concerning this comparison, it is still an open question how much "drying information" has to be incorporated into the effective parameters of networks. Will they be computed from gradients and fluxes as observed during drying (cf. Nowicki et al. 1992), or from separate numerical experiments, i.e. by applying gradients to a network with a given saturation? And, in the latter case, according to which rules will the spatial distribution of liquid for this saturation be chosen: randomly or as observed during drying (cf. Segura and Toledo 2005)? Another important issue in this context is the network size needed to be representative, or the number of small network simulations needed to get average behaviour. In this frame, it might be reasonable to introduce periodic boundary conditions.

In order to investigate the influence of structure more comprehensively, we are currently looking into random pore networks, in which not only throat radius is chosen at random but also locations of pore nodes and existence of throat connections, leading to a distributed coordination number. Furthermore, spatial correlations have to be modelled. The aim will be to discover which structural parameters are sufficient to characterize the porous medium with respect to its drying behaviour; in this sense, equivalence classes of networks might be defined and algorithms found to generate networks representative of these classes.

3 Discrete element modelling: mixing and heat transfer in mechanically agitated beds

From single particles we now turn to granular material, i.e. large ensembles of particles. Again, our aim is to go beyond average behaviour of the whole system, but rather describe the properties of individual particles.

At present, when contact drying of particulate material in mechanically agitated beds is to be modelled, heat transfer from walls is usually described by a penetration model (Schlünder 1983; Schlünder and Mollekopf, 1984). In this traditional approach, the bed of particles is viewed as a continuum with effective properties, and the continuous mixing and heating of particles is discretised by alternating static periods of duration t_R with pure heat conduction to a stagnant bed and instantaneous perfect mixing thereafter. In a rotating drum, the time t_R is obtained from

$$t_R = t_{mix} \cdot N_{mix}, \quad t_{mix} = 1/n \tag{4}$$

where n is the rotational frequency and N_{mix} the number of revolutions needed for perfect mixing. The overall (time-averaged) heat transfer coefficient α is computed from

$$\frac{1}{\alpha} = \frac{1}{\alpha_{ws}} + \frac{1}{\alpha_{bed}} \tag{5}$$

where α_{ws} is the wall-to-bed transfer coefficient—as calculated from kinetic gas theory in the gap between wall and first layer of particles—and

$$\alpha_{bed} = \frac{2}{\sqrt{\pi}} \frac{\sqrt{\rho c_p \lambda_{bed}}}{\sqrt{t_R}} \tag{6}$$

is the penetration coefficient—as obtained from time-averaged heat conduction by Fourier's law with effective volumetric heat capacity ρc_p and effective thermal conductivity λ_{bed}.

Empirical correlations based on atmospheric (Schlünder 1980) and vacuum contact (Wunschmann 1974) drying experiments are available for the mixing number N_{mix}, relating it to rotational frequency and apparatus diameter. But it is clear that this single parameter of the penetration model might not be sufficient to grasp the complex motion of particles. Note that, for rotating drums, there are up to six different regimes of particle motion, depending on particle diameter, drum diameter, rotational frequency and loading. The rolling and the slumping regime were investigated in the presented work.

We will now discuss how the discrete element method, introduced by Cundall and Strack (1979) and implemented in PFC software by ITASCA, can be used as

a modern alternative to test and upgrade penetration models—exemplified for the specific case of a horizontally rotating drum. In the discrete element approach the motion of individual particles is tracked by alternately computing forces between particles that are in contact and updating their velocities accordingly. Contact forces are computed from relative particle velocities, "overlap"of the particles and material properties describing stiffness, viscous damping and frictional slip.

At first we employed this purely mechanical model to study mixing of particles in a drum by two-dimensional simulations (Saage et al. 2005; Kwapinska et al. 2006). The authors have shown by comparison with experimental data from the literature (van Puyvelde et al. 1999, 2000) that the discrete element method has the potential for realistically describing the mixing behaviour (in respect to the character of mixing dynamics, to all trends and dependencies). A typical result is shown in Fig. 8, where spherical particles with a narrow size distribution are mixed; two (initially separated) fractions of particles, which differ only in their colour, are used to describe the extent of mixing. After a certain time, the number of contacts between particles of different colour has attained a constant level, apart from statistical fluctuations. This is the time needed for perfect mixing and can be directly compared with the parameter t_R of the penetration model. By discrete element modelling, mixing numbers N_{mix} were obtained, which are in average by a factor of 2.5 lower than those computed from the empirical correlations. A new correlation was proposed, which additionally accounts for drum loading by replacing the rotational frequency of the drum by that of the bed (for the rolling regime). Some examples of mixing times from penetration theory (t_R) and from discrete element modelling (t'_R) are given in Table 1. The mixing times t'_R are also converted into penetration coefficients α'_{bed} by Eq. (6).

Next, heat transfer was included into discrete element modelling (Kwapinska et al. 2005); to this end, a heat reservoir is associated to each particle and a thermal pipe to each contact between two particles or wall and particle (see Fig. 9). These thermal pipes are characterized by thermal resistances, obtained from heat conduction through the gas gap between the two contact partners (solid bridges and radiation are neglected); from geometric considerations, the wall-to-particle resistance is half of the particle-to-particle resistance and calculated as proposed by Schlünder (1983). The momentary heat flow rate is then computed from temperature differences. All simulations were performed for a constant mechanical and thermal time step of 2 μs. This allows us to fulfill the requirement that, within one time step, a change of particle temperature does not propagate further than a particle's immediate neighbours. A

Table 1 Comparison of simulation results with penetration theory, for 8 mm particles in a drum of diameter 0.25 m

Drum velocity, rpm	Drum load, %	Penetration theory				Penetration theory with t'_R from DEM			DEM
		t_R, s	α_{ws}, $\frac{W}{m^2K}$	α_{bed}, $\frac{W}{m^2K}$	α, $\frac{W}{m^2K}$	t'_R, s	α'_{bed}, $\frac{W}{m^2K}$	α', $\frac{W}{m^2K}$	α_{sim}, $\frac{W}{m^2K}$
28.6	15	21.7	70.5	181.0	50.7	3.10	478.9	61.4	68.2
287	30	5.46	70.5	360.8	58.9	3.16	474.3	61.3	69.2
28.6	30	21.7	70.5	181.0	50.7	7.30	312.1	57.5	67.7
4.78	30	61.8	70.5	107.2	42.5	19.25	192.2	51.6	66.3

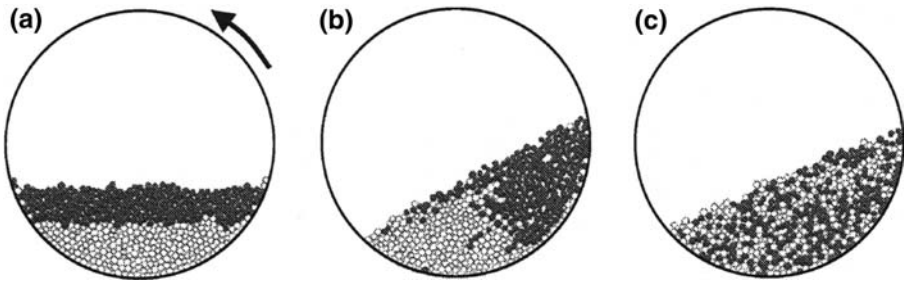

Fig. 8 Examples of different stages of mixing (in the rolling regime): (**a**) initial bed configuration, (**b**) bed after one drum revolution and (**c**) steady state

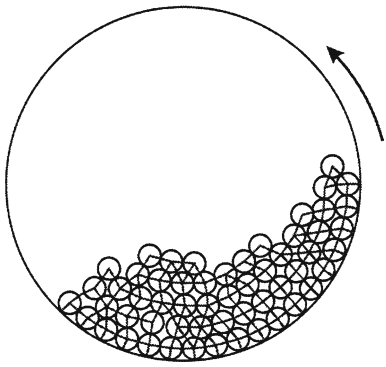

Fig. 9 Active thermal pipes for mono-sized spheres in a drum dryer

thermal pipe is made active if the respective two particles touch, i.e. if their overlap is greater than or equal to zero. After each time step, the activity status of each pipe is updated.

Computational time restricts the application of thermal discrete elements to a relatively small number of particles, so that the present investigation is of an exploratory character. Even for a maximum number of particles of 370, computational times of around 10 h on a commercial PC were necessary for about 70 s of simulated process time.

Our aim was to study heating of an agitated bed of mono-sized spheres in a rotating drum of constant wall temperature. However, we decided first to look at the limiting case when heat transfer is controlled by the wall-to-bed transfer coefficient ($\alpha \approx \alpha_{ws}$); temperature differences within the bed are then negligible and mixing does not play a role in overall heat transfer; to this end, the particle-to-particle thermal resistance was set to a value close to zero. The evolution of average bed temperature as obtained from discrete element modelling was found to coincide with the analytical solution.

Having confirmed that wall-to-bed heat transfer is correctly described, we then turned to heat transfer within the bed, which, in the penetration model, is characterised by the effective thermal conductivity of the bed λ_{bed}. If discrete element and penetration model are to be compared at full scale, this parameter must first be estimated from discrete element simulations (the remaining volumetric heat capacity is easily obtained). To this purpose, heat transfer from the drum to a stagnant bed was computed with the true resistances for the thermal pipes. In the absence of mixing, t_R in Eq. (6) is replaced by the real time and λ_{bed} is the only model parameter, which can

be obtained by fitting the analytical solution to the discrete element result and has a value of 0.44 $W\,m^{-1}\,K^{-1}$.

Finally, the combined mixing and heat transfer for a rotating drum were simulated and overall heat transfer coefficients α_{sim} estimated from the discrete element results. When comparing these to α' as predicted by the penetration model (with α_{ws} and λ_{bed} as by discrete elements), one can state that the penetration model underestimates the enhancement of heat transfer by mixing (see Table 1). Even the mixing times that had been obtained from purely mechanical simulations were too long to explain the difference, suggesting that it might not be feasible to describe the complex interaction of mixing and heat transfer by a simple penetration model.

A possible explanation for this is that the perfect mixing in the penetration model is assumed to be instantaneous and therefore "unstructured", whereas highly correlated, fluid-like particle motion can be observed in discrete element simulations (Kwapinska et al. 2005). However, another possible reason for the discrepancy will first have to be excluded: the current restriction to two dimensions and to only a few particles as compared to the experiments on which traditional correlations are based.

For illustration, we give some simulation results for combined mixing and heat transfer. Figure 10 shows the influence of mixing on the evolution of particle temperature: for a stagnant bed, the first layer of particles on the wall heats up rapidly, but the average bed temperature rises only slowly, whereas, for the rotating drum, temperature differences in the bed are leveled out. This is because—for the presented examples—contact resistance prevails over penetration resistance in the serial coupling of Eq. (5). The evolution of the particle temperature distribution is plotted in Fig. 11.

As the presented work shows, discrete element modelling has the potential for realistically describing simultaneous mixing and heat transfer in agitated beds. In the near future, the model will be extended to mass transfer so that all phenomena relevant in contact drying are accounted for. This will allow a detailed analysis and revision of existing drying models.

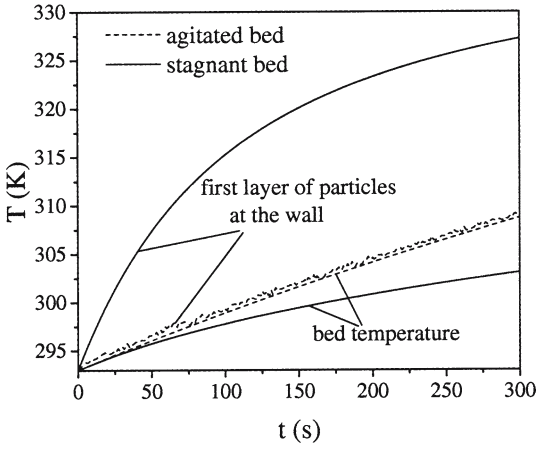

Fig. 10 Evolution of particle temperature in a drum heated by the wall (224 particles of diameter 8 mm, drum diameter 0.25 m, rotational frequency of drum 28.6 rpm, drum loading 30%)

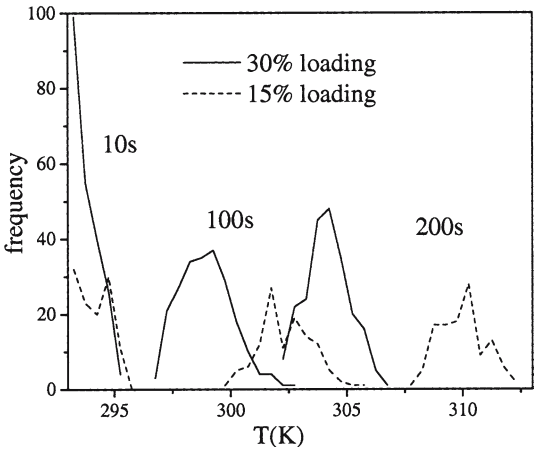

Fig. 11 Evolution of particle temperature distribution in a rotation drum heated by the wall (particle diameter 8 mm, drum diameter 0.25 m, rotational frequency of drum 28.6 rpm)

4 Population balances: distributed product quality in fluidised beds

Solids processing of particulate materials in fluidised beds, such as drying or spray granulation, are of major interest in the chemical industry. Various parameters—for material behaviour, apparatus design and operating conditions—influence the resulting products in terms of, for example, particle size, morphology and composition. Such disperse systems can best be modelled by population balances; these describe the temporal change of number density distributions of individuals of the disperse phase with respect to different external and internal coordinates.

Population balances have already been used in the past. However, these formulations were limited to relatively simple, one-dimensional models. The description of innovative and often very complex processes and operations for the production of granular materials as well as the quantification of important factors influencing product quality will require a multidimensional approach.

An example of applying population balances is continuous fluidised bed drying. The traditional approach to modelling this operation considers the disperse solids as one phase with average properties like particle size, moisture content and enthalpy. Recently, Burgschweiger (2000) proved that these models are generally suited for continuously operated dryers, but it was found, by comparison with experimental data, that such a model tends to underestimate the outlet moisture content (see Fig. 12).

Model accuracy can be significantly improved by use of population dynamics. Due to different retention times of particles, a moisture distribution in the product stream is expected. This can be modelled by introducing an additional property coordinate, the age τ of particles. The temporal evolution of the number density n for an ideally mixed system is then given by

$$\frac{\partial n(t,\tau)}{\partial t} = -\frac{\partial n(t,\tau)}{\partial \tau} + \dot{n}_{\mathrm{in}}(t) - \dot{n}_{\mathrm{out}}(t,\tau) \tag{7}$$

where $\dot{n}_{\mathrm{in}}(t)$ indicates the inlet rate of particles and $\dot{n}_{\mathrm{out}}(t,\tau)$ the particle flow rate at the outlet. The expression $\partial n(t,\tau)/\partial\tau$ represents the aging of particles. Integration of Eq. (7) results in the age distribution function of particles. Since we are not only interested in this particular aging process, but in the moisture content distribution,

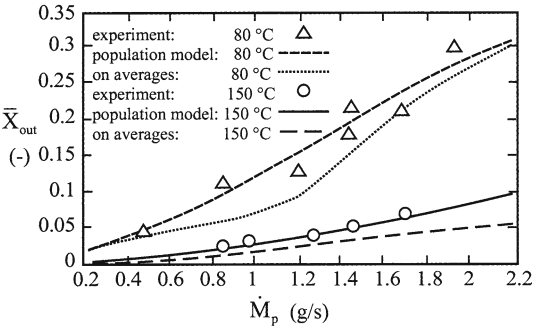

Fig. 12 Static continuous fluidised bed drying: measured and simulated (on averages and population balance) outlet moisture content of γ-Al_2O_3 particles (ϕ 1.8 mm, initial moisture content 0.60–0.65) for different particle flow rates

which is a significant parameter of product quality, we also need to apply the concept of population balances to the amount of liquid contained in the particles and to particle enthalpy. The evolution of the above number distribution will not be influenced by interaction with the gas phase. But as soon as processes such as drying and heating of particles are involved, additional sinks and sources have to be introduced in the liquid mass and enthalpy balances of the particles, respectively. A model extended in this way yields considerably better values for product moisture at the dryer outlet, as can be seen in Fig. 12 (Burgschweiger and Tsotsas 2002).

Extensive experiments are currently being carried out, in which the distribution of outlet moisture is determined by gravimetric measurement of single particles. In Fig. 13, the measured normalized particle density distribution q_0 is shown as a function of single particle moisture content. This result verifies that the outlet moisture of mono-sized particles is distributed over a relatively wide range, reflecting different retention times in the apparatus. As a consequence of this, it seems to be reasonable to find new modelling approaches, such as population balances, that have the potential to replace the existing models, which are based on averages.

Following this approach, the set of product characteristics can be arbitrarily extended to other (outlet) properties, such as colour or bioactivity, which depend on the history of the particle related to temperature and water activity.

A second research field is related to processes of particle formulation, such as particle coating and spray granulation (agglomeration), whereas the latter is the scientifically more interesting and more complex case. For these processes,

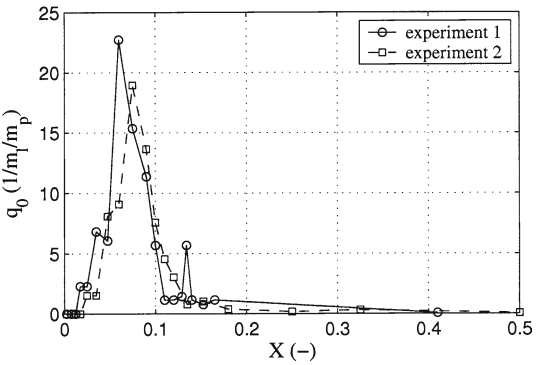

Fig. 13 Static continuous fluidised bed drying: experimental moisture content of γ-Al_2O_3 particles (ϕ 1.8 mm, initial moisture content 0.60–0.65) at dryer outlet

one-dimensional population balances have been applied in numerous approaches, whereby the particle volume v has been considered as the only significant property.

In fact, other relevant coordinates of the particle distribution are amount of liquid l and enthalpy. Assuming binary agglomeration events, the temporal change of the number density f can be described as

$$\begin{aligned}&\frac{\partial f(t,v,l)}{\partial t}+\frac{\partial G(v,l)\cdot f(t,v,l)}{\partial l}\\&=\frac{1}{2}\int_0^v\int_0^l \beta(t,v-\varepsilon,\varepsilon,l-\gamma,\gamma)\cdot f(t,v-\varepsilon,l-\gamma)\cdot f(t,\varepsilon,\gamma)\mathrm{d}\gamma\mathrm{d}\varepsilon\\&\quad-\int_0^\infty\int_0^\infty \beta(t,v,\varepsilon,l,\gamma)\cdot f(t,v,l)\cdot f(t,\varepsilon,\gamma)\mathrm{d}\gamma\mathrm{d}\varepsilon\end{aligned}\tag{8}$$

where G is the combined rate of wetting and drying—both depending on particle size, the second additionally on moisture content—and β describes the kinetics of the agglomeration process in terms of a kernel. The left term of this equation describes the accumulation of particles of certain size and amount of liquid. The first integral on the right side depicts the birth and the second integral represents the death of particles due to agglomeration. Since we have two properties of the solid phase (size and amount of liquid), double integration becomes necessary. Here ε and γ are variables of integration for the coordinates particle size and liquid mass, respectively. For simplicity, the coordinate of enthalpy is not elaborated here. Otherwise three integrals in the population balance would have been needed. Furthermore, one would have to introduce one additional advection term (such as for the drying and wetting) that takes into account the heat and enthalpy fluxes between solid and gas phase.

The solution of such multidimensional population balances requires, on the one hand, a great numerical effort (exponential in the number of particle properties) and, on the other hand, a theoretical expression for the multidimensional kernel. The marginal distributions approach offers a way to reduce the model, if the agglomeration process is assumed to depend only on particle size and not on moisture content, namely $\beta(t,v,\varepsilon,l,\gamma)=\beta(t,v,\varepsilon)$. By integrating over the amount of liquid l, we first define number density n and the liquid mass density m_l as

$$n(t,v)=\int_0^\infty f(t,v,l)\mathrm{d}l\tag{9}$$

$$m_\mathrm{l}(t,v)=\int_0^\infty l\cdot f(t,v,l)\mathrm{d}l\tag{10}$$

Then, the multidimensional population balance of Eq. (8) may be rewritten as several one-dimensional balances, one for the number distribution

$$\begin{aligned}\frac{\partial n(v)}{\partial t}&=\frac{1}{2}\int_0^v \beta(u,v-u)\cdot n(u)\cdot n(v-u)\mathrm{d}u\\&\quad-n(v)\int_0^\infty \beta(u,v)\cdot n(u)\mathrm{d}u\end{aligned}\tag{11}$$

and one for the moisture distribution

$$\begin{aligned}\frac{\partial m_\mathrm{l}(v)}{\partial t}&=\int_0^v \beta(u,v-u)\cdot n(u)\cdot m_\mathrm{l}(v-u)\mathrm{d}u\\&\quad-n(v)\int_0^\infty \beta(u,v)\cdot m_\mathrm{l}(u)\mathrm{d}u+\frac{\partial}{\partial v}\left(\dot{M}_\mathrm{np}-\dot{M}_\mathrm{ps}\right)\end{aligned}\tag{12}$$

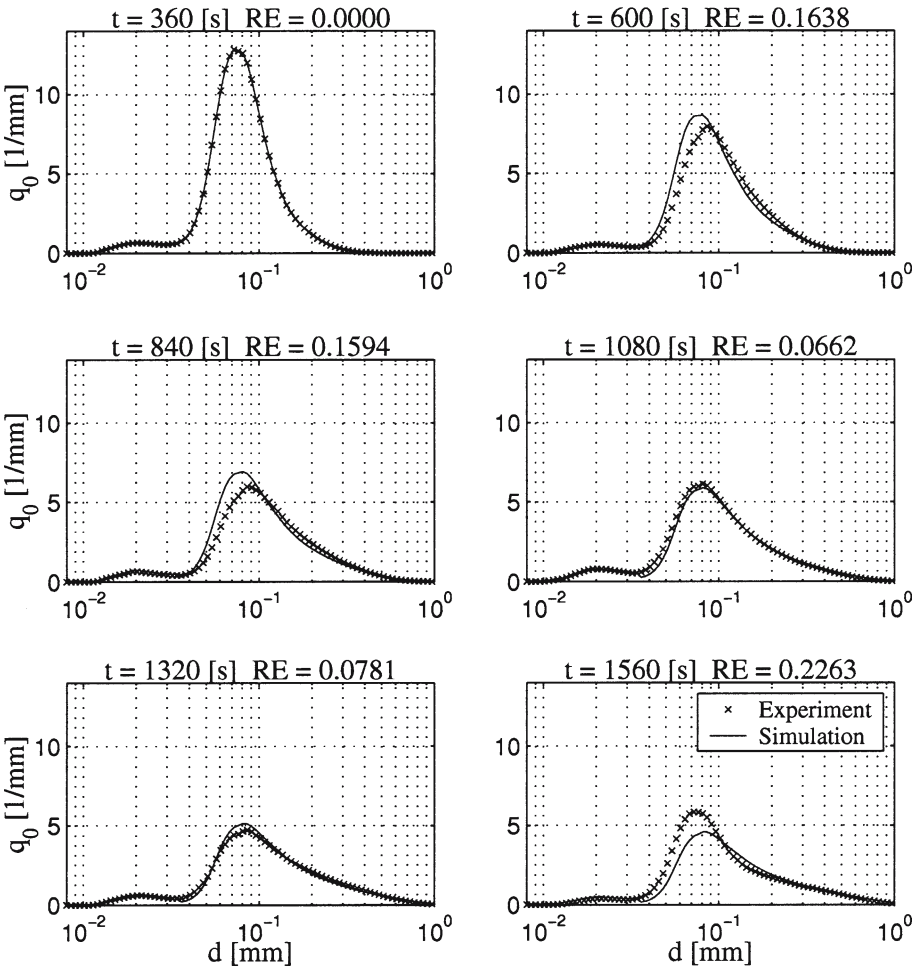

Fig. 14 Evolution of measured and simulated particle size distribution in fluidised bed spray agglomeration (RE = cumulative relative error)

where $\dot{M}_{\mathrm{np}}$ is liquid mass flow from the spray nozzle and $\dot{M}_{\mathrm{ps}}$ drying rate of the particles of size v. These terms can be deduced directly from the advection term on the left side of Eq. (8). As a result of this one obtains wetting and drying rates that depend on particle size but not on moisture content. (Again, the balance for the enthalpy distribution is not given here.) By this model reduction, the numerical effort is considerably reduced (linear in the number of properties).

The process modelled by this equation has been investigated by agglomeration experiments on microcrystalline cellulose in a fluidised bed (Peglow 2005). The governing agglomeration kernel was estimated from experimental data taking into account size-dependent nuclei formation. For this purpose, a new inverse technique was derived (Peglow et al. 2006) based on work of Bramley et al. (1996). An example for the good correspondence of model and measurement data is given in Fig. 14.

Based on work of Hounslow et al. (2001), new discretisation methods of the continuous population balance equation were developed (Peglow et al. 2006a) to solve this system. These new discretisation algorithms allow the prediction of intensive properties (temperature and moisture content) in addition to extensive properties of the disperse phase, such as size, enthalpy and amount of water.

As indicated in Eq. (12), the agglomeration process in the disperse phase was not considered in an isolated manner, but in the frame of a heterogeneous fluidised bed model with heat and mass transfer between continuous and disperse phase. More specifically, the drying rate was treated as dependent on particle size as well as on moisture content and temperature associated with this particle size.

In all existing models, the agglomeration kernel is a function of particle size only. However, other particle properties have a strong influence on the agglomeration process so that successful and first principle modelling needs to be multidimensional. As most important properties, one may consider size and moisture content of granules, but also porosity and binder content.

In a first step, the amount of liquid l in a single particle will be introduced as a full coordinate as shown in Eq. (8). Then, the agglomeration kernel β as well as the drying rate G will depend on this property, the latter establishing a direct link of mass transfer processes between granular and gas phase.

To get a better understanding of the structure of the kernel, experimental data for the temporal change of the two-dimensional distribution (size and water content) are needed. Such measurements are very demanding, but first trials with magnetic suspension gravimetry and NMR methods are promising.

5 Conclusion

Recent approaches to drying modelling have been presented. Unlike traditional techniques, relevant quantities are modelled and measured locally and not in terms of averages. In this way, processes at the pore scale (for single particles) and for individual particles (for beds of particles) are not masked. Therefore, new insight in the drying processes at different scales may well be expected.

Acknowledgements The authors would like to state that part of the presented work has been financed by the Graduiertenkolleg 828 "Micro-Macro-Interactions in Structured Media and Particle Systems"(funded by the German Research Foundation) and by the State of Saxony-Anhalt.

References

Bramley, A.S., Hounslow, M.J., Ryall, R.L.: Aggregation during precipitation from solution: A method for extracting rates from experimental data. J. Colloid Interface Sci. **183**, 155–165 (1996)

Burgschweiger, J.: Modellierung des statischen und dynamischen Verhaltens von kontinuierlich betriebenen Wirbelschichttrocknern. Dissertation, Universität Magdeburg, VDI-Verlag, Reihe 3, Nr. 665 (2000)

Burgschweiger, J., Tsotsas, E.: Experimental investigation and modelling of continuous fluidized bed drying under steady-state and dynamic conditions. Chem. Eng. Sci. **57**, 5021–5038 (2002)

Cundall, P.A., Strack, O.D.L.: A discrete numerical model for granular assemblies. Geotechnique **29**, 47–65 (1979)

Hounslow, M.J., Pearson, J.M.K., Instone, T.: Tracer studies of high shear granulation: II. Population balance modeling. AIChE J. **47**, 1984–1999 (2001)

Huinink, H.P., Pel, L., Michels, M.A.J., Prat, M.: Drying processes in the presence of temperature gradients—pore-scale modelling. Eur. Phys. J. E. **9**, 487–498 (2002)
Irawan, A., Metzger, T., Tsotsas, E.: Pore network modelling of drying: combination with a boundary layer model to capture the first drying period. Proc. 7th WCCE, Glasgow, United Kingdom (2005)
Kwapinska, M., Saage, G., Tsotsas, E.: On the way from penetration models to discrete element simulations of contact dryers. XI Polish Drying Symposium, Poznan, Poland (2005)
Kwapinska, M., Saage, G., Tsotsas, E.: Mixing of particles in rotary drums: A comparison of discrete element simulations with experimental results and penetration models for thermal processes. Powder Technol. **161**, 69–78 (2006)
Laurindo, J.B., Prat, M.: Numerical and experimental network study of evaporation in capillary porous media. Chem. Eng. Sci. **53**, 2257–2269 (1998)
Metzger, T., Tsotsas, E.: Influence of pore size distribution on drying kinetics: a simple capillary model. Drying Technol. **23**, 1797–1809 (2005)
Metzger, T., Irawan, A., Tsotsas, E.: Discrete modeling of drying kinetics of porous media. Proc. 3rd Nordic Drying Conference, Karlstad, Sweden (2005)
Nowicki, S.C., Davis, H.T., Scriven, L.E.: Microscopic determination of transport parameters in drying porous media. Dry. Technol. **10**, 925–946 (1992)
Peglow, M.: Beitrag zur Modellbildung eigenschaftsverteilter Feststoffsysteme am Beispiel der Wirbelschicht-Sprühagglomeration. Dissertation, Universität Magdeburg (2005)
Peglow, M., Kumar, J., Warnecke, G., Heinrich, S., Mörl, L., Hounslow, M.J.: Improved discretized tracer mass distribution of Hounslow et al., AIChE J. **52**, 1326–1332 (2006a)
Peglow, M., Kumar, J., Warnecke, G., Heinrich, S., Mörl, L.: A new technique to determine rate constants for growth and agglomeration with size- and time-dependent nuclei formation. Chem. Eng. Sci. **61**, 282–292 (2006a)
Perré, P., Turner, I.W.: A 3-D version of TransPore: a comprehensive heat and mass transfer computational model for simulation the drying of porous media. Int. J. Heat Mass Transfer **42**, 4501–4521 (1999)
Plourde, F., Prat, M.: Pore network simulations of drying of capillary porous media. Influence of thermal gradients, Int. J. Heat Mass Transfer **46**, 1293–1307 (2003)
Saage, G., Kwapinska, M., Tsotsas, E.: Discrete element simulation of the mixing time of granular solids. In: Proc. 16th International Symposium on Trends in Applications of Mathematics to Mechanics (pp. 441–450). Shaker Verlag (2005)
Schlünder, E.U.: Der Wärmeübergang an ruhende, bewegte und durchwirbelte Schüttschichten. VT-Verfahrenstechnik **14**, 459–468 (1980)
Schlünder, E.U.: Heat transfer to packed and stirred beds from the surface of immersed bodies. Chem. Eng. Process. **18**, 31–53 (1983)
Schlünder, E.U., Mollekopf, N.: Vacuum contact drying of free flowing, mechanically agitated particulate material. Chem. Eng. Process. **18**, 93–111 (1984)
Segura, L.A., Toledo, P.G.: Pore-level modeling of isothermal drying of pore networks. Effects of gravity and pore shape and size distributions. Chem. Eng. J. **111**, 237–252 (2005)
van Puyvelde, D.R., Young, B.R., Wilson, M.A., Schmidt, S.J.: Experimental determination of transverse mixing kinetics in a rolling drum by image analysis. Powder Technol. **106**, 183–191 (1999)
van Puyvelde, D.R., Young, B.R., Wilson, M.A., Schmidt, S.J.: Modelling transverse mixing kinetics in a rolling drum. CJChE **78**, 635–642 (2000)
Wunschmann, J.: Wärmeübertragung von beheizten Flächen an bewegte Schüttungen bei Normaldruck und Vakuum. Dissertation, Universität Karlsruhe (1974)
Yiotis, A.G., Stubos, A.K., Boudouvis, A.G., Yortsos, Y.C.: A 2-D pore network model of the drying of single-component liquids in porous media. Adv. Water Resour. **24**, 439–460 (2001)
Yiotis, A.G., Stubos, A.K., Boudouvis, A.G., Tsimpanogiannis, I.N., Yortsos, Y.C.: Pore-network modeling of isothermal drying in porous media. Trans. Porous Media **58**, 63–86 (2005)

AIChE WILEY InterScience DISCOVER SOMETHING GREAT

FLUID MECHANICS AND TRANSPORT PHENOMENA

Influence of Pore Structure on Drying Kinetics: A Pore Network Study

Thomas Metzger, Anton Irawan, and Evangelos Tsotsas
Thermal Process Engineering, Otto-von-Guericke-University, P.O. 4120, 39016 Magdeburg, Germany

DOI 10.1002/aic.11307
Published online October 12, 2007 in Wiley InterScience (www.interscience.wiley.com).

A pore network model for convective drying is applied to investigate the influence of structure on drying behavior. The isothermal drying model is based on the work of Prat, and uses invasion percolation concepts, neglecting any viscous or gravitational effects. Pore structures of different pore-size distribution and coordination number are studied in two- and three-dimensions. Results are given as phase distributions or moisture profiles during drying, as well as drying rate curves. Significant differences in drying kinetics are reported for a variation in coordination number of monomodal networks. Bimodal pore structures can produce dramatically higher drying rates, but only for certain spatial correlations of small and large pores. Finally, influence of product thickness and importance of boundary layer modeling are addressed. © 2007 American Institute of Chemical Engineers *AIChE J,* 53: 3029–3041, 2007
Keywords: drying rate, phase distributions, porous media, pore-size distribution, coordination number

Introduction

Drying kinetics of porous media depend on two classes of parameters: the first describes drying conditions, the second the material itself. In convective drying, the initial drying rate of a liquid-saturated material is only given by temperature, humidity and velocity of drying air and outer geometry of the porous body; this rate is identical to the evaporation rate of a liquid surface, and structural properties of the material will not influence it. Pore structure will, however, determine for how long this initial rate can be maintained (first drying period), and how drying rate will decrease during the so-called second drying period. Then, heat and mass transfer are controlled by inner resistances. Theoretical description of drying behavior is a challenging task, but can be of great benefit for optimal process design and product innovation.

One way to describe the transport phenomena in partially saturated porous media is by a continuous model based on volume-averaging;[1] this model employs effective parameters for thermodynamic equilibrium, such as capillary pressure and sorption isotherm, and for transport, such as absolute and relative permeabilities, diffusivity and thermal conductivity. All these parameters are functions of saturation and do strongly depend on pore structure. They may either be measured by independent experiments, or modeled from more fundamental structural information.

Discrete models of drying use a simplified geometry to represent the real pore space, such as a bundle of capillaries or a network of pores, and describe transport phenomena at the pore level. Depending on the complexity of the model, more or less structural information can be implemented. A bundle-of-capillaries geometry can only account for pore-size distribution, whereas pore networks can also account for spatial correlations of pore size, connectivity of pores, or pore shape. Such representative pore spaces can serve either to simulate the drying process directly or to compute effective parameter functions to be used in a continuous model. In this way, the influence of pore-size distribution on drying behavior has recently been studied for a bundle of capillaries, directly by a discrete model,[2] as well as via effective parameters in a continuous model.[3,4] This work aims to start similar investigations with the more versatile tool of pore networks.

Correspondence concerning this article should be addressed to T. Metzger at thomas.metzger@ovgu.de.

Since the early 1990s, pore network modeling has become increasingly popular in the field of drying. In most studies, only mass transfer is modeled, mainly as vapor diffusion in the gas phase and capillary flow in the liquid phase. The seemingly first work by Nowicki et al.[5] represents pore space by a network of biconical throats; liquid flow is subject to viscous effects. Drying is simulated for a representative network in order to compute effective parameters as used in the continuous approach.

One year later, Prat[6] proposed a network drying model with cylindrical pore throats, which is based on an invasion percolation algorithm; gravity is modeled, but viscous effects are neglected. This model is applied at the sample scale; accordingly, results are reported as phase distributions in the porous structure. Recently, an algorithm to include viscous effects in the liquid has been proposed for this model.[7,8]

A third network model has been presented by Yiotis et al.[9] who investigated drying of porous rock by purging gas through an adjacent fracture. The network is built from spherical pores that contain all pore volume; the connecting cylindrical throats only act as conductors and capillary barriers. Viscous effects are accounted for in both gas and liquid, but mainly play a role in the gas. Simulation results are presented as phase patterns and drying curves.

The latter two approaches have recently been extended to film effects,[10,11] which can produce a first drying period if pores have corners and wetting conditions are favorable. Drying experiments with etched networks could confirm the simulated phase distributions[12] and show the important role of film flow for drying rates.[13]

Due to computational limitations, three-dimensional (3-D) simulations are still rare and have only been presented for basic model versions, i.e., without viscous or film effects, to realistically analyze the drying curve with respect to percolation phenomena, such as disconnected cluster formation and breakthrough.[14,15] The role of lateral vapor transfer in the gas-side boundary layer in producing a first drying period has been pointed out in this context (see also Ref. 16).

Further investigations with model variants include evaporation of binary liquids[17] and influence of imposed thermal gradients;[18,19] only recently a network model accounting for heat transfer in convective drying has been proposed.[20]

Phase distributions during drying have been analyzed by invasion percolation concepts as proposed by Ref. 21 and Ref. 22; viscous effects will always stabilize the drying front, whereas gravity and temperature gradients can be stabilizing or destabilizing depending on their orientation with respect to the open side of the network. In any of these cases, the width of pore-size distribution plays a significant role since it defines the available pressure differences for capillary pumping.

This brief review shows that, step by step, more and more effects have been included into pore network models, so that an assessment of the continuous model is within reach. In this context, the network approach is seen as the more fundamental description. A major task is to investigate the range of validity of continuous concepts, e.g., the generalized Darcy law for two-phase flow might well describe a stabilized invasion, whereas it is difficult to imagine how it shall describe mass transfer near a percolation threshold, or when the liquid phase has split up into many disconnected clusters. If equivalence between discrete and continuous approach can be shown, representative pore networks may indeed serve to compute effective parameters. Furthermore, the stepwise approach illustrates the power of network modeling: the macroscopic effect of any pore-level transport phenomenon can be studied individually.

Besides this investigation of effects, network modeling can help to analyze the influence of pore space geometry and topology on drying behavior. The effect of pore shape has been studied with model versions accounting for corner films.[23,11] Investigation of the influence of pore-size distribution and pore structure has only been started recently by the authors.[24,16,8] Previously, only large-scale inhomogeneities of the porous medium were considered as structural effects influencing phase distributions.[25]

The objective of this work is to systematically study the influence of pore structure on drying behavior. First, the drying model of Prat is recalled, relevant transport phenomena in network and adjacent boundary layer are pointed out and aspects of the drying algorithm explained. In the next step, this model is applied to regular square pore networks (2-D) with mono- and bimodal pore-size distributions; several pore structures are studied for the same bimodal distribution by varying the spatial correlation of macropores. Simulation results are discussed on the basis of drying rate curves and liquid phase distributions. It is found that pore-size distribution and pore structure have a big effect on drying kinetics.

For further investigation, the Monte-Carlo method is introduced as an appropriate tool to compare results for different structural classes. With this method, drying behavior of regular 2-D networks of different coordination number is compared. A significant effect of this structural property on drying kinetics can be shown. All these 2-D simulations show that the major effect of structure on drying kinetics is by the disintegration of the liquid phase into separate clusters (resulting in interruption of capillary flow), which depends on coordination number and spatial correlation of pore sizes.

In the last section, the computationally more demanding simulation of three-dimensional networks is addressed, again by comparing drying behavior (drying curves and moisture profiles) for different pore-size distributions and coordination numbers. These Monte-Carlo simulations confirm the previous 2-D findings. Finally, the influence of porous medium thickness is studied, and the importance of boundary layer modeling is demonstrated for the 3-D geometry.

Pore Network Drying Model

Throughout this article, we consider the drying process as isothermal which is a reasonable approximation only for moderate drying conditions. Pore size is always chosen big enough so that viscosity, Kelvin and Knudsen effects are negligible; film effects are not relevant for the chosen cylindrical geometry of pore throats. Gravity could be easily modeled, but is deliberately set to zero to simplify the analysis of phenomena. Furthermore, we restrict our investigations to capillary porous media and model only free water, not adsorbed water. These strong assumptions are valid only for a limited range of materials and drying conditions, but such a restriction is justified since our major interest is in the role of structural influences; the use of a simple algorithm allows

investigating the problem by the appropriate, but time-consuming Monte-Carlo method.

In this section, we discuss the main elements of the drying algorithm as introduced by Prat[6] pointing out recent developments; a more detailed description is given in Ref. 26.

Pore network and gas-side boundary layer

The porous medium is represented by a network of pore nodes (without volume) that are connected by cylindrical pore throats of random radius; the solid phase need not be modeled for isothermal conditions. We restrict ourselves to regular networks of constant coordination number, but go beyond previous work that used only square or cubic networks. In all simulations, the network is initially saturated with water; then, water is removed by convective drying through the top side of the network. In horizontal direction(s), periodic boundary conditions are applied; the network bottom is impermeable. Figure 1 shows part of a partially dried 2-D square network with mono-modal throat radius distribution. Because of the random spatial distribution, capillary flow from large to small throats and liquid cluster formation are random processes as well.

Throughout this article, we use normal number distributions to generate throat radii. Monomodal networks are characterized by mean and standard deviation of radius; for bimodal distributions, the volume fraction of the two normal modes must additionally be given.

Drying rate depends on the liquid-phase distribution in the network and vapor diffusion through empty network regions and gas-side boundary layer. Traditionally, boundary-layer vapor transfer has been described for each surface pore by a mass-transfer coefficient β that can be obtained from dimensionless correlations. This will induce a sharp decrease in the drying rate as soon as the first surface throats dry out, leading to a drying rate roughly proportional to surface saturation. More recently, lateral vapor diffusion in the boundary layer is included into modeling[16,15] by extending the discrete network of pore nodes into the gas by boundary-layer thickness $s = \delta/\beta$ where δ is vapor diffusivity (see Figure 2). This phenomenon is seen as a major reason for the occurrence of an extended constant rate drying period.[27] Another explanation is by film flow in gas-filled throats that can transport liquid to the network surface and keep it sufficiently wet; but this effect is negligible for pores without corners.

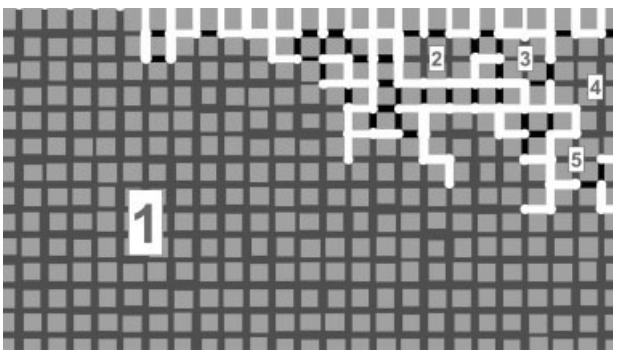

Figure 1. Part of pore network with monomodal throat-size distribution during convective drying by the top.

Empty throats are in white, liquid throats belonging to a cluster in dark gray (with respective cluster label), and single liquid throats in black.

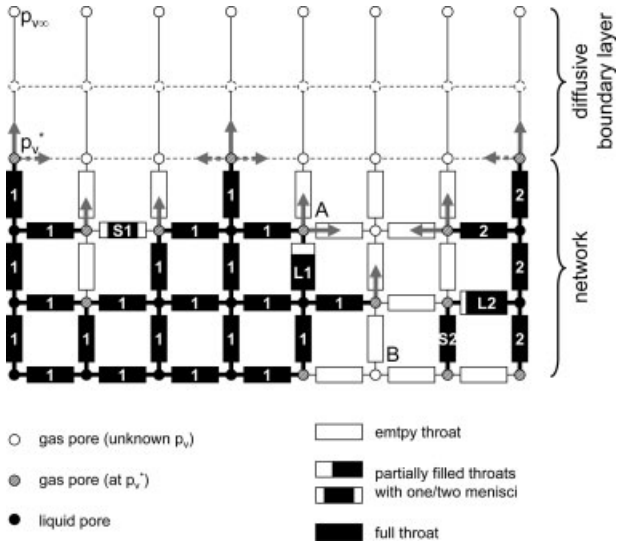

Figure 2. Example of a small partially dried pore network with discretized boundary layer to describe vapor transfer under convective drying conditions.

Boundary conditions for vapor diffusion are given, and resulting vapor flows are sketched at the liquid-gas interface (gray arrows), indicating the enhancement due to lateral diffusion in the boundary layer (dashed arrows). The liquid phase consists of two separate clusters, in either of which only the largest meniscus throat is emptying (L1 and L2), and two single throats (S1 and S2).

Vapor diffusion and capillary pumping

Since gas is the invading phase, it stays continuous, whereas the liquid typically splits up into numerous clusters. Mass transfer is controlled by vapor diffusion in the gas-filled part of the network and capillary pumping in liquid-filled regions. As capillary forces are assumed dominant over viscous forces, only the largest meniscus throat in a cluster will empty at a time, while water is pumped to all other meniscus throats at their respective evaporation rates, so that their menisci remain stationary. Local evaporation rates are computed from mass balances in the gas phase describing vapor diffusion as a quasi-steady process during the emptying of one throat

$$\sum_j \dot{M}_{v,ij} = \sum_j A_{ij} \frac{\delta}{L} \frac{p\tilde{M}_v}{\tilde{RT}} \cdot \ln\left(\frac{p - p_{v,i}}{p - p_{v,j}}\right) = 0 \qquad (1)$$

The mass flow rate $\dot{M}_{v,ij}$ between two gas pores i and j, which are connected by an empty throat, is computed from its length L and cross-sectional area

$$A_{ij} = \begin{cases} \pi r_{ij}^2 & \text{in network} \\ L^2 & \text{in boundary layer} \end{cases}, \qquad (2)$$

total pressure p, molar mass of vapor $\tilde{M}_v$, ideal gas constant R, absolute temperature T, and partial vapor pressures $p_{v,i}$ and $p_{v,j}$, respectively. Here, the logarithmic law describes combined vapor diffusion and (nonviscous) gas convection next to an evaporating liquid-gas interface. Boundary conditions to Eq. 1 are given by vapor pressure of drying air $p_{v\infty}$ at the far end of the boundary layer, and by assuming equilibrium vapor pressure p_v^* in pores next to a (partially) filled throat as indicated in Figure 2. There, an example is given of a small partially saturated network with two liquid clusters and two single liquid throats; evaporation is shown by gray arrows. If several menisci are neighbor to a pore (A), total vapor flow away from this pore is distributed to them according to their cross-sections in order to obtain local evaporation rates. Note that, in the depth of the network, whole gas regions (B) can be at equilibrium vapor pressure if surrounded by menisci (then nonevaporating). At any time, largest cluster menisci (L1 and L2), as well as single liquid throats (S1 and S2), are candidates for emptying. If ideal capillary pumping within each liquid cluster is assumed, timescale and order of invasion are only given by the respective cluster sums of local evaporation rates. (Individual clusters can be temporarily trapped, such as single liquid throat S2.) It, is, therefore, crucial to correctly track cluster affiliation of liquid throats during drying.

Cluster labeling

Initially, all throats are liquid-filled and belong to the same cluster (with label 1). In each time step, normally only one throat is emptied completely. If this throat belongs to a liquid cluster, a neighboring pore is also emptied leading to local separation of liquid throats by creation of new menisci. Therefore, we must check if the former throat members of this cluster are still connected by other capillary flow paths, or if the cluster has split up into separate clusters or single throats; in the latter case, relabeling is necessary. Since single throats do not participate in capillary flow, they get no throat label.

For relabeling, it is suitable to use a variant of the Hoshen-Kopelman algorithm[28,29] that starts at the emptied throat and is restricted to the corresponding cluster. The principle of the Hoshen-Kopelman algorithm is to scan the liquid throats one by one, check each time for already labeled neighboring liquid throats (connected by a liquid pore) and store information about labels that are found to be identical; only after scanning, labels will be corrected. If suitable stopping criteria are defined, the scanning can usually be limited to a small number of throats; this is explained in the following by help of Figure 3.

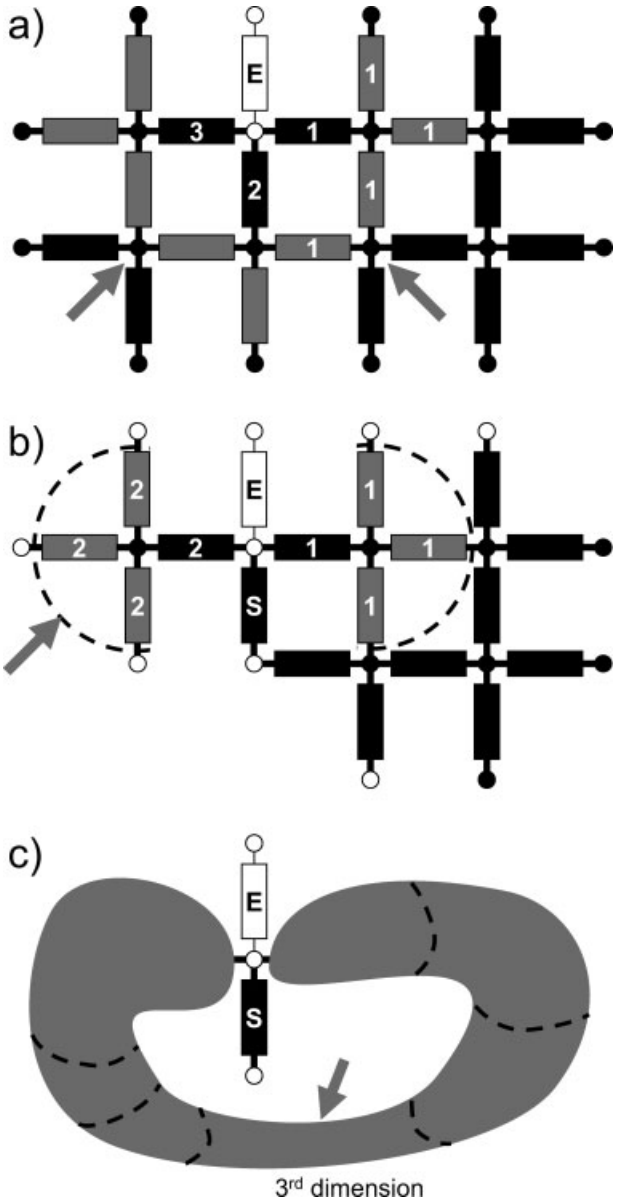

Figure 3. Relabeling of liquid throats adjacent to the throat emptied in last time step (E).

(a) After first throat is emptied, (b) situation as in upper righthand corner of Figure 1 and (c) case of a far-end connection of locally separated liquid regions (dashed lines indicate the successive generations scanned by the Hoshen-Kopelman algorithm, gray arrows show when the algorithm stops; more explanations are given in the text).

After emptying of the first surface throat (a), all liquid throats are still connected, but in the general case, this must be checked. The algorithm starts by attributing different labels to all former neighbors of the emptied throat (except single liquid throats). Then, consecutive generations of connected liquid neighbor throats are identified; these generations are labeled one after the other by the method of Hoshen-Kopelman, always attributing to a throat the minimum label already existing among direct neighbors, and storing information about identical labels. In our example, all new labels are in fact identical; the arrows indicate that this can be known after labeling the first generation. In general, several generations—and, in the worst case, all throats of the old cluster—must be scanned before the new cluster topology is known.

In practice, the algorithm may stop if all members of a new generation have been given the same label. This can have two reasons: either all except one of the newly created clusters are completely labeled or all remaining different clusters are found to be connected. An example of the first

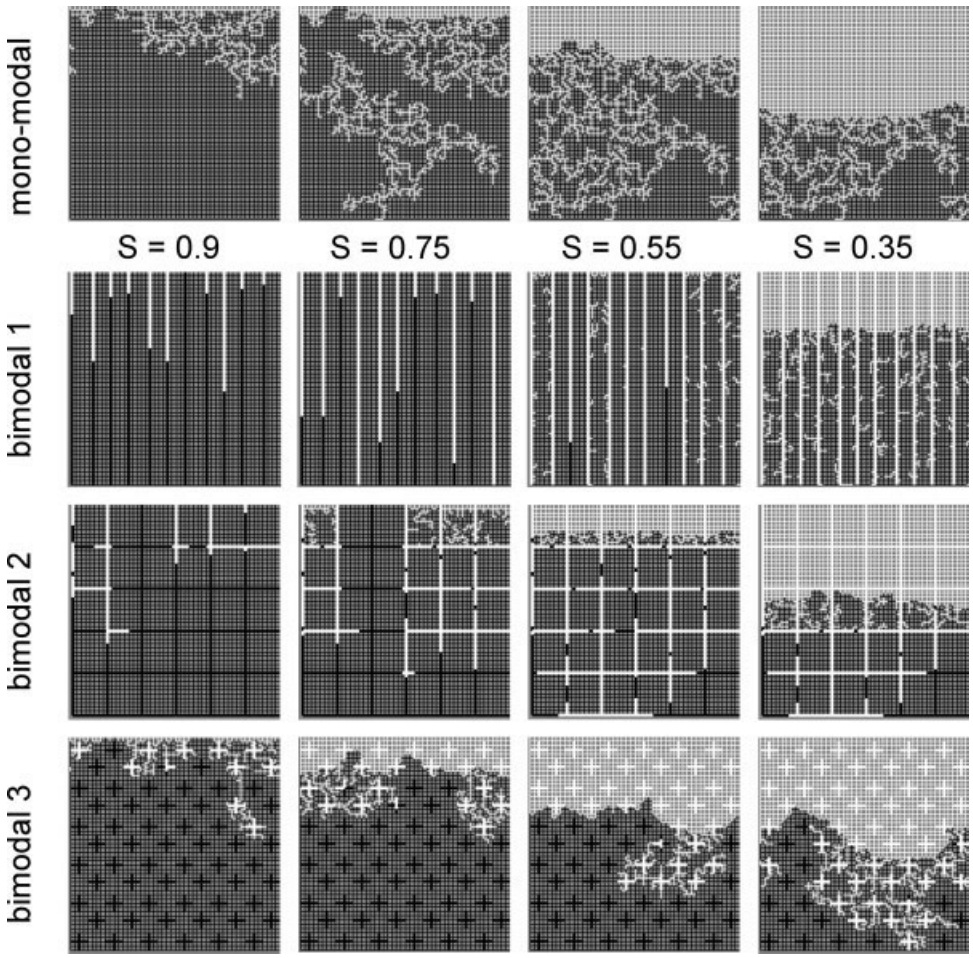

Figure 4. Drying behavior of 2-D networks with different pore structures: the first network has a monomodal pore-size distribution; the others have (almost) the same bimodal pore-size distribution, but different spatial distributions of small and large pores.

Phase distributions are shown for the indicated network saturations. (Liquid-filled throats are in black, empty throats in white.)

condition is shown in Figure 3b (situation as in the upper righthand corner of Figure 1) where cluster 2 has been scanned completely, and all further generations must, therefore, belong to cluster 1. The second condition has simple examples (such as in Figure 3a), but also nontrivial ones, such as liquid loops providing far-end connections occurring in three-dimensions (Figure 3c).

After scanning, these intermediate labels are updated, and only if new clusters have been created, the old cluster labels need to be shifted to accommodate them.

2-D Pore Networks

The aforementioned drying model is applied to a range of pore networks starting with 2-D ones. The first focus is on the role of macrothroats and their spatial correlation for drying behavior. Then, Monte-Carlo simulations are carried out, and an appropriate average presentation is chosen to compare behavior of different network classes, and to dispose of random variations between representatives of one class. With this method, we investigate the influence of coordination number for mono- and bimodal networks.

Influence of pore-size distribution

The first drying simulation is for a square 48 × 51 network, with throat length 500 μm and monomodal radius distribution of mean 40 μm, and standard deviation 2 μm. Drying air with zero moisture is at 20°C and atmospheric pressure; the boundary layer has 10 vertical nodes corresponding to a mass-transfer coefficient of 5.1 mm/s. The first line of Figure 4 shows phase distributions at the indicated network saturations (remember horizontal periodicity). The dimensionless drying rate curve is plotted in Figure 5 (solid line); the initial evaporation flux for a completely wet network surface is 0.32 kg/m^{2}h.

One can see that most of the surface rapidly dries out. This is accompanied by a drastic decrease in drying rate; a first drying period of constant rate is not observed. Due to an uncorrelated radius distribution, capillary pumping is a random process. Quasi-constant rate periods, random in start

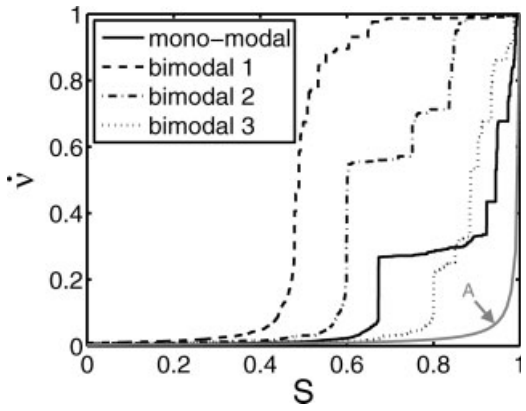

Figure 5. Normalized drying rate versus network saturation for the two-dimensional networks depicted in Figure 4.

The result for a sharply receding drying front, i.e., with no capillary pumping, is shown as curve A (for the monomodal network).

and duration, are observed, e.g., around network saturation S = 0.75, when inner-network throats are invaded, but near surface saturation, which controls mass transfer to bulk air, stays unchanged. When a zone of disconnected liquid clusters has formed, capillary pumping looses its importance and surface dries out completely (for 2-D simulations, this zone does not always span the whole network). The disconnected clusters dry out one by one, with a receding evaporation front. Soon we will see that in networks with a bimodal pore-size distribution, capillary flow can significantly enhance drying rates; but even in the unfavorable monomodal case, capillary pumping plays an important role as shows a comparison with the simulation with immobile water — and, therefore, a sharp drying front (see solid line in Figure 5 in contrast to curve A). A systematic investigation of this capillary enhancement effect has recently been presented by Chapuis and Prat.[30]

Many real porous media have a bimodal pore-size distribution; therefore, corresponding networks are generated by rescaling some throat radii to 100 ± 5 μm. As can be seen from Figure 4, these macro throats are spatially correlated in three different ways, as:

1. long channels perpendicular to network surface, so that the two "phases" of micropores and macropores are continuous (note that strict continuity cannot be achieved in 2-D);
2. long channels in both space directions, so that only the macropore phase is continuous, and we obtain a simple representation of an agglomerate of microporous particles;
3. regularly distributed small clusters—representing isolated "macro pores"—so that only micropores form a continuous phase.

All three structures have about the same volume fraction of macropores (0.447, 0.442 and 0.436, respectively); hence, their macroscopic properties porosity and pore-size distribution are similar. Their drying behavior under the same drying conditions as for the monomodal network is presented in Figures 4 and 5.

For the *first* structure, a long first drying period is observed during which the macrochannels empty, and liquid is pumped to the surface by the microthroats. The initial drying rate is maintained because of a good spatial distribution of wet surface throats, and lateral vapor transfer in the boundary layer. When almost all macrothroats are empty, disconnected clusters of microthroats develop (at S = 0.55) leading to drying out of whole surface regions and a drop in drying rate (see Figure 5). When no liquid is left in macrochannels, preferential capillary pumping stops and eventually disconnected clusters evaporate with a receding front.

The examples of the other two pore structures show that both micro- and macropores must constitute continuous phases for efficient drying. In the *second* bimodal structure, random emptying of horizontal macrochannels stops capillary flow to whole surface regions at an early stage ($S \geq 0.75$ in Figure 4), resulting in a short first drying period ($S > 0.9$ in Figure 5). In fact, the grid of macrochannels favors formation of clusters, which have small size and contain only microthroats so that capillary pumping plays a minor role, and the network dries out more or less layer by layer ($S \leq 0.55$ in Figure 4). The random disconnection and drying out of microporous regions is indeed quite similar to that of single throats in the monomodal network, only the respective length scales and timescales are larger.

Drying behavior of the *third* bimodal network structure is still closer to the monomodal case: here the randomness of throat emptying is only overruled for a short time when the gas-liquid interface reaches a macropore which is then first emptied completely (S = 0.9 in Figure 4). The presence of macrothroats does not dramatically influence drying efficiency (compare solid line and dotted line in Figure 5) since capillary pumping remains a random effect.

In conclusion, it shall be stressed that pore-size distribution does not sufficiently characterize a porous medium with respect to its drying behavior, but that spatial correlations of pore size are crucial: bimodal structures with unfavorable (or none at all) spatial correlation will behave similarly as monomodal ones. For the presented model, width of pore-size distribution plays a minor role: in the absence of pressure or temperature gradients, invasion order is dominated by relative size differences; and absolute throat size mainly affects evaporation rates. If gravitational, viscous or thermal effects are modeled, their influence will typically be significant when throats of similar size compete for liquid,[19] i.e., for monomodal networks or for bimodal networks at low saturations.

Monte-Carlo simulations

Previously, only one representative of each network structure was discussed. Naturally, the randomness of network generation will reflect in drying behavior, and different representatives of one class may have quite different drying curves. By performing 100 Monte-Carlo simulations per class, and looking at average behavior and random distributions, we will now assess this randomness to find out characteristic features of each class. The randomness of drying behavior for square monomodal networks has recently been studied by looking at the distributions of drying curves (saturation over time) and drying times.[30] The drying time distri-

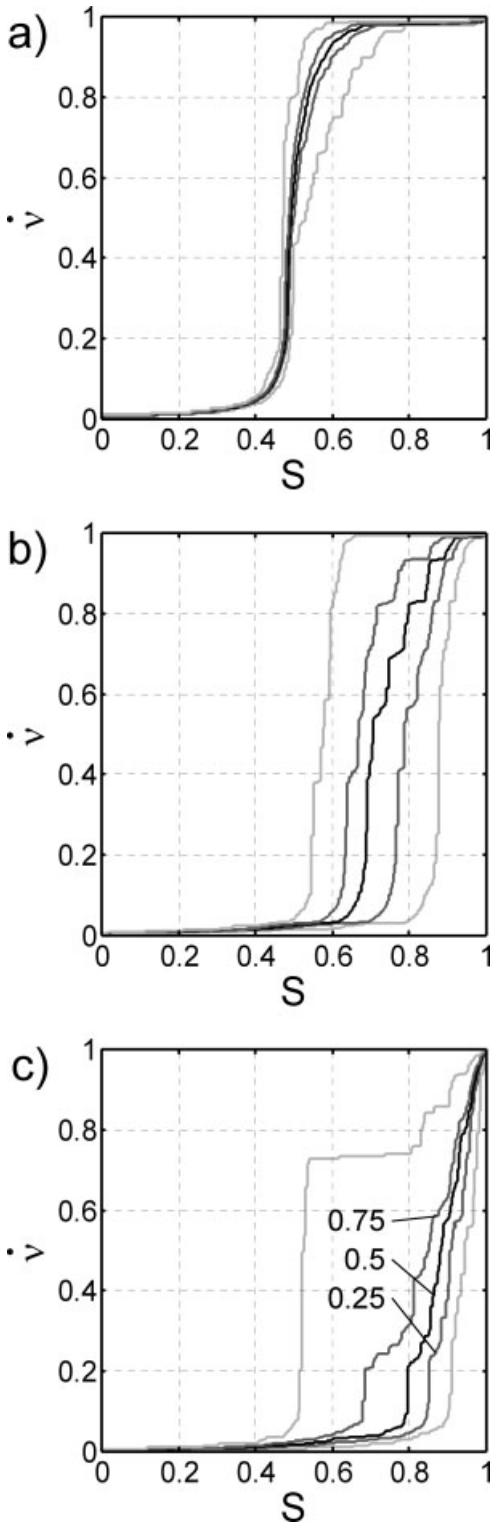

Figure 6. Drying rate curves for 2-D bimodal networks.

Normalized drying rate is plotted vs. network saturation (at 0.25 levels of cumulative distribution for 100 MC runs): (a) structure 1, (b) structure 2, and (c) structure 3. For representatives of these structures refer to Figure 4.

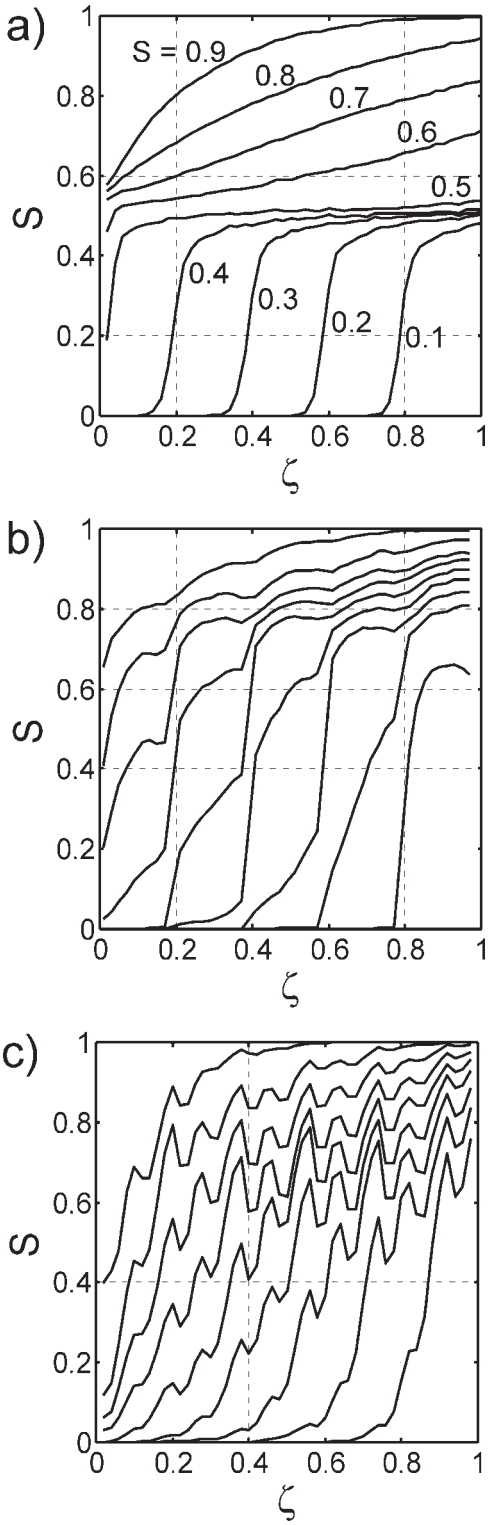

Figure 7. Saturation profiles during drying for 2-D bimodal networks.

Slice-averaged saturation is plotted vs. normalized network depth ζ as the average of 100 MC runs, for multiples of 0.1 in network saturation: (a) structure 1, (b) structure 2, and (c) structure 3. For representatives of these structures see Figure 4.

bution was found to be nearly Gaussian; dependencies on network size, and the role of film effects were also investigated. In this work, we inspect drying rate curves (drying

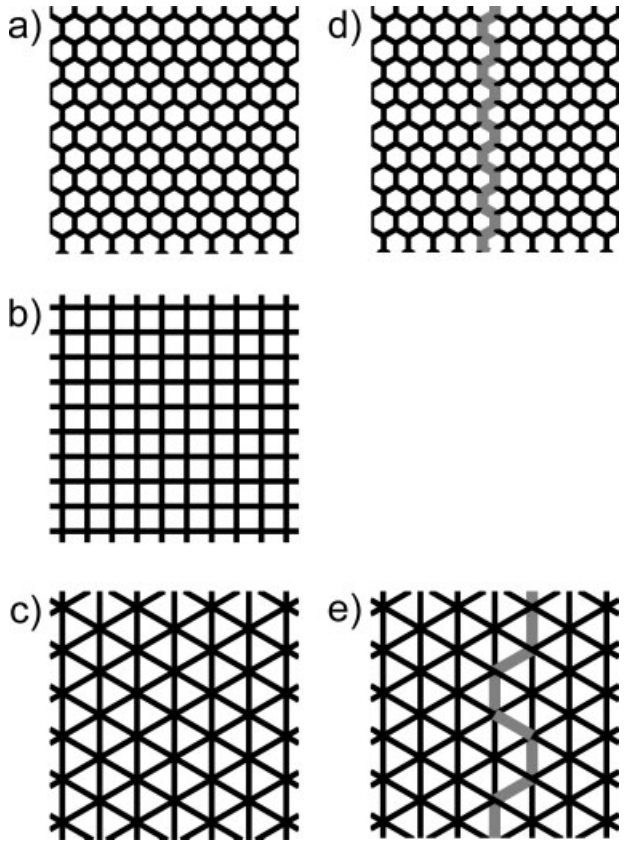

Figure 8. Representations of 2-D networks of different coordination number (a) Z = 3, (b) Z = 4 and (c) Z = 6 with monomodal pore-size distribution, as well as bimodal realizations (d), and (e) with macropore throats in gray.

rate over saturation), believing that they better reveal drying information, and accordingly choose network saturation as a variable to compute distributions of drying rate, as well as average moisture profiles.

In order to plot the distributions of drying rates, as in Figures 6a–c and 9b for the mentioned bimodal and monomodal networks, the following procedure is applied: for a given network saturation (small interval), the Monte-Carlo drying rates are combined to a cumulative frequency distribution. The light gray lines give the envelope of all 100 drying rate curves; the dark gray and black lines show 0.25 levels of the normalized cumulative distributions. (Note that an individual drying curve, as in Figure 5, may be quite different.) Corresponding averaged saturation profiles are plotted against normalized network depth ζ in Figures 7 and 10b.

Drying curves of the first bimodal structure (Figure 6a) show little variation owing to the favorable correlation of pore space; average saturation profiles (Figure 7a) are first getting progressively flatter during the emptying of macrochannels down to a saturation of approximately 0.5, and only then a relatively sharp front recedes.

For the monomodal structure (Figure 10b), and the other bimodal structures (Figures 7b–c), such two distinct periods do not exist. The respective saturation profiles show that, at *local* saturations higher than 0.7, gas can penetrate into the depth of the network at a relatively low gradient, whereas at lower saturations (i.e., at the drying front) a larger saturation gradient is observed. Certainly, the regular pore structure (of the bimodal networks) is reflected in the average saturation profiles: as separated microporous zones in structure 2 (Figure 7b), or as macropores, which have higher probability to empty in structure 3 (Figure 7c). At a larger scale, however, a resemblance between the saturation profiles of bimodal structures 2 and 3, and those of the monomodal structure (Figure 10b) can be stated.

Analyzing drying curve distributions, it can be seen that drying rate decreases rapidly for the monomodal network (Figure 9b). For bimodal structure 3, a small overall enhancement due to the macropores can be noted (e.g., compare drying rates at $S = 0.8$ in Figures 6c and 9b). Bimodal structure 2 shows a short first drying period (for $S < 0.9$ in Figure 6b) because of temporarily enhanced capillary flow to network surface. Here, the distribution of drying curves is relatively wide, because the random emptying of a few macrothroats decides on the drying out of whole microporous surface regions (this "amplifying effect" has already been mentioned in the previous section).

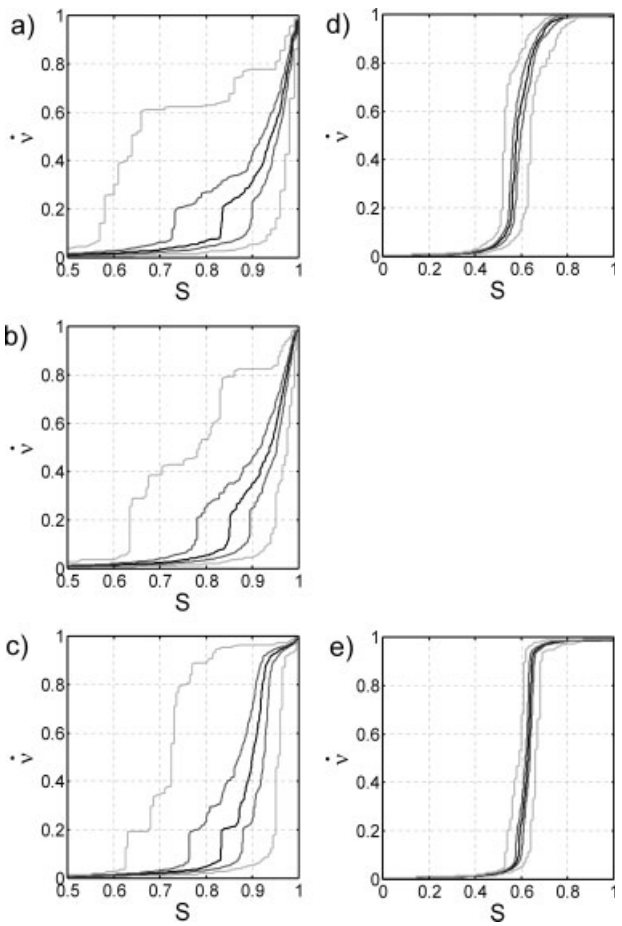

Figure 9. Drying rate curves of the 2-D networks sketched in Figure 8.

Normalized drying rate is plotted vs. network saturation, at 0.25 levels of cumulative distribution for 100 MC runs.

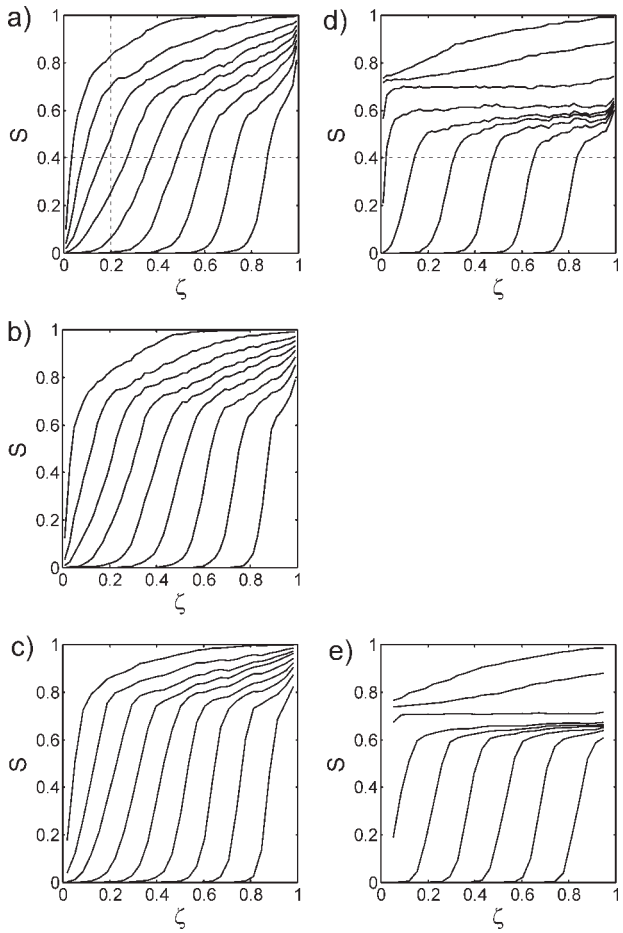

Figure 10. Saturation profiles during drying for the 2-D networks sketched in Figure 8.

Slice-averaged saturation is plotted versus normalized network depth ζ as the average of 100 MC runs, for multiples of 0.1 in network saturation.

Influence of coordination number

After investigating the influence of macrothroats, interconnectivity of pores shall now be varied. Regular monomodal networks of different coordination number Z were generated to this purpose by arranging throats in hexagons and triangles as seen in Figure 8a–c. Care was taken that porosity (defined as throat volume per area) is unchanged, and outer network dimensions are almost the same as for the square network. Consequently, throat length had to be adjusted to 289 μm for $Z = 3$ (Figure 8a) and 866 μm for $Z = 6$ (Figure 8c); the networks consist of 8,352 and 2,784 throats, respectively, as compared to 4,800 in the square case. (Radius distribution and drying conditions are unchanged.)

Cumulative distributions of drying curves and average saturation profiles for 100 Monte-Carlo simulations are shown in Figure 9a–c and 10a–c, respectively. Although overall drying behavior has the same features for all three coordination numbers, there are significant quantitative differences. The following trends can be observed: for *lower* Z, initial saturation gradients in the depth of the network are steeper, surface dries out at lower network saturations, and the receding drying front is smoother (compare Figure 10a–c); consequently, drying rate drops more drastically at the beginning (see Figure 9a at $S > 0.9$), but then may stay elevated down to lower saturations ($S < 0.8$).

It is difficult to explain these observations, and at present only possible reasons can be given. Of course, coordination number itself plays a crucial role in terms of liquid connectivity: for each liquid pore, the emptying of the first neighbor throat cuts off capillary flow between the remaining $Z - 1$ liquid throats. Throat length should be of importance as well, since it constitutes the smallest indivisible unit for liquid flow. At last, the very different initial behavior of drying rates for $Z = 6$ (see Figure 9c at $S > 0.9$) suggests that density, spatial distribution and orientation of throats at the network surface have an influence (confer to Figure 8a–c). In fact, if several throats are connected to a surface node (Figure 8c), this node and its neighborhood are assumed saturated (for discrete modeling of boundary layer), as long as one of the throats contains liquid. Therefore, the fraction of surface, which is considered to be wet, may be higher than the saturation of surface throats. Such surface effects ought to lose importance for a larger network size.

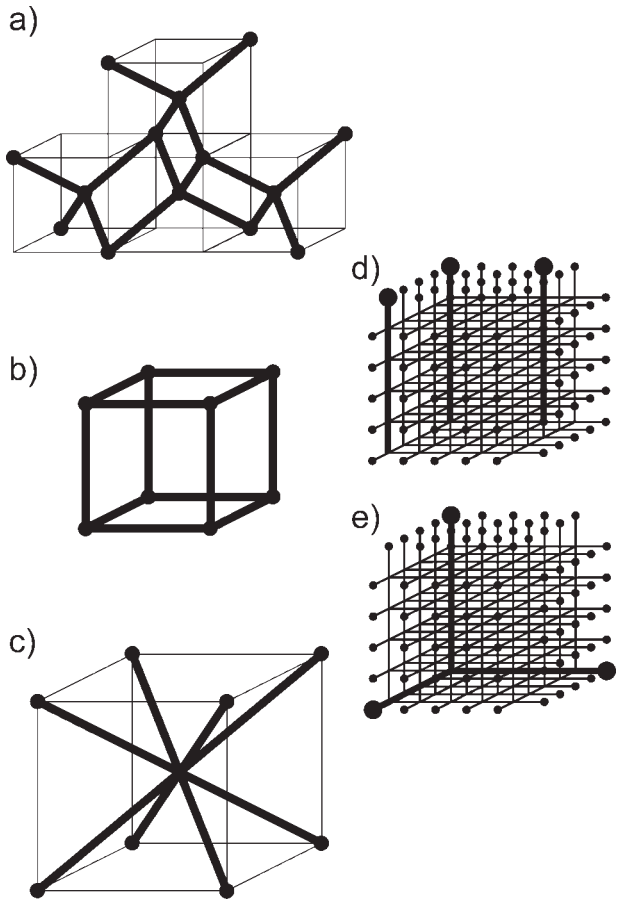

Figure 11. Representations of 3-D network structures of different coordination number (a) Z = 4, (b) Z = 6, and (c) Z = 8, and with macrochannels (d) and (e).

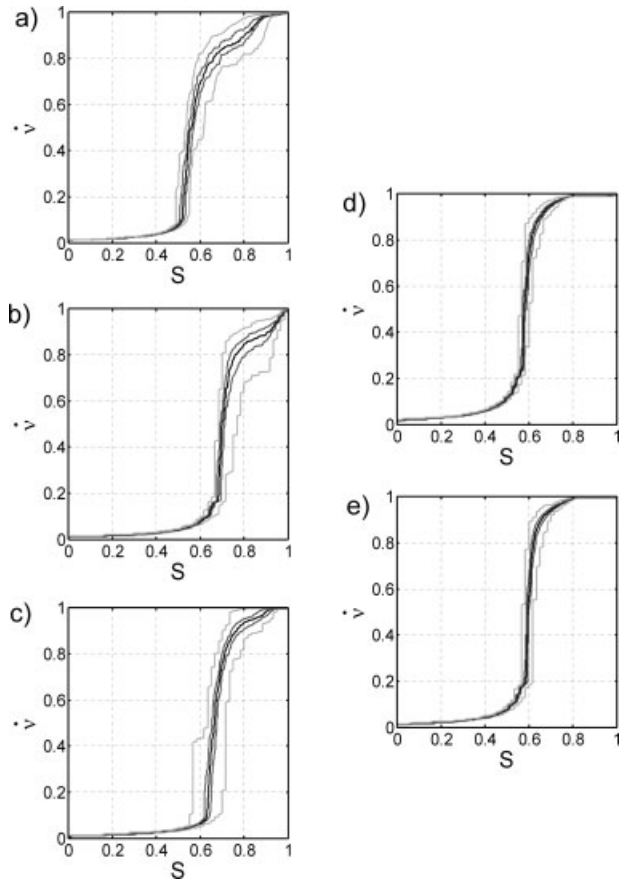

Figure 12. Normalized drying rate vs. network saturation for the 3-D networks as seen in Figure 11 (shown as 0.25 levels of cumulative distribution of MC simulations).

Drying of bimodal networks of coordination numbers Z = 3 and Z = 6 was also simulated; to this purpose, four macro channels (gray in Figure 8d and 8e) were introduced as described previously for Z = 4, in both cases having the same tortuosity and accounting for 0.281 of the total pore volume. A comparison of drying rate curves (Figures 9d–e), as well as saturation profiles (Figures 10d–e) shows that the process becomes dependent on the coordination number only after the macrochannels have emptied, i.e., at $S \approx 0.7$. Then, for *low*er Z, the decrease in drying rate starts earlier, but is less steep (Figures 9d and e); and more water can be removed before the evaporation front eventually recedes (for $S < 0.6$ in Figure 10d, for $S > 0.6$ in Figure 10e). The saturation gradient at this front is the same for both cases.

3-D Pore Networks

In this section, the aforementioned investigations are extended to 3-D networks. In three-dimensions, capillary flow paths can more easily be maintained so that a different drying behavior is found.[14] Due to computational limitations, only few 3-D network simulations can be found in literature,[14,15,23] and for large networks, only single network realizations have been investigated.[14,15] In the previous section, we recognized the need for Monte-Carlo simulations; therefore, we choose a network size that allows for a sufficient number of realizations. A periodic cubic 15 × 15 × 16 network (Z = 6), built of 10,125 throats with length 500 μm, serves as reference; for lower coordination number (Z = 4), 16,000 throats of length 329 μm are arranged as tetrahedra; a higher coordination number (Z = 8) is achieved by building octahedra of 8,000 throats (L = 658 μm). All networks have identical porosity (0.060), and approximately the same outer dimensions. To study the influence of a bimodal pore-size distribution, two different arrangements of macrochannels (accounting for a pore-volume fraction of 0.207) are realized for the cubic network. Part of each network is illustrated in Figure 11. For each network, 50 MC simulations were run, except for Z = 4, where only 25 networks were simulated. Drying conditions were chosen as in the 2-D case. Simulation results are again presented as cumulative distributions of all drying rate curves (Figure 12), and averaged saturation profiles (Figure 13).

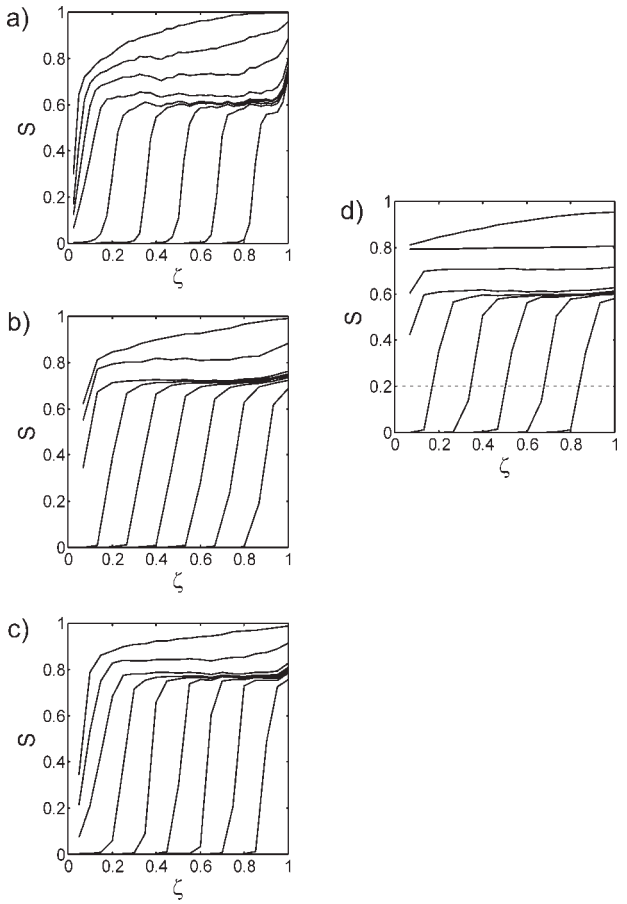

Figure 13. Saturation profiles during drying for 3-D networks of Figure 11; slice-averaged saturation vs. normalized network depth is plotted as the average of MC simulations, for multiples of 0.1 in network saturation.

Influence of coordination number

We start our discussion with the cubic monomodal network (Figures 12b and 13b): a fundamental difference to the 2-D case is that gas can penetrate into the depth of the network, while the so-called main liquid cluster remains connected to network surface, and drying rate stays relatively elevated, although not at the initial value. The formation of disconnected clusters occurs throughout the network at almost uniform saturation, and only then the evaporation front recedes. These characteristics are independent of network size; only the saturation level, at which the front starts to recede, is expected to be lower for larger networks.[14,15]

The saturation profiles (Figure 13b) are similar to those of the bimodal 2-D network with macrochannels perpendicular to network surface (Figure 7a). There, the higher number and ideal spatial distribution of liquid surface throats could produce a true first drying period (see Figure 6a at $S > 0.7$). In contrast, dimensionless drying rate for the 3-D monomodal network drops to $\dot{v} \approx 0.85$ and stays almost constant for $0.95 > S > 0.75$ (Figure 12b); this value of $\dot{v}$ could be raised to unity by increasing boundary-layer thickness.

From the saturation profiles (Figures 13a–c), the following major effect of coordination number can be stated: the *lower* Z, the lower is the saturation level down to which liquid can be removed before the surface dries out completely (as in 2-D). The corresponding drying rate curves (Figures 12a–c) suggest that the surface effects, as discussed in 2-D, play a role in producing higher drying rates and even short first drying periods for the noncubic structures $Z = 4$ and $Z = 8$ (for $S > 0.9$). In three-dimensions, however, surface effects are not expected to disappear with increasing network size, because surface saturation may stay constant during invasion of inner network regions (see discussion later on).

To summarize, we found that, for regular networks of identical porosity, a variation of coordination number has a significant effect on drying behavior. At *lower* coordination number (associated with a shorter throat length), both 2- and 3-D networks could more easily be invaded by the gas (see flatter saturation profiles in Figures 9a–c, and lower saturation level when front recedes in Figure 13a–c). The effect on drying rate is more pronounced in three-dimensions; here, higher rates could be achieved for *lower* coordination number (see Figures 12 a and c).

Influence of pore-size distribution

Based on the 2-D findings, the investigation of bimodal networks is restricted to cubic networks and spatial correlations of macrothroats for which significant changes in drying behavior may be expected. Figures 11d–e show the investigated cases, for both of which liquid-filled microthroats form a continuous phase independent of the filling of macrochannels. Consequently, the drying rate curves in Figures 12d–e show first drying periods ($S > 0.8$) during which all macrothroats are emptied. The orientation of macrochannels has almost no influence on drying rates. Saturation profiles are only plotted for the first case (Figure 13d), because those for the second case have great artifacts due to empty horizontal macrochannels. They show that 40% of liquid can be removed at flat saturation gradients, although only 20% are contained in macrothroats.

Note that for these bimodal networks, like in 2-D, the wet surface spots are more numerous and better spatially distributed than in the monomodal case. In such a way, the presence of macrothroats can enhance drying rates.

Influence of porous medium thickness

In the following, attention is given to network depth; to this purpose, one cubic $15 \times 15 \times 51$ network is generated and decorated with a mono- and bimodal throat radius distribution (as before, see Figures 11b and e). For both structures, drying is first simulated for the entire network, then for the top 31 pore levels, and for the top 16 pore levels. In this way, the surface region remains identical and we can easily investigate the influence of network depth. The results are shown as drying curves in Figure 14, and as saturation profiles for the monomodal case in Figure 15 (network depth z is normalized by throat length L).

Drying behavior of the bimodal structure shows little dependence on network depth. Macrothroats dry out first in any case, and only when the evaporation front recedes, the drying curves diverge because of different distances contributing to mass-transfer resistance (see Figure 14 for $S < 0.6$). Naturally, thinner networks can produce higher drying rates.

The monomodal structure shows initially diverging drying rates if plotted against saturation (see Figure 14 for $S > 0.8$); but if evaporated liquid is used as abscissa, the curves coincide in this region (see circle in inserted figure). In fact, surface saturation only changes up to a critical evaporated mass, before gas penetrates into network depth at constant surface state and drying rate. During this stage, liquid is removed to a uniform level throughout the network ($S \approx 0.75$; see Figure 15) and drying rate curves, as plotted upon saturation (Figure 14), will converge again at that saturation. When the evaporation front recedes, drying curves behave as in the bimodal case.

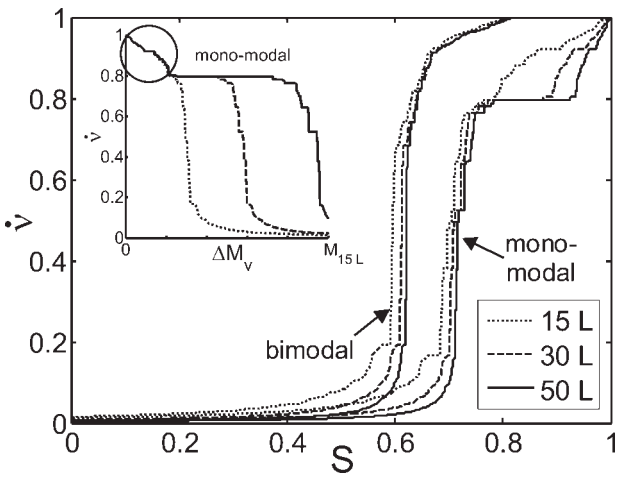

Figure 14. Drying rate curves for the same cubic network with different "active" depth.

Normalized drying rate is plotted vs. network saturation or, in the inserted figure, against mass of evaporated liquid ΔM_v (here, M_{15L} corresponds to the liquid mass contained in the first 15 layers of the network).

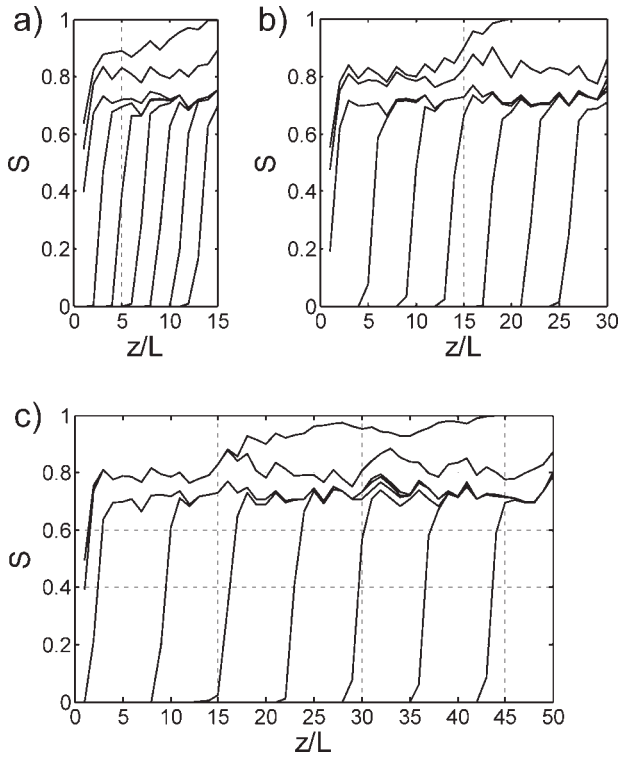

Figure 15. Saturation profiles for the same monomodal cubic network with different "active" depth.

Slice-averaged saturation is plotted vs. dimensionless network depth (for multiples of 0.1 in network saturation).

In conclusion, it may be stated that network depth plays a minor role in the absence of effects that can lead to a stabilization of the drying front, e.g., liquid viscosity.

Influence of boundary layer modeling

At last, we assess the role of lateral vapor transfer in the gas-side boundary layer for the occurrence of a first drying period. Drying of cubic networks ($15 \times 15 \times 16$) of mono- and bimodal throat radius distribution is first simulated with the model described in this work; then, lateral vapor diffusion in the boundary layer is suppressed which corresponds to the use of a mass-transfer coefficient (as was common in literature work for a long time). The major effect, shown in Figure 16, is on drying rates, not on phase distributions. A monomodal structure can only maintain a drying rate close to the initial value if the boundary layer allows for lateral mass transfer. Similarly, the first drying period of the bimodal network can be prolonged.

Conclusion

This investigation assumes that a major influence of structure on drying behavior is by capillary effects, and by how the emptying of individual pores affects the continuity of the liquid phase. Other effects like gravity, viscosity or temperature gradients may enhance or more often reduce capillary pumping. Accordingly, a pore network drying model has been used that combines nonviscous capillary flow with diffusive vapor transport. This model has been applied to a range of 2- and 3-D networks representing different pore structures: networks with a monomodal pore-size distribution, and different coordination number and bimodal networks, with different spatial correlations of micro- and macropores. For a good comparison of the drying behavior of different structures, Monte-Carlo simulations were run, and the results plotted as drying curve distributions and averaged saturation profiles.

It was found that pore space connectivity has an influence on drying: networks with lower coordination number (and smaller throat length), showed more favorable drying kinetics. A bigger enhancement effect of capillary pumping can be achieved for bimodal pore size distributions. In this case, microporous regions and macrochannels must form continuous "phases", otherwise, sustained capillary flow from large inner-network pores to small surface pores cannot be guaranteed. This study shows clearly that pore size distribution is no sufficient information but that connectivity and spatial correlations of pore size play an important role.

Furthermore, the role of network depth has been investigated. It was found that in the absence of gradients (due to gravity, liquid viscosity or heat transfer), which could stabilize or destabilize the drying front, network depth has little effect on drying behavior. Only at lower saturations, when the evaporation front starts to recede, thicker networks have lower drying rates due to a higher overall mass-transfer resistance. At last, different model versions for mass transfer through the gas-side boundary layer have been compared; here, the importance of lateral vapor transfer for a constant drying period has been pointed out.

Further investigations are recommended in the context of pore connectivity to better understand the influence of throat length as well as the role of density and orientation of surface throats. Certainly, the presented approach can easily be extended to pore networks with random pore node locations, randomly established throat connections and random spatial correlations of throat radius.

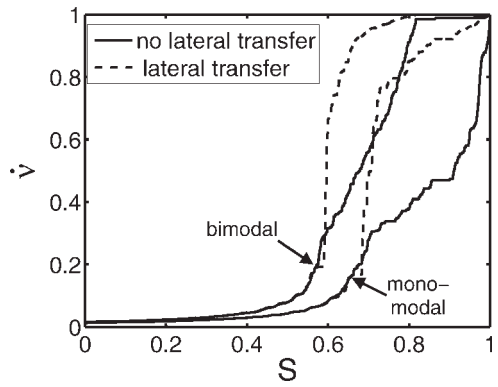

Figure 16. Drying rate curves for cubic networks with and without lateral transfer in boundary layer.

Normalized drying rate is plotted vs. network saturation for mono- and bimodal network.

This work confirms how pore network models allow investigating transport phenomena in porous media at a more fundamental level than continuous models with effective parameters. Specifically, they are an ideal tool to study the influence of structural effects on the process. Their physical significance has been proven at the laboratory scale, e.g., in drying.[12] At present, the amount of data needed for simulating real porous media and computational time are limiting so that pore network studies are still qualitative. Nevertheless, such studies can help to identify favorable pore structures, such as for drying in this work. By their fundamental nature, pore networks are a versatile tool and can be applied to many other processes of practical relevance, such as chemical reactions in porous catalysts,[31] helping to improve product quality for specialized applications in many fields.

Acknowledgments

The first author would like to thank the German Research Foundation (DFG) which financed the contributions by the second author in the frame of Graduate School 828 "Micro-Macro-Interactions in Structured Media and Particle Systems".

Literature Cited

1. Perré P, Turner IW. A 3-D version of TransPore: a comprehensive heat and mass transfer computational model for simulating the drying of porous media. *Int J Heat Mass Transfer*. 1999;42:4501–4521.
2. Metzger T, Tsotsas E. Influence of pore size distribution on drying kinetics: a simple capillary model. *Drying Technol*. 2005;23:1797–1809.
3. Vu TH. Influence of pore size distribution on drying behaviour of porous media by a continuous model. Otto-von-Guericke-University, Magdeburg; 2006. PhD thesis.
4. Vu TH, Metzger T, Tsotsas E. Influence of pore size distribution via effective parameters in a continuous drying model. Proceedings 15th Intern. Drying Symposium. Budapest, Hungary, August 20-23, 2006:B 554–560.
5. Nowicki SC, Davis HT, Scriven LE. Microscopic determination of transport parameters in drying porous media. *Drying Technol*. 1992;10:925–946.
6. Prat M. Percolation model of drying under isothermal conditions in porous media. *Int J Multiphase Flow*. 1993;19:691–704.
7. Irawan A. Isothermal drying of pore networks: influence of pore structure on drying kinetics. Otto-von-Guericke-University, Magdeburg; 2006. PhD thesis.
8. Metzger T, Irawan A, Tsotsas E. Isothermal drying of pore networks: Influence of friction for different pore structures. *Drying Technol*. 2007;25:49–57.
9. Yiotis AG, Stubos AK, Boudouvis AG, Yortsos YC. A 2-D pore-network model of the drying of single-component liquids in porous media. *Adv Water Resour*. 2001;24:439–460.
10. Yiotis AG, Boudouvis AG, Stubos AK, Tsimpanogiannis IN, Yortsos YC. The effect of liquid films on the drying of porous media. *AIChE J*. 2004;50:2721–2737.
11. Prat M. On the influence of pore shape, contact angle and film flows on drying of capillary porous media. *Int J Heat Mass Transfer*. 2007;50:1455–1468.
12. Laurindo JB, Prat M. Numerical and experimental network study of evaporation in capillary porous media, phase distributions. *Chem Eng Sci*. 1996;51:5171–5185.
13. Laurindo JB, Prat M. Numerical and experimental network study of evaporation in capillary porous media, drying rates. *Chem Eng Sci*. 1998;53:2257–2269.
14. Le Bray Y, Prat M. Three dimensional pore network simulation of drying in capillary porous media. *Int J Heat Mass Transfer*. 1999; 42:4207–4224.
15. Yiotis AG, Tsimpanogiannis IN, Stubos AK, Yortsos YC. Pore-network study of the characteristic periods in the drying of porous materials. *J Colloid Interface Sci*. 2006;297:738–748.
16. Irawan A, Metzger T, Tsotsas E. Pore network modeling of drying: combination with a boundary layer model to capture the first drying period. 7th World Congress of Chemical Engineering. Glasgow, Scotland; July 10–14, 2005:P42–033.
17. de Freitas DS, Prat M. Pore network simulation of evaporation of a binary liquid from a capillary porous medium. *Transport in Porous Media*. 2000;40:1–25.
18. Huinink HP, Pel L, Michels MAJ, Prat M. Drying processes in the presence of temperature gradients, pore-scale modeling. *Eur Physical J E*. 2002;9:487–498.
19. Plourde F, Prat M. Pore network simulations of drying of capillary media, influence of thermal gradients. *Int J Heat Mass Transfer*. 2003;46:1293–1307.
20. Surasani VK, Metzger T, Tsotsas E. Consideration of heat transfer in pore network modelling of convective drying. doi: 10.1016/j.ijheatmasstransfer. 2007.07.033. *Int J Heat Mass Transfer*.
21. Tsimpanogiannis IN, Yortsos YC, Poulou S, Kanellopoulos N, Stubos AK. Scaling theory of drying in porous media. *Phys Rev E*. 1999;59:4353–4365.
22. Prat M, Bouleux F. Drying of capillary porous media with stabilized front in two dimensions. *Phys Rev E*. 1999;60:5647–5656.
23. Segura LA, Toledo PG. Pore-level modeling of isothermal drying of pore networks, effects of gravity and pore shape and size distributions on saturation and transport parameters. *Chem Eng J*. 2005; 111:237–252.
24. Metzger T, Irawan A, Tsotsas E. Discrete modeling of drying kinetics of porous media. Proceedings 3rd Nordic Drying Conference. Karlstad, Sweden, June 15-17, 2005.
25. Laurindo JB, Prat M. Modeling of drying of capillary porous media, the discrete approach. *Drying Technol*. 1998;16:1769–1787.
26. Metzger T, Tsotsas E, Prat M. Chapter 2: Pore network models. In: Tsotsas E, Mujumdar AS, eds. *Modern Drying Technology 1: Computational Tools at Differents Scales*. John Wiley & Sons, 2007, pp. 57–102.
27. Schlünder EU. On the mechanism of the constant drying rate period and its relevance to diffusion controlled catalytic gas phase reactions. *Chem. Eng. Sci*. 1988;43:2685–2688.
28. Al-Futaisi A, Patzek TW. Extension of Hoshen-Kopelman algorithm to non-lattice environments. *Physica A*. 2003;321:665–678.
29. Metzger T, Irawan A, Tsotsas E. Remarks on the paper Extension of Hoshen-Kopelman algorithm to non-lattice environments: by Al-Futaisi A, Patzek TW. *Physica A*. 2003;321:665–678. *Physica A*. 2006; 363:558–560.
30. Chapuis O, Prat M. Influence of wettability conditions on slow evaporation in two-dimensional porous media. *Physical Review E*. 2007; 75: article no. 046311.
31. Wood J, Gladden LF, Keil F. Modelling diffusion and reaction accompanied with capillary condensation using three-dimensional pore networks, part 2: dusty gas model and general reaction kinetics. *Chem Eng Sci*. 2002;57:3047–3059.

Manuscript received Apr. 17, 2007, and revision received Aug. 7, 2007.

Drying Technology, 25: 49–57, 2007

ISSN: 0737-3937 print/1532-2300 online
DOI: 10.1080/07373930601152640

Taylor & Francis
Taylor & Francis Group

Isothermal Drying of Pore Networks: Influence of Friction for Different Pore Structures

Thomas Metzger, Anton Irawan, and Evangelos Tsotsas
Thermal Process Engineering, Otto-von-Guericke-University, Magdeburg, Germany

An existing network model for isothermal drying of capillary porous media is extended to account for viscosity in the liquid phase so that it is no longer restricted to structures with large pores. Modeling challenges and solution methods are presented in detail. The model is compared with a bundle of capillaries model of drying. Finally, simulation results for two-dimensional pore networks with mono-modal and bimodal pore structure are shown and discussed.

Keywords Bundle of capillaries; Capillary porous media; Drying curves; Phase distribution; Pore size distribution; Viscous effect

INTRODUCTION

Pore network models have become a powerful tool for the investigation of transport phenomena in porous media in general and of drying in particular. The basic idea of network modeling is to represent the porous medium by a network of pores, which are interconnected by throats, and to describe transport at the pore level. Of course, current network models cannot predict quantitatively the drying behavior of a given porous structure due to the enormous amount of data required to characterize the real pore space, which is usually not accessible by experiments and additionally faces computational limits. But they allow qualitative description of the different transport mechanisms which determine the drying kinetics.

Different approaches have been taken in the literature concerning network geometry; either pore bodies contain all volume,[1] leaving the throats as mere conductors and capillary barriers; or pores are only nodes, and all volume is attributed to the throats, which can be biconical[2] or of constant cross section.[3] Practically all literature studies investigate convective drying under isothermal conditions, an assumption that is reasonable for slow drying processes. The only exception are Huinink et al.[4] and Plourde and Prat,[5] who studied drying in the presence of thermal gradients; for convective drying conditions, a stabilized receding drying front was found. However, a truly non-isothermal model with free evolution of temperature has not yet been reported.

Viscous effects have been modeled for the liquid by Nowicki et al.[2] and for both liquid and gas phase by Yiotis et al.[1] Whereas Nowicki et al. concentrated on the determination of effective transport parameters and did not report drying curves or phase distributions during drying, Yiotis et al. investigated the drying of a porous rock when gas is purged through large fractures and viscous effects play a role in the gas mainly. In both works, a systematic investigation of the influence of viscosity on drying kinetics and moisture profiles during drying has not been done. Prat reports the stabilizing effect of gravitation on the drying front and predicts a similar effect in the presence of liquid viscosity.[6,7] Also, scaling laws, e.g., for the drying front width, have been derived as function of Bond number and capillary number, respectively.[8] In this context, two-dimensional drying simulations with liquid viscosity have been performed for the stationary case; however, the dynamic drying process has not yet been modeled.

It is worth mentioning that experiments with micro models confirm network simulation results of phase distributions,[9] but the drying rates were greatly underestimated.[7] Model versions including film flows can explain this difference qualitatively, as well as the occurrence of the first drying period.[10,11]

Apart from investigating the role of different physical effects in drying, network models can also be used to study the influence of pore structure on drying kinetics. Work in this direction has started only recently:[12,13] the isothermal model of Prat, which neglects viscous effects, was applied to the drying of networks of different structures. It was found that, for networks with a monomodal pore size distribution (as used in all literature work so far), and in the absence of film flow, the drying rate decreases from the very beginning; only materials with bimodal pore size

Correspondence: Thomas Metzger, Chair of Thermal Process Engineering, Otto-von-Guericke-University, P.O. 4120, 39106 Magdeburg, Germany; E-mail: thomas.metzger@vst.uni-magdeburg.de

distribution and highly correlated pore structure, in which large pores are formed in long channels, show the presence of first drying period and overall favorable drying rates. This initial period of constant drying rate could only be obtained by modeling lateral vapor transfer in the gas-side boundary layer, implementing an idea of Laurindo and Prat.[7] For monomodal pore structures, moisture gradients during drying were found to be steep, whereas networks with large pore channels allowed for efficient capillary pumping.

However, since this model neglects friction, the only mechanism counteracting capillary pumping is the splitting up of the liquid phase into disconnected clusters, which is determined only by the spatial distribution of relative pore size: within one cluster, large throats will empty first, no matter their absolute size (differences).

In parallel, a one-dimensional capillary model including liquid viscosity was proposed[14] that is in some ways complementary to the network model: here, the liquid phase is continuous, and only viscosity is responsible for the decrease of the drying rate. With this model, we found that broader size distributions lead to faster drying and that absolute values of mean pore size are of minor importance.

In the present article, a combination of both models is presented as an isothermal pore network model accounting for liquid viscosity, increasing the validity region of pore network modeling down to small pore sizes where friction must not be neglected.

In the gas phase, viscosity is not modeled and constant pressure is assumed. However, as is well known, during drying, a convective Stefan flow is established because molecular transfer cannot be equimolar due to the semipermeable character of the liquid–gas phase boundary (air molecules do not dissolve in the liquid, whereas liquid molecules can evaporate into the bulk air). In our model, the Stefan correction for vapor mass flow is included, but the Stefan flow is not subject to any resistance. This is true for the first drying period when evaporation takes place at the product surface and vapor transfer is in the gas-side boundary layer. But in the second drying period, when vapor has to be evacuated from the core of the porous body, significant pressure gradients can build up as simulations with a continuous model show.[15] Therefore, the model presented here may need to be extended in the future to accommodate gaseous friction for a better description of the second drying period.

The new network model is applied first to a bundle of capillaries for comparison with the existing one-dimensional model and then to two-dimensional networks having different pore structures with monomodal and bimodal pore size distributions; drying curves and moisture profiles or phase distributions are computed and analyzed. The cases of negligible and infinite liquid viscosity are discussed as limiting cases of the general model.

NETWORK DRYING MODEL WITHOUT VISCOSITY EFFECTS

In this section, the isothermal drying model for negligible viscosity is recalled.[12] The network consists of pore nodes without volume that are interconnected by cylindrical throats of randomly distributed radius. In this work, only two-dimensional networks with square grid geometry are investigated because, for realistic three-dimensional simulations with liquid viscosity, computational time is still limiting, and the influence of friction can be nicely shown in two dimensions as well.

Initially, the network is completely saturated with liquid water. It is then subjected to convective drying from the top. To describe vapor transfer in the boundary layer, the grid of pores is extended to the average boundary layer thickness $\varepsilon = \beta/\delta$ with mass transfer coefficient β and vapor diffusivity δ. Liquid water evaporates from all the surface menisci, but only the meniscus in the largest pore throat withdraws from the surface into the interior, because in the absence of friction even a small difference in capillary pressure is enough to supply water to all other throats at the local evaporation rate so that their menisci can remain stationary. Since the throat radii r_{ij} are chosen at random, the order of emptying is also random. Each throat can be seen as a link between other throats; therefore, the emptying of a throat can interrupt a liquid connection and separate liquid clusters may form during drying. Figure 1 shows a small partially saturated network with two such clusters (1 and 2) and a single liquid throat (S) as well as the diffusive boundary layer. The state of pore nodes is determined by the filling state of the pore

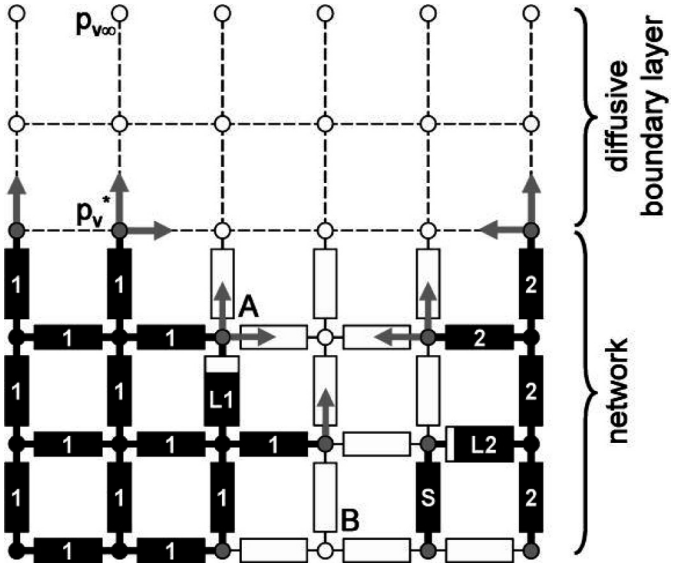

FIG. 1. Network with boundary layer during drying (liquid water is shown in black, gas in white; gas nodes at saturation vapor pressure are gray).

throats: if at least one neighboring throat is empty, the node is a gas pore; otherwise, it is a liquid pore.

To obtain drying kinetics, we assume vapor diffusion to be quasi-steady; i.e., during the emptying of one throat, the mass flow rates $\dot{M}_{v,ij}$ to each gas pore i must fulfill

$$\sum_j \dot{M}_{v,ij} = \sum_j A_{ij} \frac{\delta}{L} \frac{p\tilde{M}_v}{\tilde{R}T} \cdot \ln\left(\frac{p - p_{v,i}}{p - p_{v,j}}\right) = 0 \qquad (1)$$

where the sum is over all neighboring gas pores j, which are connected by an empty throat. Here,

$$A_{ij} = \begin{cases} \pi r_{ij}^2 & \text{in network} \\ L^2 & \text{in boundary layer} \end{cases} \qquad (2)$$

is the exchange area and L the distance between nodes, $\tilde{M}_v$ molar vapor mass, $\tilde{R}$ universal gas constant, p gas pressure, T absolute temperature, and $p_{v,i}$ are vapor pressures at the nodes. As boundary conditions to Eq. (1) we take vapor pressure of drying air $p_{v,\infty}$ at the edge of the boundary layer and saturation vapor pressure p_v^* at nodes next to a meniscus (see Fig. 1). With this, we can solve Eq. (1) to obtain the vapor pressure field from which evaporation rates at every meniscus can be computed. If several menisci are neighbor to one pore (A), the sum of vapor flow rates is distributed to them as evaporation rates according to their surface. Note that for partially filled pores the additional diffusional resistance in the empty part is neglected, in accordance with the quasi-steady assumption. (Another reason will be given below.)

In the depth of the network, pores may be at saturation vapor pressure, even if they are not directly neighbor to a meniscus (B). Therefore, some clusters may be temporarily trapped; i.e., have zero evaporation rate (like the single throat S in Fig. 1).

To obtain the time step, we compute for each cluster the time Δt_k it takes to empty its largest throat (L1 and L2)—by dividing its liquid mass by the sum of evaporation rates at all menisci of the cluster—and select the minimum. After this time, (at least) one throat in the network has emptied and throat saturations must be updated. As a consequence, additional gas pores may be created so that Eq. (1) must be updated; and cluster affiliation of throats may also change, if new clusters or single throats are created. To check this, liquid-filled throats are relabeled after each time step by a variant of the Hoshen-Kopelman algorithm.[16,17]

Throat saturations during drying can be visualized as phase distributions, and drying curves are obtained by plotting for each time step total evaporation rate as a function of network saturation. It is worth mentioning that, in empty throats, neither film flow nor adsorbed water are modeled.

MODEL EXTENSION TO INCLUDE LIQUID VISCOSITY EFFECT

If the network drying model is applied to small-sized pores, viscous effects must be accounted for. Then, within one cluster, differences in capillary pressure may no longer be adequate to pump liquid from the meniscus in the largest throat to all other menisci for keeping them stationary. This can be discussed qualitatively by looking at cluster 2 of Fig. 1.

Figure 2 shows the relative size of throat radii ($r_2 < r_1 = r_4 < r_3 < r_5$) as well as the places of evaporation. Initially, throat 3 has the largest meniscus radius and therefore the highest liquid pressure $p_{w,3} = p - 2\sigma/r_3$ (for zero contact angle); consequently, it must empty. At the same time, throat 1 will also empty, because its liquid pressure is not low enough to supply liquid at the local evaporation rate, whereas throat 2 (lower pressure and lower evaporation rate) and throat 4 (no evaporation at all) can remain stationary.

When throat 3 has emptied completely (after Δt_3), cluster size is reduced by separation of single throat 4 (then trapped), leaving throat 5 with the largest meniscus radius. Since its liquid pressure is higher than the former $p_{w,3}$ and since the distance to the meniscus in throat 1 has been reduced, the pressure difference can now pump more liquid to throat 1 than is evaporated. As a consequence, the throat fills again (in Δt_1) and its meniscus stays stationary, until throat 5 is empty.

Strictly speaking, the partial emptying and refilling of throat 1 would be accompanied by a drop and increase in the local evaporation rate (due to vapor diffusion resistance in the empty throat section), leading to oscillations in the overall drying rate. This unrealistic behavior can be avoided by neglecting the resistance to vapor transfer in the partially filled throats (see above).

For quantitative results we must compute the actual liquid flow rates from liquid mass balances. A major problem is to correctly identify all moving menisci in a cluster. As above, we assume quasi-steady transport so that for the liquid mass flow rates $\dot{M}_{w,ij}$ at each liquid pore i are given by:

$$\sum_j \dot{M}_{w,ij} = \sum_j \frac{\pi r_{ij}^4}{8\nu_w L_{ij}} (p_{w,i} - p_{w,j}) = 0 \qquad (3)$$

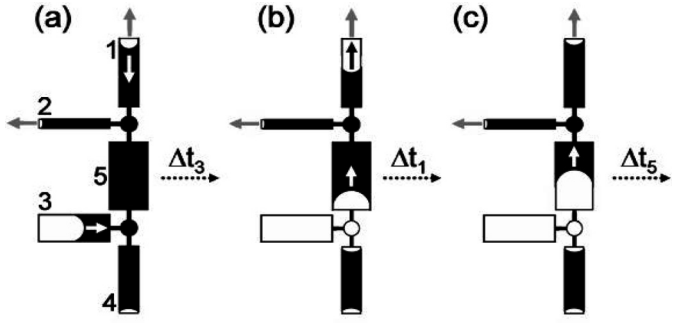

FIG. 2. Emptying and refilling of throats in cluster 2 (cf. Fig. 1) when friction controls liquid flow rates.

where $0 < L_{ij} \leq 1$ is the liquid-filled length of throats, ν_w kinematic viscosity of water, and $p_{w,j}$ liquid pressure at the neighboring meniscus or node. (The sum is over all neighbor throats because a pore node is only liquid if all connected throats contain liquid.) Gravitational effects are not considered.

Boundary conditions to Eq. (3) are given by the menisci. For all stationary menisci (in full throats where the liquid pressure can be low enough to pump water at the evaporation rate), we have a second kind of boundary condition: the liquid mass flow in the throat equals the evaporation rate at the meniscus $\dot{M}_{w,ij} = \dot{M}_{v,ij}$. For all moving menisci (in the largest throat of each cluster, in all partially filled throats and in full throats where liquid cannot be supplied at the evaporation rate), we assume the meniscus to be fully developed, the liquid having zero contact angle no matter if the throat is filling or emptying, so that the first kind boundary condition $p_{w,j} = p - 2\sigma/r_{ij}$ is applied. Figure 3 shows two possible ways to find the unique set of boundary conditions for the liquid.

The first algorithm starts with the situation as in the nonviscous case; i.e., only the largest throat of each cluster has a moving meniscus. As long as there are menisci that were declared stationary but cannot provide a low enough liquid pressure, they are, one by one, corrected to moving, starting with the one having the largest discrepancy. The procedure must be stepwise because the correction of one boundary condition will raise the pressure in the cluster, possibly making further corrections unnecessary.

In the second algorithm, initially all menisci are treated as moving. Then, all menisci that can pump enough liquid will be corrected to become stationary. This rise in cluster pressure will allow more menisci to be stationary, and iteration is necessary until the boundary conditions are without contradiction. A first comparison of the two algorithms for a test case showed the first one to be faster, although a systematic investigation is still missing.

Once the true boundary conditions are found, the liquid flow rates can be computed. Then, menisci motion can be obtained from the difference between evaporation rate and liquid flow rate, and the times required for complete filling or emptying of throats can be calculated to choose the global time step.

It should be noted that the redistribution of water after a meniscus has passed from a narrow to a wide throat (as in Fig. 2) is known as a ''Haines jump'' and can, in principle, lead to the refilling of already empty throats. However, in the present model, throat filling is assumed to stop at the next pore node.

COMPARISON WITH BUNDLE OF CAPILLARIES MODEL

Recently, we proposed a one-dimensional isothermal drying model in which the porous medium is represented by a bundle of capillaries with a radius distribution.[14] The transport mechanisms are exactly the same as in the above network model, namely viscous capillary pumping in the liquid and vapor diffusion in the gas. Lateral resistances between the capillaries and in the boundary layer are entirely neglected.

We will now use such a bundle of capillaries as a test case for the viscous network model. In our previous work, a set of capillary classes of equidistant radii r_k was defined and the number of capillaries in each class N_k chosen according to a given distribution. The plot in Fig. 4 shows,

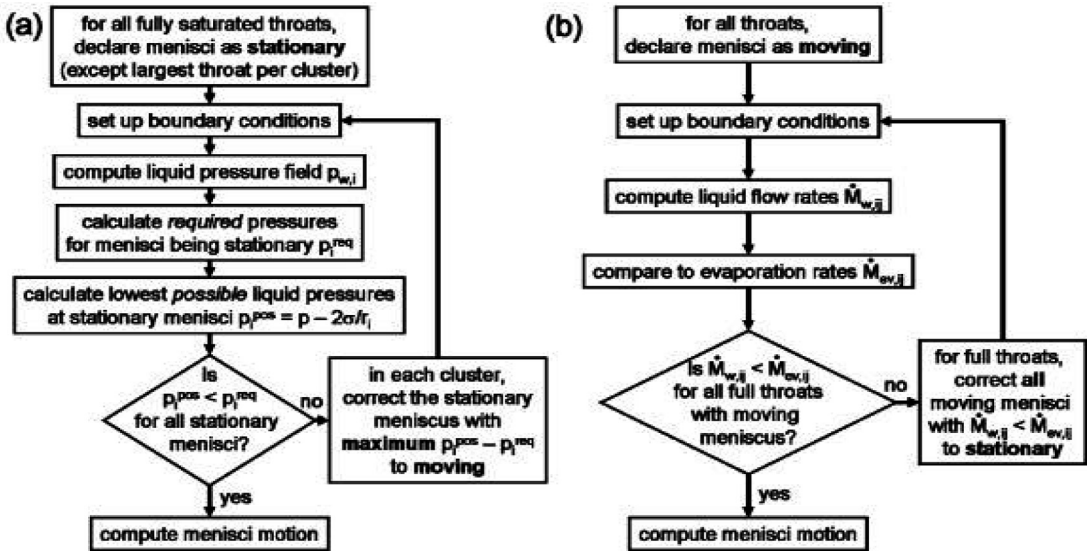

FIG. 3. Two possible algorithms to find the correct boundary conditions for liquid flow (see text).

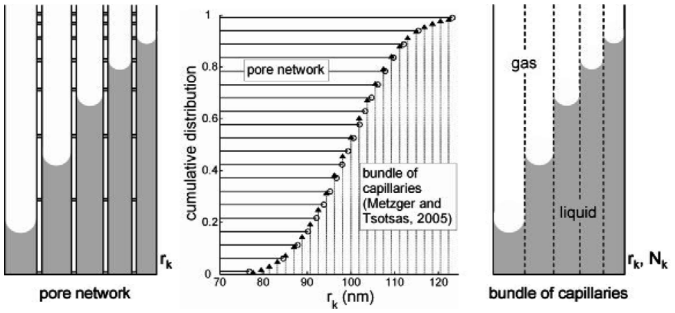

FIG. 4. Bundle of capillaries and network equivalent; the example shows only 20 (classes of) capillaries.

as an example, 20 such classes with a normal number distribution of mean radius 100 nm and standard deviation 10 nm.

In the two-dimensional network representation, the vertical throats play the role of the capillary tubes, and the horizontal ones must allow for good lateral exchange between them. Network size is limited for computational reasons; therefore, all capillary classes have now only one representative, and their radii are chosen so that the number density follows the given distribution (see Fig. 4). For the best possible comparison, the same radii are used in the one-dimensional model. The horizontal throats have small radii so that they will empty last and a continuous liquid phase for capillary pumping is guaranteed at all times. Their flow resistance is independently set close to zero. Finally, the vertical distance between horizontal connections decreases toward the network surface to keep the effect of the following difference in modeling small: in the capillary model, when the last meniscus withdraws only a little from the surface, the drying rate drops drastically, whereas in the network model a row of vertical throats must empty completely before an additional resistance appears.

Computations were performed for 50 capillary tubes of 0.1 m length and normally distributed radius of mean r_0 and standard deviation σ_0 for the network, with 50 horizontal connections (geometric progression grid). Convective drying was simulated for a flow of absolutely dry air at 20°C and atmospheric pressure, with a mass transfer coefficient $\beta = 0.1\,\mathrm{m/s}$. In Figs. 5 and 6, the results for the network model are plotted in thick lines; the thin dashed lines give respective results of the bundle of capillaries model. Figure 5b shows the moisture profiles when the last meniscus has reached (the position of) the first horizontal connection. The overall behavior of drying curve and moisture profile is correctly described by the network model: a wider pore size distribution is favorable for drying, whereas the absolute pore size is of minor importance.[14] However, the duration of the first drying period is slightly overestimated and moisture profiles are flatter than for the capillary model, especially in the depth of

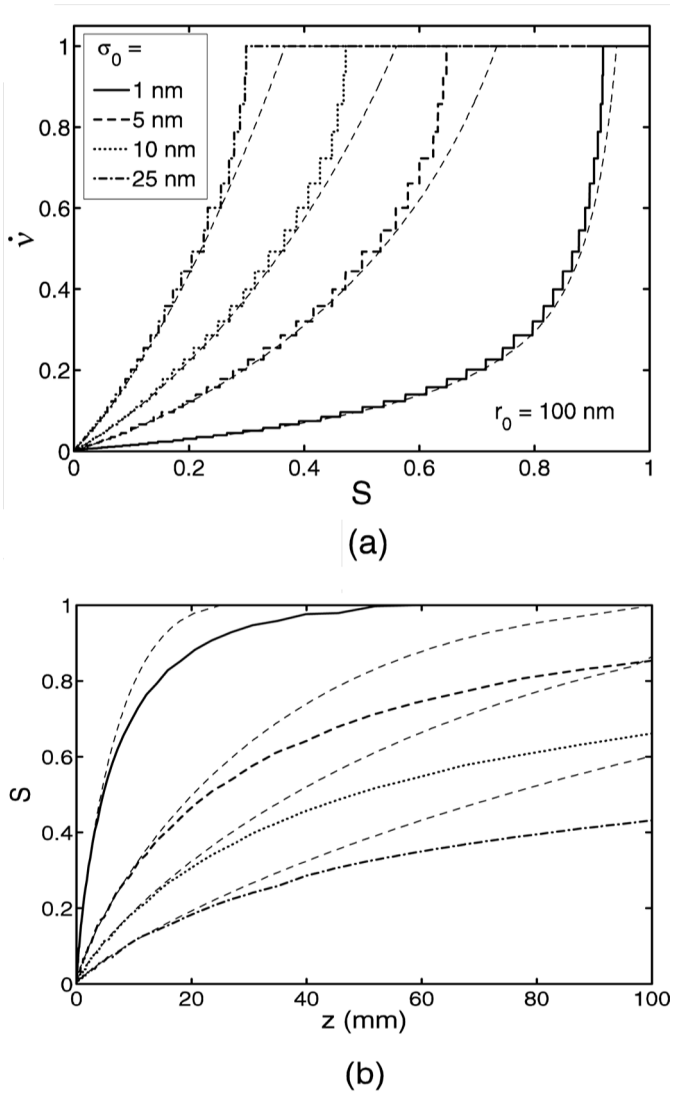

FIG. 5. Drying curves (a) and moisture profiles at end of first drying period (b) for a bundle of capillaries with normally distributed radius: comparison between capillary and network model (see text).

the network. Possible reasons are the discrete lateral exchange in the network model and different boundary conditions at the bottom: no flux is assumed in the network, whereas menisci move out one by one in the capillary model, rather imposing a first kind boundary condition for (capillary) pressure.

TWO-DIMENSIONAL PORE NETWORKS

After this comparison with a bundle of capillaries, we now turn to truly two-dimensional pore networks.

Monomodal Pore Size Distribution

First, we investigated networks with 50×50 nodes, 500 nm throat length, and mean throat radius 50 nm; the

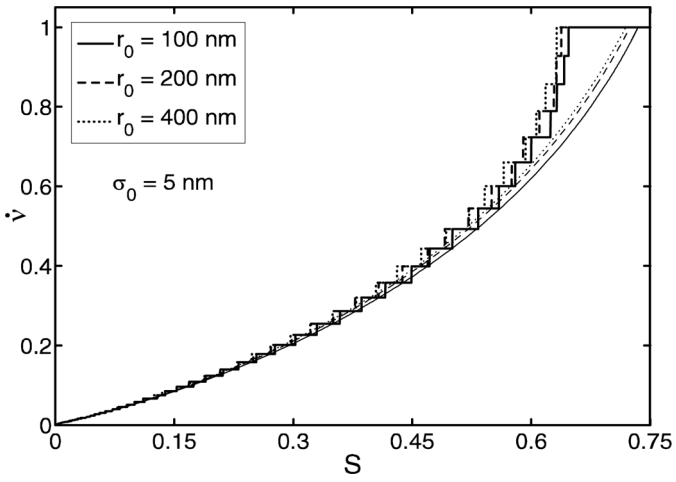

FIG. 6. Drying of a bundle of capillaries: comparison between capillary and network model (see text).

total network size is hence $(25\,\mu\text{m})^2$. Note that this throat radius is atypically small for capillary porous media; it has been chosen to illustrate viscous effects for a small network size. Significantly larger networks still pose a problem to computation. Knudsen effect in vapor diffusion and possible effects of small throat size on liquid flow are not accounted for. The networks are open for convective drying at the top with a boundary layer thickness of $50\,\mu\text{m}$ (using ten vertical nodes) corresponding to a mass transfer coefficient $\beta = 0.5\,\text{m/s}$. At the bottom, the networks are closed, but in the lateral direction, periodic boundary conditions are applied; i.e., the right side of a network is connected to the left side.

In the first run, the radii are normally distributed with 10 nm standard deviation; and viscosity is neglected. The results are shown in Figs. 7a and 8 as phase distributions and drying curve, respectively.

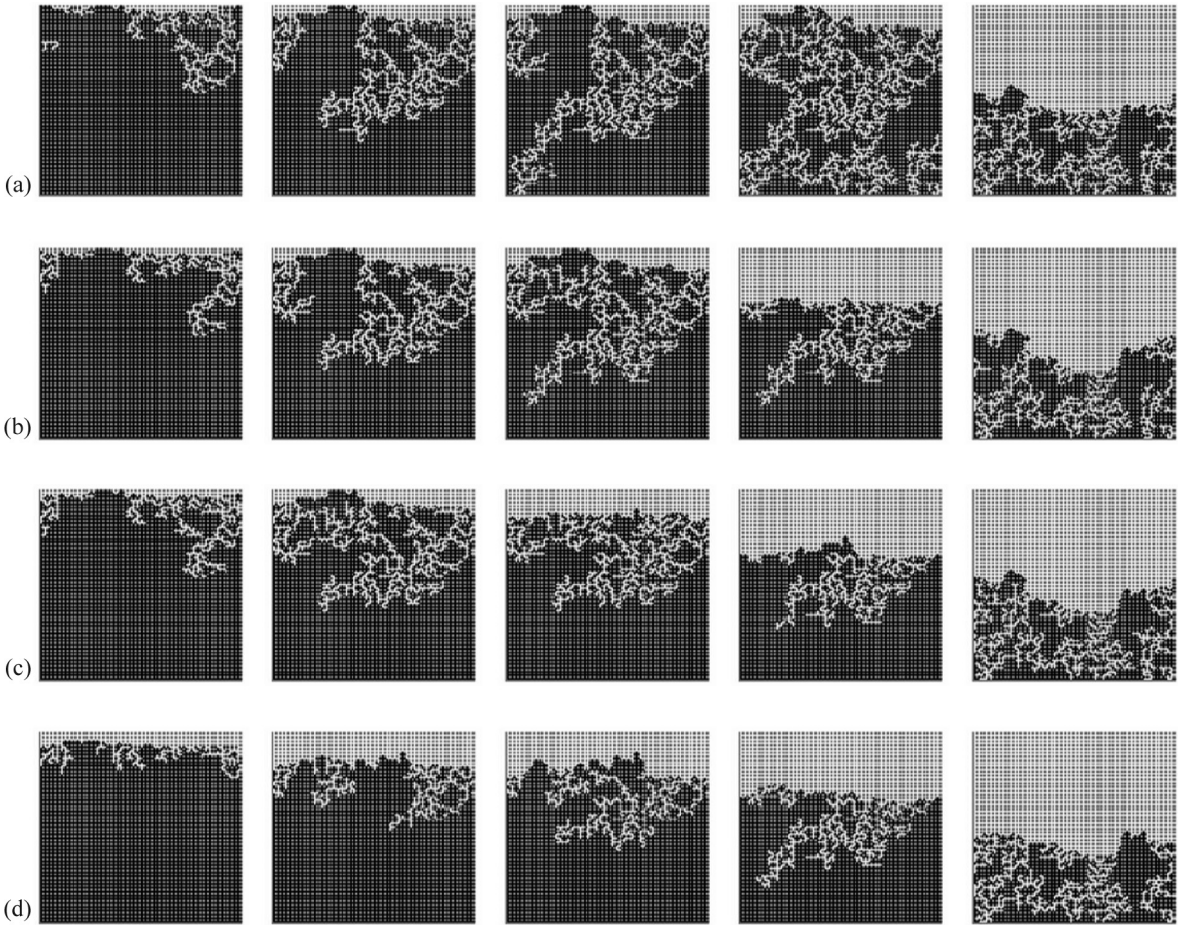

FIG. 7. Phase distributions during drying of monomodal network for S = 0.9, 0.78, 0.72, 0.58, and 0.3 where (a) $\sigma_0 = 10\,\text{nm}$ is without viscosity, and (b) $\sigma_0 = 10\,\text{nm}$, (c) $\sigma_0 = 5\,\text{nm}$, and (d) $\sigma_0 = 1\,\text{nm}$ are with liquid viscosity.

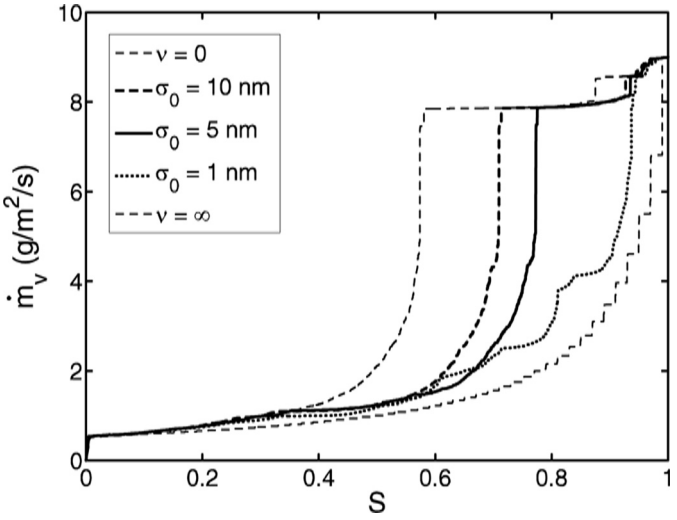

FIG. 8. Drying curves for different width of normal radius distribution and for zero and infinite viscosity.

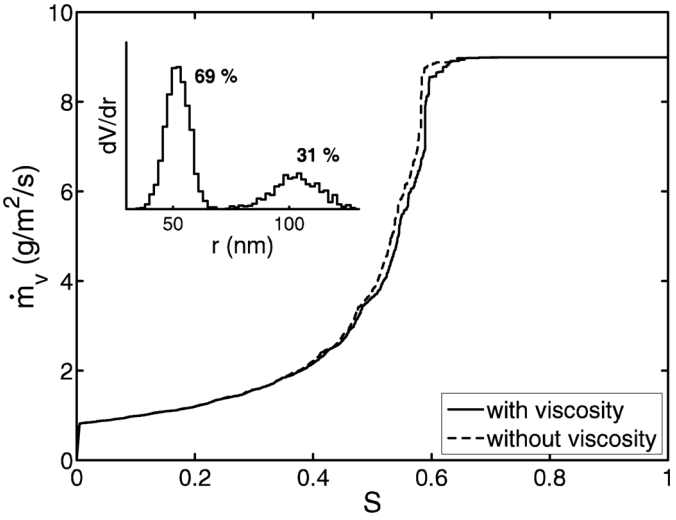

FIG. 10. Drying curves and pore volume distribution for bimodal network (see text).

One can see that liquid may be pumped from the depth of the network so that the surface stays partially wet down to low saturations. The relatively thick boundary layer allows for efficient lateral vapor transfer so that the drying rate stays almost constant.

If liquid viscosity is accounted for (Fig. 7b), capillary pumping is limited so that the drying front is stabilized and the surface dries out more rapidly.

In further simulations, the throat radii were rescaled to have a narrower absolute size distribution but the same spatial distribution of relative size. With decreasing σ_0, viscous effects dominate (Figs. 7c and d): at the high initial rates, capillary forces cannot efficiently pump liquid, so that the drying front is sharper and only breaks up when the rate has dropped significantly. For low network saturations, phase distributions show little difference. For comparison, Fig. 8 also shows the drying curve for the limit $\nu = \infty$, when no capillary pumping takes place and the drying front is sharply receding.

Bimodal Pore Size Distribution

Many technical porous media have a bimodal pore size distribution, often with strong spatial correlation. In previous work,[12] we found that a significant change in drying behavior, as compared to the monomodal case, can only be observed if both small and large pores form continuous phases. In such a pore structure, large throats for gas invasion are available over an extended period, and capillary flow to the network surface through small throats is not interrupted by emptying of large throats; therefore, a sustained first drying period appears. In two dimensions, such a structure can only be simulated by arranging large throats to long channels perpendicular to the network surface as in Fig. 9.

One drying simulation was performed, taking the monomodal network with $\sigma_0 = 5$ nm, rescaling ten vertical channels by a factor of two, and applying the same drying conditions as above. Phase distributions are shown in Fig. 9; the drying curve is presented together with pore volume distribution in Fig. 10.

It can be seen that the large throats dry out more or less completely before the small throats empty with a receding drying front. (In three dimensions, this front is expected to be less pronounced because, after the large throats are emptied, the small ones still form a continuous phase and more flow paths are available.) Viscous forces play no

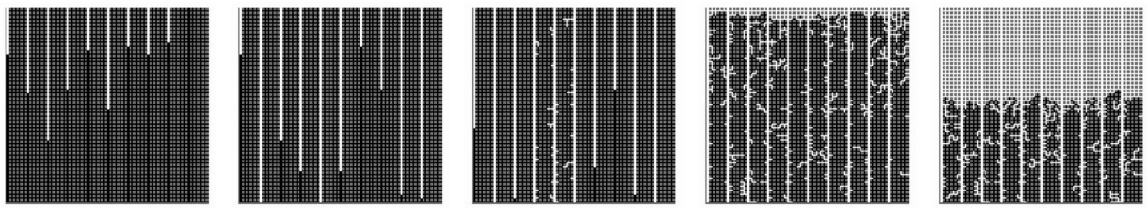

FIG. 9. Phase distributions during drying of bimodal network for S = 0.9, 0.78, 0.72, 0.58, and 0.3 (see text).

significant role: a simulation with zero viscosity yields almost the same result (see Fig. 10). The reason for this is the relatively large difference in radius between small and large pores ($\Delta r = 50\,nm$), which would be enough to pump water at the initial drying rate from more than 1 mm network depth, as simple calculus can show. This implies that, even for a much deeper network, the first drying period would extend to the same overall saturation, and only in the second drying period would lower drying rates be observed.

CONCLUSIONS

A pore network drying model that accounts for liquid viscosity has been presented and applied to two-dimensional networks with mono- and bimodal pore size distribution. It was found that only for narrow pore size distributions will liquid viscosity play a significant role, limiting the capillary flow and stabilizing the drying front. However, for broad or bimodal distributions with strong spatial correlations, capillary forces will clearly dominate over liquid friction.

In the near future, more efficient programming will make the algorithm applicable to larger networks and three-dimensional simulations. In terms of modeling, the influence of friction in the gas phase will have to be investigated.

It should be mentioned that the present work is part of a larger project with the aim of developing a pore network model comprising all relevant transport phenomena, and that model extension to heat transfer has already been started.[18] With such a complete network model it will be possible to assess rigorous continuous drying models such as the one proposed by Perré and Turner.[19] In a first step, effective transport parameters were computed from a bundle of capillaries and used in this continuous model.[15]. In the future, they shall be obtained from a pore network, as in the approach of Nowicki et al.,[2] which is recommended by Prat,[20] hence allowing for a direct comparison between continuous and network modeling.

NOMENCLATURE

A	Exchange area (m^2)
L	Throat length (m)
$\tilde{M}$	Molar mass (kg/kmol)
$\dot{M}$	Mass flow rate (kg/s)
$\dot{m}$	Mass flux (kg/m^2s)
N	Number of capillaries in one class
p	Pressure (Pa)
p_v^*	Saturation vapor pressure (Pa)
$\tilde{R}$	Ideal gas constant (J/kmolK)
r	Capillary/throat radius (m)
r_0	Mean capillary/throat radius (m)
S	Saturation
T	Temperature (K)
z	Length coordinate (m)

Greek Symbols

β	Mass transfer coefficient (m/s)
δ	Vapor diffusion coefficient (m^2/s)
ν	Kinematic viscosity (m^2/s)
$\dot{\nu}$	Normalized drying rate
σ	Surface tension of water (N/m)
σ_0	Standard deviation of radius (m)

Subscripts and Superscripts

v	Vapor
w	Liquid water
*	Saturation/equilibrium

ACKNOWLEDGEMENTS

This work was financed by the German Research Foundation (DFG) in the frame of Graduate School 828 "Micro-Macro-Interactions in Structured Media and Particle Systems."

REFERENCES

1. Yiotis, A.G.; Stubos, A.K.; Boudouvis, A.G.; Yortsos, Y.C. A 2-D pore-network model of the drying of single-component liquids in porous media. Advances in Water Resources **2001**, *24*, 439–460.
2. Nowicki, S.C.; Davis, H.T.; Scriven, L.E. Microscopic determination of transport parameters in drying porous media. Drying Technology **1992**, *10*, 925–946.
3. Prat, M. Percolation model of drying under isothermal conditions in porous media. International Journal of Multiphase Flow **1993**, *19*, 691–704.
4. Huinink, H.P.; Pel, L.; Michels, M.A.J.; Prat, M. Drying processes in the presence of temperature gradients. Pore-scale modelling. European Physical Journal E **2002**, *9*, 487–498.
5. Plourde, F.; Prat, M. Pore network simulations of drying of capillary porous media. Influence of thermal gradients. International Journal of Heat and Mass Transfer **2003**, *46*, 1293–1307.
6. Laurindo, J.B.; Prat, M. Modeling of drying in capillary-porous media: A discrete approach. Drying Technology **1998**, *16*, 1769–1788.
7. Laurindo, J.B.; Prat, M. Numerical and experimental network study of evaporation in capillary porous media, drying rates. Chemical Engineering Science **1998**, *53*, 2257–2269.
8. Prat, M.; Bouleux, F. Drying of capillary porous media with stabilized front in two-dimensions. Physical Review E **1999**, *60*, 5647–5656.
9. Laurindo, J.B.; Prat, M. Numerical and experimental network study of evaporation in capillary porous media, phase distributions. Chemical Engineering Science **1996**, *51*, 5171–5185.
10. Yiotis, A.G.; Boudouvis, A.G.; Stubos, A.K.; Tsimpanogiannis, I.N.; Yortsos, Y.C. The effect of liquid films on the drying of porous media. AIChE Journal **2004**, *50*, 2721–2737.
11. Prat, M. On the influence of pore shape, contact angle and film flows on drying of capillary porous media. International Journal of Heat and Mass Transfer. In press.
12. Irawan, A.; Metzger, T.; Tsotsas, E. *Pore Network Modelling of Drying: Combination with a Boundary Layer Model to Capture the First Drying Period*; 7th World Congress of Chemical Engineering, Glasgow, Scotland, July 10–14, 2005.

13. Metzger, T.; Irawan, A.; Tsotsas, E. *Discrete Modeling of Drying Kinetics of Porous Media*; 3rd Nordic Drying Conference, Karlstad, Sweden, June 15–17, 2005.
14. Metzger, T.; Tsotsas, E. Influence of pore size distribution on drying kinetics: A simple capillary model. Drying Technology **2005**, *23*, 1797–1809.
15. Vu, T.H.; Metzger, T.; Tsotsas, E. Influence of pore size distribution via effective parameters in a continuous drying model, In *Proceedings of the 15th International Drying Symposium*, Budapest, Hungary, August 20–23, 2006; 554–561.
16. Al-Futaisi, A.; Patzek, T.W. Extension of Hoshen-Kopelman algorithm to non-lattice environments. Physica A **2003**, *321*, 665–678.
17. Metzger, T.; Irawan, A.; Tsotsas, E. Remarks on the paper ''Extension of Hoshen-Kopelman algorithm to non-lattice environments'' by A. Al-Futaisi and T.W. Patzek, Physica A 321 (2003) 665–678. Physica A **2006**, *363*, 558–560.
18. Surasani,V.K.; Metzger, T.; Tsotsas, E. Towards a complete pore network drying model: First steps to include heat transfer. In *Proceedings of the 15th International Drying Symposium*, Budapest, Hungary, August 20–23, 2006; 125–132.
19. Perré, P.; Turner, I.W. A 3-D version of TransPore: A comprehensive heat and mass transfer computational model for simulation the drying of porous media. International Journal of Heat and Mass Transfer **1999**, *42*, 4501–4521.
20. Prat, M. Recent advances in pore-scale models for drying of porous media. Chemical Engineering Journal **2002**, *86*, 153–164.

CHEMICAL ENGINEERING RESEARCH AND DESIGN 86 (2008) 739–744

available at www.sciencedirect.com

ScienceDirect

journal homepage: www.elsevier.com/locate/cherd

Viscous stabilization of drying front: Three-dimensional pore network simulations

Thomas Metzger, Evangelos Tsotsas*

Thermal Process Engineering, Otto-von-Guericke-University, P.O. 4120, D-39016 Magdeburg, Germany

ARTICLE INFO

Article history:
Received 24 October 2007
Accepted 9 March 2008

Keywords:
Capillary porous media
Phase distributions
Drying rate curves

ABSTRACT

In this study, a recently developed pore network drying model [Metzger, T., Irawan, A. and Tsotsas, E., 2007, Isothermal drying of pore networks: influence of friction for different pore structures, Dry Technol, 25: 49–57], which accounts for liquid viscosity, is applied to three dimensions for the first time. Isothermal convective drying is simulated for a cubic network ($25 \times 25 \times 50$) with pore throats with a narrow radius distribution. The role of liquid viscosity is assessed by comparison with non-viscous drying of the same network. Simulation results are presented as phase distributions, saturation profiles and drying rate curves. In the viscous case, a stabilization of the drying front is observed. However, as the network dries out from the surface, the finite drying front gradually widens up and does not approach an asymptotic limit.

1. Introduction

Pore network models are a suitable tool to examine the role of pore-scale transport phenomena and pore structure on the process behaviour of porous media. During the past one-and-a-half decades, several research groups have applied pore network modelling to drying of capillary porous media, continuously adding new transport phenomena and increasing network size.

In network models, the porous medium is represented by a network of interconnected pores which have a prescribed geometry (cylindrical in our study) but are random in their size. Our model approach is based on the work of Prat (1993) who interpreted the drying process as an invasion percolation driven by evaporation. At every moment of the process, the largest pore at the gas–liquid interface empties because its meniscus can produce the highest liquid pressure. Due to random spatial distribution of pore size, the liquid phase typically splits up into numerous clusters that may be temporarily trapped, but eventually all liquid will evaporate. The time scale of the process is given by vapour diffusion in the empty regions of the network.

In this isothermal model, capillary flow is only determined by the spatial distribution of pore size. However, if other effects like gravity, liquid viscosity or non-uniform temperature play a role, drying behaviour can differ significantly. The model extension to gravity is straightforward by allocating to each pore a potential which then determines the order of invasion (Prat, 1993). If the network dries out from the top, gravity has a stabilizing effect on the drying front. Laurindo and Prat (1996) performed experiments with two-dimensional micro models which nicely confirmed the simulated phase patterns as well as their modification due to gravity.

Recently, the stabilizing effect of gravity has also been studied in three dimensions by Yiotis et al. (2006) who simulated drying of an $80 \times 80 \times 80$ network. If gravity plays no role and lateral diffusion in the gas-side boundary layer is modelled, they found a constant drying rate period. Such computationally intensive three-dimensional network simulations are important, because the additional dimension leads to less trapping (see also Le Bray and Prat, 1999).

Prat and Bouleux (1999) predicted a stabilization of the drying front if liquid viscosity must be accounted for (i.e. for large networks of small pores with a narrow size distribution); however, they only performed stationary network simulations. Other researchers have included viscous effects into their (two-dimensional) pore network models, but the effect of liquid viscosity on drying kinetics and phase distributions has

* Corresponding author. Tel.: +49 391 6711362: fax: +49 391 6711160.
E-mail address: thomas.metzger@ovgu.de (T. Metzger).

0263-8762/$ – see front matter
doi:10.1016/j.cherd.2008.03.003

never been studied systematically: Nowicki et al. (1992) were interested in effective parameters and did not report on phase distributions and drying rates at the sample scale; and Yiotis et al. (2001) simulated drying of porous rock when gas is purged through large fractures and viscous effects mainly play a role in the gas phase.

The stabilization of the gas invasion front in drying for gravity and liquid viscosity has also been characterized by scaling laws (Tsimpanogiannis et al., 1999; Prat and Bouleux, 1999); experimental data for the viscous stabilization had already been reported by Shaw (1987) for the drying of a bed of small glass spheres.

In the present work, we will study viscous stabilization of the front by a three-dimensional pore network drying model and discuss its effect on the drying rate curve. We will focus on the special character of this stabilization: whereas front width is constant throughout the drying process in the gravity-stabilized case, viscous effects depend on current flow rates so that the drying front can widen up during the process.

It is worth mentioning that temperature gradients will also lead to a stabilization of the drying front (Huinink et al., 2002; Plourde and Prat, 2003) if the open surface of the network is hotter—as in convective drying. The reason for this is temperature dependence of surface tension, so that out of two pores of identical radius the warmer one will empty first.

Another stabilization effect is obtained if the pores are not cylindrical but have corners so that gas-invaded pores may still contain corner films. Film flow, which is induced by capillarity and limited by liquid viscosity, has been modelled by Yiotis et al. (2003, 2004) and Prat (2007). The film region typically covers the liquid cluster region as well as part of the completely invaded region. As a result of film flow, the evaporation front is smoothened in space and shifted towards network surface, resulting in higher drying rates. Experimental evidence of film flows and their effect on drying kinetics has been given by Laurindo and Prat (1998).

In general, stabilization effects are seen as crucial if drying is to be described by a continuous model (see, e.g. Tsimpanogiannis et al., 1999). In non-stabilized percolation, drying front width has no upper limit, and continuum models lack their basis, namely gradient-based (liquid) transfer.

Besides this research on transport phenomena, an investigation of structural influences on drying behaviour has recently been started. Prat (2007) has studied the role of pore shape in the context of film flow; Segura and Toledo (2005) have investigated the role of pore shape and pore size distributions for drying behaviour and effective transport parameters; Metzger et al. (2007a) have shown that pore structures with a bimodal pore size distribution may show very different drying behaviour and that coordination number of the pore network and spatial correlations of pore size play a crucial role (Metzger et al., 2007b). In the present work, we will however restrict ourselves to isothermal drying of a network of cylindrical pores (i.e. without corner films) with mono-modal radius distribution.

2. Drying model

In the following, the main concepts of non-viscous and viscous network drying model are recalled (for more details refer to Metzger et al., 2007c).

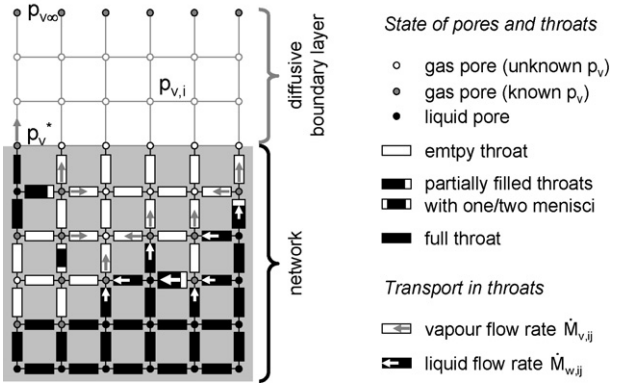

Fig. 1 – Small pore network during drying with discretized gas-side boundary layer. Definitions of pore and throat states are given; vapour and liquid transport are indicated.

2.1. Non-viscous model

The cubic pore network is built from cylindrical pore throats with radii r_{ij} obeying a normal number distribution. Initially, the network is fully saturated with water. During drying, it is open for evaporation at the top whereas the bottom is closed and the sides are connected for periodic boundary conditions in horizontal directions. Fig. 1 shows a small two-dimensional (non-periodic) pore network in the course of convective drying as a visual support for model description.

Vapour transfer to the dry air flow is modelled by diffusion through a boundary layer of uniform thickness which is discretized by extending the nodes of the network. In the gas phase (dry part of network and boundary layer), quasi-steady vapour diffusion between two nodes is described by

$$\sum_j \dot{M}_{v,ij} = \sum_j A_{ij} \frac{\delta}{L} \frac{\tilde{M}_v p}{\tilde{R}T} \ln\left(\frac{p - p_{v,i}}{p - p_{v,j}}\right) = 0 \quad (1)$$

where L is distance between nodes, A_{ij} exchange area (πr_{ij}^2 for network, L^2 for boundary layer), δ vapour diffusivity, $\tilde{M}_v$ molar vapour mass, $\tilde{R}$ universal gas constant, T absolute temperature, p gas pressure and $p_{v,i}$ vapour pressure. The system of Eq. (1) is solved to compute the unknown vapour pressures in the gas pores (white circles) by applying as boundary conditions the known vapour pressure (gray circles) of drying air $p_{v,\infty}$ at the top edge of the boundary layer and saturation vapour pressure p_v^* in pores next to the gas–liquid interface. From this, vapour diffusion rates can be computed for the empty throats (white rectangles) and evaporation rates for the menisci at the liquid–gas interface.

Note that adsorption in the empty pores is not modelled and liquid films are not accounted for. The hydraulic conductivity of thin liquid films that develop in cylindrical throats is so low that they have no significant contribution to mass transfer (Metzger et al., 2007c). We will consider pores of diameter 100 nm with a narrow distribution so that the reduction of vapour pressure due to the Kelvin effect is almost uniform for all pores and only about 2%. At atmospheric pressure, Knudsen effect in vapour diffusion only plays a significant effect if pore size is smaller than the chosen one (Kast, 1988). Therefore, we are neglecting both Kelvin and Knudsen effect.

Concerning the liquid-filled part of the network, random pore size distribution and capillary flow lead to irregular emptying of pores and the appearance of disconnected clusters. If

viscous (and gravity) effects are neglected, water flow within these liquid clusters is entirely controlled by capillary pressure differences so that (unlike in Fig. 1) *only the largest* meniscus throat of the cluster empties. The rate at which this happens is obtained by summing up the evaporation rates for all menisci of the respective cluster. This choice of largest meniscus and computation of the emptying rate is done for all clusters. At every moment during drying, the time step is given by complete emptying of *first* throat in the network since this will change liquid connectivity as well as the set of Eq. (1) for vapour diffusion. In this way, drying is described as a discrete process and the kinetics are given by a steady-state expression for vapour diffusion.

2.2. *Viscous model*

If liquid viscosity is accounted for, liquid flow rates depend on actual pressures $p_{w,i}$ and at each liquid pore node (black circles in Fig. 1) add up to zero as

$$\sum_j \dot{M}_{w,ij} = \sum_j \frac{\pi r_{ij}^4}{8\nu_w L_{ij}}(p_{w,i} - p_{w,j}) = 0 \qquad (2)$$

where ν_w is kinematic viscosity of water and L_{ij} liquid-filled length of pore throats. Boundary conditions to Eq. (2) are given at the menisci at the liquid–gas interface. For stationary menisci (in full throats where liquid can be provided at the local evaporation rate), the second kind boundary condition $\dot{M}_{w,ij} = \dot{M}_{v,ij}$ is applied. For moving menisci (in the largest throat of the cluster, in all partially filled throats and where liquid cannot be supplied at the local evaporation rate), the boundary condition of first kind $p_{w,j} = p - 2\sigma/r_{ij}$ (with surface tension σ and assuming perfect wetting of the liquid, i.e. zero contact angle) is used. Since choice of boundary conditions and flow rates are interdependent, iteration is used to determine the actual liquid flow field. The quasi-steady motion of menisci (now possibly several per cluster as in Fig. 1) is obtained as the difference between vapour and liquid flow, and the same principle of time stepping is applied as in the non-viscous case. (Note that, in the gas phase, viscosity is not modelled and constant pressure is assumed.)

Table 1 – Physical constants for simulation

Physical constant	Value
T (K)	293
p (Pa)	10^5
p_v^* (Pa)	2339
δ (mm^2/s)	25.69
σ (N/m)	0.072
ν_w (mm^2/s)	1.002

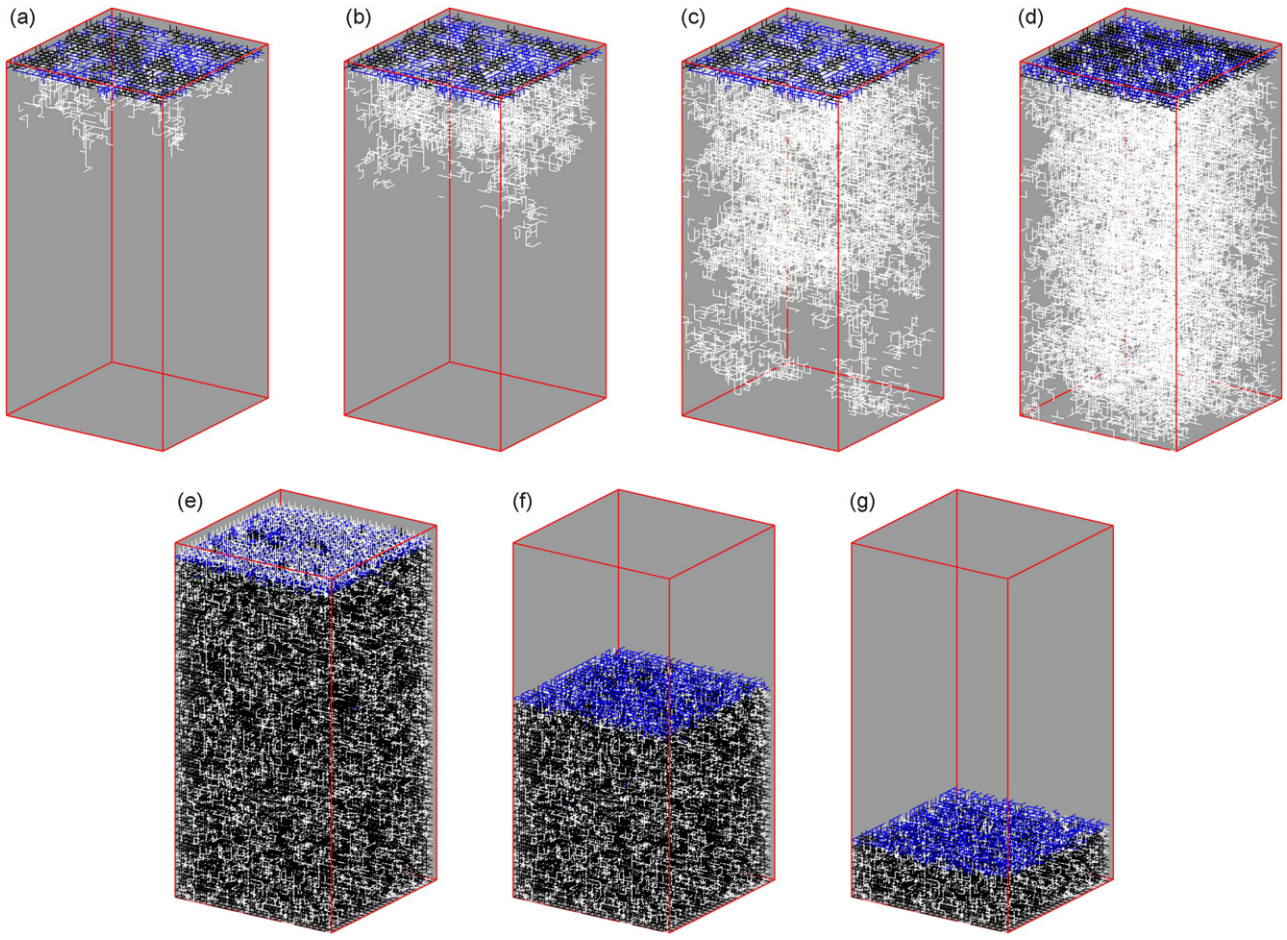

Fig. 2 – Phase distributions for *non-viscous* case at network saturations (a) 0.98; (b) 0.95; (c) 0.86; (d) 0.75; (e) 0.67; (f) 0.39; (g) 0.11; white lines represent empty throats, black is for liquid throats and blue for partially filled throats. The network is open for evaporation at the top; periodic boundary conditions are applied in horizontal directions. (For better readability, empty throats are not shown in top layers with an average saturation lower than 0.26; neither are full throats shown in bottom layers with an average saturation higher than 0.74.) (For interpretation of the references to colour in this figure legend, the reader is referred to the web version of the article.)

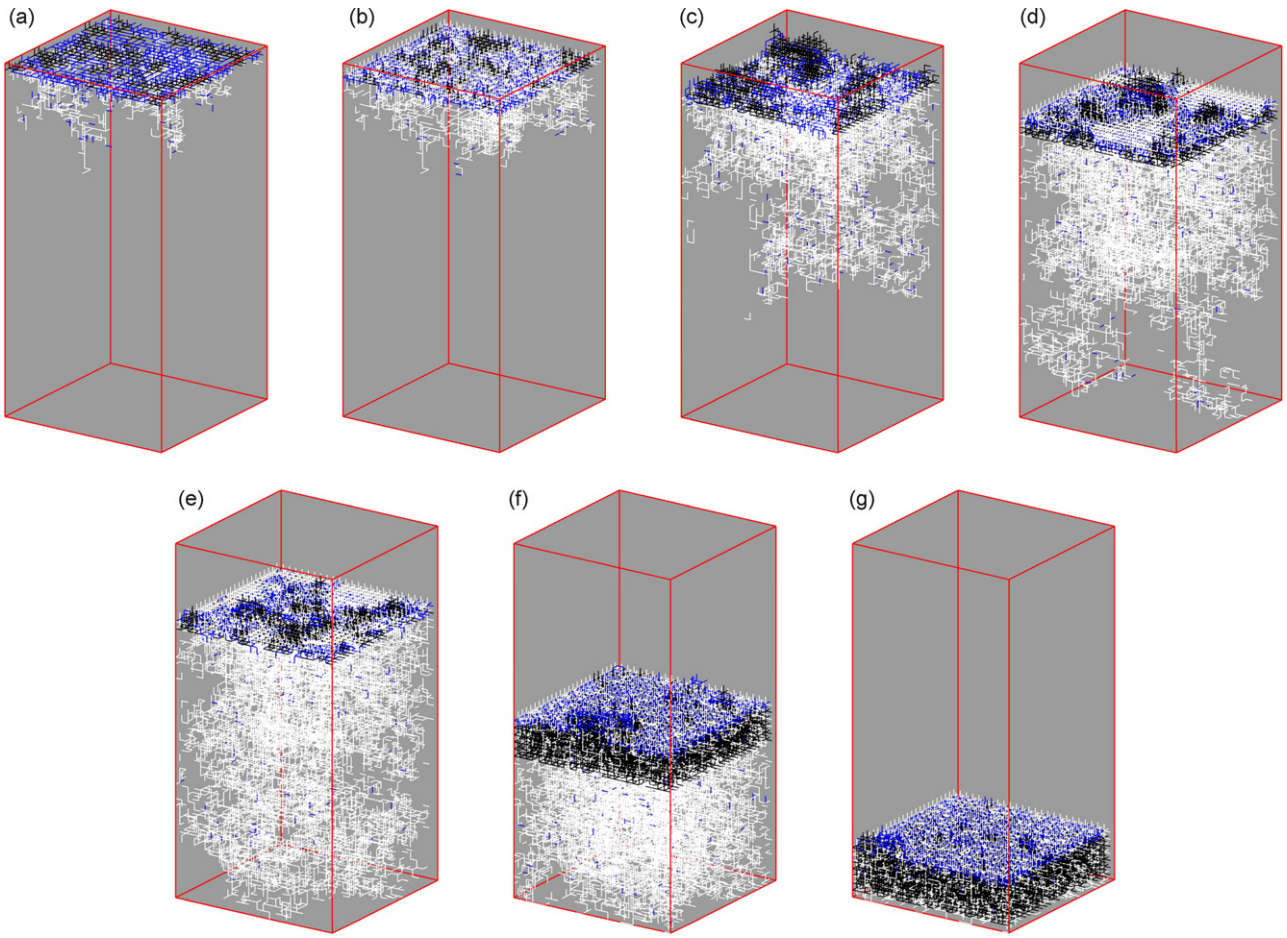

Fig. 3 – Phase distributions for *viscous* case at network saturations (a) 0.98; (b) 0.95; (c) 0.86; (d) 0.75; (e) 0.67; (f) 0.39; (g) 0.11; white lines represent empty throats, black is for liquid throats and blue for partially filled throats. The network is open for evaporation at the top; periodic boundary conditions are applied in horizontal directions. (For better readability, empty throats are not shown in top layers with an average saturation lower than 0.26; neither are full throats shown in bottom layers with an average saturation higher than 0.74.) (For interpretation of the references to colour in this figure legend, the reader is referred to the web version of the article.)

3. Simulation results

Present computational limitations impose a relatively small network size ($25 \times 25 \times 50$) so that rather unrealistic values have to be chosen for pore geometry and drying conditions to observe significant viscous effects. Air flow is at room temperature and atmospheric pressure and contains no moisture ($p_{v,\infty} = 0$); we consider water as a liquid (the physical constants for the simulation are given in Table 1); boundary layer is 50 μm thin, corresponding to a mass transfer coefficient $\beta = 0.51$ m/s and an initial drying rate of 9 g/m^2 s (for a completely wet surface). Throats have a very narrow radius distribution (50 ± 1 nm) and length 500 nm; this means that porosity is low (9.4%) and that only a thin near-surface region (depth 25 μm) of the porous medium is described. Effects sim-

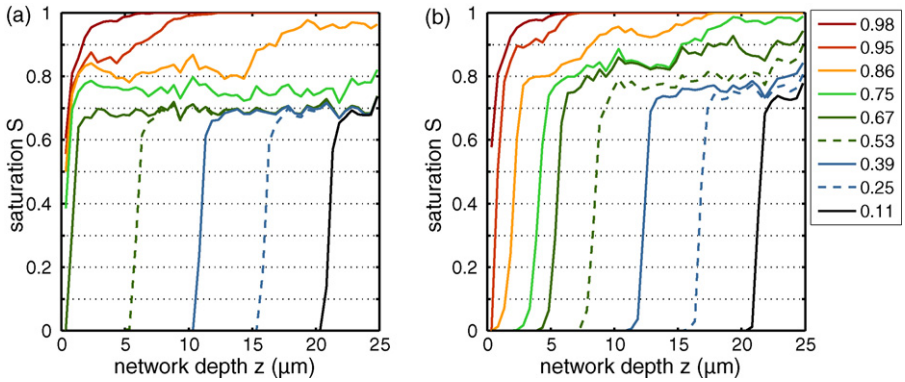

Fig. 4 – Profiles of slice-averaged saturation during drying: (a) non-viscous (b) viscous. (Solid lines correspond to the choice of phase distributions shown in Figs. 1 and 2.)

ilar to the ones discussed below will also occur for realistic conditions, but over longer distances.

Being interested in the role of liquid viscosity, drying of the same network is once simulated neglecting the viscous effects and once accounting for them. Respective phase distributions during drying are shown in Figs. 2 and 3; by slice averaging, they are converted into one-dimensional saturation profiles as plotted in Fig. 4. Corresponding drying rate curves are given in Fig. 5; the drying rate is put into dimensionless form by setting its initial value to unity.

If liquid viscosity is neglected, capillary pumping experiences no constraint as long as the liquid is connected over the whole network. During this period, no drying front occurs, but gas penetrates into the depth of the network and saturation level drops more or less uniformly throughout the network (Figs. 2a–d and 4a). Network surface stays sufficiently wet so that lateral vapour transfer in the gas-side boundary layer can ensure that liquid is evaporated at a constant rate (Fig. 5). At a critical saturation of about 0.7, the liquid phase has split up into small disconnected clusters, network surface dries out (Fig. 2e) and a receding evaporation front is observed (Figs. 2f and g and 4a). Drying rate drops due to the additional vapour transfer resistance in the network (Fig. 5). The mentioned critical saturation is expected to be lower for larger pore networks (Le Bray and Prat, 1999; Yiotis et al., 2006).

If viscous effects are modelled, they do not play a significant role in the very initial drying phase (here $S > 0.98$) which is still dominated by capillary forces (compare Figs. 2a and 3a). But as flow distances become longer and surface saturation decreases, differences in capillary pressure are not enough to supply liquid at the high local evaporation rates (which are even enhanced by lateral diffusion in the boundary layer). Therefore, all surface throats dry out (Fig. 4b) and a quite narrow drying front recedes into the pore network. As a consequence, drying rates are strongly reduced (Fig. 5), so that, as drying proceeds, this receding front can widen up gradually (Figs. 3c and d and 4b). In the viscous case, breakthrough occurs long after network surface is dry. Note also that the competition between menisci for liquid flow is documented by many moving menisci in one cluster (blue throats in Fig. 3).

With further decreasing drying rate, saturation gradient is reduced more and more (Fig. 4b) and local saturations approach the limit for liquid disconnection (Fig. 3e and f). In the final stages of drying, viscous effects play only a little role (compare Figs. 2g and 3g, see Fig. 5). This non-viscous limit ought to gain significance for deeper networks.

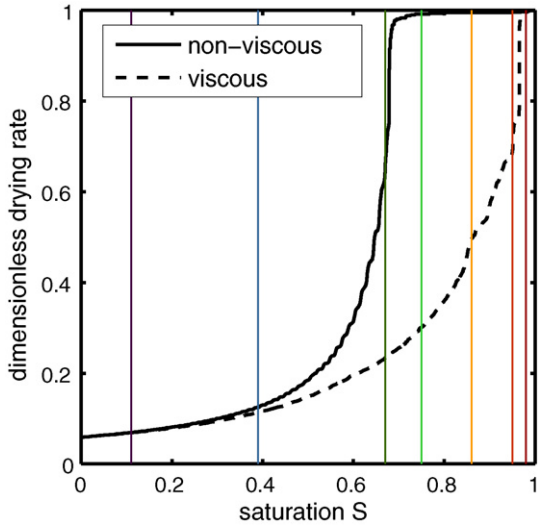

Fig. 5 – Drying rate curves for non-viscous and viscous case. (Vertical lines correspond to the choice of network saturations in the other figures.)

If we consider a characteristic length over which liquid can be pumped at a given available capillary driving force (Metzger et al., 2007c), this is found to be inversely proportional to drying rate and – neglecting vapour transfer resistance in the boundary layer – proportional to the thickness of the dried layer of the pore network. Therefore, the drying front can widen up with no upper bound if the network is arbitrarily deep, unlike in the gravity-stabilized case where front width fluctuates around a *constant* value.

Note that one of our assumptions has been perfect wetting of the liquid; for contact angles greater than zero the capillary pressures at the menisci will be less pronounced as well as the available pressure differences for driving capillary flow. This means that we have taken the minimum ratio of viscous to capillary effects; viscosity may still play a role if the pore size distribution is chosen slightly wider.

Conclusions

We have observed that viscous effects play a major role in the intermediate stages of drying whereas short- and long-time drying behaviour are similar to the non-viscous case. The relative size of viscous effects is decisive for phase distributions and drying rates in these intermediate stages of the drying process – and will especially determine the duration of the constant drying rate period. For our specific case, we observed a near-disappearance of this period whereas in many real porous media it is of considerable importance. The reason is that we have chosen a very narrow pore size distribution. Two-dimensional simulations for more realistic cases of pore size distributions – wider or even bimodal ones – show little effect of liquid viscosity (Metzger et al., 2007a).

Future work shall further investigate the local variation of saturation in the drying front and the scaling behaviour of its width with capillary number as already studied by Prat and Bouleux (1999). This shall pave the way to describe drying behaviour of much larger porous structures.

In the same context, a continuous model will be assessed that accounts for vapour diffusion in a dry zone and for viscous flow in the partially saturated zone driven by differences in capillary pressure (described by the generalized Darcy law). To this purpose, effective model parameters, such as liquid permeability and capillary pressure, will first be computed from the phase distributions as observed in a drying pore network (described by the above viscous model); then, saturation profiles shall be computed by the continuous model and compared to the profiles obtained from network simulations (as in Fig. 4b).

REFERENCES

Huinink, H.P., Pel, L., Michels, M.A.J. and Prat, M., 2002, Drying processes in the presence of temperature gradients. Pore-scale modelling. Eur Phys J E, 9: 487–498.

Kast, W., (1988). *Adsorption aus der Gasphase*. (VCH, Weinheim).

Laurindo, J.B. and Prat, M., 1996, Numerical and experimental network study of evaporation in capillary porous media. Phase distributions. Chem Eng Sci, 51: 5171–5185.

Laurindo, J.B. and Prat, M., 1998, Numerical and experimental network study of evaporation in capillary porous media. Drying rates. Chem Eng Sci, 53: 2257–2269.

Le Bray, Y. and Prat, M., 1999, Three dimensional pore network simulation of drying in capillary porous media. Int J Heat Mass Transfer, 42: 4207–4224.

Metzger, T., Irawan, A. and Tsotsas, E., 2007, Isothermal drying of pore networks: influence of friction for different pore structures. Dry Technol, 25: 49–57.

Metzger, T., Irawan, A. and Tsotsas, E., 2007, Influence of pore structure on drying kinetics: a pore network study. AIChE J, 53: 3029–3041.

Metzger, T., Tsotsas, E. and Prat, M., 2007, Chapter 2—Pore-network models: a powerful tool to study drying at the pore level and understand the influence of structure on drying kinetics, in Modern Drying Technology, Vol. 1, Computational Tools at Different Scales, Tsotsas, E. and Mujumdar, A.S., Mujumdar, A.S. (eds) (Wiley-VCH, Weinheim, Germany), pp. 57–102.

Nowicki, S.C., Davis, H.T. and Scriven, L.E., 1992, Microscopic determination of transport parameters in drying porous media. Dry Technol, 10: 925–946.

Plourde, F. and Prat, M., 2003, Pore network simulations of drying of capillary media. Influence of thermal gradients. Int J Heat Mass Transfer, 46: 1293–1307.

Prat, M., 1993, Percolation model of drying under isothermal conditions in porous media. Int J Multiphase Flow, 19: 691–704.

Prat, M. and Bouleux, F., 1999, Drying of capillary porous media with stabilized front in two-dimensions. Phys Rev E, 60: 5647–5656.

Prat, M., 2007, On the influence of pore shape, contact angle and film flows on drying of capillary porous media. Int J Heat Mass Transfer, 50: 1455–1468.

Segura, L.A. and Toledo, P.G., 2005, Pore-level modeling of isothermal drying of pore networks. Effects of gravity and pore shape and size distributions on saturation and transport parameters. Chem Eng J, 111: 237–252.

Shaw, T.M., 1987, Drying as an immiscible displacement process with fluid counterflow. Phys Rev Lett, 59: 1671–1674.

Tsimpanogiannis, I.N., Yortsos, Y.C., Poulou, S., Kanellopoulos, N. and Stubos, A.K., 1999, Scaling theory of drying in porous media. Phys Rev E, 59: 4353–4365.

Yiotis, A.G., Stubos, A.K., Boudouvis, A.G. and Yortsos, Y.C., 2001, A 2-D pore-network model of the drying of single-component liquids in porous media. Adv Water Resour, 24: 439–460.

Yiotis, A.G., Boudouvis, A.G., Stubos, A.K., Tsimpanogiannis, I.N. and Yortsos, Y.C., 2003, Effect of liquid films on the isothermal drying of porous media. Phys Rev E, 68: 037303-1–037303-4.

Yiotis, A.G., Boudouvis, A.G., Stubos, A.K., Tsimpanogiannis, I.N. and Yortsos, Y.C., 2004, The effect of liquid films on the drying of porous media. AIChE J, 50: 2721–2737.

Yiotis, A.G., Tsimpanogiannis, I.N., Stubos, A.K. and Yortsos, Y.C., 2006, Pore-network study of the characteristic periods in the drying of porous materials. J Colloid Interface Sci, 297: 738–748.

Available online at www.sciencedirect.com
ScienceDirect
International Journal of Heat and Mass Transfer 51 (2008) 2506–2518
International Journal of HEAT and MASS TRANSFER
www.elsevier.com/locate/ijhmt

Consideration of heat transfer in pore network modelling of convective drying

V.K. Surasani, T. Metzger *, E. Tsotsas

Thermal Process Engineering, Otto-von-Guericke-University, Universitaetsplatz 2, 39106 Magdeburg, Germany

Received 19 April 2007; received in revised form 5 July 2007
Available online 27 September 2007

Abstract

The influence of heat transfer on the drying behaviour of capillary porous media saturated with water is studied. To overcome the limitations of continuum approaches, a pore network model based on statistical physics and invasion percolation is used. The presented non-isothermal model is the first of its kind to describe free evolution of temperatures in convective drying. Gas-side mass transfer is modelled by a discretised boundary layer. Model assumptions are purely conductive heat transfer in the network and negligible viscosity. Vapour condensation is partially modelled. Simulations are conducted on two-dimensional square lattice networks. Overall drying rates and corresponding evolution of phase distributions and temperature fields are presented for mono- and bi-modal pore structures. The influence of heat transfer on phase distributions and drying behaviour is discussed in comparison with isothermal simulations.

Keywords: Porous structure; Drying kinetics; Phase distributions; Temperature fields; Diffusive boundary layer; Invasion percolation

1. Introduction

Drying of porous media imposes a challenging modelling task since it involves mass, momentum and heat transfer in a three-phase (solid, liquid and gas) system. Classical models are based on homogenization [1] or volume averaging techniques [2] and treat the porous medium as a fictitious continuum describing its behaviour at the macroscale. The macroscale is defined by the length over which the system can be considered as homogeneous. Every continuous model requires the knowledge of effective transport parameters, which are averaged properties and need to be found by fitting to experimental data or theoretically by assumptions about the pore space. Many of the past theories attempt to derive effective parameters of porous media by some simple representation of the pore space, often as a bundle of capillary tubes [3]. However, these models will fail when the interconnectivity of pore space or fluid phase plays a major role. It is unclear, how fractal or cluster formations in two-phase flow can be described in a continuous way. In general, drying in porous media is a random process [4] due to stochastic geometry of the void space and transport steps that can hardly be accounted by any continuous model.

Discrete models using a network representation of pore structure and based on statistical physics, i.e. percolation theory, are particularly suited where the continuous approach fails [5]. The geometry of void space in porous media is represented as a network of pores connected with throats. Various geometrical shapes have been adapted for pores and throats in literature. Spherical pore bodies may be considered to contain the entire void space of the network, with the throats acting only as conductors [6]. Alternatively, the entire void space may be attributed to either bi-conical [7] or uniform cross section [8] throats, regarding the pores as merely the volumeless nodes of the network. Pore network modelling was first developed for drying by Daian and Saliba [9] in order to describe moisture migration in porous media. Nowicki et al. [7] worked on drying of porous media, including viscous effect in the liquid

* Corresponding author. Tel.: +49 391 6711362; fax: +49 391 6711160.
E-mail address: thomas.metzger@ovgu.de (T. Metzger).

0017-9310/$ - see front matter © 2007 Elsevier Ltd. All rights reserved.
doi:10.1016/j.ijheatmasstransfer.2007.07.033

Nomenclature

A	area of cross section (m^2)
c_p	specific heat capacity (J/kg/K)
g	mass transfer conductance (kg/s)
H	enthalpy content (J)
L	length of throat (m)
$\widetilde{M}$	molar mass (kg/kmol)
$\dot{M}$	mass flow rate (kg/s)
N	number of pores/clusters (–)
P	pressure (Pa)
$\dot{Q}$	heat flow rate (W)
$\widetilde{\widetilde{R}}$	ideal gas constant (J/kmol/K)
r	throat radius (m)
S	saturation (–)
T	temperature (K)
t	time (s)
V	volume (m^3)
W	network thickness (m)
Δh	specific phase change enthalpy (J/kg)

Greek symbols

α	heat transfer coefficient ($W/m^2/K$)
β	mass transfer coefficient (m/s)
γ	surface tension (N/m)
δ	vapour diffusivity (m^2/s)
κ	thermal diffusivity (m^2/s)
λ	thermal conductivity (W/m/K)
ν	kinematic viscosity (m^2/s)
ρ	density (kg/m^3)

Subscripts/superscripts

BL	boundary layer
c	capillary
C	condensation
ev	evaporation
g	gas
i or j	pore or node
ij	throat connecting pores i and j
l	liquid
lm	number of menisci
nc	cluster number
s	solid
T	total network
v	vapour
*	equilibrium

phase, to determine effective transport parameters; Yiotis et al. [6] studied the effect of viscosity in both the gas and the liquid phase for drying of porous rocks. Prat et al. [8] investigated the stabilization of the drying front in the presence of gravity. A similar stabilization has been observed for viscous effects in the liquid [10]. Micro-model experiments have shown similar invasion patterns as the simulations [11]. However, simulated drying rates are greatly underestimated [12]. Film flows, which can contribute largely to the first drying period [13,14] can explain the difference between experimental and numerically simulated drying rates. Segura and Toledo [15,16] studied pore scale models based on the previous work by Prat [8].

Most of the above work on pore networks studied the influence of physical effects, i.e. capillary pumping, viscous flow, film flows and gravity, on overall drying behaviour under isothermal conditions. Metzger et al. [10,17], based on models similar to those of Prat, describe the influence of pore structure on drying behaviour also under isothermal conditions.

Despite of significant progress in the last decade, most pore network drying models are isothermal and, therefore, applicable only to low drying rates [5]. In convective drying, however, energy needed for evaporation is supplied to the moist product by dry airflow. Simultaneously, evaporated moisture is released to the ambient medium, making drying a coupled heat and mass transfer problem. Failing consideration of this coupling may lead to wrong results for drying kinetics. Until now, very little work has been done concerning the inclusion of heat transfer into pore network modelling. To our knowledge, only the influence of temperature gradients – which were imposed onto the drying product – has been investigated by Plourde and Prat [18], Huinink et al. [19]. Temperature dependence of liquid surface tension and equilibrium vapour pressure were accounted for and respective gradients made responsible for stabilization or destabilization of the drying front and for changes in drying rates. However, product temperature did not evolve freely as corresponding to convective drying boundary conditions.

As a step towards a complete pore network model, the present paper introduces heat transfer to the existing isothermal model version [20] that neglects viscous effects. The solid is considered non-hygroscopic, thus neglecting adsorption phenomena. Heat transfer in the network is assumed to take place only by conduction. Heat transfer parameters, i.e. thermal conductivity and heat capacity, are only functions of saturation. The non-isothermal model for convective drying and the numerical solution are presented first. Then, simulation results of drying kinetics, temporal evolution of phase distributions (cluster formation) and temperature fields are discussed for mono- and bi-modal pore size distributions.

2. Non-isothermal modelling

The non-isothermal model developed and implemented in the present work is an extension of an isothermal pore network drying model, which is based on the work of Prat [21] and includes discrete modelling of the boundary layer

[17]. Since, pore network models take geometry into account, the data structure for representing geometry will be discussed briefly before presenting model equations for heat and mass transfer.

2.1. Pore network

Void space in the porous medium is regarded as a network of cylindrical throats with randomly distributed radius connected by pore nodes without volume. In this paper, we restrict ourselves to two-dimensional square networks. Fig. 1 shows such a network of pores and throats and how is associated a control volume to each pore. As known from literature, the invasion behaviour of two-dimensional networks is slightly different to that of three-dimensional networks due to the lower connectivity of the pore space, e.g. [21]. The proposed algorithm is general enough to be applied to three-dimensional networks but still faces computational limits.

Throughout the paper white space (inside throats) represents the air and vapour phase, and black space stands for liquid. Initially, the network is fully saturated with water and has room temperature (20 °C). Only the top edge of the network is open to evaporation and subjected to heating or cooling; the remaining faces are impervious to heat and mass transfer.

2.2. Boundary layer model

For drying, the network is subjected at its open edge to lateral air flow with velocity u, bulk vapour pressure $P_{v,\infty}$ and bulk temperature T_∞. To realistically describe the drying kinetics, especially the first drying period with its constant drying rate, it is necessary to model the boundary layer in a discretised way, extending the network into the gas by additional nodes (see Fig. 2).

Assuming laminar flow over the network, the Sherwood number describing mass transfer is given by

$$Sh = \frac{\beta L_T}{\delta} = 0.664 Re^{1/2} Sc^{1/3} \tag{1}$$

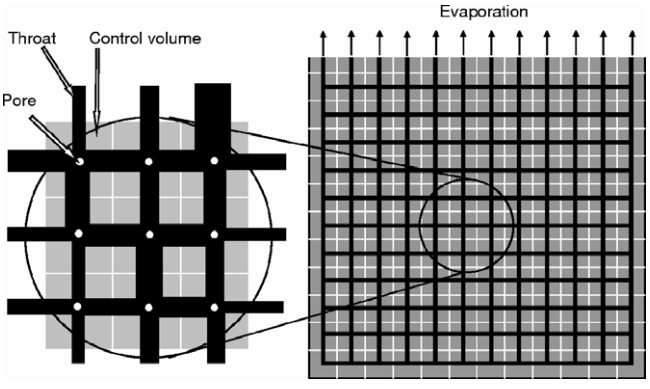

Fig. 1. Schematic representation of the porous medium by a 2D square network.

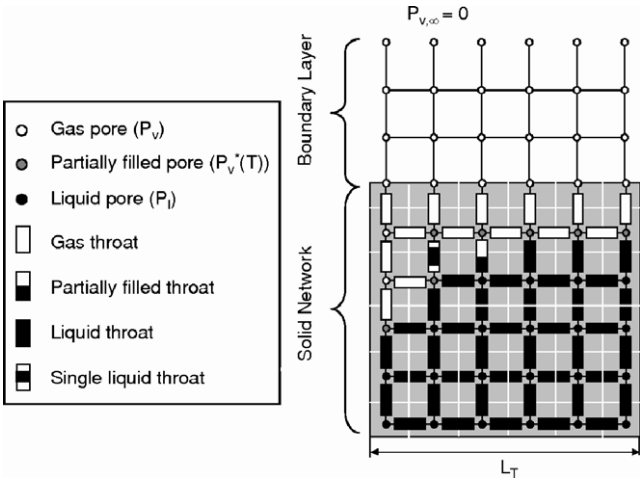

Fig. 2. Illustration of boundary layer over the network and state of pores and throats at some time during the drying process.

with Reynolds number $Re = uL_T/\nu_g$ and Schmidt number $Sc = \delta/\nu_g$. Here, β is mass transfer coefficient, L_T network length, δ vapour diffusivity and ν_g kinematic viscosity of the gas. However, Eq. (1) is derived for a plate at uniform partial pressure which is not necessarily fulfilled for drying porous medium (see [22]). From this, boundary layer thickness and the number of additional vertical nodes N_{BL} are obtained as

$$\varepsilon = \frac{\delta}{\beta} = N_{BL} L, \tag{2}$$

where the distance between nodes L is the same as the length of network throat. Vapour pressure of bulk air (here $P_{v,\infty} = 0$) provides the boundary condition for the extended network. Heat transfer between bulk air and network surface is described by a heat transfer coefficient α, which can be calculated by

$$\alpha = \beta \frac{\lambda_g}{\delta} \left(\frac{Pr}{Sc}\right)^{\frac{1}{3}} \tag{3}$$

based on the analogy between heat and mass transfer. Here λ_g is thermal conductivity of the gas and $Pr = \delta/\kappa_g$ is Prandtl number with thermal diffusivity κ_g. Fig. 2 illustrates the structure of the network and the boundary layer in the process of drying. For clarity, imaginary spherical pores are shown.

2.3. Pore and throat conditions

The state of throats plays a vital role in determining transport mechanisms during drying. Throats contain all void space and serve as the conductors in the network, carrying heat and mass flows due to temperature and vapour or liquid pressure gradients between the pores. Throats can be classified as gas throats, liquid throats and partially filled throats based on their saturation S_{ij} (see Fig. 2). The type of transport in the throats is also determined by saturation. If throat saturation S_{ij} is unity, liquid flow will

take place due to capillary pumping; if S_{ij} is equal to zero, vapour will be transferred by diffusion; and if S_{ij} is between 0 and 1, combined liquid flow, evaporation at the meniscus, and vapour diffusion will take place in a throat.

Pores represent the structural parameters of the void space and the state variables in each control volume. Structural parameters, constant in time, are the spatial positions of pores and their relative positions with respect to other pores and throats. State variables are saturations S_i, temperatures T_i, vapour pressures $P_{v_{i,i}}$ (eventually also total gas pressure) and liquid pressures $P_{l,i}$. Pore saturation S_i is determined by its neighbour throat saturations S_{ij}. If all neighbour throats are full, saturation is unity (liquid pore); and it is zero (gas pore) if all neighbour throats are empty. In general, pore saturation is equal to the fraction of full or partially filled throats ($0 \leqslant S_i \leqslant 1$). In partially filled pores, we assume equilibrium vapour pressure (see Fig. 2), which sets the boundary condition for evaporation during the drying process. Nodes in the boundary layer are always at unknown vapour pressures.

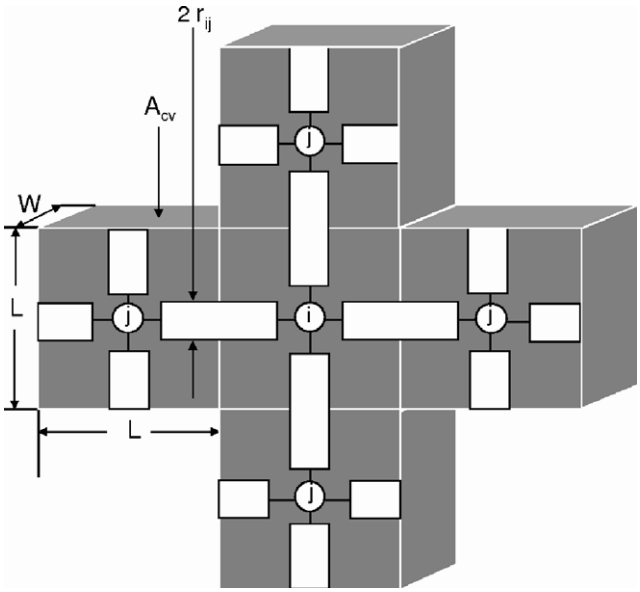

Fig. 3. Control volume i with neighbours j and exchange areas.

2.4. Heat and mass transfer relations

The implemented model is based on the following assumptions:

1. Constant boundary layer thickness;
2. constant total pressure in the gas phase;
3. quasi-stationary diffusive vapour transport;
4. negligible viscosity of liquid (capillary forces dominate over viscous forces);
5. heat transfer in the network only by conduction;
6. local thermodynamic equilibrium in each control volume.

The vapour flow rate between two gas pores due to vapour pressure gradients is given by Stefan's law as

$$\dot{M}_{v,ij} = -A_{ij}\frac{\delta}{L_{ij}}\frac{P\widetilde{M}_v}{\widetilde{R}T}\ln\left(\frac{P-P_{v,i}}{P-P_{v,j}}\right), \tag{4}$$

where $\widetilde{M}_v$ is molar mass of vapour, $\widetilde{R}$ ideal gas constant and T absolute temperature. Eq. (4) also describes the vapour flow rate between two nodes in the boundary layer, only the cross sectional area A_{ij} must be chosen accordingly. It is

$$A_{ij} = \pi r_{ij}^2 \quad \text{for network,} \tag{5}$$

$$A_{ij} = LW \quad \text{for boundary layer,} \tag{6}$$

where r_{ij} is throat radius and W network thickness in the third dimension (see Fig. 3). Since we neglect the overlap of throats at pore nodes, all throats in the network are assumed as equal in length ($L_{ij} = L$).

The liquid flow rate in the network between pores i and j due to different liquid pressures $P_{l,i}$ and $P_{l,j}$ can be calculated by Poiseuille's law as

$$\dot{M}_{l,ij} = \frac{\pi r_{ij}^4}{8\nu_l L}(P_{l,i} - P_{l,j}) \tag{7}$$

with the kinematic viscosity of water ν_l. However, Eq. (7) is not used in the present model because of the fourth assumption; instead, we apply a rule valid when viscous effects are negligible compared to capillary effects that will be discussed in Section 3.2.

Since heat transfer is only by conduction, heat flow rates due to temperature gradients are given by Fourier's law

$$\dot{Q}_{ij} = A_{cv,ij}\lambda_{ij}\frac{T_i - T_j}{L}, \tag{8}$$

where the exchange area is $A_{cv,ij} = LW$ (because both voids and solid can contribute to heat transfer). The effective thermal conductivities λ_{ij} are functions of throat saturation

$$A_{cv,ij}\lambda_{ij} = (A_{cv,ij} - \pi r_{ij}^2)\lambda_s + \pi r_{ij}^2 S_{ij}\lambda_l \tag{9}$$

with thermal conductivities of solid and liquid λ_s and λ_l, respectively. For simplicity, solid and liquid are considered as resistances in parallel, conduction in the gas is neglected. The enthalpy content H_i of control volume V_i is given by

$$H_i = V_i(\rho c_p)_i(T_i - T_{ref}), \tag{10}$$

where the total heat capacity of the control volume is

$$V_i(\rho c_p)_i = \left(V_i - \frac{L}{2}\sum_{j=1}^{4}\pi r_{ij}^2\right)(\rho c_p)_s + \frac{L}{2}\sum_{j=1}^{4}\pi r_{ij}^2 S_{ij}(\rho c_p)_l. \tag{11}$$

Fig. 3 shows how each control volume is represented by one pore and contains four-half throats, i.e. each throat participates in two control volumes. Liquid of partially filled throats are equally distributed to neighbour pores.

From the law of conservation and the assumption of quasi-steady vapour transport, total mass flow from any gas pore is equal to zero. By applying Eq. (4) to gas pore i, we obtain

$$\sum_{j=1}^{4} \dot{M}_{v,ij} = \sum_{j=1}^{4} A_{ij} \frac{\delta}{L} \frac{P\widetilde{M}_v}{\widetilde{R}T} \ln\left(\frac{P - P_{v,i}}{P - P_{v,j}}\right) = 0, \tag{12}$$

where $\dot{M}_{v,ij}$ is the mass flow rate of vapour. For partially saturated pores the vapour balance can be written as

$$\sum_{j=1}^{4-lm} \dot{M}_{v,ij} = \sum_{j=1}^{lm} \dot{M}_{ev,ij} \tag{13}$$

with evaporation or condensation rates $\dot{M}_{ev,ij}$ in the connected meniscus throats (lm). Similarly, for a model with liquid viscosity, we have for the liquid pores

$$\sum_{j=1}^{4} \dot{M}_{l,ij} = \sum_{j=1}^{4} \frac{\pi r_{ij}^4}{8\nu_l L}(P_{l,i} - P_{l,j}) = 0 \tag{14}$$

The boundary conditions to this set of equations are given at the menisci and must be found by an iterative algorithm (Metzger et al., [10]). If a meniscus is moving, a pressure boundary condition of first kind is applied ($P_{l,ij} = P - P_{c,ij}$); if it is stationary, the local evaporation rate gives a boundary condition of second kind ($\dot{M}_{l,ij} = \dot{M}_{ev,ij}$). The dynamic energy balance over the control volume can be derived from Eqs. (8) and (10) as

$$V_i(\rho c_p)_i \frac{dT_i}{dt} = -\sum_{j=1}^{4} \dot{Q}_{ij} - \Delta h_{v,i}(T_i) \sum_{j=1}^{lm} \dot{M}_{ev,ij}, \tag{15}$$

where $\Delta h_{v,i}(T_i)$ is phase change enthalpy (absolute value). The mass flow rate $\dot{M}_{ev,ij}$ is positive for evaporation and negative for condensation. The meniscus position is used to allocate heat sink/source to a control volume.

2.5. Coupling of heat and mass transfer

The interaction between heat and mass transfer influences considerably the drying process, particularly at the phase boundaries in the network. At an evaporating meniscus, the vapour takes up the enthalpy of evaporation and the liquid temperature is reduced (heat sink); likewise, we have heat sources at places of condensation. This coupling of mass transfer with heat transfer is already implemented by including rates of evaporation and condensation in the dynamic energy balance equation (Eq. (15)).

As a second major coupling effect, equilibrium vapour pressures $P^*_{v,i}(T_i)$ at the menisci are strongly temperature dependent. In the presence of a temperature field, equilibrium vapour pressure varies spatially. These vapour pressures have to be updated after each time step by use of an Antoine equation.

At the same time, due to temperature differences, gradients in surface tension γ will develop and instigate gradients in capillary pressure

$$P_{c,ij} = \frac{2\gamma(T_{ij})}{r_{ij}} \tag{16}$$

that contribute to liquid flow additionally to the effect of different throat radii.

3. Numerical solution

In drying of porous media, capillary pressure gradients exist and cause liquid flow by capillary pumping. Viscous forces will counteract capillary forces and always stabilize the receding drying front, because they reduce the distance over which liquid can be pumped at a given rate [10]. As we will see the assumption of zero liquid viscosity leads to a discrete way of solving the model for liquid transport. The continuous conservation equations for vapour and energy, Eq. (12) and Eq. (15), have to be solved together with the discrete model part that describes liquid transport due to capillary pumping. The quasi-steady vapour balances of Eq. (12) are solved for the current boundary conditions at the meniscus throats. Dynamic energy balances Eq. (15) are solved by an explicit scheme using the current phase distribution and temperature field.

3.1. Vapour transport

Rewriting Eq. (12) for each pore of unknown vapour pressure i and introducing mass transfer conductances g_{ij} leads to

$$\sum_{j=1}^{4} g_{ij}(lp_i - lp_j) = \sum_{j=1}^{4} g_{ij} lp^*_j, \tag{17}$$

where the logarithmic pressure differences are

$$lp_i = \ln(P - P_i)$$
$$lp_j = \begin{cases} \ln(P - P_j) & \text{for } S_j = 0 \\ 0 & \text{for } 0 < S_j < 1 \end{cases} \tag{18}$$

The right hand side of Eq. (17) gives the boundary conditions at the liquid–gas interface and at the edge of the gas-side boundary layer as

$$lp^*_j = \begin{cases} 0 & \text{for } S_j = 0 \\ \ln(P - P^*_{v,j}(T_j)) & \text{for } 0 < S_j < 1 \\ \ln(P - P_{v,\infty}) & \text{edge of boundary layer} \end{cases} \tag{19}$$

Applying Eq. (17) to all gas pores in network and boundary layer at a given time, forms the linear system

$$\mathbf{G} \bullet \mathbf{LP} = \mathbf{LP}^* \tag{20}$$

where $\mathbf{G}$ is a sparse symmetric matrix containing mass transfer conductances g_{ij}, $\mathbf{LP}$ represents the unknown vector of lp_i and $\mathbf{LP}^*$ the vector of boundary conditions. Eq. (20) is solved using the conjugate gradient method (CGM); then, vapour flow rates $\dot{M}_{v,ij}$ can be calculated from Eq. (4).

3.2. Liquid transport

The assumption of negligible viscous effects implies that, in each cluster, liquid can be pumped from the throat with the highest liquid pressure to all other menisci at their

respective rates of evaporation, and that only this one throat will empty. So, it is necessary to identify the throat with the lowest capillary pressure $P_{c,ij}$ (i.e. highest liquid pressure $P_{l,ij}$) for the current temperatures at each time step.

Fig. 4 shows liquid transport in a single cluster with a moving meniscus (MM) throat; all remaining menisci are stationary. For each time step, the mass lost due to evaporation from all menisci in the cluster must be removed from the throat with the lowest capillary pressure (shaded volume). For isothermal conditions, this will always be the throat with largest r_{ij} in a cluster (see Eq. (16)).

When a throat has emptied completely, throat and pore saturations must be updated, changing the linear system of Eq. (20). Therefore, we must introduce a mass transfer time step $\Delta t_{m,nc}$ for each cluster nc, which is calculated as the ratio of liquid mass left in the MM throat and sum of evaporation rates at the menisci of the cluster:

$$\Delta t_{m,nc} = \frac{\rho_l V_{MM,nc}}{\sum_{j=1}^{mt} \dot{M}_{ev,ij,nc}}. \tag{21}$$

Here, mt is the number of evaporating throats in a cluster.

3.3. Condensation

If the system is considered to be non-isothermal, spatial temperature gradients build up over the network during the drying process. Since equilibrium vapour pressure is highly sensitive to the temperature, equilibrium vapour pressure gradients will develop. At the same time, capillary pressure gradients may cause splitting of the continuous liquid phase into disconnected wet patches (liquid clusters) at different temperatures. Due to the above phenomena, vapour evaporating from hot clusters or single throats may move against the main direction of mass flow and condense on cold clusters or single throats (vapour back diffusion may take place instead of the escape of vapour from the top surface).

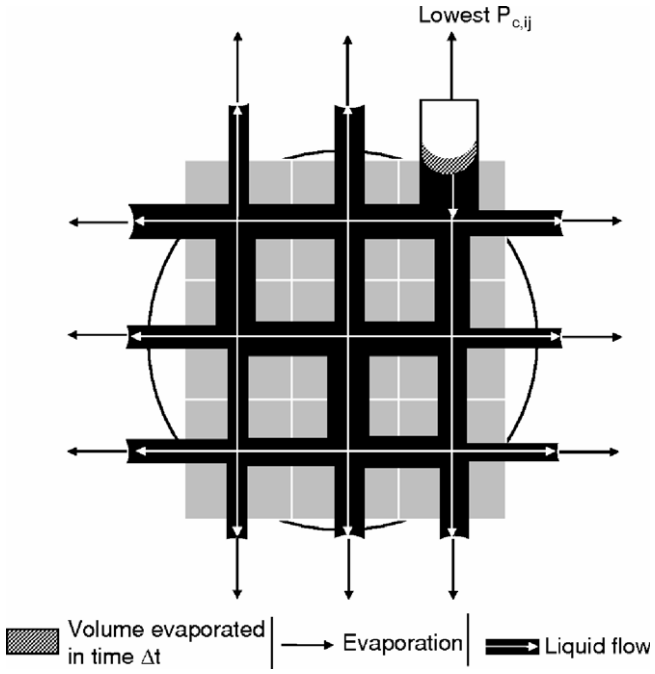

Fig. 4. Liquid flow due to capillary pumping as well as stationary and moving menisci for a single cluster.

The effect of condensation is fully included in heat transfer, Eq. (15), but it is only partially accounted for in mass transfer. For each cluster or single liquid throat, the net phase change rate is computed as the sum of all meniscus evaporation/condensation rates. If there is net evaporation in a cluster, the previously described algorithm (Section 3.2) can be used. For clusters with net condensation, we can either refill a partially emptied throat (MM throat) with mass transfer time step

$$\Delta t_{m,nc} = -\frac{(1 - S_{MM})\rho_l V_{MM,nc}}{\sum_{j=1}^{mt} \dot{M}_{ev,ij,nc}} \tag{22}$$

or we have to neglect condensation because imbibition of completely emptied throats is not included in the model. Therefore, not all condensing vapour can be accommodated but the committed error can be assessed because the true condensation rates are known. When simulation results will be presented in Section 4, the error on condensation rates will also be discussed.

3.4. Cluster labelling

One of the main advantages of discrete network models over continuous models is that the former can describe the disintegration of the liquid phase into disconnected clusters, while the latter are limited to smooth variations of pore saturation. In the isothermal case, clusters will form due to random throat size distribution. In the presence of thermal gradients, surface tension gradients may cause additional capillary pressure differences. To describe correctly liquid transport in the network, the connectivity of the liquid phase must be known, so that cluster labelling of throats is necessary. To this purpose, the Hoshen–Kopelman algorithm (well documented in literature) can be used [23,24].

Fig. 5 shows how a mass transfer time step $\Delta t_{m,nc}$ computed by Eq. (21) or Eq. (22) is associated to every cluster and every isolated throat. From these, the minimum must be chosen as the mass transfer time step of the network $\Delta t_{m,min}$.

3.5. Dynamic heat transfer by explicit scheme

Heat transfer is continuous in the presence of thermal effects, even though mass transfer naturally imposes discrete time steps (by the emptying of throats). Therefore, a different time discretisation will be necessary. For the updating of temperature fields in the entire network, dynamic energy balance was implemented in an explicit

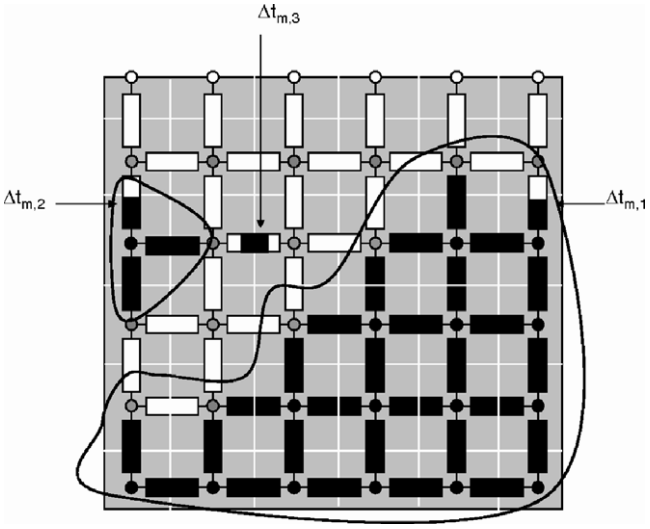

Fig. 5. Cluster formation during drying and different mass transfer time steps.

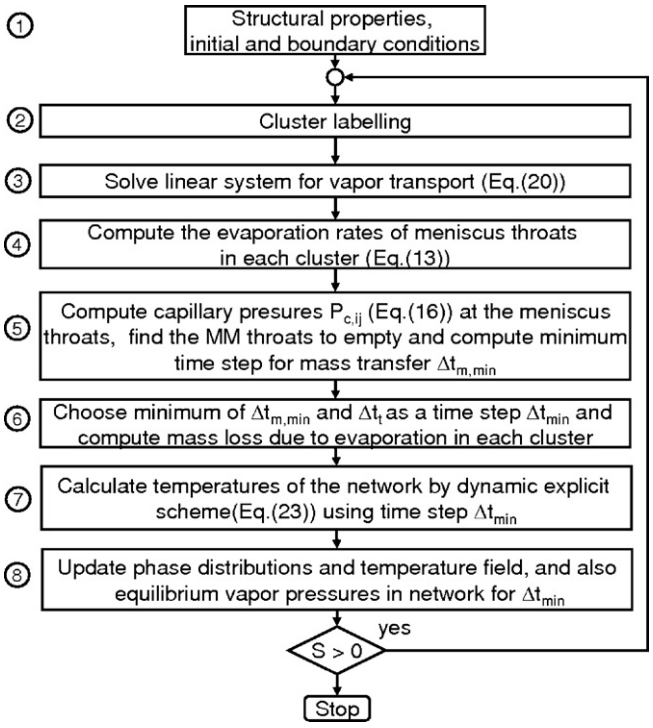

Fig. 6. Flow sheet for the drying algorithm.

scheme. By substituting Eq. (8) into Eq. (15) and integrating this equation over the thermal time step Δt_t we obtain

$$T_i|_{t+\Delta t} = T_i + \frac{\Delta t_t}{V_i(\rho c_p)_i}\sum_{j=1}^{4}\left(-A_{cv,ij}\lambda_{ij}\frac{T_i - T_j}{L} - \Delta h_v(T_i)\dot{M}_{ev,ij}\right). \quad (23)$$

The stability of the explicit method is only guaranteed if the thermal time step fulfils the condition

$$\Delta t_t < \frac{(\rho c_p)_i L^2}{\sum_j \lambda_{ij}} \quad (24)$$

for all control volumes i. If this critical value is exceeded, physically unrealistic results like negative temperatures may be observed. The major disadvantage of the explicit scheme is the small time step that causes large computational times.

3.6. Drying algorithm

Fig. 6 illustrates the numerical solution of the non-isothermal network drying model. First, the data structures describing the pore grid of network and boundary layer must be formed from network size (e.g. 51 × 51); additionally drying air velocity, initial and boundary conditions are set (step 1). After cluster labelling (step 2), the linear system for vapour transport (Eq. (20)) is solved (step 3) and the evaporation rates at each meniscus are computed (step 4). Then, from the capillary pressures $P_{c,ij}$ in meniscus throats,

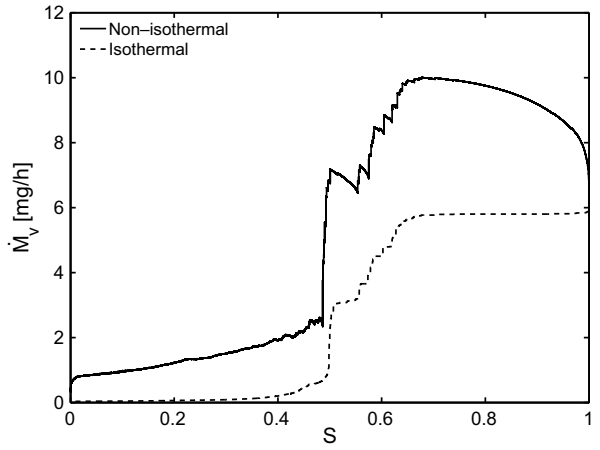

Fig. 7. Isothermal and non-isothermal drying rate curves for bi-modal network.

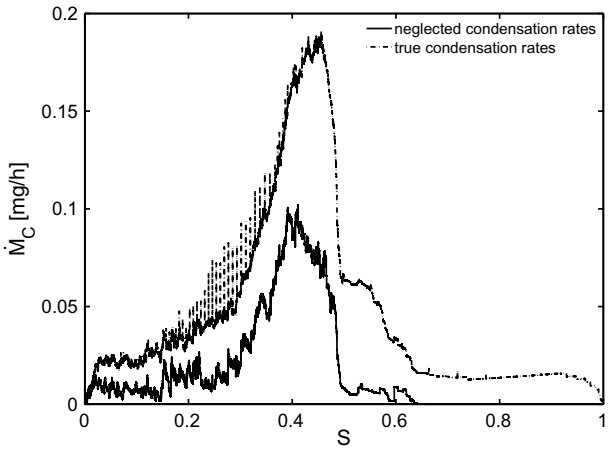

Fig. 8. Actual and neglected condensation rates in the non-isothermal model due to temperature gradients.

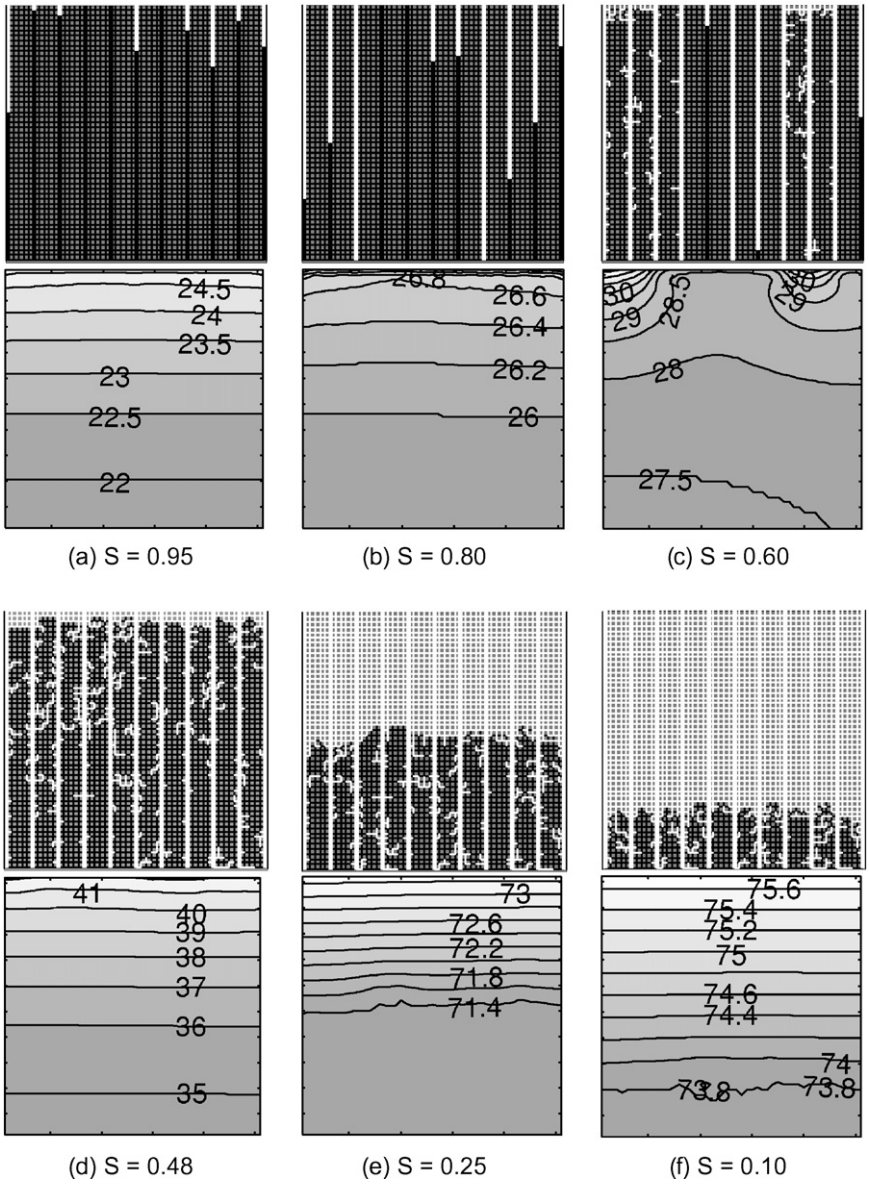

Fig. 9. Evolution of phase and temperature distributions for bimodal case network (saturations are indicated).

the MM throat is identified for each cluster, and the minimal mass transfer time step $\Delta t_{m,min}$ calculated (step 5). The time step Δt_{min} is chosen as the minimum out of mass transfer time step $\Delta t_{m,min}$ and heat transfer time step Δt_t, which obeys stability criteria of Eq. (24) (step 6). The mass loss due to evaporation is computed for the time step Δt_{min}.

Next, the new temperature field is computed by using Eq. (23) for same time step (step 7). Finally, phase distributions (pore and throat saturations) and temperature fields (as well as temperature dependent variables) are updated (step 8). The procedure will be repeated in a loop until all water is removed from the network.

4. Simulation results

The results presented in this section have been obtained for networks of size 51×51 with mono- and bi-modal throat size distribution. The radius of throats is randomly varied according to the normal number density function

$$f(r) = \frac{1}{\sqrt{2\pi}\sigma_0} e^{\frac{(r-r_0)^2}{2\sigma_0^2}} \tag{25}$$

with mean r_0 and standard deviation σ_0. A mean radius of 40 μm and a standard deviation of 2 μm are used for the mono-modal network (see Fig. 13 for realization). In the bi-modal pore network, radii from a distribution with 100 ± 5 μm are applied to every fifth vertical throat, leaving the remaining throats as of mono-modal network (Fig. 9). Throat length is 500 μm for all networks.

Initially, the network is saturated with water and has a uniform temperature of 20 °C. The heat transfer parameters of the solid are chosen as for glass: $(\rho c_p)_s = 1.7 \times 10^6$ J/(m^3 K) and $\lambda_s = 1$ W/(m K). Bulk air is at

$T_\infty = 80$ °C, has zero moisture content and velocity such that the boundary layer contains 7 nodes ($\beta = 7.3$ mm/s).

Fig. 7 shows the drying kinetics for the bi-modal pore network as evaporation rate $\dot{M}_v$ versus network saturation S. Both the isothermal and the non-isothermal curve start at the same rate. The initial warming-up to constant drying conditions can be clearly seen in the non-isothermal process. The constant rate period extends for both curves to a saturation of approximately 0.6, i.e. almost until all the macro-throats (43% of volume) are emptied.

As explained above, the order of emptying of throats is determined by capillary pressure. In the isothermal model, it depends on the throat radius alone since temperature is constant throughout the network. In the non-isothermal model, the order of emptying may also be influenced by surface tension at the menisci (Eq. (16)). However, at the beginning, influence of temperature on capillary pressure via surface tension is negligible and the macro-throats will empty first because here capillary pressure is always lowest. Liquid will be pumped through the micro-throats to the network surface so that the surface can stay almost completely wet down to relatively low overall saturations. Lateral vapour transfer in the boundary layer assures a constant drying rate [17].

The evaporation rate drops drastically when the surface starts to dry out after all macro-throats are emptied. Short quasi-constant rate periods can be observed in this falling rate period in isothermal drying when – due to random radius distribution – throat saturation near the surface stays unchanged while internal throats empty. In the case of non-isothermal modelling, during these short periods the surface will heat up and evaporation rate increases, until another near surface throat empties; then, drying rate drops to a lower value in both model versions.

Fig. 8 shows the condensation rate $\dot{M}_C$ plotted against overall network saturation in two forms; true condensation rate and neglected condensation rate. The neglected condensation rate corresponds to the error by un-accommodated condensing vapour as explained in Section 3.3. In the first drying period, the error on condensation rate is zero. There is condensation at inner network throats but it can be compensated because clusters are still big of size; therefore, capillary flow to surface menisci, evaporating at higher rates, is not yet interrupted. Consequently, clusters as a whole are evaporating and no error is committed. The formation of relatively small clusters in the second drying period may cause net condensation in clusters, which cannot fully be accounted for. The amount of vapour condensed during the entire drying process is 2.17% of the initial amount of water present in the void space; however, only 0.90% of the initial water is neglected. This shows that the effect of condensation on overall behaviour of the drying curve can be neglected for the given example.

Fig. 9 shows the evolution of phase distributions and temperature fields at different overall saturations of the network. The situation of Fig. 9a ($S = 0.95$) is located within the warming-up period, when temperature rises towards the wet bulb temperature (see Figs. 7 and 10). Fig. 9b and c correspond to the constant rate period in which almost uniform temperature fields exist and only macro-throats will empty. Surface throats empty between $S = 0.6$ and 0.48 (Fig. 9c and d). In this period, larger temperature gradients develop and network temperature starts to rise drastically. At the same time, drying rate drops, as can be clearly seen from the sudden change of slope for the saturation curve of Fig. 10. After all the macro-throats have been emptied, a drying front recedes (see transition from Fig. 9d–f) towards the bottom of the network. This increases the resistance to mass transfer. However, rising temperatures cause, at the same time, higher driving forces for vapour diffusion. Due to the latter effect, evaporation rates are much larger than according to the isothermal model in this region (Fig. 7).

Fig. 10 illustrates the variation of temperature at the top of the network (T_{max}), temperature at the bottom of the network (T_{min}), and network saturation S with time. Fig. 11 shows the number of clusters formed N_{nc} and network saturation S with time. Wet bulb temperature (25 °C) is obtained approximately at the end of the first drying period. Only few clusters are formed during this first drying period because only macro-throats are emptying. A large increase of temperature is observed during the emptying of small surface throats. Simultaneously, the number of clusters increases drastically. The number of clusters reaches a maximum during the drastic fall of evaporation rate, decreases (with fluctuations) with time as the drying front recedes towards the bottom of the network and becomes zero at the end of the drying process.

To see the influence of pore structure, drying of a mono-modal network has been simulated for isothermal and non-isothermal conditions and compared with the results for the bi-modal network. In Fig. 12, the respective drying curves are shown. Evolution of phase distributions and temperature fields for the non-isothermal drying of the mono-modal pore network are shown in Fig. 13 for the indicated saturations.

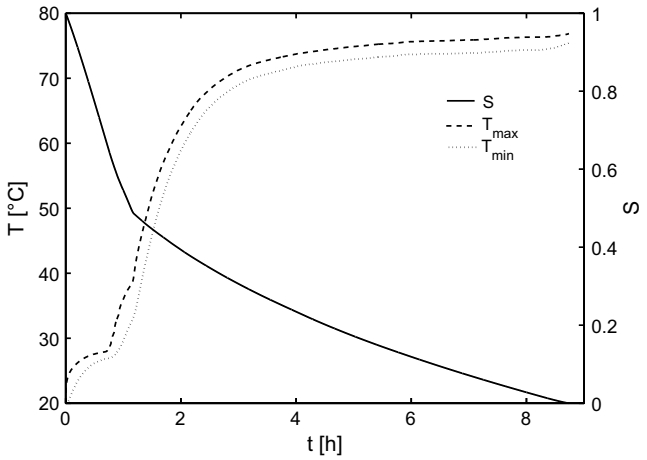

Fig. 10. Evolution of network saturation and temperature.

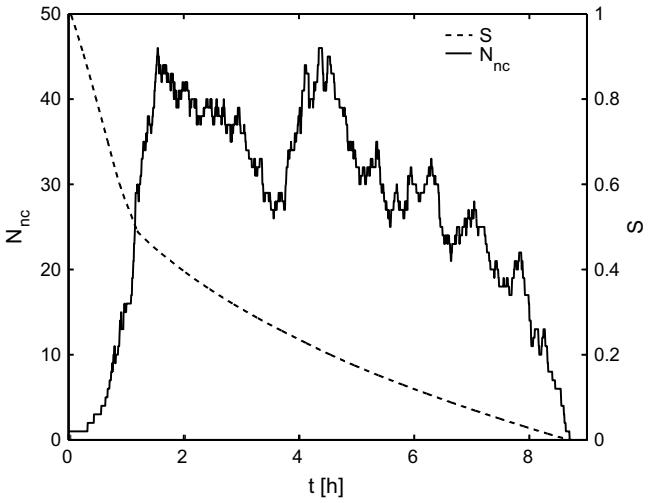

Fig. 11. Evolution of number of liquid clusters and saturation S.

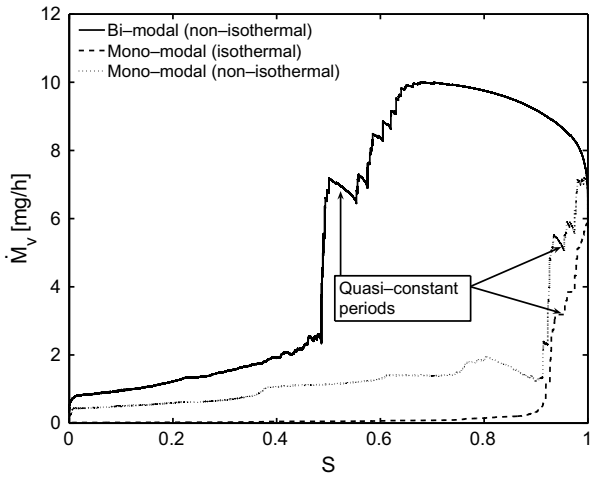

Fig. 12. Influence of pore structure on drying curve.

For all simulations, drying rate curves start at the same point because of identical initial conditions. Rapid warming leads to a sharp rise in the drying curve in both non-isothermal simulations. In the bi-modal case, the ordered emptying of macro-throats is a reason for the long constant rate period. Since macro-throats are not present in the mono-modal network, the respective first drying period is very short. Sooner or later, the gradual emptying of surface throats leads to a drastic fall of drying rates in all simulations. During this transitional period, inner throats may empty at constant wet surface fraction. This causes quasi-constant rate periods (Fig. 12). The duration of these periods depends on pore size distribution in the isothermal case. In the non-isothermal case, it depends on the dominance of capillary pressure of surface throats over that of inner throats. The temperature of the network increases in a time that is very short in comparison to total drying time. This can be seen in the temperature fields of Fig. 13a and b. A similar rise of temperature is observed at smaller overall saturations for the bi-modal network, as already discussed.

Fig. 14 gives a comparison of phase distributions obtained from isothermal and non-isothermal drying simulations for the mono-modal network. In the following, we will explain why these phase distributions are almost (but not exactly) the same. The relative change in radius of menisci throats is about 5% for the mono-modal network with a throat radius distribution of 40 ± 2 μm. The influence of temperature on surface tension γ [N/m] of water can be represented by the equation

$$\gamma[\mathrm{N/m}] = -1.704 \times 10^{-04}(T[\mathrm{K}] - 273.15) + 7.636 \times 10^{-02}, \tag{26}$$

so that the relative change in surface tension per 1 K temperature variation is approximately 0.2% (Eq. (27)). The maximal temperature gradient is about 8 K across the network and about 4 K across the drying front (see temperature fields in Fig. 14). This corresponds to a surface tension variation among the meniscus throats of maximally 0.8%. Consequently, when selecting the lowest capillary pressure throats (Eq. (17)) in a cluster, the influence of radius variation is in general larger than the influence of temperature dependent surface tension. However, when throats of very similar radius compete for the lowest capillary pressure, the influence of temperatures may have a stabilizing effect on the drying front. This stabilizing effect is due to reduction of capillary pressure with increasing temperature via surface tension under constant throat radius (Eq. (17)). Fig. 14 shows one such example of thermal stabilization at the saturation $S = 0.7$. Throats at the top of the drying front are chosen for invasion of air in the non-isothermal case, instead of throats located deeper in the network in the isothermal simulation.

5. Conclusions

In this paper, we presented a non-isothermal pore network model for the convective drying of capillary porous media. The necessity of considering heat transfer has been recognized before [18,19]. It results from the strong coupling between heat and mass transfer in the drying process, mainly due to phase change enthalpy and temperature dependent equilibrium vapour pressure, but also to temperature dependent surface tension. In the mentioned literature, however, temperature gradients were imposed on the network. Consequently, the present model is the first to describe the free evolution of temperature fields in convective drying. The model assumes dominant capillary forces and neglects both viscous forces and gravity. Vapour diffusion in the empty pore space and gas-side boundary layer is modelled as quasi-stationary; this boundary layer is discretised so that lateral vapour transfer can assure a constant rate period. Heat transfer is due to conduction, heat sinks/sources account for the evaporation/condensation of water. An algorithm to solve this model has been

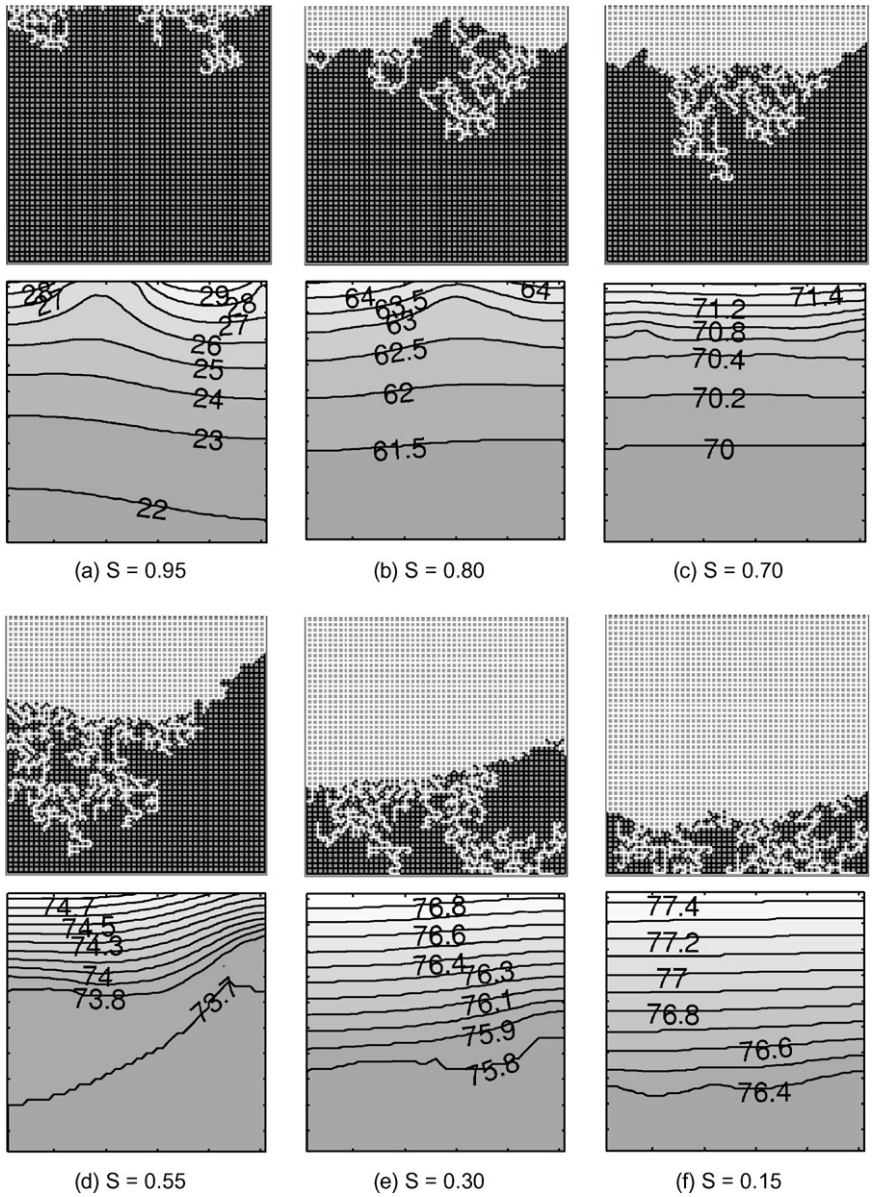

Fig. 13. Phase and temperature distributions for the non-isothermal drying of mono-modal pore network.

presented and the drying model has been applied to two-dimensional square pore networks with mono-modal and bi-modal throat radius distributions.

Characteristics of convective drying, i.e. warming-up period, constant drying rate period and falling rate period, can be observed in the simulation with a bi-modal pore network. The preferential emptying of macro-throats due to capillary pumping keeps the surface wet down to low network saturations and causes a first drying period. In the case of a mono-modal pore size distribution, after a very short warming-up period, drying rate falls drastically without a first drying period. This underlines the important role of pore structure in drying behaviour.

The influence of heat transfer on drying is mainly by an overall increase in drying rates due to the strong temperature dependency of equilibrium vapour pressure. Besides this, the invasion order of throats, which is controlled by capillary pressure differences, can be influenced by temperature gradients: capillary pressure depends both on throat radius and on temperature dependent surface tension. For the investigated case, this effect on phase distributions is relatively small, since capillary pressure differences are controlled primarily by the relative variation of throat radius. The effect is illustrated for the mono-modal pore size distribution by comparison with the isothermal simulation. For weakly disordered porous media and high temperature gradients, this thermal influence on phase patterns is expected to lead to a significant stabilization of the drying front [18,19].

In the present model version, condensation is accounted for only partially because imbibition effects would require different rules. Therefore, local condensation is only

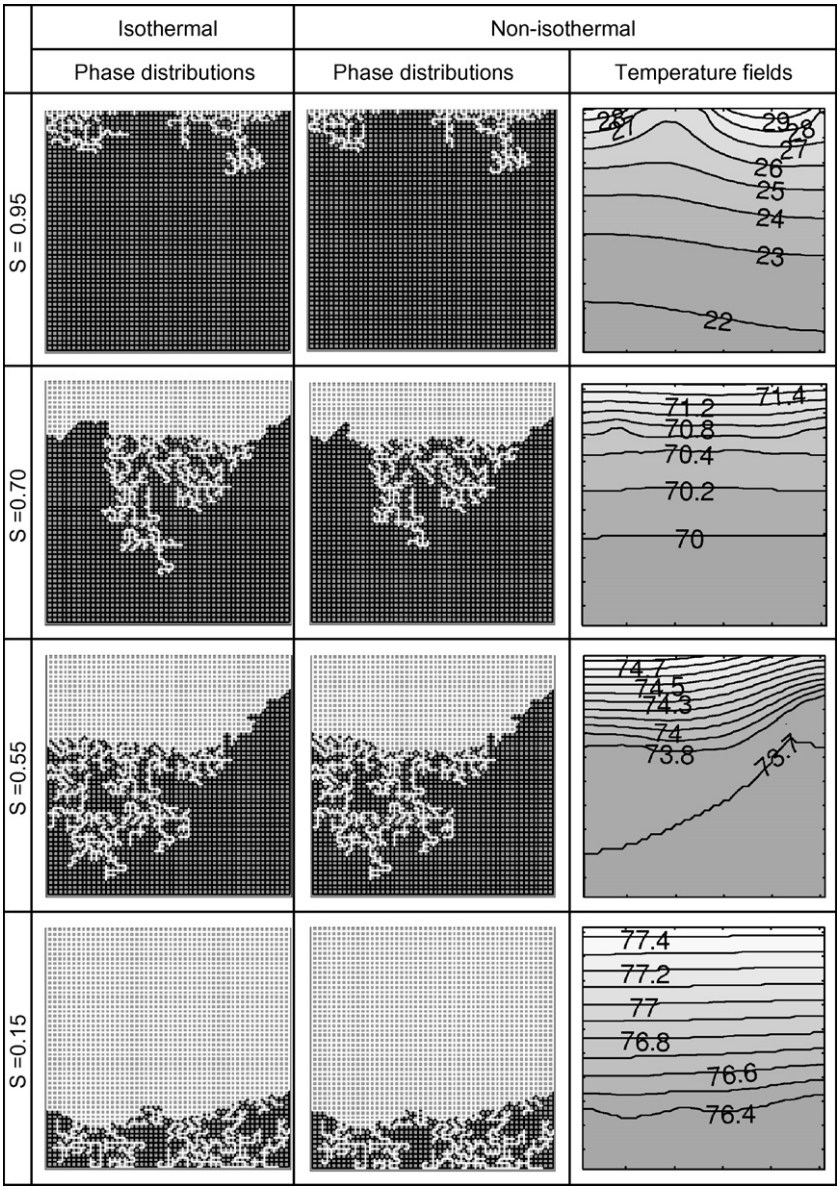

Fig. 14. Comparison of phase distributions for isothermal and non-isothermal simulations with a mono-modal pore network.

accommodated as long as the net phase change rate of a cluster does not require refilling of emptied throats. Due to low temperature gradients in the investigated cases, overall condensation rates are low and the committed error is shown to be negligible. Other ongoing work of the authors involves the application of the present model to contact drying where temperature gradients are significantly larger and in opposite direction [25]; in that case, the error on condensation rates can be important. Model improvement is under way for such more general applications. Additionally, the efficiency of the algorithm will be increased to simulate the drying of three-dimensional networks.

A further goal for the future is to develop a pore network drying model including all relevant transport processes, i.e. accounting also for viscous effects and gravity. A complementary project also aims to describe mechanical effects on the solid matrix, such as cracks and shrinkage, by the discrete network approach. Discrete modelling of porous media is seen as a fundamental method with a wider application range than classical continuum models. It offers a direct way to study the influence of microstructure on macroscopic behaviour, and it will help to develop highly specialized products and to integrate product and process optimization. Additionally, it will allow assessing continuous models and might provide a possibility to use structural information for computing effective parameters for these computationally more efficient models.

Acknowledgements

This work was financed by the German Research Foundation (DFG) in the frame of Graduate School 828 "Micro–Macro-Interactions in Structured Media and Particle Systems". The first author would like to express his special

thanks to Max-Buchner-Forschungsstiftung for its additional support.

References

[1] E. Sanchez-Palencia, Non-Homogeneous Media and Vibration Theory Lecture Notes in Physics, vol. 127, Springer-Verlag, 1980.
[2] M. Quintard, S. Whitaker, Transport in ordered and disordered porous media: volume-averaged equations, closure problems and comparison with experiments, Chem. Eng. Sci. 41 (14) (1993) 2537–2564.
[3] T.H. Vu, T. Metzger, E. Tsotsas, Influence of pore size distribution via effective parameters in a continuous drying model, in: Proceedings of 15th International Drying Symposium, Budapest, Hungary,Volume A, 20–23 August, 2006, pp. 554–561.
[4] M. Sahimi, Flow and Transport in Porous Media and Fractured Rock. From Classical Methods to Modern Approaches, VCH Verlagsgesellschaft GmbH-Weinheim, 1995.
[5] J.B. Laurindo, M. Prat, Modeling of drying in capillary-porous media: a discrete approach, Dry. Technol. 16 (9&10) (1998) 1769–1787.
[6] A.G. Yiotis, A.K. Stubos, A.G. Boudouvis, Y.C. Yortsos, Pore network model of drying of single-component liquids in porous media, Adv. Water Res. 24 (2001) 439–460.
[7] S.C. Nowicki, H.T. Davis, L.E. Scriven, Microscopic determination of transport parameters in drying porous media, Dry. Technol. 10 (4) (1992) 925–946.
[8] M. Prat, Percolation model of drying under isothermal conditions in porous media, Int. J. Multipha. Flow 19 (4) (1993) 641–704.
[9] J.F. Daian, J. Saliba, Determining a representative random pore-network for moisture sorption and migration in cement mortar, Int. J. Heat Mass Transfer 34 (8) (1991) 2081–2096.
[10] T. Metzger, A. Irawan, E. Tsotsas, Isothermal drying of pore networks: Influence of friction for different pore structures, Dry. Technol. 25 (2007) 49–57.
[11] J.B. Laurindo, M. Prat, Numerical and experimental network study of evaporation in capillary porous media. Phase distributions, Chem. Eng. Sci. 51 (1998) 5171–5185.
[12] J.B. Laurindo, M. Prat, Numerical and experimental network study of evaporation in capillary porous media. Drying rates, Chem. Eng. Sci. 53 (1998) 2257–2269.
[13] A.G. Yiotis, A.G. Boudouvis, A.K. Stubos, I.N. Tsimpanogiannis, Y.C. Yortsos, The effect of liquid films on the drying of porous media, AIChE J. 50 (2004) 2721–2737.
[14] M. Prat, On the influence of pore shape, contact angle and film flows on the drying of capillary porous media, Int. J. Heat Mass Transfer 50 (7&8) (2007) 1455–1468.
[15] L.A. Segura, P.G. Toledo, Pore-level modeling of isothermal drying of pore networks. Effect of gravity and pore shape and size distributions on saturation and transport parameters, Chem. Eng. J. 111 (2005) 237–252.
[16] L.A. Segura, P.G. Toledo, Pore-level modeling of isothermal drying of pore networks accounting for evaporation, viscous flow and shrinking, Dry. Technol. 23 (2005) 2007–2019.
[17] T. Metzger, A. Irawan, E. Tsotsas, Discrete modeling of drying kinetics of porous media, in: Proceedings of 3rd Nordic Drying Conference, Karlstad, Sweden, 15–17 June 2005.
[18] F. Plourde, M. Prat, Pore network simulations of drying of capillary porous media. Influence of thermal gradients, Int. J. Heat Mass Transfer 46 (2003) 1293–1307.
[19] H. Huinink, L. Pel, M.A.J. Michels, M. Prat, Drying processes in the presence of temperature gradients-pore-scale modeling, The Eur. Phys. J. E 9 (2002) 487–498.
[20] V.K. Surasani, T. Metzger, E. Tsotsas, Towards a complete pore network drying model: first steps to include heat transfer, in: Proceedings of 15th International Drying Symposium, Budapest, Hungary, Volume A, 20–23 August, 2006, pp. 125–132.
[21] M. Prat, Recent advances in pore-scale modeling for drying of porous media, Chem. Eng. J. 86 (2002) 153–164.
[22] W. Masmoudi, M. Prat, Heat and mass transfer between a porous media and a parallel external flow, application to drying of porous materials, Int. J. Heat Mass Transfer 34 (8) (1991) 1975–1981.
[23] A. Al-Futaisi, T.W. Patzek, Extention of Hoshen–Kopelman algorithm to non-lattice environments, Physica A 321 (2003) 665–678.
[24] T. Metzger, A. Irawan, E. Tsotsas, Remarks on the paper "Extension of Hoshen–Kopelman algorithm to non-lattice environment" by A. Al-Futaisi, T.W. Patzek, Physica A 321 (2003) 665–678, Physica A 363 (2006) 558–560.
[25] V.K. Surasani, T. Metzger E. Tsotsas, Influence of heat transfer on drying of capillary porous media: pore scale modeling, in: Proceedings of European Drying Conference AFSIA 2007, 24–25 May, 2007, Biarritz, France.

Chemical Engineering Science 63 (2008) 5218 – 5228

Contents lists available at ScienceDirect

Chemical Engineering Science

journal homepage: www.elsevier.com/locate/ces

Influence of heating mode on drying behavior of capillary porous media: Pore scale modeling

V.K. Surasani, T. Metzger*, E. Tsotsas

Thermal Process Engineering, Otto-von-Guericke-University, Universitaetsplatz 2, P.O. 4120, 39016 Magdeburg, Germany

ARTICLE INFO

Article history:
Received 4 February 2008
Received in revised form 1 July 2008
Accepted 5 July 2008
Available online 12 July 2008

Keywords:
Pore networks
Phase distributions
Temperature fields
Bimodal pore size distribution
Invasion percolation
Imbibition

ABSTRACT

Invasion percolation (IP) rules under non-isothermal conditions are applied to model the pore-scale events occurring during drying of capillary porous media, namely displacement of immiscible phases and cluster formation. A saturated two-dimensional network with a bimodal pore size distribution is dried by applying two different heat transfer boundary conditions; one corresponds to convective drying and the other to less resistive contact drying. Simulated macroscopic drying behavior is presented in conjunction with freely evolved microscopic temperature fields and phase distributions for both heating modes. Convective heating exhibits similar invasion patterns as those in isothermal simulations; both are dominated by the spatial distribution of pore radii. However, in contact heating, temperature dependency of surface tension produces significantly different invasion patterns.

1. Introduction

Drying of capillary porous media has been of significant scientific interest for many researchers since it depicts a complex, coupled, and multiphase process with a wide range of applications in industry. Because of its high cost in energy, drying is an operation with a high potential for optimization with respect to energy savings. In addition, drying plays an important role in weathering of monuments, buildings, and rocks. For many years, it has been studied experimentally for measuring drying kinetics on the macro-scale and the most advanced techniques like magnetic resonance imaging (MRI) (Guillot et al., 1989; Pel et al., 1996), and neutron scattering (Pel et al., 1993) are used to measure the spatial liquid distributions in porous media. However, in most of the cases, theoretically, drying is a remarkably little understood process. Numerous theoretical models that have been proposed in the past are based on rigorous heat, mass, and momentum balance equations on a fictitious continuum. The methods, which are mostly used in such a continuum approach, are homogenization (Sanchez-Palencia, 1980) or volume averaging techniques (Quintard and Whitaker, 1993). Even though much knowledge has been gained through this macroscopic approach to drying, and validated with experiments, it fails in relating the macroscopic phenomena to the microscopic, i.e. pore-scale, events during the drying process. These events refer to the immiscible displacement of the defending phase (wetting fluid) by the invading phase (non-wetting fluid), and formation of dry and wet patches (clusters) in the pore space caused by interfacial effects on the phase boundaries. Discrete network models based on fractal concepts and statistical physics such as percolation theory, and their applications to drying of porous media, mainly reviewed by Prat (1993) and Yiotis et al. (2001), are particularly suited for studying the situations where the continuum approach fails (Laurindo and Prat, 1998).

A network model is a comprehensive model which incorporates the description of pore space and the physics of the pore-scale events (Berkowitz and Ewing, 1998). The basic understanding of pore network modeling commences with the geometric representation of the void space in the porous medium. Most of the literature work has adopted a network representation in the form of sites (pores) connected with bonds (throats) (Nowicki et al., 1992; Prat, 1993; Yiotis et al., 2001). Prat (1993) showed that the immiscible displacements in the drying process can be treated as a special case of invasion percolation (IP). Menisci in the pore space will respond to capillary, viscous, and buoyancy forces, and the interplay between these forces has been studied in literature. In the absence of viscous forces, gravity or thermal gradients, phase distributions (IP patterns) completely depend on the spatial disorder of pore size (Laurindo and Prat, 1998). In the presence of gravity, the phase distributions are patterns of IP in a stabilizing gradient (IPSG) or in a destabilizing gradient (IPDG) depending on the direction of the gravity vector to the main direction of vapor flow (Laurindo and Prat, 1998). Similarly, IPSG patterns can be observed in the presence of viscous forces (Yiotis et al., 2001; Metzger et al., 2007a). Additionally, the influence of pore structure on drying kinetics has been investigated using pore network modeling

* Corresponding author. Tel.: +49 391 67 11362; fax: +49 391 67 11160.
E-mail address: thomas.metzger@ovgu.de (T. Metzger).

0009-2509/$ - see front matter © 2008 Elsevier Ltd. All rights reserved.
doi:10.1016/j.ces.2008.07.011

(Metzger et al., 2007b) for various two- and three-dimensional networks. For a comprehensive record on the use of pore network models in drying refer to the reviews by Prat (2002) and Metzger et al. (2007c).

In the above-mentioned literature, invasion is considered at slow drying rates. Heat transfer aspects of drying are neglected when studying the physical and structural influences on IP patterns. The influence of temperature gradients—which were imposed onto the drying product—has been investigated by Plourde and Prat (2003), Huinink et al. (2002). However, product temperature did not evolve freely as corresponding to real drying boundary conditions. Recently, Surasani et al. (2008a) considered heat transfer in a pore network model that assumes dominant capillary forces and neglects both viscous forces and gravity. This network model was the first to describe the free evolution of temperature fields in convective drying. The present work applies an improved model version to the contact heating mode and simulates the evolution of invasion patterns and temperature fields, which are then compared with those of the convective heating mode (Surasani et al., 2008a). The concept of condensation in clusters, partially implemented in the algorithm, is discussed in this article.

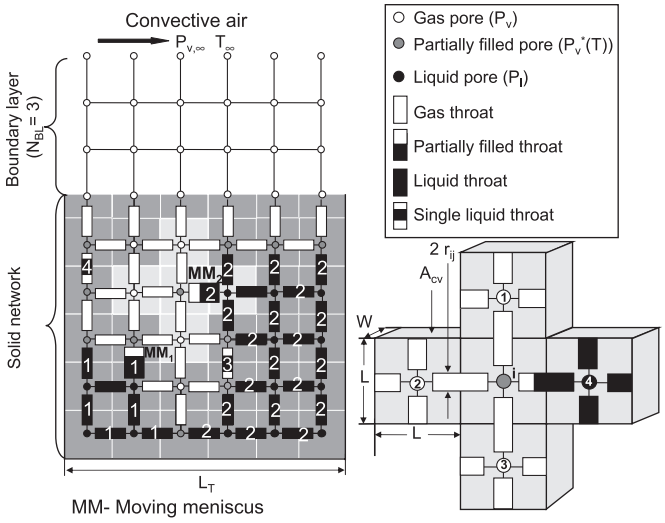

Fig. 1. Partially dried pore network with boundary layer and several liquid clusters, definitions of pore and throat conditions and magnified control volume *i* (CV).

2. Pore network model

Pore network models are unique in accounting both for a geometrical description of the pore space and for the physics of the pore-scale events, i.e. transport mechanisms at the pore scale. In this section, we will present the data structure model, i.e. the geometry of the porous network, boundary layer formation, and pore and throat conditions. Further, the model equations that represent quasi-stationary mass transfer relations in each phase and transient heat transfer are presented. The coupling relations between heat and mass transfer are also discussed in this section.

2.1. Data structure model

Void space in the porous medium is envisaged as a network of cylindrical throats connected by pore nodes. In general, the connectivity of pores, i.e. co-ordination number, will determine the topology of void space in two- and three-dimensional domain. Even though the implemented algorithm is independent of connectivity, we stick to a two-dimensional square network (see Fig. 1) due to computational limitations of the present algorithm Surasani et al. (2008a). A pictorial representation of the solid network and the gas-side boundary layer flow conditions is given in Fig. 1. Radii of the throats are distributed randomly. The pores are volume less; each pore is associated with a control volume (CV).

To describe the first drying period with its constant drying rate, boundary layer is modeled in a discretized way, by extending the network into the gas phase with additional nodes (see Fig. 1); their number is given by mass transfer coefficient and vapor diffusivity (Metzger et al., 2005; Irawan et al., 2005; Yiotis et al., 2006):

$$\varepsilon = \frac{\delta}{\beta} = N_{BL} L. \tag{1}$$

The mass transfer coefficient β can be obtained from an empirical correlation as

$$Sh = \frac{\beta L_T}{\delta} = f(Re, Sc), \tag{2}$$

with Reynolds number $Re = uL_T/v_g$ and Schmidt number $Sc = \delta/v_g$. Here, δ is vapor diffusivity, u bulk air velocity, L_T network length, and v_g kinematic viscosity of the gas. However, Eq. (1) is derived for a plate at uniform partial pressure which is not necessarily fulfilled for drying porous media (see Masmoudi and Prat, 1991). Heat transfer between bulk air and network surface is described by a heat transfer coefficient α, which can be obtained from the analogy of heat and mass transfer as

$$\alpha = \beta \frac{\lambda_g}{\delta} \left(\frac{Pr}{Sc}\right)^{1/3}, \tag{3}$$

where λ_g is gas thermal conductivity and Pr Prandtl number. Immiscible displacements upon evaporation of liquid will cause evolving IP patterns in the network. One such pattern is shown in Fig. 1 which represents the continuous vapor phase and disconnected liquid patches (clusters) in the solid network. Pore and throat conditions (Surasani et al., 2008a) (Fig. 1) will determine the transport within and between the phases. At the phase boundary, where the menisci exist, liquid flow, phase change, and vapor diffusion are simultaneous. In interfacial throats (full or partially filled), the phase boundary is either a moving meniscus or a stationary meniscus as evaporated liquid diffuses through air and, at the same time, liquid flows from or to the meniscus depending upon boundary liquid pressures. In gas throats, diffusion takes place due to vapor pressure gradients; and in liquid throats, capillary flow takes place due to capillary pressure gradients in the cluster. Pore saturations are given as the mean of the saturations of connected throats. Equilibrium vapor pressure $P_v^*(T)$ exists in partially filled pores, giving boundary conditions to the linear system of vapor transport. The missing boundary condition comes from partial vapor pressure ($P_{v,\infty}$) of convective air.

2.2. Drying model

Initially, the network is saturated completely with water and has temperature $T_{in} = 20\,^\circ$C, whereas drying air has zero absolute humidity and temperature T_∞. Since we only investigate situations well below the boiling temperature, gradients in total pressure P are neglected; constant total pressure is applied in the whole gas phase (boundary layer and network). The number of boundary layer nodes formed due to convective air is assumed to be constant. Transport mechanisms within and in between the phases are given by pore and throat conditions. Vapor diffusion through the air is assumed to be quasi-stationary and the displacements of the immiscible phases act only upon capillary forces, i.e. viscous effects are neglected in both phases. In each CV local thermal equilibrium is applied and heat transfer in the network is only by conduction.

2.2.1. Vapor transport

The vapor flow rate $\dot{M}_{v,ij}$ between two gas pores is given by Stefan's law. From the law of conservation and the assumption of quasi-stationary vapor transport, total mass flow rates from any gas pore are equal to zero:

$$\sum_{j=1}^{4} \dot{M}_{v,ij} = -\sum_{j=1}^{4} A_{ij} \frac{\delta}{L} \frac{P\tilde{M}_v}{\tilde{R}T} \ln\left(\frac{P - P_{v,i}}{P - P_{v,j}}\right) = 0. \quad (4)$$

Here, A_{ij} is the cross-sectional area of the throat in the solid network ($A_{ij} = \pi r_{ij}^2$). Since we neglect the overlap of throats at pore nodes, all throats in the network are assumed as equal in length ($L_{ij} = L$). Vapor transfer in the boundary is assumed as molecular diffusion. Thus, Eq. (4) is equally valid to represent the vapor transport in the boundary layer; in this case A_{ij} in Eq. (4) is the area of cross section between the two pores in the boundary layer ($A_{ij} = LW$). The first boundary condition to Eq. (4) is equilibrium vapor pressure in partially filled gas pores ($P_{v,j} = P_v^*(T)$). As second boundary condition, vapor pressures in bulk fluid, are applied to the gas pores at the edge of the boundary layer ($P_{v,j} = P_{v,\infty}$). The system of equations for vapor transport (Eq. (4)) for gas pores both in network and boundary layer can be put in linear form to be solved for partial vapor pressures ($P_{v,i}$) using the conjugate gradient method (CGM).

The partially filled pores should be treated differently since they are the boundaries of the clusters/single throats and the vapor flow rates will play an important role in calculating the cluster evaporation rates. The right-hand side of Fig. 1 represents partially filled pore i(CV_i) with neighbor pores named as 1, 2, 3 at unknown vapor pressures ($P_{v,j}$) and the remaining pore is at liquid pressure ($P_{l,4}$). Unknown vapor pressures at pores 1, 2, 3 have to found by solving the above system of equations (Eq. (4)). Then, the phase change rate at the partially filled throat ($\dot{M}_{ev,i4}$) can be found by the sum of the vapor flow rates in the gas throats ($\dot{M}_{v,i1}, \dot{M}_{v,i2}, \dot{M}_{v,i3}$). In general, for partially saturated pores, the vapor balance can be written as

$$\sum_{j=1}^{4-\mathrm{lm}} \dot{M}_{v,ij} = \sum_{j=1}^{\mathrm{lm}} \dot{M}_{\mathrm{ev},ij}, \quad (5)$$

with evaporation or condensation rates $\dot{M}_{ev,ij}$ in the pore neighboring meniscus throats (lm). (For several menisci, the phase change rate is distributed according to cross-sectional areas).

2.2.2. Cluster labeling

Before we proceed into discrete liquid transport modeling (Section 2.2.3), it is worth to recall the definition of a cluster and explain how to set up data structures for the formed clusters, needed for the discrete description of non-viscous capillary pumping. Cluster by definition is a region of single phase (either gas or liquid) in porous media. Here, we deal only with liquid phase clusters; for the assumed network geometry, a cluster is a group of liquid throats connected by liquid pores. For better understanding see the visualization of clusters 1 and 2 in Fig. 1. Every cluster contains (saturated or unsaturated) meniscus throats, and may or may not contain saturated throats without a meniscus.

In every cluster, meniscus throats, where mass transfer in vapor and liquid phase is coupled, must be maintained at capillary equilibrium. So it is necessary to know the exact geometric structure of a cluster to solve the discrete invasion process (Section 2.2.3) due to phase change and to monitor the disintegration process due to invasion. The process of obtaining the structural data of every cluster combined with the method of effective storing of these data for computation of liquid transport is called cluster labeling. To this purpose, the Hoshen–Kopelman algorithm (well documented in literature, Al-Futaisi and Patzek, 2003; Metzger et al., 2006a, b) can be used for cluster labeling.

2.2.3. Liquid transport

In the present model, viscous forces are neglected in both liquid and gas phases since throats are of relatively large size; additionally, throats are cylindrical, so that film flow is negligible. Literature work with polygonal throat cross sections shows that film flow in the corners may be important: Yiotis et al. (2004) analyzed different film regimes and also predicted that thermal gradients should usually have little influence on the extension of the film region, but that for large temperature gradients, films ought to be shortened; Prat (2007) mainly investigated the role of pore shape and contact angle.

The assumption of negligible viscous forces implies that, in each cluster, liquid can be pumped from the throat with the highest liquid pressure to all other meniscus throats, resulting in one throat with a moving meniscus (MM) and stationary menisci (SM) in all remaining throats. In each cluster, the MM throat will empty first since this throat alone contributes to the total evaporation of the cluster through capillary pumping. The criterion for selecting MM throats is given by capillary pressures $P_{c,ij}$, i.e. in each cluster, the throat with highest liquid pressure

$$P_{l,ij} = P - P_{c,ij} \quad (6)$$

is selected as MM throat. Capillary pressures can be given by the ratio of temperature dependent surface tension and throat radius:

$$P_{c,ij} = \frac{2\gamma(T_{ij})}{r_{ij}}. \quad (7)$$

Using Eq. (7), the MM throat is chosen as the throat with the lowest capillary pressure. Fig. 1 shows an example of two clusters (labeled 1 and 2) in each of which the MM throat is partially filled.

Since all mass loss due to evaporation is attributed to MM throats, the time steps to empty these throats can be obtained in each cluster (nc) from the saturation of the MM throat S_{MM}, liquid density ρ_l, total throat volume $V_{MM,\mathrm{nc}}$ and total evaporation rate of the cluster as

$$\Delta t_{m,\mathrm{nc}} = \frac{S_{MM}\rho_l V_{MM,\mathrm{nc}}}{\sum_{j=1}^{mt} \dot{M}_{\mathrm{ev},ij,\mathrm{nc}}}. \quad (8)$$

2.2.4. Condensation

Consideration of heat transfer in a pore network drying model poses difficulties because condensation effects have to be included. In a non-isothermal system evolved temperature gradients over the network instigate equilibrium vapor pressure gradients at phase boundaries. The above phenomenon causes the liquid to evaporate from hotter spots in the network and condense at colder spots. At the same time, capillary effects let the continuous liquid phase split up into disconnected clusters. For a cluster or a single throat, the net phase change rate is calculated as the sum of evaporation/condensation rates on the phase boundaries. Fig. 2 represents the definitions of an evaporating and a condensing cluster. In the sample cluster (Fig. 2a), if the net phase change rate ($\sum \dot{M}_{\mathrm{ev},ij}$) is positive (=net evaporation), normal invasion rules apply in updating the phase distributions. In this case, capillary pumping nullifies the effect of local condensation. If the net phase change rate is negative, net condensation takes place, and the liquid cluster (Fig. 2b) should grow. For the growth of a condensing cluster, the rules for liquid transport as presented above do not apply.

To maintain capillary equilibrium it is reasonable to fill the lowest capillary pressure throat (MM) until it is completely full because, in

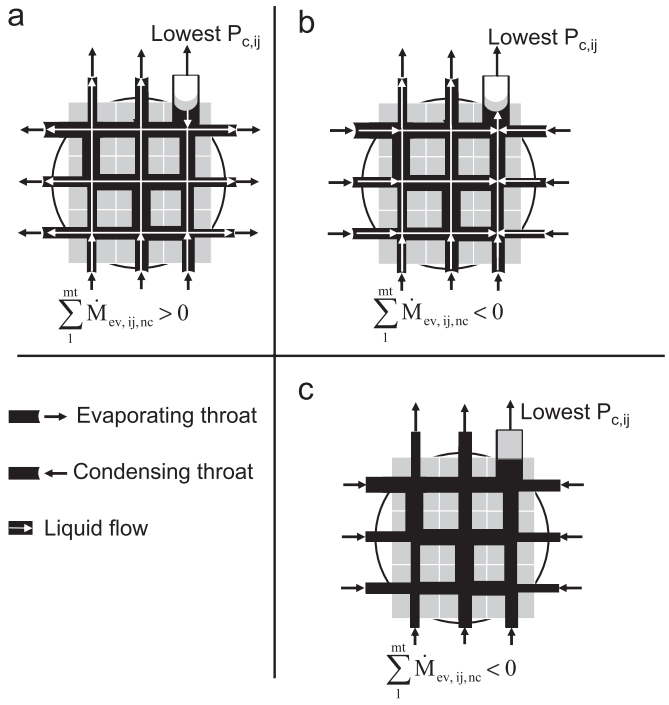

Fig. 2. The concept of: (a) evaporating and (b) condensing clusters; (c) condensing clusters (saturated).

the capillary dominated regime, capillary pressure at every meniscus in a cluster must be constant: in condensing meniscus throats, the flattening of the meniscus by vapor deposition is compensated by capillary flow to the moving meniscus which has a prescribed curvature. Eventually, when the MM throat is full, all menisci in the cluster will become flat (i.e. having infinite radius of curvature); this situation of a completely saturated condensing cluster is represented in Fig. 2c. The time step to fill the MM throat in each condensing cluster (nc) can be obtained from the ratio of mass of liquid required to fill the MM throat to the total condensation rate of the cluster.

$$\Delta t_{m,\mathrm{nc}} = -\frac{(1-S_{MM})\rho_l V_{MM,\mathrm{nc}}}{\sum_{j=1}^{mt}\dot{M}_{\mathrm{ev},ij,\mathrm{nc}}}. \tag{9}$$

If the MM throat of a condensing cluster is full but it is next to an evaporating cluster, the condensation rate is subtracted from the evaporation rate of this neighboring cluster. Further condensation is not taken into account in the present algorithm, i.e. empty throats are not filled with condensed liquid (imbibition).

2.2.5. Transient heat transfer

In many processes, during transport in porous materials, solid, liquid, and gas phases coexist in a chosen scale of CV. In each CV, temperatures of gas ($T_{g,i}$), liquid ($T_{l,i}$), and solid ($T_{s,i}$) may be different. But in most of the drying processes of capillary porous media are characterized by relatively low convective transport in liquid and gas phases so that only small temperature differences exist between the phases in a CV (Whitaker, 1977); therefore, we assume local thermal equilibrium ($T_{s,i}=T_{l,i}=T_{g,i}=T_i$). In the same spirit, heat conduction between the CVs (mainly by the solid phase) is assumed dominant over convective heat transfer. In other processes, convection plays a more important role and has been modeled in literature (Satik and Yortsos, 1996; Lu and Yortsos, 2005).

Fig. 1 shows how each CV represents one pore and contains four half throats, i.e. each throat participates in two CVs. Liquid in partially filled throats is equally distributed to the neighboring CVs. The dynamic energy balance equation over the CV is given by

$$V_i(\rho c_p)_i\frac{\mathrm{d}T_i}{\mathrm{d}t} = -\sum_{j=1}^{4}Q_{ij} - \Delta h_{v,i}(T_i)\sum_{j=1}^{\mathrm{lm}}\dot{M}_{\mathrm{ev},ij}, \tag{10}$$

where $\Delta h_{v,i}(T_i)$ is phase change enthalpy (as positive value). The mass flow rate $\dot{M}_{\mathrm{ev},ij}$ is positive for evaporation and negative for condensation. The meniscus position is used to allocate the heat sink/source to either CV. The heat exchange rates $\dot{Q}_{ij}$ between CVs i and j are given by Fourier's law of heat conduction as

$$\dot{Q}_{ij} = A_{cv,ij}\lambda_{ij}\frac{T_i - T_j}{L}. \tag{11}$$

The exchange area for heat conduction is $A_{cv,ij}=L^2$ because both void space and solid can contribute. For simplicity, solid and liquid phase resistances are considered as parallel (Strumillo and Kudra, 1986), and contribution of gas is neglected. The effective thermal conductivities λ_{ij} and CV heat capacities $V_i(\rho c_p)_i$ are functions of throat saturation (Surasani et al., 2008a). Two kinds of heat transfer boundary conditions are applied for the convective drying mode; first is heat transfer through the boundary layer as

$$\dot{Q}_{ij} = A_{cv,ij}\alpha,(T_i - T_\infty), \tag{12}$$

and second, heat transfer through insulated sides of the pore network is zero ($\dot{Q}_{ij}=0$). In the case of contact heating, a heating plate (at temperature T_{con}) is applied to the bottom edge of the network with perfect contact (numerical implementation is done by taking Eq. (11) and replacing T_j by T_{con}). The explicit scheme for solving Eq. (10) can only be stable if the thermal time step fulfills the condition

$$\Delta t_t < \frac{(\rho c_p)_i L^2}{\sum_j \lambda_{ij}}. \tag{13}$$

2.3. Coupling of heat and mass transfer

Heat and mass transfer coupling plays an important role in the drying process, particularly at the phase boundaries (menisci) in the network. At an evaporating meniscus, the vapor takes up the enthalpy of evaporation and liquid temperature is reduced (heat sink); likewise there are heat sources at places of condensation. This coupling of mass transfer with heat transfer is already implemented by including the phase change rates ($\dot{M}_{\mathrm{ev}}$) in the energy balance equation (Eq. (10)).

Further coupling is introduced by the temperature dependency of local equilibrium vapor pressure $P^*_{v,i}(T_i)$ and local surface tension $\gamma(T_{ij})$. In a non-uniform temperature field, equilibrium vapor pressure varies spatially. This has two major effects on vapor diffusion: first, it causes higher drying rates at hot spots and, second, it causes back diffusion in the network with condensation at colder spots. Equilibrium vapor pressures have to be updated after each time step by use of an Antoine equation. At the same time, surface tension γ varies inversely with temperature. By Eq. (7), a surface tension gradient may have an effect on IP patterns depending on magnitude and orientation of the temperature gradient (Plourde and Prat, 2003).

2.4. Drying algorithm

A flow sheet representation of the drying algorithm is given in Fig. 3. First, the data structures describing the solid network and boundary layer must be formed from network size; additionally, initial and boundary conditions are set (step 1) and the liquid cluster needs to be identified using the cluster labeling algorithm (step 2). The linear system for vapor transport (Eq. (4))

is solved and evaporation rates of each cluster are computed as the sum of the evaporation rates on their respective menisci using Eq. (5) (steps 3 and 4). Then, from the capillary pressures $P_{c,ij}$ in meniscus throats, the MM throat is identified for each cluster and the time step $\Delta t_{\min}$ is chosen as a minimum from the values of Eqs. (8), (9), and (13) (step 5). The mass loss due to evaporation is computed for the time step $\Delta t_{\min}$ and phase distributions (pore and throat saturations) are updated (step 6). Next, the new temperature field is computed by use of Eq. (10) for same time step; and, finally, temperatures as well as temperature dependent variables are updated (step 7). The procedure will be repeated until all liquid is removed from the network.

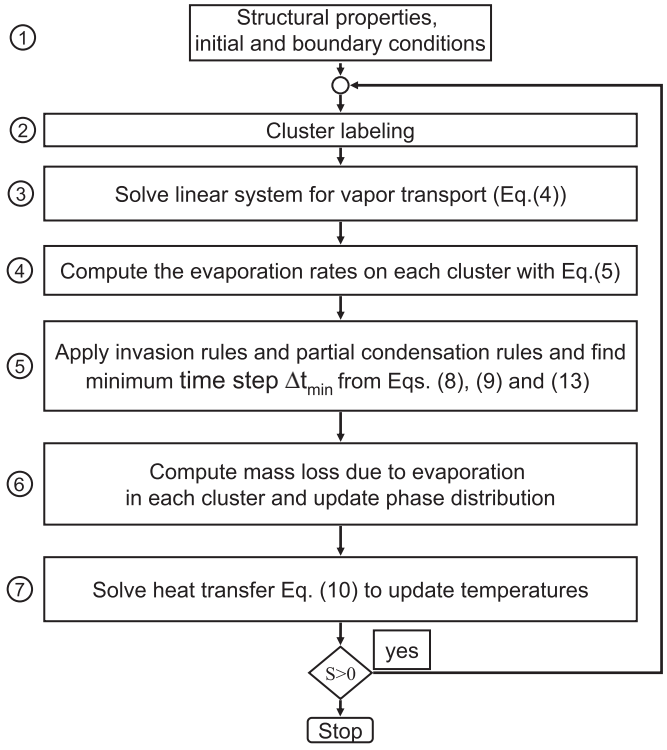

Fig. 3. Algorithm of pore-scale drying model.

3. Drying simulations

3.1. Heating modes and parameters

We are interested in demonstrating the influence of heat transfer by changing the thermal boundary conditions. To this purpose two different drying methods are used; the first one is classical convective heating, and the second is less resistive contact heating. The pictorial representations of the two modes are shown in Fig. 4. In both cases, the top surface of the solid network is open to vapor diffusion through the boundary layer and all the remaining sides are impermeable to mass transfer. A boundary layer forms parallel to the open surface of the solid network due to air convection. It is supplied at velocity such that the boundary layer contains seven nodes ($\beta = 10.4$ mm/s). Dry air has zero humidity ($P_{v,\infty} = 0$). In convective heating mode, its temperature is 80 °C and all three faces of the network are insulated (Fig. 4a). In contact heating mode, drying air is at 20 °C and the heat transfer is due to perfect thermal contact of the bottom edge of the solid network (Fig. 4b) with a heating plate at 80 °C; again the left and right sides are insulated.

One of the major features of the pore network model is to account for the geometry of void space, and its major outcome is the formation of liquid clusters as a consequence of spatial variation in pore size distribution. Thus, radii of the throats are chosen randomly according to a normal number density function and the length of every throat is 350 μm. The results presented in this section have been obtained for networks of size 51 × 51 with a bimodal throat size distribution. Every fifth throat orthogonal to the open surface of the network is chosen from a radius distribution of 100 ± 5 μm (macro-throats) and all remaining throats from a distribution of 40 ± 2 μm (micro-throats). Applied throat radius distributions for bimodal pore network are large enough to justify the assumption of neglecting viscous effects, which are dominant in network of small radius distributions (Metzger et al., 2007a).

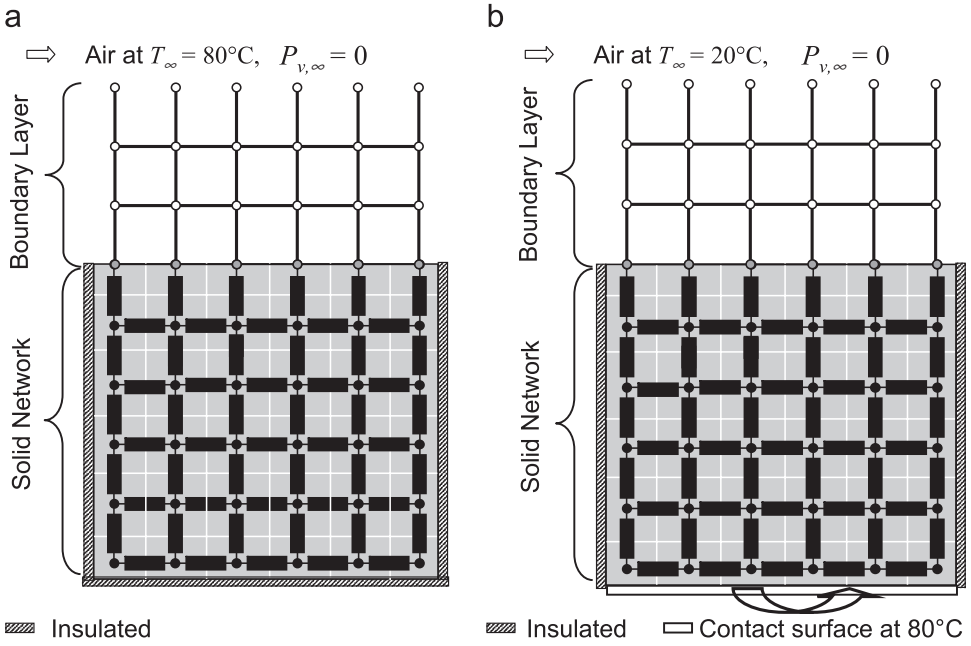

Fig. 4. Heating modes used in simulations. (a) Convective heating; (b) contact heating.

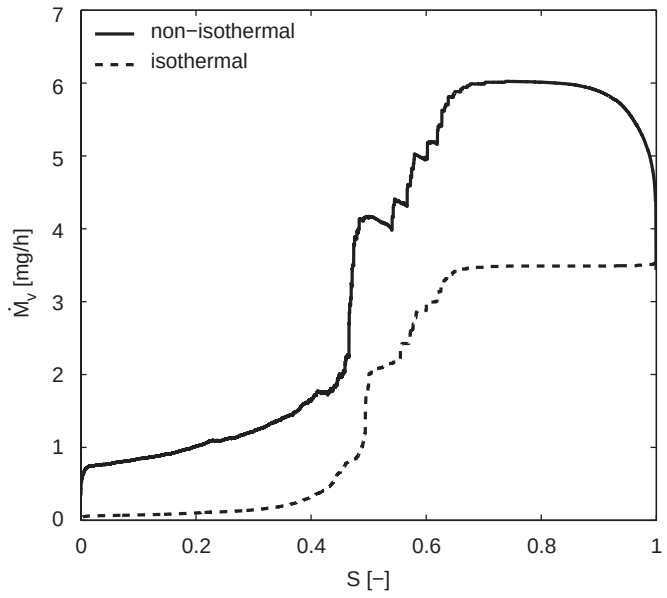

Fig. 5. Isothermal mode and convective heating mode drying rate curves for bi-modal network.

Many technical porous media exhibit bimodal pore size distribution and both micro- and macro-throats need to be continuous in reality. However, in the two-dimensional pore network such a topology is strictly not possible, but real drying behavior can be simulated by the above-described network (Metzger et al., 2007b). Three-dimensional simulations with more realistic spatial distributions of macro-throats will be presented in Surasani et al. (2008b).

Initially, the network is saturated with water and has a uniform temperature of 20 °C. The heat transfer parameters of the solid are chosen as for glass: $(\rho c_p)_s = 1.7 \times 10^6$ J/(m^3 K) and $\lambda_s = 1$ W/(m K). Simulation results of both convective heating and contact heating modes are presented in the following.

3.2. Results for convective heating mode

Fig. 5 shows the drying kinetics as evaporation rate $\dot{M}_v$ versus network saturation S. The isothermal curve is plotted for uniform temperature of 20 °C to show the effect of heat transfer. Both the isothermal and the non-isothermal curve start at the same rate. The initial warming-up to constant drying conditions can be clearly seen in the non-isothermal process. The constant rate period extends for both curves to a saturation of approximately 0.65. The order of emptying of throats is determined by capillary pressure at the menisci (Eqs. (6) and (7)). In the isothermal model, invasion of air depends on throat radius alone, since temperature is constant throughout the network. In the convective heating mode, the order of empting may also be influenced by surface tension (Eq. (7)). At the start of the drying process, macro-throats empty since the effect of temperature on capillary pressure via surface tension is negligible (see below discussion). Macro-throats at high liquid pressures (low capillary pressures) can pump liquid to the micro-throats at the network surface which stays almost completely wet down to relatively low overall saturations. As a consequence, a first drying period can be observed (the few dry surface throats are additionally masked by lateral vapor transfer in the boundary layer, see Metzger et al., 2005). The evaporation rate drops drastically when micro-throats on the surface start to dry out.

The evolution of IP patterns and temperature fields, corresponding to the isothermal mode and convective heating mode drying simulations in Fig. 5, are shown in Fig. 6 at different overall saturations of the network. Fig. 7 illustrates the variation of temperature at the top of the network ($T_{\max}$), temperature at the bottom of the network ($T_{\min}$), and network saturation S with time. The situations in convective heating at saturation S equal to 0.8 and 0.65 are located within the constant-rate period (see Figs. 5 and 7), in which the network has almost uniform temperature and only macro-throats will empty. Near wet bulb temperatures are attained at the end of the first drying period. These attained temperatures are higher than wet bulb temperature (25 °C) due to the warming up of dry spots formed after emptying of macro-surface throats. Surface throats empty in the approximate saturation range of 0.65–0.48. Short quasi-constant rate periods can be observed in this falling rate period in isothermal drying when—due to random radius distribution—throat saturation near the surface stays unchanged while internal throats are invaded. In the case of convective heating, the surface heats up and evaporation rate increases, until another near surface throat empties. Then, drying rate drops to a lower value in both model versions. These quasi-constant rate periods can be seen in the drying curve (Fig. 5) between saturations 0.65 and 0.48. In the falling rate period, larger temperature gradients develop and network temperature starts to rise drastically. At the same time, drying rate drops, as can be clearly seen from the sudden change of slope on the saturation curve in Fig. 7. After all the macro- and surface throats have been emptied, the drying front recedes (see transition from $S = 0.48$ to 0.10) towards the bottom of the network. This increases the resistance to mass transfer; however, the resulting rise in temperature causes a higher driving force for vapor diffusion. Due to the latter effect, evaporation rates are much larger than those of the isothermal model in this region (Fig. 5). The evolved temperature profiles shown in Fig. 7 reach a uniform temperature (of drying agent) in post drying period.

Fig. 6 also presents the comparison of simulated phase evolutions obtained from isothermal and convective heating mode. Very similar IP patterns are observed in the two cases, the reason for which shall now be discussed. The influence of temperature on surface tension γ of water can be represented by the equation

$$\gamma\ (\mathrm{N/m}) = -1.704 \times 10^{-4} T\ (^\circ\mathrm{C}) + 7.636 \times 10^{-2}, \qquad (14)$$

so that the relative change in surface tension per 1 K temperature variation is approximately 0.2%. The maximal temperature difference over the network is about 6 K (see temperature fields in Fig. 6). This corresponds to a surface tension variation among the meniscus throats of maximally 1.2%. The relative standard deviation of throat radius is 5% for both modes of the distribution (100±5 and 40±2 μm). Only macro-throats will empty at the start of the drying process. As long as a cluster contains macro-throats, they are so much larger in radius that a temperature gradient cannot lead to preferential emptying of micro-throats ($S = 0.8$). When a complete macro-channel is invaded, this leads to splitting up of the liquid phase into clusters (2D artifact), and micro-throats start emptying. Since the temperature gradient is very small in this period, the invasion order is essentially the same as for the isothermal case ($S \geqslant 0.65$). When surface micro-throats start emptying, temperatures start to rise. And if the relative variation of competing meniscus radii is lower than that of surface tension, we expect preferential invasion of throats at higher local temperatures (see Fig. 6 at $S = 0.48$). However, in convective heating mode, evolved temperature gradient is low, and surface tension will not play a big role for the given network disorder (i.e. standard deviation of radii). This implies IP patterns are similar to that of isothermal simulations. However, if the disorder of the network is very small then the effect of surface tension gradients can become more important (see also Plourde and Prat, 2003).

3.3. Results for contact heating mode

To depict the influence of heat transfer on macroscopic behavior, simulated drying rates for convective and contact heating modes are

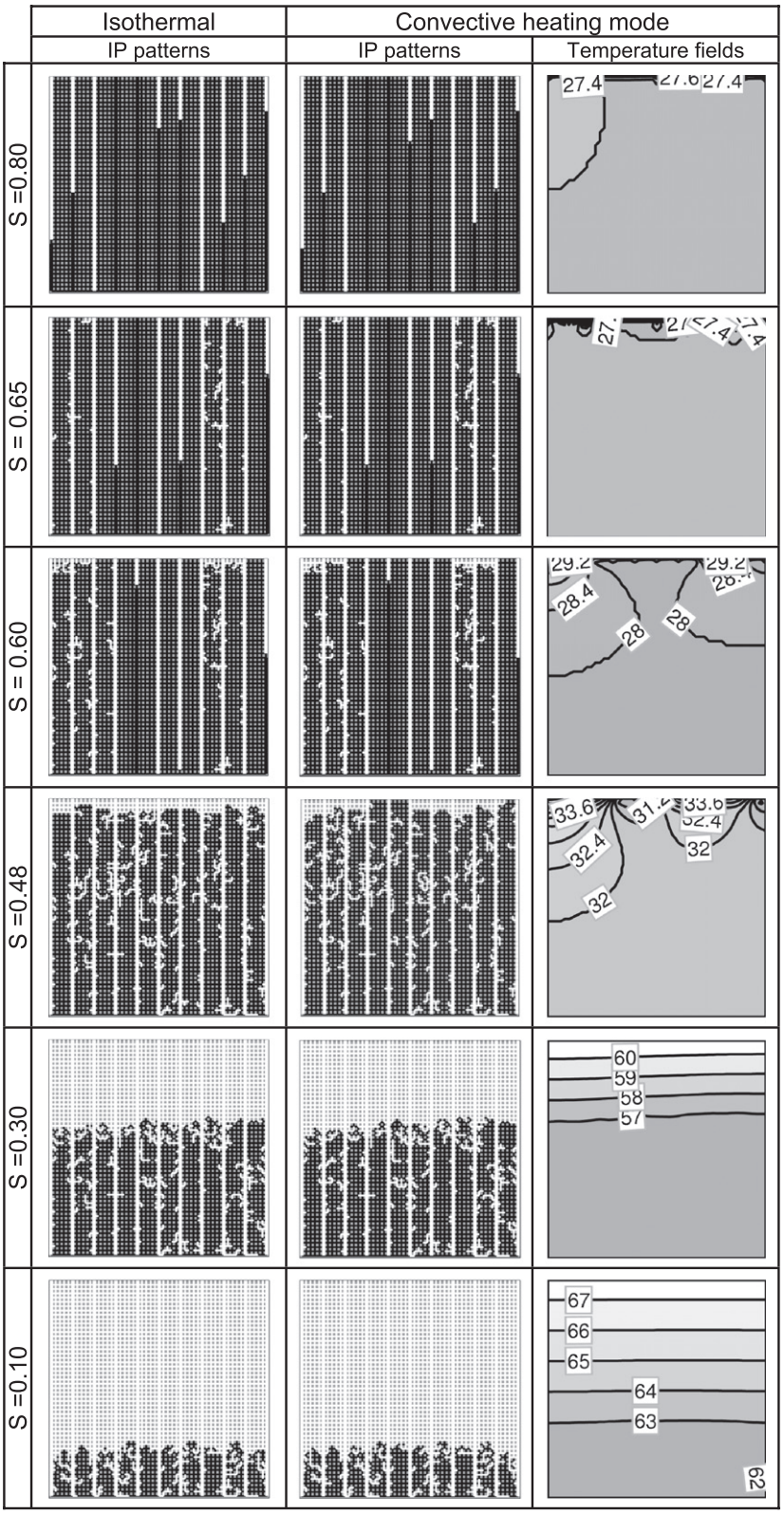

Fig. 6. Evolution of IP patterns and temperature fields for convective heating mode and comparison with simulated IP patterns of isothermal mode (network saturations are indicated; temperatures values are in °C).

compared with isothermal drying rates (Metzger et al., 2007b) at room temperature in Fig. 8. Temperature dependency of equilibrium vapor pressure directly affects evaporation rates leading to overall higher drying rates for both non-isothermal simulations (Fig. 8). All three simulations show a first drying period because macro-throats empty first keeping the surface wet down to low network

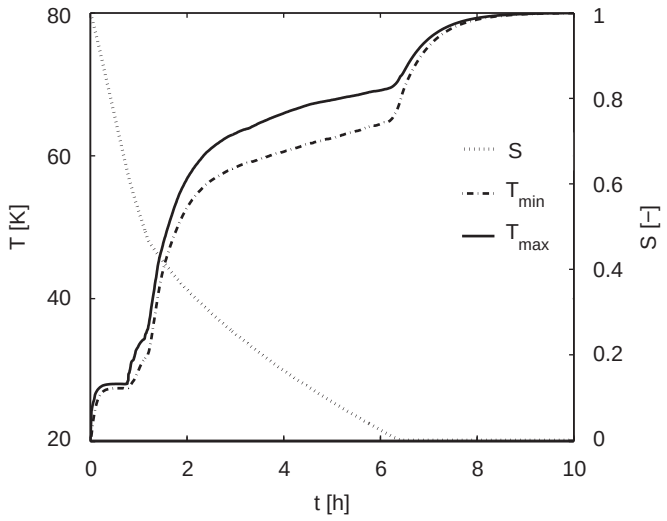

Fig. 7. Temporal evolution of temperatures at (T_{max}) top and bottom (T_{min}) of the network and its overall saturation S.

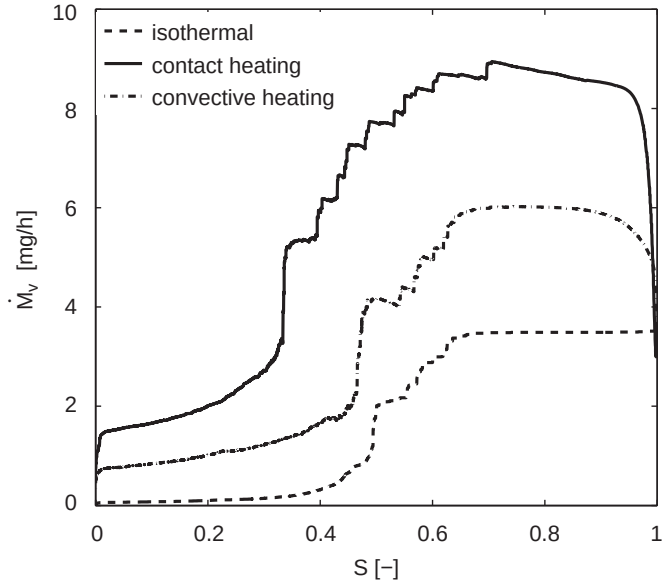

Fig. 8. Drying curves for isothermal case and both considered heating modes.

saturations. Additionally, a constant surface temperature is approached which corresponds to wet-bulb temperature for pure convective heating; for contact heating, it is higher and results from steady-state heat conduction from network bottom to top of boundary layer and from the cooling by surface evaporation.

The order of throat emptying depends on the temperature field by capillary pressure (Eq. (7)); this determines the position of the evaporation front which in turn controls drying rates. The evolutions of IP patterns and temperature fields for contact heating mode are shown in Fig. 9 and, for comparison, the results for the convective heating mode are also presented. In contact drying, again only macro-throats empty at the start (see Fig. 9 at $S = 0.80$) because of the high difference in radii for the two modes in throat size distribution. In this period, maximum temperature gradient develops in contact heating mode. Therefore, the invasion order of macro-throats differs from that of convective heating mode (Fig. 9).

After breakthrough (BT), i.e., air reaching the network bottom, and when clusters without macro-throats are created, invasion also takes place at the bottom of the network (see Fig. 9 at $S = 0.60$) due to the high gradient in temperature. A 40 K temperature difference at $S = 0.60$ corresponds to a variation of approximately 9% in capillary pressures through surface tension gradients in comparison to the relative standard deviation in one mode of the radius distribution of 5%. Therefore, a lower surface tension at the bottom will allow to empty throats which would not have been emptied for their relatively small size. Considering the network saturations 0.60–0.40, capillary fingering occurs in the entire network, i.e., forming of numerous clusters. This complex behavior is determined by the random dominance of radius distribution over surface tensions or vice versa. The small disconnected clusters evaporate not only at the top of the network, but also clusters at the network bottom can be eroded because of the significantly higher equilibrium vapor pressure in that region. As a result, two drying fronts will form which progress to the middle of the network (see Fig. 9 from S=0.40 to 0.10). With increasing mass transfer resistance for the upper evaporation front, drying rates decrease and evaporative cooling becomes less important; consequently, temperature gradients become smaller and smaller.

One of the major consequences of heat and mass transfer coupling of equilibrium vapor pressures (in pore network modeling) is diffusion of vapor from hot to cold neighboring liquid–gas interfaces and subsequent condensation. This process replaces non-wetting fluid by wetting fluid and does not follow IP rules as proposed in liquid transport. As explained in Section 2.2.4 only part of the condensing clusters (Fig. 2b) are chosen for accommodating condensed vapor. Fig. 10 shows the total condensation rate of the network $\dot{M}_C$ for both heating modes as a function of network saturation S. The actual rate as computed from vapor balances—and used for heat balances—is plotted along with the neglected rate which could not be accommodated (because imbibition is not modeled). During the initial phase of drying, while only macro-throats are emptying, capillary effects in a spanning liquid cluster nullify condensation, so that no error is made. When the liquid phase is discontinuous, condensation cannot fully be accounted for, and the error is higher in contact mode than in convective mode. In the case of convective heating, with stabilized drying front and low temperature the neglected condensation rates appear to be negligible (see also Surasani et al., 2008a). In contact heating mode, with high temperature gradient, two drying fronts and many liquid clusters, the error in condensation is relatively high.

3.4. Evolution of phase regions

Fig. 11 represents the evolution of phase regions of the bimodal network for both cases of convective and contact heating. The phase evolutions are plotted in terms of dimensionless drying front position in the network ζ versus network saturation S. The regions of evolved phases, i.e., gas, liquid, and liquid–gas interface, are named in the figure. The upper boundary in the liquid–gas interface indicates the dimensionless height above which only gas exists. Above this boundary, only vapor diffusion takes place. One can see the disconnection point (DP) in both figures. It indicates the point where all the surface throats dry out and the overall drying rates fall drastically. In convective heating, the lower boundary of liquid–gas interface indicates the dimensionless height below which only liquid exists. Only liquid flow due to capillary pumping takes place in this region. The point, at which air invades the bottom of the network, is called breakthrough point (BT). In contact heating, the liquid–gas interface lower boundary progresses in a similar way as in convective heating until BT. Later on, however, it moves upwards to give way to a gas region by empting of bottom throats. Unlike monomodal pore network drying simulations (Surasani et al., 2007) in which BT occurs after main cluster disconnection (MCD), bimodal simulations exhibit BT before DP (both MCD and DP represent the point where the surface dries out). This is due to the emptying of

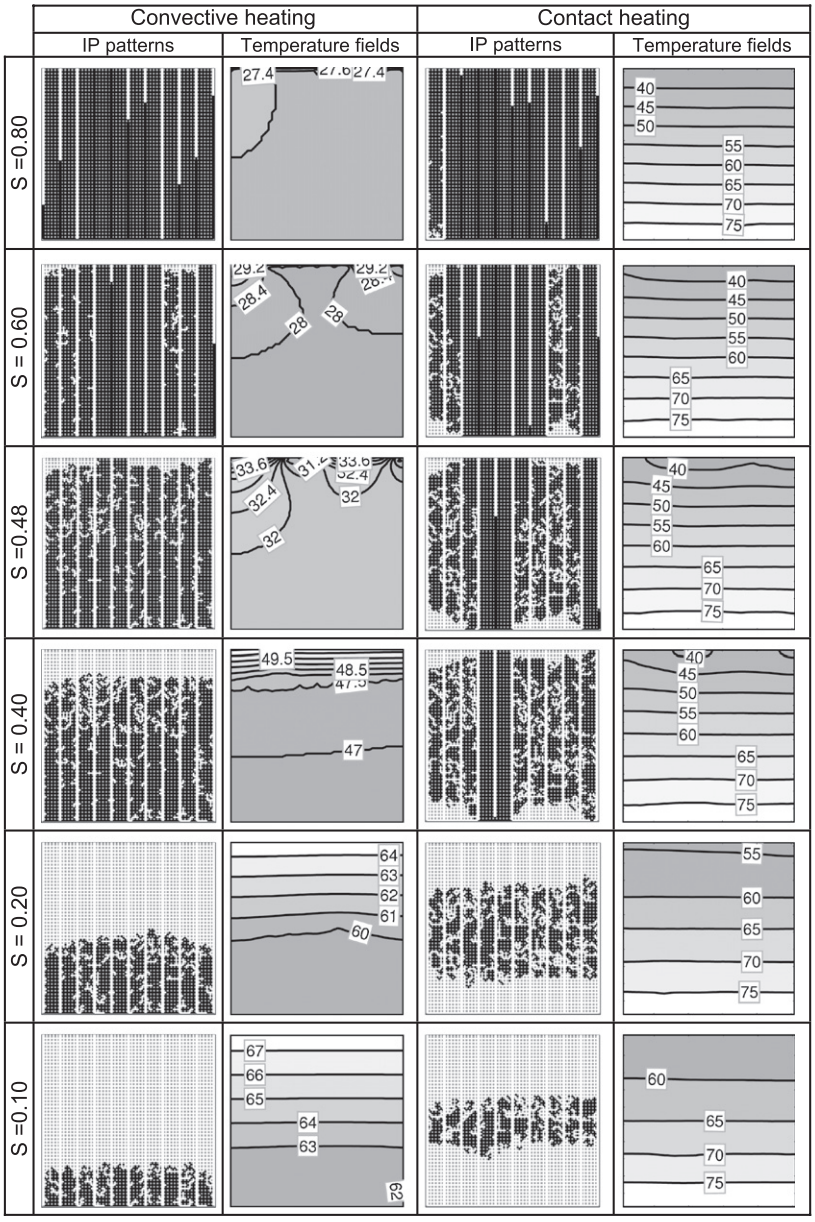

Fig. 9. Influence of heating modes on IP patterns and temperature fields (network saturations are indicated; temperatures values are in °C).

macro-throats at the beginning of drying process in the bi-modal network, whereas in the case of mono-modal surface throats will empty first.

4. Conclusions

A recently proposed non-isothermal pore network drying model (Surasani et al., 2008a), has been modified to compare convective and contact heating modes for the drying of a two-dimensional square pore network with a bimodal radius distribution. As already discussed in literature (Plourde and Prat, 2003; Huinink et al., 2002; Surasani et al., 2008a), the coupling between heat and mass transfer can have influences on both drying rates and evolving phase patterns in the porous medium. The first major expected effect is the enhancement of evaporation rate because the warming up of the porous body during drying significantly increases equilibrium vapor pressures at the evaporation front. Second, the temperature dependency of surface tension is expected to alter the order of pore emptying, leading to different phase patterns than under isothermal conditions.

A bimodal network has been chosen because many real porous media exhibit micro- and macro-pores. A major feature of such a pore network is that capillary pumping empties macro-pores first while the micro-pores stay saturated with liquid. This ensures a period of almost constant drying rate because the network surface remains nearly saturated. In the two-dimensional representation with several macro-channels (see Fig. 8), micro-porous network-spanning liquid clusters are formed in this period (Metzger et al., 2007b). In both non-isothermal drying modes (convective and contact), the macro-channels still empty preferentially because surface tension gradients have negligible effect on capillary pressure in comparison to the large difference in pore radii between micro- and macro-pores.

In the convective heating mode, evolving temperature gradients in the liquid–gas region are small throughout the drying process

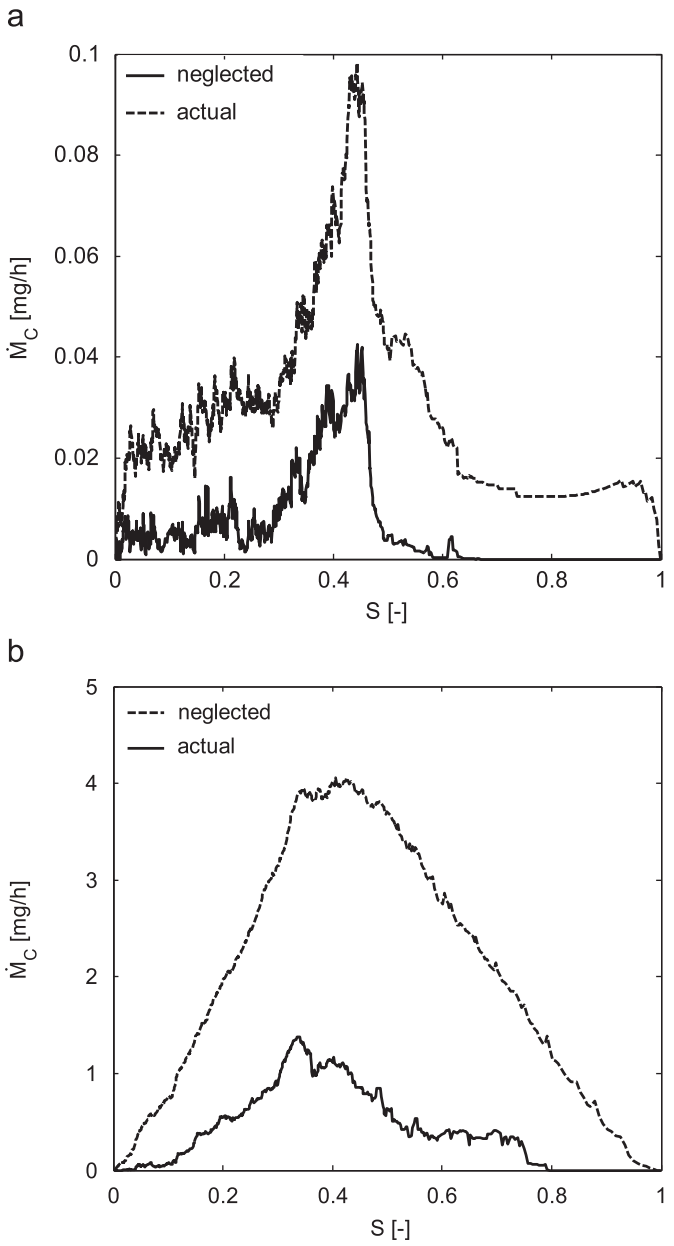

Fig. 10. Actual and neglected condensation rates for (a) convective and (b) contact heating.

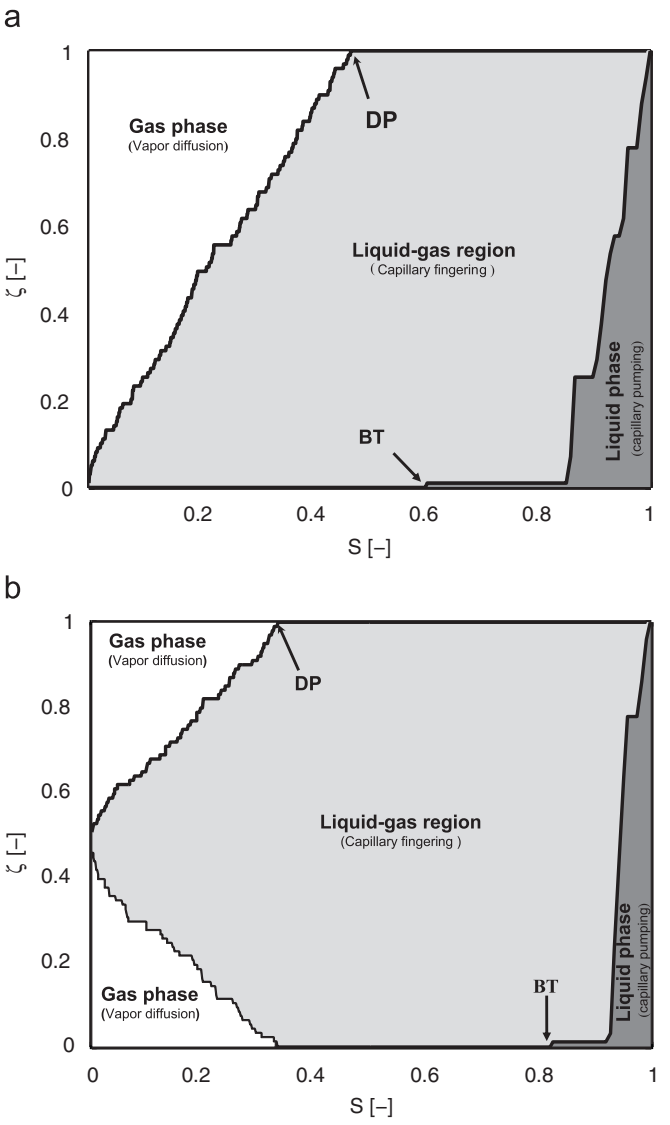

Fig. 11. Evolution of phase regions in both (a) convective and (b) contact heating modes.

so that only minor surface tension gradients develop. As a consequence, invasion order is almost not affected in both periods, i.e., during emptying of macro-throats and during drying out of micro-porous clusters. However, the temperature level gradually rises as the convective heating overrules evaporative cooling; this is because vapor diffusion resistance increases when the evaporation front recedes into the porous medium. With rising temperature, equilibrium vapor pressure at the phase boundary also increases leading to significantly higher drying rates than for the isothermal case.

A similar, but even more pronounced effect on overall drying rates is observed for the contact heating mode, since higher temperatures are reached for this less resistive heat transfer. At the same time, temperature gradients are much higher, so that surface tension variation plays a vital role in this case. Already when macro-throats are emptied, the order of invasion is modified. And after micro-porous clusters have been formed, the direction of temperature gradient leads to preferential emptying of throats at the bottom of the network. We observe what in literature is called *IP in a destabilizing gradient* (IPSG) (Plourde and Prat, 2003). A second effect occurs when the micro-porous regions have split up into small clusters. Then, the high variation in local equilibrium vapor pressure at the menisci leads to fast evaporation of clusters near the network bottom. The vapor is evacuated through the partially saturated center region of the network by the empty macro-channels. This second mechanism continues the destabilized emptying of throats. In the same time, near surface clusters also evaporate, due to the easy vapor diffusion to the dry convective air. This means that two drying fronts move towards the core of the network until they meet and the network is completely dry. Very similar behavior has been reported by Huinink et al. (2002).

As described above, the present model does not fully account for condensation, and the error has been quantified (Fig. 10). The main target of future work is to couple the invasion rules (for gas) with new imbibition rules (for liquid) so that fully saturated condensing clusters may grow into adjacent pores with free void volume. To this purpose, rules for the choice of the wetted pore throat have to be set up and details of reorganizing capillary equilibrium and cluster coalescence will be developed.

Notation

A	area of cross section, m^2
c_p	specific heat capacity, J/kg/K
g	mass transfer conductance, kg/s
H	enthalpy content, J
L	length of throat, m
$\tilde{M}$	molar mass, kg/kmol
$\dot{M}$	mass flow rate, kg/s
N	number of pores/clusters, dimensionless
P	pressure, Pa
$\dot{Q}$	heat flow rate, W
r	throat radius, m
$\tilde{R}$	ideal gas constant, J/kmol/K
S	saturation, dimensionless
t	time, s
T	temperature, K
u	velocity, m/s
V	volume, m^3
W	network thickness, m
Δh	specific phase change enthalpy, J/kg

Greek letters

α	heat transfer coefficient, $W/m^2/K$
β	mass transfer coefficient, m/s
γ	surface tension, N/m
δ	vapor diffusivity, m^2/s
ε	boundary layer thickness, m
ζ	dimensionless height, dimensionless
λ	thermal conductivity, W/m/K
ν	kinematic viscosity, m^2/s
ρ	density, kg/m^3

Subscripts/superscripts

BL	boundary layer
c	capillary
C	condensation
con	contact
ev	evaporation
g	gas
i or j	pore or node
ij	throat connecting pores i and j
l	liquid
lm	number of menisci
nc	cluster label
s	solid
T	total network
v	vapor
$*$	equilibrium

Acknowledgments

This work was financed by the German Research Foundation (DFG) in the frame of Graduate School 828 "Micro-Macro-Interactions in Structured Media and Particle Systems" and received additional support from Max-Buchner-Forschungsstiftung. The first author would like to express his special thanks to Dr. M. Prat for the fruitful discussion.

References

Al-Futaisi, A., Patzek, T.W., 2003. Extension of Hoshen–Kopelman algorithm to non-lattice environments. Physica A 321, 665–678.

Berkowitz, B., Ewing, R.P., 1998. Percolation theory and network modeling applications in soil physics. Surveys in Geophysics 19, 23–72.

Guillot, G., Trokiner, A., Darrasse, L., Saint-Jalmes, H., 1989. Drying of a porous rock monitored by NMR imaging. Journal of Physics D—Applied Physics 22, 1646–1649.

Huinink, H., Pel, L., Michels, M.A.J., Prat, M., 2002. Drying processes in the presence of temperature gradients—pore-scale modeling. European Physical Journal E 9, 487–498.

Irawan, A., Metzger, T., Tsotsas, E., 2005. Pore network modeling of drying: combination with boundary layer model to capture the first drying period. In: Proceedings of Seventh World Congress of Chemical of Chemical Engineering, Glasgow, Scotland.

Laurindo, J.B., Prat, M., 1998. Modeling of drying in capillary-porous media: a discrete approach. Drying Technology 16 (9 and 10), 1769–1787.

Lu, C., Yortsos, Y.C., 2005. Dynamics of forward filtration combustion at the pore-network level. A.I.Ch.E. Journal 51 (4), 1279–1296.

Masmoudi, W., Prat, M., 1991. Heat and mass transfer between a porous media and a parallel external flow, application to drying of porous materials. International Journal of Heat and Mass Transfer 34 (8), 1975–1981.

Metzger, T., Irawan, A., Tsotsas, E., 2005. Discrete modeling of drying kinetics of porous media. In: Proceedings of Third Nordic Drying Conference, Karlstad, Sweden, 2005.

Metzger, T., Irawan, A., Tsotsas, E., 2006a. Remarks on the paper "Extension of Hoshen–Kopelman algorithm to non-lattice environment" by Al-Futaisi, A., Patzek, T.W., 2003. Physica A 321, 665–678.

Metzger, T., Irawan, A., Tsotsas, E., 2006b. Remarks on the paper "Extension of Hoshen–Kopelman algorithm to non-lattice environment" by Al-Futaisi, A., Patzek, T.W., 2003. Physica A 363, 558–560.

Metzger, T., Irawan, A., Tsotsas, E., 2007a. Isothermal drying of pore networks influence of friction for different pore structures. Drying Technology 25, 49–57.

Metzger, T., Irawan, A., Tsotsas, E., 2007b. Influence of pore structure on drying kinetics: a pore network study. A.I.Ch.E. Journal 53, 3029–3041.

Metzger, T., Tsotsas, E., Prat, T., 2007c. Chapter 2: Pore-network models: a powerful tool to study drying at the pore level and understand the influence of structure on drying kinetics. In: Tsotsas, E., Mujumdar, M. (Eds.), Modern Drying Technology Computational Tools at Different Scales, vol. 1. Wiley, New York, pp. 57–102.

Nowicki, S.C., Davis, H.T., Scriven, L.E., 1992. Microscopic determination of transport parameters in drying porous media. Drying Technology 10 (4), 925–946.

Pel, L., Ketelaars, A.A.J., Adan, O.C.G., van Well, A.A., 1993. Determination of moisture diffusivity in porous media using scanning neutron radiography. International Journal of Heat and Mass Transfer 36, 1261–1267.

Pel, L., Brockem, H., Kopinga, K., 1996. Determination of moisture diffusivity in porous media using moisture concentration profiles. International Journal of Heat and Mass Transfer 39, 1273–1280.

Plourde, F., Prat, M., 2003. Pore network simulations of drying of capillary porous media. Influence of thermal gradients. International Journal of Heat and Mass Transfer 46, 1293–1307.

Prat, M., 1993. Percolation model of drying under isothermal conditions in porous media. International Journal of Multiphase Flow 19 (4), 641–704.

Prat, M., 2002. Recent advances in pore-scale models for drying of porous media. Chemical Engineering Journal 86, 153–164.

Prat, M., 2007. On the influence of pore shape, contact angle and film flows on drying of capillary porous media. International Journal of Heat and Mass Transfer 50, 1455–1468.

Quintard, M., Whitaker, S., 1993. Transport in ordered and disordered porous media: volume-averaged equations, closure problems and comparison with experiments. Chemical Engineering Science 41 (14), 2537–2564.

Sanchez-Palencia, E., 1980. Non-homogeneous media and vibration theory. Lecture Notes in Physics, vol. 127. Springer, Berlin.

Satik, C., Yortsos, Y.C., 1996. A pore-network study of bubble growth in porous media driven by heat transfer. Journal of Heat Transfer 118, 455–462.

Strumillo, C., Kudra, T., 1986. Drying principles applications and design. In: Hughes, R. (Ed.), Topics in Chemical Engineering, vol. 3. Gordon and Beach Science Publishers.

Surasani, V.K., Metzger, T., Tsotsas, E., 2007. A non-isothermal pore network drying modal: influence of gravity. In: Proceedings of European Congress of Chemical Engineering (ECCE-6), Copenhagen, 2007.

Surasani, V.K., Metzger, T., Tsotsas, E., 2008a. Consideration of heat transfer in pore network modelling of convective drying. International Journal of Heat and Mass Transfer 51, 2506–2518.

Surasani, V.K., Metzger, T., Tsotsas, E., 2008b. Drying simulations of various 3D pore structures by a non-isothermal pore network model. Submitted to 16th International Drying Symposium, Hyderabad, India.

Yiotis, A.G., Stubos, A.K., Boudouvis, A.G., Yortsos, Y.C., 2001. Pore network model of drying of single-component liquids in porous media. Advances in Water Resources 24, 439–460.

Yiotis, A.G., Boudouvis, A.G., Stubos, A.K., Tsimpanogiannis, I.N., Yortsos, Y.C., 2004. Effect of liquid films on the drying of porous media. A.I.Ch.E. Journal 50 (11), 2721–2737.

Yiotis, A.G., Tsimpanogiannis, I.N., Stubos, A.K., Yortsos, Y.C., 2006. Pore-network study of characteristic periods in the drying of porous media. Journal of Colloid and Interface Science 297, 738–748.

Whitaker, S., 1977. Simultaneous heat, mass, and momentum transfer in porous media: a theory of drying. Advances in Heat Transfer 13, 119–203.

Transp Porous Med
DOI 10.1007/s11242-009-9372-7

A Non-isothermal Pore Network Drying Model with Gravity Effect

V. K. Surasani · T. Metzger · E. Tsotsas

Received: 25 January 2008 / Accepted: 24 February 2009

Abstract The concept of immiscible displacement as an invasion percolation (IP) process driven by heat and mass transfer is used in a pore network model for convective drying of capillary porous media. The coupling between heat and mass transfer occurs at the liquid–gas interface through temperature-dependent equilibrium vapor pressure and surface tension as well as the phase change enthalpy (in evaporation and condensation). The interfacial effects due to capillary forces and gravity are combined in an invasion potential; viscous forces are neglected. Simulation results show stabilized invasion patterns and finite drying front width by the influence of gravity.

Keywords Capillary porous media · Mono-modal pore size distribution · Invasion percolation · Phase distributions · Temperature field

List of Symbols

A	Area of cross section (m^2)
c_p	Specific heat capacity (J/kg/K)
g	Mass transfer conductance (kg/s)
L	Length of throat (m)
$\tilde{M}$	Molar mass (kg/kmol)
$\dot{M}$	Mass flow rate (kg/s)
N	Number of pores/clusters (−)
P	Pressure (Pa)
$\dot{Q}$	Heat flow rate (W)
$\tilde{R}$	Ideal gas constant (J/kmol/K)
r	Throat radius (m)

V. K. Surasani · T. Metzger (✉) · E. Tsotsas
Institute of Process Engineering, Chair of Thermal Process Engineering, Otto-von-Guericke-University Magdeburg, P.O. Box 4120, 39016 Magdeburg, Germany
e-mail: thomas.metzger@ovgu.de

Published online: 19 March 2009

S Saturation (−)
T Temperature (K)
t Time (s)
V Volume (m^3)
W Network thickness (3rd dimension) (m)
Δh Specific phase change enthalpy (J/kg)

Greek Symbols

α Heat transfer coefficient ($W/m^2/K$)
γ Surface tension (N/m)
δ Vapor diffusivity (m^2/s)
ζ Dimensionless height (−)
λ Thermal conductivity (W/m/K)
ρ Density (kg/m^3)
Φ Throat potential (Pa)

Subscripts/superscripts

c Capillary
ev Evaporation
g Gas
i or j Pore or node
ij Throat connecting pores i or j
l Liquid
lm Number of menisci
m Mass transfer
nc Cluster index
s Solid
t Thermal/heat transfer
v Vapor
* Equilibrium
∞ Bulk air

1 Introduction

The fundamental understanding of pore network modeling commences with the network representation of the void space (Berkowitz and Ewing 1998), i.e., geometry, in the porous medium. Further, drying can be treated as a special case of invasion percolation (IP) (Prat 1993) due to the immiscible displacements of air and liquid in the pore space upon evaporation of liquid. During this invasion process, liquid menisci will respond to capillary, viscous, and buoyancy forces. In the absence of viscous forces, gravity, and thermal gradients, phase distributions completely depend on the spatial disorder of pore size (Laurindo and Prat 1998). In the presence of gravity, the phase distributions are patterns of invasion percolation in a stabilizing gradient (IPSG) or in a destabilizing gradient (IPDG) depending on the direction of the gravity vector to the main direction of vapor flow (Laurindo and Prat 1998). Similarly,

IPSG patterns can be observed in the presence of viscous forces (Yiotis et al. 2001; Metzger et al. 2007a).

In the above-mentioned literature, invasion is considered at slow drying rates; energy aspects of the drying are neglected when studying the physical and structural influences on invasion patterns. The influence of temperature gradients—which were imposed onto the drying product—has been investigated by Plourde and Prat (2003) and Huinink et al. (2002). However, product temperature did not evolve freely as corresponding to convective drying boundary conditions. Surasani et al. (2008) considered heat transfer in a pore network model that neglects viscous effects and gravity. This model was the first to describe the free evolution of temperature fields in convective drying.

The present work extends this first model (Surasani et al. 2008) to investigate the influence of invasion percolation in a stabilized pressure gradient due to capillary and gravitational forces (still neglecting viscous effects) as occurring in convective heating. Simulation results are shown as drying curves, temporal evolution of phase distributions (cluster formation), temperature fields, and phase diagrams for a mono-modal pore size distribution.

2 Model Description

In the present work, void space in the porous medium is regarded as a network of cylindrical throats with randomly distributed radius, and connections are by pore nodes. Figure 1 shows the network of pores and throats in a two-dimensional square lattice and how each pore is associated with a control volume. Initially, the network is saturated completely with water at room temperature T_{in} ($=20°\text{C}$) and drying air flows at zero humidity ($P_{\text{v},\infty} = 0$) and temperature T_∞ over the top edge of the network. In order to describe the first drying period with its constant drying rate (Metzger et al. 2007b; Yiotis et al. 2006), it is necessary to model vapor diffusion in the convective boundary layer in a discretized way, by extending the network into the gas-phase with additional nodes (see Fig. 1); their number is given by the mass transfer coefficient and vapor diffusivity. Immiscible displacements upon evaporation of liquid will cause the invasion percolation gradient (IPG) patterns in the network. One such pattern is shown in Fig. 1, which represents the continuous vapor phase and disconnected liquid clusters in the solid network. Pore and throat conditions (Surasani et al. 2008) will determine the transport within and between the phases. At the phase boundary, liquid flow, evaporation, and vapor diffusion are simultaneous, and are influenced by capillary forces and gravity. In partially filled throats, the meniscus moves as evaporated liquid diffuses through air, and at the same time, liquid flows in either direction depending on the boundary liquid pressure at the meniscus. In this process, vapor transfer is only due to molecular diffusion at constant total pressure, and viscous forces due to liquid flow are neglected. Pore saturations are given by the average saturation of connected throats.

The vapor flow rate between two gas pores is given by Stefan's law. From the law of conservation and the assumption of quasi-stationary vapor transport, the mass flow rates ($\dot{M}_{\text{v},ij}$) at any gas pore i add up to zero.

$$\dot{M}_{\text{v},ij} = A_{ij} \frac{\delta}{L} \frac{P \tilde{M}_{\text{v}}}{\tilde{R} T} \ln\left(\frac{P - P_{\text{v},i}}{P - P_{\text{v},j}}\right) \tag{1a}$$

$$\sum_{j=1}^{4} \dot{M}_{\text{v},ij} = 0 \tag{1b}$$

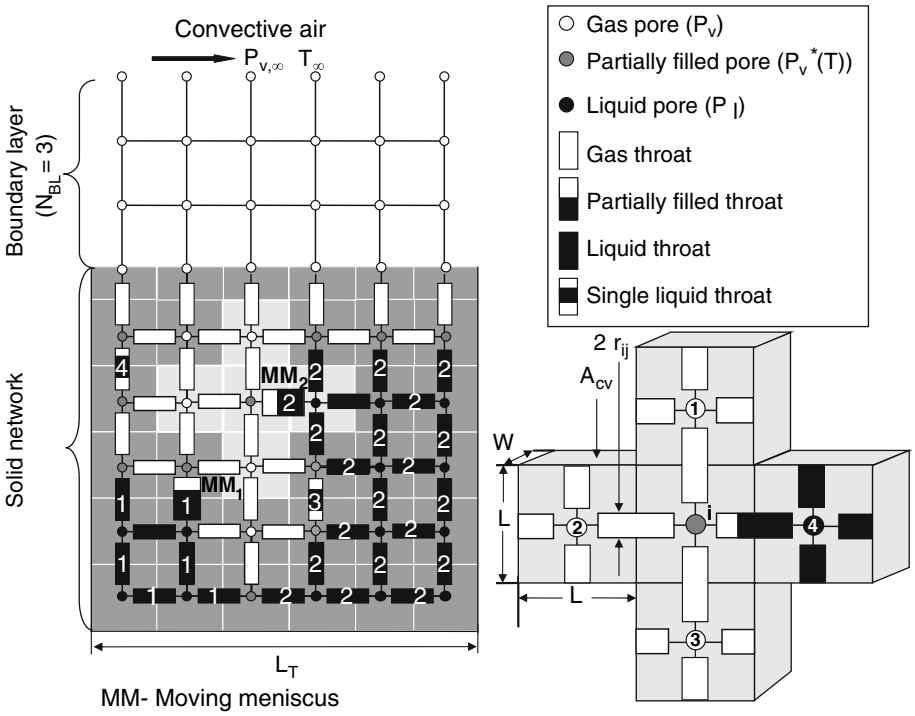

Fig. 1 Pore network with boundary layer, cluster formations, pore and throat conditions and control volume *i*

Here, cross-sectional area varies from the pore network ($A_{ij} = \pi r_{ij}^2$) to the boundary layer ($A_{ij} = LW$). Since we neglect the overlap of throats at pore nodes, all throats in the network are assumed as equal in length ($L_{ij} = L$). The linear system of vapor transport, Eq. 1, is solved for partial vapor pressures ($P_{v,i}$) using the conjugate gradient method. Equilibrium vapor pressure exists in partially filled pores, which give boundary conditions to the linear system of vapor transport. The remaining boundary is at the vapor pressure of convective air ($P_{v,\infty} = 0$). Then, vapor flow rates $\dot{M}_{v,ij}$—and especially, evaporation rates $\dot{M}_{ev,ij}$ from menisci throats—are computed from gas pore vapor pressures by Eq. 1a.

Yiotis et al. (2004) analyzed different film regimes and also predicted that thermal gradients should usually have little influence on the extension of the film region, but that for large temperature gradients, films ought to be shortened. Literature work (Prat 2007) with polygonal throat cross sections shows that film flow in the corners may be important. Thus, with the cylindrical throats and in the presence of non-uniform temperatures film effects are neglected in this model (Surasani et al. 2008).

Concerning liquid transport, the assumption of negligible viscous forces implies that, in each cluster, liquid can be pumped from the throat with the highest liquid pressure to all other meniscus throats, making them moving meniscus (MM) throats and stationary meniscus (SM) throats, respectively. In each cluster, the MM throat will empty first since this throat alone will contribute to the total evaporation rate of the cluster through capillary pumping. The criterion for selecting MM throats is given by the throat potential $P_{l,ij} = P + \Phi_{ij}$, i.e., in each cluster, the throat with the highest invasion potential is selected as MM throat, where

the invasion potential combines the effects of capillary forces and gravity

$$\Phi_{ij} = -\frac{2\sigma(T_{ij})}{r_{ij}} + (\rho_\mathrm{l} - \rho_\mathrm{g}) g h_{ij} \tag{2}$$

So, it is necessary to identify the continuous liquid phases, i.e., clusters, and within each cluster the highest invasion potential $\Phi_{\mathrm{nc,MM}}$ throat. For cluster labeling, the Hoshen–Kopelman algorithm can be used (Metzger et al. 2006). Figure 1 shows the realization for the clusters 1 and 2.

The time step Δt to empty the MM throat in each cluster (nc) can be obtained from the ratio of current mass in the MM throat to the total evaporation rate of the cluster as

$$\Delta t_{\mathrm{m,nc}} = \frac{\rho_\mathrm{l} V_{\mathrm{MM,nc}}}{\sum_j \dot{M}_{\mathrm{ev},ij,\mathrm{nc}}}. \tag{3}$$

(The sum is taken over all liquid–gas interface pores of the respective cluster.) The minimum time step $\Delta t_{\mathrm{m,min}}$ has to be chosen among all existing clusters and single throats as mass transfer time step, because a single throat invasion can change liquid connectivity and vapor diffusion conditions.

Figure 1 also shows how each control volume is represented by one pore and contains four-half throats, i.e., each throat participates in two control volumes. Liquid of partially filled throats is equally distributed to the neighbor pores. Conductive heat transfer is assumed between the CVs, and local thermal equilibrium is applied in each CV. The transient energy balance over control volume i is

$$V_i (\rho c_\mathrm{p})_i \frac{dT_i}{dt} = -\sum_{j=1}^{4} A_{\mathrm{cv},ij} \lambda_{ij} \frac{T_i - T_j}{L} - \Delta h_{\mathrm{v},i}(T_i) \sum_{j=1}^{\mathrm{lm}} \dot{M}_{\mathrm{ev},ij}, \tag{4}$$

where control volume heat capacities $V_i (\rho c_\mathrm{p})_i$ and effective thermal conductivities λ_{ij} are functions of throat saturation (Surasani et al. 2008). The exchange area is $A_{\mathrm{cv},ij} = LW$ because both voids and solid do contribute to heat transfer. Heat and mass transfer are strongly coupled at evaporating/condensing menisci by phase change enthalpy $\Delta h_{\mathrm{v},i}(T_i)$. Meniscus position in the throat is used to allocate heat sinks/sources to a control volume. In Eq. 4, the evaporation flow rates $\dot{M}_{\mathrm{ev},ij}$ are summed up for all neighbor throats that have a meniscus within control volume i; they are positive for evaporation and negative for condensation. The stability of the explicit method is only guaranteed if the thermal time step fulfils the condition

$$\Delta t_\mathrm{t} < \frac{(\rho c_\mathrm{p})_i L^2}{\sum_j \lambda_{ij}}. \tag{5}$$

The minimum of heat and mass transfer time step is used to update the phase distributions and temperature fields of the network. Then, in a loop, vapor diffusion rates, liquid flow, and heat transfer are computed and network saturation as well as temperature updated, until the network is completely dry.

3 Simulation Results

The results presented in this section have been obtained for networks of size 51×51 with mono-modal throat size distribution $40 \pm 2\,\mu\mathrm{m}$ (see Fig. 3 for realization) and, throat length is $500\,\mu\mathrm{m}$. Initially, the network is saturated with water and has a uniform temperature of 20°C.

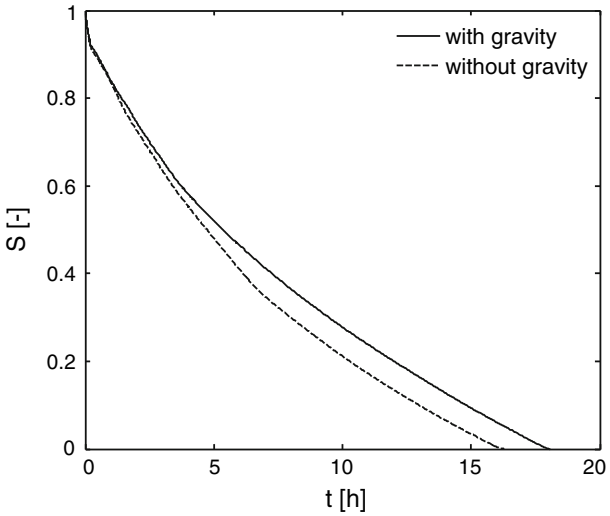

Fig. 2 Overall saturation of the network versus time

The heat transfer parameters of the solid are chosen as for glass: $(\rho c_p)_s = 1.7 \times 10^6\,\mathrm{J/(m^3K)}$ and $\lambda_s = 1\,\mathrm{W/(mK)}$. Bulk air is at $T_\infty = 80°\mathrm{C}$, has zero moisture content and velocity such that the boundary layer contains seven nodes ($\beta = 7.3\,\mathrm{mm/s}$). Simulations of convective heating mode with and without gravity are presented.

Figure 2 shows the drying kinetics as network saturation over time. The evolutions of phase distributions (IP patterns) and temperature fields are shown in Fig. 3; the respective network saturation S is indicated for simulations of both without and with gravity. At the start of the drying process, both curves in Fig. 2 show similar drying rates (i.e., slopes) and similar IP patterns can be seen at network saturation $S = 0.95$ (Fig. 3) since capillary forces are dominant over gravity in selecting the highest invasion potential throat. In both cases, drying rate falls drastically due to the increase in vapor diffusion resistance when surface throats have emptied. Further, drying rates are lower in the case of gravity and longer drying times are observed.

Figure 3 also shows the IP patterns simulated with and without gravity under isothermal conditions and a comparison with that of non-isothermal convective heating. Both isothermal and non-isothermal simulations show similar invasion patterns when compared in the presence ($B > 0$) or in the absence of gravity ($B = 0$) due to less influence of the low temperature gradient on capillary pressures. In the absence of gravity, i.e., with Bond number $B = 0$, capillary forces alone will determine the order of throat invasion; they are given by random throat radius distribution and current local temperatures (Eq. 2). If temperature gradients are low, then the gas phase will rapidly invade the depth of the pore network creating many liquid clusters in the whole network. This results in IP patterns without significant stabilization as shown in Fig. 3 (case without gravity at $S = 0.55$). For the given geometry, gravity counteracts capillary forces. Throat invasion order is then determined by the invasion potential Φ, which combines both capillary force and gravity. Capillary pumping is limited to a finite distance resulting in a stabilized drying front (with small clusters), which recedes into the network without major changes (see Fig. 3 with gravity). The observed drying rates are low in the case of gravity (see Fig. 2 with gravity) because of the increased resistance to vapor diffusion for a stabilized front.

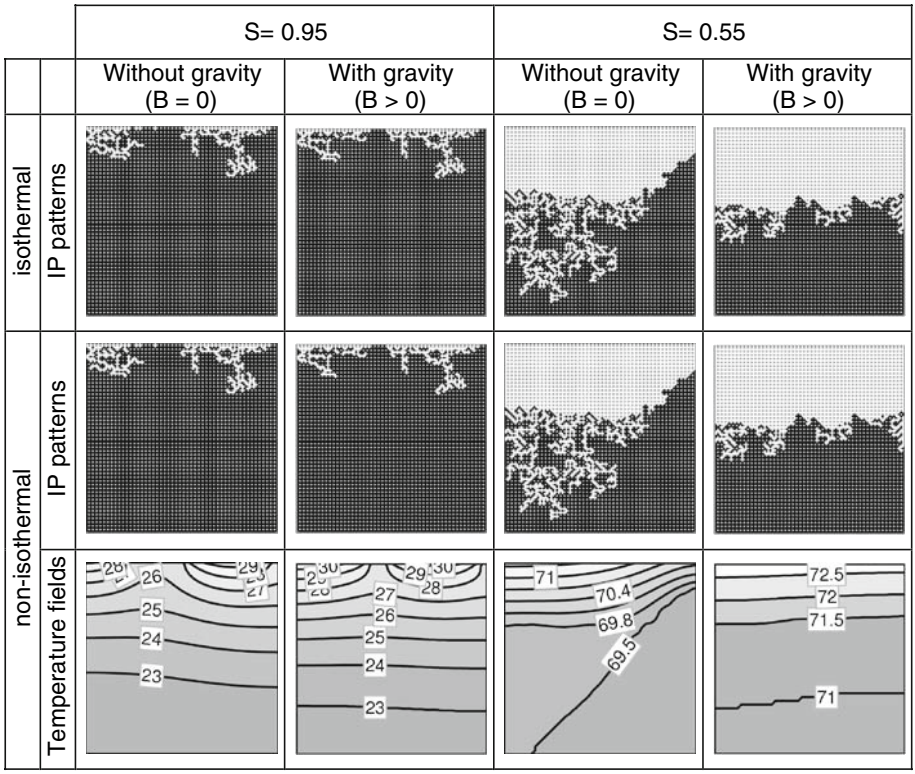

Fig. 3 Comparison of evolved phase distributions and temperature fields without and with gravity under isothermal and non-isothermal conditions (temperature fields are represented by isothermal lines with temperature in °C)

Figure 4 represents phase distributions in the mono-modal network without and with gravity. The phase evolutions are plotted in terms of dimensionless height ζ versus total network saturation S. The regions of evolved phases, i.e., gas, liquid, and liquid–gas interface, are named in the figure. The upper boundary in the liquid–gas interface indicates the dimensionless height above which the network is completely dry so that only vapor diffusion takes place. One can see the main cluster disconnection point (MCD) in both figures. MCD indicates the point where all the surface throats dry out and the surface losses contact with main liquid cluster. At this point, the overall drying rates will fall drastically. The lower boundary of liquid–gas interface indicates the dimensionless length below which only liquid phase exists. Only liquid flow due to capillary pumping takes place in this region. The point, at which air invades the bottom of the network, i.e., where the liquid–gas interface reaches the bottom of the network, is called breakthrough (BT). Invasion percolation in a stabilizing gradient is characterized by the width of liquid–gas interface. At the start of the drying process, both cases of without and with gravity represent same drying front width and similar invasion patterns (Fig. 3 at $S = 0.95$); and also similar main cluster disconnection (MCD) points are observed.

In the absence of gravity, the vertical extension of the liquid–gas interface increases while its upper boundary stays almost constant resulting in an earlier BT point (see Fig. 3 at $S = 0.55$, $B = 0$). This characterizes unstabilized invasion percolation patterns. In the

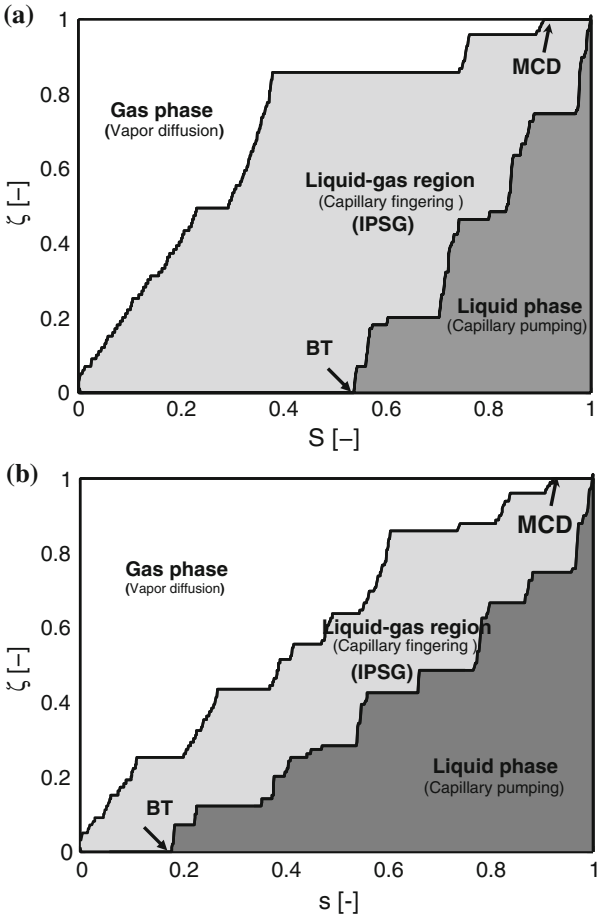

Fig. 4 Evolution of phase regions of the network in terms of dimensionless height and network saturation, without gravity (**a**) and with gravity (**b**)

presence of gravity, the liquid–gas interface has an almost constant vertical extension (see also Fig. 3 at $S = 0.55$, $B > 0$), which is characteristic for IPSG patterns. In both cases, after BT, the extension of the liquid–gas interface diminishes as its upper boundary recedes into the network.

4 Conclusions

A non-isothermal pore network drying model including gravity and capillary forces is presented which shows invasion percolation stabilizing gradient (IPSG) patterns. In the presence of gravity, IP patterns completely depend on the invasion potential Φ, i.e., the net pressure due to combined capillary forces and gravity. In convective drying, the porous medium heats up from the surface; this leads to favorable invasion of near surface throats (influence of temperature dependent surface tension in Φ). This thermal stabilization becomes important for weakly disordered networks (Surasani et al. 2008). The above-mentioned thermal

stabilization of the drying front is now superimposed by a gravitational stabilization. However, the evolved temperature gradients over the network are small and play a minor role on IP patterns in the presented case. Unstabilized invasion percolation patterns with large drying front width, without gravity, and invasion percolation stabilizing gradient (IPSG) patterns with finite drying front width, with gravity, are shown as the result of simulations on a mono-modal pore network. The characteristic liquid–gas interface is presented for both cases, with and without gravity, in the form of "phase diagram." For the gravity-controlled case, the evolved constant width of the liquid–gas interface indicates the finite drying front width in which only few cluster will form, and the observed drying rates are low due to the increased vapor diffusion resistance. Future work will include the investigation of combined influence of all forces acting on the menisci. This necessitates including viscous forces in liquid flow.

Acknowledgments This work was financed by the German Research Foundation (DFG) in the frame of Graduate School 828 "Micro-Macro-Interactions in Structured Media and Particle Systems." The first author would like to express his special thanks to Max–Buchner–Forschungsstiftung for its additional support.

References

Al-Futaisi, A., Patzek, T.W.: Extention of Hoshen–Kopelman algorithm to non-lattice environments. Phys. A **321**, 665–678 (2003). doi:10.1016/S0378-4371(02)01586-8

Berkowitz, B., Ewing, R.P.: Percolation theory and network modeling applications in soil physics. Surv. Geophys. **19**, 23–72 (1998). doi:10.1023/A:1006590500229

Huinink, H., Pel, L., Michels, M.A.J., Prat, M.: Drying processes in the presence of temperature gradients-pore-scale modeling. Eur. Phys. J. E. **9**, 487–498 (2002). doi:10.1140/epje/i2002-10106-1

Laurindo, J.B., Prat, M.: Numerical and experimental network study of evaporation in capillary porous media drying rates. Chem. Eng. Sci. **53**, 2257–2269 (1998). doi:10.1016/S0009-2509(97)00348-5

Metzger, T., Irawan, A., Tsotsas, E.: Remarks on the paper "Extension of Hoshen–Kopelman algorithm to non-lattice environments" by Al-Futaisi, A., Patzek, T.W.: Phys. A 321 665–678 (2003). Phys. A **363**, 558–560 (2006). doi:10.1016/j.physa.2005.08.026

Metzger, T., Irawan, A., Tsotsas, E.: Isothermal drying of pore networks: influence of friction for different pore structures. Dry. Technol. **25**, 49–57 (2007a). doi:10.1080/07373930601152640

Metzger, T., E. Tsotsas Prat, M.: Pore network models: a powerful tool to study drying at the pore level. In: Tsotsas, E., Mujumdar, A.S. (eds.) Computation Tools at Different Scales, vol. 1 of Modern Drying Technology, chap. 2, pp. 57–102. Wiley-VCH Velag GmbH & Co KGaA, Weinheim (2007b).

Prat, M.: Percolation model of drying under isothermal conditions in porous media. Int. J. Multiph. Flow **19**(4), 641–704 (1993). doi:10.1016/0301-9322(93)90096-D

Prat, M.: On the influence of pore shape, contact angle and film flows on drying of capillary porous media. Int. J. Heat Mass Transf. **50**, 1455–1468 (2007). doi:10.1016/j.ijheatmasstransfer.2006.09.001

Plourde, F., Prat, M.: Pore network simulations of drying of capillary porous media: influence of thermal gradients. Int. J. Heat Mass Transf. **46**, 1293–1307 (2003). doi:10.1016/S0017-9310(02)00391-5

Surasani, V.K., Metzger, T., Tsotsas, E.: Consideration of heat transfer in pore network modelling of convective drying. Int. J. Heat Mass Transf. **51**, 2506–2518 (2008). doi:10.1016/j.ijheatmasstransfer.2007.07.033

Yiotis, A.G., Stubos, A.K., Boudouvis, A.G., Yortsos, Y.C.: Pore network model of drying of single-component liquids in porous media. Adv. Water Resour. **24**, 439–460 (2001). doi:10.1016/S0309-1708(00)00066-X

Yiotis, A.G., Boudouvis, A.G., Stubos, A.K., Tsimpanogiannis, I.N., Yortsos, Y.C.: Effect of liquid films on the drying of porous media. A. I. Ch. E. J. **50**(11), 2721–2737 (2004)

Yiotis, A.G., Tsimpanogiannis, I.N., Stubos, A.K., Yortsos, Y.C.: Pore-network study of characteristic periods in the drying of porous materials. J. Colloid Interface Sci. **297**, 738–748 (2006). doi:10.1016/j.jcis.2005.11.043

Drying Technology, 28: 615–623, 2010

ISSN: 0737-3937 print/1532-2300 online
DOI: 10.1080/07373931003788676

Taylor & Francis
Taylor & Francis Group

Drying Simulations of Various 3D Pore Structures by a Nonisothermal Pore Network Model

V. K. Surasani, T. Metzger, and E. Tsotsas
Thermal Process Engineering, Otto-von-Guericke-University Magdeburg, Universitaetsplatz, Magdeburg, Germany

During drying of a porous medium, pores are subsequently invaded by gas upon evaporation of water, typically disintegrating the liquid phase into clusters. Pore network models describe this invasion process on the basis of void space geometry and physics of pore-scale events. In the recent modeling by Surasani et al., (2008) invasion percolation rules under nonisothermal conditions are described with strong coupling between heat and mass transfer. In this work, the drying of various three-dimensional (3D) cubic pore structures with mono- and bimodal pore radius distributions is simulated for convective heat and mass transfer boundary conditions. Drying rate curves differ significantly for mono- and bimodal networks. A pronounced first drying period is seen for the bimodal case; here, macropore channels empty first and water is evaporated from the still-wet micropores at the surface. Additionally, freely evolving temperature fields in conjunction with phase distributions are presented.

Keywords Capillary porous media; Invasion percolation; Nonisothermal drying; Phase distributions; Temperature fields

INTRODUCTION

Drying of capillary porous media has been the subject of applied and scientific interest for many researchers due to coupled heat and mass flows occurring in a complex geometry of void space. Classical models of drying are based on the assumption of the porous medium as fictitious continuum for which heat and mass balances are derived by either homogenization[1] or volume averaging.[2] The main motivation for the emergence of pore network models is the failure of continuous modeling[3] to represent cluster formation and to investigate the influence of transport phenomena at the pore level. One route is to use a representative pore network to obtain the effective parameters that represent transport and equilibrium properties of the partially saturated porous medium; a second route is to overcome length-scale constraints by analyzing drying behavior of small sample scale networks. For both routes, a network representation of void space is adopted so that exact description of transport in the porous medium is greatly simplified to that of individual phases; i.e., gas and liquid. This description leads to a discrete model, in which every pore is treated as an entity instead of averaging many pores in the continuous approach. Therefore, pore network modeling faces computational limits to perform simulations on real-size porous structures.[4]

Pore network models in drying of capillary porous media were first used by Daian and Saliba[5] and Nowicki et al.[6] to study the behavior of effective parameters as a function of liquid saturation. More extensive works over the last decade on pore network models have been accomplished by two prominent groups lead by Prat (since 1993[7]) and Yiotis (since 2001[8]). In their work the influence of capillary,[7] gravity,[9] and viscous forces[8] on invasion percolation (IP) patterns as well as the effect of film flows on overall drying rates[10] were studied. In recent years, the influence of pore structure on drying kinetics was studied by Metzger et al.[11] Despite a significant amount of literature on pore network models, the majority of contributions are devoted to two-dimensional cases and few drying simulations are three-dimensional.[12–14] Le Bray and Prat[12] discussed the constant rate period (CRP) for a pore network with monomodal pore size distribution but with a reduced drying rate as compared to the initial one. Applying lateral vapor diffusion in the boundary layer, Yiotis et al.[13] captured a CRP with the initial rate of drying. Later, Metzger and Tsotsas[14] studied the influence of liquid viscosity on the occurrence of a first drying period. All the above-mentioned investigations are isothermal.

Heat transfer aspects of drying, with imposed temperature gradient on the network, were investigated by Huinink et al.[15] and Plourde and Prat.[16] In these studies, two different aspects of heat and mass transfer coupling are highlighted: the temperature dependency of either equilibrium vapor pressure or surface tension, respectively. Recently, Surasani et al.[17–19] developed a nonisothermal pore network model of drying with convective boundary conditions. Unlike previous models, it delivers temperatures as they evolve freely due to the coupling of heat and mass

Correspondence: T. Metzger, Thermal Process Engineering, Otto-von-Guericke-University Magdeburg Universitaetsplatz 2, 39106 Magdeburg, Germany; E-mail: thomas.metzger@ovgu.de

transfer. So far, the nonisothermal model has only been applied to two-dimensional (2D) networks. In this article, we present the first results for 3D pore structures.

NONISOTHERMAL PORE NETWORK MODEL

The presented simulations are on regular pore networks, namely, 3D cubic lattices (with coordination number 6), as in the literature; however, the model can be easily extended to irregular networks in which every pore may have a different coordination number.

Data Structure Model

Figure 1 presents a 3D cubic lattice of void space in which pores are nodes without volume and throats containing all void volume are connectors between these pores. For visualization purpose, the network is sketched as nontransparent. Throats are cylindrical in shape with randomly varying radius according to a given distribution law.

For drying, the network is subjected at its open edge to lateral air flow with velocity u, bulk vapor pressure $P_{v,\infty}$, and bulk temperature T_∞. To realistically describe drying kinetics, especially the first drying period with its constant drying rate, it is necessary to model the boundary layer as discretized, extending network nodes into the gas (see Fig. 1). The number of additional vertical nodes N_{BL} is obtained by from boundary layer thickness ε as

$$\varepsilon = \frac{\delta}{\beta} = N_{BL} L \tag{1}$$

where L is the distance between nodes (throat length), δ is a binary diffusion coefficient, and β is the mass transfer coefficient, as obtained from empirical correlations of Sherwood number $Sh = \beta L_{network}/\delta$ and Reynolds $Re = uL_{network}/\nu_g$ and Schmidt number $Sc = \delta/\nu_g$ (with kinematic viscosity ν_g). However, Eq. (1) is derived for a plate at uniform partial pressure, which is not necessarily fulfilled for drying porous media.[20] Heat transfer between bulk air and network surface is described by a heat transfer coefficient α, which can be obtained from the analogy of heat and mass transfer as

$$\alpha = \beta \frac{\lambda_g}{\delta} \left(\frac{Pr}{Sc}\right)^{\frac{1}{3}} \tag{2}$$

where λ_g is gas thermal conductivity and $Pr = \kappa/\delta$ and Prandtl number (with thermal diffusivity κ).

Immiscible displacements upon evaporation of liquid will cause evolving IP patterns in the network, which represent the continuous vapor phase and disconnected liquid patches (clusters) in the solid network. Pore and throat conditions in a pore network are defined similarly as in Surasani et al.[17] and these will determine the transport within and between the phases (see Fig. 2a). At the phase boundary (Fig. 2b), where the menisci exist, liquid flow, phase change, and vapor diffusion are simultaneous. In partially filled throats, the phase boundary is either a moving meniscus or a stationary meniscus as evaporated liquid diffuses through air and, at the same time, liquid flows from or to the meniscus depending upon boundary liquid pressures. In gas throats (see Fig. 2c), diffusion takes place due to vapor pressure gradients. In liquid throats, capillary flow takes place due to capillary pressure gradients in the cluster (Fig. 3). Pore saturations are given by average throat saturations of connected throats.

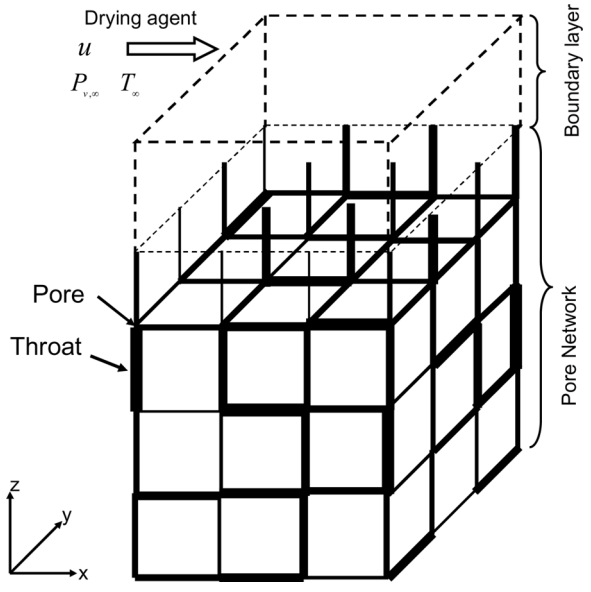

FIG. 1. Conceptualization of cubic pore network with boundary layer.

Vapor Transport

The vapor flow rate $\dot{M}_{v,ij}$ between two gas pores is given by Stefan's law. From the law of conservation and the assumption of quasi-stationary vapor transport, total mass flow rate to any gas pore i (Fig. 2c) is equal to zero:

$$\sum_{j=1}^{6} \dot{M}_{v,ij} = -\sum_{j=1}^{6} A_{ij} \frac{\delta}{L} \frac{P\widetilde{M}_v}{\widetilde{R}T} \ln\left(\frac{P - P_{v,i}}{P - P_{v,j}}\right) = 0 \tag{3}$$

Here, P is total pressure, $\widetilde{M}_v$ is molar mass of vapor, $\widetilde{R}$ ideal gas constant, T is absolute temperature, and $P_{v,i}$ is vapor pressure in pore i. The cross-sectional area A_{ij} for vapor diffusion varies from the network (πr_{ij}^2) to the boundary layer (L^2). Equilibrium vapor pressure exists in partially filled pores, giving boundary conditions to Eq. (3); the missing boundary condition comes from partial vapor pressure of convective air $P_{v,\infty}$. The system of equations for vapor transport (Eq. (3)) on gas pores can

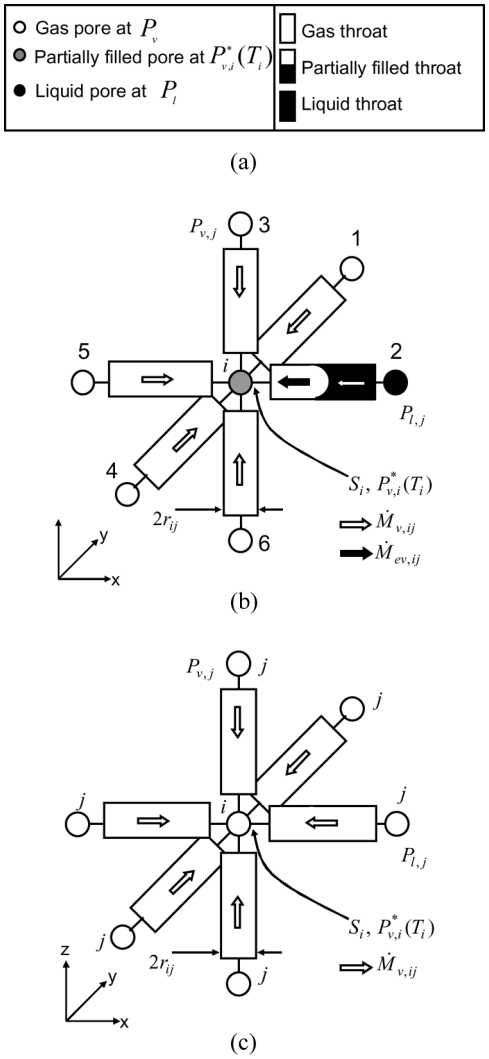

FIG. 2. Pore and throat conditions (a) and mass balances around partially saturated pores (b) and gas pores (c).

be put in linear form and solved for partial vapor pressures ($P_{v,i}$) using the conjugate gradient method (CGM).

The partially filled pores should be treated differently and the vapor flow rates through these will play an important role in calculating the cluster evaporation rates. Figure 2b represents partially filled pore i with neighbor pores 1, 3, 4, 5, and 6 at unknown vapor pressures ($P_{v,i}$) and the remaining pore 2 at liquid pressure ($P_{l,i}$). The unknown vapor pressures have to be found by solving Eq. (3). Then, the phase change rate at the partially filled throat 2 can be computed as the sum of the vapor flow rates in the gas throats as

$$\dot{M}_{ev,i2} = \sum_{j\neq 2} \dot{M}_{v,ij} \tag{4}$$

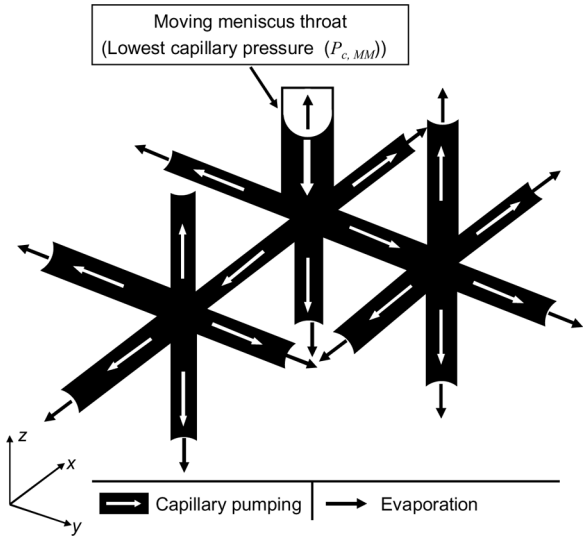

FIG. 3. Capillary pumping in a liquid cluster.

In general, for partially saturated pores, the vapor balance can be written as

$$\sum_{j=1}^{6-lm} \dot{M}_{v,ij} = \sum_{j=1}^{lm} \dot{M}_{ev,ij} \tag{5}$$

with evaporation or condensation rates $\dot{M}_{ev,ij}$ in the pore neighboring meniscus throats (lm).

Cluster Labeling

Cluster by definition is a region of single phase (either gas or liquid) in porous media. Here, we deal only with liquid-phase clusters; for the assumed network geometry, a cluster is a group of liquid throats connected by liquid pores. For better understanding, see the visualization of a cluster in Fig. 3. Every cluster contains meniscus throats (saturated or partially saturated) and may or may not contain saturated throats without a meniscus. In the absence of viscous effects, all meniscus throats in a cluster must be maintained at capillary equilibrium. So it is necessary to know the structure of a cluster to solve the discrete invasion process due to phase change and to monitor the cluster transformation and disintegration process due to gas invasion. The process of obtaining the structural data of every cluster combined with the method of effective storing of these data for computation of liquid transport is called *cluster labeling*. For this purpose, the Hoshen-Kopelman algorithm was used for previous models[21] in the literature and the present work uses a cluster labeling technique developed by Surasani.[19]

Liquid Transport

The assumption of negligible viscous forces implies that, in each cluster, liquid can be pumped from the throat with the highest liquid pressure to all other meniscus throats,

resulting in one throat with a moving meniscus (MM) and stationary menisci (SM) in all remaining throats. In each cluster, the MM throat will empty first because this throat alone contributes to the total evaporation of the cluster through capillary pumping. The criterion for selecting MM throats is given by capillary pressures $P_{c,ij}$; i.e., in each cluster, the throat with highest liquid pressure

$$P_{l,ij} = P - P_{c,ij} \tag{6}$$

is selected as MM throat. Capillary pressures can be computed from temperature-dependent surface tension γ and throat radius r_{ij}

$$P_{c,ij} = \frac{2\gamma(T_{ij})}{r_{ij}} \tag{7}$$

Using Eq. (7), the MM throat is chosen as the throat with the lowest capillary pressure. Figure 3 shows an example of a cluster in which the MM throat is a partially filled throat, and the remaining full throats are SM throats.

Since all mass loss due to evaporation is attributed to MM throats, the time steps to empty these throats can be obtained in each cluster (nc) from the saturation of the MM throat S_{MM}, liquid density ρ_l, total throat volume $V_{MM,nc}$, and cluster evaporation rate (sum over all evaporating menisci) as

$$\Delta t_{m,nc} = \frac{S_{MM}\rho_l V_{MM,nc}}{\sum_{j=1}^{mt} \dot{M}_{ev,ij,nc}}. \tag{8}$$

Condensation

If the system is considered to be nonisothermal, spatial temperature gradients build up over the network during the drying process. Because equilibrium vapor pressure is highly sensitive to the temperature, equilibrium vapor pressure gradients will develop. At the same time, random capillary pumping causes splitting of the continuous liquid phase into disconnected wet patches (liquid clusters), which are at different temperatures. Due to this, vapor evaporating from hot clusters or single throats may move against the main direction of mass flow and condense on cold clusters or single throats (vapor back diffusion may take place along with the escape of vapor from the top surface).

The effect of condensation will be fully included in heat transfer (see Eq. (10)), but it is only partially accounted for in mass transfer. For each cluster or single liquid throat, the net phase change rate is computed as the sum of all meniscus evaporation/condensation rates. If there is net evaporation in a cluster, the previously described liquid transport algorithm can be used. For clusters with net condensation, we can either refill a partially emptied throat (MM throat) with mass transfer time step

$$\Delta t_{m,nc} = -\frac{(1 - S_{MM})\rho_l V_{MM,nc}}{\sum_{j=1}^{mt} \dot{M}_{ev,ij,nc}} \tag{9}$$

or neglect the condensing vapor. In fact, new algorithmic rules (for liquid imbibition) will have to be set up to fully account for condensation.

Transient Heat Transfer

Figure 4 shows how each control volume represents one pore and contains six half throats; i.e., each throat participates in two control volumes. Liquid in partially filled throats is equally distributed to the neighboring control volumes (CVs). The dynamic energy balance equation over the control volume is given by

$$V_i(\rho c_p)_i \frac{dT_i}{dt} = -\sum_{j=1}^{6} Q_{ij} - \Delta h_{v,i}(T_i) \sum_{j=1}^{lm} \dot{M}_{ev,ij} \tag{10}$$

where $\Delta h_{v,i}(T_i)$ is phase change enthalpy (as absolute value). The mass flow rate $\dot{M}_{ev,ij}$ is positive for evaporation and negative for condensation. The meniscus position is used to allocate the heat sink/source to either control volume. The heat exchange rates $\dot{Q}_{ij}$ between CVs i and j are given by Fourier's law of heat conduction as

$$\dot{Q}_{ij} = A_{cv,ij}\lambda_{ij}\frac{T_i - T_j}{L} \tag{11}$$

The exchange area for heat conduction is $A_{cv,ij} = L^2$ because both void space and solid can contribute. The effective thermal conductivities λ_{ij} and control volume heat

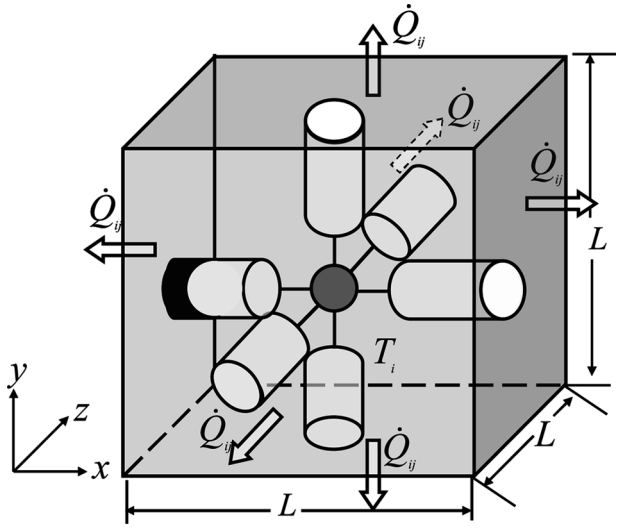

FIG. 4. Energy balance around control volume CV i.

capacities $V_i(\rho c_p)_i$ are functions of throat saturation.[17] Heat transfer by liquid convection is not accounted for. Two kinds of heat transfer boundary conditions are applied; first, heat transfer through the boundary layer as

$$\dot{Q}_{ij} = A_{cv,ij}\ \alpha(T_i - T_\infty), \tag{12}$$

and second, heat transfer through insulated sides of the pore network is zero ($\dot{Q}_{ij} = 0$). The system of Eqs. (10) is solved using semi-implicit scheme.[19]

Coupling of Heat and Mass Transfer

Heat and mass transfer coupling plays an important role in the drying process, particularly at the phase boundaries (menisci) in the network. At an evaporating meniscus, the vapor takes up the enthalpy of evaporation and liquid temperature is reduced (heat sink); likewise, there are heat sources at places of condensation. This coupling of mass transfer with heat transfer is already implemented by including the phase change rates ($\dot{M}_{ev}$) in the energy balance equation (Eq. (10)).

Further coupling is introduced by the temperature dependency of local equilibrium vapor pressure $P^*_{v,i}(T_i)$ and local surface tension $\gamma(T_{ij})$. In a nonuniform temperature field, equilibrium vapor pressure varies spatially. This has two major effects on vapor diffusion: first, it causes higher drying rates at hot spots and, second, it causes back diffusion in the network with condensation at colder spots. Equilibrium vapor pressures have to be updated after each time step by use of an Antoine equation. At the same time, surface tension γ varies inversely with temperature. A surface tension gradient may have an effect on IP patterns depending on magnitude and orientation of the temperature gradient.[15]

SIMULATION RESULTS

The simulation results presented in this work are obtained from a cubic network of size $13 \times 13 \times 13$. The radii of the throats are distributed randomly according to a normal number density function and the length of throats is chosen as 350 μm. Two kinds of throat radius distributions are applied to the pores in the simulated networks; the first one is a 40 ± 2 μm distribution for what we call *microthroats*, and the second is a 100 ± 5 μm distribution for what we call *macrothroats*. The heat transfer parameters are chosen as $(\rho c_p)_s = 1.7 \times 10^6\ \mathrm{J/(m^3\ K)}$ and $\lambda_s = 1\ \mathrm{W/(m\ K)}$ which corresponds to the glass.

Results for Monomodal Pore Network

A monomodal pore network is formed from only microthroats. The completely saturated network is subjected to convective air at temperature $T_\infty = 80°\mathrm{C}$ and with zero humidity. The simulation results obtained are presented in the following.

Figure 5 shows the drying kinetics for the monomodal pore network as evaporation rate $\dot{M}_v$ versus overall network saturation S. Both the isothermal (for 20°C) and the nonisothermal curve start at the same rate. The initial warming-up to constant drying conditions can be clearly seen in the nonisothermal process, and in the case of isothermal, it is called the *initial rate period*.[12] The constant rate period extends for both curves to a saturation of approximately 0.7. Then, the falling rate period (FRP) commences with a drastic initial fall in drying rates. In the isothermal case, drying rate slowly decreases as in a receding front model. Le Bray and Prat[12] denoted this as a receding front period (RFP). In the nonisothermal case, drying rate will not only decrease globally but increase in discrete events. This corresponds to receding and subsequent warming up of the evaporation front. The observed oscillations are large because the simulated network is of small size.

The evolutions of temperatures at the top ($T_{\max}$) and bottom ($T_{\min}$) of the network as well as network saturation are plotted in Fig. 6. Figure 7 shows the freely evolved IP patterns and surface temperature fields at different overall saturations. For visualization only the gas phase is shown in IP patterns. At the start of the process, drying rates increase significantly for a short period; during this warming up, some portion of the surface throats are invaded before the invasion process reaches deep into the network (Fig. 7 at $S = 0.95$). The wet (black) and dry (white) portions of the opened surface and its temperature field are shown in Fig. 7 at $S = 0.95$. One can relate the hot spots to dry spots where the depth of invasion (see Fig. 7 at $S = 0.95$) influences the heating of the surface; similarly, cold spots relate to wet surface regions. The increase in

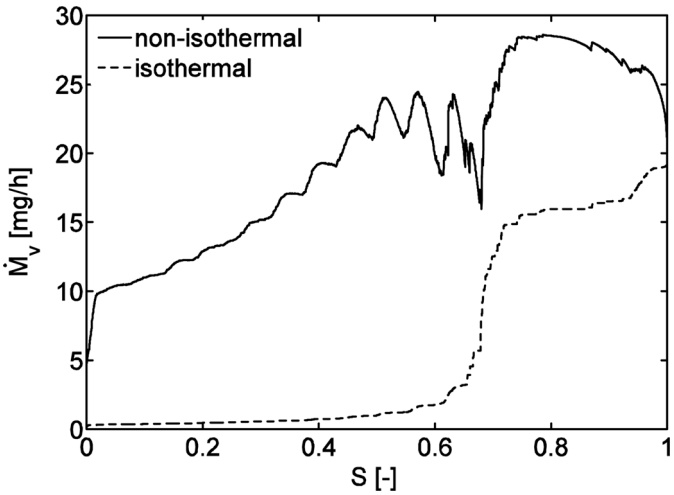

FIG. 5. Drying rate curves for monomodal network.

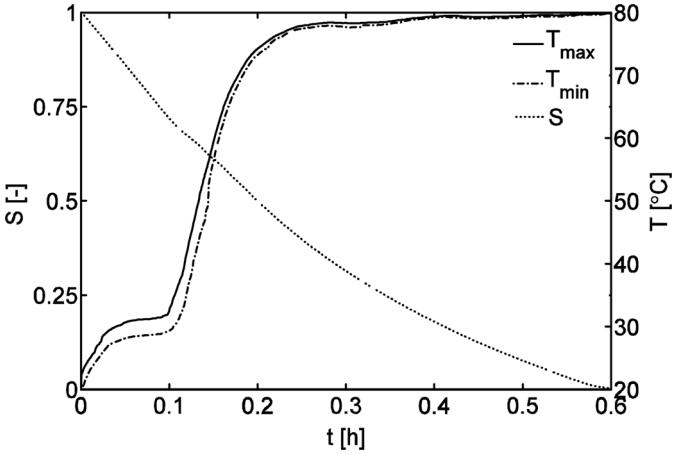

FIG. 6. Evolution of temperature and saturation for monomodal network.

drying rates in comparison with the isothermal model is due to temperature dependency of equilibrium vapor pressure. Later, gas invasion progresses, and liquid is pumped from the bottom of the network, keeping the surface of the network sufficiently wet. The point at which air invades the bottom of the network (Fig. 7 at $S = 0.885$) is called *breakthrough* (BT). After BT, the sample spanning liquid cluster splits into many disconnected clusters and loses its connection to the surface (main cluster disintegration MCD at $S = 0.7$). Until this point, drying rates and temperatures are almost constant (Fig. 6 and corresponding temperature field in Fig. 7 at $S = 0.885$). From network saturation 0.7 to 0.64, drying rates fall drastically because all remaining surface throats are emptied. As a consequence, temperatures start increasing drastically as can be seen in Figs. 6 and 7 from $S = 0.7$ to $S = 0.64$. When all surface throats are empty, the drying front recedes toward the bottom of the network. In Fig. 7, a situation for well advanced drying and almost complete heating up is shown at $S = 0.4$.

The important variable that determines the invasion process is liquid pressure (Eq. (6)) at the menisci of interfacial throats in the cluster. In the absence of gravity, the liquid pressures completely depend on the capillary pressures (Eq. (7)) and determine the order of emptying of throats. In the isothermal model, it depends on throat radius alone. In the nonisothermal model, the order of emptying may also be influenced by nonuniform surface tension at the menisci (Eq. (7)). And if the relative variation of competing meniscus radii is lower than that of surface tension, we expect preferential invasion of throats at higher local temperatures. However, in convective heating mode, the evolved temperature gradient is low, and surface tension will not play an important role for the given network disorder (i.e., standard deviation of radii).

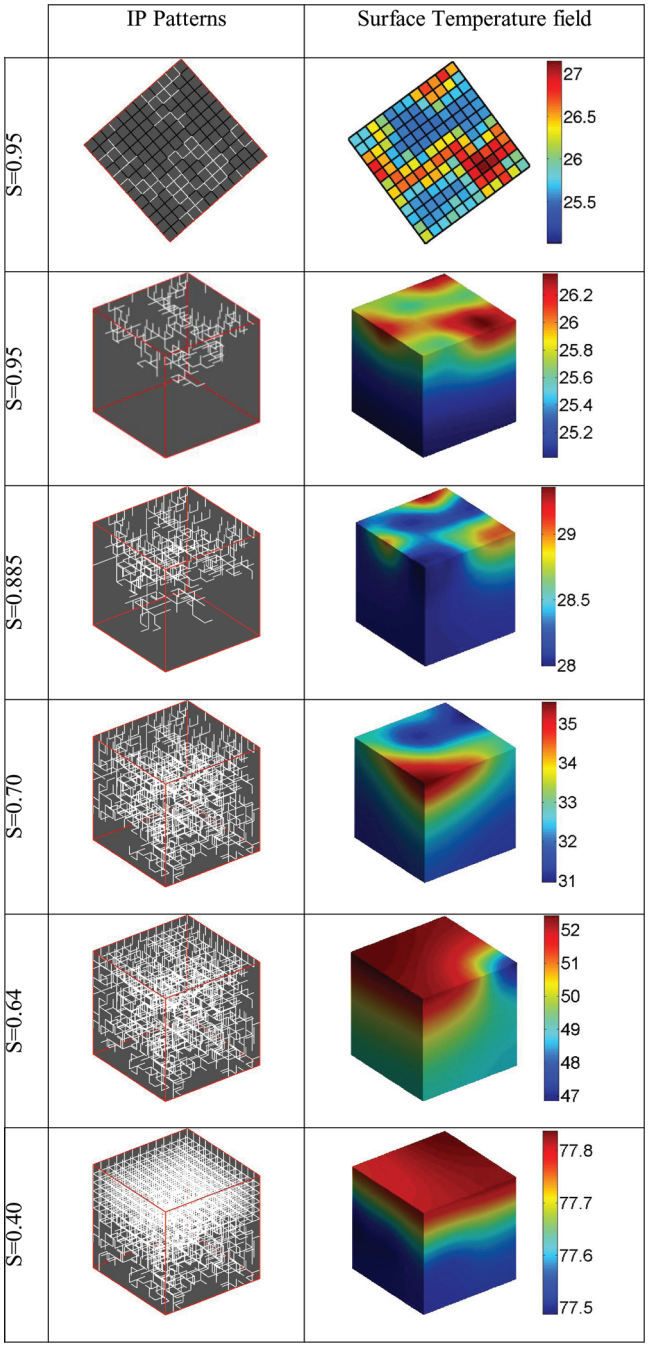

FIG. 7. Evolved IP patterns and temperature fields for monomodal pore network.

Results for Bimodal Pore Network

The bimodal pore network is obtained from the monomodal network by replacing every fourth throat in x-, y-, and z-directions by a macrothroat. Initially, the network is fully saturated and the macrothroats account for 50% of pore water. Simulated drying rate curves are compared with monomodal simulations in Fig. 8. The evolution of temperatures on the top and bottom of the network and

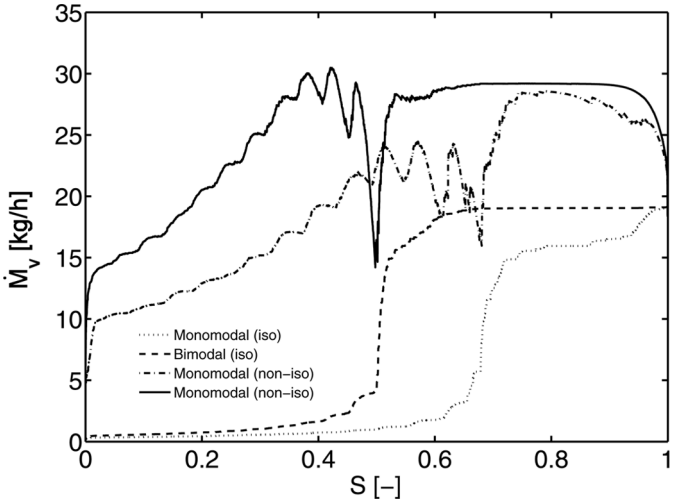

FIG. 8. Comparison between drying rate curves for mono- and bimodal pore network.

its overall saturation are shown in Fig. 9. Figure 10 presents both IP patterns and the freely evolved temperature fields at different saturations of the network.

The constant rate period is observed for both mono- and bimodal pore networks in isothermal as well as nonisothermal cases. A more pronounced CRP down to saturations lower than 0.6 is observed for the bimodal pore network; i.e., until almost all of the macrothroats (50% of void volume) are emptied. Influence of temperature on capillary pressure via surface tension is negligible and the macrothroats will empty first in the bimodal pore network (nonisothermal) because here capillary pressure is always lowest. Liquid is pumped through the microthroats to the network surface so that the surface can stay almost completely wet down to relatively low overall saturations. During this period, the network surface reaches near

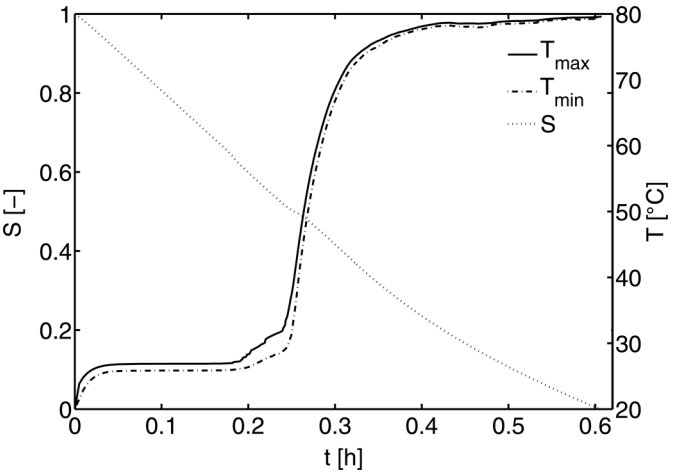

FIG. 9. Evolution of network temperature and saturation for bimodal pore network.

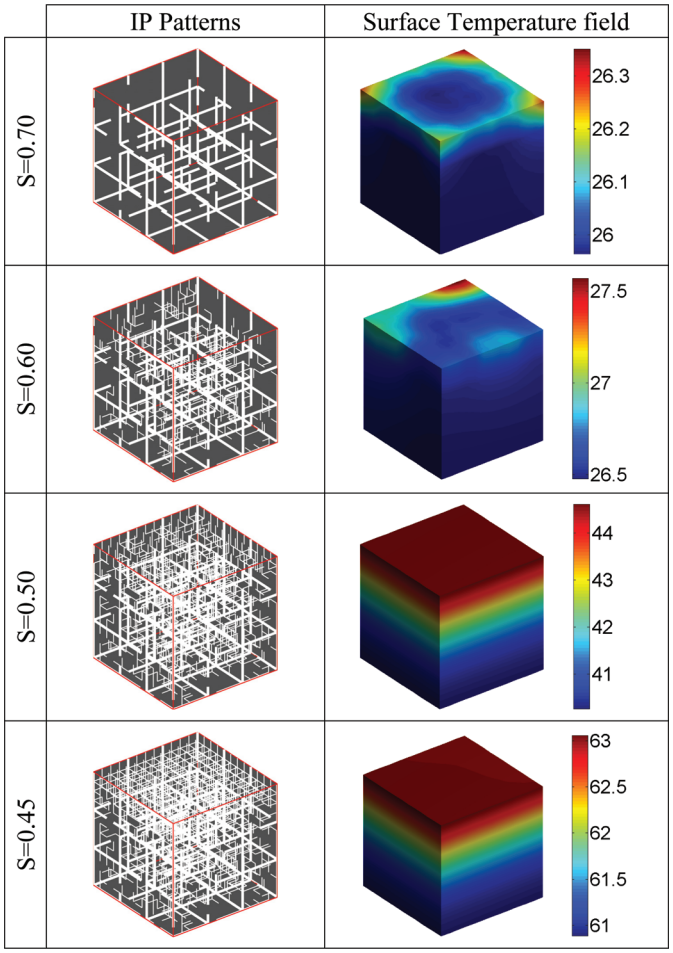

FIG. 10. Evolving IP patterns and temperature fields for bimodal pore network.

wet-bulb temperature (25°C) as one can see in Fig. 9, which exhibits a uniform temperature (T_{max}), and in Fig. 10 as an almost uniform temperature field at $S = 0.70$, where only the corners of the top surface exhibit hot spots, because those dry macrothroats are not completely surrounded by wet regions with a cooling effect. In the case of the monomodal pore network, the CRP is much shorter and the constant temperature of the surface of pore network attained is much higher (30°C) because of the lower fraction of wet surface throats in comparison with the bimodal case. For the bimodel network, the initial lone spanning cluster is ensured by the microthroats and persists until all macrothroats are invaded.

Further, microthroats will start to be invaded by air as shown in Fig. 10 at $S = 0.60$. The drying rate in the nonisothermal bimodal case starts to decrease (as the surface throats empty) and falls drastically until $S = 0.5$. At this beginning of the FRP, the temperature of the network increases as a result of an increased dry fraction of the surface where heat transfer is predominant; this behavior

can be seen by a huge rise in temperatures in Fig. 9 and the transition in temperature field from Fig. 10 from $S = 0.6$ to 0.5. The situations in Fig. 10 from $S = 0.6$ to 0.5 represent the start of the receding front period. During the start of the RFP, a rise in drying rates back to the original level is observed, which is the consequence of two opposing effects: an increase in vapor resistance and a high increase in the driving saturation vapor pressure at the front due to an increased temperature. The higher drying rate observed at the end of the RFP on nonisothermal bimodal pore network (in comparison to monomodal network) is because the macrothroats, with their larger cross sections, allow for higher vapor transfer rates.

CONCLUSIONS

Drying simulations on mono- and bimodal 3D cubic pore networks have been studied by a nonisothermal pore network model. This is the first work of applying a nonisothermal pore network model on 3D pore structures. The results presented in this work are obtained from relatively small networks of size $13 \times 13 \times 13$ due to computation limitations of the present algorithm. Simulations are obtained for conditions under which viscous and gravity effects are negligible. Heat transfer is due to conduction and local thermal equilibrium is applied in every control volume.

Previous isothermal works[11–13] are limited to slow drying rates; dry and wet patch formation and the occurrence of constant rate period (CRP) have been obtained by simulations on 3D pore networks. In this work, all fundamental aspects of drying such as warming up, constant rate, falling rate, and receding front periods are obtained by a nonisothermal model on 3D pore networks. These features are the outcome of IP patterns formed in 3D pore structures.

Both mono- and bimodal pore networks exhibit CRP; due to preferential emptying of macrothroats, the bimodal network exhibits a more pronounced CRP and the network surface reaches near wet-bulb temperature. In the monomodal case, the intermediate temperature attained is higher than wet-bulb temperature. Concerning the heat and mass transfer coupling, temperature-dependent equilibrium vapor pressure had a great effect on drying rates; surface tension had almost no effect on IP patterns because the evolved temperature gradient is not large enough to change invasion order.

NOMENCLATURE

A	Area of cross section (m^2)
c_p	Specific heat capacity (J/kg/K)
Δh	Specific phase change enthalpy (J/kg)
L	Length of throat (m)
$\widetilde{M}$	Molar mass (kg/kmol)
$\dot{M}$	Mass flow rate (kg/s)
P	Pressure (Pa)
$\dot{Q}$	Heat flow rate (W)
$\widetilde{R}$	Ideal gas constant (J/kmol/K)
r	Throat radius (m)
S	Saturation
T	Temperature (K)
t	Time (s)
V	Volume (m^3)

Greek Symbols

α	Heat transfer coefficient ($W/m^{2/}K$)
β	Mass transfer coefficient (m/s)
γ	Surface tension (N/m)
δ	Diffusivity coefficient (m^2/s)
λ	Thermal conductivity (W/m/K)
ρ	Density (m^3)

Subscripts

c	Capillary
ev	Evaporation
g	Gas
i	Pore or node
ij	Throat
lm	Number of menisci
s	Solid
v	Vapor

ACKNOWLEDGMENTS

This work was financed by the German Research Foundation (DFG) in the frame of Graduate School 828 ''Micro-Macro-Interactions in Structured Media and Particle Systems'' and has received additional support from Max-Buchner-Forschungsstiftung.

REFERENCES

1. Sanchez-Palencia, E. *Non-Homogeneous Media and Vibration Theory*; Lecture Notes in Physics 127; Springer-Verlag: New York, 1980.
2. Quintard, M.; Whitaker, S. Transport in ordered and disordered porous media: Volume-averaged equations, closure problems and comparison with experiments. Chemical Engineering Science **1993**, *41* (14), 2537–2564.
3. Laurindo, J.B.; Prat, M. Modeling of drying in capillary-porous media: A discrete approach. Drying Technology **1998**, *16* (9&10), 1769–1787.
4. Prat, M. Recent advances in pore-scale modeling for drying of porous media. Chemical Engineering Journal **2002**, *86*, 153–164.
5. Daian, J.F.; Saliba, J. Determining a representative random pore-network for moisture sorption and migration in cement mortar. International Journal of Heat and Mass Transfer **1991**, *34* (8), 2081–2096.
6. Nowicki, S.C.; Davis, H.T.; Scriven, L.E. Microscopic determination of transport parameters in drying porous media. Drying Technology **1992**, *10* (4), 925–946.
7. Prat, M. Percolation model of drying under isothermal conditions in porous media. International Journal of Multiphase Flow **1993**, *19* (4), 641–704.
8. Yiotis, A.G.; Stubos, A.K.; Boudouvis, A.G.; Yortsos, Y.C. Pore network model of drying of single-component liquids in porous media. Advances in Water Resources **2001**, *24*, 439–460.

9. Laurindo, J.B.; Prat, M. Numerical and experimental network study of evaporation in capillary porous media. Phase distributions. Chemical Engineering Science **1996**, *51*, 5171–5185.
10. Laurindo, J.B.; Prat, M. Numerical and experimental network study of evaporation in capillary porous media. Drying rates. Chemical Engineering Science **1998**, *53*, 2257–2269.
11. Metzger, T.; Irawan, A.; Tsotsas, E. Influence of pore structure on drying kinetics: A pore network study. AIChE Journal **2007**, *53* (12), 3029–3041.
12. Le Bray, Y.; Prat, M. Three-dimensional pore network simulation of drying in capillary porous media. International Journal of Heat and Mass Transfer *42*, 4207–4224.
13. Yiotis, A.G.; Tsimpanogiannis, I.N.; Stubos, A.K.; Yortsos, Y.C. Pore network study of the characteristic periods in the drying of porous materials. Journal of Colloid and Interface Science **2006**, *297*, 738–748.
14. Metzger, T.; Tsotsas, E. Viscous stabilization of drying front: Three-dimensional pore network simulations. Chemical Engineering Research Design **2008**, *86* (7), 739–744.
15. Huinink, H.; Pel, L.; Michels, M.A.J.; Prat, M. Drying processes in the presence of temperature gradients-pore-scale modelling. The European Physical Journal E **2002**, *9*, 487–498.
16. Plourde, F.; Prat, M. Pore network simulations of drying of capillary porous media. Influence of thermal gradients. International Journal of Heat and Mass Transfer **2003**, *46*, 1293–1307.
17. Surasani, V.K.; Metzger, T.; Tsotsas, E. Consideration of heat transfer in pore network modelling of convective drying. International Journal of Heat and Mass Transfer **2008**, *51*, 2506–2518.
18. Surasani, V.K.; Metzger, T.; Tsotsas, E. Influence of heating mode on drying behavior of capillary porous media: Pore scale modeling. Chemical Engineering Science **2008**, *63*, 5218–5228.
19. Surasani, V.K. A non-isothermal pore network drying model; Ph.D. thesis, Docupoint Verlag, Magdeburg, 2008.
20. Masmoudi, W.; Prat, M. Heat and mass transfer between a porous media and a parallel external flow, application to drying of porous materials. International Journal of Heat and Mass Transfer **1991**, *34* (8), 1975–1981.
21. Metzger, T.; Tsotsas, E.; Prat, M. Pore-network models: A powerful tool to study drying at the pore level and understand the influence of structure on drying kinetics. In *Modern Drying Technology: Vol. 1. Computational Tools at Different Scales*; Tsotsas, E., Mujumdar, A.S., Eds.; Wiley-VCH: Weinheim, 2007.

Drying Technology, 28: 991–1000, 2010

ISSN: 0737-3937 print/1532-2300 online
DOI: 10.1080/07373937.2010.497088

Taylor & Francis
Taylor & Francis Group

Empirical Macroscopic Model for Drying of Porous Media Based on Pore Networks and Scaling Theory

N. Vorhauer, T. Metzger, and E. Tsotsas
Thermal Process Engineering, Otto von Guericke University Magdeburg, Magdeburg, Germany

Capillary effects as they occur on the pore scale during drying of porous media lead to the development of fractal drying fronts that cannot be described by classical continuous approaches. Recently, pore network models from hydrology and the petrol industry have been applied to drying. The possibility of studying drying front patterns depending on pore network topology and spatial distribution of pore size to investigate their influence on drying rates is very advantageous. However, the discrete approach has drawbacks when drying of larger sample sizes is of interest, because solving the mass balances for individual gas and liquid pores is very time consuming. An empirical model to overcome this size limitation was first presented in Metzger et al.[1] In this, we applied the theory of scaling viscous stabilized drying fronts with capillary number and combined this theoretical physical approach with a dimensionless saturation profile obtained from 3D pore network simulations. In this article, we recall the model and complete the results for 2D networks. The resulting drying rate curves are compared to the results of both the pore network model and a receding front model with a sharp drying front.

Keywords Dimensionless saturation profiles; Invasion percolation; Scaling law; Stabilized drying front

INTRODUCTION

Drying experiments in porous media show that the drying front, which invades the porous medium, usually is not sharp but of fractal character.[2–4] This cannot be explained by means of classical continuous models, which either use a sharp drying front without spatial extension or produce smooth variations of average liquid saturation. Because transport phenomena in porous media are strongly dependent on the state of individual pores, liquid distribution is essentially influenced by pore structure and pore size distribution. Fractal drying front patterns as they develop during drying can be compared to liquid distributions observed in drainage.[2,4,5] Hence, efforts have been made to investigate the macroscopic drying behavior of porous media by means of invasion percolation models originally developed for applications in hydrology and petroleum engineering. An overview on pore network models in drying technology is given in Metzger et al.[6]

During the drying of porous media, capillary effects are competing with other mechanisms, which may result in a stabilization or destabilization of the drying front: liquid films, viscous forces, gravity, and thermal gradients. Though viscous effects always lead to stabilized drying fronts, that is, fronts of limited extension,[2,3,7,8] imposed gravity fields and thermal gradients either stabilize or destabilize the drying front and therefore can also lead to breakthrough of the gas phase by individual branches.[4,8,9] Furthermore, stabilization of the front is reached in the case of viscous flow through liquid films. When the liquid phase recedes into the network, liquid films can remain at the surface of either rough or smooth pores or in corners of polygonal pores.[3,10,11] If capillary numbers are sufficiently high, the film region is stabilized through viscous transport in the liquid films.[12]

In stabilized cases, dimensionless numbers such as Bond number for gravity and capillary number for viscosity are used to relate the additional effects to capillarity, and drying front width scales with these numbers. Scaling laws have been derived by Wilkinson[13,14] from percolation concepts for the displacement front in the presence of buoyancy and viscous forces; he correlates front width with Bond and capillary number. Shaw[2] performed drying experiments with a thin random packing of small silica spheres in which viscous effects are prominent, and he correlated front width to front velocity. Prat and Bouleux[8] obtained scaling exponents from 2D pore network simulations for gravitational stabilization.

In this work, we recall results from 2D and 3D isothermal pore network simulations with stabilized drying front width.[15] The application of scaling laws is discussed and the progression of saturation profiles across the drying front is analyzed. As will be shown by use of a transformation of the space coordinate, all these profiles are similar and hence can be approximated by respective dimensionless master curves for the 2D and 3D cases. Therefore, a macroscopic drying model can be established in the following way: For any front position z_f (i.e., the least advanced

Correspondence: Thomas Metzger, Thermal Process Engineering, Otto von Guericke University Magdeburg, Universitaetsplatz 2, 39106 Magdeburg, Germany; E-mail: thomas.metzger@ovgu.de

point of the front measured from the open side of the network), the width of the front can be determined by the scaling law from the capillary number that is associated with the current evaporation rate. Dimensional saturation profiles can be obtained by bringing the master curves to the actual front width, and overall drying rate curves can be computed from total network saturation. Drying rate curves of 2D and 3D models are compared to those of a receding front model (with sharp front) and to those of the original pore network simulation.

PORE NETWORK MODEL

Model Description

First, the pore network drying model that is used for the simulations is briefly recalled; a detailed description can be found in Metzger et al.[16] Both 2D and 3D networks contain cylindrical pores of uniform length and normally distributed radii that are connected through nodes without any volume. Furthermore, periodical boundary conditions are chosen. At the beginning, all pores are saturated with liquid; then, evaporation of liquid leads to an emptying of surface pores. The pore with the largest radius empties first because it produces the smallest capillary pressure and supplies surrounding pores with liquid. In principle, liquid pressure P_w of a meniscus pore of index ij can be as low as

$$P_{w,ij} = P - \frac{2\sigma}{r_{ij}} \tag{1}$$

(with gas pressure P, surface tension σ, and pore radius r_{ij} for the case of zero contact angle). Because viscous forces interfere with liquid pumping, viscous drying processes require the solution of the liquid pressure field. In a liquid-filled pore, viscous flow is described by

$$\dot{M}_{w,ij} = \frac{\pi r_{ij}^4}{\nu_w 8L}(P_{w,i} - P_{w,j}) \tag{2}$$

where ν_w denotes kinematic viscosity of water, L is pore length, and $P_{w,i}$ is liquid pressure at node i. The vapor diffusion rate through a gas pore between network nodes i and j is given by

$$\dot{M}_{v,ij} = \pi r_{ij}^2 \frac{\delta}{L}\frac{\widetilde{M}_v P}{\widetilde{R}T} \cdot \ln\left(\frac{P - P_{v,i}}{P - P_{v,j}}\right) \tag{3}$$

where δ is vapor diffusivity, $\widetilde{M}_v$ is molar mass of vapor, $\widetilde{R}$ is ideal gas constant, T is absolute temperature, and $P_{v,i}$ is vapor pressure at node i. Convective drying conditions are described by a discretized diffusive boundary layer allowing for lateral diffusion and with bulk air vapor pressure $P_{v,\infty}$. By this, a first drying period can be simulated.[17] At the gas–liquid phase boundary, equilibrium vapor pressure P_v^* is assumed.

For a given network saturation, a quasi-stationary vapor diffusion problem is solved to obtain the evaporation rates at all menisci. From liquid balances, another quasi-stationary problem is set up, which is coupled to the vapor problem at the menisci. For liquid menisci, two different boundary conditions must be distinguished. A meniscus is stationary if liquid can be supplied to match the local evaporation rate ($\dot{M}_{w,i,j} = \dot{M}_{v,i}$); this is only fulfilled if the pressure in Eq. (1) can be low enough. If this condition is not met or if the meniscus pore is partially filled, a meniscus is moving. In the latter case, curvature of the meniscus is assumed to be fully developed in order to calculate liquid pressure at the meniscus from Eq. (1). The procedure to find meniscus states and correct boundary conditions (either a flow or a pressure condition) is iterative. Then, liquid flow rates at the menisci are computed (by solving the liquid mass balances for all liquid nodes) and meniscus velocities are obtained by subtracting evaporation rates. Time-stepping is imposed by complete emptying (or refilling) of a meniscus pore. Then, new quasi-stationary vapor and liquid flow problems must be solved.

If temperature and gas pressure are constant and gravity is neglected, then capillary flow is always from large to small pores. Due to distributed pore radii, the pores are emptied in random order so that the liquid phase splits up and forms individual clusters. As a consequence of viscosity, the distance over which capillary flow may take place at a given rate is limited, and hence the width of the drying front is finite. The two competing forces can be related by the capillary number, which gives the ratio of viscous to capillary forces:[6]

$$Ca = \frac{4\nu_w L^3 \dot{m}_v}{\sigma\pi r_0^2 \sigma_0} \tag{4}$$

(with average surface evaporation flux $\dot{m}_v$, mean pore radius r_0, and standard deviation of radius σ_0). Equation (4) follows from the ratio of pressure drop for Poiseuille flow (at average velocity v through a cylinder of radius r_0) to a typical difference in capillary pressure, $\Delta P_c = 2\sigma((r_0 - \sigma_0/2)^{-1} - (r_0 + \sigma_0/2)^{-1})$:[6]

$$Ca = \frac{4\eta v L}{\sigma\sigma_0} \tag{5}$$

and the mass balance around a stationary surface meniscus relating liquid velocity to evaporation flux

$$v = \frac{L^2}{\pi r_0^2}\frac{\dot{m}_v}{\rho_w}. \tag{6}$$

2D Simulation

Simulation results have been obtained for convective drying (at 1 bar and 20°C, with mass transfer coefficient 5.14 m/s) for a 300×120 pore network with lateral periodicity. Pores have length $L = 500$ nm with normally distributed radii with mean $r_0 = 50$ nm and standard deviation $\sigma_0 = 1$ nm. Simulations have been stopped at breakthrough; that is, when the most advanced point of the front reaches the bottom of the network.

A sequence of phase distributions at different network saturations S is shown in Fig. 1. Pores that emptied during subsequent periods of drying are shown in grey in Figs. 1b–1e. Corresponding saturation profiles are presented in Fig. 2; these are computed as slice averages of liquid pore saturation. Figure 3 shows how drying front width L_f (defined as the perpendicular distance in the z-direction of the most advanced and least advanced points of the front to network surface) changes with the capillary number. The standard deviation σ_f of perpendicular distances of all menisci (i.e., pores building the fractal drying front) to the network surface[18] is also shown (obviously $\sigma_f < L_f$). Both quantities, L_f and σ_f, are plotted

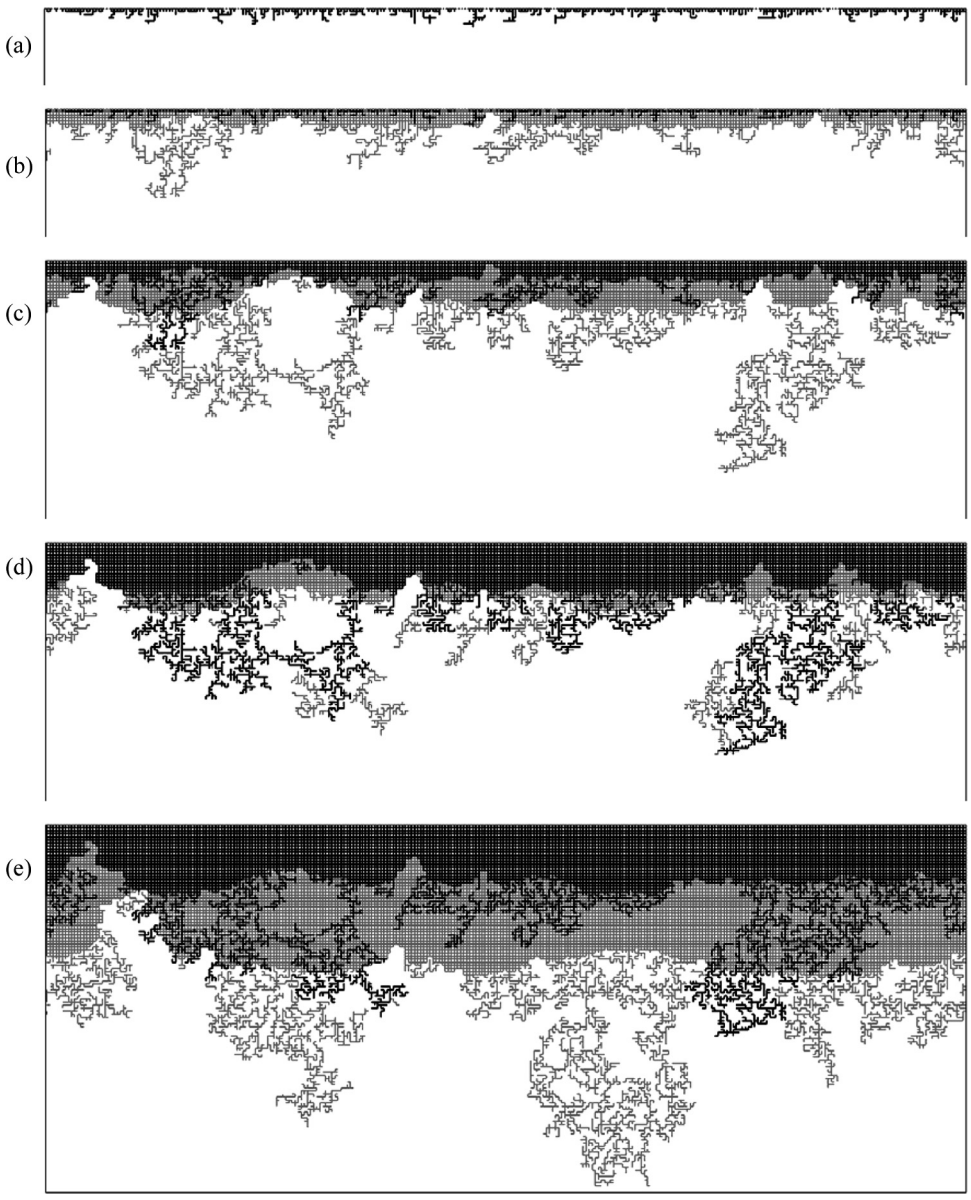

FIG. 1. Liquid distributions (in white) during drying (from the top) of a 300×120 pore network at overall saturations (a) 0.99, (b) 0.99–0.94, (c) 0.94–0.84, (d) 0.84–0.79, and (e) 0.79–0.5514 when breakthrough occurs. From (b) to (e), pores that are emptied during the given saturation interval are shown in grey. The gas phase is shown as black pores.

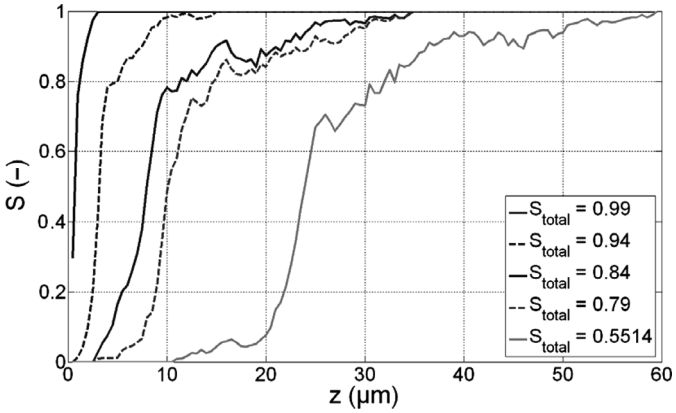

FIG. 2. Saturation profiles at decreasing overall network saturations as shown for phase distributions of the 2D network in Fig. 1.

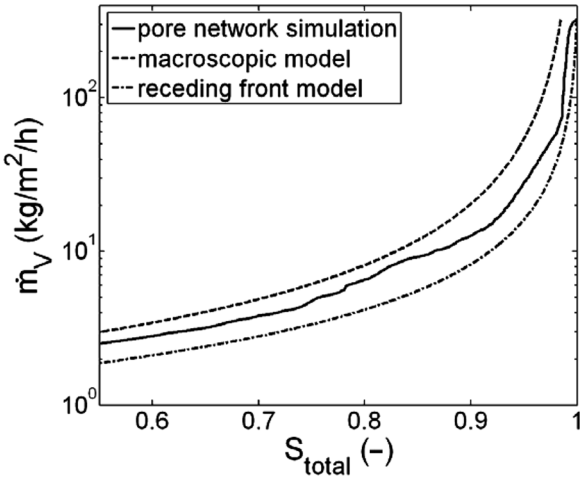

FIG. 4. Drying curves for 2D pore network simulation (run 2), macroscopic and receding front model.

in dimensionless, double-logarithmic form, once computed for the whole liquid phase and once computed for the main liquid cluster only.

At the beginning, when the front has not yet detached from the surface, high capillary numbers indicate the strong viscous forces resulting from high drying rates (quantified by evaporation mass flux $\dot{m}_v$). Because viscous forces are dominating, capillary pumping, that is, liquid supply due to distributed pore radii, can only act over short distances so that the drying front is very narrow. When the front moves away from the network surface, vapor transfer resistance is increased and drying rate drops drastically (for the drying rate curve see Fig. 4). Consequently, capillary forces can sustain viscous liquid flow over larger distances so that capillary pumping becomes the dominating effect; hence, the drying front can widen up as gas penetrates into the network. Additionally, intervals with constant front width L_f can occur (Fig. 3). In these, an erosion of the front (Fig. 1) by emptying of near surface pores and disconnected liquid clusters leads to a decrease in capillary number.

The three main effects, penetration, expansion, and erosion of the front, are random processes causing a fractal geometry of the front; L_f does not increase smoothly with decreasing Ca but in random fluctuations (Fig. 3). Under isothermal conditions, all gas pores within the drying front are at saturation vapor pressure. Consequently, evaporation only occurs at the near surface edge of the front, whereas all other menisci do not contribute to evaporation due to a screening effect.

Randomness of the invasion process leads to noticeable variations of the L_f (Ca) curve for several runs as shown in Fig. 5, where the results of five drying simulations for pore networks of same size but with different spatial pore radius

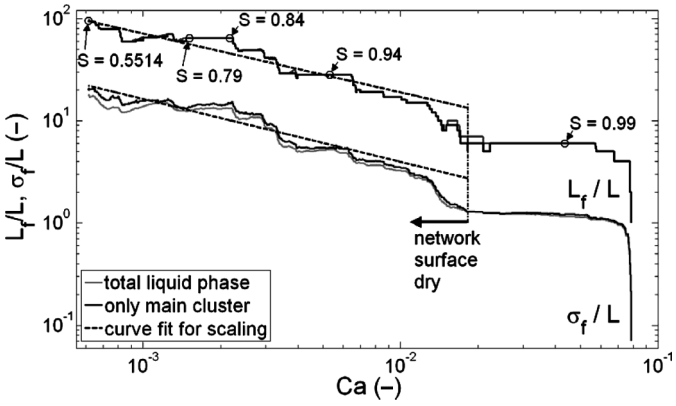

FIG. 3. Drying front width of 2D network simulation versus capillary number as defined in Eq. (4). Phase distributions for subsequent saturation intervals are shown in Fig. 1; corresponding saturation profiles are plotted in Fig. 2.

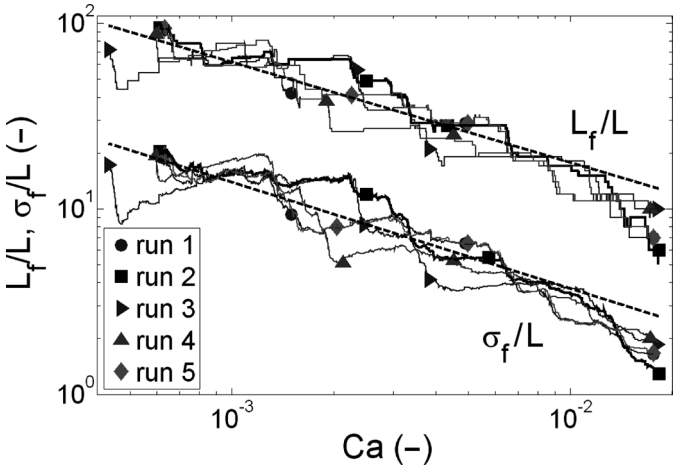

FIG. 5. Scaling of 2D drying front width for the 300×120 networks (run 1 as in Metzger et al.[1]).

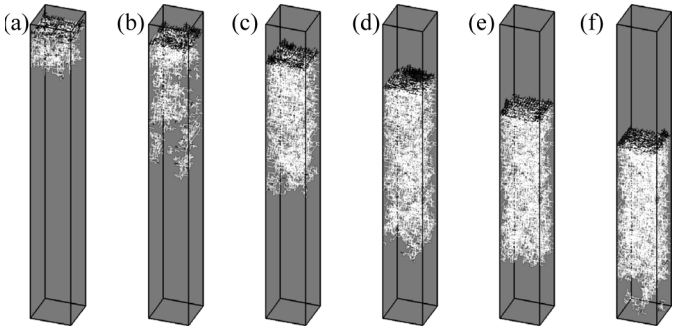

FIG. 6. Phase distributions during drying of a $15 \times 15 \times 121$ pore network at overall saturations (a) 0.95, (b) 0.9, (c) 0.8, (d) 0.7, (e) 0.6, and at breakthrough with $S = 0.4878$ (f). The top of the network is dry, the bottom saturated with liquid, and only the drying front is shown (full pores are plotted in black for slice saturations lower than 0.6; empty pores are plotted in white for higher slice saturations; all partially filled pores are drawn in black).

distributions are plotted (the above discussed realization is denoted as run 2).

For a more detailed future evaluation of the problem, it may be reasonable to choose relatively small networks (due to high computational cost of the algorithm) and perform many simulation runs to obtain more accurate statistical knowledge on drying behavior.

3D Simulation

Drying simulations have also been performed for a $15 \times 15 \times 121$ pore network with all other settings equal to the 2D runs. The resulting phase distributions for one simulation are shown in Fig. 6; for better visibility, only relevant pores in the drying front are plotted. A similar widening of the front is observed; the L_f (Ca) curve for the example in Fig. 6 is plotted in Fig. 7 (as run 2) along with the results from two more network realizations.

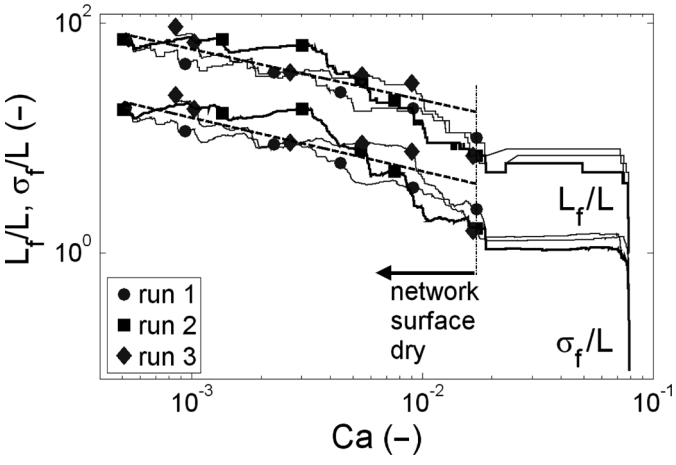

FIG. 7. Scaling of 3D drying front width for the $15 \times 15 \times 121$ networks (run 1 as in Metzger et al.[1]).

ANALYSIS OF STABILIZED DRYING FRONT

Scaling of Drying Front Width in 2D and 3D

As discussed in the literature,[4] analogies of fractal liquid patterns in drainage and drying allow the application of percolation theory to describe the drying front width by a scaling law

$$\frac{L_f}{L} = B \cdot Ca^{-\chi} \tag{7}$$

with prefactor B and scaling exponent χ. The scaling exponent χ has been derived by Wilkinson[13,14] for immiscible displacement in porous media (i.e., invasion percolation); he scaled the correlation length of clusters in the stabilized front with $\nu/(\nu+1)$, where ν denotes the correlation length exponent from "classical" percolation theory. This is also supported by Tsimpanogiannis et al.[3] for the case of drying. Prat and Bouleux[8] have pointed out that this should only be valid for the scaling of σ_f; that is, the standard deviation of perpendicular distances of all menisci to the network surface. These authors derived the exponent $1-(1+\beta)/(1+\nu)$ for the scaling of L_f in two dimensions, with percolation probability exponent β. Table 1 gives values of the involved percolation probability exponent β and the correlation length exponent ν[19] along with proposed literature values for the χ. Prat and Bouleux[8] furthermore conducted 50 simulations on a 200×200 pore network with a gravity-stabilized drying front to evaluate exponent χ numerically; they found values of 0.573 ± 0.009 for the scaling of σ_f and 0.514 ± 0.008 for L_f. By experimental work, Shaw[2] found a scaling of L_f with drying front velocity by an exponent of 0.48 ± 0.1; the experiments where performed with a packing of 0.5 μm spheres in a box of 15–20 μm × 2.5 cm × 4.0 cm, which does not correspond to a strict 2D geometry.[3,8]

In the following, pore network drying simulations are used to analyze the expansion of drying front width L_f and standard deviation σ_f. In Figs. 5 and 7, both quantities are plotted in dimensionless, double-logarithmic form for several simulations on 2D and 3D pore networks. (All plots and the following discussion are restricted to the lengths as computed for the main cluster.) In order to estimate the

TABLE 1
Scaling exponents from the literature

	2D	3D
Percolation probability exponent β	5/36	0.41
Correlation length exponent ν	4/3	0.88
$\nu/(\nu+1)$	0.5714	0.4681
$1-(1+\beta)/(1+\nu)$	0.5119	–

TABLE 2
Estimated scaling parameters for simulations on the 300×120 and $15 \times 15 \times 121$ pore networks with different radii distribution. Besides estimated scaling parameters of individual simulations in 2D and 3D, the results of a fit to all data are given for both cases

Simulations		L_f		σ_f	
		B	χ	B	χ
2D	Run 1[a]	1.2131	0.5665 ± 0.0009	0.2054	0.6115 ± 0.0010
	Run 2	1.3395	0.5748 ± 0.0010	0.2339	0.6141 ± 0.0011
	Run 3	2.7841	0.4365 ± 0.0014	0.6037	0.4334 ± 0.0017
	Run 4	0.8171	0.6287 ± 0.0013	0.1296	0.6837 ± 0.0013
	Run 5	1.3367	0.5519 ± 0.0009	0.2085	0.6094 ± 0.0010
	All runs	1.4733 ± 0.0016	0.5404 ± 0.0006	0.2657 ± 0.0018	0.5727 ± 0.0006
3D	Run 1[a]	1.9000	0.4703 ± 0.0005	0.3790	0.4992 ± 0.0005
	Run 2	3.6297	0.4214 ± 0.0012	0.7932	0.4466 ± 0.0014
	Run 3	2.0432	0.5025 ± 0.0010	0.4523	0.5238 ± 0.0012
	All runs	2.7537 ± 0.0019	0.4435 ± 0.0007	0.5968 ± 0.0022	0.4659 ± 0.0008

[a]The first runs of both 2D and 3D are as in Metzger et al.[1]

scaling exponent χ and the prefactor B of Eq. (7), one ordinary least squares fit (linear in the logarithmic representation) has been performed on *all* simulation runs, for the 2D and 3D cases, respectively; the results are shown as dashed lines in each diagram (Figs. 5 and 7). Care has been taken to exclude the initial period of drying, when the front has not yet detached from the network surface and border effects play a role. (Due to the discrete description of pore space, drying front width L_f can only be resolved down to pore length L, so that L_f/L values close to unity have low significance anyway.) Breakthrough sets the other limit of scaling analysis.

The estimated scaling parameters for 2D and 3D simulations are in given in Table 2; besides the fit on all runs, parameters have also been estimated for *each* run individually. All given standard deviations are estimated from the least squares fits. (Note that the variation between individual estimates is much larger than these standard deviations.) Because percolation in 3D networks is qualitatively different, scaling exponents χ for 3D should be taken with care because they only apply to part of the front.[20,21] In the 3D simulation, additionally, the small lateral extension of the network in comparison to the obtained front width is expected to introduce a finite size effect.[19]

Estimated values of scaling exponents χ for the stabilized front in drying of porous media are found to be close to the predicted theoretical values for 2D.[8] Furthermore, the exponents for scaling L_f are found to be slightly smaller than the exponents for σ_f, as expected from the literature. In order to estimate scaling exponents for viscous stabilized drying fronts more accurately, more Monte Carlo simulations on a reasonable network size are required. Because the depth of the networks cannot be reduced if a sufficient range of L_f is spanned, future computational efforts have to aim at the simulation of adequate large networks, especially in 3D, in order to avoid finite size effects.

Dimensionless Saturation Profile across Drying Front

The internal character of the drying front can be described by means of saturation profiles; that is, the evolution of saturation of network slices along the network depth. As exemplarily shown in Fig. 2 for one 2D simulation (run 2), saturation profiles at different overall network saturations S_{total} are qualitative similar; the same behavior is observed for the 3D pore networks. Except at the very beginning of drying, an S-shaped (2D) and a double S-shaped curve with a plateau between the two transition zones (3D) has been found for each simulation. Because of this similarity, saturation profiles are normalized in the z-direction so that $\zeta = 0$ corresponds to the least advanced point (liquid saturation $S = 0$) and $\zeta = 1$ to the most advanced point ($S = 1$) of the front. As shown in Fig. 8 (2D) and Fig. 9 (3D), where normalized profiles from the whole drying process are plotted, in both cases, distinctive master curves can be observed. The S-shape curve of 2D pore network simulations is approximated by a Gaussian step with a superposed line

$$S(\zeta) = \frac{S_{cr}}{\sqrt{2\pi}\Delta\zeta} \int_{-\infty}^{\zeta} \exp\left(-\frac{1}{2}\left(\frac{\zeta' - \zeta}{\Delta\zeta}\right)^2\right) d\zeta' + (1 - S_{cr}) \cdot \zeta. \quad (8)$$

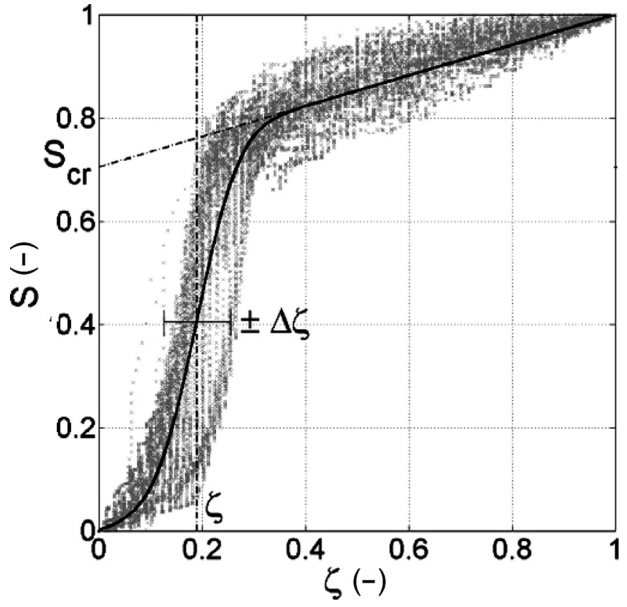

FIG. 8. Dimensionless representation of saturation profiles from the 2D pore network simulation shown in Figs. 1 and 2 (run 2) and fit of the master curve. Profiles are shown for every 0.001 step in network saturation S_{total}.

The profiles of 3D simulations can be approximated by a double Gaussian step

$$S(\zeta) = \frac{S_{cr}}{\sqrt{2\pi}\Delta\zeta_1}\int_{-\infty}^{\zeta}\exp\left(-\frac{1}{2}\left(\frac{\zeta'-\zeta_1}{\Delta\zeta_1}\right)^2\right)d\zeta' + \frac{1-S_{cr}}{\sqrt{2\pi}\Delta\zeta_2}\int_{-\infty}^{\zeta}\exp\left(-\frac{1}{2}\left(\frac{\zeta'-\zeta_2}{\Delta\zeta_2}\right)^2\right)d\zeta'. \quad (9)$$

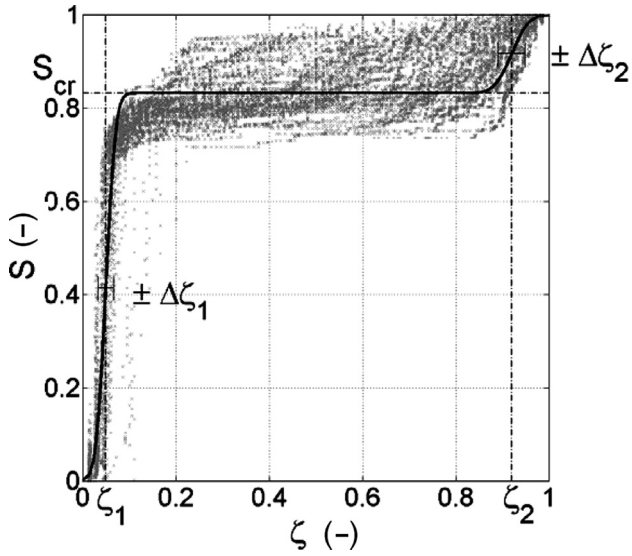

FIG. 9. Dimensionless representation of saturation profiles from the 3D pore network simulation shown in Fig. 4 (run 2) and fit of the master curve. Profiles are shown for every 0.001 step in network saturation S_{total}.

TABLE 3
Fitted parameters of dimensionless saturation profiles for 2D and 3D pore networks with different radii distribution. Given are the values for a fit to all data

	ζ	$\Delta\zeta$	S_{cr}
Runs in 2D	0.1882	0.0713	0.7193

	ζ_1	$\Delta\zeta_1$	ζ_2	$\Delta\zeta_2$	S_{cr}
Runs in 3D	0.0573	0.0204	0.8673	0.0558	0.8259

Estimated values for the parameters of these functions are given in Table 3; because profiles are found to be very similar for all simulations, in either 2D or the 3D case, parameters given are as estimated from the fit to the data of all runs. The (first) Gaussian step is to a critical saturation value S_{cr} in both cases. For 3D pore network simulation results, it is noted that the value of S_{cr} is quite high in comparison to literature data,[22] possibly due to the small lateral size of the present network and because all pore volume is contained in (bond-type) pores and the nodes (or sites in percolation terminology) do not contribute to liquid saturation, in contrast to literature work.

SIMPLE MACROSCOPIC DRYING MODEL

Model Description

Now, the above scaling laws for L_f (Ca) and the dimensionless saturation profiles are combined into an empirical macroscopic model to evaluate drying curves $\dot{m}_v$ (S) as in Figs. 4 and 10. For this model, parameters are applied as estimated for the overall fits of all data (values given for all runs in Tables 2 and 3). A key model parameter is the position of the least advanced point of the drying front $z = z_f$ that corresponds to the (perpendicular) distance of the evaporation front to network surface. The discrete formulation of the front position with parameter z_f neglects any expansion of the front. Therefore, the resulting mass flux computed for the planar evaporation front

$$\dot{m}_v = -\left(\frac{s}{\delta} + \frac{z_f}{D_{eff}}\right)^{-1}\frac{\tilde{M}_v P}{\tilde{R}T}\cdot\ln\left(1-\frac{P_v^*}{P}\right) \quad (10)$$

(with boundary layer thickness s and effective diffusivity in the network $D_{eff} = \delta\pi r_0^2/L^2$) will overestimate drying rate; individual branches already advancing deeper into the network than position z_f lead to a reduction of evaporation rates due to increasing diffusion resistances. For the evaporation rate obtained from Eq. (10), the capillary number is computed from Eq. (4) and the drying front width L_f from Eq. (7). Then, the dimensionless profiles of Eq. (8) or Eq. (9) can be applied to the interval

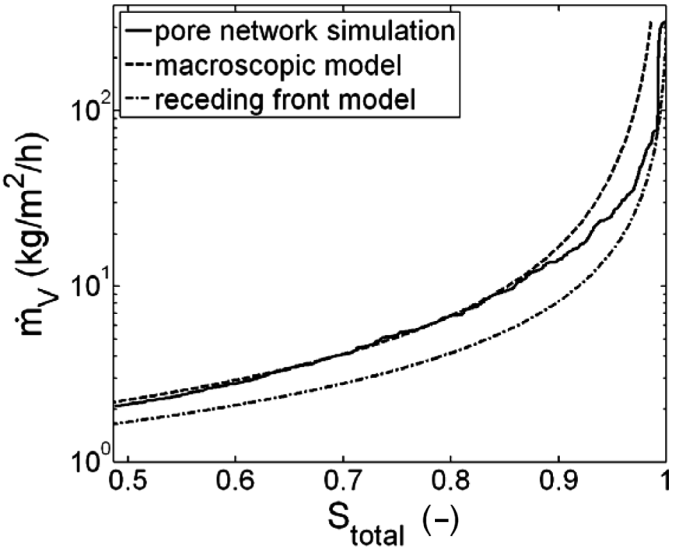

FIG. 10. Drying curves for 3D pore network simulation (run 2), macroscopic and receding front model.

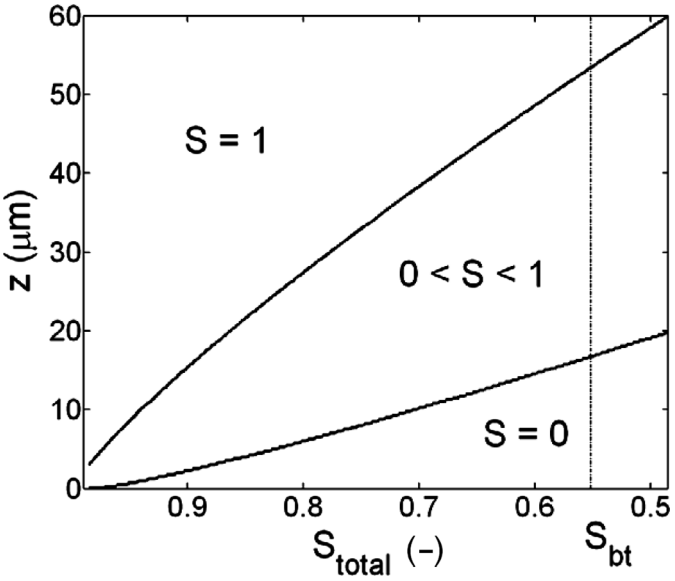

FIG. 12. Penetration and widening of the 2D drying front as computed from the macromodel; S_{bt} shows breakthrough in simulation run 2. (Saturation contours are plotted for ε and $(1-\varepsilon)$, where $\varepsilon = 10^{-4}$.).

$(z_f, z_f + L_f)$ to get an average saturation profile and the corresponding network saturation S_{total}. In this way, moisture profiles and drying rate curve can be approximated.

Comparison with Pore Network Simulation

2D Simulation

The approximated saturation profiles of the macroscopic model are compared to selected profiles from one pore network simulation (run 2). In Fig. 11, the grey surface area represents the macroscopic model showing good overall agreement with the results of the 2D pore network simulation, which are plotted as solid lines. At the very start of drying, the theoretical profile is not yet developed. This is due to the problem of finite initial drying rates; a vanishing drying front width would correspond to an infinite drying rate, but the boundary layer imposes a finite value. The contour plot in Fig. 12 shows the propagation of the drying front (z_f to $z_f + L_f$) into the network and visualizes the extension of the zone in which $0 < S < 1$. In simulation run 2, the overall network saturation at breakthrough is $S_{bt} = 0.5514$; in Fig. 12 a line is plotted to that value. From the macroscopic model, breakthrough is expected at a slightly smaller network saturation.

Finally, the drying rate curve for 2D simulations is given in Fig. 4 (as a semi-logarithmic plot) and compared to results from pore network simulations. Initially, drying rates are strongly overestimated by the macroscopic model: due to the mentioned problem of finite initial drying rates, the curve starts at network saturation less than 0.99 ($S = 0.985$). Later on, the overestimation is probably a consequence of the nonplanarity of the evaporation front. The result for a planar receding front (with $L_f = 0$) is also shown. This corresponds to the limit of infinite liquid viscosity and may serve as a lower bound for drying rates. (Contrarily to the least advanced point of the drying front as used to compute drying rates for the macroscopic model, the position of the planar receding front can be interpreted as a mean front position.)

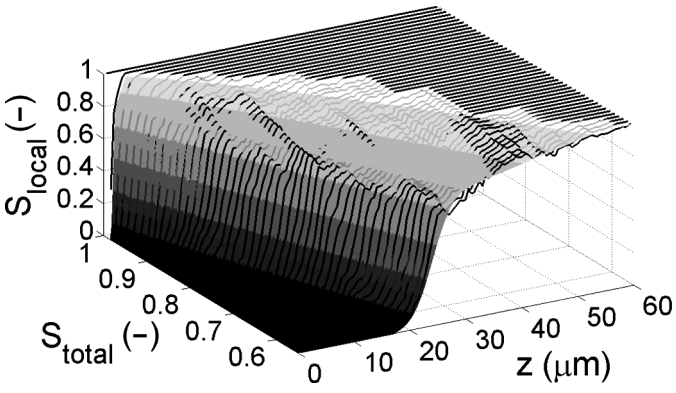

FIG. 11. Saturation profiles of 2D pore network simulation run 2 (lines) and macroscopic model (surface).

3D Simulation

Analogous to diagrams presented for the 2D case, results for 3D simulations are given in Figs. 10, 13, and 14. In the contour plot in Fig. 14, several saturation levels are plotted to highlight the distinct plateau between the two

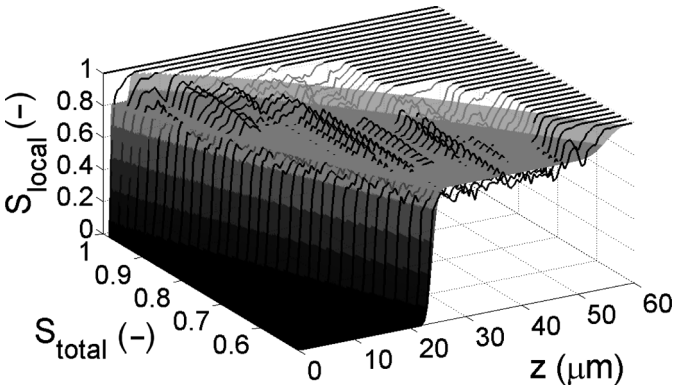

FIG. 13. Saturation profiles of 3D pore network simulation run 2 (lines) and macroscopic model (surface).

Gaussian steps. Network saturation at breakthrough is slightly overestimated by the macroscopic model, because $S_{bt} = 0.4878$ in the pore network simulation (run 2). Although scaling for 3D is qualitatively different[20,21] and finite size effects in the networks might have occurred, drying rates estimated by the macroscopic model describe the behavior of the pore network very well in a certain range (Fig. 10). The overestimation of drying rates at the start of drying is caused by the above mentioned effects.

CONCLUSIONS AND OUTLOOK

In this article, we have shown how scaling laws from percolation theory can be combined with empirical parameters obtained from pore network simulations in order to formulate a simple macroscopic model for the drying of porous media. The proposed macroscopic model of drying may serve to extrapolate the drying behavior of porous structures that are too large in number of pores to be simulated as a whole. Resulting drying rate curves from the model have been compared to pore network simulations of convective drying under isothermal conditions with a viscous-stabilized drying front; additionally, the results of a model with a sharp front have been shown. It has been confirmed that the overall agreement between pore network simulation results and results from the macroscopic model is good. Furthermore, obtained scaling exponents from simulations on relatively small networks are in the range of literature values. This suggests that future computational efforts are worthwhile to determine the exponent accurately and resolve the question of which of the competing theories is correct. Future attention should also address the dependencies of factor B in the scaling law.

Complementary future work should focus on the comparison of the macroscopic and pore network model to a traditional continuous model of drying with gradient-driven transport including the same effects as the pore network model. Then, pore network simulations may be used to estimate effective parameters, which are liquid permeability, vapor diffusivity, and capillary pressure, as proposed, for example, by Nowicki et al.[23]

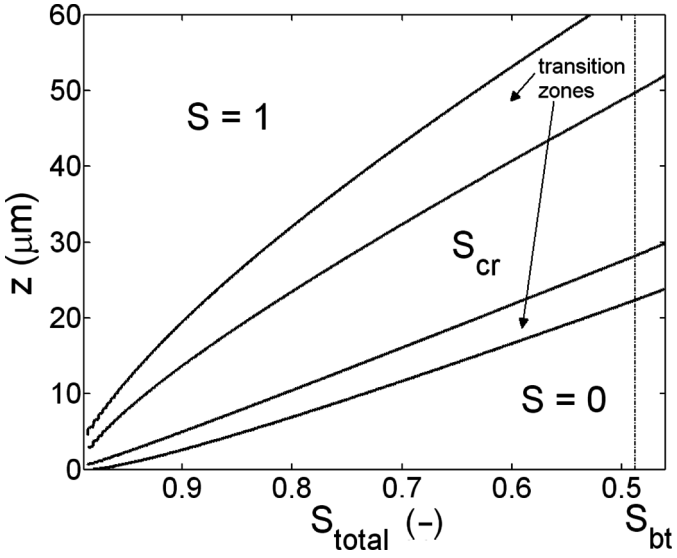

FIG. 14. Penetration and widening of the 3D drying front as computed by the macromodel; S_{bt} shows when breakthrough occurred in simulation run 2. (Saturation levels are plotted for ε, $(S_{cr} - \varepsilon)$, $(S_{cr} + \varepsilon)$, and $(1 - \varepsilon)$, where ε is 10^{-4}.).

NOMENCLATURE

B	Factor in scaling law
Ca	Capillary number
D_{eff}	Effective diffusivity ($m^2 s^{-1}$)
L	(Pore) length (m)
L_f	Front length (m)
$\tilde{M}$	Molar mass ($kg\,kmol^{-1}$)
$\dot{M}$	Mass flow rate ($kg\,s^{-1}$)
$\dot{m}$	Mass flux ($kg\,m^{-2}\,s^{-1}$)
P	Pressure (Pa)
$\tilde{R}$	Ideal gas constant ($J\,kmol^{-1}\,K^{-1}$)
r	Pore radius (m)
r_0	Mean pore radius (m)
S	Liquid saturation
S_{cr}	Critical saturation
s	Boundary layer thickness (m)
T	Temperature (K)
v	Average pore liquid velocity ($m\,s^{-1}$)
z	Distance to network surface (m)

Greek Letters

β	Percolation probability exponent
δ	Vapor diffusivity ($m^2 s^{-1}$)
ζ	Dimensionless position in front
$\Delta\zeta$	Standard deviation of position ζ
η	Dynamic viscosity ($Ns\,m^{-2}$)
ν	Correlation length exponent

ν_w	Kinematic viscosity ($m^2 s^{-1}$)
ρ	Density ($kg m^{-3}$)
σ	Surface tension (Nm^{-1})
σ_0	Standard deviation of radius (m)
σ_f	Standard deviation of front (m)
χ	Scaling exponent

Subscripts and Superscripts

1, 2	Step 1 and 2 of dimensionless profiles
bt	Breakthrough
c	Capillary
f	Front
i, ij	Indices of node, pore
total	Overall (saturation)
v	Vapor
w	Liquid water
$*$	Saturation/equilibrium
∞	Bulk air

REFERENCES

1. Metzger, T.; Vorhauer, N.; Tsotsas, E. Use of pore networks for macroscopic modelling of drying. *Proceedings of 16th International Drying Symposium*; Vol. A, Hyderabad, India, 9–12 November 2008; 242–249.
2. Shaw, T.M. Drying as an immiscible displacement process with fluid counterflow. Physical Review Letters **1987**, *59*, 1671–1674.
3. Tsimpanogiannis, I.N.; Yortsos, Y.C.; Poulou, S.; Kanellopoulos, N.; Stubos, A.K. Scaling theory of drying in porous media. Physical Review E **1999**, *59*, 4353–4365.
4. Laurindo, J.B.; Prat, M. Numerical and experimental network study of evapouration in capillary porous media. Phase distributions. Chemical Engineering Science **1996**, *51*, 5171–5185.
5. Lenormand, R. Flow through porous media: Limits of fractal patterns. Proceedings of the Royal Society of London A **1989**, *423*, 159–168.
6. Metzger, T.; Tsotsas, E.; Prat, M. Pore-network models: A powerful tool to study drying at the pore level and understand the influence of structure on drying kinetics. In *Modern Drying Technology, Vol. 1: Computational Tools at Different Scales*; Tsotsas, E., Mujumdar, A.S., Eds.; Wiley-VCH: Weinheim, 2007, 57–102.
7. Prat, M. Recent advances in pore-scale models for drying of porous media. Chemical Engineering Journal **2002**, *86*, 153–164.
8. Prat, M.; Bouleux, F. Drying of capillary porous media with a stabilized front in two dimensions. Physical Review E **1999**, *60*, 5647–5656.
9. Surasani, V.K.; Metzger, T.; Tsotsas, E. Influence of heating mode on drying behaviour of capillary porous media: Pore scale modelling. Chemical Engineering Science **2008**, *63*, 5218–5228.
10. Yiotis, A.G.; Stubos, A.K.; Boudouvis, A.G.; Tsimpanogiannis, I.N.; Yortsos, Y.C. Pore-network modeling of isothermal drying in porous media. Transport in Porous Media **2005**, *58*, 63–86.
11. Laurindo, J.B.; Prat, M. Numerical and experimental network study of evapouration in capillary porous media. Drying rates. Chemical Engineering Science **1998**, *53*, 2257–2269.
12. Yiotis, A.G.; Boudouvis, A.G.; Stubos, A.K.; Tsimpanogiannis, I.N.; Yortsos, Y.C. Effect of liquid films on the drying of porous media. AIChE Journal **2004**, *50*, 2721–2737.
13. Wilkinson, D. Percolation model of immiscible displacement in the presence of buoyancy forces. Physical Review A **1984**, *30*, 520–531.
14. Wilkinson, D. Percolation effects in immiscible displacement. Physical Review A **1986**, *34*, 1380–1391.
15. Metzger, T.; Tsotsas, E. Viscous stabilization of drying front: Three-dimensional pore network simulations. Chemical Engineering Research and Design **2008**, *86*, 739–744.
16. Metzger, T.; Irawan, A.; Tsotsas, E. Isothermal drying of pore networks: Influence of friction for different pore structures. Drying Technology **2007**, *25*, 49–57.
17. Irawan, A.; Metzger, T.; Tsotsas, E. Pore network modelling of drying: Combination with a boundary layer model to capture the first drying period. *Proceedings of 7th World Congress of Chemical Engineering*, Glasgow, Scotland, 10–14 July 2005.
18. Prat, M. Isothermal drying of non-hygroscopic capillary-porous materials as an invasion percolation process. International Journal of Multiphase Flow **1995**, *21*, 875–892.
19. Stauffer, D.; Aharony, A. *Introduction to Percolation Theory*; Taylor & Francis: London, 1992.
20. Rosso, M.; Gouyet, J.-F.; Sapoval, B. Gradient percolation in three dimensions and relation to diffusion fronts. Physical Review Letters **1986**, *57*, 3195–3198.
21. Gouyet, J.-F.; Rosso, M.; Sapoval, B. Fractal structure of diffusion and invasion fronts in three-dimensional lattices through the gradient percolation approach. Physical Review B **1988**, *37*, 1832–1838.
22. Yiotis, A.G.; Tsimpanogiannis, I.N.; Stubos, A.K.; Yortsos, Y.C. Pore network study of the characteristic periods in the drying of porous materials. Journal of Colloid and Interface Science **2005**, *297*, 738–748.
23. Nowicki, S.C.; Davis, H.T.; Scriven, L.E. Microscopic determination of transport parameters in drying porous media. Drying Technology **1992**, *10*, 925–946.

DOI: 10.1002/cite.201000023

Network models for capillary porous media: application to drying technology

Thomas Metzger* and Evangelos Tsotsas

Network models offer an efficient pore-scale approach to investigate transport in partially saturated porous materials and are particularly suited to study capillarity. Drying is a prime model application since it involves a range of physical effects: capillary pumping, viscous liquid flow, phase transition, vapor diffusion, heat transfer, but also cracks and shrinkage. This review article gives an introduction to this modern technique addressing required model input, sketching important elements of the computational algorithm and commenting on the nature of simulation results. For the case of drying, it is illustrated how network models can help analyze the influence of pore structure on process kinetics and gain a deeper understanding of the role of individual transport phenomena. Finally, a combination of pore network model and discrete element method is presented, extending the application range to mechanical effects caused by capillary forces.

Keywords: capillary pressure, composite material, discrete element method, drying, heat transfer, phase change, pore network model, pore structure, scaling law, viscous effect

Submitted: January 29, 2010; *accepted:* March 05, 2010

1 Introduction

Porous media are ubiquitous in daily life, ranging from natural materials such as rock, sand, soil or plants to man-made products such as concrete, ceramics, paper, textiles, and various agglomerates for technical, medical or food purposes. In many production processes and applications involving porous materials, the crucial step consists in replacing one pore fluid by a second, immiscible one; examples range from oil recovery (oil by water) to drying of ceramics (water by air) and infiltration of instant products (air by water). In partially saturated porous media, interfacial, or capillary, effects between the two (or more) phases may play the dominant role for fluid transport and material behavior.

For such capillary porous media, the classical approach, which treats the partially saturated body as an effective continuum and describes liquid transport as driven by gradients in average saturation, proves to be inadequate. Instead, the filling state of every single pore may decide on the macroscopic connectivity of the phases, and concepts from percolation theory have to be used. Pore network models offer an efficient way to account for these effects: the complex pore space is represented by a large number of interconnected pores that are geometrically similar but have a size distribution. Instead of tracking the phase boundary exactly, simple rules are developed to decide whether the discrete pores change their filling state. In this way, structural features of the pore space may be modeled at dramatically reduced computational costs.

Drying technology has become one important and very illustrative application of pore network modeling.

Originally, pore networks have been used in hydrogeology and petroleum engineering to model pollutant dispersion in groundwater flow [1] or immiscible displacement in oil recovery [2], but their aptitude for other materials and technical processes has soon been discovered. Drying technology has become one important and very illustrative application of pore network modeling. Since the pioneering works in the 1990s [3, 4], several researchers have become active in this field, varying pore geometry and topology of the simulated networks and adding more physical effects to the drying

model [5 – 9]; further attention has been given to the experimental validation of modeling results [5].

2 Pore network model

In this Sect., an overview over the basic pore network drying model is given. For technical details, especially concerning data structures and algorithmic rules, but also parameters for the presented drying simulations, the reader is referred to a recent review [10].

Depending on model complexity, the solid phase must be added as complementary to the pore network.

2.1 Network generation

The first step in pore network modeling is to choose the geometry of the pore elements, from which the network shall be built. In literature, several options can be found, often distinguishing between pore bodies and pore throats [11]. In this work, cylindrical capillaries are interconnected by nodes without any volume, as depicted in Fig. 1. Next, a network topology must be defined by spatial placement of nodes and node connections. Typically, square and simple cubic networks are used for 2D and 3D investigations, respectively, but the proposed model can easily be applied to other regular and irregular networks. Further, a probability distribution needs to be selected, according to which pore sizes are sampled. At last, the network is decorated, i.e., the generated pores are placed into the network, either randomly or with spatial correlations of pore size. Fig. 1 shows a normal number distribution for the radii of cylindrical pores in a square network. Depending on model complexity, the solid phase must be added as complementary to the pore network. The mentioned structural properties are based on experimental knowledge about the real porous structure: ideally, from tomographic measurements; typically, from pore volume measurements by, e.g., mercury porosimetry.

The liquid pressure in small pores is lower than in large pores, resulting in capillary pumping from large into small pores.

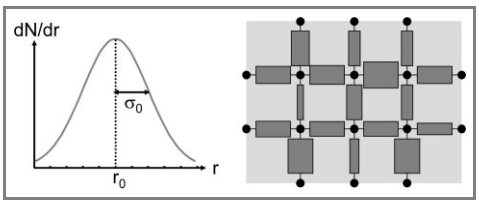

Figure 1. Number distribution of pore radius for a square network of cylindrical pores (r_0 and σ_0 are mean and standard deviation of the normal distribution, respectively).

2.2 Transport phenomena

Besides defining the pore network itself, physical effects that are relevant for the simulated process – here drying – must be identified and modeled. The most important effect in partially saturated porous media is capillary pressure P_c, which indicates by how much liquid pressure P_w is lower than gas pressure P_g due to the curved liquid-gas interface. For a cylindrical pore of radius r that is filled with a perfectly wetting liquid of surface tension σ, capillary pressure is

$$P_\mathrm{c} = \frac{2\sigma}{r} \tag{1}$$

Therefore, the liquid pressure in small pores is lower than in large pores, resulting in capillary pumping from large into small pores, as illustrated in Fig. 2a.

The most important phenomenon in drying is evaporation of pore liquid so that vapor flow from the evaporating liquid-gas menisci towards the drying air needs a model description. Assuming saturation vapor pressure P_v^* at the meniscus and vapor pressure P_v at a distance L, as depicted in Fig. 2b, then the rate of vapor diffusion in a cylindrical capillary is approximately given by

$$\dot{M}_\mathrm{v} = \pi r^2 \frac{\delta_\mathrm{v}}{L} \frac{\tilde{M}_\mathrm{v}}{\tilde{R}T} \left(P_\mathrm{v}^* - P_\mathrm{v}\right) \tag{2}$$

where δ_v is vapor diffusivity, $\tilde{M}_\mathrm{v}$ molar mass of vapor, $\tilde{R}$ ideal gas constant and T absolute temperature.

Further, secondary effects may be included, one of them being liquid viscosity. Fig. 2c shows the parabolic velocity profile of laminar flow in a cylinder. Liquid flow rate then depends linearly on the pressure difference as

$$\dot{M}_\mathrm{w} = \frac{\pi r^4}{8 \nu_\mathrm{w} L} (P_\mathrm{w1} - P_\mathrm{w2}) \tag{3}$$

where ν_w is kinematic liquid viscosity. Obviously, friction sets an upper limit to capillary flow; the effects on drying behavior will be discussed in Sect. 4.1.

If pores are not cylindrical, capillary liquid flow may also occur in the corners of gas-filled pores, thereby enhancing mass transfer as compared to vapor diffusion. The interested reader is referred to literature work, in which film effects are modeled – and shown to be crucial – for pores with square or polygonal cross Sect. [6, 12]. Besides this, gravitational effects can be modeled by introducing height-dependent hydrostatic pressure [4]. Gravity may prevent capillary flow, if vertical distances are too large and if capillary pressures are small due to large pore radii. Important non-

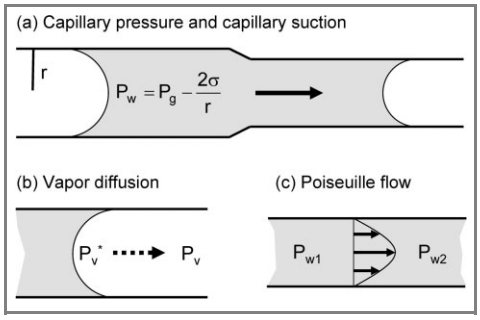

Figure 2. Pore level phenomena of equilibrium and transport (see text for details).

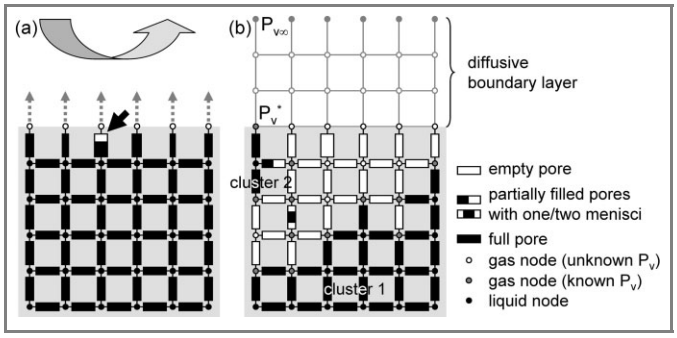

Figure 3. Drying of a pore network: (a) combined effect of evaporation and capillary pumping for full network; (b) liquid clusters, different states of pores/nodes and discretized boundary layer for partially saturated network.

isothermal effects will be addressed in Sect. 4.2.

At last, it shall be stressed that in all mentioned pore network models the interaction between liquid and solid is only described by the wetting properties. This means that sorbed (or bound) liquid is not modeled and that all pore liquid is considered as free. Sorption, which essentially modifies the vapor transfer in gas-filled pores, could be included in the model; but is not expected to affect the capillary effects which are in the focus of this network approach.

2.3 Drying algorithm

When pore network and physical rules are set, the network process model can be developed. Fig. 3a shows a square pore network that is filled with water (shown in black) and subjected to a flow of drying air over its top side so that liquid is evaporated from all surface pores. For the simplest case of negligible viscous effects, only the largest surface pore is emptied and ideal capillary flow keeps the other surface pores full. As drying continues, the largest of the pores at the current liquid-gas interface, i.e., of those containing a meniscus, are preferentially emptied. The spatial distribution of pore size determines the order for gas invasion. After a while, the partially saturated network typically contains several disconnected liquid clusters. Fig. 3b gives an example of a phase distribution and defines the different states of pores and nodes.

To describe vapor transport, the network of pore nodes is extended to span the gas-side boundary layer [13]. Lateral diffusion in the boundary layer is necessary for the constant rate period that will be observed for certain pore structures. Vapor flow rates between the nodes are computed from a diffusion problem with boundary conditions for vapor pressure (saturation value P_v^* at liquid-gas interface and value of drying air $P_{v\infty}$ at top of boundary layer). For every liquid cluster, evaporation rates of all meniscus pores are summed up and liquid is subtracted at that rate from the largest interface pore of the respective cluster. When the state of one pore has changed, liquid connectivity must be updated by a cluster labeling algorithm [14]. In this way, the network is emptied pore by pore, at drying rates depending on current phase distributions.

2.4 Simulation results

The drying algorithm yields the evolution of phase patterns and the overall drying rate curve, typically plotted as evaporation rate versus network saturation. In order to reduce effects due to finite network size, periodic boundary conditions are chosen in lateral direction. Fig. 4 shows the phase patterns of in a drying network with a normal pore size distribution. (Pores are large, i.e. of the order of 100 µm, and drying rate is moderate so that viscous effects can be neglected.) Gas invasion into the depth of the network before its surface dries out completely (a-b), formation of disconnected liquid clusters with fractal geometry (b), and subsequent erosion of these clusters from the top (c-d) can be observed. Indeed, capillary pumping is advantageous for drying kinetics: the evaporation front, i.e., the top envelope of the liquid cluster region, remains closer to the network surface than for an immobile liquid, for which the liquid-filled region sharply recedes into the network and vapor diffusion resistance is high.

Concerning the simulation results, network generation, and therefore gas invasion, are random processes, so that the phase patterns of different pore networks with the same statistical properties may differ significantly. In fact, the sample network of Fig. 4 nicely illustrates the different phenomena during drying, but its favorable capillary pumping is rather typical

Sorption is not expected to affect the capillary effects which are in the focus of this network approach.

The network is emptied pore by pore, at drying rates depending on current phase distributions.

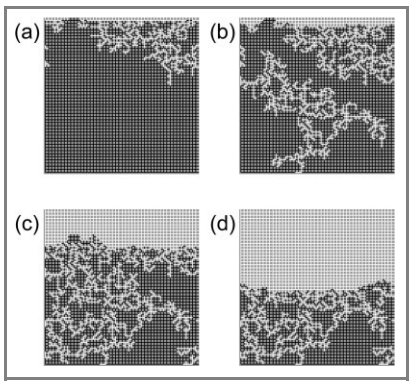

Figure. 4. Liquid distributions (in black) in a drying network with normal pore size distribution for network saturations (a) 0.9, (b) 0.75, (c) 0.55 and (d) 0.35 (adapted from [8]).

for 3D networks; in 2D networks, trapping of liquid, interrupting capillary flow, is quite pronounced and network surface will often dry out before breakthrough of gas at the network bottom [15].

For representative results, many pore networks have to be sampled by use of the same distribution function (see Fig. 1) and drying kinetics have to be computed for all of them. In Fig. 5, the results of 100 such Monte Carlo simulations are presented. Dimensionless drying rate $\dot{v}$ (initial value is set to unity) is plotted as a function of liquid saturation of the network S in Fig. 5a. The shaded area comprises all 100 drying curves; the black curves indicate the quartiles of the drying rate distribution for any network saturation. Fig. 5b gives saturation profiles as a function of dimensionless network depth ζ for 0.1 steps in network saturation, the curves being averages of 100 individual profiles.

Many pore networks have to be sampled and drying kinetics have to be computed for all of them.

It can be stated for the square pore network with a mono-modal pore size distribution that network surface dries out very soon and drying rate decreases drastically. The drying front consists of two regions (see Fig. 5b): the first is situated next to the dry network region and has a steep saturation gradient, it contains the small disconnected clusters that evaporate one by one; the second region has a shallow saturation gradient, it contains the gas branch that gradually invades the saturated network region.

Many porous media exhibit a wide pore size distribution with distinct modes.

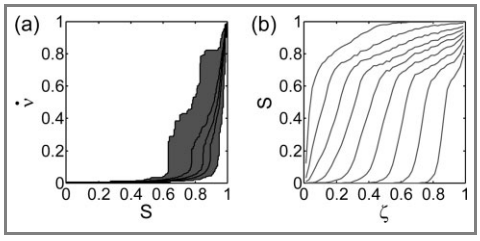

Figure 5. Average drying behavior of 2D square network with mono-modal (normal) pore size distribution (see Fig. 4): (a) drying rate curve, (b) saturation profiles (adapted from [8]).

3 Influence of structure

One major purpose of pore network modeling is to study how structural properties of the porous medium influence process behavior. In the following, the above described drying model is applied to networks with different pore space characteristics.

3.1 Bimodal pore size distributions

Many porous media, both natural and technical, exhibit a wide pore size distribution with distinct modes, and pores of different sizes often build up a hierarchical structure. Here, we choose a bimodal pore size distribution and investigate three different configurations for the spatial correlation of large pores. For each configuration, the positions of large (and small) pores in the network are fixed, but their exact sizes are randomly selected. All three structures have the same overall porosity and pore size distribution.

Fig. 6 depicts the first structure, in which large pores are arranged as network-spanning channels away from the surface, and illustrates the specific drying behavior for this arrangement. Corresponding drying curves and saturation profiles are given in Fig. 7 for 100 Monte Carlo runs. As can be easily seen, capillary pumping ensures that the large channels are emptied first, while the small pores stay full of liquid and keep most of the network surface wet. Hence, a constant rate period, or first drying period, can be distinguished: (almost) all liquid contained in large pores can be evaporated at the high initial rate. Only when the large pores are empty, the small ones start to dry out from the surface, the evaporation front recedes into the network and drying rate drops drastically. The saturation profiles first reflect the random invasion of large channels by gas (with a macroscopic gradient), then assume a uniform saturation level, before a relatively sharp front recedes. For this struc-

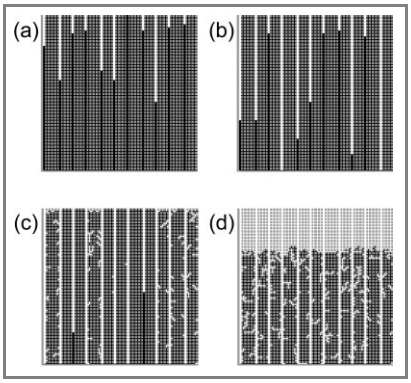

Figure 6. Liquid distributions in a drying network with a bimodal pore size distribution and macropores arranged as long channels for network saturations (a) 0.9, (b) 0.75, (c) 0.55 and (d) 0.35 (adapted from [8]).

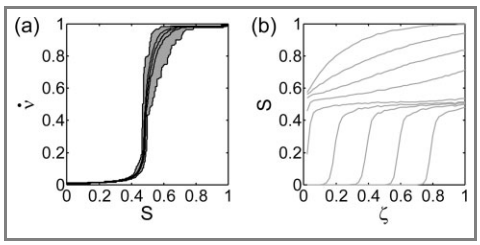

Figure 7. Drying behavior of square network with bimodal pore size distribution as in Fig. 6: (a) drying rate curve, (b) saturation profiles (adapted from [8]).

ture, drying behavior shows very limited random variation.

In the second structure, large pores are arranged in vertical and horizontal channels, dividing the 2D network into subregions of small pores; therefore, the structure might be interpreted as an agglomerate of porous particles. The third structure consists of a matrix of small pores with isolated large pores representing inclusions or fractures. Fig. 8 shows both configurations and their respective drying behavior. Neither of them can ensure a constant rate period, and both exhibit a large randomness.

For the agglomerate structure, the random emptying of large channels cuts off capillary flow to whole subregions of the evaporation front, which gradually dry out from the network surface. (The first drying period observed for some Monte Carlo runs is a random effect and not characteristic for the average behavior.) During drying of the third bimodal structure, random gas invasion is only temporarily overruled, namely when a large pore is reached and must be emptied preferentially. The overall drying behavior of both structures is very similar to the mono-modal case, since capillary pumping remains a random effect. However, the presence of large pores enhances the randomness in the drying rate curves; and the imposed spatial correlations are visible as a texture on the saturation profiles.

For effective capillary pumping, large pores and small pores must form two sample-spanning, interpenetrating networks. Only then, all liquid contained in the large pores can be pumped through the small-pore network and evaporated at the high initial rate, because network surface remains almost completely wet. Clearly, spatial continuity of both networks cannot be fully achieved in 2D; respective 3D network simulations are documented in [10].

3.2 Pore connectivity

Another important structural property of the pore network is the coordination number Z

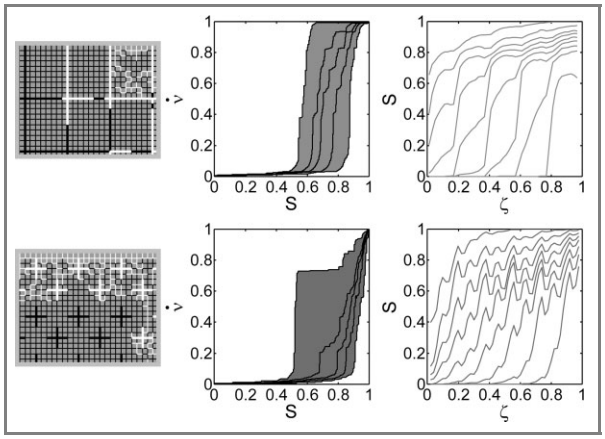

Figure 8. Drying behavior of square networks with different bimodal pore structure: detail of partially dried network, drying rate curve, and saturation profiles (adapted from [8]).

that measures to how many neighbors a network node is connected. Here, drying behavior of three regular 3D networks is analyzed; their unit cells are illustrated in Fig. 9. Besides the simple cubic arrangement ($Z=6$), networks built from tetrahedra ($Z=4$) or octahedra ($Z=8$) are simulated. All three networks are decorated with the same mono-modal pore size distribution, and pore length is adjusted so that all networks have the same porosity.

The averaged saturation profiles in Fig. 9 all show a fundamental difference to the 2D profiles for a mono-modal pore size distribution (see Fig. 5): pore liquid is removed from the

For effective capillary pumping, large pores and small pores must form two sample-spanning, interpenetrating networks.

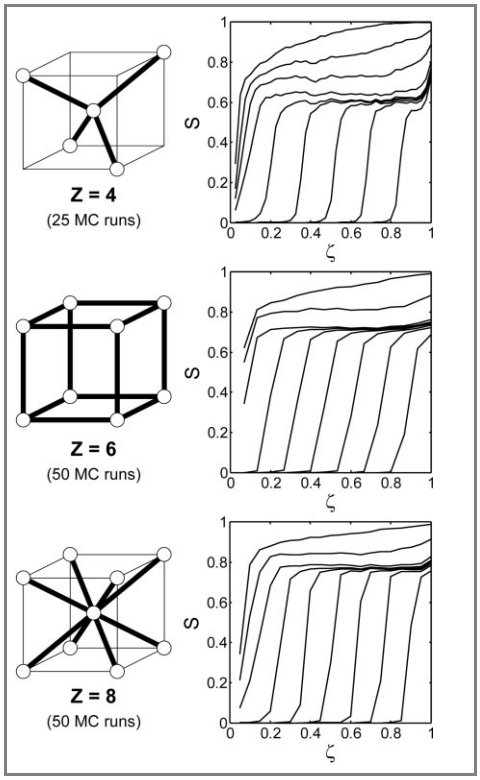

Figure 9. Regular 3D networks with different coordination number and their respective averaged saturation profiles during drying (adapted from [8]).

whole network before a uniform saturation level is reached and the evaporation front recedes into the network. Therefore, unlike in 2D, a constant rate period can be observed.

Concerning pore connectivity, it may be stated that, for networks with lower coordination number, gas invasion is facilitated and more liquid can be removed from the network at the high initial drying rate. As expected from 2D behavior, a bimodal pore structure can further improve drying rates [8].

4 Influence of transport phenomena

Network models are well suited to look at the details of heat and mass transport.

Besides accounting for structural effects, network models are well suited to look at the details of heat and mass transport. By activating or deactivating individual transport phenomena in the algorithm, their specific role can be studied and a deeper understanding gained. In this paper focus is on the role of liquid viscosity and the importance of non-isothermal effects. The basic network algorithm that has been introduced in Sect. 2 serves as reference. For studies on gravity and corner films in pores with edges the reader is referred to [10].

4.1 Liquid viscosity

Drying is a non-isothermal process and heat transfer can substantially affect drying behavior.

In Sect. 2, the pore-scale description of viscous liquid flow has already been given. In order to account for liquid viscosity in the drying algorithm for the pore network, the rules for gas invasion have to be changed. For negligible viscosity, only the largest interface pore of each cluster has been emptied at any time. However, if viscosity slows down capillary liquid flow to the smaller interface pores, the flow rates in all pores have to be known for tracking the menisci. To this aim, the pressure field has to be computed from appropriate boundary conditions at the liquid-gas phase boundary [16]. (An alternative algorithm to account for liquid viscosity and corner films has been proposed in [17].)

Figs. 10 and 11 show two drying simulations for a cubic network of small pores (around 100 nm in size) which is subjected to high drying rates so that viscous effects are pronounced: in (a) liquid viscosity has not been modeled, whereas (b) fully accounts for it.

For non-viscous flow, liquid can be pumped by differences in capillary pressure over any distance. Gas breaks through at the bottom of the network (see Fig. 10a) and the whole network looses liquid, well before the network surface dries out. In the saturation profiles (see Fig. 11a), no macroscopic gradient is observed during this constant rate period. The front recedes into the network when capillary flow is stopped by discontinuity of the liquid phase.

With viscosity, liquid flow rate is a function of distance and pressure difference. Since the available pressures are determined by pore size distribution, the distance, over which liquid can be pumped, depends on the current evaporation rate. For the full network, this rate is high, so that gas can invade only a thin layer of the network, before surface pores are emptied. As the evaporation front is receding, drying rate drops and the distance for capillary pumping increases so that the drying front can gradually widen up (see Figs. 10b and 11b). Experimental evidence for such a rate-dependent front width is given in [19]. The saturation profiles show a significant gradient in the capillary flow region, i.e. above the saturation level 0.7, at which the liquid phase becomes disconnected.

Hence, by the influence of friction, the drying front, i.e., the partially saturated region, becomes limited in size. This is known as viscous stabilization and leads to less favorable drying rates.

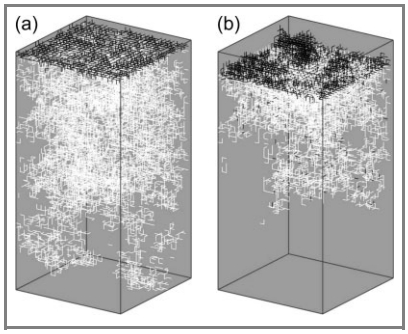

Figure 10. Phase distributions for (a) non-viscous and (b) viscous drying simulation, both at network saturation 0.86; from the top, only liquid pores are plotted, from the bottom, only empty pores (source [18]).

4.2 Heat transfer

So far, only mass transfer has been modeled. However, drying is a non-isothermal process and heat transfer can substantially affect drying behavior. Therefore, the basic, non-viscous drying model has been extended to account for the latent heat of evaporation and the temperature dependencies of saturation vapor pressure and surface tension [20, 21]. In the presence of thermal gradients, both evaporation and condensation occur in the partially saturated pore region, transferring heat from warm to cold places by vapor flow. This heat pipe effect is

accounted for in the non-isothermal drying algorithm. However, some of the condensing vapor is not accommodated, since refilling of empty pores needs new algorithmic rules. Further, heat is transferred by conduction where effective conductivity and heat capacity depend on the local saturation. At every node, local thermal equilibrium between the phases is assumed.

To illustrate the effects of heat transfer, a bimodal pore structure with constant rate period is dried by hot air. Fig. 12a shows the distribution of liquid and temperature at a network saturation of 0.4. The major effect in this example is the almost uniform heating of the network, to wet bulb temperature during the constant rate period, and further when evaporative cooling becomes less important at the lower drying rates of the receding front. The gradual temperature rise is accompanied by substantially higher drying rates, as plotted in Fig. 13 (convective heating curve), especially in the second drying period, due to the temperature dependency of saturation vapor pressure. For convective drying, the model extension to heat transfer eliminates a deficiency of the isothermal model, namely the unrealistically large decrease of drying rate in the falling rate period. For 3D simulations with a bimodal pore structure, still better results are achieved [22]. The effect on phase distributions is of minor importance; for the drying of monomodal structures, a thermal stabilization of the drying front is expected [23].

Further, the non-isothermal model allows to study the influence of the heating mode on drying behavior. If the above bimodal network is dried with contact heating, as illustrated in Fig. 12b, the phase patterns are dramatically modified. Due to the large temperature gradient and the temperature dependency of surface tension, the emptying order is changed. Interface pores at the hot bottom of the network are preferentially emptied, because along with surface tension also capillary pressure decreases with increasing temperature. Consequently, two fronts are observed which propagate into the drying network and meet in its core (see also [24]). Fig. 12b also nicely shows the effect of evaporative cooling; at the network surface, dry hot spots coexist with cooler wet patches. In the contact mode, more heat can be transferred to the drying network, so that drying rates are further increased (see Fig. 13).

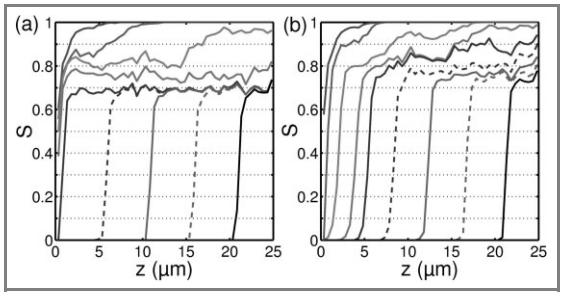

Figure 11. Saturation profiles for the (a) non-viscous and (b) viscous drying simulations of Fig. 10 (source [18]).

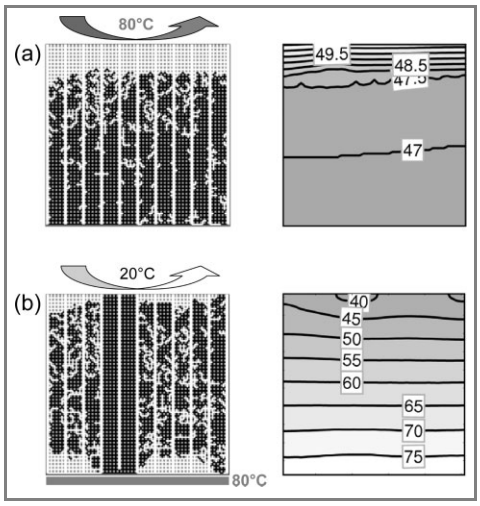

Figure 12. Phase patterns and temperature fields (values in °C) during non-isothermal drying of bimodal pore structure, for (a) convective heating and (b) contact heating (adapted from [21]).

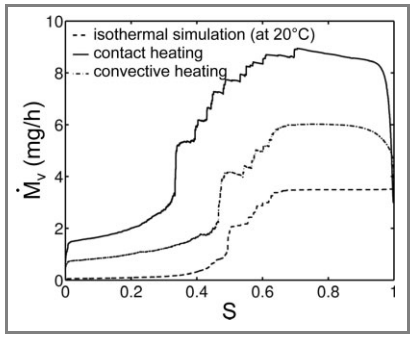

Figure 13. Evaporation rates during drying of a bimodal network with convective and contact heating as in Fig. 12 (adapted from [21]).

5 Macro-scale behaviors

For technical applications, it is important that the findings of pore-scale modeling can be used for macroscopic descriptions. The viscous-stabilized drying front offers a good example to illustrate how such up-scaling can be achieved. In Fig. 14, phase front and corresponding saturation profile are shown for a large network. Phenomena of invasion percolation can be appropriately described at a macroscopic level by scaling laws [25]. In this example, front width – either measured by its total extent L_f or by its standard deviation σ_f – scales with capillary number

$$Ca \propto \frac{v_w}{\sigma}\frac{\dot{M}_v}{\sigma_0} \qquad (4)$$

which measures the ratio of viscous to capillary effects and contains relevant liquid properties,

The non-isothermal model allows to study the influence of the heating mode on drying behavior.

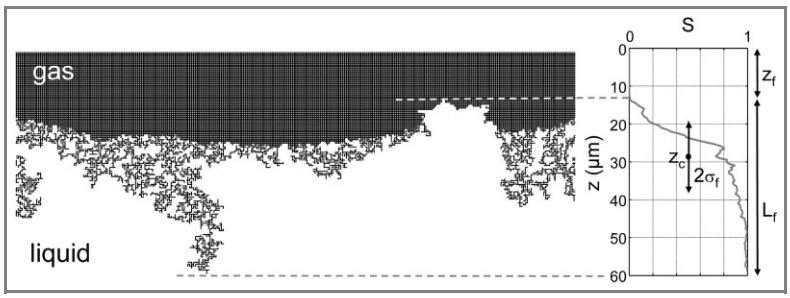

Figure 14. Viscous-stabilized drying front in a large pore network and saturation profile with definitions for description of front width and location.

drying rate $\dot{M}_v$ and width of the pore size distribution. As shown in Fig. 15, pore network simulations can be used to estimate the exponent in the scaling law for front width (in units of pore length)

$$\frac{L_f}{L} \propto Ca^{-\chi} \tag{5}$$

The negative sign of the exponent reflects the above-described widening of the front with decreasing drying rate. Additional analysis reveals that all saturation profiles are similar and can be approximated by one dimensionless profile. Furthermore, drying rate depends on the position of the evaporation front, approximated by z_f, so that a macroscopic model for saturation profiles and drying rates can be developed [26]. The same procedure can be applied to 3D networks with different empirical model parameters.

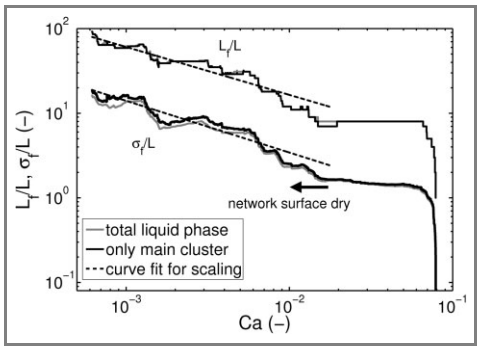

Figure 15. Scaling of front width with capillary number for the example of Fig. 14.

An alternative link to macroscopic modeling is seen in the parameterization of continuous models. The effective parameters, e.g., liquid permeability, are determined by numerical experiments on partially saturated pore network. In drying technology, the authors are currently developing this approach; some pioneering work can already be found in literature [3, 7].

6 Drying of composite materials

Up to here, all simulated pore structures have been homogeneous at the macroscopic scale. But network models are more versatile than this, and composite materials represent another interesting application of this tool. Such composites may, e.g., consist of a small-pore and a large-pore material. In the following, three different spatial arrangements of the two materials with respect to the evaporating surface of the network are considered. Respective phase distributions are shown in Fig. 16; the corresponding drying rate curves are plotted in Fig. 17.

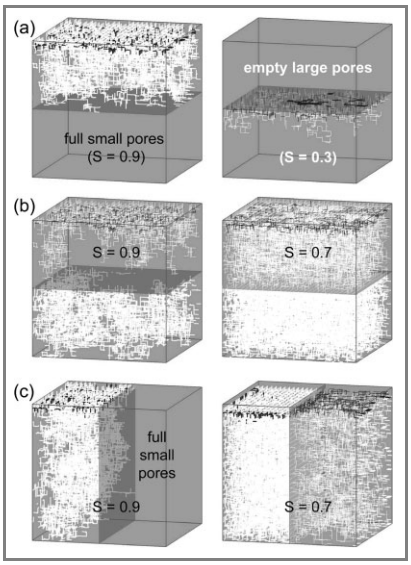

Figure 16. Phase patterns of drying composite pore networks: (a) large-pore region on top, (b) small-pore region on top and (c) both regions side by side.

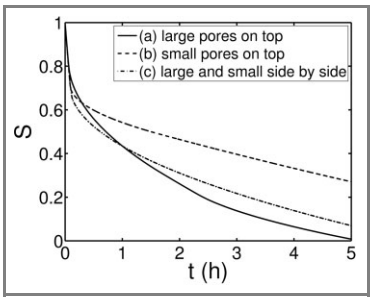

Figure 17. Drying curves – as total saturation over time – for the three spatial arrangements of composite material in Fig. 16.

If the large-pore region is on top of the small-pore region (Fig. 16a), capillary pumping ensures that the small pores stay saturated until all large pores have been emptied. The network surface dries out completely at a high saturation ($S = 0.77$). In contrast, capillary

pumping is more effective, if the small-pore region is on top (Fig. 16b). After breakthrough of the gas to the lower large-pore region, this one is evacuated until liquid connectivity is lost. Then, more small pores are emptied until the whole liquid phase has split up into small clusters and the network surface dries out (at $S < 0.7$).

For the side-by-side arrangement of the two regions (Fig. 16c), the large-pore region and the small-pore region are successively emptied down to their respective loss of liquid discontinuity. Then, the evaporation front recedes into the network (at $S < 0.7$).

Besides capillarity, vapor diffusion through dry network regions affects the overall drying behavior. Assuming a uniform pore length (i.e., lattice constant), the small-pore region has a lower porosity (0.094) than the large-pore region (0.212). Consequently, long-time drying rates are lower if vapor has to diffuse through the small-pore region, as in Fig. 16b. In turn, large pores permit higher drying rates in the falling rate period. Therefore, the first configuration (Fig. 16a) has the shortest overall drying time, even though its initial drying rates are lowest, and the second configuration takes the longest time to dry out completely (see Fig. 17). The third arrangement combines high initial drying rates with a relatively short overall drying time.

Recent literature work on 2D networks [27] nicely confirms the simulated phase patterns by experiments on small networks; it also addresses the role of non-uniform porosity.

7 Drying mechanics

In the above Sections, the focus has been on drying kinetics; the network model has been used to simulate phase distributions and drying rates for a range of pore structures. But structure is not necessarily independent of drying; instead, drying can modify or destroy the pore structure by capillary forces.

Recently, a network approach has been proposed to study such drying mechanics [28]. For rather dense particle aggregates, both solid phase and pore space can be represented by complementary networks, as illustrated in Fig. 18. Phase distributions are simulated by a pore network model; the capillary forces on the particles of the agglomerate are computed from pore saturations; and the mechanical response of the network of bonded particles to this mechanical load is obtained by the discrete element method. Cracks and shrinkage have already been simulated with a basic model version for cubic networks. An extension to irregular networks is currently being developed.

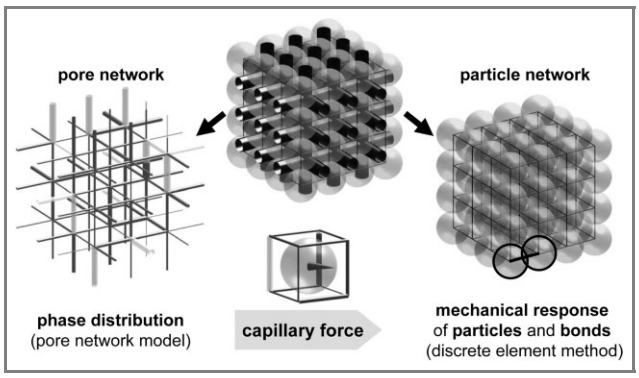

Figure 18. Complementary networks of pores and particles to simulate the mechanical effects of capillary forces.

An example of the capillary force distribution during non-viscous drying is given in Fig. 19: for every particle, a cone represents direction and magnitude of the local capillary force. Depending on drying conditions and strength of the inter-particle bonds, different crack patterns are obtained. Fig. 20 shows the final distribution of normal and shear cracks as a function of bond strength. In the first model version, capillary forces merely depend on pore saturation and hence are truly local

Structure is not necessarily independent of drying; instead, drying can modify or destroy the pore structure by capillary forces.

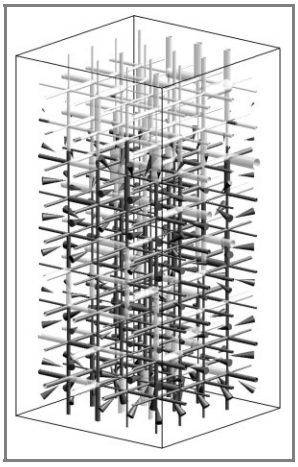

Figure 19. Distribution of capillary forces resulting from the saturation of individual pores in a partially dried network.

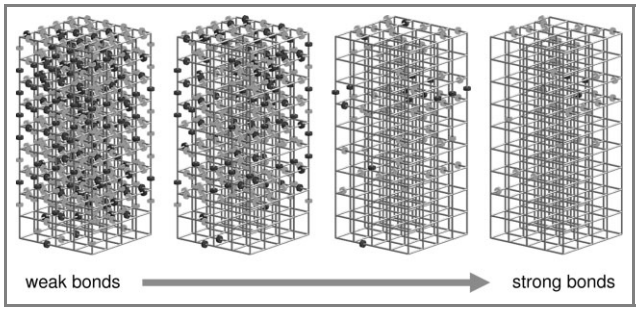

Figure 20. Distribution of cracks (dark disk: normal, light disk: shear) in the dried network different values of bond strength.

effects; if macroscopic tensions – resulting from gradients in liquid pressure – are included, then propagating cracks are expected rather than isolated micro cracks.

With modern experimental devices such as atomic force microscope, it will soon be possible to parameterize the laws for particle contacts and bonds so that the model can become predictive.

8 Summary

Pore network modeling has been presented as a novel, fascinating opportunity for engineering, providing a virtual micro-lab to study processes involving partially saturated porous media. The approach establishes a link between structural properties of a product and its process behavior; it can connect product quality and process optimization; it brings together chemical and material engineering.

Thomas Metzger, born 1972 in Berlin, studied Physics at Tübingen University, including a one-year stay at University of Birmingham, United Kingdom. In 2002, he obtained his doctoral degree at Institut National Polytechnique de Lorraine in Nancy, France, with an experimental work on thermal dispersion in porous media. Moving on to Otto von Guericke University Magdeburg, he started his research on drying of solids investigating inner-particle transport phenomena and the role of pore structure. In 2007, he became Juniorprofessor for Pore Network Models in Process Engineering with a focus on capillary effects in partially saturated porous materials.

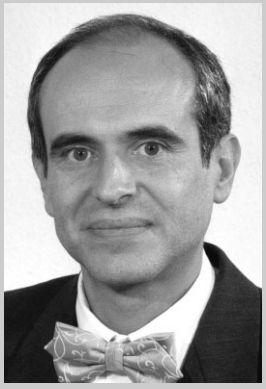

Evangelos Tsotsas was born in 1959 in Thessaloniki, Greece. After his graduation in Mechanical Engineering at Aristotle University of Thessaloniki in 1981, he became research assistant at Karlsruhe University. He obtained his doctoral degree in the field of vacuum contact drying in 1985 and completed his habilitation on heat and mass transfer in packed beds with fluid flow in 1990. From 1991 until 1994, he was responsible as senior process specialist at Dow Deutschland for drying technology and fluidization technology. Since 1994, he holds the Chair of Thermal Process Engineering at Otto von Guericke University Magdeburg with a focus on particle systems and porous solids. He was chairman of the EFCE Working Party on Drying from 2004 to 2008 and presides over the ProcessNet committee on Drying since 2005.

Evidently, network modeling is not limited to the presented process example of drying, but suited for many other processes. The engineer's challenge is to appropriately extend the model to the respective physical mechanisms and to the involved pore structures.

Besides theoretical developments, modern experimental techniques such as X-ray tomography will allow pore-scale validation and parameterization of the model. A further challenge is seen in handling and evaluating the huge data sets of 3D simulations. Model reductions, by approximate algorithmic rules, and up-scaling techniques have to be elaborated to make the simulation tool fully available for technical applications in product and process design.

Acknowledgements

Several PhD students have been member of the pore network modeling team in Magdeburg, and every one of them has contributed to the development of the new simulation tool. The authors would like to express their thanks to Dr.-Ing. Anton Irawan (doctoral degree in 2006 [29]), Dr.-Ing. Vikranth K. Surasani (doctoral degree in 2008 [30]), M.Sc. Abdolreza Kharaghani (doctoral thesis submitted in 2010 [31], M.Sc. Cagda Akdag and Dipl.-Ing. Nicole Vorhauer.

Jun.-Prof. T. Metzger
(thomas.metzger@ovgu.de),
Prof. E. Tsotsas,
Thermal Process Engineering, Otto von Guericke University, P.O. 4120, 39016 Magdeburg, Germany.

Literature

[1] M. Sahimi, B. D. Hughes, L. E. Scriven, H. Ted Davis, *Chem. Eng. Sci.* **1986**, *41*, 2103.
[2] R. Lenormand, E. Touboul, C. Zarcone, *J. Fluid Mech.* **1988**, *189*, 165.
[3] S. C. Nowicki, H. T. Davis, L. E. Scriven, *Drying Technol.* **1992**, *10*, 926.
[4] M. Prat, *Int. J. Multiphase Flow* **1993**, *19*, 691.
[5] J. B. Laurindo, M. Prat, *Chem. Eng. Sci.* **1996**, *51*, 5171.
[6] A. G. Yiotis et al., *Transp. Porous Med.* **2005**, *58*, 63.
[7] L. A. Segura, P. G. Toledo, *Drying Technol.* **2005**, *23*, 2007.
[8] T. Metzger, A. Irawan, E. Tsotsas, *AIChE J* **2007**, *53*, 3029.
[9] J.-G. Salin, *Drying Technol.* **2008**, *26*, 560.
[10] T. Metzger, E. Tsotsas, M. Prat, *Pore-network models*, Ch. 2 in *Modern Drying Technology*, Vol. 1

(Eds.: E. Tsotsas, A. S. Mujumdar), Wiley-VCH, Weinheim, **2007**.
[11] A. Yiotis et al., *Adv. Water Resour.* **2001**, *24*, 439.
[12] M. Prat, *Int. J. Heat Mass Transfer* **2007**, *50*, 1455.
[13] A. Irawan, T. Metzger, E. Tsotsas, in *Proc. Of the 7th World Congress of Chemical Engineering*, Glasgow, Scotland, July **2005**.
[14] T. Metzger, A. Irawan, E. Tsotsas, *Physica A* **2006**, *363*, 558.
[15] Y. Le Bray, M. Prat, *Int. J. Heat Mass Transfer* **1999**, *42*, 4207.
[16] A. Irawan, T. Metzger, E. Tsotsas, *Drying Technol.* **2007**, *25*, 47.
[17] F. Debaste, *Modélisation de l'évaporation en milieu poreux: développement de modèles fondamentaux et appliqués*, Dissertation, Université Libre de Bruxelles, **2008**.
[18] T. Metzger, E. Tsotsas, *Chem. Eng. Res. Des.* **2008**, *86*, 739.
[19] T. M. Shaw, *Phys. Rev. Lett.* **1987**, *59*, 1671.
[20] V. K. Surasani, T. Metzger, E. Tsotsas, *Int. J. Heat Mass Transfer* **2008**, *51*, 2506.
[21] V. K. Surasani, T. Metzger, E. Tsotsas, *Chem. Eng. Sci.* **2008**, *63*, 5218.
[22] V. K. Surasani, T. Metzger, E. Tsotsas, to appear in *Drying Technol.* **2010**, *28*. DOI: 10.1080/07373931003788676
[23] F. Plourde, M. Prat, *Int. J. Heat Mass Transfer* **2003**, *46*, 1293.
[24] H. P. Huinink, L. Pel, M. A. J. Michels, M. Prat, *Eur. Physical J.* **2002**, *E9*, 487.
[25] M. Prat, F. Bouleux, *Phys. Rev.* **1999**, *E60*, 5647.
[26] N. Vorhauer, T. Metzger, E. Tsotsas, to appear in *Drying Technol.* **2010**, *28*.
[27] K. M. Pillai, M. Prat, M. Marcoux, *Int. J. Heat Mass Transfer* **2009**, *52*, 1643.
[28] A. Kharaghani, T. Metzger, E. Tsotsas, in *Proc. of 16th International Drying Symposium*, Hyderabad, India, Now. **2008**.
[29] A. Irawan, Isothermal drying of pore networks: influence of pore structure on drying kinetics, *Dissertation*, Otto von Guericke University Magdeburg, **2006**.
[30] V. K. Surasani, Non-isothermal network model for drying of porous media, *Dissertation*, Otto von Guericke University Magdeburg, **2008**.
[31] A. Kharaghani, Irregular pore networks and mechanical effects during drying of porous media, *Dissertation*, Otto von Guericke University Magdeburg, **2010**.

A Proposal for Discrete Modeling of Mechanical Effects During Drying, Combining Pore Networks With DEM

Abdolreza Kharaghani, Thomas Metzger, and Evangelos Tsotsas
Thermal Process Engineering, Otto von Guericke University, P.O. 4120, 39016 Magdeburg, Germany

DOI 10.1002/aic.12318
Published online July 13, 2010 in Wiley Online Library (wileyonlinelibrary.com).

A discrete modeling approach is introduced to investigate the influence of liquid phase distributions on damage and deformation of particle aggregates during convective drying. The approach is illustrated on a simple 3D aggregate structure, in which monosized spherical particles are arranged in a cubic packing and bonded together at their contacts; the mechanical behavior of this aggregate is simulated by discrete element method (DEM). Liquid phase distributions in the void space are obtained from drying simulations for a pore network. In a one-way coupling approach, capillary forces are computed over time from the filling state of pores and applied as loads on each particle in DEM. A nonlinear bond model is used to compute interparticular forces. Simulations are conducted for various drying conditions and for aggregates with different mechanical properties. Microcracks induced by bond breakage are observed in stiff material, whereas soft material tends to shrink reversibly without damage. © 2010 American Institute of Chemical Engineers *AIChE J,* 57: 872–885, 2011
Keywords: pore network modeling, discrete element method, multiphase, microcracks, shrinkage

Introduction

Drying is undeniably a complex process involving various transport processes, such as two-phase flow with liquid-vapor phase change, which are accompanied by undesired mechanical effects. These effects—widely encountered, but poorly understood—are a major problem in drying industry and present a challenge for modeling and simulation of drying. Therefore, a profound study is essential to learn about the fundamental reasons of these effects and to find ways to control them, to analyze them, and to develop, as the result of such analysis, methods and conditions of drying, which would lead not only to a preservation of the quality of the dried material but also to its improvement. It is known that convective-drying induced mechanical effects mainly depend upon moisture distribution, which is influenced by drying conditions and the porous material itself. As major aspects, a theoretical investigation should consider structural and mechanical properties of the solid as well as the mechanisms controlling liquid flow (mainly capillary and viscous effects) that depend on process parameters.

Several approaches in this sense have been taken in literature. Lewis et al.[1] coupled classical heat and mass transfer equations with an elastic constitutive model to find drying-induced stresses in capillary porous bodies. A thermomechanical approach to shrinkage and cracking phenomena in drying, which is based on thermodynamics of irreversible processes and continuum mechanics of porous media, was proposed by Kowalski.[2] X-ray microtomography was used to monitor shrinkage and cracks of drying organic gels under different drying conditions.[3] Recently, simulated drying stresses were compared with measured tensile strength to

Correspondence concerning this article should be addressed to T. Metzger at thomas.metzger@ovgu.de.

give a criterion for crack initiation.[4] In this work, the first crack appears at the point where the strength curve crosses the simulated tensile stress curve. Different strategies are used in literature[5] to model shrinkage during drying. In these works, the partially saturated porous medium is treated as a fictitious continuum and coupling between the transfer processes and mechanical interactions are considered as follows. First, fundamental balance equations together with phenomenological rate equations for heat and mass transfer—involving effective parameters, which themselves depend on one or more physically independent variables—are solved by use of traditional numerical techniques to obtain time-dependent temperature and moisture content distributions. Then, depending on the drying period and material itself, rheological behaviors, such as elasticity, viscoelasticity, and plasticity, are applied to model mechanical effects that appear in drying. Despite the strengths and extensive applications of these models, they are phenomenological and primarily concerned with mathematical modeling of the observed phenomena without detailed attention to pore-scale physics, such as transport phenomena and direct interactions between solid and liquid phase.

As a more fundamental approach to drying, pore network models (PNMs) have more recently been adopted by scientists. In these models, the porous medium is represented by a network of interconnected pores, which have a prescribed geometry but are random in their size; and pore-scale transport phenomena for each phase are described explicitly. This ensures that effects are not lost or masked during up-scaling to the product scale. So far, investigations with PNMs have predominately considered the influence of physical effects and structural properties on drying kinetics. Concerning physical effects, viscosity is either completely neglected[6] or accounted for in liquid phase[7] or in both liquid and gas phase.[8] A stabilization of the drying front has been observed by considering gravity and liquid viscosity.[9,10] Further model extensions include film effects[11,12] and heat transfer.[13–15] Apart from physical effects, some studies focus on the influence of structural properties, such as pore shape[12,16] and pore size distribution (mono- and bimodal), spatial correlation of pore size, and coordination number of the regular network.[17]

Few notable works have been published on the understanding of mechanical effects arising during drying from pore level effects. Brinker and Scherer[18] have done comprehensive investigations on the driving forces causing shrinkage and cracks during drying of gels. Surface deformation of solids has also been analyzed as due to capillary forces.[19] Recently, numerical drying curves have been studied to see the influence of shrinkage for a network of pores whose radii are reduced with increasing capillary pressure.[20] In the above-mentioned work, driving force for cracking and shrinkage is understood, but never modeled at the microlevel. This work sets out to explore these effects by means of discrete networks of pores and particles, respectively.

In spite of significant advances in pore network drying models, there are still open issues. For instance, these network models do not include solid phase geometry explicitly. Therefore, local effects on solid phase (such as cracks) can not be described. In principle, these effects are due to capillary forces, which induce stresses on the solid phase causing displacement. This work sets out to explicitly model the solid phase in the case that the porous material can be reasonably represented by a network of spherical particles, such as particle aggregates obtained by sintering, sol-gel processing, or agglomeration. Capillary forces obtained from a PNM are applied to these particles, and their mechanical response is computed by discrete element method (DEM).

DEM is an alternative to the classical continuum mechanics approach, which has originally been developed for rock mechanics. Unlike traditional numerical methods, this mesh-free technique can treat the solid phase as an assembly of discrete elements, starting with basic constitutive laws at interparticle contacts and providing microscopic interactions of the particles and their contacts under different loading conditions. Indeed, such microscopic information not only can be significant for a better understanding of the phenomenon but also opens up possibilities for microstructural material design. However, computational requirements in DEM simulations are inevitably demanding, as the number of equations governing the system depends on the number of particles used to capture the microstructure, so that simulations are usually carried out on a limited number of spherical particles (instead of more complex particle geometries).

Initially, DEM has been widely used to model disaggregated media[21] that occur naturally, such as sand, rocks, and rock-falls. Recent work includes fundamental studies on breakage processes and strength of individual dry agglomerates[22,23] proving that DEM can be successfully applied to particle systems with solid bonds to describe their experimental cracking and breakage behavior. Furthermore, wet granular materials have been modeled,[24,25] in which capillary force has been expressed as a function of interparticle distance, water bridge volume, contact angle, and surface tension. To date little report of DEM application on drying has been found in literature.[26]

In this article, we propose a discrete approach to model and simulate the mechanical effects as a result of liquid phase evolution during convective drying of porous materials. The scope of this work is to explain the new simulation tool, demonstrate that it can describe relevant phenomena during drying at a qualitative level, and—on a simple example—illustrate what chances the numerical results offer regarding a microscale analysis of drying. Only future work will allow the model to become predictive, both by model development and parameterization in well-defined experiments.

The several assumptions that are made in this pioneering work have to be seen in this light that they are not inherent to the modeling approach, but can be disposed of by model extensions. Specifically, the considered particle aggregates are of cubic arrangement, for which the pore network is also cubic and local capillary forces are easily computed. Pore size, however, needs to be randomized to obtain the typical capillary effects. The generalization to irregular aggregate structures is possible; then, the pore network can be obtained, for example, by the use of a Voronoi method,[27] allowing for a natural computation of pore sizes and yielding a complementary pore network in a strict sense. Furthermore, heat transfer is not modeled, and macroscopic stresses because of liquid pressure gradients are not yet accounted for; both effects can be included as has been done for pure pore network modeling.

Supporting the isothermal model assumption, it shall be stressed that mechanical effects induced by moisture removal

are typically one or two orders of magnitude larger than effects solely caused by thermal expansion of the drying material.[2] Furthermore, temperature gradients in the liquid-filled pore regions are usually small for convective drying so that thermal effects on the phase distributions can be neglected.[13–15]

First, the pore network drying model of Prat, which has recently been extended concerning geometrical and physical aspects,[28] is recalled and governing structural and mass transport rules are paraphrased. Then, the DEM is briefly introduced and its assumptions and limitations are discussed. Further, the porous structure is encoded into discrete phases using pore network and DEM approaches. On this basis, a one-way coupling of pore and particle networks is introduced by describing capillary forces as a function of pore saturations. The model is consecutively applied to particle aggregates under different drying conditions. Two limiting cases are considered that can be interpreted as (1) slow and fast drying or as (2) two pore liquids with very different ratios of surface tension to viscosity. Simulation of the two cases leads to different capillary force distributions in the particle network. The respective mechanical response is captured by tracking contact forces and, for stiff aggregates, simulating and analyzing the resulting cracks. The influence of material properties on cracks formation is illustrated. For specific material properties, reversible shrinkage without cracks is obtained as observed experimentally as spring-back during drying of certain gels. We end with a summary of the main findings and mention potential works for the future.

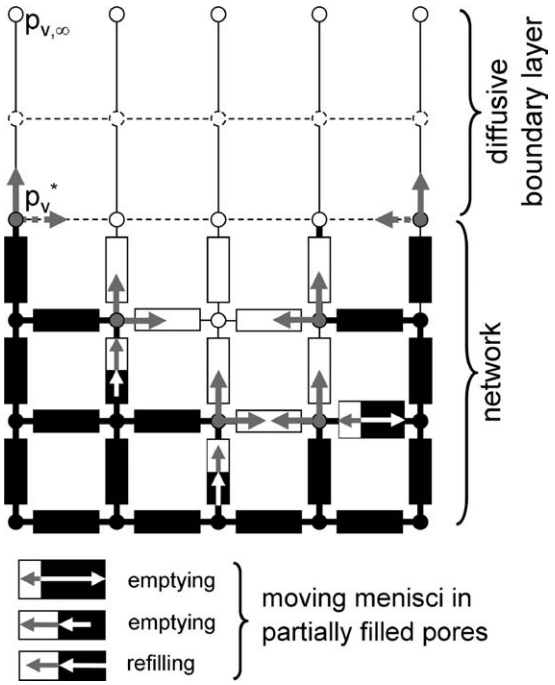

Figure 1. Partially saturated pore network including diffusive boundary layer.

Liquid pores and nodes are in black; gas ones in white; gray nodes are at saturation vapor pressure. Vapor diffusion is shown as gray arrows; its boundary conditions are illustrated. For partially filled pores, liquid flow is shown as white arrows.

Description of Pore Network Drying Model

The PNM is a modern discrete approach for the study of transport phenomena in porous media in general and of drying in particular. In this approach, the complicated pore space geometry is conceptualized by a network of nodes (standard is 2D square and 3D cubic), which are interconnected by cylindrical pores. Transport phenomena are described by using some local rules straightly at the pore level. The PNM used in our study was initiated in pioneering works by Prat, who elucidated the drying phenomenon as an invasion percolation driven by evaporation. In this work, we recall the isothermal PNM, which is based on the following elements and rules.

Data structure

The data structure describes the connectivity of the (cylindrical) pores and nodes in the network and its boundary layer. The conceptual model of a pore network is depicted in Figure 1. The network consists of pores of uniform length L, the radii r_{ij} of which are randomly assigned according to a probability density function; the saturation states of pores and nodes evolve during drying.

Mass transfer mechanisms

Mass transfer in the network is controlled by vapor diffusion in the gas-filled region and liquid flow in the liquid-filled part of the network by taking into account the following assumptions. Liquid films and adsorption are not modeled; porous media are considered as capillary with only free water and perfect wetting. Gravity deliberately is set to zero but could be included if larger pores and large objects shall be studied; and viscosity in gas phase is not modeled (reasonable for moderate drying conditions) so that gas pressure is constant. Both Kelvin and Knudsen effects are neglected. Initially, the network is completely saturated with water. Its top surface is open for evaporation, however, the bottom is closed and the other surfaces are impervious (see Figure 1). To compute the vapor diffusion, quasisteady balances for mass flow rates (in kg/s) are set up for any gas pore i by

$$\sum_j \dot{\mathrm{M}}_{v,ij} = \sum_j A_{ij} \frac{\delta}{L} \frac{p_g \tilde{\mathrm{M}}_v}{\tilde{R}T} \cdot \ln\left(\frac{p_g - p_{v,i}}{p_g - p_{v,j}}\right) = 0 \qquad (1)$$

(regardless of its position in the network or in the boundary layer) where L is distance between nodes, A_{ij} exchange area ($\pi {r_{ij}}^2$ for network, L^2 for boundary layer), δ vapor diffusivity, $\tilde{\mathrm{M}}_v$ molar vapor mass, $\tilde{\mathrm{R}}$ universal gas constant, p_g gas pressure, T temperature (in K) and $p_{v,i}$ vapor pressure (in Pa). The system of Eq. 1 is solved for unknown vapor pressures by applying the vapor pressure of drying air at the top edge of the boundary layer and saturation vapor pressure next to the gas-filled interface. In the liquid domain, if viscosity can be neglected, the following algorithm is implemented. (1) Every liquid cluster is identified. (2) According to the invasion percolation rule, the pore connected to the gas-invaded region, which has lowest capillary pressure is identified for each cluster. (3) The evaporation flux at the boundary of each

cluster is computed. (4) For each cluster, the mass loss corresponding to this evaporation flux is assigned to the invasion pore. (5) The pore of all clusters that empties first sets the time step as liquid connectivity as well as the set of Eq. 1 for vapor diffusion may change. (6) The phase distribution within the network is updated and the above-described procedure is repeated.

To compute liquid flow rates (in kg/s) if viscosity cannot be neglected, the mass balance in any liquid node is expressed by

$$\sum_j \dot{\mathrm{M}}_{w,ij} = \sum_j \frac{\pi r_{ij}^4}{8 v_w L_{ij}} \left(p_{w,i} - p_{w,j}\right) = 0 \tag{2}$$

where v_w is kinematic viscosity of water (in m^2/s) and L_{ij} liquid-filled length of pore. The linear system of Eq. 2 must be solved for unknown liquid pressures $p_{w,i}$. Boundary conditions to Eq. 2 are given at the liquid-gas interface. For a stationary meniscus, that is, where capillary pressure can provide liquid water at the local evaporation rate, the second type boundary condition $\dot{M}_{w,ij} = \dot{M}_{v,ij}$ is applied. For a moving meniscus, that is, where evaporation takes place at a higher rate than capillary flow (or for any partially filled pore), the boundary condition of first kind $p_{w,j} = p_g - 2\sigma/r_{ij}$ (with surface tension σ) is used. As boundary conditions on the flow problem depend on meniscus states themselves, an iterative procedure is used to find the states of the menisci.[10] For correct boundary conditions, the motion of menisci is obtained as the difference between evaporation flow rate and liquid flow rate. In the viscous case, several menisci per cluster may move. Depending on meniscus motion, pores may empty and partially saturated pores may refill again. Time stepping is imposed by the complete emptying (or refilling) of a meniscus pore; then, vapor and liquid flow problems must be solved for new boundary conditions.

DEM Formulation

The DEM is a numerical technique to study the mechanical behavior of complex systems, not only homogenous but also heterogeneous (in particle and bond properties), of discrete bodies or particles. They are mostly modeled as circular disks (2D) or spheres (3D) though they can also be arbitrarily shaped. The interaction between particles is described by applying the equations of motion to each particle, and a contact law to each inter-particle contact. The DEM used in this study was developed by Cundall,[29] who restricted himself to modeling of spherical particles, so that the numerical simulation is based on the following assumptions and rules:

- All particles are treated as undeformable balls.
- In (elastic) contacts, shape deformation of particles is not described explicitly, but represented by a virtual overlap (soft-contact approach).
- Overlap distance is related to contact force via the contact law; it is small as compared to particle size.

Linear contact law

The contact law relates the relative displacement of two particles at a contact to the contact force acting on them. Figure 2 shows a contact model by two particles at positions $\mathbf{x}_i$ and $\mathbf{x}_j$, with radii R_i and R_j, respectively. The unit normal vector $\mathbf{n}_{ij}$ (the suffix denotes the contact between particles i and j) is defined by

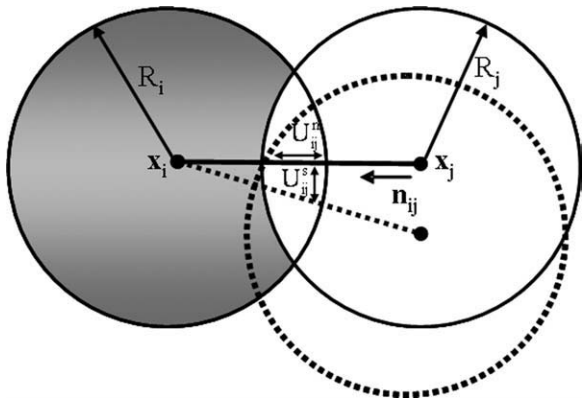

Figure 2. Interaction between two particles.

$$\mathbf{n}_{ij} = \frac{\mathbf{x}_j - \mathbf{x}_i}{d_{ij}}, \; d_{ij} = \left|\mathbf{x}_j - \mathbf{x}_i\right|. \tag{3}$$

The contact force vector $\mathbf{F}_{ij}$ can be resolved into normal and shear components with respect to the contact plane as

$$\mathbf{F}_{ij} = \mathbf{F}_{ij}^n + \mathbf{F}_{ij}^s. \tag{4}$$

The normal contact force vector is computed by

$$\mathbf{F}_{ij}^n = \mathrm{F}_{ij}^n \mathbf{n}_{ij} = \mathrm{K}_{ij}^n U_{ij}^n \mathbf{n}_{ij} \tag{5}$$

where K_{ij}^n is normal contact stiffness (in N/m) and $\mathrm{U}_{ij}^n = \mathrm{R}_i + \mathrm{R}_j - \mathrm{d}_{ij}$ normal overlap distance. The shear contact force is computed in an incremental fashion. When the contact is formed, the total shear contact force is initialized to zero. Each subsequent relative shear-displacement increment (resulting from a shear contact velocity $\mathbf{V}_{ij}^s$ for the numerical time step Δt)

$$\Delta \mathbf{U}_{ij}^s = \mathbf{V}_{ij}^s \Delta t \tag{6}$$

results in an increment of shear force

$$\Delta \mathbf{F}_{ij}^s = -\mathrm{K}_{ij}^s \Delta \mathbf{U}_{ij}^s \tag{7}$$

(with contact shear stiffness K_{ij}^s) that is added to the current value of contact shear force

$$\mathbf{F}_{ij}^s \leftarrow \mathbf{F}_{ij}^s + \Delta \mathbf{F}_{ij}^s. \tag{8}$$

To obtain realistic behavior and numerical stability, viscous damping needs to be added to the contact model.[21,30] Damping forces act in both normal and shear directions and are proportional to the respective contact velocities; the proportionality factor is $2\zeta\sqrt{\mathrm{K}_{ij} m_i m_j/(m_i + m_j)}$, where ζ is the damping ratio (see Table 2), m_i and m_j denote the particle masses and K_{ij} the contact stiffness.

It should be noted that for contacts between unbonded spherical particles, which experience small strain conditions and exclusively compressive stresses, the Hertz model is a more suitable contact law.[30] But, in the present case of

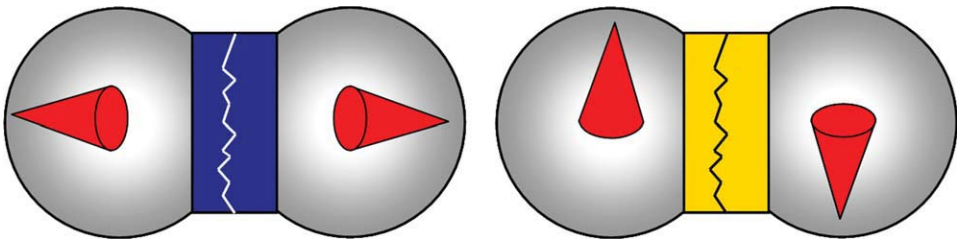

Figure 3. Schematic illustration of (external) forces on the particles (red cones) and resultant cracks of the parallel bond, normal (in dark blue) or shear (in yellow).

[Color figure can be viewed in the online issue, which is available at wileyonlinelibrary.com.]

bonded particles, the simple linear contact model is mostly used because it naturally incorporates tensile forces and is computationally efficient.[23,30]

Motion equations

The motion of a single particle is determined by the resultant force and moment vectors acting upon it. Particle motion can be divided into translational and rotational motion. For each particle, the equations of motion can be expressed as two vector equations, the first relating resultant force to the translational motion

$$m\ddot{\mathbf{x}} + \mathbf{F}^{\text{int}} = \mathbf{F}^{\text{ext}} \tag{9}$$

and the second resultant moment to rotational motion

$$\mathrm{I}\ddot{\boldsymbol{\theta}} + \mathbf{M}^{\text{int}} = \mathbf{M}^{\text{ext}} \tag{10}$$

Here, $\mathbf{x}$ and θ are translational and angular position vectors of the particle, respectively; the double dots denotes a second time derivative; and m and I are mass and moment of inertia, respectively (both scalar for spherical particle). $\mathbf{F}^{\text{int}}$ denotes internal forces at the particle contacts; $\mathbf{F}^{\text{ext}}$ stands for external forces, for example, gravitational force, and will be used for capillary forces from the fluid phase. $\mathbf{M}^{\text{int}}$ and $\mathbf{M}^{\text{ext}}$ are the internal and external moment (both in Nm) acting on the particle, respectively. In our case, $\mathbf{M}^{\text{ext}}$ is set to zero, no moment being induced by capillary forces.

Computing particle motion

In DEM calculation, one mechanical time step is as follows. First, particle positions and velocities are initialized. Once neighbors are determined, contacts between particles are identified (which is the most time-consuming procedure) and contact forces computed for touching particles. Then, particle forces and moments are updated including potential external forces and moments. The particle accelerations hence can be computed and the magnitudes of particle velocities and displacements can be integrated. These computations are adopted for each particle in every time step. If the external forces change, many such mechanical time steps are necessary to track the evolution of the particle system. Time-stepping is stopped when particles reach a mechanical equilibrium state. Concerning the present application of DEM to aggregates, one should keep in mind that particle displacements are typically very small, often corresponding to only a tiny fraction of particle diameter.

Bonding models

DEM allows proximate particles to be bonded together by using contact and parallel bond models.[30] The contact bond model extends the linear contact response to particle configurations with negative overlap. This is achieved by simple continuation of the response curve: the contact force is computed by (5) even for negative values of U_{ij}^{n}, up to a predefined maximum force $F_{ij}^{n,\max}$ beyond which the bond breaks and contact force is set to zero. This "breakage of the bond" is interpreted as a normal crack. In shear direction, if the magnitude of the contact force computed by (8) equals or exceeds a prescribed maximum shear contact force $F_{ij}^{s,\max}$, the bond breaks, and the contact force is set to the friction limit $F_{ij}^{s,\max} = \mu_{ij}|\mathbf{F}_{ij}^{n}|$, where μ_{ij} is the friction coefficient of the contact. We will use the contact bond model to describe shrinkage of soft material.

A parallel bond can be envisioned as a set of elastic springs uniformly distributed over a circular cross-section lying on the contact plane and centered at the contact. Unlike the contact bond, the parallel bond can be associated to a physical solid bridge between particles, as in a real aggregate. Parallel bonds establish an elastic interaction between particles that acts in parallel to the particle-based portion of the force-displacement behavior. Thus, the existence of a parallel bond does not totally prevent slip. Parallel bonds can transmit both force and moment between particles, whereas particles can transmit only force. Relative motion at a contact causes a force and a moment to develop within the bond as a result of the parallel bond stiffnesses (see Figure 3). The force and moment that act on the two bonded particles are related to the maximum normal and shear stresses acting within the bond. If either of these maximum stresses reaches the corresponding bond strength, that is, cracking threshold, the parallel bond breaks and its contributions to force and moment are no longer considered. We will use the parallel bond model to describe cracks in stiff material.

Model parameters

The physical meaning of the micromechanical properties in DEM, such as normal and shear particle stiffness, that is, K^{n} and K^{s}, is not yet completely understood. So far, two common strategies are used to estimate these crucial model

parameters[30]: For the general case of arbitrary packings of arbitrarily sized particles, model parameters are found by means of a calibration process, in which a particular instance of a model with a particular packing arrangement and set of model parameters is used to simulate a set of material tests (e.g., unconfined compression test, three-point bend test, Brazilian test, etc.). The model parameters are then chosen to reproduce the relevant material properties as measured in such tests. For simple packing arrangements, the relation between model parameters and commonly measured material properties is known a priori.[30] As an example, for a cubic array of spheres with radius R, the apparent Young's modulus can be expressed as $E = \frac{K^n}{4R}$. In this work, the goal has not been to find the micromechanical properties from own experiments; instead, we have used calibration results from literature where available, and known micro-macro relations otherwise.

Currently, a growing research activity can be observed to supply DEM models with parameters obtained from advanced microscale experiments, for example, atomic force microscopy or nanoindentation,[31,32] which directly investigate particle-particle interactions.

Coupling of Pore Network with DEM

Representation of porous structure

We have used the two aforementioned discrete approaches to describe the porous structure. The solid phase is represented by a cubic packing of monosized particles bonded at their contact points (see Figure 4a). Accordingly, void space is represented by a cubic network of cylindrical pores. The radii of these pores, however, have been randomized (with a small standard deviation) to produce the typical capillary effects. Therefore, the two networks are not complementary in a strict sense. Figure 4b shows a network that is partially saturated by a single-component liquid. (For better visualization of differences in pore radii, they are scaled exponentially in the graphical representation.) Throughout the article light gray space (inside pores) represents the air and vapor phase, and dark blue stands for liquid. All simulations start with networks fully saturated with water and drying from the top (at 20°C and atmospheric pressure).

Model coupling scheme

The coupling of the two models (see Figure 4c) is via capillary forces on the particles, which depend on liquid saturation in the pore network and thus change over time. For such a coupled simulation, we compute in a first pass the evolution of pore saturations in a given pore network and the capillary forces as described in the next section. These forces are stored over time in the capillary force protocol. In the second pass, the capillary forces are consecutively applied to the complementary particle network (with its given material properties) to compute the response using DEM. The coupling is one-way, and pore sizes are not updated with changing particle positions. However, for the considered stiff aggregates, the actual change in network geometry because of capillary forces can be neglected. More important than shrinkage are the exerted forces and the resulting cracks. (The case of soft aggregates that exhibit considerable shrinkage will be discussed later.)

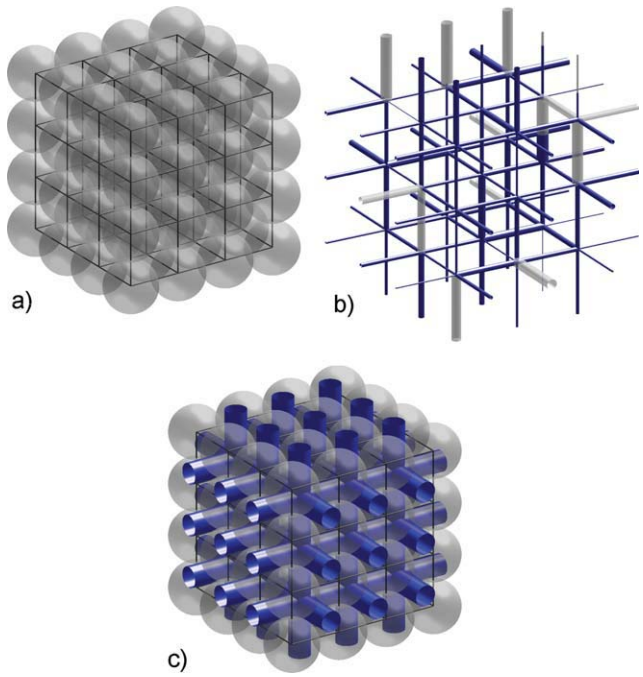

Figure 4. Model porous medium where (a) represents solid phase (bonds are represented as lines), (b) complementary pore network (liquid is plotted in dark blue, gas in light gray), and (c) both networks.

[Color figure can be viewed in the online issue, which is available at wileyonlinelibrary.com.]

As mass transfer is much slower than the mechanical response, for every drying time step, a new (and only slightly different) quasistatic equilibrium is approached in a limited number of mechanical DEM time steps (500); the equilibrium condition is checked by monitoring the mean unbalanced force on the particles, which must tend to zero. Interparticle bond breakage is recorded during simulations to obtain spatial and temporal information on cracks and contact forces.

Capillary forces on particle network

Capillary forces are commonly encountered in nature[33] during processes, such as evaporation and condensation, leading to the formation of liquid bridges with menisci at the liquid-gas interfaces. The surface curvature of the meniscus determines the negative Young–Laplace pressure inside the liquid. This pressure acts in the direction normal to the liquid-solid interface and pulls the solid together. Additionally, there is the direct action of the liquid surface tension, which pulls the contact line of meniscus and solid in the direction of the tangent to the liquid interface. In modeling of the capillary force, many expressions ranging from binary systems—for instance, plate-sphere and sphere-sphere[34]—to an arbitrarily shaped granular medium[35] (multiple systems) have already been developed.

In a cubic particle aggregate, every particle is bonded to six neighboring particles and surrounded by 12 pores. The mean radius of the (cylindrical) pores is computed to match the constrictions of pore space between two pore bodies (see

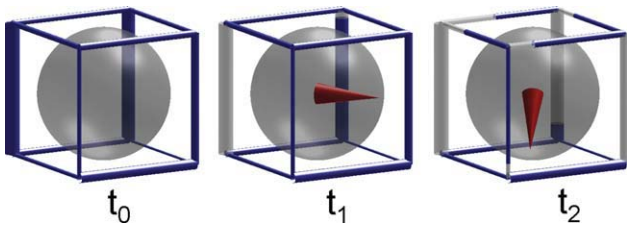

Figure 5. One selected cell of the network with a particle, its neighboring pores and resulting capillary force vector (red cone) as it evolves with pore saturations (liquid in dark blue) during drying.

[Color figure can be viewed in the online issue, which is available at wileyonlinelibrary.com.]

Figure 4c); and the radius of (circular) solid bridges is set to touch those pore cylinders. Therefore, solid phase, that is, primary particles plus solid bridges, and void space are to a certain extent complementary. (Of course, the widening of pores on either side of a constriction is not modeled; furthermore, there is an overlap of the cylindrical pores at the nodes.) The described geometry of pore space justifies that liquid bridges are not modeled because they cannot exist between two neighboring particles, the corresponding space being occupied by solid. Consequently, liquid is considered to be located in the cylindrical pores. However, liquid films[11,12] and—if bonds are not solid—liquid bridges might be subject to future analysis.

Assuming perfect wetting, the capillary force on the particle depicted in Figure 5 depends on effective wet area, A_w, that is, the projection of the wetted area onto a plane perpendicular to the local capillary force, and capillary pressure, $P_c = 2\sigma/r$, in full pores. The mechanical moment that may result from the contribution of the contact line is not considered here. To approximate the capillary force from pore network geometry and pore saturations, we use the following approach. The contributions of all twelve neighboring pores are summed up, where each pore's contribution is a vector directed from particle centre to pore centre (defined as the centre of mass of the full cylindrical pore). For the sake of simplicity, we postulate wet area fractions to be proportional to pore saturations S_j. (Specifically, variations in pore size or capillary pressure are not accounted for.) Thus, for the time-dependent capillary force on each particle, we obtain

$$\mathbf{F}_c(\mathbf{x}_p, t) \propto \sum_{j=1}^{12} S_j(t) \frac{\mathbf{x}_j - \mathbf{x}_p}{|\mathbf{x}_j - \mathbf{x}_p|} \tag{11}$$

where $\mathbf{x}_p$ and $\mathbf{x}_j$ are coordinates of particle centre and pore centers, respectively. In subsequent simulations, we have chosen the proportionality factor in (11) such that capillary pressure in a given network assumes a realistic value and $\mathbf{F}_c$ has the unit of a force.

Evolution of capillary forces during drying

Dynamic simulations are run to see the evolution of capillary forces during drying. In doing so, the aforesaid drying model is applied to the same pore network to investigate the role of liquid phase distributions for mechanical load onto the material. Previous work has shown that phase patterns mainly depend on the relative importance of capillarity and liquid viscosity.[36] Here, the two limiting cases are considered:

1. Liquid viscosity is considered as negligible (for capillary pumping). It must be stressed that this is not only an idealization for liquids with low viscosity but also—and mainly—an approximation of the case that pores are sufficiently large and/or drying rates rather low, so that capillary liquid flow is not affected by friction.
2. Pore liquid is considered as immobile. This case is intended to represent high drying rates and/or drying of small pores, for which viscous effects largely suppress capillary flow. And it can also describe highly viscous liquids such as binder solutions.

Figure 6 shows the respective drying rate curves in dimensionless form. As we are interested in observing the capillary force evolution in the whole system, we generated relatively small networks ($5 \times 5 \times 10$) with particle diameter (and pore length) 500 nm. The boundary layer is 5 μm thin, corresponding to a mass transfer coefficient of 5.1 m/s. Pore radius is normally distributed with 103 nm mean and standard deviation 1 nm. (For the studied system, typical capillary pressure is of the order of 1.4 MPa, and net capillary forces as shown in Figure 5 are in the range of 0.35 μN.) The width of pore size distribution determines the ratio of capillary to viscous effects and therefore plays no major role in the two limiting cases. For drying conditions between the two discussed limits, intermediate behavior is observed as shown in Figure 6 for the case of water. Pore network saturations and capillary forces during the drying process are depicted in Figure 7 for negligible liquid viscosity, whereas the result of the immobile water simulation is presented in Figure 8.

Discussing the capillary force evolution and starting with the nonviscous case, one can see from Figure 7a that in the fully saturated network, capillary forces appear on the top surface as well as on the other surfaces (on which empty

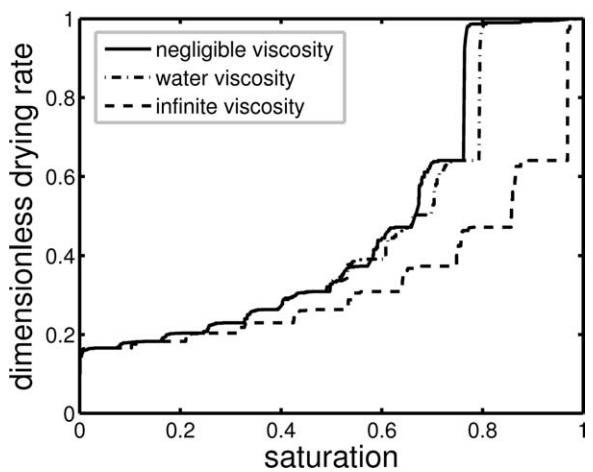

Figure 6. Normalized drying rate vs. network saturation for the simulations depicted in Figures 7 and 8, as well as for the case of water viscosity.

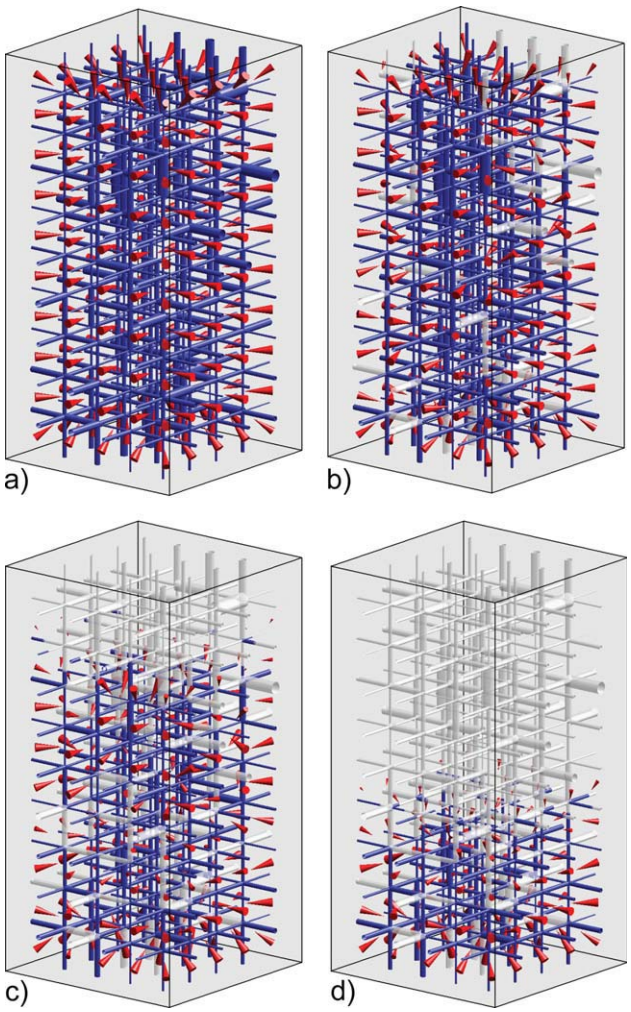

Figure 7. Evolution of capillary forces for negligible liquid viscosity at (a) full saturation and at network saturations, (b) 0.9, (c) 0.6, and (d) 0.3; gray cylinders represent empty pores, and dark blue is for liquid; capillary forces are presented by red cones, and cone size scales with force magnitude.

The network is subjected to evaporation at the top. (For better visualization of differences in pore radii, they are scaled exponentially). [Color figure can be viewed in the online issue, which is available at wileyonlinelibrary.com.]

pores have been imposed). In this regime, the compressive capillary forces are symmetric and the net capillary force on inner particles is zero. As evaporation continues, the liquid phase splits up into small disconnected clusters (Figures 7b, c). Accordingly, capillary forces get less organized such that they are still compressive for the individual clusters whereas, at the local level, tension forces can develop. Globally, capillary forces decline downwards and eventually vanish at the bottom of the network by the end of drying. However, in the high viscosity limit, liquid stays in a single cluster and a sharp drying front propagates through the network, accompanied by a capillary force front that keeps the wet region under compression (Figure 8); therefore, the force gradient in this case is rather significant. At the bottom of the network, the local capillary forces stay constant until this region eventually dries out at the end of the process.

In conclusion, it shall be stressed that—depending on drying conditions—capillary forces evolve in different ways. In the following, the question is addressed whether these capillary interactions may promote mechanical effects and whether these depend on drying conditions.

Evolution of contact force distribution

In this part, we describe the impact of local capillary force evolution during drying on the global bond network. This is demonstrated by a network of contact forces and cracks. Figure 9 represents interparticle contact forces in a small $5 \times 5 \times 10$ particle network with 625 bonds (with material parameters as in Table 1). The resultant contact forces are computed by applying the capillary forces from the previous section (for the high viscosity limit) in Eqs. 4–8. If capillary forces are comparable with bond strength, microcracks may occur. Figure 9a illustrates the situation in the early stage of drying (saturation 0.6), where 4% of the network bonds have broken. We can see that the contact forces are less pronounced in the dried network region because bond failures allow the particles to reorganize and thus relieve the tensile forces in the contact points. As drying progresses to network saturation 0.3, cracks (8% of bonds) propagate downwards resulting in a network that is practically free of tensile forces. These simulation results are in qualitative accord with numerical[4,18] and experimental[37] observations.

To provide a detailed insight into how a microcrack initiates, we have analyzed a normal contact force evolution while applying the capillary forces in two different drying conditions. In fact, we assume in our model that the history of the contact force is not involved in crack formation. Despite the crack being only a result of the current state of the contact force, this force is a result of the emptying order of pores; therefore the drying conditions are crucial. Simulations start with a fully saturated network where the capillary forces are pronounced; and the particles are in mechanical equilibrium state. Figure 10 shows an example of normal contact force evolutions in one specific (vertical) bond near the center of the network for the two limiting drying conditions (see Table 1 for material parameters). Initially, capillary forces cause compression of the particles (positive values of contact force). When the drying front passes the bond, the action changes into tension (negative value of contact force), which may eventually result in the breakage of the bond if the current force reaches bond strength (in the given example, -10.8×10^{-10} N). In the highly viscous limit, the capillary force field in the wet part is rather uniform in lateral directions with a sharp change near the drying front (see Figure 8). In this case, the gas invasion takes time to reach the bond and the bond experiences strong local compression for longer. In the nonviscous case, pores are invaded throughout the network leading to a disordered capillary force field, and a weakening of normal compressive contact force in the partially saturated region (at saturation 0.88). A preliminary analysis of these two different behaviors at the sample scale is done in the next section.

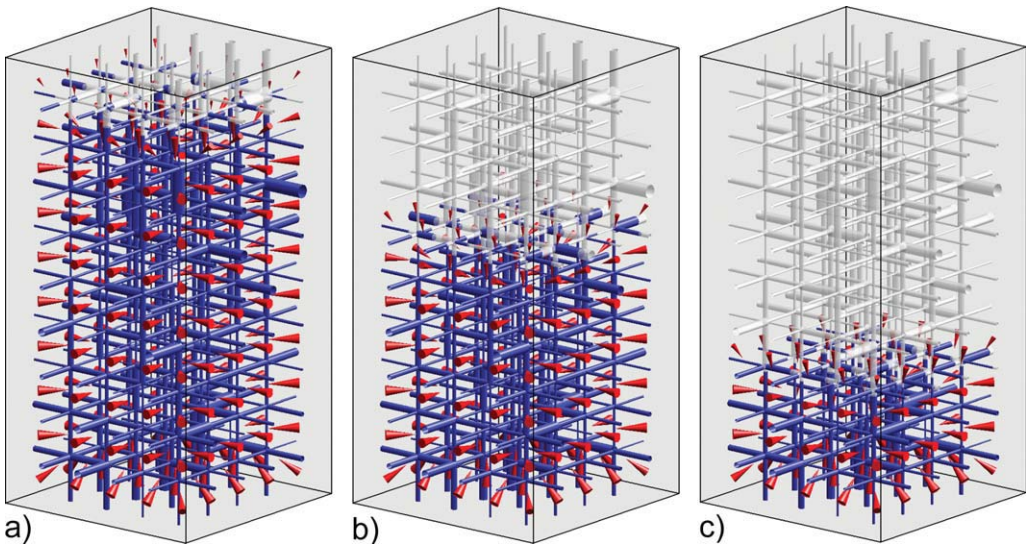

Figure 8. Evolution of capillary forces for immobile water at network saturations (a) 0.9, (b) 0.6, and (c) 0.3; gray cylinders represent empty pores, and dark blue is for liquid; capillary forces are presented by red cones, and cone size scales with force magnitude.

The network is subjected to evaporation at the top. (For better visualization of differences in pore radii, they are scaled exponentially). [Color figure can be viewed in the online issue, which is available at wileyonlinelibrary.com.]

Simulation of Cracks and Shrinkage During Drying

In practice, damage by cracks is rather observed during drying of stiff materials (with high elastic modulus), whereas shrinkage is the main effect when soft materials (with low elastic modulus) are dried. In the DEM approach, the terms "stiff" and "soft" are translated into the behavior of primary particle contacts, for example, soft particles can have significant virtual overlap. (We restrict our analysis to elastic behavior, which is no general constraint to the method.) In this section, we present numerical results for different drying conditions as well as for both types of materials to show these phenomena. Such simulations shall in future help to find criteria for material properties and drying conditions to preserve the solid structure. At first, we use a relatively small network for qualitative discussion of phenomena; later on, larger networks aim at more representative results.

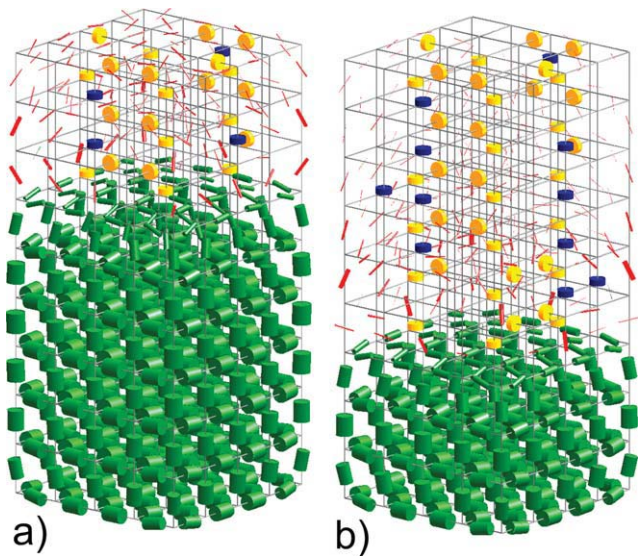

Figure 9. Contact force distributions and crack developments at network saturations (a) 0.6 and (b) 0.3. Compressive and tensile contact forces are represented by green and red cylinders, respectively (radius indicating force magnitude, orientation accounting for normal and shear components).

Normal and shear cracks are visualized by dark blue and yellow discs, respectively. [Color figure can be viewed in the online issue, which is available at wileyonlinelibrary.com.]

Influence of drying conditions

We show how the dynamics of crack formation in stiff particle aggregates is influenced by drying conditions. To this purpose, we have chosen microparameters for a rather dense porous agglomerate, namely activated alumina γ-Al_2O_3 (as used in[23]); as particle radii are about two orders of magnitude smaller in our work, we have scaled parallel bond stiffness accordingly (to get similar values in units N/m). For simplicity, a uniform bond radius has been used,

Table 1. Microparameters of Stiff Particle Networks

Characteristic	Value
Particle radius (m)	250×10^{-9}
Particle density (kg/m^3)	3230
Friction coefficient between particles	0.5
Damping ratio	0.7
Normal/shear stiffness of particles (N/m)	3×10^4
Normal/shear stiffness of parallel bonds (N/m^3)	8×10^{14}
Normal/shear strength of parallel bonds (N/m^2)	1.6×10^4
Bond radius (fraction of particle radius)	0.5858

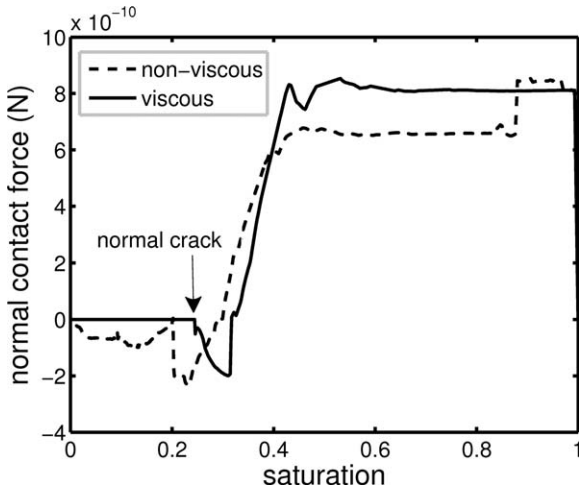

Figure 10. Evolution of normal contact forces at one specific contact in nonviscous and highly viscous limit.

which is computed from interparticle distances and mean pore radius as explained above.

First, we analyze the case of negligible liquid viscosity: capillary flow and resulting liquid phase distributions have been discussed in context with Figure 7. In a second simulation step, the capillary forces corresponding to these phase distributions have been applied to the stiff particle aggregate; the resulting normal and shear cracks of bonds are shown in Figure 11.

At high network saturations, when the network as a whole loses liquid but stays partially saturated to the surface (first drying period), it remains under compression by capillary forces. During this initial period, only shear cracks are observed, their number rising with drying time. At later stages of drying, the drying front recedes and a completely dry region develops (second drying period). This dry region is no longer under compression because of the absence of capillary forces. Therefore, also normal cracks may occur. In this second period, normal cracks gradually appear as the dry region moves into the network; and also more shear cracks occur in the vicinity of the drying front. At the end of drying, 66 shear cracks and 15 normal cracks are counted, that is, 81 out of 625 bonds have broken. These cracks are not uniformly distributed in space: the decrease of cracks from top to bottom of the sample is attributed to the nonsymmetric force load on the different regions.

If liquid is immobile, all surface pores dry out immediately and a sharp drying front recedes into the pore network as shown in Figure 8. The mechanical response of the solid network is presented in Figure 12. At the beginning, the bottom of the network stays completely saturated, and therefore, experiences no changes in capillary forces, no cracks are observed in that region. Only in the vicinity of the receding phase front, cracks occur. As argued for the nonviscous case, normal cracks may only occur in the dry region where the network is no longer under compression. In this way, together with the propagating drying front, a crack front moves towards the bottom of the network, resulting in a total of 42 shear cracks and 12 normal cracks. This means that 54 out of 625 bonds have failed during the drying process. These final numbers are very similar to those of the nonviscous case. The main difference seems to be in the time-dependence of crack appearance, because cracks only occur in the neighborhood of local changes in liquid saturation.

Influence of bond strength

To show the future potential of this modeling approach, bond strength has been systematically varied to determine its effect on crack formation and distribution. To this purpose, a nonviscous drying simulation has been used with the same pore and particle network parameters as before (see Table 1). As shown in Figure 13 and Table 2, by increasing bond strength, the total number of cracks can be reduced. This is

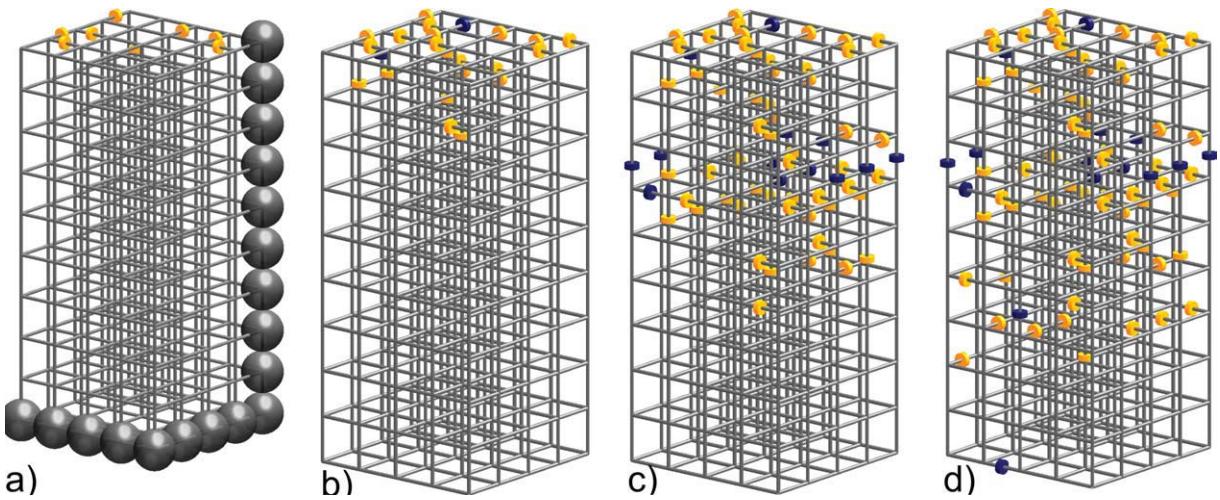

Figure 11. Distribution of microcracks for negligible liquid viscosity at network saturations (a) 0.9, (b) 0.6, and (c) 0.3 as well as (d) for the completely dry aggregate.

Dark blue and yellow cylinders stand for normal and shear cracks, respectively. (For better readability, only the bond network is shown.). [Color figure can be viewed in the online issue, which is available at wileyonlinelibrary.com.]

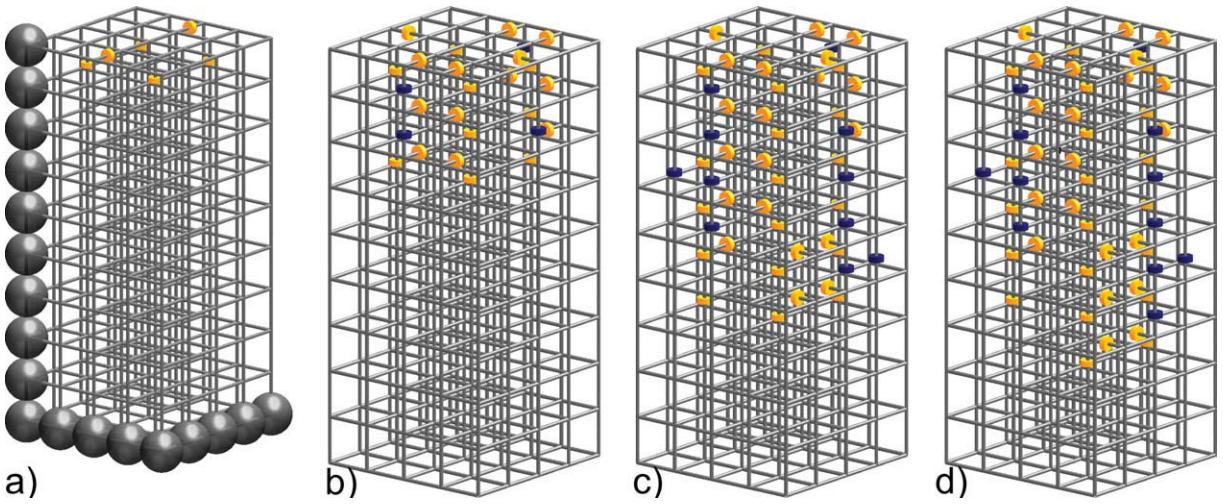

Figure 12. Distribution of microcracks for immobile liquid at network saturations (a) 0.9,(b) 0.6, (c) 0.3, and (d) for the completely dry aggregate.

Dark blue and yellow cylinders stand for normal and shear cracks, respectively. [Color figure can be viewed in the online issue, which is available at wileyonlinelibrary.com.]

clear as the bonds can better withstand the capillary forces occurring during drying. As a second effect, the type of cracks is changed: for higher bond strength, shear cracks are dominating, whereas the numbers of normal and shear cracks are comparable for weak bonds. Moreover, the time-dependency of the process can be observed, and influence of the bond strength on the number of cracks seems to be stronger in the second drying period than in the first. In the first drying period, when liquid is removed from the whole network, mainly shear cracks may occur. In the second period, when the drying front recedes (here at network saturation <0.75), still intact bonds may be broken by additional shear cracks and also normal cracks. This means that cracks occur to a great extend in the second drying period.

Monte-Carlo simulations

In the previous parts, only one realization of the network structure in each drying condition was considered; simulation results showed slightly more cracks for the nonviscous limit of drying. To push the analysis further and being aware of the fact that randomness of network generation may lead to quite different network saturation distributions and accordingly varied mechanical responses, Monte-Carlo simulations on larger networks have to be run. Present computational cost and memory limitations impose a relatively small particle network size ($10 \times 10 \times 20$, corresponding to 5500 interparticle bonds) and a limited number (10) of MC simulations per drying condition. Simulations are carried out with the same pore and particle parameters as above (see Table 1).

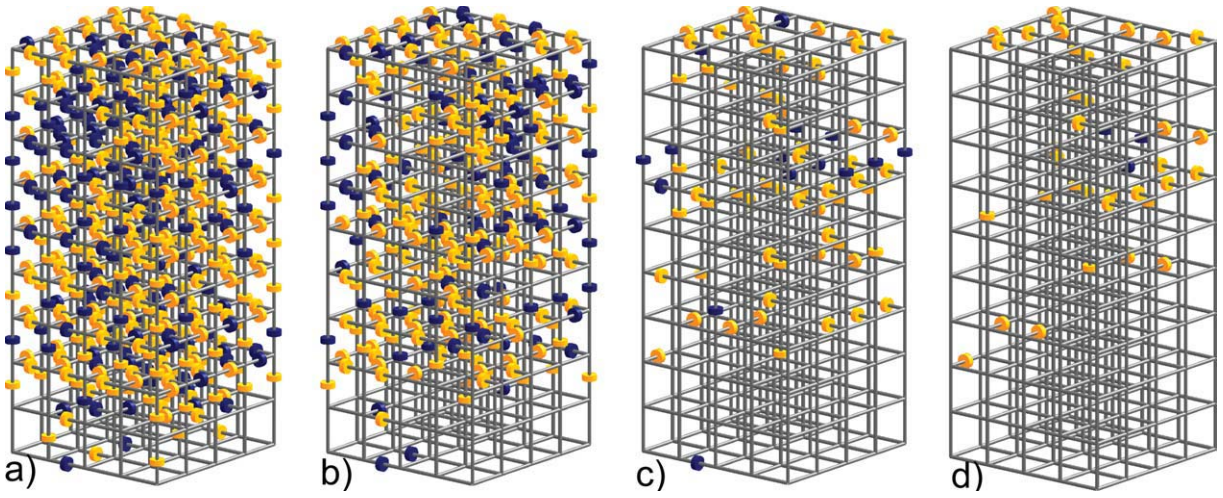

Figure 13. Cracks at the end of drying of brittle aggregates for different bond strengths when liquid viscosity is neglected (see Table 2 for numbers).

[Color figure can be viewed in the online issue, which is available at wileyonlinelibrary.com.]

Table 2. Stiff Aggregate Behavior for Varying Bond Strength

	a	b	c	d
Normal and shear bond strength (10^4 N/m^2)	0.4	0.8	1.6	2
Number of cracks during first drying period				
Shear	52	23	13	10
Normal	13	14	2	0
Total	65	37	15	10
Number of cracks during second drying period				
Shear	290	197	53	26
Normal	162	90	13	3
Total	452	287	66	29
Total number of cracks	517	324	81	39

Simulations results are summarized in Table 3 as average numbers of cracks with respective statistical standard deviations. First, one can notice a size effect: for the same micromechanical parameters as above, the fraction of broken bonds is considerably larger for this larger network. Second, the results indicate that more normal cracks, but less shear cracks have occurred in the viscous limit than in the nonviscous. These two opposing effects compensate each other and the discrepancy in total number of cracks is not significant. In other words, in both cases, the order of emptying the pores is different, but a representative bond experiences—sooner or later in the drying process—similar local tensions, which mainly occur when its direct-neighbor pores are emptied. Regarding the spatial distributions of cracks, very regular crack patterns are obtained for the viscous limit, whereas the nonviscous limit produces correlated, but irregular crack patterns (not shown).

In reality, the liquid pressure in the pores has a gradient that depends on drying rate; this gradient is expected to be negligible in the nonviscous limit and to be pronounced for the viscous limit. As discussed in literature,[18] this pressure gradient leads to tensile forces near the evaporating surface and the combination of macroscopic tension and local ''switching off'' of capillary forces is expected to result in macroscopic cracks. Such differences in liquid pressures are not yet included in the modeling of forces, so that cracks are only described on a ''local'' basis.

Shrinkage for soft materials

At last, an application of the new method to soft materials is outlined. One prominent example is highly porous gels that show considerable—and sometimes reversible—shrinkage during drying. To our knowledge, no DEM simulation of such materials has yet been performed, so that in the lack of literature parameters, we use the simple linear contact bond model with parameters (see Table 4) that correspond to typical macroscopic moduli. It is not evident that the mechanisms during elastic compaction of a gel matrix, that is, the reversible folding of solid filaments, can be approximated by overlapping of soft discrete particles. Indeed, the particles in DEM simulation now rather represent small portions of solid material than real primary particles, and the liquid distribution in the pore network is an averaged one. Nevertheless, we will see that qualitative effects can be correctly reproduced by the chosen DEM approach. Contact force distribution during shrinkage is shown in Figure 14 for a $10 \times 5 \times 5$ network. Initially, the aggregate is in mechanical equilibrium and capillary forces are not yet loaded (Figure 14a). Then, in one step, the full capillary forces are applied to the aggregate leading to a new equilibrium between attractive capillary and repulsive contact forces with considerable shrinkage (Figure 14b). In fact, this single step corresponds to a complete first drying period during which liquid removal is compensated by ideal shrinkage, that is, all pores remain fully saturated but reduce their size. The kinetics of this period are not yet modeled; specifically, volume change of pores is not accounted for and viscous effects leading to nonuniform shrinkage (or even a ''premature'' end of the first drying period by emptying of pores) are not yet addressed. Therefore, we restrict ourselves to the nonviscous limit, where uniform shrinkage can be assumed.

As evaporation continues in the second drying period, capillary forces gradually disappear from the top and repulsive contact forces bring the particles back to their initial positions (see Figure 14c). Such a spring-back phenomenon is known to occur for certain gels.[38,39] Eventually, mechanical equilibrium for the dried aggregate will be reached, without cracks having occurred. A near equilibrium state is shown in Figure 14d. In the second period, the results are meaningful even if volume change is neglected, because it concerns the gas pores, which play a minor role in transport phenomena.

Table 3. Number Distributions of Cracks for 10 MC Runs of Nonviscous and Viscous Drying

	Nonviscous	Viscous
Normal cracks	1245 ± 57	1490 ± 20
Shear cracks	1660 ± 50	1350 ± 29
Total cracks	2900 ± 36	2850 ± 39

Conclusions

A discrete approach has been presented to model mechanical effects during isothermal drying of porous materials. The solid phase is represented by a particle network, the void space by a complementary pore network. Local capillary forces are computed from pore saturations as obtained from

Table 4. Microparameters of Soft Particle Networks

Characteristic	Value
Particle radius (m)	250×10^{-9}
Particle density (kg/m^3)	2000
Friction coefficient between particles	0.5
Normal/shear stiffness of particles (N/m)	10
Normal/shear contact bond strength/capillary force	2

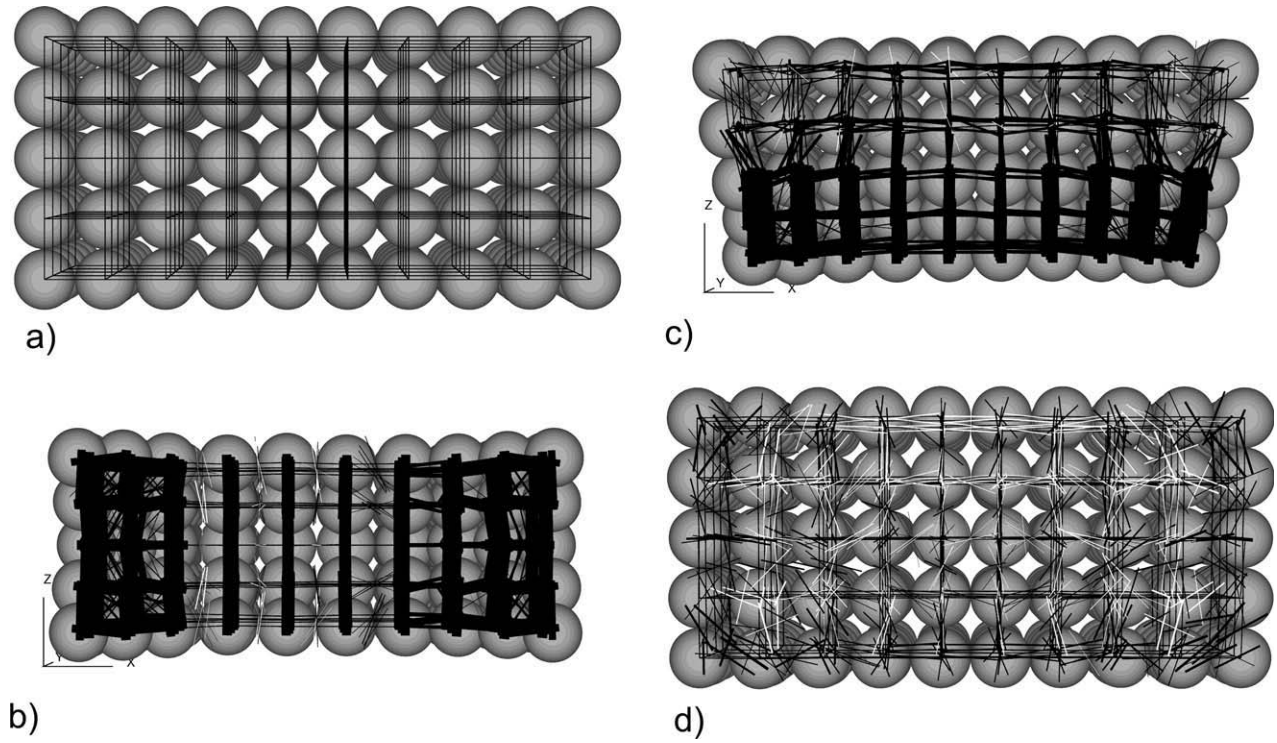

Figure 14. Volumetric shrinkage and contact force distribution of a soft aggregate at four different times during drying: (line thickness indicates relative force; black color means compression and white tension).

a pore network drying algorithm and then applied to the particle network by use of DEM.

For soft materials, such as gels, spring-back of the material, which has shrunken during the first drying period, has been described. For stiff materials, influence of liquid phase distributions during drying and material properties on material response (i.e., the occurrence of cracks) has been investigated. Our results suggest that different spatial distributions of liquid and resulting capillary forces during drying cannot explain the fact that faster drying leads to greater material damage. Instead, our simulations seem to confirm the hypothesis that only the combination of local forces and macroscopic stress leads to this damage.[18]

Although the current model version is still limited, the presented results correctly describe material behavior at a qualitative level. By this, the aptitude of the discrete approach to describe drying phenomena has been demonstrated; and appropriate model extensions are believed to make the model predictive. For example, two-way coupling shall be introduced by accounting for shrinkage in the pore network. Another major effect is the pressure gradient[18] in the liquid, which causes differential stress and nonuniform shrinkage of the solid. A model extension accounting for exact liquid pressures is expected to allow the simulation of differential stress in the solid and of (propagating) macrocracks. Further, the approach may be extended to nonisothermal effects, which are already included in PNMs. Ongoing research work extends the presented model to irregular particle aggregates and their complementary pore networks. Additionally, DEM offers the possibility to use more complex contact and particle properties. Advanced microscale experiments will allow parameterization of the DEM model, and analysis of damaged dry material will help assess simulation results for cracks in a more rigorous way.

In conclusion, the presented technique is seen as a new powerful tool to analyze interactions between fluid and solid phases during drying at the pore level. In this approach, as microscopic behavior can be directly investigated, truly local information is available from simulations (as opposed to continuous models). Indeed, such modeling efforts are undertaken in the belief that discrete approaches to classical problems can help for a fundamental understanding and that more refined model versions will allow studying mechanical effects for a wide range of materials and drying conditions.

Acknowledgments

This work was financed by the German Research Foundation (DFG) in the frame of Graduate School 828 "Micro-Macro-Interactions in Structured Media and Particulate Systems".

Literature Cited

1. Lewis RW, Strada M, Comini G. Drying-induced stresses in porous bodies. *Int J Numer Methods Eng*. 1977;11:1175–1184.
2. Kowalski SJ. *Thermomechanics of Drying Processes*. Berlin: Springer, 2003.
3. Job N, Sabatier F, Pirard JP, Crine M, Léonard A. Towards the production of carbon xerogel monoliths by optimizing convective drying conditions. *Carbon*. 2006;44:2534–2542.
4. Pourcel F, Jomaa W, Puiggali JR, Rouleau L. Criterion for crack initiation during drying: alumina porous ceramic strength improvement. *Powder Technol*. 2007;172:120–127.
5. Katekawa ME, Silva MA. A review of drying models including shrinkage effects. *Drying Technol*. 2006;24:5–20.

6. Prat M. Percolation model of drying under isothermal conditions. *Int J Multiphase Flow*. 1993;46:691–704.
7. Nowicki SC, Davis HT, Scriven LE. Microscopic determination of transport parameters in drying porous media. *Drying Technol*. 1992;10:925–946.
8. Yiotis AG, Stubos AK, Boudouvis AG, Yortsos YC. A 2-D pore network model of the drying of single-component liquids in porous media. *Adv Water Resour*. 2001;24:439–460.
9. Laurindo JB, Prat M. Modeling of drying in capillary-porous media: a discrete approach. *Drying Technol*. 1998;16:1769–1787.
10. Metzger T, Irawan A, Tsotsas E. Isothermal drying of pore networks: influence of friction for different pore structures. *Drying Technol*. 2007;25:49–57.
11. Yiotis AG, Boudouvis AG, Stubos AK, Tsimpanogiannis IN, Yortsos YC. The effect of liquid films on the drying of porous media. *AIChE J*. 2004;50:2721–2737.
12. Prat M. On the influence of pore shape, contact angle and film flows on drying of capillary porous media. *Int J Heat Mass Transfer*. 2007;50:1455–1468.
13. Huinink HP, Pel L, Michels MAJ, Prat M. Drying processes in the presence of temperature gradients, pores scale modeling. *Eur Phys JE*. 2002;9:487–498.
14. Plourde F, Prat M. Pore network simulations of drying of capillary media. Influence of thermal gradients. *Int J Heat Mass Transfer*. 2003;46:1293–1307.
15. Surasani VK, Metzger T, Tsotsas E. Consideration of heat transfer in pore network modeling of convective drying. *Int J Heat Mass Transfer*. 2008;51:2506–2518.
16. Segura LA, Toledo PG. Pore-level modeling of isothermal drying of pore networks. Effects of gravity and pore shape and size distributions. *Chem Eng J*. 2005;111:237–252.
17. Metzger T, Irawan A, Tsotsas E. Influence of pore structure on drying kinetics: a pore network study. *AIChE J*. 2007;53:3029–3041.
18. Brinker CJ, Scherer GW. *Sol-Gel Science*. New York: Academic Press, 1990.
19. Amaral M. Deformation of solid surface due to capillary forces. *J Colloid Interface Sci*. 1984;100:17–26.
20. Segura L, Toledo PG. Pore-level modeling of isothermal drying of pore networks accounting for evaporation, viscous flow, and shrinking. *Drying Technol*. 2005;23:2007–2019.
21. Cundall PA, Strack ODL. A discrete numerical model for granular assemblies. *Geotechnique*. 1979;29:47–65.
22. Moreno-Atanasio R, Ghadiri M. Mechanistic analysis and computer simulation of impact breakage of agglomerates: effect of surface energy. *Chem Eng Sci*. 2006;61:2476–2481.
23. Antonyuk S. *Deformations- und Bruchverhalten von kugelförmigen Granulaten bei Druck- und Stoßbeanspruchung*, PhD thesis. Otto-von-Guericke-Universität, Magdeburg; 2006.
24. Richefeu V, Youssoufi MSEI, Radjaï F. Shear strength properties of wet granular materials. *Phys Rev E*. 2006;73:051304–11.
25. Scholtès L, Chareyre B, Nicot F, Darve F. Micromechanics of granular materials with capillary effects. *Int J Eng Sci*. 2009;47:64–75.
26. Jintang L, David JM. Application of the discrete element modeling in air drying of particulate solids. *Drying Technol*. 2002;20:255–282.
27. Kharaghani A. *Irregular Pore Networks and Mechanical Effects During Drying of Porous Media*, PhD thesis. Otto-von-Guericke-Universität, Magdeburg; 2010.
28. Irawan A. *Isothermal Drying of Pore networks: Influence of Pore Structure on Drying Kinetics*, PhD thesis. Otto-von-Guericke-Universität, Magdeburg; 2006.
29. Cundall PA. A computer model for simulating progressive, large scale movements in blocky rock systems. *Proc Symp Int Soc Rock Mech. Nancy*. 1971;1:129–136.
30. Itasca Consulting Group Inc. Particle Flow Code in Three-Dimension Manual, Version 3.10 (2005), Itasca Consulting Group Inc., Minneapolis, Mn, USA.
31. Tykhoniuk R, Tomas J, Luding S, Kappl M, Heim L, Butt HJ. Ultrafine cohesive powders: from interparticle contacts to continuum behavior. *Chem Eng Sci*. 2007;62:2843–2864.
32. Dutta AK, Penumadu D. Hardness and modulus of individual sand particles using nanoindentation. *Geotech Special Publication*. 2007;173:34–43.
33. Young T. An essay on the cohesion of fluids. *Phil Trans R Soc Lond*. 1805;95:65–87.
34. Rabinovich YI, Esayanur MS, Moudgil BM. Capillary forces between two spheres with a fixed volume liquid bridge: theory and experiment. *Langmuir*. 2005;21:10992–10997.
35. Grof Z, Lawrence J, František S. Computer simulation of evolving capillary bridges in granular media. *Granular Matter*. 2008;10:93–103.
36. Metzger T, Tsotsas E. Viscous stabilization of drying front: three-dimensional pore network simulations. *Chem Eng Res Des*. 2008;86:739–744.
37. Bisschop J, van Mier GM. Effects of aggregates on drying shrinkage micro-cracking in cement-based composites. *Mater Struct*. 2002;35:453–461.
38. Dong H, Reidy RF, Brennan JD. Shrinkage and springback behavior of Methylsilsesquioxanes prepared by an acid/base two-step processing procedure. *Chem Mater*. 2005;17:6012–6017.
39. Hwang SW, Jung HH, Hyun SH, Ahn YS. Effective preparation of crack-free silica aerogels via ambient drying. *J Sol-Gel Sci Tech*. 2007;41:139–146.

Manuscript received Aug. 17, 2009, and revision received May 15, 2010.